Syracuse University

SURFACE

May 2016

Elucidating the Electronic Origins of Intermolecular Forces in Crystalline Solids

Michael Thomas Ruggiero
Syracuse University

Follow this and additional works at: https://surface.syr.edu/etd

Part of the Physical Sciences and Mathematics Commons

Recommended Citation

Abstract

It is not possible to study almost any physical system without considering intermolecular forces (IMFs), no matter how insignificant they may appear relative to other energetic factors. Countless studies have shown that IMFs are responsible for governing a wide variety of physical properties, but often the atomic-origins of such interactions elude experimental detection. A considerable amount of work throughout the course of this research was therefore placed on using quantum mechanical simulations, specifically density functional theory (DFT), to calculate the electronic properties of solid-materials. The goal of these calculations was a better understanding of the precise origins of interatomic energies, down to the single-electron level. Furthermore, experimental X-ray diffraction and terahertz spectroscopy were both utilized because they are able to broadly probe the potential energy surfaces of molecular crystals, enhancing the theoretical data. Combining DFT calculations with experimental measurements enabled in-depth studies into the nature of specific non-covalent interactions, with results that were often unexpected based on conventional descriptions of IMFs. Overall, this work represents a significant advancement in understanding how subtle changes in characteristics like orbital occupation or electron density can have profound effects on bulk properties, highlighting the fragile relationship that exists between the numerous energetic parameters occurring within condensed phase systems.

ELUCIDATING THE ELECTRONIC ORIGINS OF INTERMOLECULAR FORCES IN
CRYSTALLINE SOLIDS

by

Michael T. Ruggiero

B.S. The State University of New York – College at Geneseo, 2012
M.Phil. Syracuse University, 2014

Dissertation

Submitted in partial fulfillment of the requirements for the degree of

Doctor of Philosophy in Chemistry

Syracuse University

May 2016

ACKNOWLEDGEMENTS

Table of Contents

List of Illustrative Materials

CHAPTER 1: Introduction

1.1 Motivation

Intermolecular forces (IMFs) dictate many physical properties of materials, ranging from melting points to elasticities. There are various sources of IMFs, but their roots can all be traced to simple electrostatic interactions. In small systems consisting of only a few atoms the source of interatomic energies can be easily defined and explained. But in more complex materials, like transition metal complexes or large molecular crystals, accurately describing the origins of IMF-dependent observables becomes much more complicated due to the wide variety of possible contributing factors. This work uses a combination of density functional theory calculations and experimental measurements to directly probe the features that govern IMF generation in solids. These tools, when combined, enable a complete description of IMF and their dependent effects to be obtained, and in doing so subtleties that may have been traditionally overlooked are found to actually be of great importance. Furthermore, the development of new methods for deconstructing the obtained energetic results into individual components was prioritized, generating new techniques for interpreting and analyzing the data that have enabled more detailed descriptions of IMFs in crystalline solids.

The research is broadly grouped into the study of inorganic and organic molecular crystals. Inorganic solids provide an opportunity to study the non-covalent interactions between metal cations and ligands, and can be used to determine such things as the role of individual d-electrons on IMF characteristics (**Chapter 7**). On the other hand, the molecules in organic crystals are typically bound by London dispersion interactions, a minor source of interaction

energy but one that can be deeply impactful, for example in determining the stability of

crystalline polymorphs (**Chapter 15**).

1.2 Background and Theory

The atomic-level features of any material are governed by a complex set of factors, including atomic composition and charges, molecular structure, and electronic arrangement.[1-3] In the case of molecules, covalent bond characteristics are primarily responsible for dictating bulk properties.[4-6] But while a covalent bond can be easily described energetically using bond potential diagrams (**Figure 1-1**), it is possible to obtain greater detail by partitioning the plot into attractive and repulsive components.[7-8] The decomposition of data is the foundation for much of the work undertaken here, as even regularly utilized information is able to be deconvolved to yield a more fundamental description regarding the forces present in molecular crystals.

Non-covalent intermolecular forces (IMFs), while normally representing a small fraction of energy with respect to covalent bonds (~15 kJ/mol for a hydrogen bond compared to ~366 kJ/mol for an O-H covalent bond), are responsible for many observables including melting and boiling points, surface tension, and viscosity.[9-10] These interactions can be broadly grouped into four categories, namely ion, dipole, hydrogen bond, and London dispersion forces.[11-12] Solid materials are stabilized to a large degree by IMFs, and are often the driving force behind crystallization (**Figure 1-2**).[13-15]
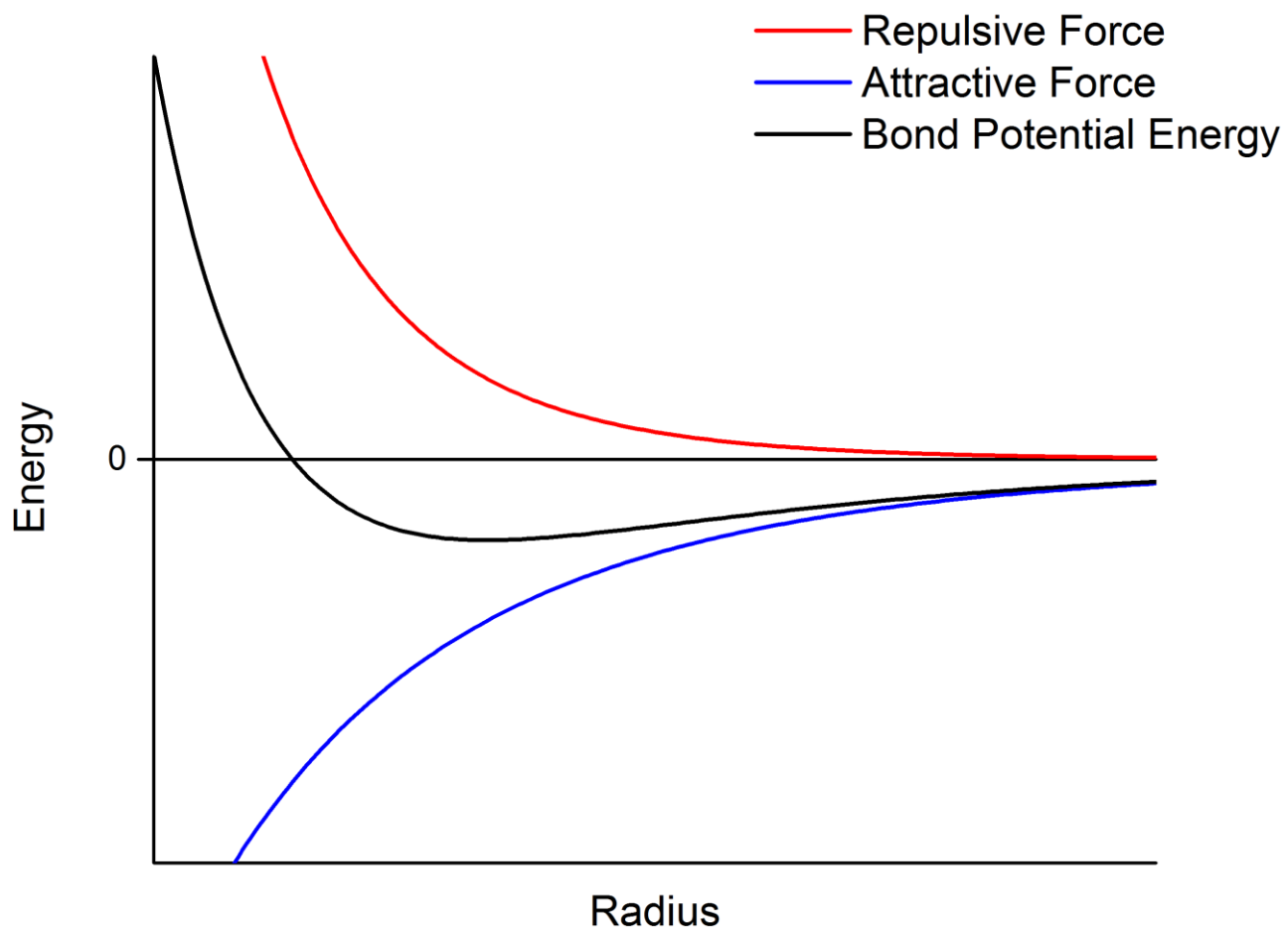
Figure 1-1. Typical covalent bond potential energy diagram (black), with the corresponding attractive (blue) and repulsive (red) components shown.
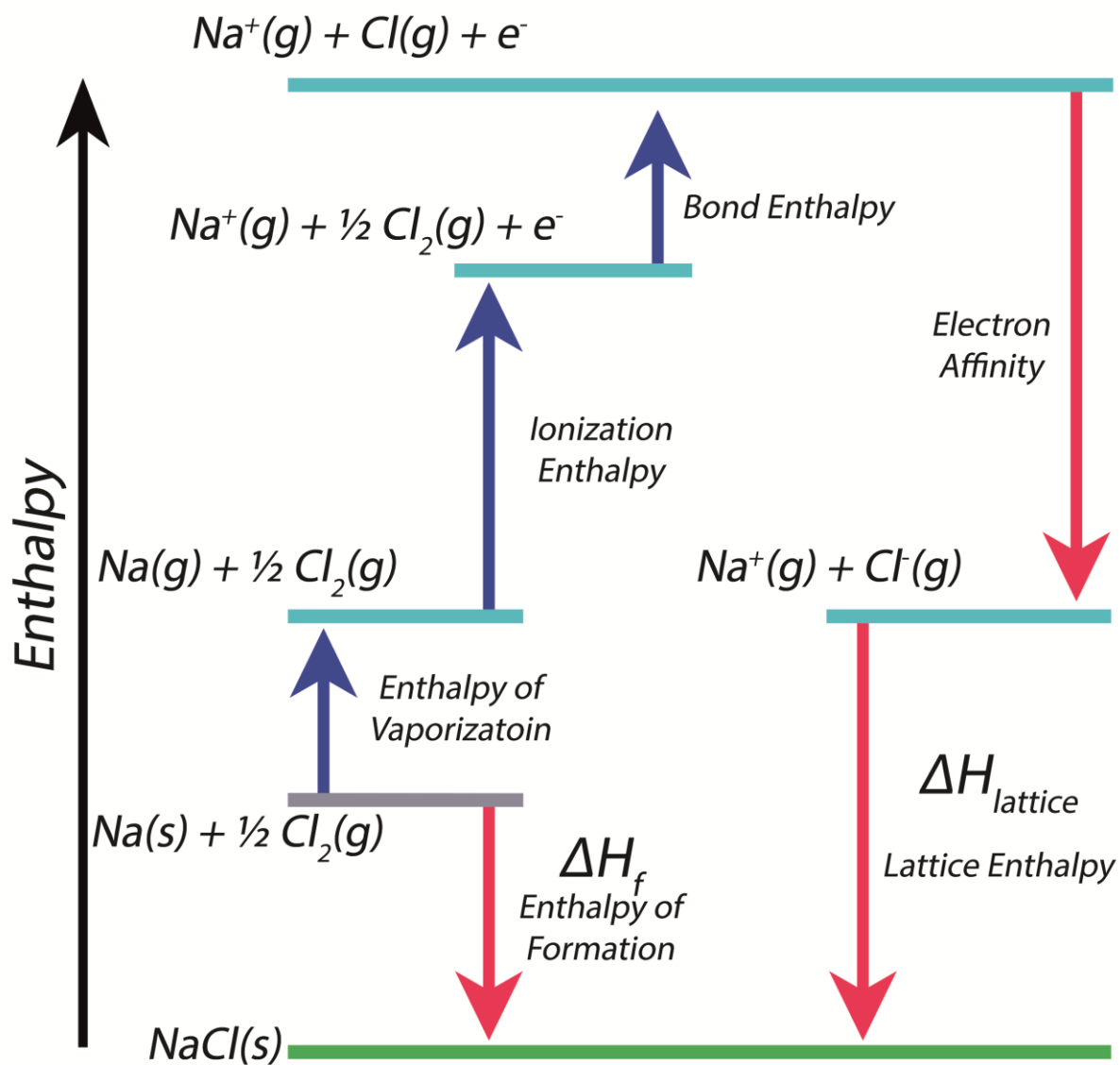
Figure 1-2. The Born-Haber cycle for an ionic crystal.

Intermolecular interactions all have the same dependence on the electron distribution of the individual atoms and molecules, only differing in the way in which the charges interact between species.[16-18] On the one hand, ionic bonding (typically the strongest IMF) can often be described simply by representing the atoms as point charges of charge q, with potential energies dictated by Coulomb's law,[19-20]

$$V_{ionic}(r) = \frac{q_1 q_2}{4\pi\varepsilon_0 R} \tag{1.1}$$

where ε_0 is the vacuum permittivity and R is the interatomic distance. On the other hand, the energy of London dispersion forces[21-23] (typically the weakest IMF) is approximated by,

$$V_{London}(r) \approx -\frac{3}{2}\frac{I_1 I_2}{I_1 + I_2}\frac{\alpha_1 \alpha_2}{R^6} \tag{1.2}$$

where I and α are the atomic ionization potential and polarizabilities, respectively. But while the two energy equations at first appear to be fundamentally different, they are actually quite similar as closer inspection reveals that q, I, and α are all dependent on the electronic distribution.[24-27] This dependence means that through an accurate knowledge of electronic structure a complete description of the IMFs can be obtained.

Electronic structure calculations, at their core, determine the energies of the molecular wavefunctions.[28-34] In many *ab initio* methods, the wavefunctions are first built from a linear combination of atomic orbitals, and therefore the atomic contribution to each molecular orbital is also determined.[35-38] These two pieces of information, while seemingly minor, are actually all that is needed in order to determine a wide range of properties such as the dipole and multipole

moments,[39-41] bond types and orders,[42-46] and X-ray structure factors.[47-49] It quickly becomes apparent that more details related to IMFs can be directly determined from a single calculation, for instance the ionic and dipolar contributions to the total IMF. Moreover, unlike many experimental methods, theoretical techniques give absolute values for the calculated quantities to many places of precision, enabling the partitioning of bulk IMFs into any number of factors.[50-51] This represents a powerful tool for investigating the roles of electronic effects on the formation and strengths of IMFs, and forms the basis for the research presented in this work.

There do exist experimental methods for probing the electronic structure and charge density, for instance ultra violet-visible (UV-vis) spectroscopy yields information about the electronic states[52-53] and X-ray diffraction can generate charge density maps based on the diffraction of X-rays by electrons.[49, 54] However directly measuring the strength and origins of intermolecular forces often proves difficult.[55] This is especially challenging when complex systems containing a variety of forces are considered, because it is not trivial to assign the origins of IMF-dependent properties to a specific interaction alone. For example, in crystals of organic molecular salts where all four types of IMF are entangled, such as pyridinium hydrochloride[56] (**Figure 1-3**), it would be difficult to experimentally define the melting point as being primarily dependent on any one value. Furthermore, the existence of certain varieties of IMFs is still under debate in the literature, even for commonly accepted interaction-types like π-stacking.[57-58] In this regard, *ab initio* simulations can provide exact quantum mechanical parameters surrounding the electronic structure, enabling the role of each individual electron to be considered in terms of its various energy contributions.
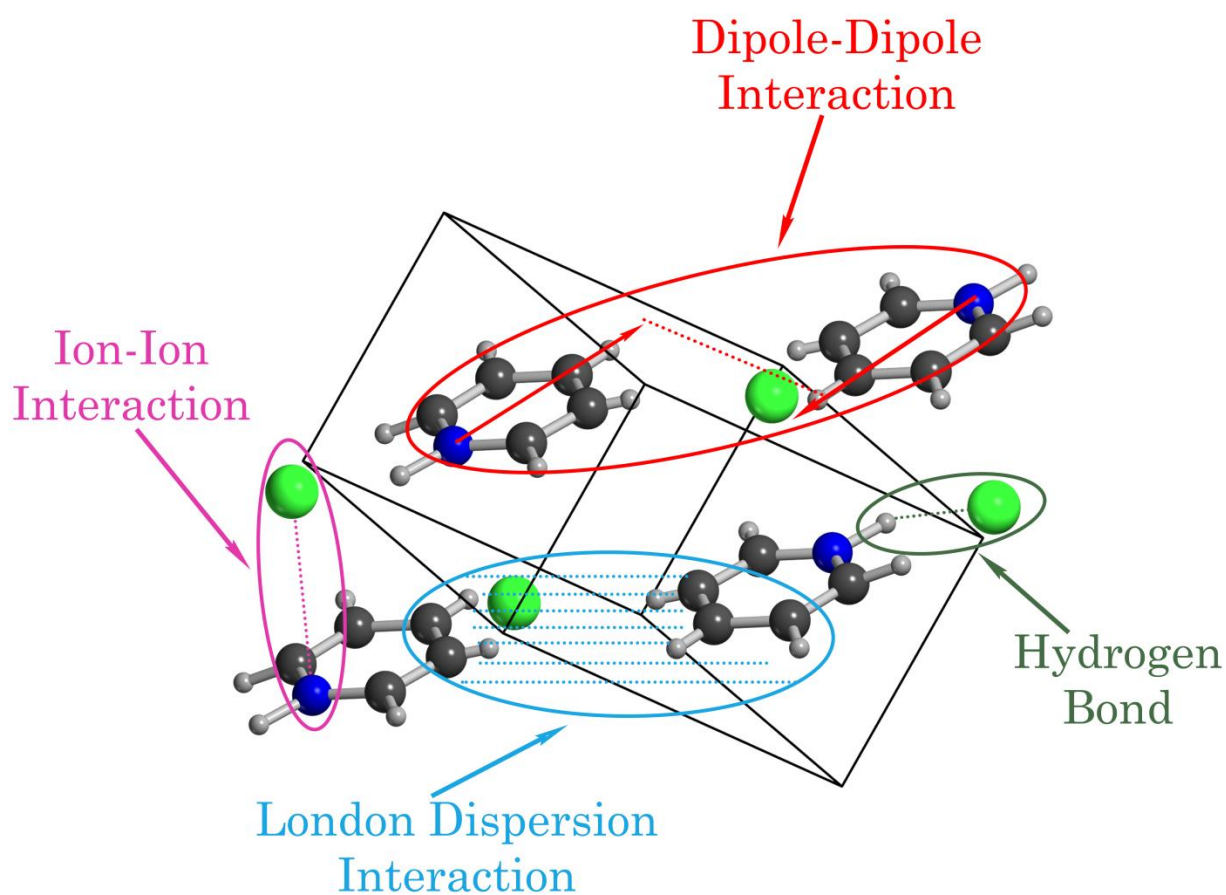
Figure 1-3. Experimental crystal structure of pyridinium hydrochloride, with the various IMFs pointed out. For the sake of comparison the atoms are described using their formal charges, with the chloride and nitrogen having a single negative and positive charge, respectively.

Yet, any simulation requires validation by experimental measurements to provide confidence in the obtained quantities.[59-61] While it may not be possible to directly measure some of the values from *ab initio* calculations, by carefully choosing experimental techniques that measure related parameters an indication of the overall quality of the simulation can be achieved. A good example of this concept is in the determination of the elastic properties of membrane lipid bilayers.[62-64] The flexibility of cell membranes is a critical aspect to proper cell function, but also in the design of new drug delivery devices that utilize lipid vesicles.[65-66] These properties are extremely difficult to measure experimentally because traditional methods are not capable of probing such delicate materials.[63-64, 67] However, studies using non-traditional combinations of experimental techniques, such as measuring the refractive index of vesicles as they experience various degrees of osmotic pressure, have produced values for the compressibility, bending, and tension moduli.[64, 68-70] By performing *ab initio* simulations and comparing the simulated values to those of experiments, additional elastic parameters (*i.e.* bulk, shear, and Young's moduli) can be generated and trusted.[67, 71-72]

For the analysis of intermolecular forces in solid materials a number of techniques are appropriate for validating the simulated results. Specifically two methods are used in this work, X-ray diffraction and terahertz spectroscopy, because they provide information regarding the charge distributions and potential energy surface minima and curvatures.[54, 73-78] In order to effectively investigate IMFs computationally, the structure must first be optimized so that the forces acting on all of the atoms are zero. This equilibrium structure, corresponding to each atomic nucleus resting in a potential energy minimum, can then be compared to the experimental single-crystal X-ray diffraction structure to determine the quality of the simulation. Values such as bond length, angles, dihedral angles, and lattice parameters can all be used to confirm the

quality of the theoretical model.[79-82] And while it might be tempting to believe that locating the correct potential energy minimum be enough, the lack of any data regarding the curvature of the potential means that no information pertaining to the inter-nuclear potential is obtained. This is illustrated in **Figure 1-4**, which shows two bond potential energy diagrams with identical equilibrium bond distances but two very different potential well depths. The variation between the inter-nuclear potentials would lead to large deviations between the interaction energies that would not be captured by a structural analysis alone.
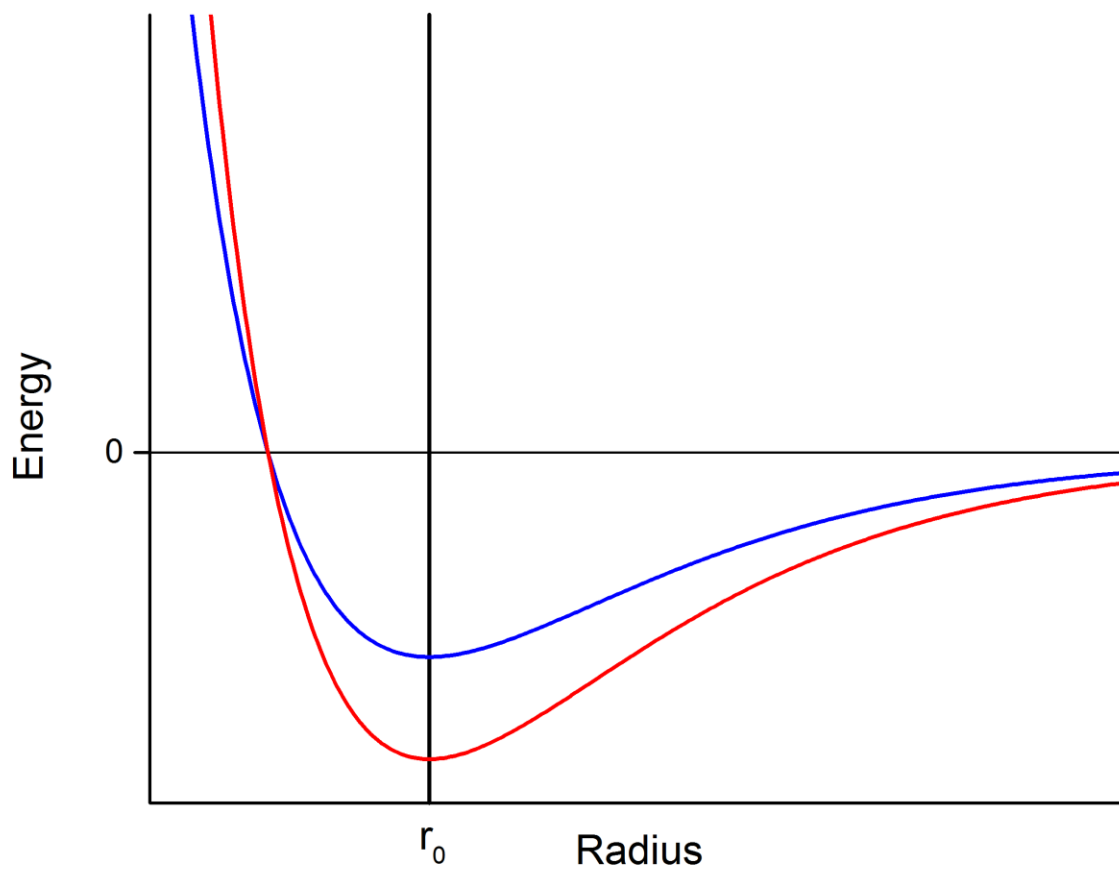
Figure 1-4. Two bond potential energy diagrams with different curvatures but identical minima at r_0. Structural determination only provides information about r_0.

Terahertz vibrational spectroscopy is a powerful technique for evaluating the potential energy surfaces in solid materials. Unlike mid-infrared spectroscopy, which typically excites vibrations of single bonds, terahertz modes involve large-amplitude motions of both the atoms and molecules in a system.[76, 78, 83-84] Low-frequency vibrations can involve external translations and librations, as well as internal molecular torsions. The complexity of the low-frequency vibrational eigenvectors means that the entire potential energy surface can be sampled using a small number of features. In turn, the accurate simulation of the terahertz vibrational spectrum of a crystal implies that, in addition to the correct minima and curvature, the electronic structure is also well determined and calculated values such as thermodynamic parameters and electronic properties can be trusted.[80, 85-87] Moreover, the accurate simulation of infrared intensities, dependent on the atomic charges and change in transient dipole moment, implies that the charge distribution and dipole moments are also well modeled.[24, 26] Therefore the confirmation of theoretical results by the combination of X-ray diffraction and terahertz spectroscopic measurements provides a great deal of confidence in the applied theory, and as such more advanced usage of the data (*e.g.* in construction of the density of states) is possible.

Terahertz spectroscopy is also valuable as an analytical method. Because the low-frequency vibrations are dependent on the global potential energy, identical molecules that form different crystal structures (polymorphs) will have a unique spectral fingerprint. This makes terahertz spectroscopy a highly utilized tool in the pharmaceutical industry, where identification of different polymorphic forms is critical for quality control.[81, 88-92]

In addition to the pharmaceutical industry, the art preservation field is beginning to realize the benefits of terahertz spectroscopy. Unlike harsh X-rays, terahertz radiation is non-ionizing and non-invasive, making it an attractive replacement for the characterization of fragile

historical artworks and documents.[79, 93-95] Many of these works used mineral-based inks and pigments where the molecular composition and hydration levels could have drastic consequences, not only for the visual appearance but also for the long term health of the document.[96-99] However, traditional spectroscopic techniques are unable to differentiate between materials made up of the same molecules, with the only way of detecting differences (*e.g.* water content) relying on subtle changes in absorption band intensities.[100-101] But in solids, different hydration levels typically cause a change in crystal structure, meaning that terahertz spectroscopy can differentiate between hydrated species with relative ease.[79, 93, 102-104]

1.3 Summary of the Chapters

      In **Chapters 2-3** the foundations for quantum theory, electronic structure methods, and density functional theory (DFT) are introduced and the relative concepts explained. **Chapter 4** specifically discusses solid-state DFT (ss-DFT), and goes into detail about how the periodicity of crystals is modelled theoretically using the CRYSTAL software package. Also, the five most utilized calculation-types for this work are reviewed, including the determination of a systems energy, equilibrium, vibrational, one-electron, and elastic properties. A shift from theoretical to experimental is made in **Chapter 5**, where the important optic and laser configuration concepts necessary to perform terahertz spectroscopic measurements are discussed. Experimental methods are presented in **Chapter 6**, specifically regarding terahertz spectroscopy as well as introducing the theory and techniques for structural determination using X-ray diffraction (XRD).

      Combining ss-DFT, terahertz spectroscopy, and XRD is a common theme throughout the work presented in this thesis. A good example of the utility of this coupled approach is the study of $3d$ transition metal-maleate tetrahydrates (MMT, M=Mn, Fe, Co, Ni, Zn) as discussed in **Chapter 7**. These crystals are unique because the maleate ligand contains a low-barrier hydrogen bond (LBHB) when packed into the solid-state, and the coordination of the ligand is similar to the geometry of many enzymatic active sites that involve proton transfer reactions, such as carbonic anhydrase.[105-113] There have been many recent studies that suggest LBHBs are the key to many catalytic processes, although there still exists debate about their formation and properties.[114-120] At least in the case of metalloenzymes, it is generally accepted that the metal cation is the protagonist for much of the chemistry that occurs, including the formation of LBHBs.[121-122] The MMT solids provide a rare opportunity to study the effects that metal cations,

specifically related to *d*-orbital occupation, have on the properties of materials. This is because they crystallize in the same space group and are generally isomorphic, although the orientation of a pair of symmetry related water molecules and the position of the proton in the LBHB deviate across the series. Through a combined experimental and theoretical study the results revealed that the metal cation actually had little direct effect on the LBHB, but rather the occupations of the 3*d*-orbitals governed the tilt angle of the coordinated water molecules, which in turn ultimately dictated the LBHB properties.

The study of the MMT crystals was made possible by deconstructing the interaction between the metal cation and the coordinated water molecules into contributions from each individual *d*-orbital. This was possible using the crystal orbital overlap population (COOP) analysis first introduced by Hoffman and Hughbanks.[45] The COOP method is similar to the density of states, but in this case only the orbitals between two selected sets (*e.g.* between two molecular fragments) are used for analysis. The data obtained from a COOP calculation yields specific information about the effective bond order, as it partitions the orbitals into bonding and antibonding regions, weighted by the overlap matrix elements for the particular interaction. Using the COOP data it was shown that specific *d*-orbitals were more prone to antibonding interactions then others, and upon population of these orbitals the coordinated water molecules were required to tilt in order to minimize their interaction and avoid harsh energetic penalties.

In **Chapter 8**, the COOP method was again used for the study of crystalline monosodium glutamate monohydrate (MSG) and monopotassium glutamate monohydrate (MPG). Unlike the MMT crystals, the two glutamate salts have slightly different crystalline packing arrangements, differing by only one space group number. These crystals afford the opportunity to explore the relationship between cation charge and their interaction with adjacent molecular anions. Here,

the two glutamic acid salts were fully characterized by low-temperature single crystal XRD and

terahertz spectroscopy, and the spectra were assigned using ss-DFT. As with the MMT solids,

the COOP method was used to describe the interaction between the metal cation with

surrounding glutamate ions, and additionally a second orbital analysis was performed, known as

the crystal orbital Hamiltonian population (COHP) analysis.[43-44, 46, 50] The COHP technique is

similar to that of COOP, but instead of weighting the DOS with the overlap matrix the

Hamiltonian matrix elements are used instead, partitioning the orbitals based on their energetic

contributions. This again provides information about the bonding and antibonding regions, but

instead of bond order it yields a measure of the bond strength.

While experimental techniques are limited to the availability of samples for testing,

theoretical methods are not held to the same constraint. This concept enabled the theoretical

study of glutamate salts that had their metal cations switched, substituting potassium cations for

sodium cations (as well as the inverse). These structures were optimized to their equilibrium

geometry and studied using both the COOP and COHP analyses. The results from this study help

to highlight the delicate balance that is struck between energetic forces in solid materials, and

how slight changes in atomic radius or charge can have profound effects on bulk properties.

The combined works of **Chapters 9-12** investigate metal sulfate hydrates, specifically

copper sulfate ($CuSO_4$) and iron sulfate ($FeSO_4$). The motivation for these studies arose from the

use of metal sulfates in many historic inks and pigments that, over time, could degrade and

damage the base (*i.e.* parchment) on which they were applied.[94, 96, 98-99, 123] This degradation

could be monitored using the hydration content of the pigments, with changes indicating more

(or less) damage potential. Although there exist numerous methods for quantitatively

determining water content using destructive techniques such as thermalgravimetric analysis,[124-]

[125] the value and delicate nature of the samples of interest (paintings, manuscripts) necessitate the use of non-destructive techniques. Terahertz spectroscopy was utilized because the only difference between the various metal sulfate hydrates was the number of co-crystallized water molecules, a property that can be easily addressed due to the different packing arrangement that results as a condition of hydration level.

In **Chapter 9**, an in-depth study of the computational methods required to accurately simulate copper sulfate compounds was performed and the role of basis set size and functional choice were studied in detail. The results revealed a strong correlation between the number of polarization functions on the oxygen and sulfur atoms and the calculated geometries, with larger polarization sets yielding a more accurate structure. Following this, the terahertz spectrum of anhydrous copper sulfate ($CuSO_4$) was fully assigned using ss-DFT simulations. However the results of the vibrational analysis showed that as-received samples of 'pure' $CuSO_4$ actually contained a nontrivial amount of contamination from hydrate species, specifically the monohydrate ($CuSO_4 \cdot H_2O$) and the trihydrate ($CuSO_4 \cdot 3H_2O$) forms. Using a combination of powder X-ray diffraction (PXRD) and ss-DFT, the terahertz spectrum of the mixed sample was fully assigned and quantitative values for the hydrate populations were extracted.

Following this, **Chapter 10** explores the most common copper sulfate hydrate, the pentahydrate form ($CuSO_4 \cdot 5H_2O$). The terahertz spectrum of $CuSO_4 \cdot 5H_2O$ had already been reported, but it was believed that those samples had been contaminated unknowingly by other hydrate forms, leading to inaccurate results.[126] Furthermore, the terahertz spectrum of $CuSO_4 \cdot 5H_2O$ contains a broad and increasing absorption that makes locating and assigning features difficult. Through the use of controlled drying, coupled with simultaneous PXRD and terahertz measurements, the true low-frequency vibrational spectrum of $CuSO_4 \cdot 5H_2O$ was

uncovered, agreeing with the simulated data from ss-DFT. Moreover, the observed broad absorption was determined to be caused by unincorporated water molecules that collect on the surface of the crystallites, highlighting the sensitivity of terahertz spectroscopy to unordered water.

The structure of $CuSO_4 \cdot 5H_2O$ was also of interest, because the crystallographic unit cell contains two unique copper coordination environments,[127-128] a rather uncommon occurrence. In **Chapter 11** the electronic origins for the differing structures were explored using the COOP and COHP methods described in **Chapters 7** and **8**. The orbital analysis proved that the two variations in geometries represented the balance that must be struck between various forces within crystalline solids, with the formation of intermolecular hydrogen bonds challenging the conformational energy of the copper-water coordination geometries.

Concluding the study of metal-sulfates, **Chapter 12** details the investigation of iron sulfate heptahydrate and tetrahydrate, $FeSO_4 \cdot 7H_2O$ and $FeSO_4 \cdot 4H_2O$, respectively. The ss-DFT vibrational analysis of $FeSO_4 \cdot 4H_2O$ proved to be in excellent agreement with the experimental observations. However in $FeSO_4 \cdot 7H_2O$, while a majority of the spectrum was well-reproduced, there existed a single anomalous feature that could not be described by the theoretical model. This notably broad feature occurred at very low frequencies well below the first predicted vibrational mode, and exhibited an uncharacteristic shift to lower energies upon cooling. This absorption was ultimately determined to be due to a phonon polariton, a quasiparticle that results from coupling of infrared photon with optical phonons.[129-133] While this feature could not be modeled theoretically, it proved to be a valuable component of the $FeSO_4 \cdot 7H_2O$ terahertz spectrum because it enabled the quantitative determination of relative hydrate concentrations from binary mixtures of $FeSO_4 \cdot 4H_2O$ and $FeSO_4 \cdot 7H_2O$ to be obtained.

The interest in accurately simulating the various components that determine the strength of IMFs led to the study of pyridinium containing crystals (**Chapter 13**). In these systems a wide range of intermolecular interactions are present, including ionic, dipolar, quadrupolar, hydrogen bonding, and London dispersion forces. Such a complex set of energetic factors makes their simultaneous simulation difficult, and the results are often highly dependent on the chosen density functional.[134-140] Recent advances in density functional development have produced range-corrected hybrid functionals, approximations that incorporate a variable amount of exact Hartree-Fock exchange in certain regions to account for non-local effects.[141-146] The consequences of including range-corrections on the simulation of the three-pyridinium containing crystals were evaluated by studying the optimized equilibrium geometries, and it was shown that the inclusion of exact exchange in both the short and long-range limits resulted in an accurate portrayal of the experimental geometry across all three solids.

The roles of internal and external forces in crystals of poly-L-proline were examined within the context of terahertz spectroscopy and elasticity in **Chapter 14**. Polyproline is unique amongst the amino acids in that it can form both *cis* and *trans*-peptide bonds, resulting in two helical forms (PP-I and PP-II, respectively). The two polyproline helices were synthesized and their structures were determined using a combination of PXRD and ss-DFT, leading to the first full structural solution of the PP-I helix. The ss-DFT vibrational simulation indicated that motions accessible by terahertz spectroscopy exhibited a spring-type character, and were therefore selected to determine Young's modulus using a relationship to Hooke's law. The results were compared to those calculated strictly from first-principles and were found to agree, marking the first time terahertz spectroscopy was used for determining the elasticity of a large biopolymer.

In **Chapter 15**, the balance between molecular conformational energy and intermolecular forces were explored within the context of the α-β-glutamic acid polymorphic phase transition. The details surrounding the transition have proven elusive, with a solvent-meditated process being the generally accepted theory.[147-151] The two glutamic acid polymorphs were synthesized, recrystallized, and the low-temperature single-crystal XRD structures determined. A full experimental and theoretical vibrational analysis was performed and the resulting thermodynamic data used to construct Gibbs free energy curves. The Gibbs curves indicate that while α-GLU is stable a low temperatures β-GLU is favored at room temperature. It was shown that α-GLU is the more stable of the two polymorphs; however β-GLU experiences a larger degree of external stabilization primarily from more favorable London dispersion forces. The study of the two glutamic acid polymorphs highlights the competition between internal conformational and external intermolecular energies.

The work presented in the following chapters, while broad, in united by the common theme of how IMF affect the simulations and properties of crystalline solids. Particular attention has been paid to the development of theoretical methodologies that can provide a more detailed theoretical description for such forces. The ultimate goal of elucidating the electronic origins of many of these effects was achieved through the use of COOP and COHP analyses, which were implemented into the CRYSTAL code specifically for this work. The research performed here has furthered the knowledge surrounding IMF generation, and will lead to a more sophisticated approach to material design, ultimately producing more advanced technologies and fueling new innovations.

1.4 References

1. Alkorta, I.; Rozas, I.; Elguero, J., Bond Length–Electron Density Relationships: From Covalent Bonds to Hydrogen Bond Interactions. *Struct. Chem.* **1998**, *9*, 243-247.

2. Grandbois, M.; Beyer, M.; Rief, M.; Clausen-Schaumann, H.; Gaub, H. E., How Strong Is a Covalent Bond? *Science* **1999**, *283*, 1727-1730.

3. Leman, G.; Friedel, J., On the Description of Covalent Bonds in Diamond Lattice Structures by a Simplified Tight-Binding Approximation. *J. Appl. Phys.* **1962**, *33*, 281-285.

4. Harrison, W. A., *Electronic Structure and the Properties of Solids: The Physics of the Chemical Bond*; Courier Corporation, 2012.

5. Cremer, D.; Kraka, E., A Description of the Chemical Bond in Terms of Local Properties of Electron Density and Energy. *Croat. Chem. Acta* **1984**, *57*, 1259-1281.

6. Salvetat, J.-P.; Bonard, J.-M.; Thomson, N.; Kulik, A.; Forro, L.; Benoit, W.; Zuppiroli, L., Mechanical Properties of Carbon Nanotubes. *Appl. Phys. A* **1999**, *69*, 255-260.

7. Su, P.; Li, H., Energy Decomposition Analysis of Covalent Bonds and Intermolecular Interactions. *J. Chem. Phys.* **2009**, *131*, 014102.

8. Bazant, M. Z.; Kaxiras, E., Modeling of Covalent Bonding in Solids by Inversion of Cohesive Energy Curves. *Phys. Rev. Lett.* **1996**, *77*, 4370.

9. Stone, A., *The Theory of Intermolecular Forces*; Oxford University Press, 2013.

10. Reed, A. E.; Curtiss, L. A.; Weinhold, F., Intermolecular Interactions from a Natural Bond Orbital, Donor-Acceptor Viewpoint. *Chem. Rev.* **1988**, *88*, 899-926.

11. Kollman, P., A General Analysis of Noncovalent Intermolecular Interactions. *J. Am. Chem. Soc.* **1977**, *99*, 4875-4894.

12. Kollman, P. A., Noncovalent Interactions. *Acc. Chem. Res.* **1977**, *10*, 365-371.

13. Glasser, L.; von Szentpály, L., Born-Haber-Fajans Cycle Generalized: Linear Energy Relation between Molecules, Crystals, and Metals. *J. Am. Chem. Soc.* **2006**, *128*, 12314-12321.

14. Braga, D.; Grepioni, F., *Crystal Engineering: From Molecules and Crystals to Materials*; Springer, 1999.

15. Aakeröy, C. B., Crystal Engineering: Strategies and Architectures. *Acta Crystallogr. Sect. B: Struct. Sci.* **1997**, *53*, 569-586.

16. Israelachvili, J. N., *Intermolecular and Surface Forces: Revised Third Edition*; Academic press, 2011.

17. Schneider, H. J.; Schiestel, T.; Zimmermann, P., Host-Guest Supramolecular Chemistry. 34. The Incremental Approach to Noncovalent Interactions: Coulomb and Van Der Waals Effects in Organic Ion Pairs. *J. Am. Chem. Soc.* **1992**, *114*, 7698-7703.

18. Gavezzotti, A., Efficient Computer Modeling of Organic Materials. The Atom–Atom, Coulomb–London–Pauli (AA-CLP) Model for Intermolecular Electrostatic-Polarization, Dispersion and Repulsion Energies. *New J. Chem.* **2011**, *35*, 1360-1368.

19. Tokura, Y., Comop Today. *Physics Today* **2003**, 50-55.

20. Stokes, R. J.; Evans, D. F., *Fundamentals of Interfacial Engineering*; John Wiley & Sons, 1997.

21. Grimme, S., Density Functional Theory with London Dispersion Corrections. *Wiley Interdiscip. Comput. Mol. Sci.* **2011**, *1*, 211-228.

22. Grimme, S., Semiempirical GGA-Type Density Functional Constructed with a Long-Range Dispersion Correction. *J. Comput. Chem.* **2006**, *27*, 1787-99.

23.   Grimme, S., Accurate Description of Van Der Waals Complexes by Density Functional Theory Including Empirical Corrections. *J. Comput. Chem.* **2004**, *25*, 1463-1473.

24.   Noel, Y.; Zicovich-Wilson, C. M.; Civalleri, B.; D'Arco, P.; Dovesi, R., Polarization Properties of Zno and Beo: An *ab initio* Study through the Berry Phase and Wannier Functions Approaches. *Phys. Rev. B.* **2001**, *65*, 014111.

25.   Burns, L. A.; Mayagoitia, Á. V.-.; Sumpter, B. G.; Sherrill, C. D., Density-Functional Approaches to Noncovalent Interactions: A Comparison of Dispersion Corrections (DFT-D), Exchange-Hole Dipole Moment (XDM) Theory, and Specialized Functionals. *J. Chem. Phys.* **2011**, *134*, 084107.

26.   Maschio, L.; Kirtman, B.; Rérat, M.; Orlando, R.; Dovesi, R., Ab Initio Analytical Raman Intensities for Periodic Systems through a Coupled Perturbed Hartree-Fock/Kohn-Sham Method in an Atomic Orbital Basis. I. Theory. *J. Chem. Phys.* **2013**, *139*, 164101.

27.   Lacivita, V.; Rèrat, M.; Orlando, R.; Ferrero, M.; Dovesi, R., Calculation of Longitudinal Polarizability and Second Hyperpolarizability of Polyacetylene with the Coupled Perturbed Hartree-Fock/Kohn-Sham Scheme: Where It Is Shown How Finite Oligomer Chains Tend to the Infinite Periodic Polymer. *J. Chem. Phys.* **2012**, *136*, 114101.

28.   Dovesi, R.; Orlando, R.; Roetti, C.; Pisani, C.; Saunders, V., The Periodic Hartree-Fock Method and Its Implementation in the Crystal Code. *Phys. Status Solidi B* **2000**, *217*, 63-88.

29.   Pisani, C., *Quantum-Mechanical Ab-Initio Calculation of the Properties of Crystalline Materials*; Springer Berlin Heidelberg, 1996.

30. Pisani, C.; Dovesi, R.; Roetti, C., *Different Approaches to the Study of the Electronic Properties of Periodic Systems*; Springer, 1988.

31. Sholl, D.; Steckel, J. A., *Density Functional Theory: A Practical Introduction*; John Wiley & Sons, 2011.

32. Dovesi, R.; Orlando, R.; Erba, A.; Zicovich-Wilson, C. M.; Civalleri, B.; Casassa, S.; Maschio, L.; Ferrabone, M.; De La Pierre, M.; D'Arco, P.*, et al.*, CRYSTAL14: A Program for the *ab initio* Investigation of Crystalline Solids. *Int. J. Quantum Chem* **2014**, *114*, 1287-1317.

33. Delley, B., From Molecules to Solids with the Dmol3 Approach. *J. Chem. Phys.* **2000**, *113*, 7756-7764.

34. Segall, M. D.; Philip, J. D. L.; Probert, M. J.; Pickard, C. J.; Hasnip, P. J.; Clark, S. J.; Payne, M. C., First-Principles Simulation: Ideas, Illustrations and the CASTEP Code. *J. Phys.: Condens. Matter* **2002**, *14*, 2717.

35. Evarestov, R. A., Quantum Chemistry of Solids. **2012**.

36. Krishnan, R.; Binkley, J. S.; Seeger, R.; Pople, J. A., Self-Consistent Molecular Orbital Methods. XX. A Basis Set for Correlated Wave Functions. *J. Chem. Phys.* **1980**, *72*, 650-654.

37. Hariharan, P. C.; Pople, J. A., The Influence of Polarization Functions on Molecular Orbital Hydrogenation Energies. *Theoret. Chim. Acta* **1973**, *28*, 213-222.

38. Hehre, W. J.; Pople, J. A., Molecular Orbital Theory of the Electronic Structure of Organic Compounds. III. Ab Initio Studies of Charge Distribution Using a Minimal Slater-Type Basis. *J. Am. Chem. Soc.* **1970**, *92*, 2191-2197.

39.   Fantin, P.; Barbieri, P.; Neto, A. C.; Jorge, F., Augmented Gaussian Basis Sets of Triple and Quadruple Zeta Valence Quality for the Atoms H and from Li to Ar: Applications in HF, MP2, and DFT Calculations of Molecular Dipole Moment and Dipole (Hyper) Polarizability. *J. Mol. Struct.* **2007**, *810*, 103-111.

40.   Kjaergaard, H. G.; Bezar, K. J.; Brooking, K. A., Calculation of Dipole Moment Functions with Density Functional Theory: Application to Vibrational Band Intensities. *Mol. Phys.* **1999**, *96*, 1125-1138.

41.   Aguado, A.; Bernasconi, L.; Jahn, S.; Madden, P. A., Multipoles and Interaction Potentials in Ionic Materials from Planewave-DFT Calculations. *Faraday Discuss.* **2003**, *124*, 171-184.

42.   Mulliken, R. S., Electronic Population Analysis on LCAO–Mo Molecular Wave Functions. I. *J. Chem. Phys.* **1955**, *23*, 1833-1840.

43.   Deringer, V. L.; Tchougréeff, A. L.; Dronskowski, R., Crystal Orbital Hamilton Population (COHP) Analysis as Projected from Plane-Wave Basis Sets. *J. Phys. Chem. A* **2011**, *115*, 5461-5466.

44.   Dronskowski, R.; Bloechl, P. E., Crystal Orbital Hamilton Populations (COHP): Energy-Resolved Visualization of Chemical Bonding in Solids Based on Density-Functional Calculations. *J. Phys. Chem* **1993**, *97*, 8617-8624.

45.   Hughbanks, T.; Hoffmann, R., Chains of Trans-Edge-Sharing Molybdenum Octahedra: Metal-Metal Bonding in Extended Systems. *J. Am. Chem. Soc.* **1983**, *105*, 3528-3537.

46.   Ruggiero, M. T.; Erba, A.; Orlando, R.; Korter, T. M., Origins of Contrasting Copper Coordination Geometries in Crystalline Copper Sulfate Pentahydrate. *Phys. Chem. Chem. Phys.* **2015**, *17*, 31023-31029.

47.   Bunău, O.; Joly, Y., Self-Consistent Aspects of X-Ray Absorption Calculations. *J. Phys.: Condens. Matter* **2009**, *21*, 345501.

48.   Rosenauer, A.; Schowalter, M.; Glas, F.; Lamoen, D., First-Principles Calculations of 002 Structure Factors for Electron Scattering in Strained in X Ga 1− X As. *Phys. Rev. B.* **2005**, *72*, 085326.

49.   Koritsanszky, T. S.; Coppens, P., Chemical Applications of X-Ray Charge-Density Analysis. *Chem. Rev.* **2001**, *101*, 1583-1628.

50.   Alexei, G.; Rajeev, A.; Olle, E., Balanced Crystal Orbital Overlap Population—a Tool for Analysing Chemical Bonds in Solids. *J. Phys.: Condens. Matter* **2003**, *15*, 7751.

51.   Volkov, A.; Coppens, P., Calculation of Electrostatic Interaction Energies in Molecular Dimers from Atomic Multipole Moments Obtained by Different Methods of Electron Density Partitioning. *J. Comput. Chem.* **2004**, *25*, 921-934.

52.   Williams, D.; Fleming, I.; Pretsch, E., Spectroscopic Methods. *Organic Chemistry* **1989**.

53.   Perkampus, H.-H.; Grinter, H.-C.; Threlfall, T., *UV-Vis Spectroscopy and Its Applications*; Springer, 1992.

54.   Madsen, G. K. H.; Iversen, B. B.; Larsen, F. K.; Kapon, M.; Reisner, G. M.; Herbstein, F. H., Topological Analysis of the Charge Density in Short Intramolecular OH⊙⊙⊙ O Hydrogen Bonds. Very Low Temperature X-Ray and Neutron Diffraction Study of Benzoylacetone. *J. Am. Chem. Soc.* **1998**, *120*, 10040-10045.

55.   Müller-Dethlefs, K.; Hobza, P., Noncovalent Interactions: A Challenge for Experiment and Theory. *Chem. Rev.* **2000**, *100*, 143-168.

56. Hensen, K.; Pullmann, P.; Bats, J. W., Die Kristall- Und Molekülstrukturen Von Chlorotrispyridinium-Bis-(Tetrachloroaluminat(III)) Und Einer Weiteren Modifikation Von Pyridiniumchlorid. *Z. Anorg. Allg. Chem.* **1988**, *556*, 62-69.

57. Grimme, S., Do Special Noncovalent Π–Π Stacking Interactions Really Exist? *Angew. Chem. Int. Ed.* **2008**, *47*, 3430-3434.

58. Scheiner, S., A New Noncovalent Force: Comparison of P··· N Interaction with Hydrogen and Halogen Bonds. *J. Chem. Phys.* **2011**, *134*, 094315.

59. Pavone, M.; Rega, N.; Barone, V., Implementation and Validation of DFT-D for Molecular Vibrations and Dynamics: The Benzene Dimer as a Case Study. *Chem. Phys. Lett.* **2008**, *452*, 333-339.

60. Nazeeruddin, M. K.; De Angelis, F.; Fantacci, S.; Selloni, A.; Viscardi, G.; Liska, P.; Ito, S.; Takeru, B.; Grätzel, M., Combined Experimental and DFT-TDDFT Computational Study of Photoelectrochemical Cell Ruthenium Sensitizers. *J. Am. Chem. Soc.* **2005**, *127*, 16835-16847.

61. Minenkov, Y.; Singstad, Å.; Occhipinti, G.; Jensen, V. R., The Accuracy of DFT-Optimized Geometries of Functional Transition Metal Compounds: A Validation Study of Catalysts for Olefin Metathesis and Other Reactions in the Homogeneous Phase. *Dalton Trans.* **2012**, *41*, 5526-5541.

62. Rawicz, W.; Olbrich, K.; McIntosh, T.; Needham, D.; Evans, E., Effect of Chain Length and Unsaturation on Elasticity of Lipid Bilayers. *Biophys. J.* **2000**, *79*, 328-339.

63. Duwe, H. d.; Sackmann, E., Bending Elasticity and Thermal Excitations of Lipid Bilayer Vesicles: Modulation by Solutes. *Physcia A* **1990**, *163*, 410-428.

64. Bloom, M.; Evans, E.; Mouritsen, O. G., Physical Properties of the Fluid Lipid-Bilayer Component of Cell Membranes: A Perspective. *Quarterly reviews of biophysics* **1991**, *24*, 293-397.

65. Huang, H. W., Elasticity of Lipid Bilayer Interacting with Amphiphilic Helical Peptides. *J. Phys. II* **1995**, *5*, 1427-1431.

66. Helfrich, W., Lipid Bilayer Spheres: Deformation and Birefringence in Magnetic Fields. *Phys. Lett. A* **1973**, *43*, 409-410.

67. Feng, S.-s., Interpretation of Mechanochemical Properties of Lipid Bilayer Vesicles from the Equation of State or Pressure-Area Measurement of the Monolayer at the Air-Water or Oil-Water Interface. *Langmuir* **1999**, *15*, 998-1010.

68. Jadidi, T.; Seyyed-Allaei, H.; Tabar, M. R. R.; Mashaghi, A., Poisson's Ratio and Young's Modulus of Lipid Bilayers in Different Phases. *Front. Bioeng. Biotechnol.* **2014**, *2*, 8.

69. Popescu, G.; Ikeda, T.; Goda, K.; Best-Popescu, C. A.; Laposata, M.; Manley, S.; Dasari, R. R.; Badizadegan, K.; Feld, M. S., Optical Measurement of Cell Membrane Tension. *Phys. Rev. Lett.* **2006**, *97*, 218101.

70. Tierney, K. J.; Block, D. E.; Longo, M. L., Elasticity and Phase Behavior of Dppc Membrane Modulated by Cholesterol, Ergosterol, and Ethanol. *Biophys. J.* **2005**, *89*, 2481-2493.

71. Ayton, G.; Smondyrev, A. M.; Bardenhagen, S. G.; McMurtry, P.; Voth, G. A., Calculating the Bulk Modulus for a Lipid Bilayer with Nonequilibrium Molecular Dynamics Simulation. *Biophys. J.* **2002**, *82*, 1226-1238.

72.   Helfrich, W., Elastic Properties of Lipid Bilayers: Theory and Possible Experiments. *Zeitschrift für Naturforschung C* **1973**, *28*, 693-703.

73.   Young, R. A., *X-Ray Diffraction*; Engineering Experiment Station, Georgia Institute of Technology, 1961.

74.   Cullity, B. D.; Weymouth, J. W., Elements of X-Ray Diffraction. *Am. J. Phys.* **1957**, *25*, 394-395.

75.   Abrahams, S.; Collin, R.; Lipscomb, W.; Reed, T., Further Techniques in Single-Crystal X-Ray Diffraction Studies at Low Temperatures. *Rev. Sci. Instrum.* **1950**, *21*, 396-397.

76.   Schmuttenmaer, C. A., Exploring Dynamics in the Far-Infrared with Terahertz Spectroscopy. *Chem. Rev.* **2004**, *104*, 1759-1780.

77.   Beard, M. C.; Turner, G. M.; Schmuttenmaer, C. A., Terahertz Spectroscopy. *J. Phys. Chem. B* **2002**, *106*, 7146-7159.

78.   Zeitler, J. A.; Taday, P. F.; Newnham, D. A.; Pepper, M.; Gordon, K. C.; Rades, T., Terahertz Pulsed Spectroscopy and Imaging in the Pharmaceutical Setting - a Review. *J. Pharm. Pharmacol.* **2007**, *59*, 209-223.

79.   Ruggiero, M. T.; Bardon, T.; Strlič, M.; Taday, P. F.; Korter, T. M., Assignment of the Terahertz Spectra of Crystalline Copper Sulfate and Its Hydrates Via Solid-State Density Functional Theory. *J. Phys. Chem. A* **2014**, *118*, 10101-10108.

80.   Delaney, S. P.; Witko, E. M.; Smith, T. M.; Korter, T. M., Investigating Tautomeric Polymorphism in Crystalline Anthranilic Acid Using Terahertz Spectroscopy and Solid-State Density Functional Theory. *J. Phys. Chem. A* **2012**, *116*, 8051-8057.

81.   King, M. D.; Buchanan, W. D.; Korter, T. M., Identification and Quantification of Polymorphism in the Pharmaceutical Compound Diclofenac Acid by Terahertz

Spectroscopy and Solid-State Density Functional Theory. *Anal. Chem.* **2011**, *83*, 3786-3792.

82.   Hakey, P. M.; Allis, D. G.; Hudson, M. R.; Korter, T. M., Density Functional Dependence in the Theoretical Analysis of the Terahertz Spectrum of the Illicit Drug MDMA (Ecstasy). *Sensors Journal, IEEE* **2010**, *10*, 478-484.

83.   McIntosh, A. I.; Yang, B.; Goldup, S. M.; Watkinson, M.; Donnan, R. S., Terahertz Spectroscopy: A Powerful New Tool for the Chemical Sciences? *Chemical Society Reviews* **2012**, *41*, 2072-2082.

84.   Smith, R. M.; Arnold, M. A., Terahertz Time-Domain Spectroscopy of Solid Samples: Principles, Applications, and Challenges. *Appl. Spectrosc. Rev.* **2011**, *46*, 636-679.

85.   Strachan, C. J.; Taday, P. F.; Newnham, D. A.; Gordon, K. C.; Zeitler, J. A.; Pepper, M.; Rades, T., Using Terahertz Pulsed Spectroscopy to Quantify Pharmaceutical Polymorphism and Crystallinity. *J. Pharm. Sci.* **2005**, *94*, 837-846.

86.   Delaney, S. P.; Pan, D.; Yin, S. X.; Smith, T. M.; Korter, T. M., Evaluating the Roles of Conformational Strain and Cohesive Binding in Crystalline Polymorphs of Aripiprazole. *Cryst. Growth Des.* **2013**, *13*, 2943-2952.

87.   Delaney, S. P.; Pan, D.; Galella, M.; Yin, S. X.; Korter, T. M., Understanding the Origins of Conformational Disorder in the Crystalline Polymorphs of Irbesartan. *Cryst. Growth Des.* **2012**, *12*, 5017-5024.

88.   Shen, Y.-C., Terahertz Pulsed Spectroscopy and Imaging for Pharmaceutical Applications: A Review. *Int. J. Pharm.* **2011**, *417*, 48-60.

89.   Chakkittakandy, R.; Corver, J. A. W. M.; Planken, P. C. M., Terahertz Spectroscopy to Identify the Polymorphs in Freeze-Dried Mannitol. *J. Pharm. Sci.* **2010**, *99*, 932-940.

90.   Taday, P. F., Applications of Terahertz Spectroscopy to Pharmaceutical Sciences. *Phil. Trans. R. Soc. A* **2004**, *362*, 351-364.

91.   Strachan, C. J.; Rades, T.; Newnham, D. A.; Gordon, K. C.; Pepper, M.; Taday, P. F., Using Terahertz Pulsed Spectroscopy to Study Crystallinity of Pharmaceutical Materials. *Chem. Phys. Lett.* **2004**, *390*, 20-24.

92.   Taday, P. F.; Bradley, I. V.; Arnone, D. D.; Pepper, M., Using Terahertz Pulse Spectroscopy to Study the Crystalline Structure of a Drug: A Case Study of the Polymorphs of Ranitidine Hydrochloride. *J. Pharm. Sci.* **2003**, *92*, 831-838.

93.   Ruggiero, M. T.; Bardon, T.; Strlic, M.; Taday, P. F.; Korter, T. M., The Role of Terahertz Polariton Absorption in the Characterization of Crystalline Iron Sulfate Hydrates. *Phys. Chem. Chem. Phys.* **2015**, *17*, 9326-9334.

94.   Bardon, T.; May, R. K.; Taday, P. F.; Strlic, M., Systematic Study of Terahertz Time-Domain Spectra of Historically Informed Black Inks. *Analyst* **2013**, *138*, 4859-4869.

95.   Fischer, B.; Hoffmann, M.; Helm, H.; Modjesch, G.; Jepsen, P. U., Chemical Recognition in Terahertz Time-Domain Spectroscopy and Imaging. *Semicond. Sci. Technol.* **2005**, *20*, S246.

96.   Strlič, M.; Menart, E.; Cigić, I. K.; Kolar, J.; de Bruin, G.; Cassar, M., Emission of Reactive Oxygen Species During Degradation of Iron Gall Ink. *Polym. Degrad. Stab.* **2010**, *95*, 66-71.

97.   Kolar., J.; Strlič., M., *Iron Gall Inks: On Manufacture, Characterisation, Degradation and Stabilisation*; National and University Library: Ljubljana, Slovenia, 2006.

98.   Kolar, J.; Štolfa, A.; Strlič, M.; Pompe, M.; Pihlar, B.; Budnar, M.; Simčič, J.; Reissland, B., Historical Iron Gall Ink Containing Documents — Properties Affecting Their Condition. *Anal. Chim. Acta* **2006**, *555*, 167-174.

99.   Hahn, O.; Malzer, W.; Kanngiesser, B.; Beckhoff, B., Characterization of Iron-Gall Inks in Historical Manuscripts and Music Compositions Using X-Ray Fluorescence Spectrometry. *X-Ray Spectrom.* **2004**, *33*, 234-239.

100.   Bratos, S.; Pick, R., *Vibrational Spectroscopy of Molecular Liquids and Solids*; Springer Science & Business Media, 2012; Vol. 56.

101.   Sherwood, P. M. A., *Vibrational Spectroscopy of Solids*; CUP Archive, 1972.

102.   Baur, W.; Rolin, J., Salt Hydrates. Ix. The Comparison of the Crystal Structure of Magnesium Sulfate Pentahydrate with Copper Sulfate Pentahydrate and Magnesium Chromate Pentahydrate. *Acta Crystallogr. Sect. B: Struct. Sci.* **1972**, *28*, 1448-1455.

103.   Zahrobsky, R. F.; Baur, W. H., On the Crystal Chemistry of Salt Hydrates. V. The Determination of the Crystal Structure of $CuSO_4 \cdot 3H_2O$ (Bonattite). *Acta Crystallogr. Sect. B* **1968**, *24*, 508-513.

104.   Baur, W., On the Crystal Chemistry of Salt Hydrates. III. The Determination of the Crystal Structure of $FeSO_4.7H_2O$ (Melanterite). *Acta Crystallographica* **1964**, *17*, 1167-1174.

105.   Avvaru, B. S.; Kim, C. U.; Sippel, K. H.; Gruner, S. M.; Agbandje-McKenna, M.; Silverman, D. N.; McKenna, R., A Short, Strong Hydrogen Bond in the Active Site of Human Carbonic Anhydrase II. *Biochemistry* **2010**, *49*, 249-251.

106. Fernández-Gacio, A.; Codina, A.; Fastrez, J.; Riant, O.; Soumillion, P., Transforming Carbonic Anhydrase into Epoxide Synthase by Metal Exchange. *ChemBioChem* **2006**, *7*, 1013-1016.

107. Breton, S., The Cellular Physiology of Carbonic Anhydrases. *Jop* **2001**, *2*, 159-164.

108. Lu, D.; Voth, G. A., Proton Transfer in the Enzyme Carbonic Anhydrase: An *ab initio* Study. *J. Am. Chem. Soc.* **1998**, *120*, 4006-4014.

109. Lindskog, S., Structure and Mechanism of Carbonic Anhydrase. *Pharmacology & Therapeutics* **1997**, *74*, 1-20.

110. Christianson, D. W.; Fierke, C. A., Carbonic Anhydrase: Evolution of the Zinc Binding Site by Nature and by Design. *Acc. Chem. Res.* **1996**, *29*, 331-339.

111. McQuate, R. S., Carbonic Anhydrase and Metalloderivatives. A Bioinorganic Chemistry Study. *J. Chem. Educ.* **1977**, *54*, 645-8.

112. Steiner, H.; Jonsson, B.-H.; Lindskog, S., The Catalytic Mechanism of Carbonic Anhydrase. *Eur. J. Biochem.* **1975**, *59*, 253-259.

113. Maren, T. H., *Carbonic Anhydrase: Chemistry, Physiology, and Inhibition*, 1967; Vol. 47, p 595-781.

114. Nadal-Ferret, M.; Gelabert, R.; Moreno, M.; Lluch, J. M., Are There Really Low-Barrier Hydrogen Bonds in Proteins? The Case of Photoactive Yellow Protein. *J. Am. Chem. Soc.* **2014**, *136*, 3542-3552.

115. Zhang, C., Low-Barrier Hydrogen Bond Plays Key Role in Active Photosystem II — a New Model for Photosynthetic Water Oxidation. *Biochim. Biophys. Acta* **2007**, *1767*, 493-499.

116. Poi, M. J.; Tomaszewski, J. W.; Yuan, C.; Dunlap, C. A.; Andersen, N. H.; Gelb, M. H.; Tsai, M.-D., A Low-Barrier Hydrogen Bond between Histidine of Secreted Phospholipase A2 and a Transition State Analog Inhibitor. *J. Mol. Biol.* **2003**, *329*, 997-1009.

117. Cleland, W. W.; Frey, P. A.; Gerlt, J. A., The Low Barrier Hydrogen Bond in Enzymatic Catalysis. *J. Biol. Chem.* **1998**, *273*, 25529-25532.

118. Frey, P.; Whitt, S.; Tobin, J., A Low-Barrier Hydrogen Bond in the Catalytic Triad of Serine Proteases. *Science* **1994**, *264*, 1927-1930.

119. Cleland, W.; Kreevoy, M., Low-Barrier Hydrogen Bonds and Enzymic Catalysis. *Science* **1994**, *264*, 1887-1890.

120. Cleland, W. W., Low-Barrier Hydrogen Bonds and Low Fractionation Factor Bases in Enzymic Reactions. *Biochemistry* **1992**, *31*, 317-319.

121. Ruggiero, M. T.; Korter, T. M., The Crucial Role of Water in Shaping Low-Barrier Hydrogen Bonds. *Phys. Chem. Chem. Phys.* **2016**.

122. Heikinheimo, P.; Tuominen, V.; Ahonen, A.-K.; Teplyakov, A.; Cooperman, B. S.; Baykov, A. A.; Lahti, R.; Goldman, A., Toward a Quantum-Mechanical Description of Metal-Assisted Phosphoryl Transfer in Pyrophosphatase. *PNAS* **2001**, *98*, 3121-3126.

123. Kolar, J.; Strlic, M., *Iron Gall Inks : On Manufacture, Characterisation, Degradation, and Stabilisation*; National and University Library: Ljubljana, 2006.

124. Gustafsson, R.; Orlov, A.; Badger, C.; Griffiths, P.; Cox, R.; Lambert, R., A Comprehensive Evaluation of Water Uptake on Atmospherically Relevant Mineral Surfaces: Drift Spectroscopy, Thermogravimetric Analysis and Aerosol Growth Measurements. *Atmos. Chem. Phys.* **2005**, *5*, 3415-3421.

125.   Guggenheim, S.; Van Groos, A. K., Baseline Studies of the Clay Minerals Society Source Clays: Thermal Analysis. *Clays Clay Miner.* **2001**, *49*, 433-443.

126.   Fu, X.; Yang, G.; Sun, J.; Zhou, J., Vibrational Spectra of Copper Sulfate Hydrates Investigated with Low-Temperature Raman Spectroscopy and Terahertz Time Domain Spectroscopy. *J. Phys. Chem. A* **2012**, *116*, 7314-7318.

127.   Lyakhov, N. Z.; Chupakhin, A. P.; Isupov, V. P.; Boldyrev, V. V., Dependence of Kinetics of Copper Sulfate Pentahydrate Dehydration on Water Vapor Pressure. *J. Solid State Chem.* **1978**, *26*, 173-178.

128.   Ruggiero, M. T.; Korter, T. M., Uncovering the Terahertz Spectrum of Copper Sulfate Pentahydrate. *J. Phys. Chem. A* **2016**, *120*, 227-232.

129.   Bittner, B.; Scherm, M.; Schoedl, T.; Tyroller, T.; Schwarz, U. T.; Max, M., Phonon-Polariton Damping by Low-Frequency Excitations in Lithium Tantalate Investigated by Spontaneous and Stimulated Raman Scattering. *J. Phys.: Condens. Matter* **2002**, *14*, 9013.

130.   Gelder, A. P. v.; Holvast, J.; Stoelinga, J. H. M.; Wyder, P., Localized Polariton Modes of Small Cubic Crystals. *J. Phys. C* **1972**, *5*, 2757.

131.   Lee, Y.-S.; Tomaino, J. L.; Jameson, A. D.; Khitrova, G.; Gibbs, H. M.; Stroech, A.; Kira, M.; Koch, S. In *Interaction of Strong Terahertz Pulses with Exciton-Polaritons in Quantum-Well Microcavity*, CLEO:2011 - Laser Applications to Photonic Applications, Baltimore, Maryland, 2011/05/01; Optical Society of America: Baltimore, Maryland, 2011; p QMB2.

132.   Stoyanov, N. S.; Ward, D. W.; Feurer, T.; Nelson, K. A., Terahertz Polariton Propagation in Patterned Materials. *Nat. Mater.* **2002**, *1*, 95-98.

133. Wiederrecht, G. P.; Dougherty, T. P.; Dhar, L.; Nelson, K. A.; Leaird, D. E.; Weiner, A. M., Explanation of Anomalous Polariton Dynamics in Litao$_3$. *Phys. Rev. B.* **1995**, *51*, 916-931.

134. Tsuneda, T.; Hirao, K., Long-Range Correction for Density Functional Theory. *Wiley Interdiscip. Comput. Mol. Sci.* **2014**, *4*, 375-390.

135. Song, J.-W.; Tsuneda, T.; Sato, T.; Hirao, K., Calculations of Alkane Energies Using Long-Range Corrected DFT Combined with Intramolecular Van Der Waals Correlation. *Org. Lett.* **2010**, *12*, 1440-1443.

136. Weintraub, E.; Henderson, T. M.; Scuseria, G. E., Long-Range-Corrected Hybrids Based on a New Model Exchange Hole. *J. Chem. Theory Comput.* **2009**, *5*, 754-762.

137. Song, J.-W.; Watson, M. A.; Nakata, A.; Hirao, K., Core-Excitation Energy Calculations with a Long-Range Corrected Hybrid Exchange-Correlation Functional Including a Short-Range Gaussian Attenuation (LCgau-BOP). *J. Chem. Phys.* **2008**, *129*, 184113.

138. Song, J.-W.; Tokura, S.; Sato, T.; Watson, M. A.; Hirao, K., An Improved Long-Range Corrected Hybrid Exchange-Correlation Functional Including a Short-Range Gaussian Attenuation (LCgau-BOP). *J. Chem. Phys.* **2007**, *127*, 154109.

139. Schwabe, T.; Grimme, S., Double-Hybrid Density Functionals with Long-Range Dispersion Corrections: Higher Accuracy and Extended Applicability. *Phys. Chem. Chem. Phys.* **2007**, *9*, 3397-3406.

140. Jacquemin, D.; Perpète, E. A.; Scalmani, G.; Frisch, M. J.; Kobayashi, R.; Adamo, C., Assessment of the Efficiency of Long-Range Corrected Functionals for Some Properties of Large Compounds. *J. Chem. Phys.* **2007**, *126*, 144105.

141.   Gerber, I. C.; Ángyán, J. G.; Marsman, M.; Kresse, G., Range Separated Hybrid Density Functional with Long-Range Hartree-Fock Exchange Applied to Solids. *J. Chem. Phys.* **2007**, *127*, 054101.

142.   Zhao, Y.; Truhlar, D. G., Density Functional for Spectroscopy: No Long-Range Self-Interaction Error, Good Performance for Rydberg and Charge-Transfer States, and Better Performance on Average Than B3LYP for Ground States. *J. Phys. Chem. A* **2006**, *110*, 13126-13130.

143.   Vydrov, O. A.; Scuseria, G. E., Assessment of a Long-Range Corrected Hybrid Functional. *J. Chem. Phys.* **2006**, *125*, 234109.

144.   Yanai, T.; Tew, D. P.; Handy, N. C., A New Hybrid Exchange–Correlation Functional Using the Coulomb-Attenuating Method (CAM-B3LYP). *Chem. Phys. Lett.* **2004**, *393*, 51-57.

145.   Tawada, Y.; Tsuneda, T.; Yanagisawa, S.; Yanai, T.; Hirao, K., A Long-Range-Corrected Time-Dependent Density Functional Theory. *J. Chem. Phys.* **2004**, *120*, 8425-8433.

146.   Dreuw, A.; Weisman, J. L.; Head-Gordon, M., Long-Range Charge-Transfer Excited States in Time-Dependent Density Functional Theory Require Non-Local Exchange. *J. Chem. Phys.* **2003**, *119*, 2943-2946.

147.   Wu, H.; Reeves-McLaren, N.; Jones, S.; Ristic, R. I.; Fairclough, J. P. A.; West, A. R., Phase Transformations of Glutamic Acid and Its Decomposition Products. *Cryst. Growth Des.* **2010**, *10*, 988-994.

148.   Di Profio, G.; Curcio, E.; Ferraro, S.; Stabile, C.; Drioli, E., Effect of Supersaturation Control and Heterogeneous Nucleation on Porous Membrane Surfaces in the Crystallization of L-Glutamic Acid Polymorphs. *Cryst. Growth Des.* **2009**, *9*, 2179-2186.

149. Schöll, J.; Bonalumi, D.; Vicum, L.; Mazzotti, M.; Müller, M., In Situ Monitoring and Modeling of the Solvent-Mediated Polymorphic Transformation of L-Glutamic Acid. *Cryst. Growth Des.* **2006**, *6*, 881-891.

150. Cashell, C.; Corcoran, D.; Hodnett, B. K., Effect of Amino Acid Additives on the Crystallization of L-Glutamic Acid. *Cryst. Growth Des.* **2005**, *5*, 593-597.

151. Kitamura, M., Polymorphism in the Crystallization of L-Glutamic Acid. *J. Cryst. Growth* **1989**, *96*, 541-546.

CHAPTER 2: Quantum Mechanics and Electronic Structure Methods

2.1 Introduction to Quantum Theory

2.1.1 The Schrödinger Equation

At the turn of the twentieth century physicists had begun to investigate the interesting properties of the dual wave-particle nature of light.[1-4] By the 1920s it was accepted that light acted simultaneously as both a particle and a wave, and attention then turned to electrons. A major breakthrough came in 1924, when Louis de Broglie proposed that not only light, but all matter, exhibited wave-particle duality using what is now known as the de Broglie relationship,[5]

$$\lambda = \frac{h}{p} \tag{2.1}$$

where λ is the wavelength, h is Planck's constant, and p is momentum. Following this, two identical formulations for describing the state of an electron emerged. Werner Heisenberg treated electrons as particles and using complicated matrix mathematics,[6-8] but it was Erwin Schrödinger who famously treated particles from a wave standpoint, for which he introduced the equation for a particle moving freely in space known as the time-dependent Schrödinger equation,[9-10]

$$\hat{H}\Psi(r,t) = i\hbar\frac{\partial}{\partial t}\Psi(r,t) \tag{2.2}$$

where $\hat{H}$ is the Hamiltonian operator and $\Psi(r,t)$ is the wavefunction. In the Schrödinger equation, the wavefunction is the function that describes the quantum state of an isolated particle, and when squared represents the probability of finding a particle at any point in space. The Hamiltonian is a mathematical operator that returns to the total energy of a system, and can have multiple forms based on the system of interest.[11-12] In the case of a freely propagating particle, the Hamiltonian returns the total energy because Planck's law[13-14] and the de Broglie relationship relate wavelength and momentum to energy, thus

$$i\hbar \frac{\partial}{\partial t}\Psi(r,t) = E\Psi(r,t) \qquad (2.3)$$

For a single particle moving in a three-dimensional external potential the Hamiltonian can be deconstructed into kinetic ($\hat{T}$) and potential ($\hat{V}$) energy operators,

$$\hat{H} = \hat{T} + \hat{V} = -\frac{\hbar}{2m}\nabla^2 + V(r) \qquad (2.4)$$

with m representing the particles mass and ∇^2 being the Laplacian operator which has the form,

$$\nabla^2 = \frac{\partial^2}{\partial x^2} + \frac{\partial^2}{\partial x^2} + \frac{\partial^2}{\partial x^2} \qquad (2.5)$$

Because the Hamiltonian is not dependent on time and wavefunctions represent stationary states (standing waves), the time-dependent wavefunction can be separated into time-dependent and independent components, ultimately yielding the time-independent Schrödinger equation

$$\hat{H}\Psi(r) = E\Psi(r) \tag{2.6}$$

Schrödinger used this equation to derive the wavefunction and energy levels of a hydrogen atom, and his calculated values exactly matched experimental observations involving the spectral lines of hydrogen (the Rydberg series).[15] In theory the wavefunction for any system can be solved for any system, but because of the nature of quantum mechanics additional non-classical concepts must be considered. For example, the indistinguishably of quantum particles must be incorporated into mathematic form of the wavefunction to obtain an accurate result.[16-17] This can be understood as simply 'switching the labels' on wavefunction ordering, which will not result in any observable changes in a system, *i.e.,*

$$|\Psi(r,r')|^2 = |\psi_1(r)\psi_2(r')|^2 = |\psi_1(r')\psi_2(r)|^2 = |\Psi(r',r)|^2 \tag{2.7}$$

However, since both $\psi_1(r)\psi_2(r')$ and $\psi_1(r')\psi_2(r)$ are solutions to the Schrödinger equation, they must be taken as a linear combination of the total wavefunction,

$$\Psi(r,r') = \frac{1}{\sqrt{2}}(\psi_1(r)\psi_2(r') \pm \psi_1(r')\psi_2(r)) \tag{2.8}$$

This results in two solutions, a symmetric case, $\Psi(r,r') = \Psi(r',r)$, and antisymmetric case, $\Psi(r,r') = -\Psi(r',r)$. Both solutions satisfy the probability density equality in (2.7) but electrons (and all fermions) must have antisymmetric wavefunctions, a consequence known as the Pauli Exclusion Principle.[18-19] Simply, only one electron can occupy a quantum state at any given time, clearly obtained if $\Psi(r) = \Psi(r')$ in the antisymmetric variant of (2.8). The antisymmetric wavefunction for a many-body system (neglecting spin) is constructed using

the Slater determinant,

$$\Psi(r_1, r_2, \dots, r_n) = \frac{1}{\sqrt{n!}} \begin{vmatrix} \psi_1(r_1) & \psi_2(r_1) & \cdots & \psi_n(r_1) \\ \psi_1(r_2) & \psi_2(r_2) & \cdots & \psi_n(r_2) \\ \vdots & \vdots & \ddots & \vdots \\ \psi_1(r_n) & \psi_2(r_n) & \cdots & \psi_n(r_n) \end{vmatrix} \tag{2.9}$$

Actually solving the Schrödinger equation for the wavefunction energy becomes much more difficult when considering systems with more than one electron, as the number of terms that must be accounted for increases greatly.[20] For an atomic system three types of Coulombic forces contribute to the Hamiltonian potential energy term: the attractive nucleus-electron ($\hat{Z}$) energy, the repulsive electron-electron ($\hat{U}$) and the nucleus-nucleus ($\hat{N}$) energies. The number of kinetic energy terms doubles when the kinetic energy of the electrons ($\hat{T}_e$) and nuclei ($\hat{T}_N$) are included. The many-body Hamiltonian then becomes the sum of these operators,

$$\hat{H} = \hat{T}_e + \hat{T}_N + \hat{Z} + \hat{U} + \hat{N} \tag{2.10}$$

$$\hat{H} = \overbrace{\sum_i^N -\frac{\hbar}{2m_i} \nabla_i{}^2}^{\hat{T}_e} + \overbrace{\sum_I^M -\frac{\hbar}{2m_I} \nabla_I{}^2}^{\hat{T}_N}$$
$$+ \xi \left(\underbrace{\sum_{i,I}^N \frac{Z_I}{|r_i - R_I|}}_{\hat{Z}} + \underbrace{\frac{1}{2}\sum_i^N \sum_{j \neq i}^N \frac{1}{|r_i - r_j|}}_{\hat{U}} + \underbrace{\frac{1}{2}\sum_I^M \sum_{J \neq I}^M \frac{Z_I Z_J}{|R_I - R_J|}}_{\hat{N}} \right) \tag{2.11}$$

Here, r and R represent the electron and nuclear coordinates with indices (i,j) and (I,J), respectively, $\textbf{Z}$ is the nuclear charge (bolded to emphasize its difference from the nuclear potential), and ξ represents the Columbic constant,

$$\xi = \frac{e^2}{4\pi\varepsilon_0} \tag{2.12}$$

where e is the elementary charge of an electron and ε_0 is the vacuum permittivity. Because of the electron-electron repulsive term in (2.11) the equation is not separable into single particle terms, and each additional electron a system gains increases the number of parameters exponentially.

The problems associated with solving the many-body wavefunction exactly have led to the development of numerous approximations for determining the energy of large systems. Two such theories will be discussed, the first being Hartree-Fock theory,[21-22] which searches for a single Slater determinant that give the lowest energy of a system, and density functional theory,[23-24] a method that relates spatial electron density to observable properties.

2.2 Theoretical Methods for Solving the Schrödinger Equation

The electronic ground state is responsible for dictating many of the physical properties of materials.[25-27] For example, because the bulk modulus is defined as the change in pressure with respect to volume, and in turn pressure is the change in energy with respect to volume, an accurate knowledge of the ground state energy can provide its value,[22]

$$B = -V \left(\frac{\partial P}{\partial V} \right)_S \tag{2.13}$$

$$P(V) = -\left(\frac{\partial E}{\partial V} \right)_S \tag{2.14}$$

$$B = -V \left(\frac{\partial P}{\partial V} \right)_S = -V \left(\frac{\partial^2 E}{\partial V^2} \right)_{T,S} \tag{2.15}$$

Therefore, the accurate calculation of the electronic ground state is paramount for any quantum mechanical simulation. But as previously mentioned, the large number of electrons and nuclei present in most real materials makes solving the Schrödinger equation explicitly nearly impossible. Fortunately approximations can be made that assist in decreasing the complexity of many body problem, with one example being the Born-Oppenheimer approximation.[28-29]

2.2.1 The Born-Oppenheimer Approximation

Separation of the many body Hamiltonian into electronic and nuclear terms yields,

$$\widehat{H}_{electronic} = \sum_i^N -\frac{\hbar}{2m_i}\nabla_i^2 + \xi\left(\sum_{i,I}^N \frac{Z_I}{|r_i - R_I|} + \frac{1}{2}\sum_i^N\sum_{j\neq i}^N \frac{1}{|r_i - r_j|}\right) \qquad (2.16)$$

$$\widehat{H}_{nuclear} = \sum_I^M -\frac{\hbar}{2m_I}\nabla_I^2 + \xi\frac{1}{2}\sum_I^M\sum_{J\neq I}^M \frac{Z_I Z_J}{|R_I - R_J|} \qquad (2.17)$$

Because the mass of a nucleus is much greater than the mass of an electron, the Born-Oppenheimer approximation allows the motion, and thus the kinetic energy of the nucleus, to be neglected. The electronic Hamiltonian therefore reduces to

$$\widehat{H} = \widehat{T}_e + \widehat{Z} + \widehat{U} + \widehat{N} \qquad (2.18)$$

$$\widehat{H} = \sum_i^N -\frac{\hbar}{2m_i}\nabla_i^2 + \xi\left(\sum_{i,I}^N \frac{Z_I}{|r_i - R_I|} + \frac{1}{2}\sum_i^N\sum_{j\neq i}^N \frac{1}{|r_i - r_j|} + \frac{1}{2}\sum_I^M\sum_{J\neq I}^M \frac{Z_I Z_J}{|R_I - R_J|}\right) \qquad (2.19)$$

It is important to note that while the last term is a nuclear term, it remains in the Hamiltonian to maintain charge balance. This nuclear-nuclear interaction is simply a classical Coulombic potential energy for point charges, and is commonly referred to as the Ewald sum. For the remainder of the discussion, it will be omitted from the Hamiltonian, as well as the dependence of $\widehat{T}_e$ on the subscript e.

2.2.2 The Variational Principle

The expectation value of the Hamiltonian is equal to the ground state energy of a system,

$$E = \frac{\langle \Psi | \hat{H} | \Psi \rangle}{\langle \Psi | \Psi \rangle} = \int_{-\infty}^{\infty} \Psi^* \hat{H} \Psi \, dr^3 \qquad (2.20)$$

From this, it becomes obvious that the exact knowledge of the wavefunction yields the exact energy of a system. However, for a many-body system, it is difficult to ascertain the true wavefunction. Therefore the variational principle is introduced, which states that for any wavefunction other than the true one the calculated energy will always be greater than the actual energy.[30] Many computational methods are based on the variational principle, as algorithms are designed to iterate over wavefunction approximations with the goal being minimization of the total energy. This forms the basis for one of the earliest computational methods for solving the Schrödinger equation, the Self-Consistent Field or Hartree-Fock technique.

2.2.3 Hartree-Fock Theory

Hartree-Fock (HF), also known as the Self-Consistent Field technique, forms the foundation of modern molecular orbital theory using the approximation that electrons do not interact and can be described using one-electron wavefunctions.[31-32] The HF technique, based on the variational principle, is an *ab initio* method that attempts to calculate the electronic energy by guessing the form of the one-electron wavefunctions iteratively while minimizing the total energy. The two key assumptions of HF are that nuclear motion is not considered (the Born-

Oppenheimer approximation) and that the electrons move independently of one another (no explicit electron correlation). These two assumptions imply that a two electron system can be described simply as the product of two wavefunctions

$$\Psi(r, r') = \psi_1(r)\psi_2(r') \tag{2.21}$$

and can be extended to a system with N electrons

$$\Psi(r_1, r_2, \dots, r_n) = \psi_1(r_1)\psi_2(r_2) \dots \psi_n(r_n) \tag{2.22}$$

However, this wavefunction does not satisfy the antisymmetric condition related to the Pauli Exclusion Principle. In order to meet this requirement, the wavefunction must be expressed as a Slater determinant,

$$\Psi(r) = \frac{1}{\sqrt{2}} \begin{vmatrix} \psi_i(r) & \psi_i(r) \\ \psi_j(r') & \psi_j(r') \end{vmatrix} = \frac{1}{\sqrt{2}}\left(\psi_i(r)\psi_j(r') - \psi_i(r')\psi_j(r)\right) \tag{2.23}$$

The Slater determinant includes the indistinguishability of electrons by mathematically representing each electron as simultaneously occupying every orbital. The HF energy (E_{HF}) is then calculated by taking the expectation value of the Hartree-Fock Hamiltonian (the Fock operator, $\hat{F}$), which is written as a combination of one- and two-electron operators,

$$\hat{F} = \overbrace{\hat{T} + \hat{Z}}^{One-Electron} + \overbrace{\hat{U}}^{Two-Electron} \tag{2.24}$$

$$F = \langle\Psi|\hat{F}|\Psi\rangle = E_\Psi \tag{2.25}$$

$$\langle \Psi | \hat{F} | \Psi \rangle = \sum_i \left(\langle \psi_i | \hat{T} | \psi_i \rangle + \langle \psi_i | \hat{Z} | \psi_i \rangle \right) + \frac{1}{2} \sum_i \sum_{j \neq i} \langle \psi_i \psi_j | \hat{U} | \psi_i \psi_j \rangle \qquad (2.26)$$

Throughout this discussion, the expectation value (energies) of the energy operators will be noted using the same symbol as the respective operator without the accent, as in (2.25), with the exception being the total energy (the expectation value of the Hamiltonian) which will sometimes be noted as E. The one-electron terms are solved relatively easily; however the two-electron terms are not. Considering the two-electron antisymmetric wavefunction,

$$\Psi(r, r') = \psi_1(r)\psi_2(r') - \psi_1(r')\psi_2(r) \qquad (2.27)$$

the two electron expectation value takes the form

$$\langle \psi_i \psi_j | \hat{U} | \psi_i \psi_j \rangle = \qquad (2.28)$$
$$\frac{1}{2} \xi \sum_i \sum_{j \neq i} \left(\psi_i(r)\psi_j(r') - \psi_i(r')\psi_j(r) \right) \frac{1}{|r - r'|} \left(\psi_i(r)\psi_j(r') - \psi_i(r')\psi_j(r) \right)$$

For simplicity, the wavefunctions are assumed to be normalized and both electron spin and imaginary components are ignored. Upon multiplication and factorization, and introducing integration over all space, four total terms are produced that can be factored into just two,

$$J_{ij} = \frac{1}{2} \xi \sum_i \sum_{j \neq i} \iint \psi_i^2(r) \frac{1}{|r - r'|} \psi_j^2(r) \, dr \, dr' \qquad (2.29)$$

$$K_{ij} = -\frac{1}{2}\,\xi \sum_i \sum_{j\neq i} \iint \psi_i(r)\psi_j(r')\frac{1}{|r-r'|}\,\psi_i(r')\psi_j(r)\,dr\,dr' \qquad (2.30)$$

The first term, J_{ij}, is the Coulombic repulsion energy, which is interaction of an electron in orbital ψ_i with the average position of all other electrons in orbitals ψ_j where $j \neq i$. The second integral, K_{ij}, is the exchange integral, a quantum mechanical phenomenon that is a result of the antisymmetric nature of the wavefunction allowing electrons to exchange orbitals. Because the Coulombic repulsion term does not take the antisymmetric nature of electron wavefunctions into account the energy is slightly greater than the true interaction.[33-34] The exchange energy corrects this (because it is negative), usually damping the pure Coulombic repulsion energy by ~25%.[35-36] It is important to note that the Coulombic repulsion term does not represent the interaction between individual electrons, instead each electron experiences a mean potential generated by the remaining electrons.

Combining the Fock operator components, it becomes clear that the Hartree-Fock energy is a simple eigenvalue problem,

$$\left[\hat{T} + \hat{Z} + \sum_{j\neq i}\hat{J}_j - \sum_{j\neq i}\hat{K}_j\right]\psi_i(r) = E_i\psi_i(r) \qquad (2.31)$$

Furthermore, because the diagonal terms ($j=i$) would result in the two-electron energy being equal to zero, the dependency on i can be removed, yielding the well-known version of the Fock operator,

$$\hat{F} = \hat{T} + \hat{V} + \sum_j \hat{J}_j - \sum_j \hat{K}_j \qquad (2.32)$$

The Fock operator is appropriate for solving the energy of a system with a wavefunction determined from the Slater determinant. However, from a purely *ab initio* approach, the Slater determinant that results in the lowest energy is most likely unknown, because the molecular orbitals are unknown. A linear combination of atomic orbitals (LCAO) is used to build the molecular orbitals,

$$\psi_i(r) = \sum_{\mu}^{N} a_{i,\mu} \varphi_\mu(r) \tag{2.33}$$

where $\varphi_\mu(r)$ are the atomic orbitals and $a_{i,\mu}$ are the orbital coefficients. The introduction of LCAO basis results in the Hartree-Fock-Roothaan equations,[37-38] which is a variation of the aforementioned HF equations,

$$\hat{F}\psi_i(r) = E_i\psi_i(r) \tag{2.34}$$

$$\hat{F} \sum_{\mu}^{N} a_{i,\mu} \varphi_\mu(r) = E_i \sum_{\mu}^{N} a_{i,\mu} \varphi_\mu(r) \tag{2.35}$$

When considering every combination of basis function, the Hartree-Fock-Roothaan equations become

$$\sum_{\mu}^{N} a_{i,\mu} \int \varphi_\mu(r) \hat{F} \varphi_\nu(r) \, dr = E_i \sum_{\mu}^{N} a_{i,\mu} \int \varphi_\mu(r)\varphi_\nu(r) \, dr \tag{2.36}$$

Introducing matrix notation, the Hartree-Fock-Roothaan terms can be expressed in terms of the overlap matrix $S_{\mu\nu}$ and Fock matrix $F_{\mu\nu}$ with respect to the introduced atomic orbitals,

$$S_{\mu\nu} = \int \varphi_\mu(r)\varphi_\nu(r)\, dr \tag{2.37}$$

$$F_{\mu\nu} = \int \varphi_\mu(r)\hat{F}\varphi_\nu(r)\, dr \tag{2.38}$$

Leading to the Hartree-Fock-Roothaan equation written as

$$\sum_\mu^N \sum_\nu^N F_{\mu\nu} a_{i,\mu} = E_i \sum_\mu^N \sum_\nu^N S_{\mu\nu} a_{i,\mu} \tag{2.39}$$

and simplified to matrix notation,

$$\mathbf{FA} = \mathbf{SA}E \tag{2.40}$$

This solution demonstrates that diagonalization of $\mathbf{F}$ will produce values for E for every molecular orbital $\psi_i(r)$. The elements of $\mathbf{S}$ are dependent only on the atomic orbitals and do not change with molecular orbital index, with $\mathbf{A}$ (and by definition, $\mathbf{F}$) depending on molecular orbital index.

In many cases the exact orbital coefficients that yield the lowest energy configuration are not known. In such a scenario, the variational principle states that the energy of the incorrect LCAO will result in an energy higher than that of the correct one. Therefore, an iterative procedure for determining the linear combination coefficients is performed, by varying the coefficients with the goal being minimization of the total energy, and is known as the Self-

Consistent Field (SCF) technique, illustrated in **Figure 2-1.** Initially, the system of interest and atomic orbitals with predetermined orbital coefficients are used to construct the overlap matrix and the Fock matrix. Diagonalization of the Fock matrix yields the energy for every molecular orbital, and the result is fed back into itself in order to guess new orbital coefficients, and the process repeats until no discernable change in energy is observed between two adjacent steps.
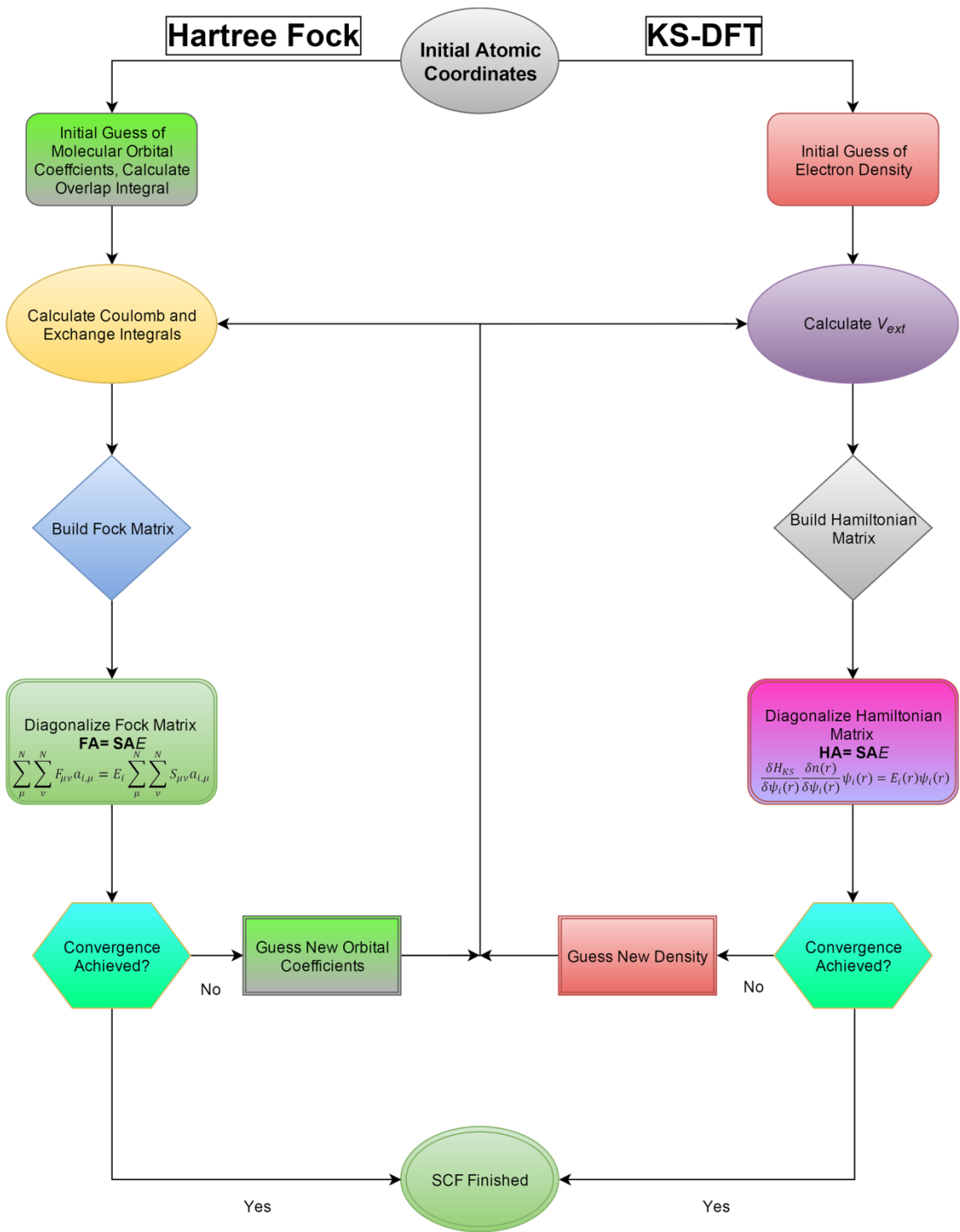
Figure 2-1. Diagram of the SCF technique for Hartree-Fock and Kohn-Sham density functional theory (KS-DFT).

2.2.4 Density Functional Theory

While HF theory was groundbreaking in its handling of the many-body problem, there still exists a large computational cost associated with building the many-electron wavefunction and solving the eigenvalue problem for large systems.[31] The dimension of the wavefunction is directly related to the number of electrons (three-dimensions per electron), and for example the full wavefunction of the relatively simple CO_2 molecule has 66-dimensions. Because the electron wavefunction is not directly observable, an alternative method of solving the Schrödinger equation would be to shift the focus away from the wavefunction and instead use something that can be observed, specifically the electron density (n) that has an operator,

$$\hat{n} = \delta(r - r') \tag{2.41}$$

with the expectation value of the density given by,

$$n(r) = \langle \Psi | \hat{n} | \Psi \rangle = \int |\Psi(r)|^2 dr \tag{2.42}$$

The electron density can be used in place of many of the wavefunction terms in the total energy Hamiltonian,

$$\hat{H} = \hat{T} + \hat{Z} + \hat{U} \tag{2.43}$$

$$\hat{H} = \sum_i^N -\frac{\hbar}{2m_i} \nabla_i^2 + \xi \left(\sum_{i,I}^N \frac{Z_I}{|r_i - R_I|} + \frac{1}{2} \sum_i^N \sum_{j \neq i}^N \frac{1}{|r_i - r_j|} \right) \tag{2.44}$$

For example, the electron-nuclei potential energy Z, can be determined from the expectation value of the electron-nuclei potential energy operator $\hat{Z}$, given by

$$\langle \Psi(r)|\hat{Z}|\Psi(r)\rangle = \langle\hat{Z}\rangle_{\Psi(r)} = \xi \sum_{i}^{N_e} \sum_{I}^{N_n} \int \psi_i(r) \frac{\mathbf{Z}_I}{|r - R_I|} \psi_i(r) dr \qquad (2.45)$$

$$\langle\hat{Z}\rangle_{\Psi(r)} = \xi \sum_{i}^{N_e} \sum_{I}^{N_n} \int |\psi_i(r)|^2 \frac{\mathbf{Z}_I}{|r - R_I|} dr \qquad (2.46)$$

Substituting the expression for electron density, the equation becomes

$$\langle\hat{Z}\rangle_{n(r)} = \xi \sum_{I}^{N_n} \int n(r) \frac{\mathbf{Z}_I}{|r - R_I|} dr \qquad (2.47)$$

Expressing the energy of a system in terms of electron density rather than the many-body wavefunction is good in theory, but without knowledge of the exact wavefunction determining $n(r)$ is still an impossible task. However in 1964 Pierre Hohenberg and Walter Kohn developed a theory that claimed the ground state energy for a many-body wavefunction can be found by solving the non-interacting electron equations in an effective potential determined solely from the electron density.[23] Hohenberg and Kohn supported this by introducing two important theorems: (1) that there cannot be two different external potentials that yield the same non-degenerate ground state charge density, and (2) that the external potential (and therefore the total energy), is a unique functional of the electron density.

The first theorem can be proven using a *reductio ad absurdum* argument. Assuming that there exist two different external potentials, $V_{ext}^{(1)}(r)$ and $V_{ext}^{(2)}(r)$ that yield the same ground state

electron density, $n(r)$, the potentials would be a result of two distinct Hamiltonians, $\hat{H}^{(1)}$ and $\hat{H}^{(2)}$, which give way to unique wavefunctions $\Psi^{(1)}(r)$ and $\Psi^{(2)}(r)$. The variational principle states that that no wavefunction can yield an energy for $\Psi^{(1)}(r)$ less than the expectation value using $\hat{H}^{(1)}(r)$,

$$E^{(1)} = \left\langle \Psi^{(1)} \middle| \hat{H}^{(1)} \middle| \Psi^{(1)} \right\rangle < \left\langle \Psi^{(2)} \middle| \hat{H}^{(1)} \middle| \Psi^{(2)} \right\rangle \tag{2.48}$$

Because of the initial assumption that states the two systems have identical densities, the second expectation value in the above expression can be rewritten as

$$\left\langle \Psi^{(2)} \middle| \hat{H}^{(1)} \middle| \Psi^{(2)} \right\rangle = \left\langle \Psi^{(2)} \middle| \hat{H}^{(2)} \middle| \Psi^{(2)} \right\rangle + \int n(r) \left(\hat{V}_{ext}^{(1)}(r) - \hat{V}_{ext}^{(2)}(r) \right) dr \tag{2.49}$$

Switching the labels, it is equally shown that the following expression is valid,

$$\left\langle \Psi^{(1)} \middle| \hat{H}^{(2)} \middle| \Psi^{(1)} \right\rangle = \left\langle \Psi^{(1)} \middle| \hat{H}^{(1)} \middle| \Psi^{(1)} \right\rangle + \int n(r) \left(\hat{V}_{ext}^{(2)}(r) - \hat{V}_{ext}^{(1)}(r) \right) dr \tag{2.50}$$

And by combining (2.46) and (2.47) the relationship,

$$E^{(1)} + E^{(2)} < E^{(2)} + E^{(1)} \tag{2.51}$$

is obtained, which is clearly contradictory. This contradiction proves that each ground state electron density does in fact determine a unique external potential.

The second theorem provides a means of solving for the energy of a system based solely on the electron density, by stating that a unique functional for the energy can be defined using

the density and that the exact ground state energy is the minimum value of the functional. This uses the previous theorem, that because the external potential and therefore the wavefunction is determined uniquely by the density then all other observables must also be uniquely determined.

$$\hat{E}[n(r)] = \hat{T}[n(r)] + \hat{Z}[n(r)] + \hat{V}_{ext}[n(r)] \tag{2.52}$$

$$\hat{E}[n(r)] \equiv \hat{F}[n(r)] + \hat{V}_{ext}[n(r)] \tag{2.53}$$

Here, $\hat{F}[n(r)]$ is a universal functional (not to be confused with the HF Fock operator) because its treatment of the kinetic and internal potential energies is the same for all systems, that is it does not depend on V_{ext}. Again, introducing the variational principle, it follows that minimization of $E[n(r)]$ with respect to $n(r)$ will result in the lowest ground state energy,

$$E^{(1)} = E[n(r)] = \langle \Psi^{(1)} | \hat{H}^{(1)} | \Psi^{(1)} \rangle < \langle \Psi^{(2)} | \hat{H}^{(1)} | \Psi^{(2)} \rangle = E^{(2)} \tag{2.54}$$

These two theorems, while they showcase that the electron density can be used to effectively calculate the ground state properties of a given system, do not provide any methods for actually solving the problem. The issues arise from the fact that $\hat{F}[n(r)]$ is not known, and that it depends on the density itself.

A year after Hohenberg and Kohn published their theorems, Walter Kohn and Lu Jeu Sham developed an ansatz which stated that the exact ground state density can be written as the sum of non-interacting particle wavefunctions,

$$n(r) = \sum_i^N |\psi_i(r)|^2 \qquad (2.55)$$

enabling the use of an independent particle equation that can be solved numerically.[24]

The method used in Kohn-Sham density functional theory (KS-DFT) is very similar to what is done in HF, with a few notable exceptions.[39] First, the KS-energy is constructed in a slightly different manner, as (unlike HF) electron exchange is not taken into account. The energy can be written as,

$$\begin{aligned} E[n(r)] &= T[n(r)] + V[n(r)] + U[n(r)] \\ &= T_s[n(r)] + Z[n(r)] + U_H[n(r)] + E_{xc}[n(r)] \end{aligned} \qquad (2.56)$$

The notable differences include referring to the kinetic and electron-electron repulsion energy terms as T_s and U_H, respectively, and the addition of the exchange-correlation energy term, E_{xc}. In KS-DFT, the kinetic energy term is split into two contributions, the non-interacting kinetic energy (T_s) and the kinetic energy that arises due to correlation effects (T_c), such that,

$$T[n(r)] = T_s[n(r)] + T_c[n(r)] \qquad (2.57)$$

The correlation component is included in the exchange-correlation energy (*vide infra*). The repulsion energy in KS-DFT is referred to as the Hartree potential, since it is simple the classical electrostatic interaction between the density with itself,

$$U_H[n(r)] = \frac{1}{2}\xi \int \int \frac{n(r)n(r')}{|r-r'|} dr dr' \tag{2.58}$$

Finally, all of the missing energy factors, including electron exchange, correlation, and T_c are grouped into E_{xc}. There exist various approximations for E_{xc}, many of which are discussed in detail in **Chapter 3**.

The KS equation is a simple minimization of the total energy with respect to the KS-orbitals, in order to obtain the orbitals[22],

$$\frac{\delta E_{KS}}{\delta \psi_i(r)} = \left(\frac{\delta T_s}{\delta \psi_i(r)} + \left[\frac{\delta V}{\delta n(r)} + \frac{\delta E_{Hartree}}{\delta n(r)} + \frac{\delta E_{xc}}{\delta n(r)}\right]\right)\frac{\delta n(r)}{\delta \psi_i(r)} = E_i(r)\psi_i(r) \tag{2.59}$$

which simplifies to

$$\frac{\delta E_{KS}}{\delta \psi_i(r)} = -\frac{\hbar}{2m}\nabla_i^2 \psi_i(r) \tag{2.60}$$
$$+ \left[\xi \int \psi_i(r)\frac{Z_I}{|r-R_I|}dr + \frac{1}{2}\xi \int \int \psi_i(r)\frac{n(r')}{|r-r'|}dr dr' + \frac{\delta E_{xc}}{\delta n(r)}\right]\psi_i(r)$$

Where the bracketed term is typically represented by $v_s(r)$. Therefore, the electron density is what is used to determine the one-electron orbitals, using the same method as the Hartree-Fock-Roothaan equation (2.39), specifically using an iterative SCF technique for determining the orbital coefficients (**Figure 2-1**).

There are many similarities between HF and KS-DFT, with only minor differences in the manipulation of the mathematics governing the two techniques. Arguably the most impactful dissimilarity is the explicit exchange and lack of correlation energy in HF and the inclusion of the approximate exch[22]ange-correlation energy in KS-DFT.[20] The next chapter details the various formulations of exchange-correlation functional, as well as describing how the atomic orbitals are modeled, which is applicable to both methods.

2.3 References

1.   Selleri, F., *Wave-Particle Duality*; Springer, 1992.

2.   Heisenberg, W., Physics and Philosophy: The Revolution in Modern Science. **1958**.

3.   Müller-Kirsten, H. J., *Introduction to Quantum Mechanics: Schrödinger Equation and Path Integral*; World Scientific, 2006.

4.   Einstein, A., *A Heuristic Viewpoint Concerning the Production and Transformation of Light*, 1929.

5.   De Broglie, L., The Reinterpretation of Wave Mechanics. *Foundations of Physics* **1970**, *1*, 5-15.

6.   Green, H. S.; Born, M., Matrix Mechanics. **1965**.

7.   Heisenberg, W., *Über Quantentheoretische Umdeutung Kinematischer Und Mechanischer Beziehungen*; Springer, 1985.

8.   Waerden, B. L., *Sources of Quantum Mechanics*; Courier Corporation, 1968; Vol. 5.

9.   Schrödinger, E., An Undulatory Theory of the Mechanics of Atoms and Molecules. *Phys. Rev.* **1926**, *28*, 1049.

10.   Phillips, A. C., *Introduction to Quantum Mechanics*; John Wiley & Sons, 2013.

11.   Leforestier, C.; Bisseling, R.; Cerjan, C.; Feit, M.; Friesner, R.; Guldberg, A.; Hammerich, A.; Jolicard, G.; Karrlein, W.; Meyer, H.-D., A Comparison of Different Propagation Schemes for the Time Dependent Schrödinger Equation. *J. Comput. Phys.* **1991**, *94*, 59-80.

12.   Cohen, L., Hamiltonian Operators Via Feynman Path Integrals. *Journal of Mathematical Physics* **1970**, *11*, 3296-3297.

13.   Planck, M., *The Theory of Heat Radiation*; Courier Corporation, 2013.

14.   Griffiths, D. J.; Harris, E. G., Introduction to Quantum Mechanics. *Am. J. Phys.* **1995**, *63*, 767-768.

15.   Duncan, A., *Rydberg Series in Atoms and Molecules*; Elsevier, 2012; Vol. 23.

16.   Eckert, K.; Schliemann, J.; Bruss, D.; Lewenstein, M., Quantum Correlations in Systems of Indistinguishable Particles. *Annals of Physics* **2002**, *299*, 88-127.

17.   Zanardi, P., Quantum Entanglement in Fermionic Lattices. *Phys. Rev. A* **2002**, *65*, 042101.

18.   Murdin, P., Pauli Exclusion Principle. *Encyclopedia of Astronomy and Astrophysics* **2000**, *1*, 4896.

19.   Kittel, C., *Introduction to Solid State Physics*; Wiley, 2005.

20.   Levine, I. N., *Quantum Chemistry*; Pearson Prentice Hall Upper Saddle River, NJ, 2009; Vol. 6.

21.   Slater, J. C., A Simplification of the Hartree-Fock Method. *Phys. Rev.* **1951**, *81*, 385-390.

22.   Evarestov, R. A., Quantum Chemistry of Solids. **2012**.

23.   Hohenberg, P.; Kohn, W., Inhomogeneous Electron Gas. *Phys. Rev.* **1964**, *136*, B864-B871.

24.   Kohn, W.; Sham, L. J., Self-Consistent Equations Including Exchange and Correlation Effects. *Phys. Rev.* **1965**, *140*, A1133-A1138.

25.   Kohn, W.; Becke, A. D.; Parr, R. G., Density Functional Theory of Electronic Structure. *J. Phys. Chem* **1996**, *100*, 12974-12980.

26.   Bersuker, I. B., Electron Structure and Properties of Coordination Compounds-Introduction to the Theory. *Leningrad Izdatel Khimiia* **1976**, *1*.

27.   Harrison, W. A., *Electronic Structure and the Properties of Solids: The Physics of the Chemical Bond*; Courier Corporation, 2012.

28.   Born, M., Born-Oppenheimer Approximation. *Ann. Physik* **1927**, *84*, 457.

29.   Alexander, M. H.; Capecchi, G.; Werner, H.-J., Theoretical Study of the Validity of the Born-Oppenheimer Approximation in the Cl+ H2→ Hcl+ H Reaction. *Science* **2002**, *296*, 715-718.

30.   Ekeland, I., On the Variational Principle. *J. Math. Anal. Appl.* **1974**, *47*, 324-353.

31.   Sholl, D.; Steckel, J. A., *Density Functional Theory: A Practical Introduction*; John Wiley & Sons, 2011.

32.   Csizmadia, I. G., Theory and Practice of Mo Calculations on Organic Molecules. . *Int. J. Quantum Chem* **1978**, *13*, 159-159.

33.   Gritsenko, O.; Schipper, P.; Baerends, E., Exchange and Correlation Energy in Density Functional Theory: Comparison of Accurate Density Functional Theory Quantities with Traditional Hartree–Fock Based Ones and Generalized Gradient Approximations for the Molecules Li2, N2, F2. *J. Chem. Phys.* **1997**, *107*, 5007-5015.

34.   Lykos, P.; Pratt, G., Discussion on the Hartree-Fock Approximation. *Reviews of Modern Physics* **1963**, *35*, 496.

35.   Kerman, A.; Svenne, J.; Villars, F., Hartree-Fock Calculation for Finite Nuclei with a Nonlocal Two-Body Potential. *Phys. Rev.* **1966**, *147*, 710.

36.   Langhoff, P.; Karplus, M.; Hurst, R., Approximations to Hartree—Fock Perturbation Theory. *J. Chem. Phys.* **1966**, *44*, 505-514.

37. Clementi, E.; Roetti, C., Roothaan-Hartree-Fock Atomic Wavefunctions: Basis Functions and Their Coefficients for Ground and Certain Excited States of Neutral and Ionized Atoms, $Z \leq 54$. *At. Data Nucl. Data Tables* **1974**, *14*, 177-478.

38. McQuarrie, D. A., *Quantum Chemistry*; University Science Books, 2008.

39. Bickelhaupt, F. M.; Baerends, E. J., Kohn-Sham Density Functional Theory: Predicting and Understanding Chemistry. *Reviews in Computational Chemistry, Volume 15* **2007**, 1-86.

CHAPTER 3: Density Functional Theory

3.1 Density Functionals

The previous section describes how the electron density of a system determines all of the observable properties associated with the ground electronic state. The Kohn-Sham Hamiltonian was shown to include two terms, the universal operator that is system-independent, and the exchange-correlation operator, which is not able to be known in its entirety.[1-4] The search for functionals that accurately approximate the exchange-correlation energy has been the subject of countless studies and is an extremely active area of research.[5-8] In this section, the various formulations of the exchange-correlation functional will be described in order of increasing complexity, often referred to as the rungs of Jacob's Ladder (**Figure 3-1**).

Functional
Dependence

Funcational
Examples

Explicit Correlation

$n(r), \nabla n(r),$
$\nabla^2 n(r),$
$\varepsilon_x^{\text{exact}}, \varepsilon_c^{\text{PT2}}$

Double Hybrid

B2-PLYP,
mPW2-PLYP

$n(r), \nabla n(r),$
$\nabla^2 n(r)$

Meta-GGA

M06-2X, TPSS

$n(r), \nabla n(r),$
$\varepsilon_x^{\text{exact}}(r^*)$

Range-Corrected

HSE-06, HISS

$n(r), \nabla n(r),$
$\varepsilon_x^{\text{exact}}$

Hybrid

PBE0, B3LYP

$n(r), \nabla n(r)$

GGA

PBE, BLYP

$n(r)$

LDA

VWN, PW92

Hartree Fock
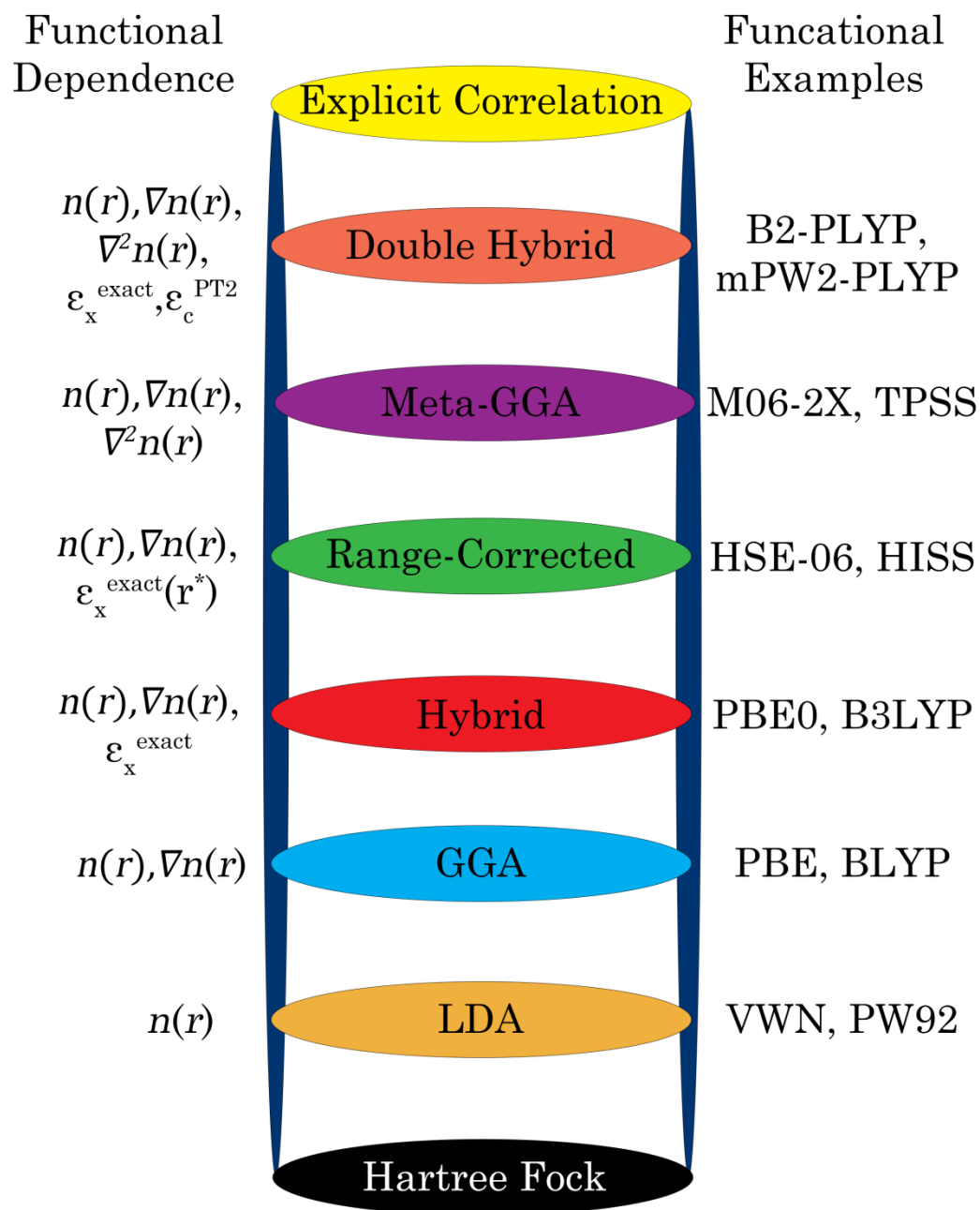
Figure 3-1. The Jacobs Ladder of functional development, showing the functional class in the middle and the dependencies (left) and examples (right).

66

3.1.1 Local Density Approximation (LDA) Functionals

The first and simplest of the exchange-correlation functionals is the Local Density Approximation (LDA).[1, 4, 9-10] In the LDA approach, the exchange-correlation energy, E_{xc}^{LDA}, is dependent on the electron density, $n(r)$, and a functional of the density, $\varepsilon_{xc}^{LDA}[n(r)]$,

$$E_{xc}^{LDA}[n(r)] = \int n(r)\varepsilon_{xc}^{LDA}[n(r)]dr \tag{3.1}$$

The exchange-correlation energy can be decomposed into the sum of the individual exchange and correlation terms,

$$E_{xc}^{LDA} = E_x^{LDA} + E_c^{LDA} \tag{3.2}$$

As the name implies, ε_{xc}^{LDA} must be approximated in some way. The most widely adopted approach uses the exchange-correlation energy of a homogenous electron gas (HEG). The HEG is a theoretical system constructed by placing N interacting electrons in a volume (V), and bringing N to infinity. The exchange energy of this system has an analytical solution, the Dirac exchange energy functional,[11-12] and has the expression,

$$\varepsilon_x^{Dirac}[n(r)] = -\frac{3}{4}\left(\frac{3}{\pi}\right)^{\frac{1}{3}} n(r)^{\frac{1}{3}} \tag{3.3}$$

ultimately yielding the Dirac exchange energy expression,

$$E_x^{Dirac}[n(r)] = \int n(r)\varepsilon_x^{Dirac}[n(r)]dr = -\frac{3}{4}\left(\frac{3}{\pi}\right)^{\frac{1}{3}}\int n(r)^{\frac{4}{3}}dr \qquad (3.4)$$

But while the exchange energy for a HEG is known completely, the correlation energy functional is not. However, values for E_c^{HEG} have been obtained using exact Monte Carlo simulations.[13] The LDA thus uses the E_{xc}^{HEG} as a reference for real systems, and simply relates the calculated density values to the energy of a HEG with the corresponding density (**Figure 3-2**),

$$E_{xc}^{LDA}[n(r)] = E_{xc}^{HEG}[n(r)] \qquad (3.5)$$

Various approaches have been taken to better approximate the correlation energy of real systems, and numerous correlation functionals (ε_c^{LDA}) have been developed, namely Vosko-Wilk-Nusair (VWN)[14], von Barth-Hedin (VBH)[15], Perdew-Zunger (PZ81)[16], and Perdew-Wang (PW92)[17].

The LDA method has proven to be effective, but many of the successes are most likely due to cancellation of errors rather than true chemical accuracy.[18-19] Conversely, the LDA commonly predicts over-binding, exhibiting cohesive energies that are larger than experimental values.[20-21] Specifically concerning solid-materials, this over binding results in lattice constants that are too small. Moreover, the LDA usually under-estimates electronic band gaps, further hindering its utility in high-level theoretical work.[22-23] Attempts to modify the LDA functional form (*i.e.* including Taylor expansions) were unsuccessful, and led to the development of more advanced techniques, specifically the generalized-gradient approximation.
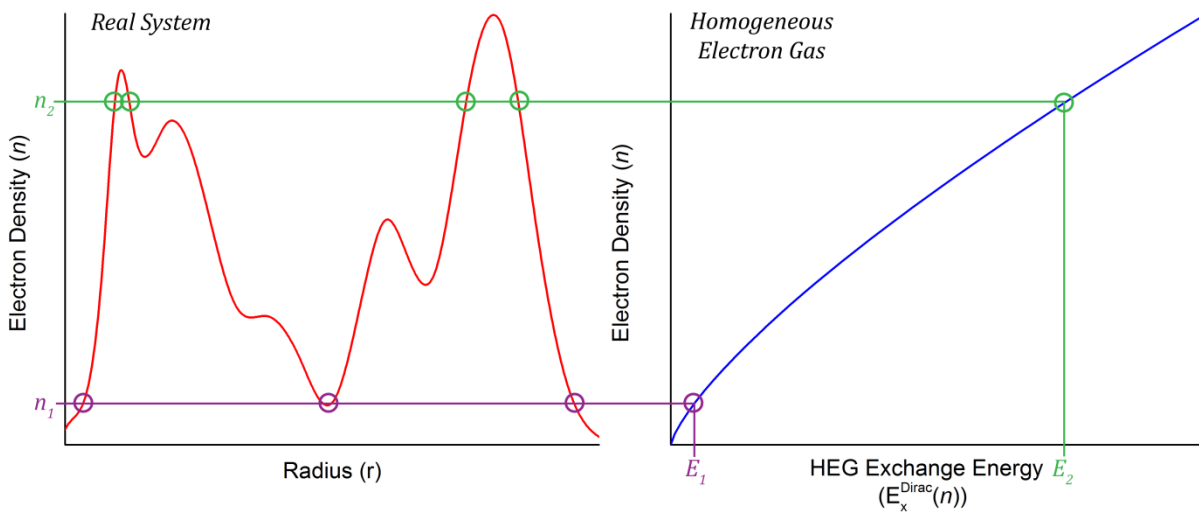
Figure 3-2. Comparison between the electron density (n(r)) of a real system and the homogeneous electron gas in order to determine the exchange energy $E_x^{Dirac}(n(r))$. This is illustrated for two densities, n_1 and n_2, that have corresponding exchange energies of E_1 and E_2.

3.1.2 Generalized Gradient Approximation (GGA) Functionals

The construction of the LDA makes it exact when considering materials of uniform electron density. Systems that slowly vary in their electron density distribution can be considered within this limit and are often well modelled by the LDA.[4] But most systems, especially those that involve covalent bonds, usually exhibit rapid changes in the election density within small regions and the LDA is insufficient in this regard.[24] The inclusion of the gradient of the electron density into the exchange-correlation functional, known as the generalized gradient approximation (GGA), improves on the LDA by giving the functional greater flexibility for dealing with the rapid changes in electron density found in real systems.[25-27] In the GGA, the exchange-correlation functional is expressed in terms of both the local electron density and the gradient of the density

$$E_{xc}^{GGA}[n(r)] = \int n(r)\varepsilon_{xc}^{GGA}[n(r), \nabla n(r)]dr \qquad (3.6)$$

It is important to note that while the literature often refers to the GGA as 'nonlocal', this is not accurate as all values depend on the local electron density.[27] It is not uncommon for GGA functionals to incorporate the energy of a HEG, effectively including the LDA into the functional form. For example, the well-known Perdew-Burke-Ernzerhof (PBE) exchange functional has the form[28-29]

$$E_{x}^{PBE}[n(r)] = \int n(r)\varepsilon_{x}^{Dirac}[n(r)]F_{x}^{PBE}[n(r), \nabla n(r)]dr \qquad (3.7)$$

70

where F_x^{PBE} represents the exchange enhancement factor, which augments the Dirac exchange functional by incorporating the gradient of the density,

$$F_x^{PBE} = 1 + \kappa \left(1 - \frac{1}{1 + \frac{x}{\kappa}} \right)$$

(3.8)

where $x = \mu p$, κ and μ are constants, and

$$p = \left(\frac{|\nabla n(r)|}{2(3\pi^2)^{1/3} n(r)^{4/3}} \right)^2.$$

(3.9)

It becomes obvious that the GGA functional form is much more flexible than the LDA functionals, because of the greater degrees of freedom that the gradient expansions allow. A large advantage when generating GGA functionals is the choice of constant parameters, which can either be chosen purely from first principles (as in PBE), or empirically (as in the Becke-Lee-Yang-Parr[30-31] (BLYP) exchange-correlation functional).

The results obtained using GGA functionals typically surpass those of pure LDA methods.[5, 10, 25] The GGA has found widespread use throughout the computational fields, and GGA functionals can be found almost ubiquitously throughout quantum mechanical software packages.

3.1.3 Hybrid Functionals

In 1993, Axel Becke introduced the first hybrid functional, which aimed to improve upon the GGA method by including a percentage of exact Hartree-Fock exchange into the exchange-correlation energy.[32-33] The idea was born out of the Adiabatic Connection formula,[34] a technique that attempts to interpolate between a non-interacting (no correlation, *ie.* Hartree-Fock) and a real system to yield an exchange correlation energy as a continuous function of particle interaction,[33]

$$E_{xc}^{Adiabatic} = \int_0^1 V(\lambda)_{xc} d\lambda \qquad (3.10)$$

where λ is the interelectronic coupling parameter that represents a completely non-interacting and a fully interacting system when equal to 0 and 1, respectively. The integral therefore represents a continuum of partially interacting systems, and by carefully selecting a value for λ a balance between exact Hartree-Fock and LDA methods can be struck. Invoking a simple two-point approximation, $(E_{xc,\lambda=0}^{Adiabatic} + E_{xc,\lambda=1}^{Adiabatic})/2$, yields the hybrid exchange-correlation energy that forms the basis for modern hybrid functionals,

$$E_{xc}^{Adiabatic} = \frac{1}{2}E_x^{HF} + \frac{1}{2}(E_x^{LDA} + E_c^{LDA}) \qquad (3.11)$$

Arguably the most well-known hybrid functional is the Beck-3-parameter-Lee-Yang-Parr (B3LYP) functional, built from the B88 (B) exchange and Lee-Yang-Par (LYP) correlation functionals.[32] The three-parameters referenced in the name refer to the linear combination

coefficients (a_0, a_x, and a_c) used to mix the LDA exchange-correlation energies (E_{xc}^{LDA}) with the HF and GGA exchange-correlation energies (E_x^{HF}, E_x^B, and E_c^{LYP}),

$$E_{xc}^{B3LYP} = E_x^{LDA} + a_0(E_x^{HF} - E_x^{LDA}) + a_x(E_x^B - E_x^{LDA}) + E_c^{LDA} + a_c(E_c^{LYP} - E_c^{LDA}) \qquad (3.12)$$

In B3LYP, the three constants were determined empirically by fitting data to experimental thermochemical data, and are set to $a_0 = 0.20$, $a_x = 0.72$, and $a_c = 0.81$.

The development of hybrid functionals has led to a rich research field of functional determination.[5, 35-37] Unlike the LDA functionals, a high level of customization is possible when developing hybrids, because the base functionals and mixing percentages can be varied at will. Just like the GGA, some functionals are strictly *ab initio* (like the PBE0 hybrid functional[38-39]), while others are empirical (B3LYP). Hybrid functionals have had an overwhelming amount of success, often predicting electronic, structural, vibrational, and thermodynamic parameters close to experimentally determined values.[10, 36, 40-42]

3.1.4 Range-Separated Hybrid (RSH) Functionals

Despite the differences between the three aforementioned functional classes, they are all dependent on local electron density (despite any references to non-locality), and thus any range-dependent phenomena (*i.e.* charge transfer dynamics[43-44]) are not well-reproduced.[45-47] Range-separated hybrid (RSH) functionals attempt to correct these issues by including exact Hartree-Fock exchange contributions in specific regions of space by scaling the exchange potential by a position dependent function.[48-51] This is performed by splitting the Coulomb operator into short (SR), medium (MR), and long-range (LR) components,

$$\frac{1}{r} = \underbrace{\frac{1 - erf(\omega_{SR}r)}{r}}_{SR} + \underbrace{\frac{erf(\omega_{SR}r) - erf(\omega_{LR}r)}{r}}_{MR} + \underbrace{\frac{erf(\omega_{LR}r)}{r}}_{LR} \quad (3.13)$$

where erf is the error function, and ω is an adjustable parameter defining the length scale of the range-separation. The range-separated hybrid exchange-correlation energy then takes the general form

$$E_{xc}^{RSH} = E_c^{DF} + c_{SR}\left(E_x^{SR,HF} - E_x^{SR,DF}\right) + c_{MR}\left(E_x^{MR,HF} - E_x^{MR,DF}\right) + c_{LR}\left(E_x^{LR,HF} - E_x^{LR,DF}\right) \quad (3.14)$$

where E_{xc}^{DF} is the exchange-correlation energy of any particular density functional and the degree of range correction is determined by the coefficients c_{SR}, c_{MR}, and c_{LR}. For example, the short-range corrected HSE06 functional[52] uses scales the SR and LR components inversely,

$$\frac{1}{r} = \underbrace{\frac{1 - erf(\omega r)}{r}}_{SR} + \underbrace{\frac{erf(\omega r)}{r}}_{LR} \quad (3.15)$$

Generating the HSE06 exchange-correlation energy as,

$$E_{xc}^{HSE06} = \frac{1}{4}E_x^{SR,HF}(\omega) + \frac{3}{4}E_x^{SR,PBE}(\omega) + E_x^{LR,PBE}(\omega) + E_c^{PBE} \quad (3.16)$$

It is interesting to highlight that when $\omega = 0$ the LR component goes to zero and the functional energy is equivalent to PBE0, while when $\omega = \infty$ the SR component goes to zero and the functional is equivalent to PBE. The published formulation of HSE06 has $\omega = 0.11a_0^{-1}$.

Similar to the tuning allowed in hybrid functional generation, the RSH functionals can be customized to large extent by changing ω and c_{XR}, as well as in the selection of base exchange-correlation functionals. Four different types of RSH have been developed, namely short ($c_{SR} \neq 0$, $c_{MR} = c_{LR} = 0$, HSE06), middle ($c_{SR} = c_{LR} = 0$, $c_{MR} \neq 0$, HISS), long ($c_{SR} = c_{MR} = 0$, $c_{LR} \neq 0$, LC-wPBE), and dual ($c_{SR} \neq 0$, $c_{LR} \neq 0$, $c_{MR} = 0$ wB97-X) range-corrected hybrids.[46, 48-50, 52-53]

3.1.5 Meta-Global Gradient Approximation (mGGA) Functionals

Meta-Global Gradient Approximation (mGGA) functionals represent the fifth rung of Jacobs Ladder, and advance the technique introduced by GGA functionals by not only including the gradient of the electron density, but also including the kinetic energy density (τ, the Laplacian (second derivative) of atomic orbitals),[8, 41, 54-56]

$$\tau(r) = \sum_{i}^{occupied} \frac{1}{2} |\nabla \psi_i(r)|^2 \tag{3.17}$$

resulting in the functional formulation,[40]

$$E_{xc}^{mGGA}[n(r)] = \int n(r) \varepsilon_{xc}^{GGA}[n(r), \nabla n(r), \tau(r)] dr \tag{3.18}$$

The Laplacian of the occupied atomic orbitals represents a non-local functional of the density. By including the non-local quantity, range effects can be effectively taken into account without

75

the need for mixing contributions of exact Hartree-Fock exchange, as is done in the RSH

methods. The mGGA functionals are built in a similar fashion to GGA functionals, for example

the M06-L mGGA exchange functional[56] has the form

$$E_x^{M06-L}[n(r)] = \int n(r)\varepsilon_x^{HEG}[n(r)]F_x^{PBE}[n(r), \nabla\rho(r)]f_x^{M06-L}[\tau(r)]dr \qquad (3.19)$$

where F_x^{PBE} is the PBE exchange energy enhancement factor (eqn. 3.8) and f_x^{M06-L} is the

kinetic energy enhancement factor given by,

$$f_x^{M06-L} = \int \frac{\tau(r)^{LDA} - \tau(r)^{M06-L}}{\tau(r)^{LDA} + \tau(r)^{M06-L}} \, dr \qquad (3.20)$$

where

$$\tau(r)^{LDA} = \frac{3}{10}(6\pi^2)^{2/3}n(r)^{5/3} \qquad (3.21)$$

The mGGA family of functionals is less tunable than hybrid or RSH functionals;

however the inclusion of the kinetic energy density in the functional framework leads is an

elegant technique for including non-local properties without arbitrary parameterization. The

difference between various mGGA functionals is found in the enhancement factors, and there are

many different mGGA functionals available in modern computational software packages,

including TPSS[40], M06-L[56], and M06-2X[8], to name a few.

3.1.6 Additional Density Functional Methods

The functional types listed above represent the current state-of-the-art techniques, however the field of functional development is broad and new methodologies are regularly being developed.[57-61] One of the largest shortcomings with density functional methodologies is the lack of explicit electron correlation, which is required in order to accurately calculate many properties of real systems.[59, 62-66] By far the largest consequence of this is the inherent inability for simulating non-covalent London dispersion interactions.[67-70] There have been many attempts at improving this, ranging from explicit calculation of electron correlation within the functional framework to *ex post facto* empirical and semi-empirical methods.[62, 69, 71-74] Coupled cluster[75-76] and Møller–Plesset (MP2, MP4, MP5, etc…) perturbation theory[77-79] are two of the more fully *ab initio* methods, and have been used with success on many small to medium sized systems. The most cutting edge density functional formulations, the double-hybrid (DH) functionals attempt to incorporate Görling-Levy perturbation theory (PT2)[80] correlation energy into the functional form,[81-84]

$$E_{xc}^{DH} = (1 - a)E_x^{DF} + aE_x^{HF} + (1 - b)E_c^{DF} + bE_c^{PT2}$$

(3.22)

These functionals are only beginning to be developed; however, the calculation of explicit electron correlation is very computationally expensive and is currently limited to small systems. Yet DH functionals show promise, but additional testing is required to fully gauge their capabilities and utility in *ab initio* simulations.[81-85]

3.2 London Dispersion Corrections

Alternatives to the explicit calculation of electron correlation have been developed for calculating London dispersion-related properties,[86-89] but the most popular are the semi-empirical methods introduced by Grimme.[74] Two of the techniques will be discussed here, known as the D2[73] and D3[72] methods. While the two techniques differ in their formulation, the manner in which the dispersion energy is added to the system is identical.

3.2.1 Grimme D2 Dispersion Correction

At the completion of the self-consistent field calculation, the pure DFT energy (E_{DFT}) augmented with the semi-empirical London dispersion energy (E_{disp}),

$$E_{DFT+D} = E_{DFT} + E_{disp} \tag{3.23}$$

with the dispersion correction given by,

$$E_{disp} = -s_6 \sum_{I}^{N} \sum_{J \neq I}^{N} \frac{C_6^{IJ}}{R_{IJ}^6} f_{dmp}(R_{AB}) \tag{3.24}$$

where s_6 is a global scaling factor, N is the number of atoms with indices I and J, C_6^{IJ} is the sixth-order dispersion coefficient for atom pair IJ, and R_{IJ} is the distance between atoms A and B.

In order to avoid singularities for small R_{IJ}, a damping function f_{dmp} is used, which has the form,

$$f_{dmp}(R_{IJ}) = \frac{1}{1 + e^{-d(\frac{R_{IJ}}{R_r}-1)}} \quad (3.25)$$

Here, d represents the steepness of the damping function and is a constant ($d = 20$), and R_r is the sum of the atomic van der Waal radii ($R_r = R_{vdw}^I + R_{vdw}^J$). The C_6^{IJ} coefficients are calculated from the mean of previously determined atomic C_6 coefficients,

$$C_6^{IJ} = \sqrt{C_6^I C_6^J} \quad (3.26)$$

where the atomic C_6 coefficients have been calculated by Grimme using the DFT/PBE0[38] calculations of atomic ionization potentials I_p and static dipole polarizabilites α,

$$C_6^a = 0.05 N I_p^a \alpha^a \quad (3.27)$$

where N has values of 2, 10, 18, 36, and 54 for atoms from rows 1-5 of the periodic table, respectively. In the D2 method, the proportionality constant in (3.27) was determined by simultaneously fitting the data to previously determined C_6 values, as well as the binding energies and bond distances of noble gas dimers.[55, 90] This is the largest criticism of the D2 method, due to the empirical nature of the reported C_6 coefficients.[59, 62] The D2 method of Grimme is an improvement over more empirical methods, and requires little user input other than providing the s_6 scaling coefficient. It has proven to be an effective technique for

79

reproducing dispersion related effects, having been tested on highly correlated systems such as noble-gas dimers and molecular crystals.[69, 71, 91-92]

3.2.2 Grimme D3 Dispersion Correction

Recently, Grimme introduced the D3 method, which is even less empirical than the D2 method and requires virtually no user input.[72] One of the major improvements of the D3 method is that the C_6^{IJ} coefficients are no longer based on empirical measurements and instead were calculated *ab initio* from time-dependent (TD-DFT) calculations. The foundation for this is the Casimir-Polder formula,[93-94]

$$C_6^{IJ} = \frac{3}{\pi} \int_0^\infty \alpha^I(i\omega)\alpha^J(i\omega)d\omega \tag{3.28}$$

where $\alpha^I(i\omega)$ is the averaged dipole polarizability of atom I at imaginary frequency ω. In theory this formula could be used to easily calculate the C_6^{IJ} coefficient for any pair of atoms, but that would lead to an inconsistent treatment of dispersion interactions in and between molecules because the polarizaiabilities of free atoms are often much different than covalently bonded atoms. Therefore, Grimme *et al.* based the calculation of C_6^{IJ} coefficients on calculations of atomic-hydride species (I_mH_n and J_kH_l, where $m, n, k,$ and l are stoichiometric factors), followed by removal of the contribution from the hydrogens,

$$C_6^{IJ} = \frac{3}{\pi} \int_0^\infty \frac{1}{m}\left[\alpha^{I_mH_n}(i\omega) - \frac{n}{2}\alpha^{H_2}(i\omega)\right] \times \frac{1}{k}\left[\alpha^{J_kH_l}(i\omega) - \frac{l}{2}\alpha^{H_2}(i\omega)\right]d\omega \tag{3.29}$$

While at first this method of determining the C_6^{IJ} coefficients may seem to be a more empirical method because of its dependence on reference molecule choice, this is avoided by the second major D3 improvement that determines the atomic C_6 coefficients on a system-by-system basis by taking chemical environment into account. Grimme *et al.* propose what they term 'coordination number dependent' dispersion coefficients, although the term is slightly misleading in that it is applicable the entire chemical and hybridization environment rather than only coordination complexes. The approach is based on the concept of fractional coordination number (CN), which attempts to classify the number of bonded neighbors to an atom *A* using a counting function,

$$CN^I = \sum_{J \neq I}^{N} \frac{1}{1 + e^{-k_1 \left(k_2 \frac{(R_{I,cov} + R_{J,cov})}{r_{AB}} - 1 \right)}}$$

(3.30)

where $R_{I,cov}$ and $R_{J,cov}$ are the single-bond radii of atoms *I* and *J*, respectively, and k_1 and k_2 are scale factors that were chosen to best reproduce CN for carbon in ethyne, ethene, and ethane (~2, 3, and 4, respectively). Taking CN into account, the system-dependent C_6^{IJ} are determined,

$$C_6^{IJ}(CN^I, CN^J) = \frac{Z}{W}$$

(3.31)

where

$$Z = \sum_{A}^{N_I} \sum_{B}^{N_J} C_{6,ref}^{IJ} \left(CN_A^I, CN_B^J \right) L_{AB}$$

(3.32)

$$W = \sum_{A}^{N_I} \sum_{B}^{N_J} L_{AB} \tag{3.33}$$

$$L_{AB} = e^{-k_3 \left[\left(CN^I - CN_A^J \right)^2 + \left(CN^J - CN_B^J \right)^2 \right]} \tag{3.34}$$

Here, L_{AB} is a Gaussian weighted average with A and B representing the two reference systems that have coordination numbers and a dispersion coefficient of CN_A^J, CN_B^J, and $C_{6,ref}^{IJ}$ respectively. Thus, the final dispersion coefficients for any particular system are a result of interpolating between numerous *ab initio* C_6^{IJ} reference systems (227 systems total) while taking chemical environment into consideration through the use of the CN weighting scheme. This drastically reduces the empirical nature of the dispersion correction, and provides a vast improvement over the methods used in the D2 scheme.

Additionally, The D3 method has a number of other modifications that represent improvements over D2, principally the inclusion of the higher order C_8 dispersion coefficients and three-body dispersion interactions. The C_8^{IJ} coefficients are calculated recursively using the C_6^{IJ} coefficients,

$$C_8^{IJ} = 3 C_6^{IJ} \sqrt{Q^I Q^J} \tag{3.35}$$

where

$$Q = s_{42} \sqrt{Z} \frac{\langle r^4 \rangle}{\langle r^2 \rangle} \tag{3.36}$$

with s_{42} being a scaling factor that was determined by fitting the C_8^{IJ} values to noble gas dimers, Z the nuclear charge, and $\langle r^4 \rangle$ and $\langle r^2 \rangle$ being multiple-type expectation values derived from atomic densities. The three-body dispersion interaction energy is taken into account by

$$E^{IJK} = \frac{C_9^{IJK} (3\cos\theta_{IJ}\cos\theta_{JK}\cos\theta_{IK} + 1)}{R_{IJ}R_{JK}R_{IK}} \tag{3.37}$$

where the three-body dispersion coefficient, C_9^{IJK}, is a geometric mean of the atomic C_6 coefficients,

$$C_9^{IJK} = -\sqrt{C_6^{IJ} C_6^{JK} C_6^{IK}} \tag{3.38}$$

Finally, the three-body term is damped similarly to the pairwise term, yielding the total three-body dispersion energy of a system as

$$E^{(3)} = \sum_{IJK} f_{damp,(3)}(R_{IJK})E^{(IJK)} \tag{3.39}$$

Overall, the two methods by Grimme represent effective methods of describing the dispersion interactions in systems of any size or state with a low computational cost. The D3 method is an improvement over D2, both in the manner in which it handles the selection of the C_6 as well as by the inclusion of higher-order and three-body dispersion coefficients.

3.3 Basis Sets

Recalling the Hartree-Fock and Kohn-Sham theories from Chapter 2, both methods (while different) both have the same foundation, the electrons are treated independently by one-electron wavefunctions (ψ, molecular orbitals) and the initial step involves construction of the many-body wavefunction (Ψ) using the Slater determinant (Hartree-Fock, (3.40)) or by calculating the electron density (Kohn-Sham DFT, (3.41)) using the one-electron wavefunctions.

$$\Psi(r) = \frac{1}{\sqrt{2}} \begin{vmatrix} \psi_i(r) & \psi_i(r) \\ \psi_j(r') & \psi_j(r') \end{vmatrix} \tag{3.40}$$

$$\Psi(r) \propto n(r) = \sum_i |\psi_i(r)|^2 \tag{3.41}$$

But the problem of constructing the one-electron wavefunction still remains, which is normally done by taking a linear combination of hydrogenic atomic orbitals, φ,[95-96]

$$\psi_i(r) = \sum_\mu a_{i,\mu} \, \varphi_\mu(r) \tag{3.42}$$

where $a_{i,j}$ are orbital coefficients unique to the molecular and atomic orbitals that have indices of i and μ, respectively. While chemical intuition suggests that simply using the set of atomic orbitals that exist on each atom-type as a basis (*i.e.* a single 1s function for hydrogen), this would not be sufficient for describing most bonding scenarios. This point can be illustrated using the hydroxyl radical, where a covalent bond is formed using what many chemists would describe as a *sp* hybridized orbital, requiring a *p*-type orbital on hydrogen in order to accurately represent it.

And while the addition of a *p*-type orbital to hydrogen would sufficiently capture that interaction, it is not limited mathematically to such a solution. For example, instead of using atom-centered atomic orbitals, a set of many plane waves can be summed (Fourier sum) to yield the same mathematical representation of the molecular orbital, and to ultimately yield the same result (**Figure 3-3**).

Thus, any combination of mathematical functions, known as a basis sets, can be used so long as the end result provides flexibility for the system to adjust to any particular scenario, and this is where a balance between basis set size and computational efficiency must be struck. Clearly an infinite basis would give the correct answer, but would be impossible to use computationally, while too small a basis set would constrict system and likely lead to an incorrect result.[4, 97-98] Therefore, much like the field of functional development, the construction and choice of basis set is an extremely active area of research that is constantly producing new methods and styles of basis functions. Here, the two basis set styles, atom-centered and plane wave, will be discussed and the relevant parameters discussed.
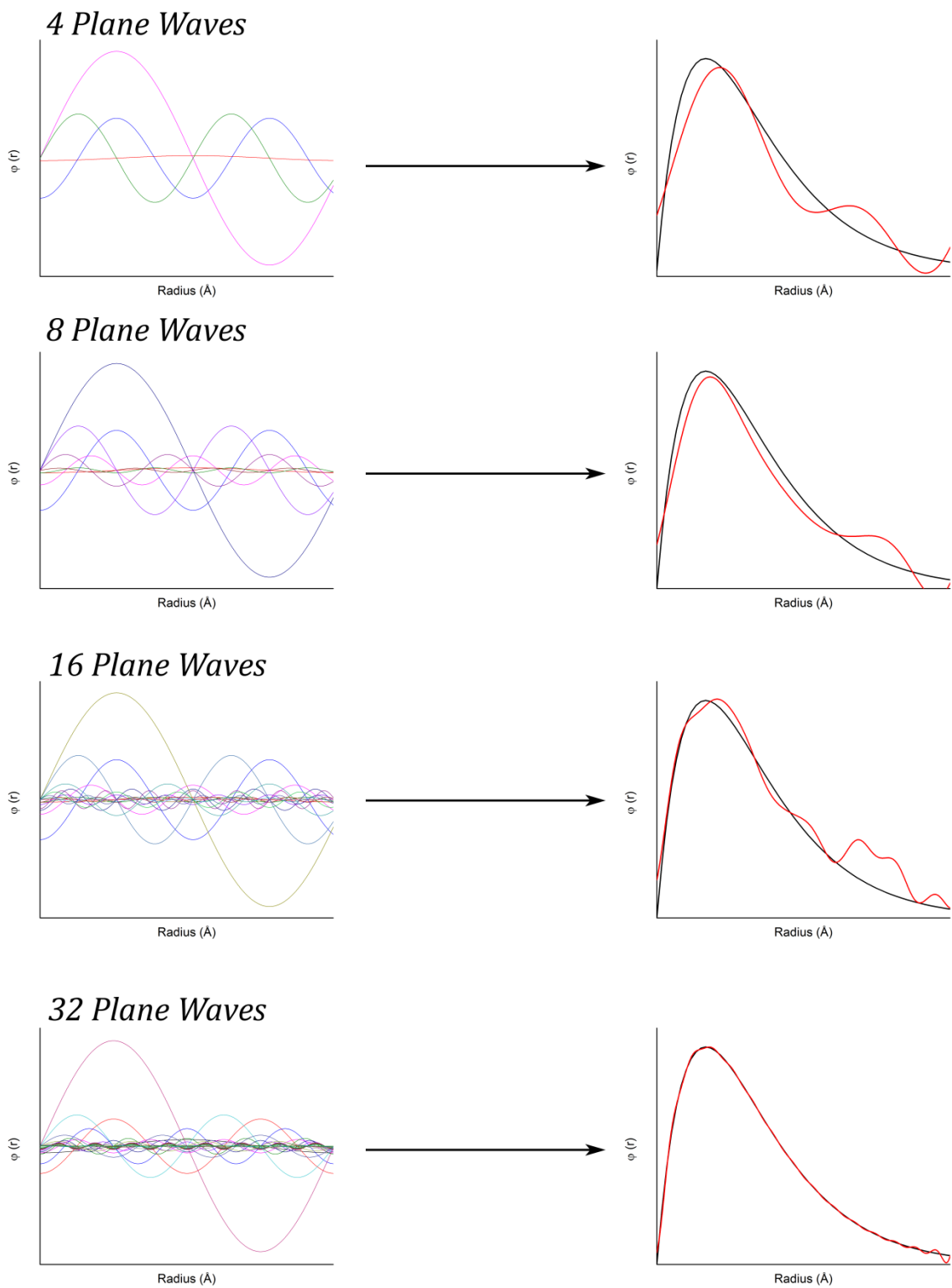
Figure 3-3. Result of using an increasing set of plane waves to reproduce a hydrogen 1*s* **orbital.**

3.3.1 Atom-Centered Basis Sets

Atom-centered basis sets are, as the name implies, functions that are centered on the atomic nuclei. They can be constructed using any mathematical function, but are usually expressed as either Slater-type orbitals (STOs) or Gaussian-type orbitals (GTOs) (**Figure 3-4**).[99-100] The atomic orbitals are then represented by a linear combination of primitive functions (γ) multiplied by a corresponding coefficient d_n,

$$\varphi(\gamma_1, \gamma_2, \dots, \gamma_i) = \sum_n d_n \gamma_n(\alpha, r) \tag{3.43}$$

where γ_n is a function of radius and Gaussian exponent (r and α, respectively).[96, 101-102] The primary choices of primitive functions are the Slater and Gaussian functions that have the forms

$$\gamma^{STO}(\alpha, r) = e^{-\alpha r} \tag{3.44}$$

$$\gamma^{GTO}(\alpha, r) = e^{-\alpha r^2} \tag{3.45}$$

While STOs are better suited for reproducing the hydrogen atomic orbitals, primarily near and far from the nucleus (the cusp and exponential decay, respectively), they are computationally ineffective because the product of two STOs does not yield a STO.[1] On the other hand, GTOs are multiplicative, because the product of two GTOs yields a new single GTO. This has major implications for computationally efficiency, as any multi-centered integrals can be reduced to simpler two-center integrals.[103-105] Moreover, the use of GTOs permits analytical first- and second-derivatives of the energy to be taken, which has consequences for optimization of

molecular structure.[106-107] Therefore, the computational cost of using more GTOs is negated by the advantages, and this is the reason most atom-centered basis sets are based on GTOs rather than STOs. For the remainder of the discussion only GTOs will be discussed.
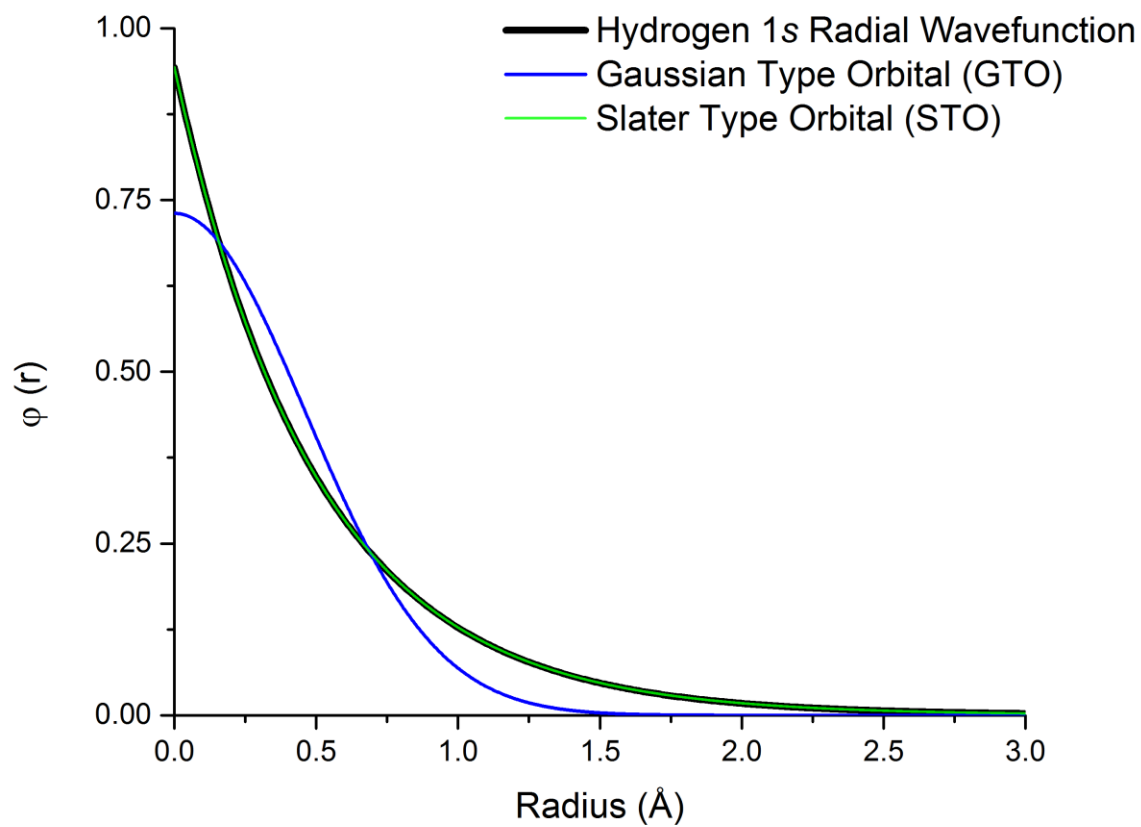
Figure 3-4. Comparison between the hydrogen 1*s* radial wavefunction (black) and the two types of primitive basis functions, the STO (green) and GTO (blue).

As mentioned, computational accuracy can be increased through the use of larger basis sets, and the simplest solution to this is the choice of the number or primitive functions used for constructing the GTOs. Three STO-nG basis functions (a basis set constructed from n primitive Gaussian functions) are shown in **Figure 3-5**, and as the number of primitive Gaussian functions is increased the deviations from the hydrogenic 1s orbital are decreased.[103] However, as previously mentioned, simply reproducing the occupied atomic orbitals mathematically does not (and usually will not) result in a better simulation. Therefore, the number of GTOs per atomic orbitals are usually increased to provide more flexibility by the computational algorithms.
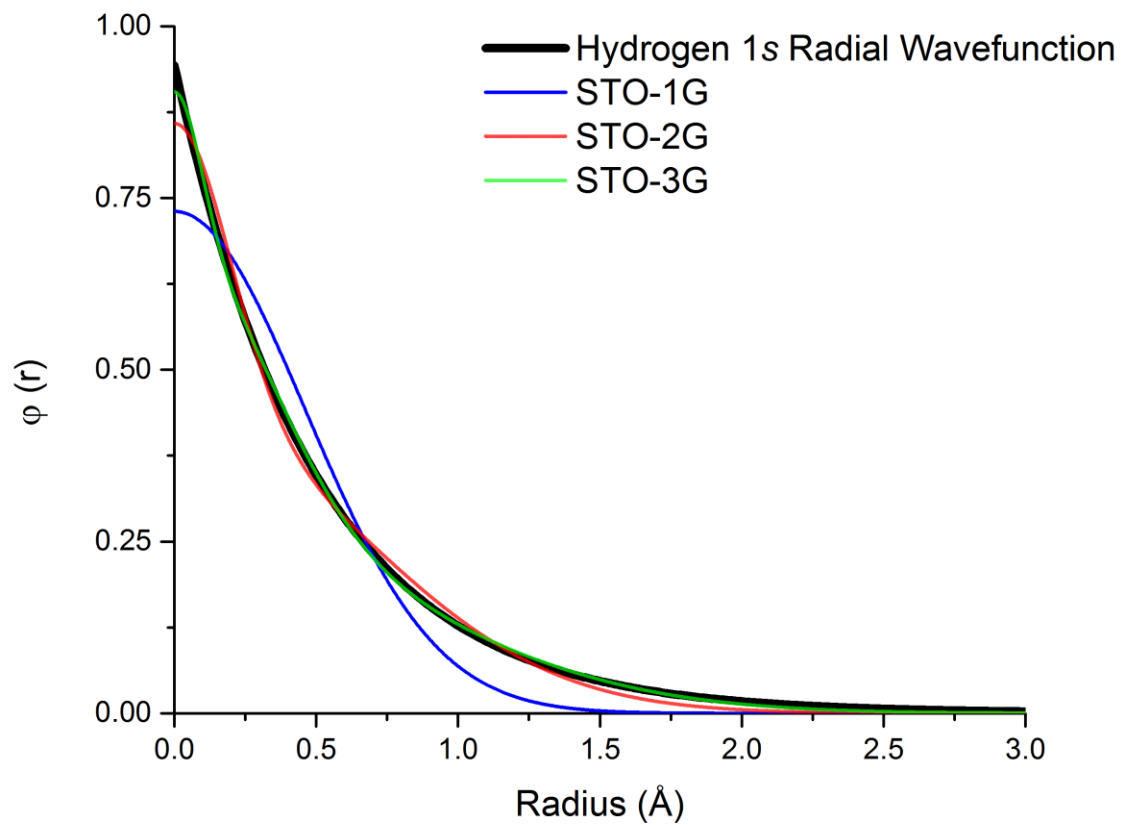
Figure 3-5. Visualization of the role that the number of primitive Gaussian functions has on the reproduction of the hydrogen 1*s* **wavefunction.**

The simplest case of using a single GTO for each occupied atomic orbital is what is known as a minimal basis set. Examples of minimal basis sets are the STO-nG and MIDI![108] sets, and are usually not very effective for most systems, with the exception of single-atom calculations.[109-111] Increasing the number of GTOs per atomic orbital results in the X-ζ (X=double, triple, …) basis sets; for example a triple-ζ basis set for hydrogen would have three $1s$ GTOs. But while the primitive functions of a GTO are typically input by the user during a calculation and fixed, the molecular orbitals are built by varying the linear combination of the individual GTOs by adjusting of the GTO coefficients iteratively. Thus, defining multiple GTOs for a particular orbital allows for a greater degree of flexibility, enabling a more accurate representation of the molecular orbitals to be found. For example, imagining that a hydrogen atom begins to be perturbed in some way (*e.g.* during the formation of a covalent bond or upon application of an electric field), the hydrogen radial distribution function would change accordingly. If this type of system was modelled using a minimal basis set, this perturbation would not be captured. However if a larger basis set, such as a triple-zeta set, were used, the perturbation is more likely to be well modelled because of the flexibility attained. This example is shown graphically in **Figure 3-6,** where an arbitrary *p*-type hybridization has been applied to a hydrogen $1s$ orbital while the resulting best fit basis function was calculated using the STO-3G and triple-ζ 6-311G basis sets.[101]
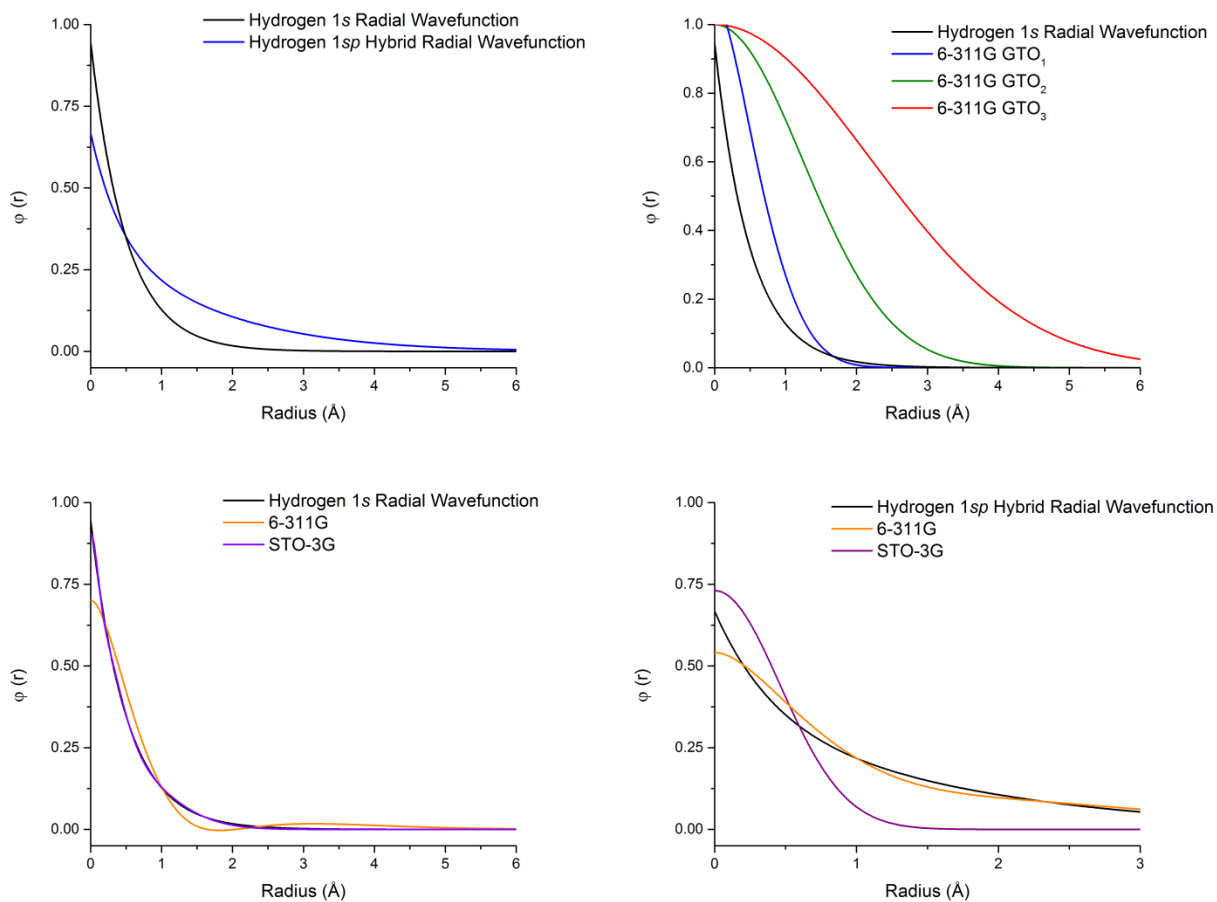
Figure 3-6. Example of the flexibility of a triple-ζ basis, containing three separate *s*-type orbital functions (top right), for both the hydrogen 1*s* radial wavefunction as well as an *sp*-type orbital (top left) compared to a minimal basis set. The minimal set accurately reproduces the unperturbed wavefunction (bottom left), but fails when the wavefunction deviates too much from the ideal 1*s* wavefunction (bottom right).

There are countless methods for improving basis set quality while reducing computational cost. One of the most effective is the split-valence basis set formulation, where the core atomic orbitals are represented by a minimal basis (one GTO per core orbital) but have multiple GTOs for the valence orbitals. These basis sets are by far the most common atom-centered basis sets, with much of the pioneering work done by John Pople, whose basis sets have the notation[96-97, 101-103]

$$W - XYZ \dots G \tag{3.46}$$

where W is the number of primitive Gaussian functions used to describe the core GTO and XYZ are the number of primitive Gaussian functions used to describe the first and second (in the case of a double-ζ) and third (in the case of a triple-ζ) valence GTOs. For example, the split-valence triple-ζ 6-311G basis set of lithium has a single $1s$ GTO that is described by 6 primitive Gaussian functions, and three $2s$ GTOs described by three, one, and one primitive Gaussian functions, respectively.

Additionally, basis sets can be augmented with additional functions to further facilitate computational flexibility. The two most common methods involve inclusion of polarization or diffuse basis functions.[102, 112-114] Polarization functions are orbitals that have an angular momentum higher than what is typically occupied, providing a more efficient means for simulating hybridized atomic orbitals.[102, 115] Diffuse functions are very broad GTOs (small α exponent) that are added somewhat arbitrarily to allow for large-scale displacements of the electron from the nuclei. Diffuse functions are necessary for anions and highly polarizable systems,[114] but often cannot be used in condensed phase simulations due to the propensity for artificial overlap with neighboring molecules, often promoting spurious conduction.[116-117]

Polarization and diffuse functions are typically use the notations * and +, respectively. However for polarization functions in particular it is becoming more conventional to use the polarization orbital lettering explicitly, for instance for the split-valence triple-ζ basis set with polarization functions added to hydrogen (*p* function) and carbon (*d* function), the following notations are equivalent

$$6\text{-}311G(d,p) = 6\text{-}311G^{**} \tag{3.47}$$

However, if two polarization functions are added there is no method of conveying this using the asterisk notation,

$$6\text{-}311G(2d,2p) \neq 6\text{-}311G^{****} \tag{3.48}$$

and therefore the alphanumeric labelling is preferred. Furthermore, confusion can arise when the added polarization function is not a *d* function (such as when adding a polarization function to a zinc atom), as both 6-311G(d) and 6-311G(f) are often applied interchangeably.

It is important to note that while the atomic orbitals are represented here in one-dimension, atomic wavefunctions are three-dimensional and must be constructed with both the radial and angular components. Therefore, the GTOs are transformed into 'real' atomic wavefunctions using the spherical harmonics, and then the molecular orbital built by varying the GTO coefficients,

$$\varphi(r,\theta,\phi) = \sum_n Y_{i,m,l}(\theta,\phi) d_n \gamma_n(\alpha_i,r) \tag{3.49}$$

This is rather trivial to perform, but this transformation has implications for computational efficiency. The transformation from a single GTO to atomic wavefunctions generates (with the exception of *s* orbitals), multiple wavefunctions, *i.e.* 3, 5, and 7 atomic orbitals per GTO for *p*, *d*, and *f*-type orbitals, respectively. Because of this, computational cost scales by N^4, where *N* is the number of basis functions. This is yet another reason why basis set selection is a very important decision when performing *ab initio* calculations.

3.3.2 Plane Wave Basis Sets

While chemists view of molecular structure leads to a bias for using atom-centered basis sets to construct molecular orbitals, physicists tend to prefer treating the molecular orbital as a whole using a sum of continuous plane waves, λ (see **Figure 3-3**),[118-119]

$$\psi(r) = \sum_n a_n \lambda_n(\alpha, r) \tag{3.50}$$

where

$$\lambda(\alpha, r) = e^{i\alpha r} \tag{3.51}$$

It is interesting to note that unlike the construction of molecular orbitals using atom-centered basis sets, the primitive PW functions are directly summed to yield the molecular orbital, there is no intermediate step of first creating the atomic orbitals. In fact, the concept of atomic orbitals does not truly exist when using a PW basis, which is one of the criticisms of using this technique.[1] It is appealing though because it is universal, and the only input condition for any

system is the number of PWs to use for the calculation. This is determined by specifying a cutoff energy (E_{cut}) that relates maximum wave vector of the PW to the energy,

$$\frac{1}{2}|\alpha|^2 < E_{cut} \qquad (3.52)$$

No construction of basis set is necessary (thus there is no pure PW-equivalent to the atom-centered basis set development field), and the accuracy of the calculation can be made better (or worse) by simply changing the E_{cut} value. However in practice the large charge density located near the nuclei would require a very large number of PWs to accurately reproduce it. To mitigate this, core psuedopotentials are introduced to model the charge density near the nuclei, and PWs are used for the valence electrons.[120-121] This means that in fact, each atom-type must have a defined pseudopotential prior to use, limiting the utility and universality of a PW basis set.

3.3.2 Advantages and Disadvantages of Atom-Centered and Plane Wave Basis Sets

The differing constructions of the two methods for representing molecular wavefunctions, while both suitable for performing quantum mechanical simulations, leads to a distinct set of advantages and disadvantages. Where thousands (and sometimes hundreds of thousands) of PWs are required to model a system, an atom centered basis set with a small number of GTOs can provide more accurate results. However, PWs are far better suited for fast Fourier transform, and are extremely efficient for computing integrals.[122-123] Moreover, because PWs are continuous functions they do not introduce any basis set superposition errors (BSSE) or Pulay forces, which commonly plague calculations that utilize atom-centered basis sets.[118, 124-125]

While correctable using the a few different techniques, the existence of BSSE can lead to spurious over binding and inaccurate results and is major drawback of atom centered basis sets, especially those that are small in size.[126-128]

PW basis are great alternatives for periodic calculations, because both the PWs and the Fourier sum are periodic.[129-130] This is not to say that atom centered basis sets are not appropriate for periodic simulations (they are through the use of Bloch functions, see **Chapter 5**), but rather to point out that a PW basis may not be the best choice for isolated or non-periodic systems.[1, 95] In order to perform an isolated PW calculation, it is necessary to place the system of interest into a very large box so that the periodicity does not influence the calculation. Moreover, a major constraint when using a PW basis is the difficulty in extracting localized information from the wavefunction.[131-133] Because the PWs are continuous, localized qualities like bond population analyses are very difficult to discern.[130, 134] That being said there is a plethora of published literature using PW codes, and the choice between PW or atom centered basis sets is usually a matter of preference and convenience.[118-119, 135-138]

3.4 References

1. Evarestov, R. A., Quantum Chemistry of Solids. **2012**.

2. Levine, I. N., *Quantum Chemistry*; Pearson Prentice Hall Upper Saddle River, NJ, 2009; Vol. 6.

3. McQuarrie, D. A., *Quantum Chemistry*; University Science Books, 2008.

4. Sholl, D.; Steckel, J. A., *Density Functional Theory: A Practical Introduction*; John Wiley & Sons, 2011.

5. Burke, K., Perspective on Density Functional Theory. *J. Chem. Phys.* **2012**, *136*, 150901.

6. Harrison, N., An Introduction to Density Functional Theory. *NATO Science Series, Sub Series III* **2003**, *187*, 45-70.

7. Perdew, J. P., Density-Functional Approximation for the Correlation Energy of the Inhomogeneous Electron Gas. *Phys. Rev. B.* **1986**, *33*, 8822.

8. Zhao, Y.; Truhlar, D. G., The M06 Suite of Density Functionals for Main Group Thermochemistry, Thermochemical Kinetics, Noncovalent Interactions, Excited States, and Transition Elements: Two New Functionals and Systematic Testing of Four M06-Class Functionals and 12 Other Functionals. *Theor. Chem. Acc.* **2008**, *120*, 215-241.

9. Parr, R. G., *Density Functional Theory of Atoms and Molecules*; Springer, 1980.

10. Segall, M. D.; Philip, J. D. L.; Probert, M. J.; Pickard, C. J.; Hasnip, P. J.; Clark, S. J.; Payne, M. C., First-Principles Simulation: Ideas, Illustrations and the CASTEP Code. *J. Phys.: Condens. Matter* **2002**, *14*, 2717.

11. Dirac, P. A. M., Note on Exchange Phenomena in the Thomas Atom. *Mathematical Proceedings of the Cambridge Philosophical Society* **1930**, *26*, 376-385.

12.   Parr, R. G.; Yang, W., *Density-Functional Theory of Atoms and Molecules*; Oxford
      university press, 1989; Vol. 16.

13.   Ceperley, D. M.; Alder, B. J., Ground State of the Electron Gas by a Stochastic Method.
      Phys. Rev. Lett. **1980**, *45*, 566-569.

14.   Vosko, S. H.; Wilk, L.; Nusair, M., Accurate Spin-Dependent Electron Liquid
      Correlation Energies for Local Spin Density Calculations: A Critical Analysis. *Can. J.
      Phys.* **1980**, *58*, 1200-1211.

15.   Barth, U. v.; Hedin, L., A Local Exchange-Correlation Potential for the Spin Polarized
      Case. . *J. Phys. C* **1972**, *5*, 1629.

16.   Perdew, J. P.; Zunger, A., Self-Interaction Correction to Density-Functional
      Approximations for Many-Electron Systems. *Phys. Rev. B.* **1981**, *23*, 5048-5079.

17.   Perdew, J. P.; Wang, Y., Accurate and Simple Analytic Representation of the Electron-
      Gas Correlation Energy. *Phys. Rev. B.* **1992**, *45*, 13244-13249.

18.   Groß, A., Theoretical Surface Science: A Microscopic Perspective. Springer (Berlin,
      2002): 2007.

19.   Langreth, D. C.; Mehl, M., Beyond the Local-Density Approximation in Calculations of
      Ground-State Electronic Properties. *Phys. Rev. B.* **1983**, *28*, 1809.

20.   van de Walle, A.; Ceder, G., Correcting Overbinding in Local-Density-Approximation
      Calculations. *Phys. Rev. B.* **1999**, *59*, 14992-15001.

21.   Kohanoff, J., *Electronic Structure Calculations for Solids and Molecules: Theory and
      Computational Methods*; Cambridge University Press, 2006.

22.   Bechstedt, F.; Del Sole, R., Analytical Treatment of Band-Gap Underestimates in the
      Local-Density Approximation. *Phys. Rev. B.* **1988**, *38*, 7710.

23. Rubio, A.; Corkill, J. L.; Cohen, M. L., Theory of Graphitic Boron Nitride Nanotubes. *Phys. Rev. B.* **1994**, *49*, 5081.

24. Ul-Haq, Z.; Madura, J. D., *Frontiers in Computational Chemistry: Volume 2: Computer Applications for Drug Design and Biomolecular Systems*; Elsevier, 2015.

25. Perdew, J. P.; Chevary, J.; Vosko, S.; Jackson, K. A.; Pederson, M. R.; Singh, D.; Fiolhais, C., Atoms, Molecules, Solids, and Surfaces: Applications of the Generalized Gradient Approximation for Exchange and Correlation. *Phys. Rev. B.* **1992**, *46*, 6671.

26. Perdew, J. P.; Yue, W., Accurate and Simple Density Functional for the Electronic Exchange Energy: Generalized Gradient Approximation. *Phys. Rev. B.* **1986**, *33*, 8800.

27. Wu, Z.; Cohen, R. E., More Accurate Generalized Gradient Approximation for Solids. *Phys. Rev. B.* **2006**, *73*, 235116.

28. Perdew, J. P.; Burke, K.; Ernzerhof, M., Generalized Gradient Approximation Made Simple. *Phys. Rev. Lett.* **1996**, *77*, 3865-3868.

29. Madsen, G. K. H., Functional Form of the Generalized Gradient Approximation for Exchange: The PBE α Functional. *Phys. Rev. B.* **2007**, *75*, 195108.

30. Becke, A. D., Density-Functional Exchange-Energy Approximation with Correct Asymptotic Behavior. *Phys. Rev. A* **1988**, *38*, 3098-3100.

31. Lee, C.; Yang, W.; Parr, R. G., Development of the Colle-Salvetti Correlation-Energy Formula into a Functional of the Electron Density. *Phys. Rev. B.* **1988**, *37*, 785-789.

32. Becke, A. D., Density-Functional Thermochemistry. III. The Role of Exact Exchange. *J. Chem. Phys.* **1993**, *98*, 5648-5652.

33. Becke, A. D., A New Mixing of Hartree--Fock and Local Density-Functional Theories. *J. Chem. Phys.* **1993**, *98*, 1372-1377.

34.   Yang, W., Generalized Adiabatic Connection in Density Functional Theory. *J. Chem. Phys.* **1998**, *109*, 10107-10110.

35.   Zhao, Y.; Lynch, B. J.; Truhlar, D. G., Development and Assessment of a New Hybrid Density Functional Model for Thermochemical Kinetics. *J. Phys. Chem. A* **2004**, *108*, 2715-2719.

36.   Kudin, K. N.; Scuseria, G. E.; Martin, R. L., Hybrid Density-Functional Theory and the Insulating Gap of U O 2. *Phys. Rev. Lett.* **2002**, *89*, 266402.

37.   Zhao, Y.; Truhlar, D. G., Density Functionals with Broad Applicability in Chemistry. *Acc. Chem. Res.* **2008**, *41*, 157-167.

38.   Adamo, C.; Barone, V., Toward Reliable Density Functional Methods without Adjustable Parameters: The PBE0 Model. *J. Chem. Phys.* **1999**, *110*, 6158-6170.

39.   Perdew, J. P.; Ernzerhof, M.; Burke, K., Rationale for Mixing Exact Exchange with Density Functional Approximations. *J. Chem. Phys.* **1996**, *105*, 9982-9985.

40.   Tao, J.; Perdew, J. P.; Staroverov, V. N.; Scuseria, G. E., Climbing the Density Functional Ladder: Nonempirical Meta-Generalized Gradient Approximation Designed for Molecules and Solids. *Phys. Rev. Lett.* **2003**, *91*, 146401.

41.   Cramer, C. J.; Truhlar, D. G., Density Functional Theory for Transition Metals and Transition Metal Chemistry. *Phys. Chem. Chem. Phys.* **2009**, *11*, 10757-10816.

42.   Bickelhaupt, F. M.; Baerends, E. J., Kohn-Sham Density Functional Theory: Predicting and Understanding Chemistry. *Reviews in Computational Chemistry, Volume 15* **2007**, 1-86.

43. Dreuw, A.; Weisman, J. L.; Head-Gordon, M., Long-Range Charge-Transfer Excited States in Time-Dependent Density Functional Theory Require Non-Local Exchange. *J. Chem. Phys.* **2003**, *119*, 2943-2946.

44. Dreuw, A.; Head-Gordon, M., Failure of Time-Dependent Density Functional Theory for Long-Range Charge-Transfer Excited States: The Zincbacteriochlorin-Bacteriochlorin and Bacteriochlorophyll-Spheroidene Complexes. *J. Am. Chem. Soc.* **2004**, *126*, 4007-4016.

45. Zhao, Y.; Truhlar, D. G., Density Functional for Spectroscopy: No Long-Range Self-Interaction Error, Good Performance for Rydberg and Charge-Transfer States, and Better Performance on Average Than B3LYP for Ground States. *J. Phys. Chem. A* **2006**, *110*, 13126-13130.

46. Vydrov, O. A.; Scuseria, G. E., Assessment of a Long-Range Corrected Hybrid Functional. *J. Chem. Phys.* **2006**, *125*, 234109.

47. Ruggiero, M. T.; Gooch, J.; Zubieta, J.; Korter, T. M., Evaluation of Range-Corrected Density Functionals for the Simulation of Pyridinium-Containing Molecular Crystals. *J. Phys. Chem. A* **2016**.

48. Henderson, T. M.; Izmaylov, A. F.; Scuseria, G. E.; Savin, A., Assessment of a Middle-Range Hybrid Functional. *J. Chem. Theory Comput.* **2008**, *4*, 1254-1262.

49. Henderson, T. M.; Izmaylov, A. F.; Scuseria, G. E.; Savin, A., The Importance of Middle-Range Hartree-Fock-Type Exchange for Hybrid Density Functionals. *J. Chem. Phys.* **2007**, *127*, 221103.

50.   Vydrov, O. A.; Heyd, J.; Krukau, A. V.; Scuseria, G. E., Importance of Short-Range

        Versus Long-Range Hartree-Fock Exchange for the Performance of Hybrid Density

        Functionals. *J. Chem. Phys.* **2006**, *125*, 074106.

51.   Paier, J.; Marsman, M.; Hummer, K.; Kresse, G.; Gerber, I. C.; Ángyán, J. G., Screened

        Hybrid Density Functionals Applied to Solids. *J. Chem. Phys.* **2006**, *124*, 154709.

52.   Krukau, A. V.; Vydrov, O. A.; Izmaylov, A. F.; Scuseria, G. E., Influence of the

        Exchange Screening Parameter on the Performance of Screened Hybrid Functionals. *J.

        Chem. Phys.* **2006**, *125*, 224106.

53.   Weintraub, E.; Henderson, T. M.; Scuseria, G. E., Long-Range-Corrected Hybrids Based

        on a New Model Exchange Hole. *J. Chem. Theory Comput.* **2009**, *5*, 754-762.

54.   Peverati, R.; Truhlar, D. G., Improving the Accuracy of Hybrid Meta-GGA Density

        Functionals by Range Separation. *J. Phys. Chem. Lett.* **2011**, *2*, 2810-2817.

55.   Zhao, Y.; Truhlar, D. G., Design of Density Functionals That Are Broadly Accurate for

        Thermochemistry, Thermochemical Kinetics, and Nonbonded Interactions. *J. Phys.

        Chem. A* **2005**, *109*, 5656-5667.

56.   Zhao, Y.; Truhlar, D. G., A New Local Density Functional for Main-Group

        Thermochemistry, Transition Metal Bonding, Thermochemical Kinetics, and

        Noncovalent Interactions. *J. Chem. Phys.* **2006**, *125*, 194101.

57.   Tsuneda, T.; Hirao, K., Long-Range Correction for Density Functional Theory. *Wiley

        Interdiscip. Comput. Mol. Sci.* **2014**, *4*, 375-390.

58.   Kronik, L.; Tkatchenko, A., Understanding Molecular Crystals with Dispersion-Inclusive

        Density Functional Theory: Pairwise Corrections and Beyond. *Acc. Chem. Res.* **2014**, *47*,

        3208-3216.

59. Ramalho, J. P. P.; Gomes, J. R. B.; Illas, F., Accounting for Van Der Waals Interactions between Adsorbates and Surfaces in Density Functional Theory Based Calculations: Selected Examples. *RSC Advances* **2013**, *3*, 13085-13100.

60. Juliano, T. R.; King, M. D.; Korter, T. M., Evaluating London Dispersion Force Corrections in Crystalline Nitroguanidine by Terahertz Spectroscopy. *IEEE Trans. Terahertz Sci. Technol.* **2013**, *3*, 281-287.

61. Labanowski, J. K.; Andzelm, J. W., *Density Functional Methods in Chemistry*; Springer Science & Business Media, 2012.

62. Ryde, U.; Mata, R. A.; Grimme, S., Does DFT-D Estimate Accurate Energies for the Binding of Ligands to Metal Complexes? *Dalton Trans.* **2011**, *40*, 11176-11183.

63. Song, J.-W.; Tokura, S.; Sato, T.; Watson, M. A.; Hirao, K., An Improved Long-Range Corrected Hybrid Exchange-Correlation Functional Including a Short-Range Gaussian Attenuation (LCgau-BOP). *J. Chem. Phys.* **2007**, *127*, 154109.

64. Yanai, T.; Tew, D. P.; Handy, N. C., A New Hybrid Exchange–Correlation Functional Using the Coulomb-Attenuating Method (CAM-B3LYP). *Chem. Phys. Lett.* **2004**, *393*, 51-57.

65. Gritsenko, O.; Schipper, P.; Baerends, E., Exchange and Correlation Energy in Density Functional Theory: Comparison of Accurate Density Functional Theory Quantities with Traditional Hartree–Fock Based Ones and Generalized Gradient Approximations for the Molecules Li2, N2, F2. *J. Chem. Phys.* **1997**, *107*, 5007-5015.

66. Becke, A. D., Density-Functional Thermochemistry. V. Systematic Optimization of Exchange-Correlation Functionals. *J. Chem. Phys.* **1997**, *107*, 8554-8560.

67. Witko, E. M.; Buchanan, W. D.; Korter, T. M., The Importance of London Dispersion Forces in Crystalline Magnesium Nitrate Hexahydrate. *Inorg. Chim. Acta* **2012**, *389*, 176-182.

68. King, M. D.; Buchanan, W. D.; Korter, T. M., Application of London-Type Dispersion Corrections to the Solid-State Density Functional Theory Simulation of the Terahertz Spectra of Crystalline Pharmaceuticals. *Phys. Chem. Chem. Phys.* **2011**, *13*, 4250-4259.

69. Grimme, S., Density Functional Theory with London Dispersion Corrections. *Wiley Interdiscip. Comput. Mol. Sci.* **2011**, *1*, 211-228.

70. Lin, I. C.; von Lilienfeld, O. A.; Coutinho-Neto, M. D.; Tavernelli, I.; Rothlisberger, U., Predicting Noncovalent Interactions between Aromatic Biomolecules with London-Dispersion-Corrected DFT. *J. Phys. Chem. B* **2007**, *111*, 14346-14354.

71. Jonas, M.; Stephan, E.; Ralf, T.; Stefan, G., A DFT-D Study of Structural and Energetic Properties of Tio 2 Modifications. *J. Phys.: Condens. Matter* **2012**, *24*, 424206.

72. Grimme, S.; Antony, J.; Ehrlich, S.; Krieg, H., A Consistent and Accurate ab initio Parametrization of Density Functional Dispersion Correction (DFT-D) for the 94 Elements H-Pu. *J. Chem. Phys.* **2010**, *132*, 154104.

73. Grimme, S., Semiempirical GGA-Type Density Functional Constructed with a Long-Range Dispersion Correction. *J. Comput. Chem.* **2006**, *27*, 1787-1799.

74. Grimme, S., Accurate Description of Van Der Waals Complexes by Density Functional Theory Including Empirical Corrections. *J. Comput. Chem.* **2004**, *25*, 1463-1473.

75. Purvis III, G. D.; Bartlett, R. J., A Full Coupled-Cluster Singles and Doubles Model: The Inclusion of Disconnected Triples. *J. Chem. Phys.* **1982**, *76*, 1910-1918.

76.   Bartlett, R. J., Many-Body Perturbation Theory and Coupled Cluster Theory for Electron Correlation in Molecules. *Annu. Rev. Phys. Chem.* **1981**, *32*, 359-401.

77.   Pople, J. A.; Krishnan, R.; Schlegel, H.; Binkley, J. S., Derivative Studies in Hartree-Fock and Møller-Plesset Theories. *Int. J. Quantum Chem* **1979**, *16*, 225-241.

78.   Ayala, P. Y.; Scuseria, G. E., Linear Scaling Second-Order Moller–Plesset Theory in the Atomic Orbital Basis for Large Molecular Systems. *J. Chem. Phys.* **1999**, *110*, 3660-3671.

79.   Manby, F. R., Density Fitting in Second-Order Linear-R12 Møller–Plesset Perturbation Theory. *J. Chem. Phys.* **2003**, *119*, 4607-4613.

80.   Görling, A.; Levy, M., Correlation-Energy Functional and Its High-Density Limit Obtained from a Coupling-Constant Perturbation Expansion. *Phys. Rev. B.* **1993**, *47*, 13105.

81.   Schwabe, T.; Grimme, S., Double-Hybrid Density Functionals with Long-Range Dispersion Corrections: Higher Accuracy and Extended Applicability. *Phys. Chem. Chem. Phys.* **2007**, *9*, 3397-3406.

82.   Tarnopolsky, A.; Karton, A.; Sertchook, R.; Vuzman, D.; Martin, J. M., Double-Hybrid Functionals for Thermochemical Kinetics. *J. Phys. Chem. A* **2008**, *112*, 3-8.

83.   Grimme, S.; Neese, F., Double-Hybrid Density Functional Theory for Excited Electronic States of Molecules. *J. Chem. Phys.* **2007**, *127*, 154116.

84.   Kossmann, S.; Kirchner, B.; Neese, F., Performance of Modern Density Functional Theory for the Prediction of Hyperfine Structure: Meta-GGA and Double Hybrid Functionals. *Mol. Phys.* **2007**, *105*, 2049-2071.

85. Goerigk, L.; Grimme, S., Efficient and Accurate Double-Hybrid-Meta-GGA Density Functionals—Evaluation with the Extended GMTKN30 Database for General Main Group Thermochemistry, Kinetics, and Noncovalent Interactions. *J. Chem. Theory Comput.* **2011**, *7*, 291-309.

86. Bučko, T.; Lebègue, S.; Hafner, J.; Ángyán, J. G., Tkatchenko-Scheffler Van Der Waals Correction Method with and without Self-Consistent Screening Applied to Solids. *Phys. Rev. B.* **2013**, *87*, 064110.

87. Tkatchenko, A.; Scheffler, M., Accurate Molecular Van Der Waals Interactions from Ground-State Electron Density and Free-Atom Reference Data. *Phys. Rev. Lett.* **2009**, *102*, 073005.

88. Dion, M.; Rydberg, H.; Schröder, E.; Langreth, D. C.; Lundqvist, B. I., Van Der Waals Density Functional for General Geometries. *Phys. Rev. Lett.* **2004**, *92*, 246401.

89. Heßelmann, A., Derivation of the Dispersion Energy as an Explicit Density- and Exchange-Hole Functional. *J. Chem. Phys.* **2009**, *130*, 084104.

90. Becke, A. D.; Johnson, E. R., A Density-Functional Model of the Dispersion Interaction. *J. Chem. Phys.* **2005**, *123*, 154101.

91. De-Li, C.; Al-Saidi, W. A.; Johnson, J. K., The Role of Van Der Waals Interactions in the Adsorption of Noble Gases on Metal Surfaces. *J. Phys.: Condens. Matter* **2012**, *24*, 424211.

92. Hu, W.; Wu, X.; Li, Z.; Yang, J., Helium Separation Via Porous Silicene Based Ultimate Membrane. *Nanoscale* **2013**, *5*, 9062-9066.

93. Casimir, H. B. G.; Polder, D., The Influence of Retardation on the London-Van Der Waals Forces. *Phys. Rev.* **1948**, *73*, 360-372.

94.   Kaplan, I. G., *Intermolecular Interactions: Physical Picture, Computational Methods and Model Potentials*; John Wiley & Sons, 2006.

95.   Zunger, A.; Freeman, A., Self-Consistent Numerical-Basis-Set Linear-Combination-of-Atomic-Orbitals Model for the Study of Solids in the Local Density Formalism. *Phys. Rev. B.* **1977**, *15*, 4716.

96.   Krishnan, R.; Binkley, J. S.; Seeger, R.; Pople, J. A., Self-Consistent Molecular Orbital Methods. XX. A Basis Set for Correlated Wave Functions. *J. Chem. Phys.* **1980**, *72*, 650-654.

97.   Denis, P. A., Basis Set Requirements for Sulfur Compounds in Density Functional Theory: A Comparison between Correlation-Consistent, Polarized-Consistent, and Pople-Type Basis Sets. *J. Chem. Theory Comput.* **2005**, *1*, 900-907.

98.   Ruggiero, M. T.; Bardon, T.; Strlič, M.; Taday, P. F.; Korter, T. M., Assignment of the Terahertz Spectra of Crystalline Copper Sulfate and Its Hydrates Via Solid-State Density Functional Theory. *J. Phys. Chem. A* **2014**, *118*, 10101-10108.

99.   Wachters, A. J. H., Gaussian Basis Set for Molecular Wavefunctions Containing Third-Row Atoms. *J. Chem. Phys.* **1970**, *52*, 1033-1036.

100.   Huzinaga, S., Basis Sets for Molecular Calculations. *Comp. Phys. Rep.* **1985**, *2*, 281-339.

101.   Krishnan, R.; Binkley, J. S.; Seeger, R.; Pople, J. A., Self-Consistent Molecular Orbital Methods. XX. A Basis Set for Correlated Wave Functions. *J. Chem. Phys.* **1980**, *72*, 650-654.

102.   Hariharan, P. C.; Pople, J. A., The Influence of Polarization Functions on Molecular Orbital Hydrogenation Energies. *Theoret. Chim. Acta* **1973**, *28*, 213-222.

103. Hehre, W. J.; Stewart, R. F.; Pople, J. A., Self-Consistent Molecular-Orbital Methods. I. Use of Gaussian Expansions of Slater-Type Atomic Orbitals. *J. Chem. Phys.* **1969**, *51*, 2657-2664.

104. Dunning Jr, T. H., Gaussian Basis Functions for Use in Molecular Calculations. I. Contraction of (9s5p) Atomic Basis Sets for the First-Row Atoms. *J. Chem. Phys.* **1970**, *53*, 2823-2833.

105. Fernández Rico, J.; Fernandez, J.; Ema, I.; Lopez, R.; Ramirez, G., Four-Center Integrals for Gaussian and Exponential Functions. *Int. J. Quantum Chem* **2001**, *81*, 16-28.

106. Fournier, R.; Andzelm, J.; Salahub, D., Analytical Gradient of the Linear Combination of Gaussian-Type Orbitals—Local Spin Density Energy. *J. Chem. Phys.* **1989**, *90*, 6371-6377.

107. Dovesi, R.; Orlando, R.; Erba, A.; Zicovich-Wilson, C. M.; Civalleri, B.; Casassa, S.; Maschio, L.; Ferrabone, M.; De La Pierre, M.; D'Arco, P.*, et al.*, CRYSTAL14: A Program for the *ab initio* Investigation of Crystalline Solids. *Int. J. Quantum Chem* **2014**, *114*, 1287-1317.

108. Easton, R. E.; Giesen, D. J.; Welch, A.; Cramer, C. J.; Truhlar, D. G., The Midi! Basis Set for Quantum Mechanical Calculations of Molecular Geometries and Partial Charges. *Theoret. Chim. Acta*, *93*, 281-301.

109. Del Bene, J.; Pople, J., Theory of Molecular Interactions. I. Molecular Orbital Studies of Water Polymers Using a Minimal Slater-Type Basis. *J. Chem. Phys.* **1970**, *52*, 4858-4866.

110.   Lambrecht, W. R.; Andersen, O. K., Minimal Basis Sets in the Linear Muffin-Tin Orbital Method: Application to the Diamond-Structure Crystals C, Si, and Ge. *Phys. Rev. B.* **1986**, *34*, 2439.

111.   Hehre, W. J.; Pople, J. A., Molecular Orbital Theory of the Electronic Structure of Organic Compounds. III. Ab Initio Studies of Charge Distribution Using a Minimal Slater-Type Basis. *J. Am. Chem. Soc.* **1970**, *92*, 2191-2197.

112.   Clark, T.; Chandrasekhar, J.; Spitznagel, G. W.; Schleyer, P. V. R., Efficient Diffuse Function-Augmented Basis Sets for Anion Calculations. III. The 3-21+ G Basis Set for First-Row Elements, Li–F. *J. Comput. Chem.* **1983**, *4*, 294-301.

113.   Check, C. E.; Faust, T. O.; Bailey, J. M.; Wright, B. J.; Gilbert, T. M.; Sunderlin, L. S., Addition of Polarization and Diffuse Functions to the Lanl2dz Basis Set for P-Block Elements. *J. Phys. Chem. A* **2001**, *105*, 8111-8116.

114.   Raffenetti, R. C., General Contraction of Gaussian Atomic Orbitals: Core, Valence, Polarization, and Diffuse Basis Sets; Molecular Integral Evaluation. *J. Chem. Phys.* **1973**, *58*, 4452-4458.

115.   Lynch, B. J.; Zhao, Y.; Truhlar, D. G., Effectiveness of Diffuse Basis Functions for Calculating Relative Energies by Density Functional Theory. *J. Phys. Chem. A* **2003**, *107*, 1384-1388.

116.   Martin, R. L.; Kress, J. D.; Campbell, I.; Smith, D., Molecular and Solid-State Properties of Tris-(8-Hydroxyquinolate)-Aluminum. *Phys. Rev. B.* **2000**, *61*, 15804.

117.   Peintinger, M. F.; Oliveira, D. V.; Bredow, T., Consistent Gaussian Basis Sets of Triple-Zeta Valence with Polarization Quality for Solid-State Calculations. *J. Comput. Chem.* **2013**, *34*, 451-459.

118. Kresse, G.; Furthmüller, J., Efficient Iterative Schemes for *ab initio* Total-Energy Calculations Using a Plane-Wave Basis Set. *Phys. Rev. B.* **1996**, *54*, 11169.

119. Blaha, P.; Schwarz, K.; Sorantin, P.; Trickey, S., Full-Potential, Linearized Augmented Plane Wave Programs for Crystalline Systems. *Comput. Phys. Commun.* **1990**, *59*, 399-415.

120. Blöchl, P. E., Projector Augmented-Wave Method. *Phys. Rev. B.* **1994**, *50*, 17953.

121. Chelikowsky, J. R.; Cohen, M. L., Nonlocal Pseudopotential Calculations for the Electronic Structure of Eleven Diamond and Zinc-Blende Semiconductors. *Phys. Rev. B.* **1976**, *14*, 556.

122. Troullier, N.; Martins, J. L., Efficient Pseudopotentials for Plane-Wave Calculations. *Phys. Rev. B.* **1991**, *43*, 1993.

123. Troullier, N.; Martins, J. L., Efficient Pseudopotentials for Plane-Wave Calculations. II. Operators for Fast Iterative Diagonalization. *Phys. Rev. B.* **1991**, *43*, 8861.

124. Lee, K.; Yu, J.; Morikawa, Y., Comparison of Localized Basis and Plane-Wave Basis for Density-Functional Calculations of Organic Molecules on Metals. *Phys. Rev. B.* **2007**, *75*, 045402.

125. Lippert, G.; Parrinello, J. H., A Hybrid Gaussian and Plane Wave Density Functional Scheme. *Mol. Phys.* **1997**, *92*, 477-488.

126. Schwenke, D. W.; Truhlar, D. G., Systematic Study of Basis Set Superposition Errors in the Calculated Interaction Energy of Two HF Molecules. *J. Chem. Phys.* **1985**, *82*, 2418-2426.

127. Simon, S.; Duran, M.; Dannenberg, J., How Does Basis Set Superposition Error Change the Potential Surfaces for Hydrogen-Bonded Dimers? *J. Chem. Phys.* **1996**, *105*, 11024-11031.

128. McLean, A.; Chandler, G., Contracted Gaussian Basis Sets for Molecular Calculations. I. Second Row Atoms, Z= 11–18. *J. Chem. Phys.* **1980**, *72*, 5639-5648.

129. Tackett, A.; Holzwarth, N.; Matthews, G., A Projector Augmented Wave (PAW) Code for Electronic Structure Calculations, Part II: PWPAW for Periodic Solids in a Plane Wave Basis. *Comput. Phys. Commun.* **2001**, *135*, 348-376.

130. Segall, M.; Shah, R.; Pickard, C.; Payne, M., Population Analysis of Plane-Wave Electronic Structure Calculations of Bulk Materials. *Phys. Rev. B.* **1996**, *54*, 16317.

131. Deringer, V. L.; Tchougréeff, A. L.; Dronskowski, R., Crystal Orbital Hamilton Population (COHP) Analysis as Projected from Plane-Wave Basis Sets. *J. Phys. Chem. A* **2011**, *115*, 5461-5466.

132. Maintz, S.; Deringer, V. L.; Tchougréeff, A. L.; Dronskowski, R., Analytic Projection from Plane-Wave and PAW Wavefunctions and Application to Chemical-Bonding Analysis in Solids. *J. Comput. Chem.* **2013**, *34*, 2557-2567.

133. Kuneš, J.; Arita, R.; Wissgott, P.; Toschi, A.; Ikeda, H.; Held, K., Wien2wannier: From Linearized Augmented Plane Waves to Maximally Localized Wannier Functions. *Comput. Phys. Commun.* **2010**, *181*, 1888-1895.

134. Sánchez-Portal, D.; Artacho, E.; Soler, J. M., Analysis of Atomic Orbital Basis Sets from the Projection of Plane-Wave Results. *J. Phys.: Condens. Matter* **1996**, *8*, 3859.

135. Schuchardt, K. L.; Didier, B. T.; Elsethagen, T.; Sun, L.; Gurumoorthi, V.; Chase, J.; Li, J.; Windus, T. L., Basis Set Exchange: A Community Database for Computational Sciences. *J. Chem. Inf. Mod.* **2007**, *47*, 1045-1052.

136. Davidson, E. R.; Feller, D., Basis Set Selection for Molecular Calculations. *Chem. Rev.* **1986**, *86*, 681-696.

137. Jensen, F., Atomic Orbital Basis Sets. *Wiley Interdiscip. Comput. Mol. Sci.* **2013**, *3*, 273-295.

138. Hill, J. G., Gaussian Basis Sets for Molecular Applications. *Int. J. Quantum Chem* **2013**, *113*, 21-34.

CHAPTER 4: Solid-State Density Functional Theory Methods and Techniques

4.1 Introduction to Solid-State Density Functional Theory

The study of crystalline materials by *ab initio* methods presents a different set of computational challenges than more traditional gas-phase calculations.[1-5] One of the most significant differences is the need to represent the infinite periodicity of these materials in an efficient manner, so that the crystalline potential is properly accounted for. Fortunately the majority of *ab initio* formulae and algorithms have been modified for use in the solid-state.[5-9] Of particular importance are the generation of crystalline orbitals that extend throughout the entire bulk, and the handling of one- and two-electron integrals to take the long-range contributions from solid into account. In this chapter, the theoretical framework of solid-state density functional theory (ss-DFT) will be examined in the context of the *ab initio* CRYSTAL software package,[5] and the various calculation methods and algorithms used and developed for this work will be discussed in detail.

4.1.1 Reciprocal Space and Bloch's Theorem

A crystalline system can be described by a unit cell that, when translated, will reproduce the entire three-dimensional structure of the solid.[10] The unit cell is defined by three constants called lattice vectors (a_1, a_2, and a_3), and any position inside the unit cell (r) can be expressed as a function of the lattice vectors,

$$r = x_1 a_1 + x_2 a_2 + x_3 a_3 \qquad (4.1)$$

A general lattice vector (g) can be defined such that

$$g = n_1 a_1 + n_2 a_2 + n_3 a_3 \qquad (4.2)$$

where n is any integer. In a crystalline system, translational invariance dictates that for any r, $r + g = r' = r$. This translational invariance is what generates the periodicity and has significant implications for ss-DFT computational techniques.

Any real-space lattice can be expressed in reciprocal space (or k-space), defined by the real-reciprocal lattice vector relationship

$$a_i b_j = 2\pi \delta_{ij} \qquad (4.3)$$

where b_j is a reciprocal lattice vector and δ_{ij} is the Kronecker delta that is equal to one if $i = j$ and zero otherwise.

Just as in real space, reciprocal lattice vectors (k) can be expressed as a linear combination of basis vectors with coefficients n,

$$k = n_1 b_1 + n_2 b_2 + n_3 b_3 \qquad (4.4)$$

Transforming a real space lattice into reciprocal space is possible using (4.3),

$$b_1 = 2\pi \frac{a_2 \times a_3}{a_1 \cdot (a_2 \times a_3)}$$

$$b_2 = 2\pi \frac{a_3 \times a_1}{a_2 \cdot (a_3 \times a_1)} \qquad (4.5)$$

$$b_3 = 2\pi \frac{a_1 \times a_2}{a_3 \cdot (a_1 \times a_2)}$$

Just like in real space, a fundamental unit cell can be defined in reciprocal space that, when repeated, will reproduce the reciprocal space lattice. This volume is termed the first Brillouin zone (BZ) and all calculations done in reciprocal space are performed within the context of the BZ, as they accurately represent (by translational symmetry) the entire bulk.

Working in reciprocal space may seem tedious, but there exist significant computational advantages to doing so.[1, 9, 11-13] The first involves the transformation of the localized atom centered basis sets to periodic Bloch functions.[14-16] Without the use of a periodic basis function, the Hamiltonian would have an infinite parameter space and ss-DFT calculations would not be possible.[17-19] Bloch functions satisfy Bloch's theorem that states that when a Bloch wave function (Φ) that has the same periodicity as the crystal is translated, the function has the same value at equivalent k points,[20-21]

$$\Phi(r + g; k) = e^{ikg}\Phi(r; k) \tag{4.6}$$

Bloch's theorem profoundly simplifies the treatment of periodic systems, because it enables only the analysis of k points in the BZ to fully describe the solid. In order to exploit Bloch's theorem, the atomic orbitals must be transformed into Bloch functions, which is done through Fourier transform of the Gaussian-type atomic orbitals (GTO, φ),[22-23]

$$\Phi(r; k) = \frac{1}{\sqrt{N}} \sum_g e^{ikg} \varphi^{(g)}(r - R_\mu) \tag{4.7}$$

where N is the number of primitive unit cells, and R_μ is the coordinate corresponding to the center of the Gaussian function (the nuclear coordinate). The solid-state GTOs also have a slightly different form than mentioned in (3.49),

$$\varphi(r - g) = \sum_n d_n \gamma_n (\alpha; r - R_\mu - g) \tag{4.8}$$

where d_n is the coefficient of the primitive Gaussian γ_n. It is important to note that the primitive Gaussian functions used in (4.8) have already been transformed using solid-state spherical harmonics.

Using the periodic Bloch functions, the periodic crystalline orbitals (CO) can be constructed in the same manner as molecular orbitals were in (2.33),

$$\psi(r; k) = \sum_\mu a_\mu \Phi_\mu(r; k) \tag{4.9}$$

118

and subsequently can be used to solve the Schrödinger equation

$$\hat{H}\psi_i(r;k) = E_i(k)\psi_i(r;k) \qquad (4.10)$$

The utility of Bloch functions can be observed here. In the real space atomic orbital basis,

the Hamiltonian matrix is infinite, running over all possible lattice vectors. However using

Bloch's theorem each k value can be treated independently from one another, with an infinite

number of k $n_f \times n_f$ blocks, where n_f is the number of Bloch functions (**Figure 4-1**). Exploiting

this property, the BZ can be sampled using a finite number of k points and the Hamiltonian

matrix diagonalized, followed by integration using interpolation techniques such as the

trapezoidal or Gaussian quadrature methods to yield the energy of the system as a function of k.[4]

All of the work dedicated to transforming atomic orbitals to periodic Bloch functions

begs the question, why do it at all? The use of atomic orbitals enables chemical properties to be

considered, and then transferred to the periodic Bloch functions. This takes the effect that

neighboring interactions have on the atomic wavefunctions into effect, increasing the accuracy of

the calculations and helping ensure a more physical result.[1, 12, 17]
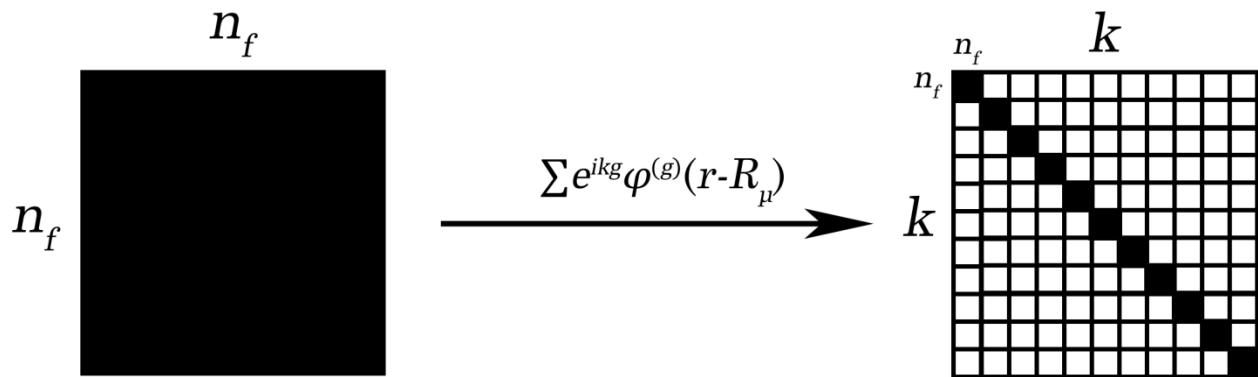
Figure 4-1. Schematic illustrating the effect that using Bloch's theorem has on the calculation of periodic systems. In the atomic orbital basis (left), the infinite periodicity results in an infinite matrix over all lattice vectors and atomic orbitals. Fourier transformation to reciprocal space reduces the problem to an infinite number of block diagonalized matrices that contain the Bloch function elements.

4.1.2 The Solid-State Density Functional Theory Matrices

As shown in the previous section, calculations in real space using an atomic orbital basis provides chemical advantages, while reciprocal space enables a high degree of computational efficiency. Therefore, all of the matrices used to solve the Schrödinger equation in CRYSTAL are initially described in real space, then subsequently transformed to reciprocal space, so that the eigenvalue matrix relationship can be solved,

$$\mathbf{H}(k)\mathbf{A}(k) = \mathbf{S}(k)\mathbf{A}(k)\mathbf{E}(k) \tag{4.11}$$

where $\mathbf{H}(k)$ is the Hamiltonian matrix, $\mathbf{A}(k)$ is the eigenvector matrix, $\mathbf{S}(k)$ is the overlap matrix, and $\mathbf{E}(k)$ is the diagonalized energy matrix,. The transformation from real space to reciprocal space is done as before using Fourier transformations. For example, the construction of the overlap elements using atomic orbitals is as follows,

$$
\begin{aligned}
S_{\mu\nu}(k) = \langle \Phi_\mu(k) | \Phi_\nu(k) \rangle &= \int \Phi_\mu^*(r;k) \Phi_\nu(r;k) dr \\
&= \frac{1}{N} \sum_g \sum_{g'} e^{-ikg} e^{ikg'} \int \varphi_\mu^*(r-g) \varphi_\nu(r-g') dr
\end{aligned}
\tag{4.12}
$$

recalling that φ and Φ are the atomic and Bloch orbitals, respectively.

The construction of the Hamiltonian matrix is the most complex, and just as shown in Chapter 2 contains the sum of four terms,

$$\hat{H} = \hat{T}_s + \hat{Z} + \hat{U}_H + \hat{E}_{xc} \tag{4.13}$$

where $\hat{T}, \hat{Z}, \hat{U}_H$, and $\hat{E}_{xc}$ are the kinetic, electron-nucleus, Coulombic repulsion, and exchange-correlation operators, respectively. For any particular crystalline orbital, the eigenvalue of the Hamiltonian operator yields the corresponding energy. The expectation value for each matrix element is defined in real space, and then transformed into reciprocal space as follows,

$$H_{\mu\nu}^g = \langle \varphi_\mu | \hat{H} | \varphi_\nu \rangle \tag{4.14}$$

$$H_{\mu\nu}(k) = \sum_g e^{ikg} H_{\mu\nu}^g \tag{4.15}$$

thus, the Hamiltonian matrix elements can be written as the sum of the expectation values of the various energy operators,

$$H_{\mu\nu}^g = T_{s\,\mu\nu}^g + Z_{\mu\nu}^g + U_{H\,\mu\nu}^g + E_{xc\,\mu\nu}^g \tag{4.16}$$

Because the formulation of these operators was discussed in detail in **Chapter 2**, a reduced notation ignoring constants will be used here for simplicity. The first two terms are monoelectronic terms representing the kinetic and nuclei-electron Coulombic attraction energies, respectively.

The kinetic energy integrals are determined using the kinetic energy operator (∇^2, the Laplacian),

$$T_{s\,\mu\nu}^{g} = -\frac{1}{2}\langle\varphi_\mu|\hat{T}_s|\varphi_\nu\rangle = -\frac{1}{2}\langle\varphi_\mu|\nabla^2|\varphi_\nu\rangle = -\frac{1}{2}\int\varphi_\mu(r)\nabla^2\varphi_\nu(r)dr \qquad (4.17)$$

And the nuclei-electron integrals are solved similarly,

$$\begin{aligned}
Z_{\mu\nu}^{g} = \langle\varphi_\mu|\hat{Z}|\varphi_\nu\rangle &= \sum_h\sum_I\left\langle\varphi_\mu\left|\frac{\mathbf{Z}_I}{r-R_I-h}\right|\varphi_\nu\right\rangle \\
&= \sum_h\sum_I\int\varphi_\mu(r)\frac{\mathbf{Z}_A}{r-R_I-h}\varphi_\nu(r)dr
\end{aligned} \qquad (4.18)$$

where R_I is the position of nucleus I and the sum over h is all lattice translation vectors, which is important for including contributions from neighboring unit cells.

The two bielectronic terms, the electron-electron mean field Coulomb repulsion and exchange-correlation integrals, are treated by examining the interaction between the total electron density (P) and the individual orbitals (a key assumption of DFT[24-26]). The density matrix elements are given by

$$P_{\mu\nu}(k) = \sum_i a_{\mu,i}^*(k)\,a_{\nu,i}(k) \qquad (4.19)$$

where i is the crystalline orbital index.

The Coulomb bielectronic term, $U_{\mu\nu}^g$, is represented as,

$$U_{H\mu\nu}^g = \sum_{\sigma,\omega}\sum_{g'} P_{\sigma\omega}^{g'} \sum_h \left\langle \varphi_\mu^0 \varphi_\nu^g \left| \frac{1}{r-r'} \right| \varphi_\sigma^h \varphi_\omega^{h+g} \right\rangle \tag{4.20}$$

$$U_{H\mu\nu}^g = \sum_{\sigma,\omega}\sum_{g'} P_{\sigma,\omega}^{g'} \sum_h \int\int \varphi_\mu(r)\varphi_\nu(r-g)\frac{1}{r-r'-h}\varphi_\sigma(r'-h)\varphi_\omega(r'-h-g') \tag{4.21}$$

where $P_{\sigma,\omega}^{g'}$ is the density matrix, g' and h are translation vectors, and r and r' are the positions

of the two electrons. The exchange-correlation term is discussed in detail in **Chapter 3**, and will

not be reproduced here.

Combining all of Hamiltonian terms, the total energy of the irreducible cell is given by

$$\begin{aligned}
E_{tot} &= N + \frac{1}{2}\sum_{\mu\nu}\sum_g P_{\mu\nu}^g H_{\mu\nu}^g \\
&= \frac{1}{2}\sum_{\mu\nu}\sum_g P_{\mu\nu}^g (2T_{s\mu\nu}^g + 2Z_{\mu\nu}^g + U_{H\mu\nu}^g + E_{xc\mu\nu}^g)
\end{aligned} \tag{4.22}$$

where *N* is the potential energy of the nuclei (the Ewald sum, see **2.2.1**), and the constants added

to prevent double counting. An important consideration of the mentioned terms is the apparent

infinite sums that appear over lattice vectors (*g* and *h*). Clearly the sums are necessary to

properly account for interactions beyond the irreducible unit cell, but the terms must be truncated

somewhat in order to minimize computational cost, while still maintaining chemical accuracy.[1-2,]

[12, 17] In the CRYSTAL software, truncation of the terms is performed based on pseudo-overlap of

the atomic orbitals, that is truncation determined by the overlap between two sets of atomic

orbitals at increasing lattice vector magnitudes.

CRYSTAL performs this truncation by first grouping all of the atomic orbitals with the same quantum numbers m and l (*i.e.* $3d$) for each atom into shells. Subsequently, a single s-type GTO is generated using a value for Gaussian exponent corresponding to most diffuse orbital in the shell (the smallest Gaussian exponent from the basis). This adjoined Gaussian is used to initially test for overlap with all other shells, and if the overlap criteria is met all of the integrals are evaluated, or otherwise discarded. Therefore, the selected tolerance not only increases the cost of the calculation, but also increases the size of the matrices by dictating that more (or less) integrals be considered. These concepts are the foundation for every calculation performed using CRYSTAL, and enable the simulation of any property dependent on ground state electronic structure. In the following sections, the major calculation types used throughout this work will be discussed, beginning with the calculation of DFT energy using the Self-Consistent Field.

4.2 Computational Techniques Used in CRYSTAL14

4.2.1 Calculation of the Electronic Energy Using the Self Consistent Field Method

Because the two-electron terms in the Hamiltonian are dependent on the crystalline orbital coefficients, values that are only known if a full solution to the Schrödinger equation is known, an iterative method to determining the energy must be used. This technique, known as the Self-Consistent Field (SCF), is an iterative method where the coefficients are determined by varying the electron density and diagonalizing the Hamiltonian matrix until convergence (usually on energy) is reached.[8-9, 25-27] The scheme (see **Figure 2-1**) is similar to the molecular case discussed in **Chapter 2**, but here the Roothaan-Hall equation is solved at discrete k-points, thus the calculations involves regularly switching between real and reciprocal space using Fourier transformations.[2, 5-6]

In CRYSTAL, the initial density P^0 is guessed from a superposition of atomic densities, and the Hamiltonian matrix in real space is calculated and subsequently Fourier transformed to reciprocal space, resulting in a set of K matrices, where K is the number of k-points selected for sampling. The Hamiltonian matrix is then diagonalized, and the new density matrix determined P^1. If convergence is not met, P^1 is used to generate a new Hamiltonian matrix, and the process repeats with a new cycle, otherwise it ends. This iterative method has proven to be effective for determining the ground-state properties of many systems, however in many cases convergence can be accelerated by mathematically damping or projecting the density matrix from one cycle to the next.[28-30] For example, a linear-mixing method uses the previous two cycles electron density as a linear combination for the new density guess,

$$P^n = (1 - \alpha)P^{n-1} + \alpha P^{n-2} \qquad (4.23)$$

This mixing helps soften numerical instabilities that may arise during the minimization routine, and is effective in keeping the minimization from deviating from its projected path.[2] There are also quadratic and higher-order mixing methodologies available, and can be chosen based on convenience and behavior of the particular system under study.

The SCF is forms the foundation for any *ab initio* simulation using CRYSTAL (and most other software packages[6-9]). For the remainder of this work, each mention of the energy is the result of one or more SCF cycles. It is a powerful method that enables the simulation of the various properties that will be outlined throughout this chapter.

4.2.2 Geometry Optimizations

The proper equilibrium geometry of a system is required in order to accurately calculate energies and related quantities.[31-33] Due to the various computational parameters possible (*i.e.* basis set, functional, k-point sampling, etc...), each set of parameters will have a different lowest energy configuration of the atoms. Therefore, geometry optimizations should be performed whenever a new calculation is initialized to ensure the results are consistent. An equilibrium geometry is defined as having all atomic nuclei centered at the minima on the potential energy surface (PES, also commonly referred to as a hypersurface).[34-35] In any system the PES is a function of the nuclear coordinate (R), and arises from the Born-Oppenheimer approximation.[36] By taking derivative(s) of the PES common observables such as the forces (F), vibrations (D), and elastic properties (C) quantities can be derived,[37-40]

$$F = \frac{\partial E}{\partial R}; \frac{\partial E}{\partial a} \qquad (4.24)$$

$$D = \frac{\partial^2 E}{\partial R_I R_J} \qquad (4.25)$$

$$C = \frac{\partial^2 E}{\partial a_i a_j} \qquad (4.26)$$

where R and a are the atomic positions and lattice constants, respectively. Therefore an accurate knowledge of both the PES and its derivatives is imperative for calculating meaningful values. But because most complex systems an analytical form of the PES is not known, determining the first and second derivatives is not a trivial task. The first derivative of the PES (the gradient) is of primary importance for geometry optimizations, while the second derivative is helpful it is not necessary to calculate in order to determining the equilibrium structure. The second derivative of the PES is required for the calculation of vibrational and elastic properties, and will be discussed in further details in the following sections.

Analyzing the PES topologically yields valuable information about the structure, for example at a minima the forces are equal to zero ($\frac{\partial E}{\partial x} = 0$), while the second derivative (the Hessian matrix) would have all positive values.[41-43] Because the PES is not known analytically, numerical algorithms for energy minimization must be employed to locate the equilibrium structure. There are countless methods for performing this optimization, but rely on the dimensionality of the derivative, namely linear, gradient, and Hessian based search routines.[44-46]

While a Hessian-based optimization would be fastest, the building of the Hessian matrix

is computationally expensive; on the other hand a linear search is computationally quick, it often converges very slowly.[44, 47-48] Gradient based methods are utilized because the first derivative of the PES can be solved analytically using the Hellman-Feynman theorem[49-50] which states that the derivative of the total energy with respect to some parameter (ζ) is equal to the derivative of the Hamiltonian with respect to the same parameter,[51-53]

$$\frac{\partial E}{\partial \zeta} = \left\langle \Psi(\zeta) \left| \frac{\partial \widehat{H}}{\partial \zeta} \right| \Psi(\zeta) \right\rangle \tag{4.27}$$

The Hellman-Feynman theorem makes the calculation of atomic forces very simple, as the derivative of the energy with respect to atomic coordinates only means the derivative of the external ionic potential operator needs to be taken, as it is the only term in the Hamiltonian dependent on atomic position.

The strategy for the common quasi-Newton (QN) gradient optimization[54-56] involves approximating the PES as a second-order Taylor expansion quadratic function,

$$E(v + \Delta v) = E(v) + \nabla E(v)^t \Delta v + \frac{1}{2} \Delta v^t D \Delta v \tag{4.28}$$

where $\Delta v = v - v_0$, D is the Hessian, and $\nabla E(v)$ is the gradient.

The gradient of this function (with respect to Δv) is given by,

$$\nabla E(v + \Delta v) = \nabla E(v) D \Delta v \qquad (4.29)$$

at the PES minimum, the $\nabla E(v + \Delta v) = 0$, and rearranging the above equation provides the calculated next optimization step (the Newton step),

$$\Delta v = -D^{-1} \nabla E(v) \qquad (4.30)$$

While $\nabla E(v)$ is known analytically using the Hellman-Feynman theorem, the Hessian is not known and must be either computed explicitly or approximated. Because the calculation of the Hessian is computationally expensive, an approximation is built using information about how the gradient changes between steps (a analogue to the second derivative). Several techniques for this approximation can be used, with the most common in solid-state DFT software packages being the Broyden-Fletcher-Goldfarb-Shanno (BFGS) scheme.[47, 54] The calculation of the gradients followed by determining the Newton step is repeated iteratively (with an SCF calculation performed after each step) until the required convergence criterion are met.

4.2.3 Frequency Analyses

The analysis of the lattice dynamics of a solid is key to interpreting experimental vibrational spectra and understanding thermodynamic properties.[57-60] The calculation of phonons in the CRYSTAL software involves building the Hessian (or dynamical) matrix and diagonalizing it, yielding the vibrational eigenvectors and eigenvalues.[5, 38-39, 61] The calculation

of the Hessian matrix is done numerically by displacing each atom along the three Cartesian axes

and computing the energy and analytical gradients,

$$D_{IJ} = \frac{\partial^2 E}{\partial R_I \partial R_J} = \frac{\partial v_I}{\partial R_J} \approx \frac{v_I(R_J^0) - v_I(R_J^0 - R_J)}{2R_J} \tag{4.31}$$

The Hessian matrix is, at this stage, a matrix of atomic force constants (k). The Hessian is

subsequently mass-weighted,

$$W_{\alpha I, \beta J} = \frac{D_{IJ}}{\sqrt{M_\alpha M_\beta}} \tag{4.32}$$

where M_α and M_β are the masses of atoms α and β associated with the I and J coordinates,

respectively. The mass-weighted Hessian matrix now populated with the atomic-pair ω^2 terms

from the harmonic oscillator solution to the Schrödinger equation,

$$E = \hbar\omega = \hbar\sqrt{\frac{k}{\mu}} \tag{4.33}$$

where k is the force constant and μ is the reduced mass of a given vibrational mode.

Diagonalization of D yields the vibrational eigenvectors and eigenvalues, and the eigenvalues

(ω) are subsequently converted to the vibrational frequencies using the simple relationship,

$$\tilde{v} = \frac{1}{2\pi c}\omega \tag{4.34}$$

The infrared intensities (A) are proportional to the square of the first derivative of the dipole moment (μ) with respect to eigenvector coordinate (Q) multiplied by the degeneracy of the vibration (d),[62]

$$A \propto d \left| \frac{\partial \mu}{\partial Q} \right|^2 \tag{4.35}$$

The change in the dipole moment with respect to the atomic displacements is related to the Born charge tensor (Z^*),

$$Z^* = \frac{\partial \mu}{\partial R} = \frac{\partial^2 E}{\partial R \partial \varepsilon} = \frac{\partial P}{\partial R} \tag{4.36}$$

where P is the polarization of the unit cell that is equal to the change in energy as a function of electric field (ε).[63] The calculation of the polarization derivative can be performed in a variety of ways, and CRYSTAL implements the Berry phase approach as a default.[5, 61] This involves calculating the polarization as the difference between the equilibrium and displaced structures,

$$\Delta P = P_\lambda - P_0 \tag{4.37}$$

The simulation of the crystalline phonons enables thermodynamic analyses to be carried out, as the heat-capacity of solids is dependent on the phonon density of states.[57, 64] This dependence is reflected in the Einstein and Debye heat capacity models that incorporate vibrational motion into their formulae, correcting the classical Dulong-Petit law.[10, 65-66] Using

statistical mechanics the various thermodynamic quantities (*i.e.* entropy, enthalpy, Gibbs free energy) can be calculated from the phonon density of states.

4.2.4 One-Electron Orbital Analyses

An array of properties can be determined using the one-electron wavefunctions produced in an SCF calculation, including the atomic electron population,[67] band structure,[68] and density of states.[69-71] These quantities can all be calculated *ex post facto* using post-processing utilities provided in the CRYSTAL software, as they are usually simple manipulations of the Hamiltonian elements produced during the SCF. Here, the scheme for calculating the density of states will be discussed, followed by two techniques that were implemented into the CRYSTAL software for this work, the crystal orbital overlap population[72] and crystal orbital Hamiltonian population analyses.[69-70, 73] This suite of tools is invaluable for characterizing the interactions within molecular crystals, with the latter two methods capable of providing insight into the role of bonding and nonbonding interactions.

4.2.4.1 Density of States

The electronic density of states (DOS) is a measure of how the crystalline orbitals (bands) are organized as a function of energy.[10] The density of states can be deconstructed into contributions for specific atoms (atomic DOS) and orbitals (and orbital DOS), and any combination therein, enabling the study of how the various contributions effect the overall

133

electronic structure of a system. The DOS ($\rho(\varepsilon)$) is calculated from the one-electron

wavefunctions for an orbital, atom, and total system, respectively,

$$\rho_\mu(\varepsilon) = \frac{2}{V_B} \sum_i \sum_v \int_{BZ} S_{\mu v}(k)\, a_{\mu,i}^*(k)\, a_{v,i}(k)\ \ \delta\big(\varepsilon - \varepsilon_i(k)\big)\, dk \tag{4.38}$$

$$\rho_A(\varepsilon) = \sum_{\mu \in A} \rho_\mu(\varepsilon) \tag{4.39}$$

$$\rho_{tot}(\varepsilon) = \sum_A \rho_A(\varepsilon) \tag{4.40}$$

where S and a are the overlap matrix and orbital coefficients, and μ and v represent are the two orbital

indices. It is important to note that the diagonal elements of the overlap matrix $S_{\mu,\mu}$ are included in the

DOS calculation, which results in all values being ≥ 0 from self-interaction. The DOS calculation yields

valuable information involving the contribution of an orbital or atom to the total electronic structure of the

solid, but it does not provide any insight regarding the chemical nature of the interaction between two

orbitals, *i.e*. bond populations or the type of interaction (bonding or antibonding). This information can be

obtained using the COOP and COHP methods, which are modifications of the DOS scheme.

4.2.4.2 Crystal Orbital Overlap and Hamiltonian Population Analyses

The crystal orbital overlap population analysis was introduced by Hoffman and

Hughbanks,[72] and is an effective method for separating the electronic DOS for two sets of

orbitals into bonding and antibonding regimes by making a slight modification to the DOS

formula. Where the formula for DOS (eqn 102.) includes diagonal elements, the COOP formula

does not,

$$COOP_{A-B}(\varepsilon) = \frac{2}{V_B} \sum_i \sum_{\mu \in A} \sum_{\nu \in B} \int_{BZ} S_{\mu\nu}(k)\, a^*_{\mu,i}(k)\, a_{\nu,i}(k)\, \delta\left(\varepsilon - \varepsilon_j(k)\right) dk \qquad (4.41)$$

Here, only the interaction between the orbitals of set A and B are considered. The COOP formula

reduces to that of the DOS if the sets A and B are identical. Here, if the overlap integral is

positive, the COOP curve is positive indicating a bonding interaction, while the inverse is true

for antibonding interactions. Integration of the COOP curves effectively renders the bond order

of the interaction between the set sets of orbitals, meaning that non-traditional interactions (*i.e.*

the interaction between two separate molecules) can be quantified using COOP data.

The COOP method partitions the electronic states into bonding and antibonding regions,

but does not provide a concise description of the energies associated with the particular

interactions. By substituting the Hamiltonian matrix for the overlap matrix, the band energies are

what is partitioned. This formalism is the crystal orbital Hamiltonian population (COHP) and has

the form,[69-70]

$$COHP_{A-B}(\varepsilon) = \frac{2}{V_B} \sum_i \sum_{\mu \in A} \sum_{\nu \in B} \int_{BZ} H_{\mu\nu,i}(k)\, a^*_{\mu,i}(k)\, a_{\nu,i}(k)\, \delta\left(\varepsilon - \varepsilon_j(k)\right) dk \qquad (4.42)$$

In the COHP analysis the data is again partitioned into bonding and antibonding regions,

however bonding regions will be negative because of their more stable energies (compared to

antibonding regions). For this reason, COHP curves are commonly plotted as the negative (-

COHP) to make the comparing to COOP data easier. Plots and a more in depth discussion of

COOP and COHP can be found in **Chapters 7** and **11**.

4.2.5 Elastic and Piezeo-Optic Properties

4.2.5.1 Calculation of Elastic Constants

The manner in which a material responds to an applied force is related to its elastic properties.[74-77] The elasticity of solids is described experimentally by measuring the stress-strain curve. The stress (σ) and strain (ε) are defined mathematically as,

$$\sigma = \frac{F}{A_0} \tag{4.43}$$

$$\varepsilon = \frac{\Delta x}{x_0} \tag{4.44}$$

where x_0 and Δx are the equilibrium and change in equilibrium lengths, F is the applied force, and A_0 is the equilibrium area of the face orthogonal to the applied force. For linear materials, the stress-strain relationship results in Hooke's law,

$$F = k\Delta x = \frac{YA_0}{x_0}\Delta x \tag{4.45}$$

where Y is Young's modulus and is equal to the strain divided by the stress.[10, 78-79]

Both the stress and strain are represented by second-rank tensors, corresponding to the various combinations of deformations possible (**Figure 4-2**), and in the case of solids can be written as,

$$\sigma_{ij} = \begin{bmatrix} \sigma_{xx} & \sigma_{xy} & \sigma_{xz} \\ \sigma_{yx} & \sigma_{yy} & \sigma_{yz} \\ \sigma_{zx} & \sigma_{zy} & \sigma_{zz} \end{bmatrix} \tag{4.46}$$

$$\varepsilon_{kl} = \begin{bmatrix} \varepsilon_{xx} & \varepsilon_{xy} & \varepsilon_{xz} \\ \varepsilon_{yx} & \varepsilon_{yy} & \varepsilon_{yz} \\ \varepsilon_{zx} & \varepsilon_{zy} & \varepsilon_{zz} \end{bmatrix} \tag{4.47}$$

The elastic constant tensor (C) of a three-dimensional solid is then required to relate the stress and strain, resulting in a fourth rank tensor with indices *i, j, k,* and *l* (not to be confused with the orbital indices *i* and *j* that are previously used),

$$\sigma_{ij} = C_{ijkl}\varepsilon_{kl} \tag{4.48}$$

The elastic constants are typically expressed using a reduced notation C_{vu} (Voigt's notation), where $v = ij$ and $u = kl$, with v and u having values that correspond to the various indices of the individual tensors (*i.e.* $v = 1, ...,6$ where 1=*xx*, 2=*yy*, 3=*zz*, 4=*yz*, 5=*xz*, and 6=*xy*).[80] The elements of the elastic tensor are defined as

$$C_{vu} = \frac{1}{V}\frac{\partial^2 E}{\partial\varepsilon_v\partial\varepsilon_u} = \frac{1}{V}\sum_{i,j=1}^{3}\sum_{k,l=1}^{3}\frac{\partial^2 E}{\partial a_{ij}\partial a_{kl}} \tag{4.49}$$

The second derivatives are determined in the same manner as the frequency analysis, the energy derivatives with respect to lattice vector strain are determined analytically while the second derivatives are evaluated numerically by applying the deformation and subsequently calculating the energy. Bravais lattice symmetry is taken into account by reducing the number of deformations required to construct the elastic tensor, for example a cubic crystal only three deformations corresponding to the C_{11}, C_{12} and C_{44} constants must performed.

The calculation of elastic constants permits the description of solids physical properties using a variety of parameters such as the Bulk, shear, and Young's moduli. The elastic properties can be used in a variety of ways, including aiding in the description of lattice dynamics, and determination of materials strengths. **Chapter 14** presents a unique method for determining the elastic constants of large biopolymers using terahertz spectroscopy, and those results are confirmed via the aforementioned *ab initio* methods. Finally, the elastic constants can be used to describe other properties of solids, such as the piezoelectric and piezo-optic effects, which will be discussed in the following section.
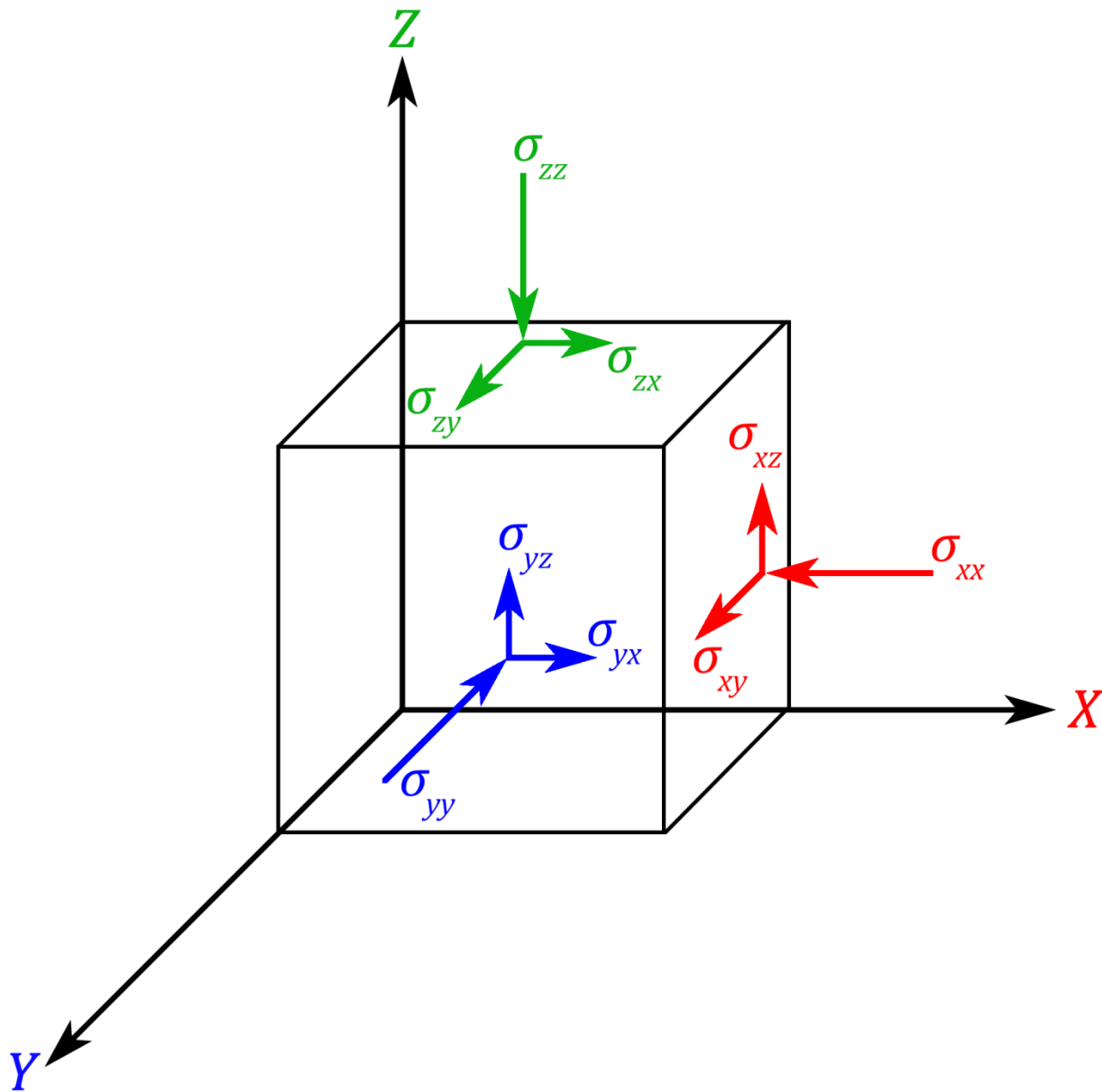
Figure 4-2. Graphical illustration of the stress tensor elements on a crystal.

4.2.5.2 Calculation of the Piezeo-Optic Tensor

The application of stress to crystalline materials can have a profound effect on electronic and optical properties, with the most well-known example being the piezoelectric effect.[81-82] An algorithm was developed for the calculation of one of these quantities in particular, the piezo-optic tensor, which is a measure of the change in a crystals refractive index as a function of stress.[83] The calculation of the piezo-optic tensor requires that the full elastic and photoelectric tensors be constructed. The photoelastic tensor (p_{ijkl}) relates the change in the inverse dielectric tensor ($\Delta \epsilon_{ij}^{-1}$) as a function of strain,

$$p_{ijkl} = \frac{\partial \epsilon_{ij}^{-1}}{\partial \varepsilon_{kl}}$$

(4.50)

and can predict if a material will become birefringent upon application of a deformation.[84-85] The dielectric tensor (and by extension its inverse) are related to the polarizability tensor (α),

$$\epsilon_{ij} = \delta_{ij} + \frac{\alpha_{ij}}{\epsilon_0 V}$$

(4.51)

where δ_{ij} is the Kronecker delta, ϵ_0 is the vacuum permittivity, and V is the unit cell volume. The polarizability tensor is calculated using the Coupled Perturbed Hartree-Fock/Kohn-Sham method,[86-88] by taking the second derivative of the energy with respect to applied electric field (**E**),

$$\alpha_{ij} = \frac{\partial^2 E}{\partial \mathbf{E}_i \partial \mathbf{E}_j} \tag{4.52}$$

The fourth-rank piezo-optic tensor (π) is then the product of the inverse of the elastic tensor ($\mathbb{S}$, the elastic compliance tensor) and the photoelastic tensor,[83]

$$\pi_{ijkl} = p_{ijkl}\mathbb{S}_{ijkl} \tag{4.53}$$

It is important to note that unlike the elastic tensor and compliance tensors, the photoelastic and piezo-optic tensors are not symmetric ($\pi_{ij,kl} \neq \pi_{kl,ij}$) and with the exclusion of Bravais lattice symmetry effects the entire tensor must be calculated.

The calculation of the piezo-optic tensor represents the utility of the DFT methods implemented into the CRYSTAL software. It builds upon the techniques described in each section of this chapter, combining results from different simulations to arrive at the final result. However, all of the theoretical equations are similar in their dependence on the ground state electron density, and this helps to highlight that the accurate determination of that energy enables obtaining results by simply manipulating the manner in which the value is used. It is important to note that these methods only represent a small fraction of the available calculation types in CRYSTAL.

4.3 References

1.   Pisani, C.; Dovesi, R.; Roetti, C., *Different Approaches to the Study of the Electronic Properties of Periodic Systems*; Springer, 1988.

2.   Evarestov, R. A., Quantum Chemistry of Solids. **2012**.

3.   Pisani, C., *Quantum-Mechanical Ab-Initio Calculation of the Properties of Crystalline Materials*; Springer Science & Business Media, 1996; Vol. 67.

4.   Sholl, D.; Steckel, J. A., *Density Functional Theory: A Practical Introduction*; John Wiley & Sons, 2011.

5.   Dovesi, R.; Orlando, R.; Erba, A.; Zicovich-Wilson, C. M.; Civalleri, B.; Casassa, S.; Maschio, L.; Ferrabone, M.; De La Pierre, M.; D'Arco, P.*, et al.*, CRYSTAL14: A Program for the *ab initio* Investigation of Crystalline Solids. *Int. J. Quantum Chem* **2014**, *114*, 1287-1317.

6.   Paolo, G.; Stefano, B.; Nicola, B.; Matteo, C.; Roberto, C.; Carlo, C.; Davide, C.; Guido, L. C.; Matteo, C.; Ismaila, D.*, et al.*, QUANTUM ESPRESSO: A Modular and Open-Source Software Project for Quantum Simulations of Materials. *J. Phys.: Condens. Matter* **2009**, *21*, 395502.

7.   Kresse, G.; Furthmüller, J., Efficient Iterative Schemes for *ab initio* Total-Energy Calculations Using a Plane-Wave Basis Set. *Phys. Rev. B.* **1996**, *54*, 11169-11186.

8.   Segall, M. D.; Philip, J. D. L.; Probert, M. J.; Pickard, C. J.; Hasnip, P. J.; Clark, S. J.; Payne, M. C., First-Principles Simulation: Ideas, Illustrations and the CASTEP Code. *J. Phys.: Condens. Matter* **2002**, *14*, 2717.

9.   Delley, B., From Molecules to Solids with the Dmol3 Approach. *J. Chem. Phys.* **2000**, *113*, 7756-7764.

10.   Kittel, C., *Introduction to Solid State Physics*; Wiley, 2005.

11.   Ramirez, R.; Böhm, M. C., The Use of Symmetry in Reciprocal Space Integrations. Asymmetric Units and Weighting Factors for Numerical Integration Procedures in Any Crystal Symmetry. *Int. J. Quantum Chem* **1988**, *34*, 571-594.

12.   Pisani, C., *Quantum-Mechanical Ab-Initio Calculation of the Properties of Crystalline Materials*; Springer Berlin Heidelberg, 1996.

13.   Sebastiani, D., Current Densities and Nucleus-Independent Chemical Shift Maps from Reciprocal-Space Density Functional Perturbation Theory Calculations. *ChemPhysChem* **2006**, *7*, 164-175.

14.   Simmons, J.; Lin, C. C.; Fouquet, D.; Lafon, E.; Chaney, R., Generalization of the Basis Functions of the LCAO Method for Band-Structure Calculations. *J. Phys. C* **1975**, *8*, 1549.

15.   Grüneich, A.; Heß, B. A., Choosing Gto Basis Sets for Periodic HF Calculations. *Theor. Chem. Acc.* **1998**, *100*, 253-263.

16.   Heaton, R. A.; Harrison, J. G.; Lin, C. C., Self-Interaction Correction for Density-Functional Theory of Electronic Energy Bands of Solids. *Phys. Rev. B.* **1983**, *28*, 5992.

17.   Dovesi, R.; Orlando, R.; Roetti, C.; Pisani, C.; Saunders, V., The Periodic Hartree-Fock Method and Its Implementation in the Crystal Code. *Phys. Status Solidi B* **2000**, *217*, 63-88.

18.   Janpugdee, P.; Pathak, P. H.; Mahachoklertwattana, P.; Burkholder, R. J., An Accelerated DFT-Mom for the Analysis of Large Finite Periodic Antenna Arrays. *Antennas and Propagation, IEEE Transactions on* **2006**, *54*, 279-283.

19.   Busico, V.; Causà, M.; Cipullo, R.; Credendino, R.; Cutillo, F.; Friederichs, N.; Lamanna, R.; Segre, A.; Van Axel Castelli, V., Periodic DFT and High-Resolution Magic-Angle-Spinning (HR-MAS) ^{1}H NMR Investigation of the Active Surfaces of $MgCl_2$-Supported Ziegler-Natta Catalysts. The $MgCl_2$ Matrix. *J. Phys. Chem. C* **2008**, *112*, 1081-1089.

20.   Landsberg, P., Solid State Theory. *Methods and Applications (6th edn) Wiley, New York* **1969**.

21.   Zhang, X.-G.; Varga, K.; Pantelides, S. T., Generalized Bloch Theorem for Complex Periodic Potentials: A Powerful Application to Quantum Transport Calculations. *Phys. Rev. B.* **2007**, *76*, 035108.

22.   Louie, S. G.; Ho, K.-M.; Cohen, M. L., Self-Consistent Mixed-Basis Approach to the Electronic Structure of Solids. *Phys. Rev. B.* **1979**, *19*, 1774.

23.   Chadi, D., Localized-Orbital Description of Wave Functions and Energy Bands in Semiconductors. *Phys. Rev. B.* **1977**, *16*, 3572.

24.   Bickelhaupt, F. M.; Baerends, E. J., Kohn-Sham Density Functional Theory: Predicting and Understanding Chemistry. *Reviews in Computational Chemistry, Volume 15* **2007**, 1-86.

25.   Kohn, W.; Becke, A. D.; Parr, R. G., Density Functional Theory of Electronic Structure. *J. Phys. Chem* **1996**, *100*, 12974-12980.

26.   Kohn, W.; Sham, L. J., Self-Consistent Equations Including Exchange and Correlation Effects. *Phys. Rev.* **1965**, *140*, A1133-A1138.

27.   Parr, R. G.; Yang, W., *Density-Functional Theory of Atoms and Molecules*; Oxford university press, 1989; Vol. 16.

28.   Badziag, P.; Solms, F., An Improved SCF Iteration Scheme. *Computers & chemistry* **1988**, *12*, 233-236.

29.   Gavin, B.; Polizzi, E., Non-Linear Eigensolver-Based Alternative to Traditional SCF Methods. *J. Chem. Phys.* **2013**, *138*, 194101.

30.   Marks, L.; Luke, D., Robust Mixing for ab initio Quantum Mechanical Calculations. *Phys. Rev. B.* **2008**, *78*, 075114.

31.   Montgomery Jr, J. A.; Frisch, M. J.; Ochterski, J. W.; Petersson, G. A., A Complete Basis Set Model Chemistry. Vi. Use of Density Functional Geometries and Frequencies. *J. Chem. Phys.* **1999**, *110*, 2822-2827.

32.   Reveles, J. U.; Köster, A. M., Geometry Optimization in Density Functional Methods. *J. Comput. Chem.* **2004**, *25*, 1109-1116.

33.   El-Azhary, A.; Suter, H., Comparison between Optimized Geometries and Vibrational Frequencies Calculated by the DFT Methods. *J. Phys. Chem* **1996**, *100*, 15056-15063.

34.   Scott, A. P.; Nobes, R. H.; Schaefer III, H. F.; Radom, L., The Wolff Rearrangement: The Relevant Portion of the Oxirene-Ketene Potential Energy Hypersurface. *J. Am. Chem. Soc.* **1994**, *116*, 10159-10164.

35.   Zhao, J.; Xie, R.-H., Genetic Algorithms for the Geometry Optimization of Atomic and Molecular Clusters. *Journal of Computational and Theoretical Nanoscience* **2004**, *1*, 117-131.

36.   Goedecker, S.; Hellmann, W.; Lenosky, T., Global Minimum Determination of the Born-Oppenheimer Surface within Density Functional Theory. *Phys. Rev. Lett.* **2005**, *95*, 055501.

37.   Handy, N. C.; Tozer, D. J.; Laming, G. J.; Murray, C. W.; Amos, R. D., Analytic Second Derivatives of the Potential Energy Surface. *Isr. J. Chem.* **1993**, *33*, 331-344.

38.   Pascale, F.; Zicovich-Wilson, C. M.; López Gejo, F.; Civalleri, B.; Orlando, R.; Dovesi, R., The Calculation of the Vibrational Frequencies of Crystalline Compounds and Its Implementation in the Crystal Code. *J. Comput. Chem.* **2004**, *25*, 888-897.

39.   Zicovich-Wilson, C. M.; Pascale, F.; Roetti, C.; Saunders, V. R.; Orlando, R.; Dovesi, R., Calculation of the Vibration Frequencies of A-Quartz: The Effect of Hamiltonian and Basis Set. *J. Comput. Chem.* **2004**, *25*, 1873-1881.

40.   Perger, W. F.; Criswell, J.; Civalleri, B.; Dovesi, R., Ab-Initio Calculation of Elastic Constants of Crystalline Systems with the Crystal Code. *Comput. Phys. Commun.* **2009**, *180*, 1753-1759.

41.   Schlegel, H. B., Geometry Optimization on Potential Energy Surfaces. *Modern Electronic Structure Theory* **1995**, *2*, 459-500.

42.   Deglmann, P.; Furche, F., Efficient Characterization of Stationary Points on Potential Energy Surfaces. *J. Chem. Phys.* **2002**, *117*, 9535-9538.

43.   Silvi, B.; Savin, A., Classification of Chemical Bonds Based on Topological Analysis of Electron Localization Functions. *Nature* **1994**, *371*, 683-686.

44.   Schlegel, H. B., Optimization of Equilibrium Geometries and Transition Structures. *J. Comput. Chem.* **1982**, *3*, 214-218.

45.   Baker, J., An Algorithm for Geometry Optimization without Analytical Gradients. *J. Comput. Chem.* **1987**, *8*, 563-574.

46.   Pulay, P.; Fogarasi, G., Geometry Optimization in Redundant Internal Coordinates. *J. Chem. Phys.* **1992**, *96*, 2856-2860.

47.   Head, J. D.; Zerner, M. C., An Approximate Hessian for Molecular Geometry Optimization. *Chem. Phys. Lett.* **1986**, *131*, 359-366.

48.   Peng, C.; Ayala, P. Y.; Schlegel, H. B.; Frisch, M. J., Using Redundant Internal Coordinates to Optimize Equilibrium Geometries and Transition States. *J. Comput. Chem.* **1996**, *17*, 49-56.

49.   Feynman, R. P., Forces in Molecules. *Phys. Rev.* **1939**, *56*, 340-343.

50.   Hellmann, H., *Einführung in Die Quantenchemie: Texte Imprimé*; F. Deuticke, 1937.

51.   Pulay, P., Direct Use of the Gradient for Investigating Molecular Energy Surfaces. In *Applications of Electronic Structure Theory*, Springer: 1977; pp 153-185.

52.   Bakken, V.; Helgaker, T.; Klopper, W.; Ruud, K., The Calculation of Molecular Geometrical Properties in the Hellmann—Feynman Approximation. *Mol. Phys.* **1999**, *96*, 653-671.

53.   St-Amant, A.; Salahub, D. R., New Algorithm for the Optimization of Geometries in Local Density Functional Theory. *Chem. Phys. Lett.* **1990**, *169*, 387-392.

54.   Head, J. D.; Zerner, M. C., A Broyden—Fletcher—Goldfarb—Shanno Optimization Procedure for Molecular Geometries. *Chem. Phys. Lett.* **1985**, *122*, 264-270.

55.   Wright, S.; Nocedal, J., Numerical Optimization. *Springer Science* **1999**, *35*, 67-68.

56.   Poppinger, D., Geometry Optimization in ab initio Molecular Orbital Theory. *Chem. Phys. Lett.* **1975**, *34*, 332-336.

57.   Kieffer, S. W., Thermodynamics and Lattice Vibrations of Minerals: 3. Lattice Dynamics and an Approximation for Minerals with Application to Simple Substances and Framework Silicates. *Reviews of Geophysics* **1979**, *17*, 35-59.

58.   Böttger, H., *Principles of the Theory of Lattice Dynamics*; Vch Pub, 1983.

59.   Bell, R., The Dynamics of Disordered Lattices. *Rep. Prog. Phys.* **1972**, *35*, 1315.

60.   Sherwood, P. M. A., *Vibrational Spectroscopy of Solids*; CUP Archive, 1972.

61.   Noel, Y.; Zicovich-Wilson, C. M.; Civalleri, B.; D'Arco, P.; Dovesi, R., Polarization

        Properties of Zno and Beo: An *ab initio* Study through the Berry Phase and Wannier

        Functions Approaches. *Phys. Rev. B.* **2001**, *65*, 014111.

62.   Izmaylov, A. F.; Scuseria, G. E., Analytical Infrared Intensities for Periodic Systems with

        Local Basis Sets. *Phys. Rev. B.* **2008**, *77*, 165131.

63.   Pasquarello, A.; Car, R., Dynamical Charge Tensors and Infrared Spectrum of

        Amorphous Sio 2. *Phys. Rev. Lett.* **1997**, *79*, 1766.

64.   Zhuravlev, Y. N.; Korabel'nikov, D. V.; Aleinikova, M. V., Ab Initio Calculations of the

        Thermodynamic Parameters of Lithium, Sodium, and Potassium Oxides under Pressure.

        Phys. Solid State **2012**, *54*, 1518-1527.

65.   Atkins, P. W.; Friedman, R. S., *Molecular Quantum Mechanics*; Oxford university press,

        2011.

66.   Fei, Y.; Saxena, S., An Equation for the Heat Capacity of Solids. *Geochim. Cosmochim.*

        Acta **1987**, *51*, 251-254.

67.   Mulliken, R. S., Electronic Population Analysis on LCAO–Mo Molecular Wave

        Functions. I. *J. Chem. Phys.* **1955**, *23*, 1833-1840.

68.   Zaanen, J.; Sawatzky, G.; Allen, J., Band Gaps and Electronic Structure of Transition-

        Metal Compounds. *Phys. Rev. Lett.* **1985**, *55*, 418.

69.   Deringer, V. L.; Tchougréeff, A. L.; Dronskowski, R., Crystal Orbital Hamilton

        Population (COHP) Analysis as Projected from Plane-Wave Basis Sets. *J. Phys. Chem. A*

        2011, *115*, 5461-5466.

70. Dronskowski, R.; Bloechl, P. E., Crystal Orbital Hamilton Populations (COHP): Energy-Resolved Visualization of Chemical Bonding in Solids Based on Density-Functional Calculations. *J. Phys. Chem* **1993**, *97*, 8617-8624.

71. Maintz, S.; Deringer, V. L.; Tchougréeff, A. L.; Dronskowski, R., Analytic Projection from Plane-Wave and PAW Wavefunctions and Application to Chemical-Bonding Analysis in Solids. *J. Comput. Chem.* **2013**, *34*, 2557-2567.

72. Hughbanks, T.; Hoffmann, R., Chains of Trans-Edge-Sharing Molybdenum Octahedra: Metal-Metal Bonding in Extended Systems. *J. Am. Chem. Soc.* **1983**, *105*, 3528-3537.

73. Ruggiero, M. T.; Erba, A.; Orlando, R.; Korter, T. M., Origins of Contrasting Copper Coordination Geometries in Crystalline Copper Sulfate Pentahydrate. *Phys. Chem. Chem. Phys.* **2015**, *17*, 31023-31029.

74. Erba, A.; Mahmoud, A.; Orlando, R.; Dovesi, R., Elastic Properties of Six Silicate Garnet End Members from Accurate ab initio Simulations. *Phys. Chem. Miner.* **2013**, *41*, 151-160.

75. Gosline, J.; Lillie, M.; Carrington, E.; Guerette, P.; Ortlepp, C.; Savage, K., Elastic Proteins: Biological Roles and Mechanical Properties. *Phil. Trans. R. Soc. B* **2002**, *357*, 121-132.

76. Helfrich, W., Elastic Properties of Lipid Bilayers: Theory and Possible Experiments. *Zeitschrift für Naturforschung C* **1973**, *28*, 693-703.

77. Tatham, A. S.; Shewry, P. R., Comparative Structures and Properties of Elastic Proteins. *Phil. Trans. R. Soc. B* **2002**, *357*, 229-234.

78. Fast, L.; Wills, J.; Johansson, B.; Eriksson, O., Elastic Constants of Hexagonal Transition Metals: Theory. *Phys. Rev. B.* **1995**, *51*, 17431.

79. Cavallini, F., The Best Isotropic Approximation of an Anisotropic Hooke's Law. *Bollettino di Geofisica Teorica ed Applicata* **1999**, *40*, 1-18.

80. Gow, M. M. In *The Thermodynamics of Crystal Lattices*, Proceedings of the Cambridge Philosophical Society: Mathematical and physical sciences, Cambridge Univ Press: 1944; p 151.

81. Labéguerie, P.; Harb, M.; Baraille, I.; Rérat, M., Structural, Electronic, Elastic, and Piezoelectric Properties of A-Quartz and M X O 4 (M= Al, Ga, Fe; X= P, as) Isomorph Compounds: A DFT Study. *Phys. Rev. B.* **2010**, *81*, 045107.

82. Erba, A.; El-Kelany, K. E.; Ferrero, M.; Baraille, I.; Rérat, M., Piezoelectricity of Srtio 3: An ab initio Description. *Phys. Rev. B.* **2013**, *88*, 035102.

83. Erba, A.; Ruggiero, M. T.; Korter, T. M.; Dovesi, R., Piezo-Optic Tensor of Crystals from Quantum-Mechanical Calculations. *J. Chem. Phys.* **2015**, *143*, 144504.

84. Chang, W., Photoelastic Stiffening by Z-Directed Acoustic-Wave-Induced Electric Fields as Extra Control of Optic Interaction in Batio 3. *Ultrasonics, Ferroelectrics, and Frequency Control, IEEE Transactions on* **2015**, *62*, 1161-1165.

85. Mahmoud, A.; Erba, A.; El-Kelany, K. E.; Rérat, M.; Orlando, R., Low-Temperature Phase of BaTiO$_3$: Piezoelectric, Dielectric, Elastic, and Photoelastic Properties from ab initio Simulations. *Phys. Rev. B.* **2014**, *89*, 045103.

86. Maschio, L.; Kirtman, B.; Rérat, M.; Orlando, R.; Dovesi, R., Ab Initio Analytical Raman Intensities for Periodic Systems through a Coupled Perturbed Hartree-Fock/Kohn-Sham Method in an Atomic Orbital Basis. I. Theory. *J. Chem. Phys.* **2013**, *139*, 164101.

87.   Rérat, M.; Maschio, L.; Kirtman, B.; Civalleri, B.; Dovesi, R., Computation of Second Harmonic Generation for Crystalline Urea and Kdp. An Ab Initio Approach through the Coupled Perturbed Hartree–Fock/Kohn–Sham Scheme. *J. Chem. Theory Comput.* **2015**, *12*, 107-113.

88.   Lacivita, V.; Rèrat, M.; Orlando, R.; Ferrero, M.; Dovesi, R., Calculation of Longitudinal Polarizability and Second Hyperpolarizability of Polyacetylene with the Coupled Perturbed Hartree-Fock/Kohn-Sham Scheme: Where It Is Shown How Finite Oligomer Chains Tend to the Infinite Periodic Polymer. *J. Chem. Phys.* **2012**, *136*, 114101.

CHAPTER 5: Terahertz Time-Domain Spectroscopy

5.1 Origins of the Interaction between Terahertz Radiation and Crystalline Materials

The condensation of molecules into a crystal lattice has a profound effect on their vibrational spectrum, often highlighted by the presence of additional features in the ≤ 600 cm^{-1} (terahertz) region.[1-3] These observations are often attributed to the onset of intermolecular interactions and crystal field effects, and can be broadly explained using the quantum harmonic oscillator model.[4-6] The Hamiltonian for a harmonic oscillator is given by,

$$\hat{H} = \frac{\hat{p}^2}{2\mu} + \frac{1}{2}\mu\omega^2 r \tag{5.1}$$

Corresponding to the time-independent Schrödinger equation,

$$\hat{H}\Psi_n(r) = -\frac{\hbar^2}{2\mu}\frac{d^2\Psi_n(r)}{dr^2} + \frac{1}{2}\mu\omega^2 r\Psi_n(r) = E_n\Psi_n(r) \tag{5.2}$$

where $\hat{p}$ is the momentum operator $(-i\hbar\frac{d}{dr})$, $\hbar$ is the reduced Planck constant, μ is the mass, ω is the angular frequency of the oscillator, and $\Psi_n(r)$ is the radial vibrational wave function for the nth level. The two terms in (5.2) represent the kinetic and potential energies, respectively.

The vibrational wavefunction for the nth level is given as

$$\Psi_n(r) = \frac{1}{\sqrt{2^n n!}} \left(\frac{\mu\omega}{\pi\hbar}\right)^{1/4} e^{-\frac{\mu\omega r^2}{2\hbar}} H_n\sqrt{\frac{\mu\omega}{\hbar}} \tag{5.3}$$

with H_n representing the Hermite polynomials,

$$H_n(r) = (-1)^n e^{r^2} \frac{d^n}{dr^n}\left(e^{-r^2}\right) \tag{5.4}$$

Solving the Schrödinger equation yields energy levels of a harmonic oscillator,

$$E_n = \hbar\omega\left(n + \frac{1}{2}\right) \tag{5.5}$$

with

$$\omega = \sqrt{\frac{k}{\mu}} \tag{5.6}$$

where k is the vibrational force (or spring) constant. Thus for a system to have vibrational levels resonant with terahertz radiation it must have a small angular frequency, meaning it has either a small force constant or a large reduced mass. This relationship is exploited in the solid-state, as the weak intermolecular interactions between the atoms and molecules often lead to vibrational motions that have small force constants, resulting in translations and external rotations of the entire molecules within a lattice.[7-11] However low-frequency vibrations are not limited to external motions, as large flexible molecules often exhibit internal torsional modes that are

153

accessible by terahertz spectroscopy.[12-14] Additionally, crystals that contain heavy atoms such as metal-organic complexes often contain low-frequency vibrational states owing to the increased reduced mass.[15-17] This makes terahertz spectroscopy better suited for characterizing intermolecular interactions than traditional vibrational methods (*e.g.* FTIR) because the large-amplitude motions transverse a large area of the potential energy surface, enabling even subtle changes in the way that molecules interact to be characterized directly.[18] Moreover, terahertz spectroscopy is a valuable analytical tool because each unique crystal will have a unique spectral fingerprint even if two solids contain the same molecular formula, as in the case of crystalline polymorphs.[18-20] In this section, the generation and detection of terahertz pulses will be discussed with respect to the laser system used for a majority of the work presented.

5.2 Relevant Optics Concepts

5.2.1 Induced Polarization

When electromagnetic radiation interacts with non-resonant states in real media the propagating electric field couples to charged particles, resulting in motion that can be described using the classical Drude model.[4, 21-22] In this formalism, the charge carriers are independent of one another with the exception of collisions, which are considered instantaneous events having a mean collision interval of τ. The motion equation for the free carriers is thus,

$$m^* \frac{d^2x}{dt^2} + \frac{m}{\tau}\frac{dx}{dt} - q\boldsymbol{E}(t) = 0 \tag{5.7}$$

where m^* is the effective mass of the charge particle, q is the charge of the particle, and $\boldsymbol{E}$ is the electric field strength. The displacement of charge carriers upon interaction with the electric field induces a polarization of the material,

$$P(t) = (\varepsilon - \varepsilon_\infty)\varepsilon_0 \boldsymbol{E}(t) = Nqx \tag{5.8}$$

where P equal to the induced polarization, ε is the relative permittivity (dielectric constant) of the material at the frequency of the propagating electromagnetic wave, ε_∞ is the high frequency relative permittivity, ε_0 is the vacuum permittivity, and N is the charge carrier density.

Using this relationship, the carrier motion equation (5.7) can be modified to yield the polarization equation,

$$\frac{d^2 P(t)}{dt^2} + \gamma \frac{dP(t)}{dt} - \frac{Nq^2}{m} \boldsymbol{E}(t) = 0 \tag{5.9}$$

where $\gamma = \frac{1}{\tau}$ (the coherent delay). Finally, because any electromagnetic wave can be represented as a Fourier sum of monochromatic waves, the polarization of a material can be deconstructed in the same fashion. Assuming small displacements of the charge carriers, their motion of the carriers (and by extension the polarization) can be modeled as harmonic oscillators. Introducing the electric susceptibility (χ, where $\chi = \varepsilon - \varepsilon_\infty$) the polarization can be expressed as,

$$P(t) = \chi \boldsymbol{E}(t) \tag{5.10}$$

Representing $\boldsymbol{E}(t)$ as a plane wave with the form $\boldsymbol{E}(t) = A(t)\cos\omega_0 t$, it is clearly apparent from (5.10) that the amplitude of the electromagnetic wave is directly proportional the polarization in a material, which also extends to the magnitude of charge carrier displacement (5.7).

5.2.2 Nonlinear Optics

The introduction of large amplitude carrier displacements means that anharmonic effects must be considered.[23-25] Expanding (5.10) as a Taylor series yields,

$$P(t) = \chi_{(1)} \boldsymbol{E}(t) + \chi_{(2)} \boldsymbol{E}(t)^2 + \chi_{(3)} \boldsymbol{E}(t)^3 \dots \tag{5.11}$$

156

This introduces the higher order nonlinear responses that drive many optical processes such as sum frequency and cross-polarized wave generations. Only considering up to the second-order term and substituting the wave equation for electric field, the polarization response of a material becomes,

$$P(t) = \chi_{(1)}A(t)cos\omega_0 t + \boxed{\frac{\chi_{(2)}A(t)^2}{2} + \frac{\chi_{(2)}A(t)^2}{2}\cos 2\omega_0 t} \qquad (5.12)$$

Here, the boxed terms represent the quadratic nonlinear response, and two separable components emerge. The latter term is clearly dependent on both the frequency and amplitude of the electromagnetic wave and is responsible for second-harmonic generation, while the former is only dependent on amplitude and is the foundation behind optical rectification (**Figure 5-1**). The dependence of optical rectification on amplitude alone leads to two very different scenarios when considering continuous and pulsed radiation.

Optical rectification caused by a continuous source yields a constant polarization, resulting in a DC voltage across the material, which is easily proven experimentally by placing a nonlinear material, effectively turning it into a capacitor (**Figure 5-2**). However when the incident radiation is pulsed, a transient polarization is induced that results in emission of radiation proportional to the second derivative of the polarization,

$$E_{radiated}(t) \propto \frac{d^2P(t)}{dt^2} \qquad (5.13)$$

Through Fourier transforming the time-domain emission waveform of polarization induced by pulsed radiation it can be shown that the radiation produced by optical rectification

157

has a frequency less than that of the pulse, contrary to the second harmonic radiation (**Figure 5-2**). In the frequency-domain optical rectification is commonly referred to as *difference-frequency mixing*; however from a fundamental standpoint this view is not entirely accurate since no actual mixing occurs.

An additional consideration when utilizing pulsed electromagnetic radiation is the relationship between pulse duration (Δt) and bandwidth ($\Delta \omega$), which follows the uncertainty principle,

$$\Delta t \Delta \omega \geq \frac{1}{2} \qquad (5.14)$$

and holds true when all frequency components are in phase (known as a Fourier transform limited pulse).[26-27] This relationship is the cause for the phenomenon of white-light generation when using ultrafast (sub-picosecond) laser pulses.

It is important to note that only non-centrosymmetric crystals are capable of producing second-order nonlinear optic effects, a result of the inversion symmetry causing cancellation of dipoles leading to no independent irreducible components in the second order electric susceptibility tensor, $\chi_{(2)}$.
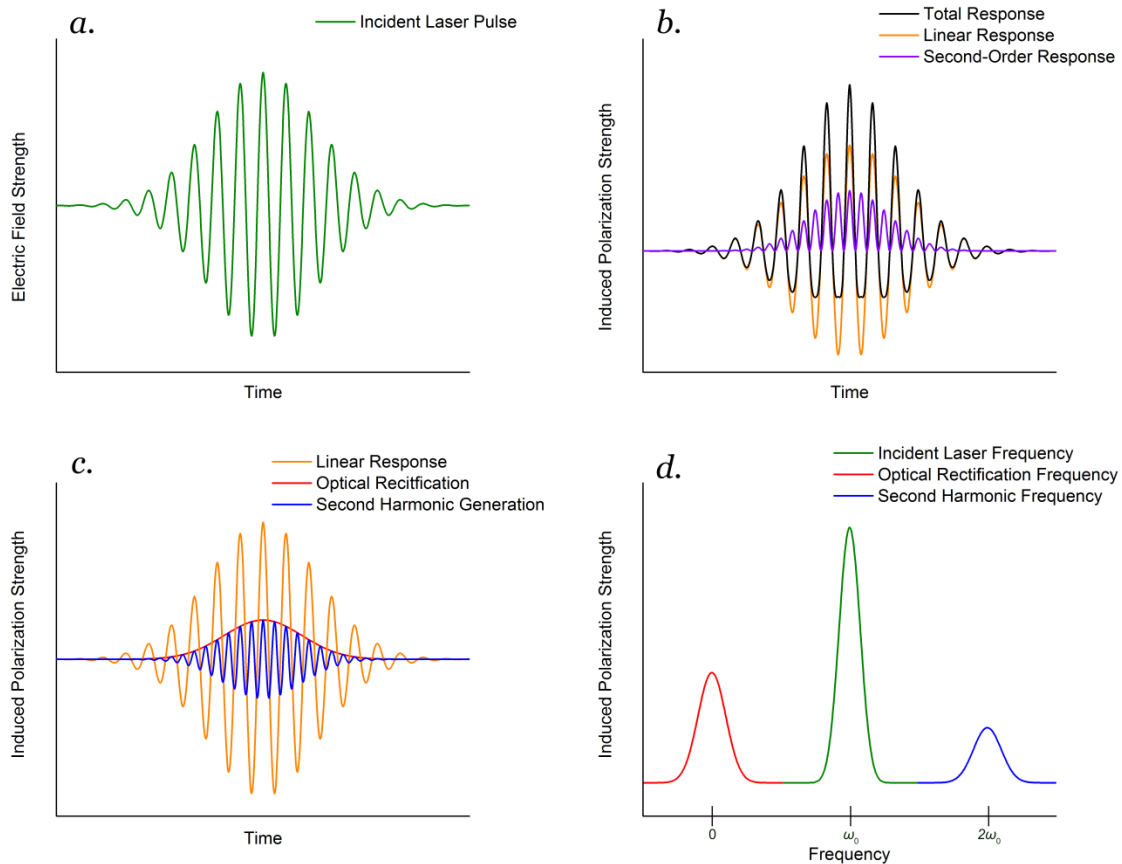
Figure 5-1. A laser pulse (*a,* green) and the linear and second-order polarizations in a nonlinear material (*b*, orange and purple, respectively) of an imaginary system are shown. The second-order components of optical rectification and second-harmonic generation (*c*, blue and purple, respectively), along with the Fourier transform of the time-domain pulse (*d*) are also provided.
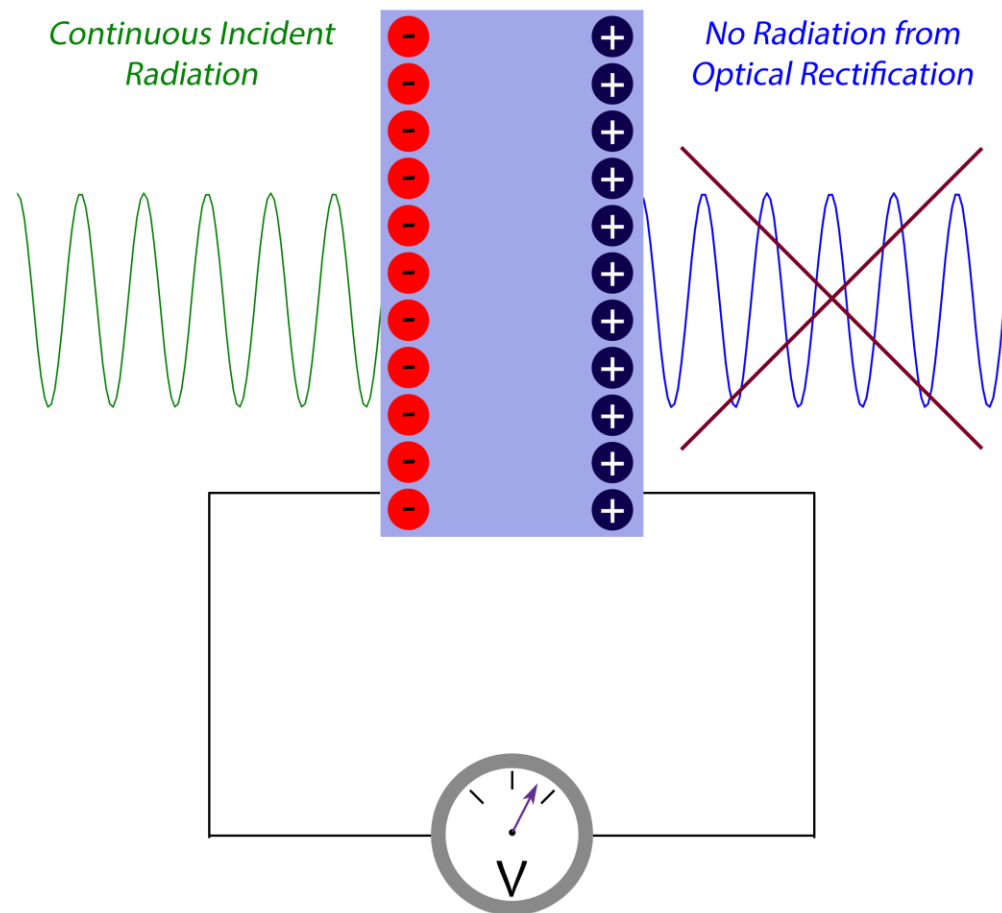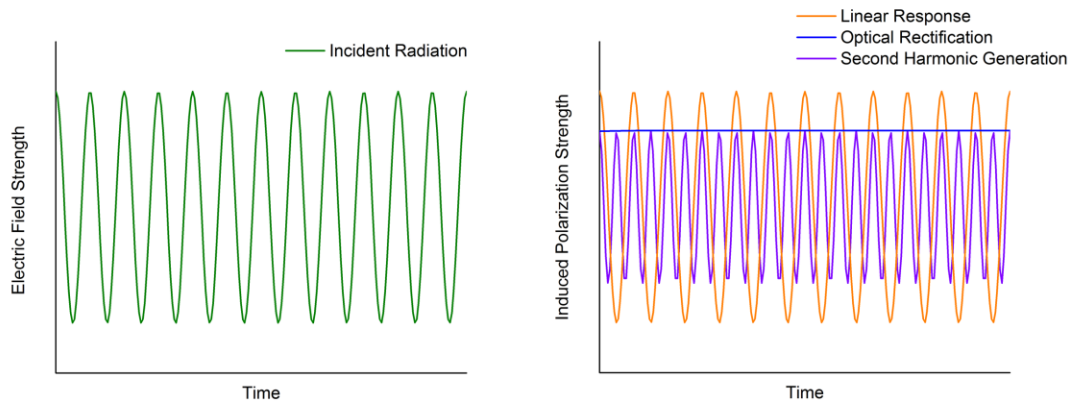
Figure 5-2. Optical rectification from a continuous source (top) results in a constant voltage across the nonlinear material (bottom).

5.3 Terahertz Laser System

The terahertz spectrometer is pumped by a modified Ti:sapphire pulsed laser system comprising four laser components (**Figure 5-3)**, which ultimately produces 35 fs pulses centered at 800 nm with a peak power of 2.5 watts that is used to both generate and detect terahertz radiation. The system has been described in detail previously, and the main components will only be briefly described here for completeness.[28-30]
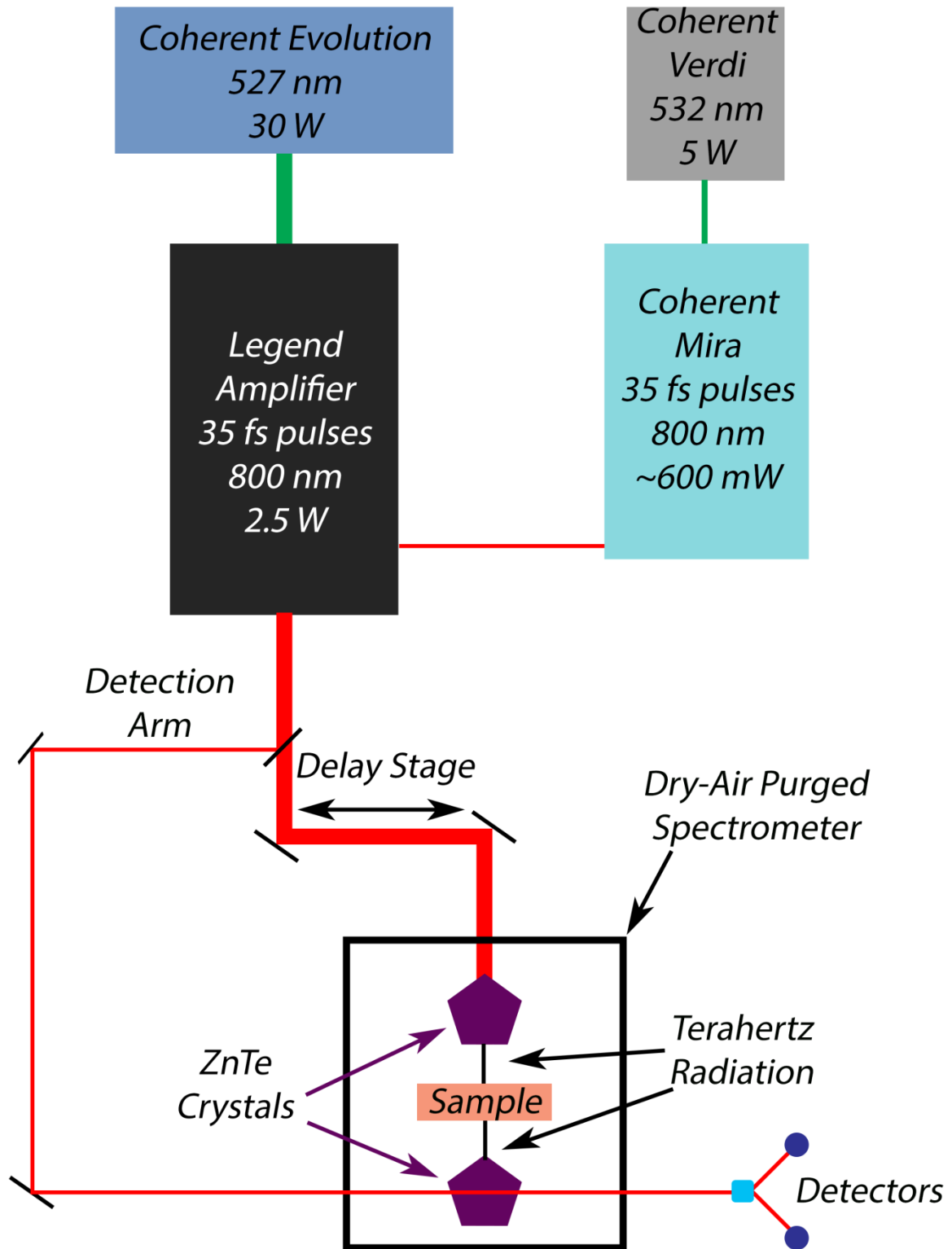
Figure 5-3. Laser system for generation of terahertz radiation.

5.3.1 Coherent Verdi-V5

The Verdi is a diode pump solid state laser responsible for generating a continuous 532 nm beam that is used to generate ultrafast pulses in the Mira oscillator. Two 804 nm fiber coupled laser diodes are used to pump the neodymium-doped yttrium orthovanadate ($Nd:YVO_4$) gain medium to produce near-infrared (NIR) light with a wavelength of 1064 nm. The NIR beam is focused onto a lithium triborate (LBO) crystal that produces visible 525 nm light though second harmonic generation. Both the visible and NIR light exits the LBO crystal and a dichroic mirror is used to transmit the visible and reflect the NIR beams. The NIR light is recycled by passing the beam through a Fabry-Perot etalon[31-32] before being redirected back into the LBO crystal. The Verdi ultimately produces continuous 5 W 532 nm radiation that is directed into the Mira oscillator system.

5.3.2 Coherent Mira

The Mira is a Ti:sapphire oscillator that generates 35 fs pulses through the Kerr lens mode locking effect.[33-34] The 532 nm continuous wave beam from the Verdi is focused onto the Ti:sapphire gain medium, producing an 800 nm beam which is directed into the laser cavity. While mode locking can occur spontaneously, a perturbative glass shaker is initiated to create rapid intensity fluctuations within the cavity in order to promote standing wave generation (mode locking). As the pulse is amplified in the cavity it undergoes group velocity dispersion, resulting in a chirped pulse.[35] This occurs due to the different frequency components of the mode locked pulse travelling at different speeds leading to time-broadening of the pulse. A pair of prisms in

the cavity compensate for this dispersion by forcing the faster components to travel a larger distance in space, correcting for any phase mismatch. As the pulse is amplified the Kerr lens effect (a third-order nonlinear property) focuses the high-energy pulses while blocking the continuous wave radiation. Finally, the cavity exit slit is designed to deflect any residual continuous wave bleed-through, ensuring that only the pulsed radiation are able to escape the cavity. The Mira produces pulses with a 35 fs duration and 76 MHz repetition rate, centered at 800 nm, and a typical peak power of 500-700 mW. The output is used to seed the Coherent Legend Ti:sapphire regenerative amplifier.

5.3.3 Coherent Evolution-30 and Legend-USP

The Coherent Evolution-Legend system is responsible for producing the high-energy pulses that are ultimately used to generate and detect terahertz radiation. Seed pulses from the Mira are used to stimulate emission from a Ti:sapphire crystal in the Legend regenerative amplifier, which is pumped by high-energy pulses from the Evolution. To minimize damage to the Ti:sapphire crystal, the ultrafast 800 nm pulses from the Mira must have a dramatically reduced peak intensity, which is accomplished through the use of a pulse stretcher. The stretcher uses a dispersion grating to introduce a positive temporal chirp that has shorter wavelengths on the leading edge of the pulse. The stretcher component produces 200 ps pulses that are used to seed the Ti:sapphire crystal in the regenerative amplifier, which is simultaneously pumped by the high-energy pulses from the Evolution.

The Evolution is a solid-state Q-switched neodymium-doped yttrium lithium fluoride (Nd:LYF$_4$, or more commonly Nd:LYF) laser that ultimately produces high-energy 527 nm

pulses that are used to pump the Ti:sapphire rod in the Legend regenerative amplifier. A continuous wave diode source pumps the Nd:LYF medium, selected over more common neodymium media because of its long excited-state lifetime (470 μs), which provides efficient energy storage for high energy pulse operation with low repetition rates. The quality of the cavity is modulated using two acousto-optic (AO) Q-switches. In AO Q-switching, an ultrasonic wave is applied to a silica block to generate an optical phase grating with a period and amplitude proportional to that of the applied acoustic wave.[36-37] When the Q-switches are enabled, intracavity light is diffracted and deflected out of the cavity, reducing the Q (quality). However when the ultrasonic wave is removed, the silica block becomes transparent and the cavity returns to its high-Q state, resulting in rapid emission of a high energy 1053 nm pulse that is then directed into frequency doubling LBO crystals, leading to the 527 nm output. The Q-switches in the Evolution are set to a 1 kHz repetition rate, yielding 30 mJ pulses and a maximum 30 W power output.

The 527 nm pump pulses from the Evolution and 800 nm seed pulses from the Mira/stretcher are directed onto the Ti:sapphire rod in the Legend regenerative amplifier. Initially, the seed pulses from the Mira/stretcher are *s*-polarized, with the electric-field of the pulse is perpendicular to the Ti:sapphire angle of incidence, resulting in total reflection. The seed pulse then passes through a disabled Pockels cell,[38] followed by double transmission through a λ/4 waveplate (with the aid of an end mirror). This rotates the polarization of the pulse by 90°, leading to *p*-polarization of the pulse. The pulse then passes through the deactivated Pockels cell, which is then activated, and passes through the Ti:sapphire rod because the angle of incidence is equal to Brewster's angle (the angle of incidence at which polarized light is totally transmitted through a material).[39] The pulse is amplified as it travels through the Ti:sapphire rod, which is

pumped by the Evolution output. The pulse then travels through an ejector crystal, which is

totally transparent due to the polarization of the pulse, as well as through an inactive Pockels cell

and finally an end mirror, directing the pulse back into the Ti:sapphire rod. The amplified pulse

then doubly passes through both the active Pockels cell and the $\lambda/4$ waveplate, resulting in no

polarization change. Finally, when the desired amplification is reached the second Pockels cell is

activated, rotating the pulse to *s*-polarization and causing it to be deflected by the ejector crystal

into the compressor, which operates in the reverse manner as the stretcher. Upon exiting from the

compressor, the pulse is no longer chirped, and the time duration is decreased back to 35 fs. The

final output of the system is a 35 fs pulse, centered at 800 nm with a bandwidth of 65 nm, a 1

kHz repetition rate and a peak power of 2.5 W.

5.4 Terahertz Generation and Detection

There are many techniques for generating and detecting terahertz radiation; however only the methods used in this work will be discussed. The custom built spectrometer utilized for the majority of this work used a nonlinear zinc telluride (ZnTe) crystal to both generate and detect terahertz radiation through optical rectification[35, 40-42] and free-space electrooptic sampling,[43-44] respectively. For the generation, the incoming laser pulse is focused onto a the <110> face of a 1 mm thick ZnTe crystal, and the emitted pulses have a bandwidth of ~10-100 cm^{-1} and a duration of 200 fs. The bandwidth of the emitted radiation is limited by self-absorption by the ZnTe solid.

The detector crystal is also a <110> cut ZnTe solid, and the terahertz absorption is measured indirectly through the use of a detection beam. When the incident terahertz beam interacts with the ZnTe crystal it introduces a birefringence proportional to the amplitude of the pulse. The time-delayed linear polarized detection pulse is directed onto the ZnTe crystal and reflected. The reflected light has a polarization proportional the amount of birefringence, and thus proportional to the amplitude of the incident terahertz pulse. It is the amount of polarization that is detected by passing the detection beam through a Wollaston prism,[45] which splits the pulse into two orthogonal linear polarized beams. The two beams are focused onto a pair of balanced photodiodes, and the difference signal (amplified by a lock-in amplifier) is recorded. A time-domain waveform is generated through the use of the delay stage that samples the spectrum in space, and therefore time.

A commercial broadband terahertz spectrometer (Advantest TAS7500TS) has been used for a few studies (see **Chapters 8**, **14**, and **15**), that uses slight different techniques for generating and detecting far-infrared light. The source module (TAS1130) generates terahertz

radiation through optical rectification using a lithium niobate ($LiNbO_3$) nonlinear crystal. Lithium niobate has similar absorption problems as ZnTe, but by taking advantage of Cherenkov radiation enables the generation of higher bandwidth terahertz pulses.[46-48] Cherenkov radiation, commonly discussed in particle physics because of its prevalence in nuclear reactions, occurs when the group velocity of the laser pulse is large than the phase velocity of the induced polarization.[49-50] This causes the radiated light to be emitted at an angle defined by the ratio of the indices of refraction for the emitted and incident pulses, similar to that of the propagating wave caused by a sonic boom. By focusing the incident laser beam to minimize the distance between it and the surface of the crystal absorption losses can be minimized, thus yielding a terahertz pulse with a larger bandwidth than optical rectification could produce alone. Detection of the terahertz radiation is performed using a photoconductive antenna (TAS1230). A semiconducting material such as doped gallium arsenide (GaAs) is connected to electrodes that introduce a bias. The incident terahertz pulse modifies the generated current, which is detected by a computer.[51]

5.5 References

1.   Schmuttenmaer, C. A., Exploring Dynamics in the Far-Infrared with Terahertz Spectroscopy. *Chem. Rev.* **2004**, *104*, 1759-1780.

2.   Sherwood, P. M. A., *Vibrational Spectroscopy of Solids*; CUP Archive, 1972.

3.   Bratos, S.; Pick, R., *Vibrational Spectroscopy of Molecular Liquids and Solids*; Springer Science & Business Media, 2012; Vol. 56.

4.   Kittel, C., *Introduction to Solid State Physics*; Wiley, 2005.

5.   Maradudin, A. A., *Theory of Lattice Dynamics in the Harmonic Approximation*; Academic Pr, 1971.

6.   Wilson, E. B.; Decius, J. C.; Cross, P. C., *Molecular Vibrations: The Theory of Infrared and Raman Vibrational Spectra*; Courier Corporation, 2012.

7.   Parlinski, K.; Li, Z.; Kawazoe, Y., First-Principles Determination of the Soft Mode in Cubic Zro 2. *Phys. Rev. Lett.* **1997**, *78*, 4063.

8.   Barron, T.; Huang, C.; Pasternak, A., Interatomic Forces and Lattice Dynamics of A-Quartz. *J. Phys. C* **1976**, *9*, 3925.

9.   Hansen, F. Y.; Wang, R.; Taub, H.; Shechter, H.; Reichel, D.; Danner, H.; Alldredge, G., Collective Excitations in Ethane Monolayers Adsorbed on Graphite (0001) Surfaces. *Phys. Rev. Lett.* **1984**, *53*, 572.

10.   Williams, M. R.; True, A. B.; Izmaylov, A. F.; French, T. A.; Schroeck, K.; Schmuttenmaer, C. A., Terahertz Spectroscopy of Enantiopure and Racemic Polycrystalline Valine. *Phys. Chem. Chem. Phys.* **2011**, *13*, 11719-11730.

11. Hermet, P.; Bantignies, J.-L.; Maurin, D.; Sauvajol, J.-L., Terahertz Spectroscopy of the Crystalline A-Quaterthiophene: A Combined Experimental and Density Functional Theory Study. *Chem. Phys. Lett.* **2007**, *445*, 47-50.

12. Delaney, S. P.; Pan, D.; Galella, M.; Yin, S. X.; Korter, T. M., Understanding the Origins of Conformational Disorder in the Crystalline Polymorphs of Irbesartan. *Cryst. Growth Des.* **2012**, *12*, 5017-5024.

13. Delaney, S. P.; Pan, D.; Yin, S. X.; Smith, T. M.; Korter, T. M., Evaluating the Roles of Conformational Strain and Cohesive Binding in Crystalline Polymorphs of Aripiprazole. *Cryst. Growth Des.* **2013**, *13*, 2943-2952.

14. Yu, B.; Zeng, F.; Yang, Y.; Xing, Q.; Chechin, A.; Xin, X.; Zeylikovich, I.; Alfano, R., Torsional Vibrational Modes of Tryptophan Studied by Terahertz Time-Domain Spectroscopy. *Biophys. J.* **2004**, *86*, 1649-1654.

15. Ghosh, S. K.; Bharadwaj, P. K., Puckered-Boat Conformation Hexameric Water Clusters Stabilized in a 2d Metal-Organic Framework Structure Built from Cu (II) and 1, 2, 4, 5-Benzenetetracarboxylic Acid. *Inorg. Chem.* **2004**, *43*, 5180-5182.

16. Ruggiero, M. T.; Korter, T. M., The Crucial Role of Water in Shaping Low-Barrier Hydrogen Bonds. *Phys. Chem. Chem. Phys.* **2016**.

17. Ruggiero, M. T.; Bardon, T.; Strlic, M.; Taday, P. F.; Korter, T. M., The Role of Terahertz Polariton Absorption in the Characterization of Crystalline Iron Sulfate Hydrates. *Phys. Chem. Chem. Phys.* **2015**, *17*, 9326-9334.

18. McIntosh, A. I.; Yang, B.; Goldup, S. M.; Watkinson, M.; Donnan, R. S., Terahertz Spectroscopy: A Powerful New Tool for the Chemical Sciences? *Chemical Society Reviews* **2012**, *41*, 2072-2082.

19. Zeitler, J. A.; Rades, T.; Taday, P., Pharmaceutical and Security Applications of Terahertz Spectroscopy. *THz Spectroscopy: Principles and Applications, CRC Press, Boca Raton, FL* **2007**, 299-323.

20. Strachan, C. J.; Taday, P. F.; Newnham, D. A.; Gordon, K. C.; Zeitler, J. A.; Pepper, M.; Rades, T., Using Terahertz Pulsed Spectroscopy to Quantify Pharmaceutical Polymorphism and Crystallinity. *J. Pharm. Sci.* **2005**, *94*, 837-846.

21. Zhang, X.-C.; Xu, J., *Introduction to Thz Wave Photonics*; Springer, 2010; Vol. 29.

22. Rulliere, C., *Femtosecond Laser Pulses*; Springer, 2005.

23. Shen, Y.-R., Principles of Nonlinear Optics. **1984**.

24. Boyd, R. W., *Nonlinear Optics*; Academic press, 2003.

25. Bloembergen, N., *Nonlinear Optics*; World Scientific, 1996.

26. Dudovich, N.; Dayan, B.; Faeder, S. M. G.; Silberberg, Y., Transform-Limited Pulses Are Not Optimal for Resonant Multiphoton Transitions. *Phys. Rev. Lett.* **2001**, *86*, 47.

27. Schiemann, S.; Hogervorst, W.; Ubachs, W., Fourier-Transform-Limited Laser Pulses Tunable in Wavelength and in Duration (400-2000 Ps). *Quantum Electronics, IEEE Journal of* **1998**, *34*, 407-412.

28. Allis, D. G.; Hakey, P. M.; Korter, T. M., The Solid-State Terahertz Spectrum of Mdma (Ecstasy) – a Unique Test for Molecular Modeling Assignments. *Chem. Phys. Lett.* **2008**, *463*, 353-356.

29. Hakey, P. M.; Allis, D. G.; Hudson, M. R.; Ouellette, W.; Korter, T. M., Investigation of (1r,2s)-(−)-Ephedrine by Cryogenic Terahertz Spectroscopy and Solid-State Density Functional Theory. *ChemPhysChem* **2009**, *10*, 2434-2444.

30. Hakey, P. M.; Allis, D. G.; Ouellette, W.; Korter, T. M., Cryogenic Terahertz Spectrum of (+)-Methamphetamine Hydrochloride and Assignment Using Solid-State Density Functional Theory. *J. Phys. Chem. A* **2009**, *113*, 5119-5127.

31. Jewell, J.; Rushford, M.; Gibbs, H., Use of a Single Nonlinear Fabry–Perot Etalon as Optical Logic Gates. *Appl. Phys. Lett.* **1984**, *44*, 172-174.

32. Mallinson, S. R., Fabry-Perot Interferometer. Google Patents: 1989.

33. Brabec, T.; Spielmann, C.; Curley, P.; Krausz, F., Kerr Lens Mode Locking. *Opt. Lett.* **1992**, *17*, 1292-1294.

34. Cerullo, G.; De Silvestri, S.; Magni, V., Self-Starting Kerr-Lens Mode Locking of a Ti: Sapphire Laser. *Opt. Lett.* **1994**, *19*, 1040-1042.

35. Nahata, A.; Weling, A. S.; Heinz, T. F., A Wideband Coherent Terahertz Spectroscopy System Using Optical Rectification and Electro-Optic Sampling. *Appl. Phys. Lett.* **1996**, *69*, 2321-2323.

36. Henningsen, T.; Conroy, J. J., Acousto-Optic Q-Switch. Google Patents: 1977.

37. Yang, K.; Zhao, S.; Li, G.; Zhao, H., Theoretical and Experimental Study of a Laser-Diode-Pumped Actively Q-Switched Nd: Yvo 4 Laser with Acoustic–Optic Modulator. *Optics & Laser Technology* **2005**, *37*, 381-386.

38. Lee, Y.-S., *Principles of Terahertz Science and Technology*; Springer Science & Business Media, 2009; Vol. 170.

39. Zhang, X. C.; Hu, B.; Darrow, J.; Auston, D., Generation of Femtosecond Electromagnetic Pulses from Semiconductor Surfaces. *Appl. Phys. Lett.* **1990**, *56*, 1011-1013.

40. Lee, Y.-S.; Meade, T.; Perlin, V.; Winful, H.; Norris, T. B.; Galvanauskas, A., Generation of Narrow-Band Terahertz Radiation Via Optical Rectification of Femtosecond Pulses in Periodically Poled Lithium Niobate. *Appl. Phys. Lett.* **2000**, *76*, 2505-2507.

41. Rice, A.; Jin, Y.; Ma, X. F.; Zhang, X. C.; Bliss, D.; Larkin, J.; Alexander, M., Terahertz Optical Rectification from 〈110〉 Zinc-Blende Crystals. *Appl. Phys. Lett.* **1994**, *64*, 1324-1326.

42. Zhang, X. C.; Ma, X. F.; Jin, Y.; Lu, T. M.; Boden, E. P.; Phelps, P. D.; Stewart, K. R.; Yakymyshyn, C. P., Terahertz Optical Rectification from a Nonlinear Organic Crystal. *Appl. Phys. Lett.* **1992**, *61*, 3080-3082.

43. Cai, Y.; Brener, I.; Lopata, J.; Wynn, J.; Pfeiffer, L.; Stark, J. B.; Wu, Q.; Zhang, X. C.; Federici, J. F., Coherent Terahertz Radiation Detection: Direct Comparison between Free-Space Electro-Optic Sampling and Antenna Detection. *Appl. Phys. Lett.* **1998**, *73*, 444-446.

44. Wu, Q.; Litz, M.; Zhang, X. C., Broadband Detection Capability of Znte Electro-Optic Field Detectors. *Appl. Phys. Lett.* **1995**, 2924.

45. Padgett, M.; Harvey, A., A Static Fourier-Transform Spectrometer Based on Wollaston Prisms. *Rev. Sci. Instrum.* **1995**, *66*, 2807-2811.

46. Kitaeva, G. K., Terahertz Generation by Means of Optical Lasers. *Laser Physics Letters* **2008**, *5*, 559-576.

47. Theuer, M.; Torosyan, G.; Rau, C.; Beigang, R.; Maki, K.; Otani, C.; Kawase, K., Efficient Generation of Cherenkov-Type Terahertz Radiation from a Lithium Niobate Crystal with a Silicon Prism Output Coupler. *Appl. Phys. Lett.* **2006**, *88*, 071122.

48.   Auston, D.; Cheung, K.; Valdmanis, J.; Kleinman, D., Cherenkov Radiation from Femtosecond Optical Pulses in Electro-Optic Media. *Phys. Rev. Lett.* **1984**, *53*, 1555.

49.   Pafomov, V., On Transition Radiation and the Vavilov-Cherenkov Radiation. *Zhur. Eksptl'. Teoret. Fiz.* **1959**, *36*.

50.   Zrelov, V. P. *Cherenkov Radiation in High-Energy Physics*; ERDA Div. Phys. Res.: 1973.

51.   Zhang, X. C., *Introduction to Thz Wave Photonics*; Springer, 2010.

CHAPTER 6: Experimental Methods

The dynamic nature of many of the studied compounds, specifically related to water content and polymorph identities, necessitated a precise knowledge of the sample contents at all stages of experimental data acquisition. By performing X-ray diffraction and terahertz measurements simultaneously, validation regarding the presence of contaminants could be obtained. In this section, the basic theory of X-ray diffraction will be discussed first, followed by the experimental methods used for practical measurements.

6.1 X-Ray Diffraction Theory

The diffraction of X-rays by crystals (of copper sulfate pentahydrate) was first discovered in 1912 by Max von Laue.[1-2] Because diffraction occurs when the wavelength of light matches the spacing between particles, crystals diffract X-rays because the atomic spacing is similar to the X-ray wavelength (~1 Å).[3-4] X-ray diffraction was almost instantly recognized for its value, and within a year of its discovery William Bragg developed Bragg's law, which related the observed scattering angles with the spacing between atoms in a crystal.[5-6] Bragg's law, illustrated schematically in **Figure 6-1**, has the popular form,

$$2d \sin(\theta) = n\lambda \tag{6.1}$$

where d is the spacing between atoms, θ is the angle between the incident X-ray vector and the plane of atoms, and λ is the wavelength of the X-rays. Bragg's law arises from the dependence of

diffraction on the inverse of the spacing between planes of atoms, easily shown by rearranging the equation,

$$\frac{\sin(2\theta)}{n\lambda} = \frac{1}{d} \qquad\qquad (5.2)$$

The $\frac{1}{d}$ dependence on diffraction means that only a particular set of reciprocal lattice vectors will result in diffraction at any particular λ, corresponding to points on the Ewald sphere.[7-8] This dependence on reciprocal space (the same reciprocal space used to perform many of the solid-state density functional theory calculations discussed in **Chapter 4**), has implications for determining both the unit cell parameters and atomic structures from an XRD measurement.

$$2d \sin(\theta) = n\lambda$$
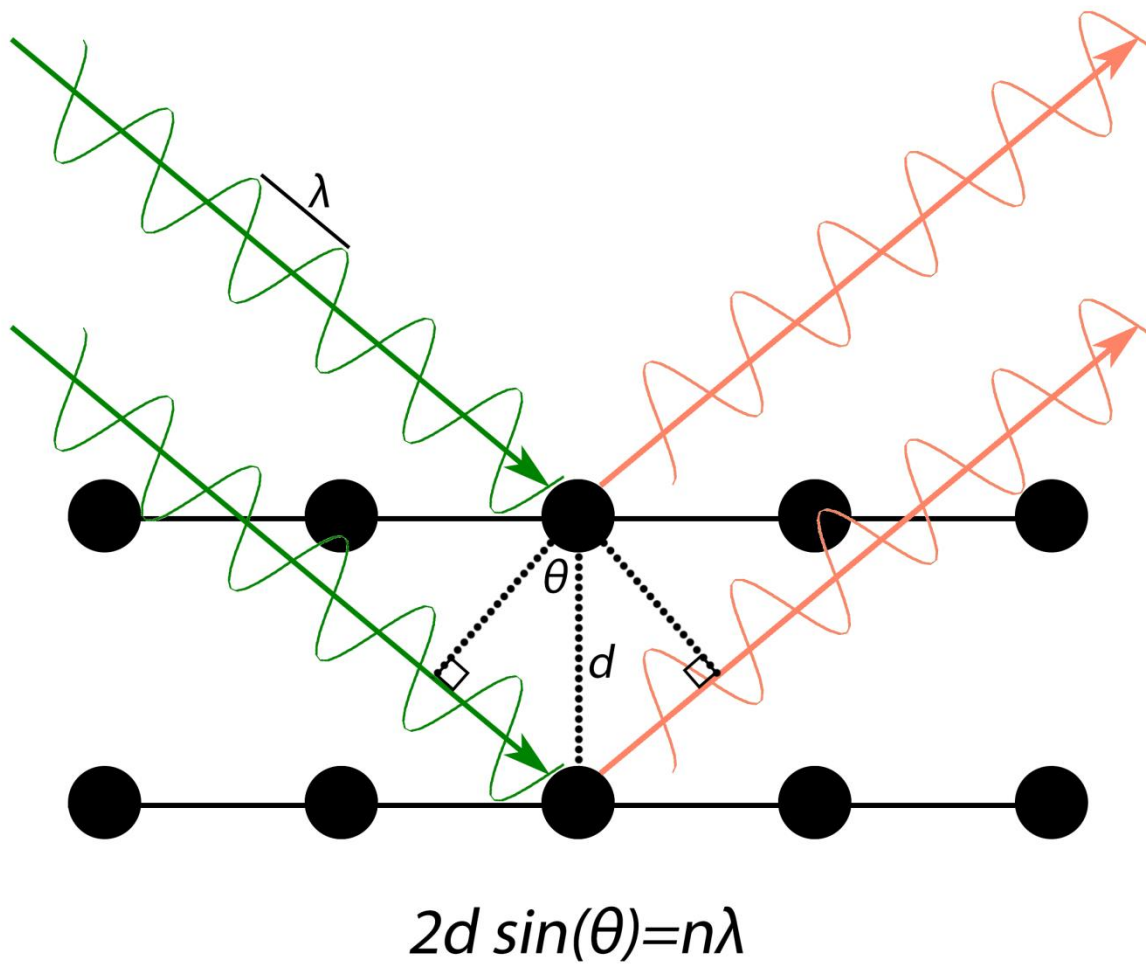
Figure 6-1. Illustration of the diffraction of X-rays by crystals and example of Bragg's law.

X-ray diffraction can be performed on single crystals (*vide infra*) or polycrystalline samples, the latter of which is known as powder X-ray diffraction (PXRD). In a PXRD measurement, the random orientation of the crystallites results in the diffracted X-rays being dispersed in all directions, effectively carving out a cone.[9-10] By either rotating the sample or the X-ray source the different Bragg conditions can be met as a function of angle, generating diffraction lines. The simplest detection method involves projecting the diffracted X-rays onto a photographic plate, known as a Debye-Shcherrer camera.[11-12] In more modern instruments, the diffracted X-rays are detected using a charge-coupled device (CCD).[13-14] Using Bragg's law, the unit cell lengths can be easily determined by the diffraction angles. For example, in the case of a cubic crystal the distance between two lattice constants (*a*) is given by,

$$\frac{1}{d} = \frac{\sqrt{h^2 + k^2 + l^2}}{a} \qquad (5.3)$$

where *h, k,* and *l* are the Miller indices of the Bragg plane, which are defined in terms of either reciprocal lattice vectors or, more commonly, as the intercepts along the real space lattice vectors. Thus, the spacing between the (100) Miller index in a cubic crystal corresponds to the spacing between two unit cell faces (*i.e.* the lattice constant, *a*) and (5.3) reduces to

$$\frac{1}{d} = \frac{\sqrt{1^2 + 0^2 + 0^2}}{a} = \frac{1}{a} \qquad (5.4)$$

Substituting for $\frac{1}{d}$ yields,

$$\frac{\sin(2\theta)}{n\lambda} = \frac{\sqrt{h^2 + k^2 + l^2}}{a} \tag{5.5}$$

Making the determination of lattice constants from PXRD relatively simple for cubic systems, however the other Bravais lattice systems are not as trivial and require more rigorous calculations.

While the lattice constants are easily obtained from PXRD, determining the individual atomic positions and identities is more complex. It is possible to use the intensity of the diffracted X-rays to determine the nuclear identities because it depends on the electron density around of the diffracting atom.[15-16] The intensity of a diffracted X-ray, known as a structure factor, is defined as,

$$F(h,k,l) = \sum_{j=1}^{N} f_j e^{2\pi i(hx_j + ky_j + lz_j)} \tag{5.6}$$

where N is the number of atoms in the unit cell, x_j, y_j, and z_j are the fractional coordinates of atom j with form factor f_j. The atomic form factor is dependent on the electron density,

$$f(r) = \int \rho(r) e^{iQ \cdot r} dr \tag{5.7}$$

and this is why light atoms (*i.e.* hydrogen, helium) are typically not able to be detected to a high degree of precision when using XRD.[17] In order to actually determine the positions of the atoms

179

from XRD data, the structure factors must be Fourier transformed to yield the electron density in real space,

$$\rho(x, y, z) = \frac{1}{V} \sum_h \sum_k \sum_l F(h, k, l) e^{-2\pi i (hx_j + ky_j + lz_j)} \tag{5.8}$$

By solving for the electron density using known atomic form factors and comparing to the experimentally determined values, the atomic structure can be elucidated with a very high amount of precision. Unfortunately in order to generate the electron density both the magnitude and phase of the structure factor must be known, while XRD only measures the former (5.9).

$$\rho(x, y, z) = \frac{1}{V} \sum_h \sum_k \sum_l |F(h, k, l)| e^{-2\pi i (hx_j + ky_j + lz_j - \varphi(hkl))} \tag{5.9}$$

This has implications for determining the structures of crystals, with many proposed techniques for overcoming the phase-problem, including the Patterson and direct methods.[18-20]

An important note is that the symmetry of the crystal is reflected in the symmetry of the diffraction pattern.[1, 3, 8] This has consequences for solving crystal structures as the determination of diffraction symmetry provides information about the bulk symmetry. There are two factors that contribute to the analysis of a diffraction pattern, the first being that the point group of the diffraction pattern is the centrosymmetric parent of the crystalline point group. This arises because for any two reciprocal space vectors (k and –k) the structure factors are complex conjugates of each other (Friedel's law). Therefore the point group of a diffraction pattern (the Laue symmetry) is the point group symmetry of the crystal plus a center of symmetry. The second piece of symmetry information obtainable from a diffraction pattern revolves around the

translational symmetry of the different symmetry elements, specifically lattice centering, screw

axes, and glide planes. The case of lattice centering will be described here to illustrate this.

Considering a face centered cubic crystal, there exist four atoms related by symmetry

with coordinates (x_j, y_j, z_j), $(\frac{1}{2} + x_j, \frac{1}{2} + y_j, z_j)$, $(\frac{1}{2} + x_j, y_j, \frac{1}{2} + z_j)$, $(x_j, y\frac{1}{2} +_j, \frac{1}{2} + z_j)$.

Substituting into (5.6) yields,

$$F(h, k, l) = 4f_j \left[e^{2\pi i (hx_j + ky_j + lz_j)} + e^{2\pi i \left(h\left(\frac{1}{2} + x_j\right) + k\left(\frac{1}{2} + y_j\right) + lz_j \right)} \right.$$
$$\left. + e^{2\pi i \left(h\left(\frac{1}{2} + x_j\right) + ky_j + l\left(\frac{1}{2} + z_j\right) \right)} + e^{2\pi i \left(hx_j + k\left(\frac{1}{2} + y_j\right) + l\left(\frac{1}{2} + z_j\right) \right)} \right] \qquad (5.10)$$

Factoring the above equation returns,

$$F(h, k, l) = \left[1 + e^{\pi i (h+k)} + e^{\pi i (h+l)} + e^{\pi i (k+l)} \right] \times 4f_j e^{2\pi i (hx_j + ky_j + lz_j)} \qquad (5.11)$$

Therefore, systematic absences arise for all *h, k,* and *l* values, except when they are all even or

odd. Using the symmetry information obtained by the analysis of the diffraction pattern, the

number of possible crystallographic space groups can be limited to either a single possibility, or

in some cases a small number of possibilities. In the case of the latter, the calculated intensities

for each possibility are compared to the experimental diffraction pattern, and the space group

that is in the best agreement is chosen.

6.2 X-Ray Experimental Measurements

Once suitable crystals had been grown, the samples were mounted on a MiTeGen tip.

Measurements were performed using a Bruker Kappa APEX DUO diffractometer, which

contained both a copper and molybdenum source capable of generating Kα radiation with

wavelengths of 1.5418 Å and 0.71076 Å, respectably. An initial determination of the lattice

parameters and Bravais lattice type was typically performed by taking 36 frames at different

angles in order to calculate the necessary images required for a full determination using the

Bruker APEX2 software package.[21] For example, the symmetry of a certain cubic lattices only

requires 1/24 of the Ewald sphere to be sampled, as all others points are generated by symmetry

(not considering Friedel's Law). X-ray diffraction measurements were capable of being

performed at a variety of temperatures from 90 K to 300 K through the use of a liquid nitrogen

gas stream cooler (Cryocool LN-3) and variable temperature controller (Cryo-con 32B). Most

measurements were performed at 90 K to mimic the theoretical simulations, as they do not take

thermal effects into account.

Once the X-ray diffraction pattern had been collected, a full structural determination was

performed. First, the unit cell parameters and Bravais lattice type were recalculated using the

entire data set, followed by integration of the diffraction images using the SAINT software

package[22] to obtain the intensities of the reflections (*i.e.* the structure factors). Because the

crystals inherently absorb X-rays, although often to a small amount, the intensity data must be

corrected for this. Absorption effects were corrected for using the SADABS software,[23] which

refines the data using standard absorption correction models. Following this, the space group

symmetry of the solid was determined using XPREP, which analyzes the reflections and finds the systematic absences.[24]

Because the studied solids all contained relatively small molecules the structures were always solved using direct methods.[25] After identification of the heavy-atom positions, the models were refined against the measured structure factor magnitudes (F^2) using the SHELXTL software.[20, 26] The structures were corrected for thermal effects by refining against anisotropic thermal displacement parameters. Finally, the positions of the hydrogen atoms were determined either from residual electron density or by their calculated positions and all atoms were subsequently refined against isotropic displacement parameters.[27]

6.3 Terahertz Spectroscopy

Samples were prepared for terahertz spectroscopic measurements by mixing with polytetrafluoroethylene (PTFE) to a w/w concentration of 0.5-5% depending on the absorption strength of the sample. There are a number of suitable matrices for terahertz spectroscopy, including high density polyethylene (HDPE), polymethylpentene (PMT), and adamantane ($C_{10}H_{16}$), with all meeting the basic requirement of little to no absorption in the sub-150 cm^{-1} region.[28] A PTFE matrix was chosen based on its low hygroscopicity[29] and the relatively low pressures required to press into pellets.[30]

The sample and matrix material were placed into a stainless-steel ball mill (Dentsply-Rinn 3110-3A) to pulverize and homogenize the sample. Pulverization is particularly important for terahertz spectroscopy, as the presence of larger particles can lead to scattering effects.[31-32] Finally, the samples were pressed into ~550 mg pellets with diameters of 13mm using a hydraulic press (ICL EZ-Press 12). A pressure of 2000 psi was typically sufficient for creating stable pellets. It was discovered that in many cases pelletization resulted in a much longer shelf-life for the sample stability then when left in air alone. In one scenario that involved extremely hygroscopic samples ($FeSO_4$), pelletization stabilized the samples for at least one week.[33]

Terahertz measurements were performed at room (300 K) and liquid nitrogen (78 K) temperatures, with the temperature controlled via liquid nitrogen and a variable temperature controller (Cryo-con 32). Because atmospheric water is a strong absorber of terahertz radiation[33-35] the spectrometer was continuously purged with dry air and the sample chamber held under vacuum throughout the entire course of an experiment. The data were acquired over a 32 ps time window consisting of 3200 points, and averaged over 32 scans. The resulting time-domain

terahertz waveform was treated with by a Hanning window and subsequently Fourier

transformed to yield a frequency-domain transmission spectrum. To arrive at absorption units,

the transmission spectrum of a sample was divided by that of a blank, and the final presented

spectra are a result of four averaged sample/blank sets. The absorption spectra were converted to

units of molar extinction coefficient ($\varepsilon = M^{-1}\ cm^{-1}$) through division by the pellet concentration

and volume, respectively.

6.4 References

1. Young, R. A., *X-Ray Diffraction*; Engineering Experiment Station, Georgia Institute of Technology, 1961.

2. Eckert, M., Max Von Laue and the Discovery of X-Ray Diffraction in 1912. *Annalen der Physik* **2012**, *524*, A83-A85.

3. Cullity, B. D.; Weymouth, J. W., Elements of X-Ray Diffraction. *Am. J. Phys.* **1957**, *25*, 394-395.

4. Born, M.; Wolf, E., *Principles of Optics: Electromagnetic Theory of Propagation, Interference and Diffraction of Light*; CUP Archive, 2000.

5. Bragg, W. H.; Bragg, W. L., The Reflection of X-Rays by Crystals. *Proc. R. Soc. London, Ser. A* **1913**, *88*, 428-438.

6. Kapitza, P.; Dirac, P. In *The Reflection of Electrons from Standing Light Waves*, Mathematical Proceedings of the Cambridge Philosophical Society, Cambridge Univ Press: 1933; pp 297-300.

7. Leslie, A. G., The Integration of Macromolecular Diffraction Data. *Acta Crystallogr. Sect. D. Biol. Crystallogr.* **2006**, *62*, 48-57.

8. Warren, B. E., *X-Ray Diffraction*; Courier Corporation, 1969.

9. Harris, K. D.; Tremayne, M.; Kariuki, B. M., Contemporary Advances in the Use of Powder X-Ray Diffraction for Structure Determination. *Angew. Chem. Int. Ed.* **2001**, *40*, 1626-1651.

10. Langford, J. I.; Louer, D., Powder Diffraction. *Rep. Prog. Phys.* **1996**, *59*, 131.

11. Hume-Rothery, W.; Reynolds, P. W., A High-Temperature Debye-Scherrer Camera, and Its Application to the Study of the Lattice Spacing of Silver. *Proceedings of the Royal Society of London. Series A, Mathematical and Physical Sciences* **1938**, 25-34.

12. Hume-Rothery, W.; Strawbridge, D., A General-Purpose Debye-Scherrer Camera and Its Application to Work at Low Temperatures. *J. Sci. Instrum.* **1947**, *24*, 89.

13. Mezouar, M.; Crichton, W.; Bauchau, S.; Thurel, F.; Witsch, H.; Torrecillas, F.; Blattmann, G.; Marion, P.; Dabin, Y.; Chavanne, J., Development of a New State-of-the-Art Beamline Optimized for Monochromatic Single-Crystal and Powder X-Ray Diffraction under Extreme Conditions at the Esrf. *J. Synchotron Radiat.* **2005**, *12*, 659-664.

14. Hammersley, A.; Svensson, S.; Hanfland, M.; Fitch, A.; Hausermann, D., Two-Dimensional Detector Software: From Real Detector to Idealised Image or Two-Theta Scan. *Int. J. High Pressure Res.* **1996**, *14*, 235-248.

15. Hubbell, J.; Veigele, W. J.; Briggs, E.; Brown, R.; Cromer, D.; Howerton, R., Atomic Form Factors, Incoherent Scattering Functions, and Photon Scattering Cross Sections. *J. Phys. Chem. Ref. Data* **1975**, *4*, 471-538.

16. Kittel, C., *Introduction to Solid State Physics*; Wiley, 2005.

17. Abrahams, S.; Collin, R.; Lipscomb, W.; Reed, T., Further Techniques in Single-Crystal X-Ray Diffraction Studies at Low Temperatures. *Rev. Sci. Instrum.* **1950**, *21*, 396-397.

18. Sheldrick, G. M.; Dauter, Z.; Wilson, K.; Hope, H.; Sieker, L., The Application of Direct Methods and Patterson Interpretation to High-Resolution Native Protein Data. *Acta Crystallogr. Sect. D. Biol. Crystallogr.* **1993**, *49*, 18-23.

19.   Egert, E., Patterson Search–an Alternative to Direct Methods. *Acta Crystallogr. Sect. A: Found. Crystallogr.* **1983**, *39*, 936-940.

20.   Sheldrick, G., A Short History of Shelx. *Acta Crystallogr. Sect. A* **2008**, *64*, 112-122.

21.   *Apex2, Data Collection Software*, Version 2011.8-0; Bruker-AXS Inc.: Madison, WI, 2011, 2011.

22.   *Saint Plus, Data Reduction Software*, Version 6.45A; Bruker-AXS Inc.: Madison, WI 2013, 2013.

23.   Sheldrick, G., SADABS. University of Göttingen, Germany Program for Empirical Absorption Correction of Area Detector Data: 1996.

24.   Bruker, S., Version 6.02 (Includes Xprep and SADABS). *Bruker AXS Inc., Madison, Wisconsin, USA* **1999**.

25.   Hauptman, H., The Direct Methods of X-Ray Crystallography. *Science* **1986**, *233*, 178-183.

26.   Sheldrick, G., SHELXTL, Version 6.1; Bruker Analytical X-Ray Systems. *Inc.: Madison, WI* **1997**.

27.   Wilson, A.; Geist, V., International Tables for Crystallography. Volume C: Mathematical, Physical and Chemical Tables. *Crystal Research and Technology* **1993**, *28*, 110-110.

28.   Bründermann, E.; Hübers, H.-W.; Kimmitt, M. F., *Terahertz Techniques*; Springer, 2012; Vol. 151.

29.   Balakrishnan, J.; Fischer, B.; Mickan, S.; Abbott, D. In *Hygroscopicity of Window Materials Using Terahertz Time-Domain Spectroscopy (Thz-Tds)*, Infrared and Millimeter Waves, 2007 and the 2007 15th International Conference on Terahertz

Electronics. IRMMW-THz. Joint 32nd International Conference on, IEEE: 2007; pp 206-207.

30.   Smith, R. M.; Arnold, M. A., Terahertz Time-Domain Spectroscopy of Solid Samples: Principles, Applications, and Challenges. *Appl. Spectrosc. Rev.* **2011**, *46*, 636-679.

31.   Strachan, C. J.; Rades, T.; Newnham, D. A.; Gordon, K. C.; Pepper, M.; Taday, P. F., Using Terahertz Pulsed Spectroscopy to Study Crystallinity of Pharmaceutical Materials. *Chem. Phys. Lett.* **2004**, *390*, 20-24.

32.   Franz, M.; Fischer, B. M.; Walther, M., The Christiansen Effect in Terahertz Time-Domain Spectra of Coarse-Grained Powders. *Appl. Phys. Lett.* **2008**, *92*, 021107.

33.   Ruggiero, M. T.; Bardon, T.; Strlic, M.; Taday, P. F.; Korter, T. M., The Role of Terahertz Polariton Absorption in the Characterization of Crystalline Iron Sulfate Hydrates. *Phys. Chem. Chem. Phys.* **2015**, *17*, 9326-9334.

34.   Xu, J.; Plaxco, K. W.; Allen, S. J., Collective Dynamics of Lysozyme in Water: Terahertz Absorption Spectroscopy and Comparison with Theory. *J. Phys. Chem. B* **2006**, *110*, 24255-24259.

35.   Ruggiero, M. T.; Korter, T. M., Uncovering the Terahertz Spectrum of Copper Sulfate Pentahydrate. *J. Phys. Chem. A* **2016**, *120*, 227-232.

CHAPTER 7: The Crucial Role of Water in Shaping Low-Barrier Hydrogen Bonds

The material contained within this chapter is published in *Physical Chemistry Chemical Physics* (Ruggiero, M.T.; Korter, T.M. *Phys. Chem. Chem. Phys.* **2016**. *In Press*) This article has been reproduced by permission of the PCCP Owner Societies.
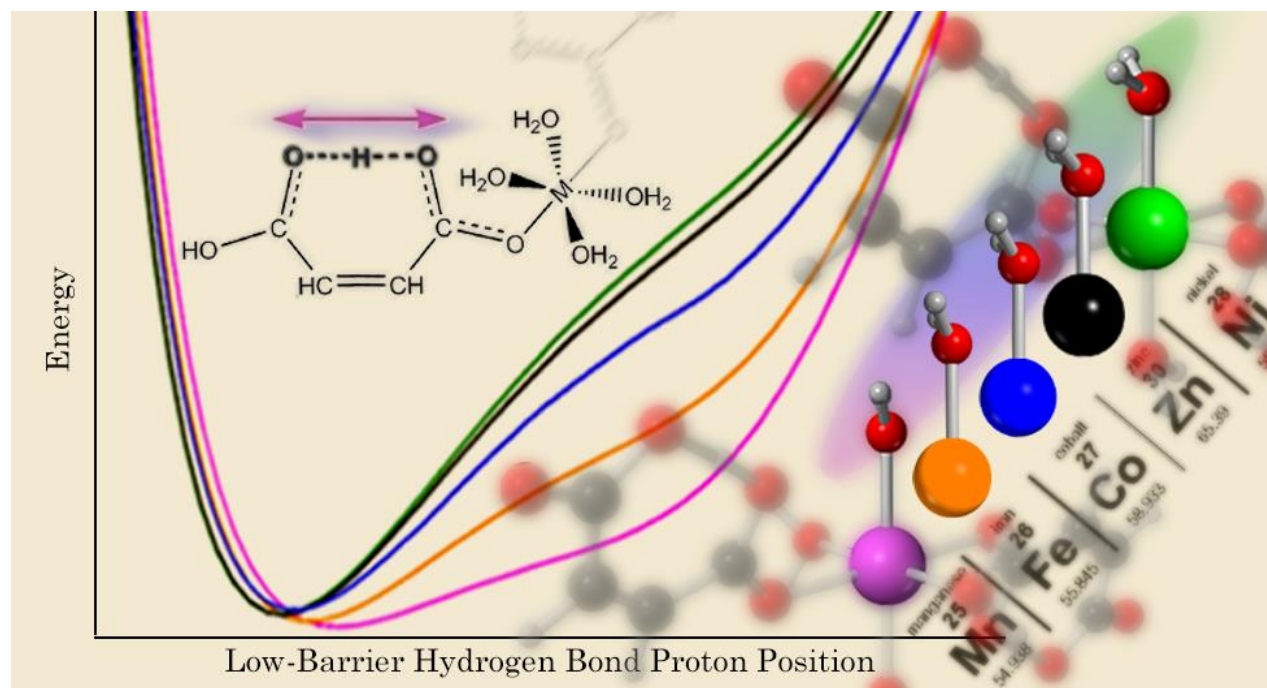
Abstract

Low-barrier hydrogen bonds (LBHBs) are key components in a range of chemical processes, often appearing in metal-mediated catalytic applications. The formation of LBHBs has generally been attributed to the particular geometric arrangement of the surrounding atoms and molecules, yet few specific atomic-level details have emerged. In this study, several metal maleate tetrahydrates have been studied using a combination of solid-state density functional theory, terahertz spectroscopy, and X-ray diffraction to evaluate the significance of both water molecules and metal cations in guiding LBHB formation and function. The findings reveal the assumption that metal identity is of paramount importance to be incomplete, and that the metal cation does not directly influence the LBHB in the maleate ligand. Rather, the characteristics are regulated by water molecule positioning, asserting the critical role of water in governing LBHBs and providing new insight into their formation mechanisms.

7.1 Introduction

Hydrogen bonding is known to be a vital phenomenon for understanding the structure and function of biological macromolecules such as nucleic acids and proteins.[1-3] More recently hydrogen bonds with unusually short heavy-atom separations, often referred to as low-barrier hydrogen bonds (LBHBs), have been shown to play a particularly important role in governing the underlying mechanisms of many enzymatic reactions.[4-10] The prevalence of LBHBs in nature has prompted numerous studies[11-15], yet there still exists debate over the significance and chemical sources of such interactions.[16-19] The electronic and structural origins of LBHBs are an active field of research that has produced multiple theories for LBHB formation, with leading hypotheses involving larger charge distributions[20-21] and resonance assistance.[22-24] Maleic acid is a small molecule with an LBHB-containing anionic form that has been the subject of previous investigations both in the gas-phase and in different condensed-phase environments.[25-27] While there has been a great deal of insight into LBHB characteristics provided by these studies, there are still questions regarding the exact origins of LBHB features, presumably due to the difficulties in recovering atomic-level details from gas-phase and solution-phase experiments. Studying the maleate anion within solid-state complexes enables precise knowledge regarding molecular structure and subsequent effects to be obtained, and can help identify the electronic sources that shape the LBHB potential energy surface.[21, 28-30] Here, crystalline transition metal maleate tetrahydrates (MMT, $M^{2+}(C_4O_4H_3^{-1})_2(H_2O)_4$, where M = Mn, Fe, Co, Ni, Zn, **Figure 7-1**), were selected to study the roles that various energetic forces have on the properties of the LBHB in the maleate ligand.
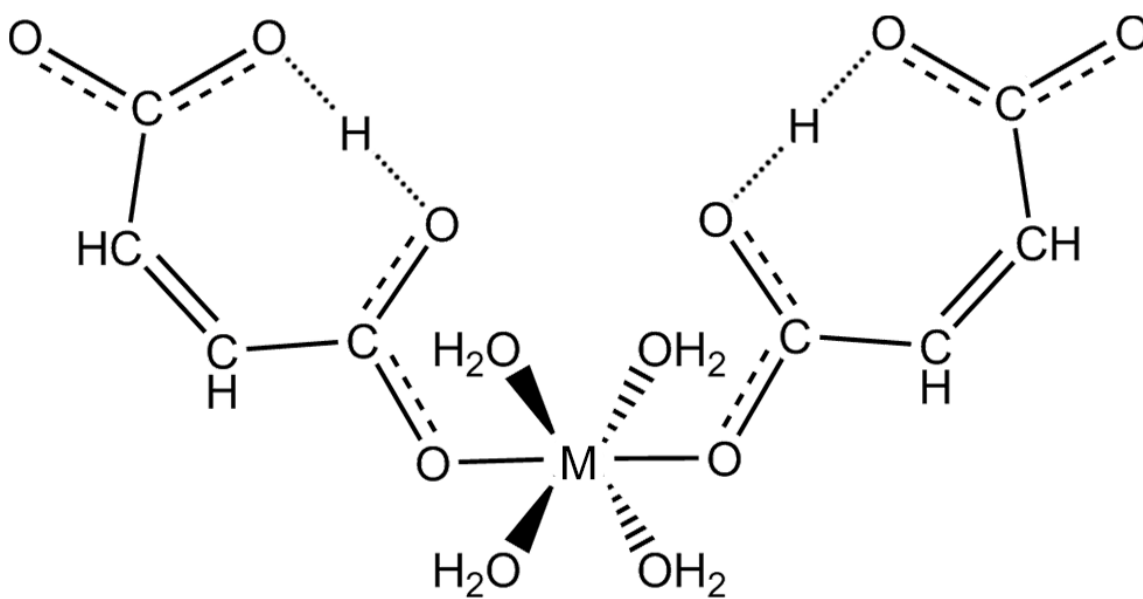
Figure 7-1. General structure of a metal maleate tetrahydrate

The MMT crystals are all generally isomorphic, and are therefore valuable systems for gauging the impact of both metal identity and external water interactions on the formation and characteristics of LBHBs. By studying these crystals with different metals from the $3d$ transition metal block, the effect that individual d-orbital occupations have on the overall electronic structure can be evaluated, with any observed differences tracked across the series. To accomplish this, the MMT solids were investigated using a combination of solid-state density functional theory (DFT), terahertz vibrational spectroscopy, and single-crystal X-ray diffraction (XRD) in order to fully describe the structures and energetic forces within these solids. By joining detailed knowledge of the electronic structure, lattice vibrational data, and precise positional information, new details surrounding LBHB formation can be achieved. Collectively, these tools have revealed that the potential energy surface of LBHB in crystalline metal maleates is governed by *both* metal identity and water positioning. This result explains the origins of the LBHB geometries found in these compounds, and ultimately helps to clarify the properties of LBHB interactions in larger systems.

7.2 Methods

7.2.1 Experimental

Maleic acid (99+%), metal nitrates, and basic metal carbonates were all purchased from Alfa Aesar. Metal maleate tetrahydrates (with the exception of FeMT) were synthesized by two methods: dissolving maleic acid and a metal nitrate at a 2:1 molar ratio in water, and by dissolving maleic acid in hot (353 K) water and adding a metal carbonate until the pH reached 5.5.[31] In the case of the carbonate route synthesis, the solution was filtered after cooling to remove excess starting carbonate. Iron maleate was synthesized by dissolving maleic acid in water and adding elemental iron powder at a 2:1 molar ratio, and refluxing for 1 h.[32] All solutions were allowed to evaporate at room temperature, which produced crystals suitable for single-crystal XRD measurements. Low-temperature single-crystal X-ray diffraction measurements were performed at 90 K using monochromatic Mo Kα radiation ($\lambda = 0.71076$ Å) on a Bruker KAPPA APEX DUO diffractometer containing an APEX II CCD system. The structures were solved using direct methods and refinements were performed with the SHELXTL software.[33] Upon assignment of the non-hydrogen atoms, the structures were refined using isotropic displacement parameters, followed by refinement using anisotropic parameters. All of the water proton positions were assigned by electron density, and the positions were then refined isotropically.

Terahertz (or far-infrared) vibrational spectra were obtained from 20-90 cm^{-1} at 78 K using a time-domain terahertz spectrometer based on an amplified femtosecond Ti:Sapphire near-infrared laser system.[34] The terahertz pulses were generated and detected with zinc telluride

crystals through optical rectification[35] and free-space electrooptic sampling[36], respectively. The samples were mixed with polytetrafluoroethylene (PTFE) with a w/w concentration of ~0.5%, pulverized in a stainless steel ball mill, and subsequently pressed into 2mm thick pellets. The collected terahertz waveforms consisted of 32 averaged waveforms over a 32 ps time window, producing ~1 cm^{-1} resolution. The absorption spectra were obtained by Fourier transformation of the waveforms, and division by a blank PTFE spectrum. The final spectra presented are an average of four separate sample/blank data sets from the same pellets.

7.2.2 Computational

The CRYSTAL14 software package was used for all solid-state DFT simulations.[37] Geometry optimizations were performed with starting atomic positions obtained from the experimental X-ray crystallography measurements of the MMT crystals. The atomic positions and lattice parameters were allowed to fully relax within the space group symmetry of the solid during the optimization, with an energy convergence criterion of 10^{-8} hartree. The hybrid Becke-3-Lee-Yang-Parr (B3LYP) functional[38] was used for all DFT calculations. Based on recent studies[39] the split-valence double-zeta 6-31G(2d,2p) basis set[40] was used to represent all non-metal atoms, while the 6-31G(d) basis set[41] was used to represent the transition metals. All of the metal cations were in their high-spin electronic configuration. The normal mode vibrations of the solids were calculated numerically within the harmonic approximation, using a central-difference equation, requiring two displacements per atom, per Cartesian axis. The infrared intensities were calculated through determination of the atomic charge tensor via the Berry phase method.[42]

Non-periodic simulations were performed with the Gaussian09 software package,[43] and were used for the calculation of the electronic eigenfunctions and eigenvalues of the MMT compounds for visualization purposes. The corresponding computational parameters utilized for the solid calculations were also employed for the non-periodic calculations. This includes using five d-orbitals as opposed to the Gaussian default of six. It is also important to note that Gaussian implements B3LYP using the VWN3 local correlation functional, but CRYSTAL14 uses the VWN5 formulation, however the results presented were not affected by changing the Gaussian B3LYP style, and thus the default setting was used. These calculations were performed on the already optimized solid-state MMT formula units, extracted from the crystals, representing the entire contents of the crystallographic unit cells (Z=1) in these samples. Crystal orbital overlap population (COOP) diagrams were created using the post-processing software AOMix[44], and molecular orbital visualizations were created with VMD.[45]

7.3 Results and Discussion

7.3.1 Structural Analysis

The crystal structures of MnMT, FeMT, CoMT, NiMT, and ZnMT (**Figure 7-2)** were redetermined at 90 K by single-crystal XRD measurements.[31-32, 46-47] Copper was omitted from this series because it does not form a comparable structure, presumably due to its d^9 electronic state promoting a Jahn-Teller distorted geometry. In all cases, the metal cation is coordinated by four water molecules and two maleate anions, with each maleate ligand maintaining an internal LBHB between its terminal carboxylate groups when packed in the solid state.

While the five MMT structures have the same basic formulas and are generally isomorphic, there exist subtle, but significant, changes in the structures moving across the $3d$ period (**Table 7-1**). Because of the lack of atomic precision when determining proton positions with XRD, all structural values which contain hydrogen atoms will be taken from the DFT-refined structure (experimental values are provided in **Appendix D**). A detailed presentation of the structures of MnMT and ZnMT is provided here; since they represent the extremes in the investigated metal series (details regarding the remaining species are available in **Appendix D**).
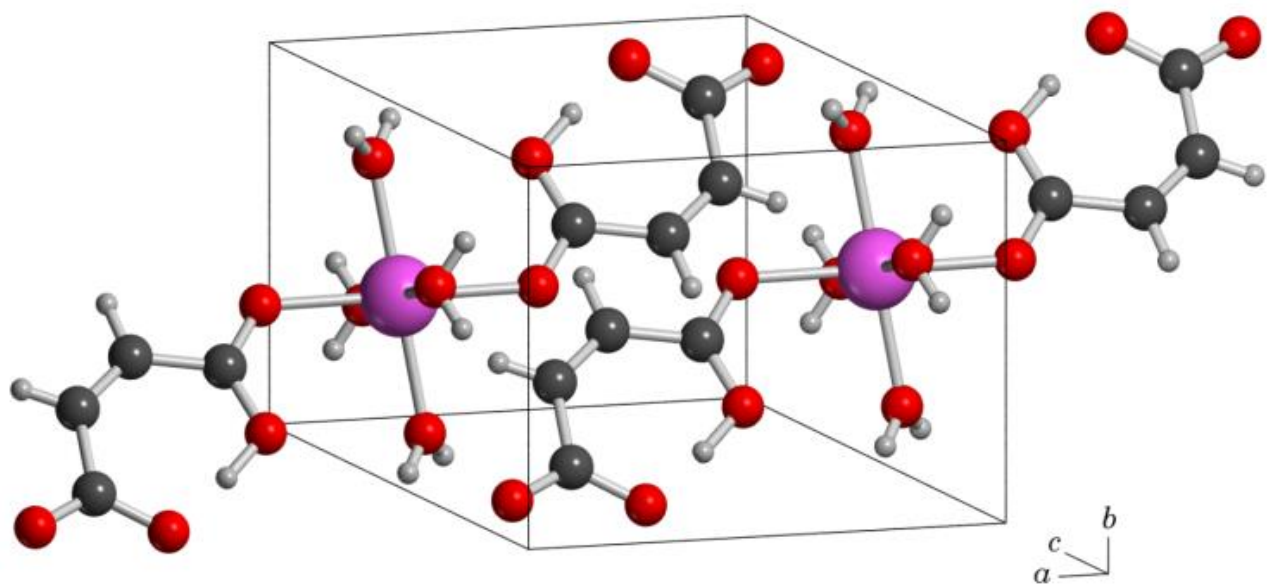
Figure 7-2. Unit cell structure of MnMT

Table 7-1. Calculated water$_a$ tilt angle and O-H$_{mal}$ bond distances.

Species	Water$_a$ Tilt Angle (°)	O$_{far}$-H$_{mal}$ Distance (Å)	O$_{near}$-H$_{mal}$ Distance (Å)
MnMT	8.88	1.077	1.362
FeMT	25.78	1.058	1.385
CoMT	34.55	1.045	1.414
NiMT	43.76	1.038	1.432
ZnMT	41.60	1.039	1.429

The MnMT structure shows deviations from complete isomorphism with the ZnMT structure, with the most apparent being the orientation of a symmetrically equivalent pair of water molecules (water$_a$), whose hydrogens are nearly co-planar (8.88°) with the metal-water$_a$ bond **(Figure 7-3).** In contrast, the water$_a$ molecules exhibit significant tilting in ZnMT (41.60°). Considering the trend across all the MMT samples, starting at MnMT and moving toward ZnMT results in a general increase of the water$_a$ tilt angle, with the greatest deviation from co-planarity with the metal-water$_a$ bond coordinate occurring in NiMT (43.76°). Simultaneously, the covalent bond distance between the oxygen and hydrogen involved in the LBHB (O$_{far}$ and H$_{mal}$) steadily shortens when moving from MnMT (1.077 Å) to ZnMT (1.039 Å). The two structural trends show similar behaviors, strongly suggesting a correlation between metal identity, orientation of water$_a$, and LBHB proton position.
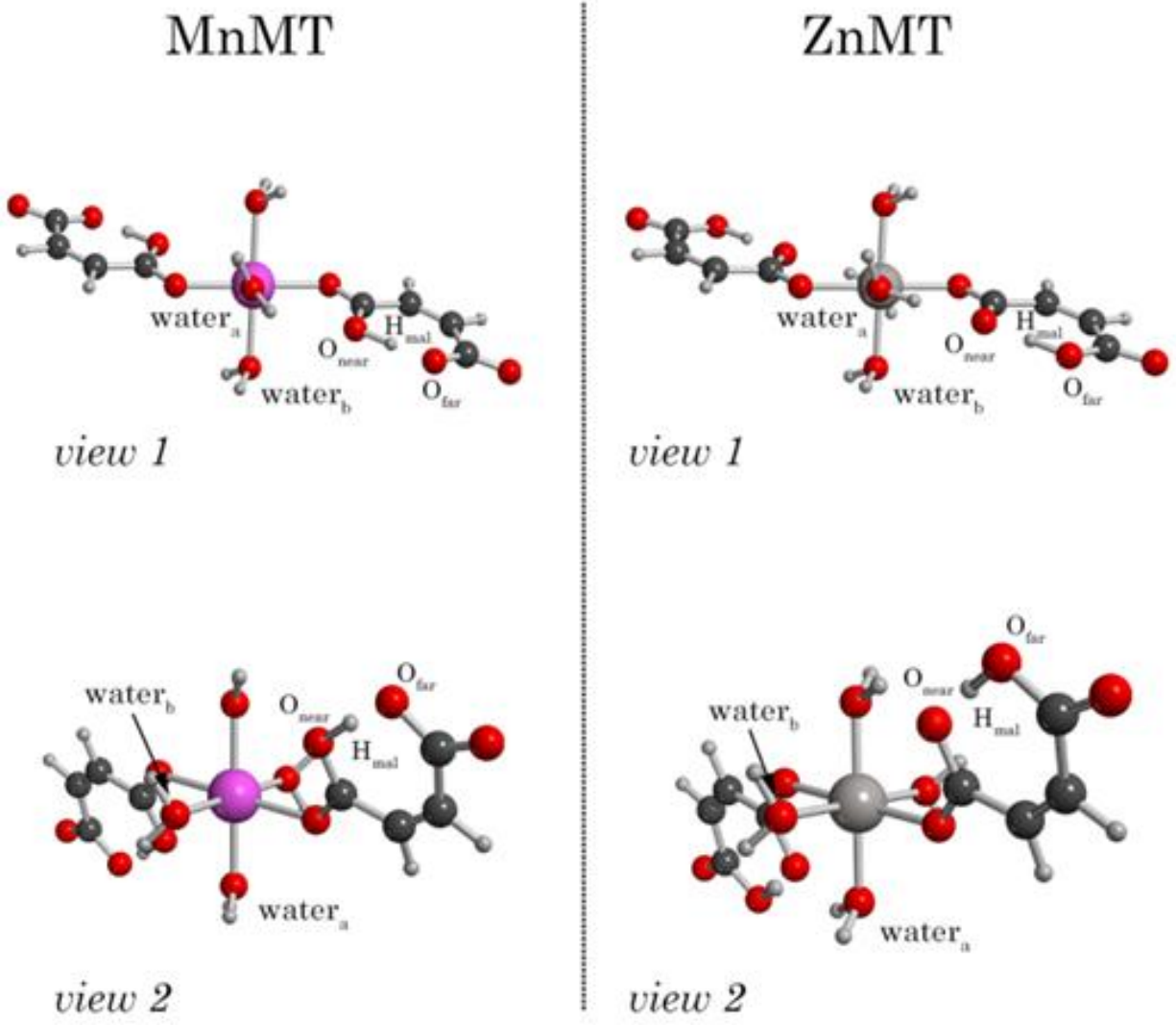
Figure 7-3. Two views of the MnMT (Mn = magenta) and ZnMT (Zn = gray) formula units in the solid state. Note the different orientations of water_a.

7.3.2 Terahertz Vibrational Analysis

The lattice vibrations of the MMT crystals were investigated using terahertz spectroscopy to probe the changes in the large-amplitude motions of the metal and ligands induced by the observed structural differences. The terahertz vibrational spectra were recorded at 78 K and are shown in **Figure 7-4**. The spectra appear very similar to each other, with all five containing two clearly defined absorption features occurring between 54-61 cm^{-1} and 79-83 cm^{-1} for the two peaks, respectively. The similarity of the spectra seems to suggest that the differences between the structures may be too minor to affect the potential energy surfaces governing the specific vibrational motions in the terahertz region. However, there is distinct shifting of the peak centers when moving across the $3d$ metals. In order to determine the exact origins of the frequency shifting, solid-state DFT vibrational simulations were performed on the optimized MMT structures (**Figure 7-5**). The spectral simulations resulted in very good agreement with both the experimental frequencies and intensities, confirming the quality of both the calculated structures and charge distributions within the systems.
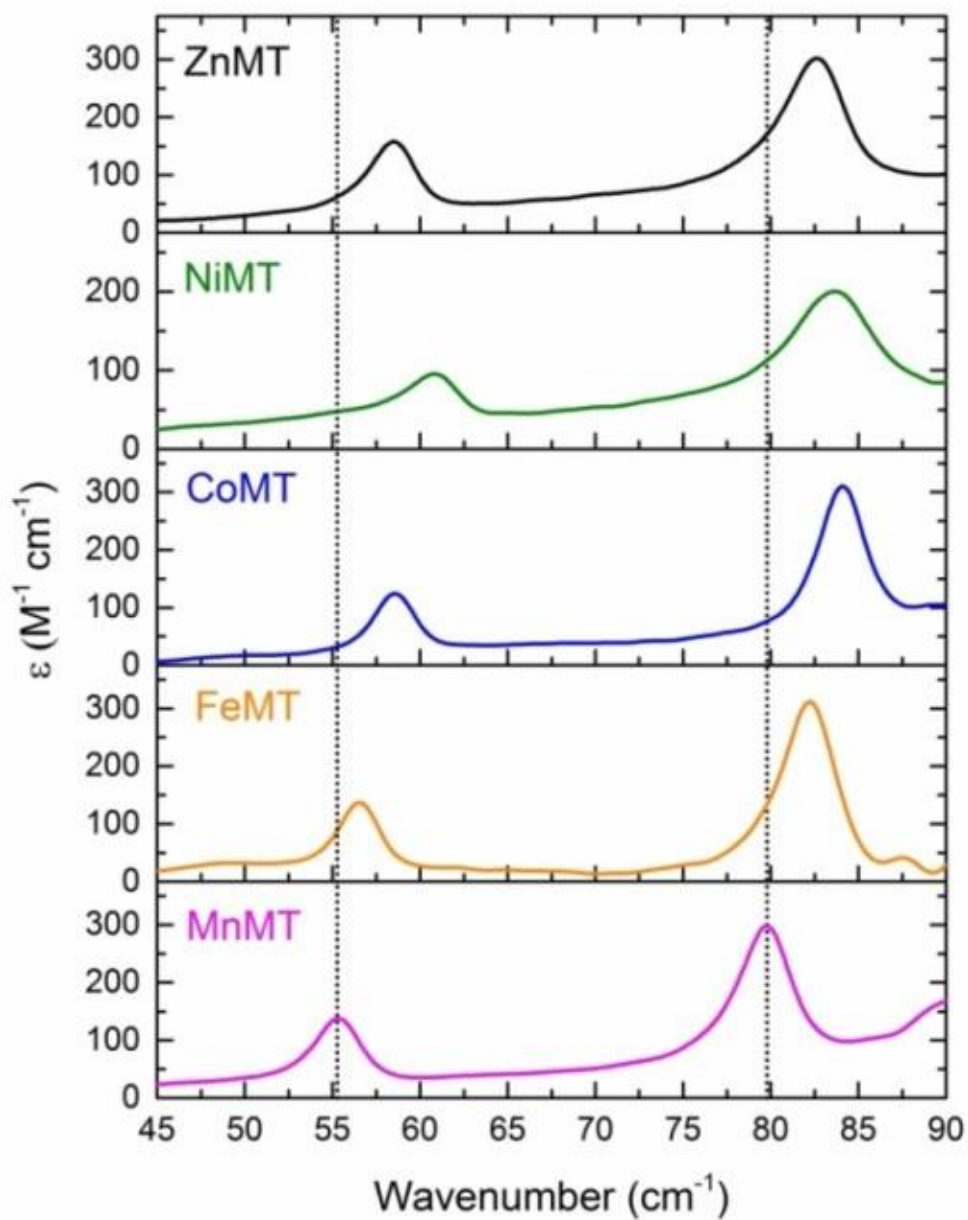
Figure 7-4. Terahertz spectra (78 K) of the crystalline MMT species. The dotted lines have been added at the peak centers of the MnMT spectrum as visual guides.
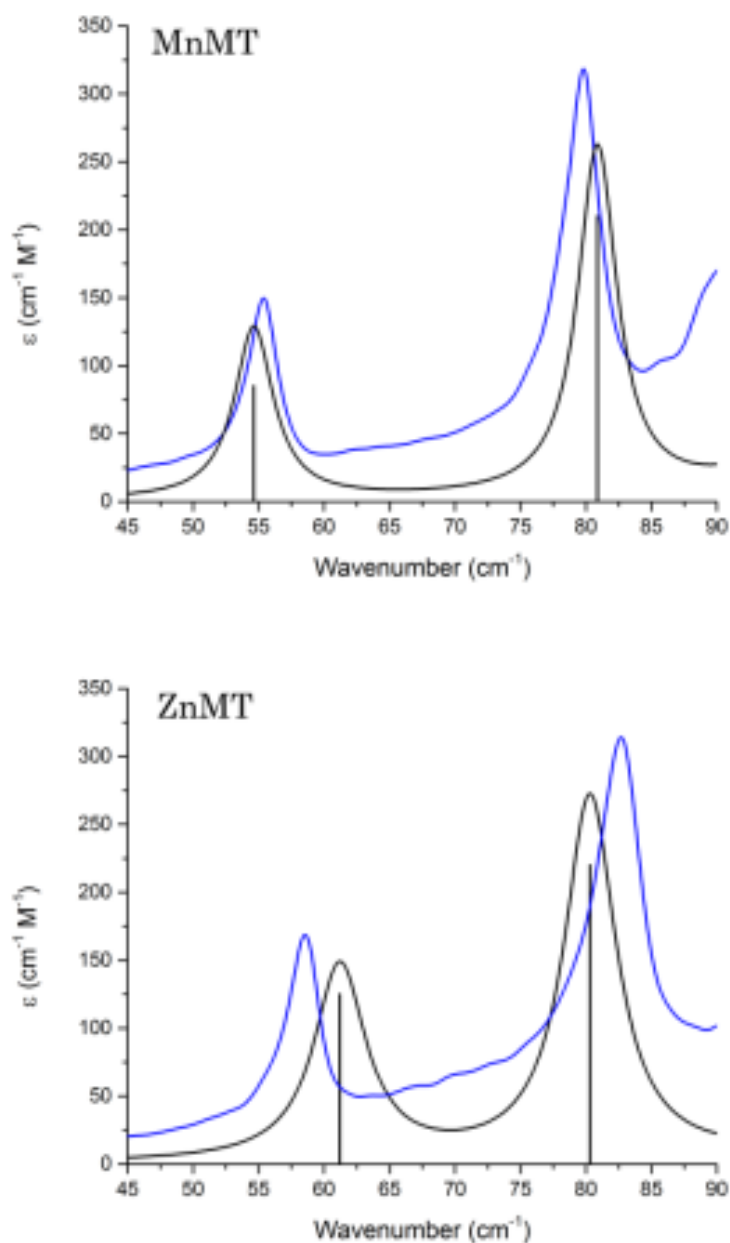
Figure 7-5. Experimental (blue) and DFT-simulated (black) terahertz spectra of MnMT (top) and ZnMT (bottom). The theoretical spectra have been convolved with Lorentzian line shapes with full-width half-maxima (FWHM) of 3.8 and 4.6 cm^{-1} based on the experimental terahertz spectra for MnMT and ZnMT, respectively.

The terahertz frequency trends can be explained by considering the positions of the water$_a$ ligands. Inspection of the vibrational eigenvectors of the two species revealed that the mode types are the same between the various MMT species, and a common component of both terahertz vibrational motions is significant water$_a$ oscillations, with the average amount of water$_a$ displacement (relative to all other displacements) being 19 % and 25 % of the total motion for the lower and higher frequency modes, respectively. A clear trend emerges when the experimental frequencies for the two absorptions are plotted as a function of the water$_a$ tilt angles (**Figure 7-6**), connecting the water$_a$ orientation to the terahertz vibrational motions. The calculated spectra also follow the same trend, although the higher frequency eigenvalue was ~1-2 cm^{-1} offset from the experimental frequency (spectra available in the **Appendix D**). The influence of metal cation mass and size was also investigated and was shown to not influence the spectra in the observed fashion (**Appendix D**). These results highlight that the alterations in the MMT structures that are seen primarily as angular changes in water$_a$ positioning are sufficiently large to change the character of the normal modes in the terahertz spectral region. The agreement between the experiment and *ab initio* calculations not only confirms the correct modeling of the geometry, but also the accurate capturing of the potential energy surfaces involving the water$_a$ molecule and maleate ligands, key components of the LBHB.
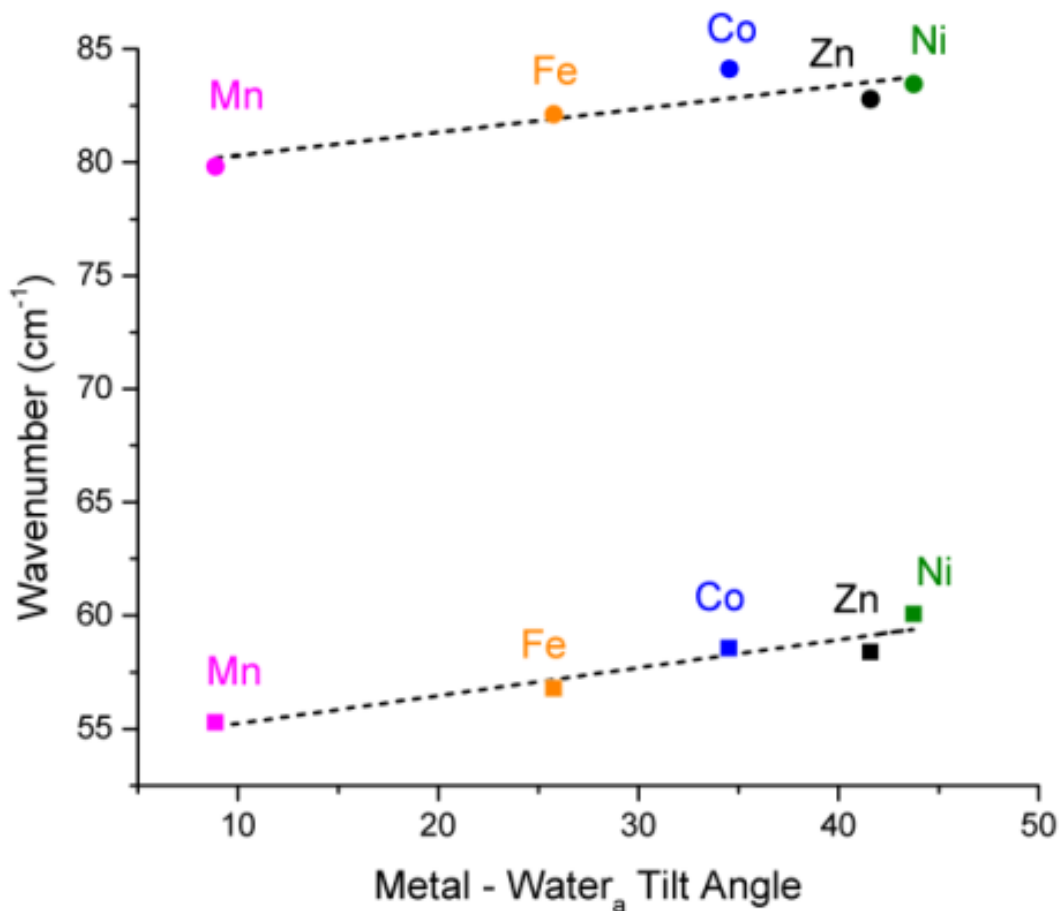
Figure 7-6: Absorption frequencies and metal-water$_a$ tilt angles for the two peaks in the MMT terahertz spectra. The dashed lines represent linear least-squared trend fits for each mode type.

The dependence of the terahertz features on the water$_a$ tilt angle also provides a possible explanation for the varying FWHM of the absorptions in the experimental spectra. It has been shown that the vibrational lifetime (and thus, spectral linewidth) of the modes is inversely proportional to hydrogen bonding strength.[48] The linearity of the hydrogen bond geometry between water$_a$ and O$_{near}$ is directly related to the water$_a$ rotation angle, with the furthest from linear (weakest) in MnMT and closest to linear (strongest) in NiMT. Therefore it can be surmised that the increasing linewidths are a result of stronger hydrogen bonding networks.

7.3.3 Maleate Low-Barrier Hydrogen Bond

Potential energy curves along the LBHB coordinate were created by calculating the energy of the solid with varying H$_{mal}$ positions around the midpoint of the LBHB (+/- 0.300 Å in 0.015 Å increments), while the remainder of the structure was kept rigid. The potential energy curves describing the intramolecular proton transfer of H$_{mal}$ in the MMT species are shown in **Figure 7-7**. The H$_{mal}$ potential energy curves in the solids were found to vary considerably with metal cation identity, as well as deviating from the LBHB potential of the quasi-isolated maleate anion[28] (which is a shallow, symmetric double well). In the case of MnMT, the H$_{mal}$ potential is the widest and most asymmetric, and is the closest to a double well out of all the MMT species. The potentials become increasingly narrow with more single-well character moving across the period, with NiMT showing only a weak shoulder instead of a near second minimum along the LBHB coordinate. The shapes of these potentials help provide an explanation for the observed variation of the O$_{far}$-H$_{mal}$ bond in the MMT compounds. In MnMT, the potential is very wide,

and thus the expectation value for the hydrogen position is closer to the midpoint. The opposite

is true in ZnMT, where the narrow potential leads to a preferred proton position closer to O_{far}.

Given the similar trends noted in the LBHB bond distances and metal-water$_a$ tilt angles across

the MMT series, it is apparent that water$_a$ plays a critical role in the shape of the potential energy

curve of the LBHB. The influence that water$_a$ has on the LBHB arises from the strength of the

hydrogen bonding interaction between the water and the maleate ligands. The tilted orientations

of water$_a$ in NiMT and ZnMT result in a more direct hydrogen bonding interaction with O_{near},

stabilizing the carboxylate character of the maleate anion and driving H_{mal} to have its preferred

position on O_{far}. However in MnMT, the orientation of water$_a$ prohibits a direct interaction with

O_{near}, resulting in a much shallower potential energy surface for H_{mal}. To demonstrate the

dependency on water$_a$, the two water$_a$ molecules were removed from the MnMT, CoMT, and

ZnMT calculated solids (the series intermediate and extremes). The H_{mal} atom was again scanned

as before, but the new simulations revealed the LBHB potentials to be greatly changed, with all

three being essentially the same (see **Figure 7-4**). No indication of a second minimum along the

LBHB coordinate was found. Additionally, the effect of the two water$_b$ molecules was

considered in ZnMT, and removal of those waters resulted in very little change in the H_{mal}

potential (plot provided in the **Appendix D**). These omitted water tests provide compelling

evidence that water$_a$ bears the full responsibility for the shape of the LBHB potential, and any

other effects (such as resonance assistance) are a secondary consideration. That stated, the

identity of the metal does determine the orientation of water$_a$, thus indirectly influencing the H_{mal}

potential energy curves.
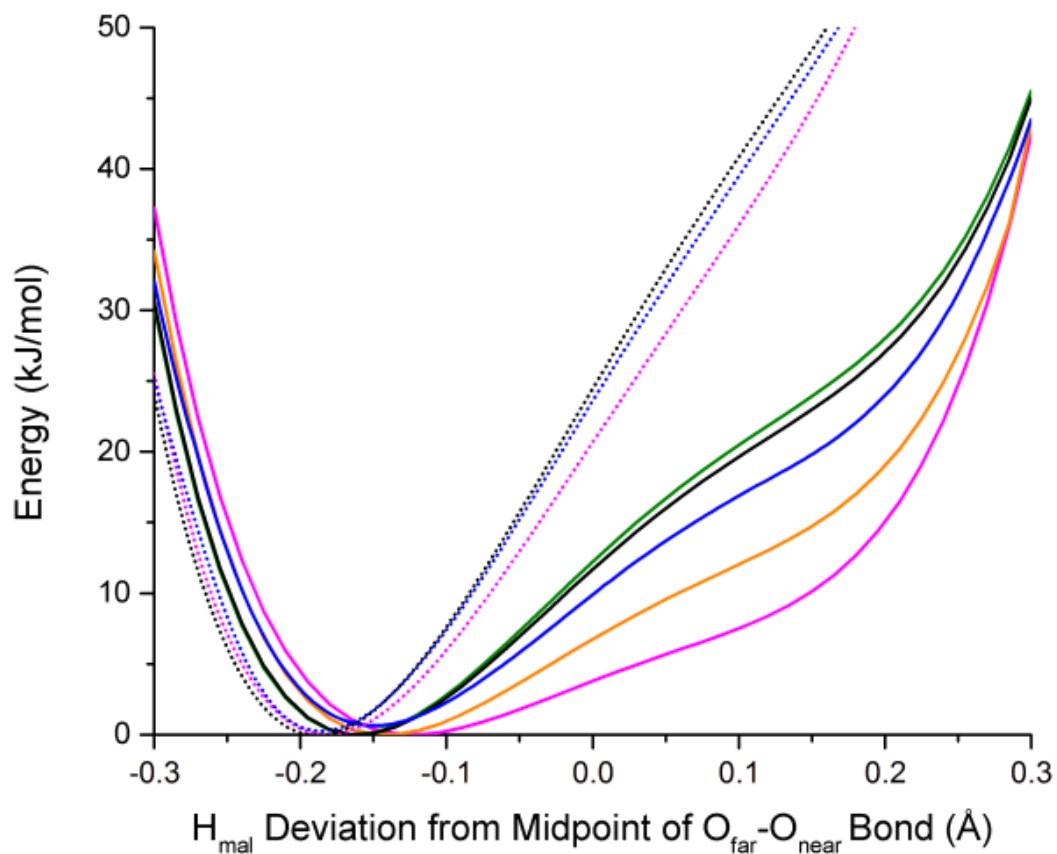
Figure 7-7. Potential energy curves (minima normalized to zero) along the LBHB coordinate for each MMT species (Mn=magenta, Fe=orange, Co=blue, Ni=green, Zn=black). Also shown are the same potential energy surfaces in MnMT, CoMT, and ZnMT after removal of the water$_a$ molecules (dotted magenta, blue, and black curves, respectively). Negative values are towards O$_{far}$, and positive values are towards O$_{near}$.

The pattern in the LBHB potential energy curves prompted the question of whether or not a divalent metal cation could be found where complete proton transfer to O_{near} is realized. This possibility was investigated computationally by creating a purely theoretical structure of calcium maleate tetrahydrate (CaMT) and optimizing its solid-state structure. The CaMT structure results in a water$_a$ tilt angle of 0.0° with respect to the metal-water$_a$ bond coordinate, and the proton in the LBHB was completely transferred to O_{near}. Certainly the use of calcium to achieve proton transfer is extreme, given its total lack of d-orbital electrons, yet this system demonstrates the sensitivity of the water$_a$ tilt and subsequent H_{mal} position to the electron configuration of the metal cation.

7.3.4 Molecular Orbital Analysis

The specific metal clearly plays an important role in the structures of these species, and an investigation of the occupied electronic states of the metal in each system was performed to clarify the origins of the observed differences. While the observed phenomena may be explained using traditional explanations such as pKa variations, it is the electronic origin of such factors that has been elucidated here. In keeping with the detailed presentation of the two extremes of the transition metal series, MnMT and ZnMT exhibit very different metal-water orbital interactions, leading to the dissimilar orientations of water$_a$. For MnMT, the water$_a$ molecular orbitals (which resemble the $1b_1$ and $3a_1$ molecular orbitals of an isolated water molecule) are in an orientation that results in collinear bonding with the d-orbitals of manganese, maximizing overlap ($\varepsilon = -11.00$ eV). However, this orientation also leads to a collinear *antibonding* interaction between the water and the metal ($\varepsilon = -6.61$ eV). In the case of ZnMT, the twisted

211

orientation of water$_a$ results in much less direct orbital overlap (ε = -10.44 eV) than in the corresponding MnMT orbital. This also produces a lessened antibonding interaction (ε = -7.95 eV). Plots of all four molecular orbitals are presented in **Figure 7-8**. The stronger bonding interaction of MnMT is reflected in the energies of the corresponding molecular orbitals, as the MnMT bonding orbital is 0.56 eV lower in energy than ZnMT. MnMT is also more directly antibonding, with the antibonding orbital higher in energy by 1.34 eV than the corresponding ZnMT orbital. This orbital analysis also provides an explanation for the observed behavior in CaMT (no occupied d-orbitals), where the water$_a$ molecules bond in a way which maximizes their overlap with the calcium s and p-type orbitals, resulting in a planar water$_a$-metal geometry.

While visualization of the molecular orbitals is useful for initial characterization of the metal-water$_a$ interactions, it does not provide a detailed picture regarding the specific electronic populations in the bond. A more quantative analysis can be achieved by calculating the density of states and weighting it by the corresponding overlap elements between the metal and water$_a$ orbitals. This method is commonly referred to as a crystal orbital overlap population (COOP) analysis and has been used in the past to characterize the interactions between fragments in molecular species.[49-50] The COOP data presented in **Figure 7-9** was produced by multiplying the density of states by the overlap matrix (7.1),

$$COOP_{\mu,\nu} = \sum_i \sum_\mu \sum_\nu S_{\mu\nu} C_{\mu,i} C_{\nu,i}^* \delta(E - \varepsilon_i) \qquad (7.1)$$

Where μ and ν are the orbital indices from the respective fragments, $\boldsymbol{C}$ and $\boldsymbol{C}^*$ are the eigenvectors, $\boldsymbol{S}_{\mu,\nu}$ is the overlap between $\boldsymbol{C}_\mu$ and $\boldsymbol{C}_\nu$, and $\boldsymbol{\delta}(E - \varepsilon_i)$ is the sampling interval.
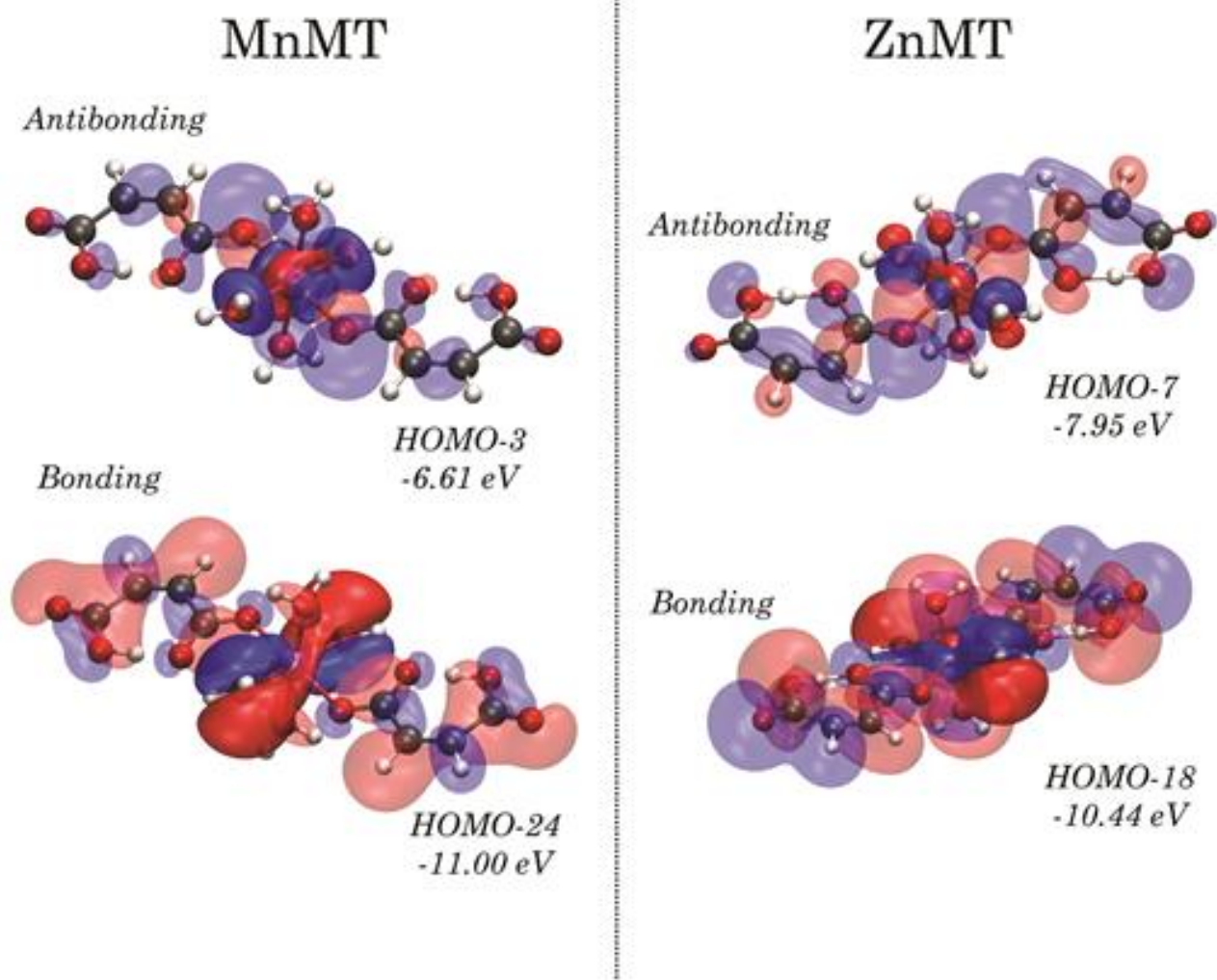
Figure 7-8. Occupied antibonding (top) and bonding (bottom) molecular orbitals of MnMT and ZnMT. The orbital lobes in the area of interest have been darkened for clarity.
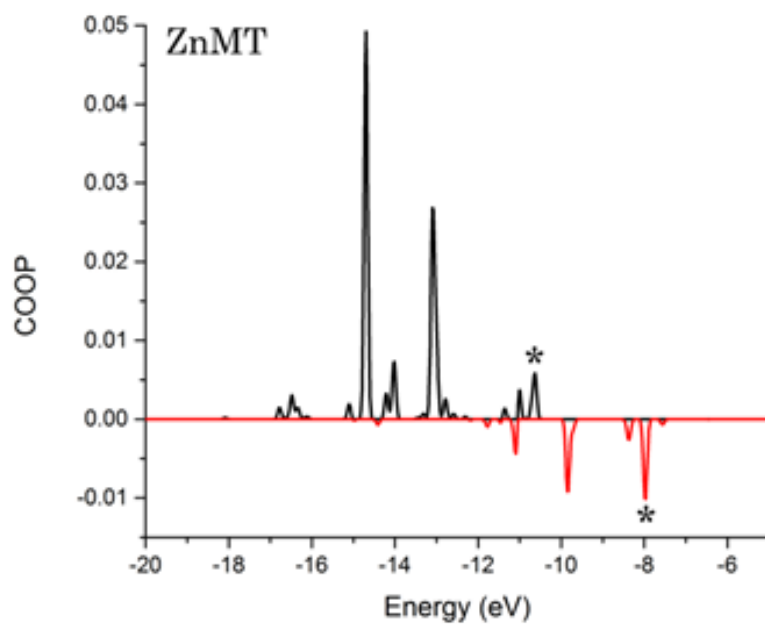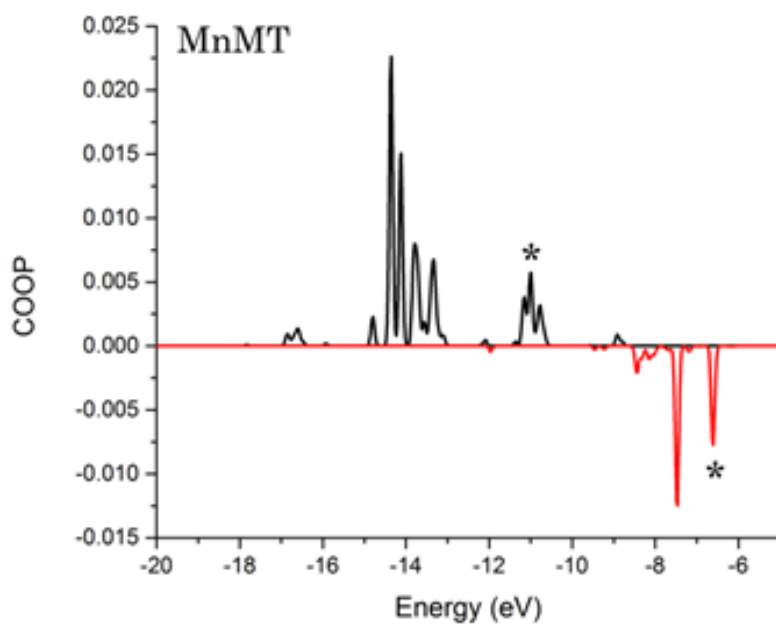
Figure 7-9. MnMT and ZnMT crystal orbital overlap population diagrams, showing both bonding (black, positive) and antibonding (red, negative) interactions. Asterisks denote the molecular orbitals shown in this work.

The total amount of bonding and antibonding populations were determined for each MMT by integration of the positive and negative regions of the COOP diagrams, respectively (**Figure 7-10**). When moving across the MMT series, the total amount of favorable and unfavorable interactions can be attributed to the individual d-orbital occupations on the metal. The total COOP bonding and antibonding energies manifests itself in the magnitude of water$_a$ tilting, ultimately relating the water positioning and subsequent LBHB potential to the electronic configuration of the specific metal cation. For example, there is a considerable decrease in both the bonding and antibonding densities in NiMT. This is mediated by two related factors: the addition of an electron into the primarily antibonding d_{xy} or d_{yz} orbitals and the resultant tilting of the water$_a$ molecules. The electron gained by nickel increases the antibonding character of the metal-water$_a$ bond, which ultimately disrupts the balance between the bonding and antibonding energies. This causes water$_a$ to tilt, reducing its overlap with nickel and thus avoiding the energetic penalty of a direct antibonding interaction. The consequence of this tilting is a reduced bonding interaction and therefore a total reduction in the bonding character of the nickel-water$_a$ bond.
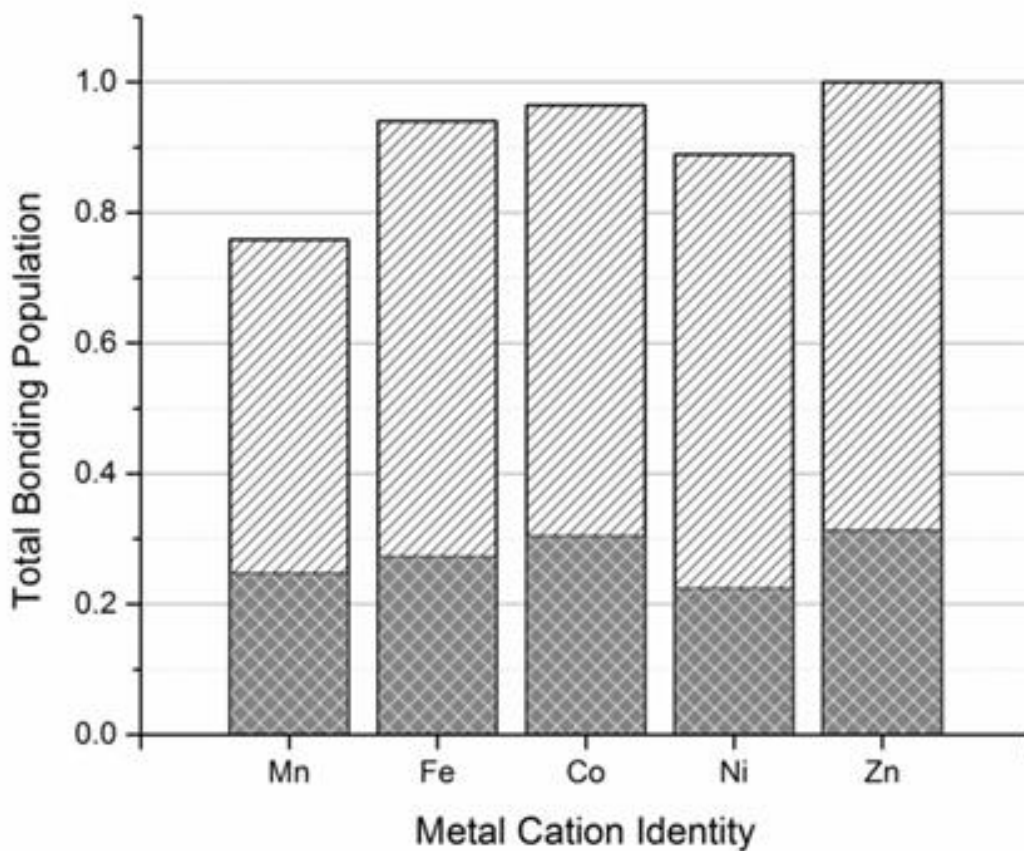
Figure 7-10. The total metal-water$_a$ bond populations (relative to ZnMT) of all MMT species studied. The height of each column represents the total bond population, with the contributions from bonding (light grey) and antibonding (dark grey) interactions indicated.

The largest change in the amount of bonding and antibonding populations occurs at the interface between the d^7-CoMT and the d^8-NiMT, meaning that CoMT represents the most even distribution between the two energetic factors in the MMT series. FeMT and NiMT are then thought to be the most "rigid" because any change in the $water_a$ positioning would reduce the most favorable bonding situation in FeMT, while a tilt of $water_a$ in NiMT would cause a significant increase in the antibonding character. To show this, the ratio of bonding to antibonding interactions in the metal maleates can be calculated as a function of d-orbital populations, where NiMT has the highest proportion of bonding character per electron of any of the MMT species studied, followed by FeMT. The same can be said for each MMT, where the metal-$water_a$ bond angle is determined by the maximization of the bonding to antibonding population ratios. The data provided in **Figures 7-9** and **7-10** help to highlight the delicate balance between the electronic interactions and the geometric arrangements of the atoms and molecules in the studied solids, and how the final properties are achieved through minimization of diametrically opposed energetic factors in complex crystalline materials.

7.4 Conclusions

A combination of single-crystal X-ray diffraction, terahertz spectroscopy, and solid-state density functional theory has enabled a complete picture to be achieved of the role of electronic interactions in determining the structures of transition metal maleates. The subtle geometry differences between these species, including the orientation of the coordinated water molecules and shape of the LBHB potential in the maleate ligand, were shown to play an important role in the low-frequency vibrations of these systems. Through the use of DFT calculations, the origin of these differing geometries was discovered to be directly related to the occupations of individual $3d$ orbitals in the metals and the extent of their overlap with specific coordinated waters. The metal-induced tilt of the water molecules profoundly impacts the LBHB potential energy surface within the maleate ligand, altering its features and symmetry. The proton transfer coordinate in the maleate ligand is therefore shaped by the concerted influences of the metal ion dictating the water positions, and the subsequent modification of the LBHB potential by these waters. While the traditional assumption that metal cation size and charge are responsible for variations in LBHB characteristics may generally be correct, the results presented in this work provide a detailed description regarding the specific electronic origins of the observed behavior, ultimately revealing that water is the key to understanding the properties of LBHBs in complex materials.

7.5 Acknowledgements

Supporting Information (see APPENDIX D)

CCDC 1408922-1408926 contain the supplementary crystallographic data for this paper. These data can be obtained free of charge from The Cambridge Crystallographic Data Centre via www.ccdc.cam.ac.uk/data_request/cif.

7.6 References

1. Zundel, G., *Hydrogen Bonds with Large Proton Polarizability and Proton Transfer Processes in Electrochemistry and Biology*; Wiley Online Library, 2007.

2. Guerra, C. F.; Bickelhaupt, F. M.; Snijders, J. G.; Baerends, E. J., The Nature of the Hydrogen Bond in DNA Base Pairs: The Role of Charge Transfer and Resonance Assistance. *Chem. Eur. J.* **1999**, *5*, 3581.

3. Tarek, M.; Tobias, D., Role of Protein-Water Hydrogen Bond Dynamics in the Protein Dynamical Transition. *Phys. Rev. Lett.* **2002**, *88*, 138101.

4. Cassidy, C. S.; Lin, J.; Frey, P. A., A New Concept for the Mechanism of Action of Chymotrypsin: The Role of the Low-Barrier Hydrogen Bond. *Biochemistry* **1997**, *36*, 4576-4584.

5. Cleland, W.; Kreevoy, M., Low-Barrier Hydrogen Bonds and Enzymic Catalysis. *Science* **1994**, *264*, 1887-1890.

6. Stasko, D.; Hoffmann, S. P.; Kim, K.-C.; Fackler, N. L. P.; Larsen, A. S.; Drovetskaya, T.; Tham, F. S.; Reed, C. A.; Rickard, C. E. F.; Boyd, P. D. W., *et al.*, Molecular Structure of the Solvated Proton in Isolated Salts. Short, Strong, Low Barrier (Sslb) H-Bonds. *J. Am. Chem. Soc.* **2002**, *124*, 13869-13876.

7. Kiefer, L. L.; Paterno, S. A.; Fierke, C. A., Hydrogen Bond Network in the Metal Binding Site of Carbonic Anhydrase Enhances Zinc Affinity and Catalytic Efficiency. *J. Am. Chem. Soc.* **1995**, *117*, 6831-6837.

8. Ramaswamy, S.; Park, D.-H.; Plapp, B. V., Substitutions in a Flexible Loop of Horse Liver Alcohol Dehydrogenase Hinder the Conformational Change and Unmask Hydrogen Transfer. *Biochemistry* **1999**, *38*, 13951-13959.

9.   Heikinheimo, P.; Tuominen, V.; Ahonen, A.-K.; Teplyakov, A.; Cooperman, B. S.; Baykov, A. A.; Lahti, R.; Goldman, A., Toward a Quantum-Mechanical Description of Metal-Assisted Phosphoryl Transfer in Pyrophosphatase. *PNAS* **2001**, *98*, 3121-3126.

10.   Schiøtt, B.; Iversen, B. B.; Madsen, G. K. H.; Larsen, F. K.; Bruice, T. C., On the Electronic Nature of Low-Barrier Hydrogen Bonds in Enzymatic Reactions. *PNAS* **1998**, *95*, 12799-12802.

11.   Smirnov, S. N.; Golubev, N. S.; Denisov, G. S.; Benedict, H.; Schah-Mohammedi, P.; Limbach, H.-H., Hydrogen/Deuterium Isotope Effects on the NMR Chemical Shifts and Geometries of Intermolecular Low-Barrier Hydrogen-Bonded Complexes. *J. Am. Chem. Soc.* **1996**, *118*, 4094-4101.

12.   Pan, Y.; McAllister, M. A., Characterization of Low-Barrier Hydrogen Bonds. 1. Microsolvation Effects. An ab initio and DFT Investigation. *J. Am. Chem. Soc.* **1997**, *119*, 7561-7566.

13.   Kumar, G. A.; McAllister, M. A., Characterization of Low-Barrier Hydrogen Bonds. 8. Substituent Effects on the Strength and Geometry of the Formic Acid-Formate Anion Model System. An ab initio and DFT Investigation. *J. Am. Chem. Soc.* **1998**, *120*, 3159-3165.

14.   García-Fernández, P.; García-Canales, L.; García-Lastra, J. M.; Junquera, J.; Moreno, M.; Aramburu, J. A., Pseudo-Jahn-Teller Origin of the Low Barrier Hydrogen Bond in N2h7+. *J. Chem. Phys.* **2008**, *129*, 124313.

15.   Bieńko, A. J.; Latajka, Z.; Sawka-Dobrowolska, W.; Sobczyk, L.; Ozeryanskii, V. A.; Pozharskii, A. F.; Grech, E.; Nowicka-Scheibe, J., Low Barrier Hydrogen Bond in

Protonated Proton Sponge. X-Ray Diffraction, Infrared, and Theoretical ab initio and Density Functional Theory Studies. *J. Chem. Phys.* **2003**, *119*, 4313-4319.

16.   Perrin, C. L., Are Short, Low-Barrier Hydrogen Bonds Unusually Strong? *Acc. Chem. Res.* **2010**, *43*, 1550-1557.

17.   Perrin, C. L.; Nielson, J. B., "Strong" Hydrogen Bonds in Chemistry and Biology. *Annu. Rev. Phys. Chem.* **1997**, *48*, 511-544.

18.   Warshel, A.; Papazyan, A., Energy Considerations Show That Low-Barrier Hydrogen Bonds Do Not Offer a Catalytic Advantage over Ordinary Hydrogen Bonds. *PNAS* **1996**, *93*, 13665-13670.

19.   Nadal-Ferret, M.; Gelabert, R.; Moreno, M.; Lluch, J. M., Are There Really Low-Barrier Hydrogen Bonds in Proteins? The Case of Photoactive Yellow Protein. *J. Am. Chem. Soc.* **2014**, *136*, 3542-3552.

20.   Gilli, G.; Gilli, P., Towards an Unified Hydrogen-Bond Theory. *J. Mol. Struct.* **2000**, *552*, 1-15.

21.   Ward, M. D., Design of Crystalline Molecular Networks with Charge-Assisted Hydrogen Bonds. *Chem. Commun.* **2005**, 5838-5842.

22.   Gilli, P.; Bertolasi, V.; Ferretti, V.; Gilli, G., Evidence for Resonance-Assisted Hydrogen Bonding. 4. Covalent Nature of the Strong Homonuclear Hydrogen Bond. Study of the O-H--O System by Crystal Structure Correlation Methods. *J. Am. Chem. Soc.* **1994**, *116*, 909-915.

23.   Gilli, G.; Bellucci, F.; Ferretti, V.; Bertolasi, V., Evidence for Resonance-Assisted Hydrogen Bonding from Crystal-Structure Correlations on the Enol Form of the B-Diketone Fragment. *J. Am. Chem. Soc.* **1989**, *111*, 1023-1028.

24.   Beck, J. F.; Mo, Y., How Resonance Assists Hydrogen Bonding Interactions: An Energy Decomposition Analysis. *J. Comput. Chem.* **2007**, *28*, 455-466.

25.   Woo, H.-K.; Wang, X.-B.; Wang, L.-S.; Lau, K.-C., Probing the Low-Barrier Hydrogen Bond in Hydrogen Maleate in the Gas Phase: A Photoelectron Spectroscopy and Ab Initio Study. *J. Phys. Chem. A* **2005**, *109*, 10633-10637.

26.   McAllister, M. A., Characterization of Low-Barrier Hydrogen Bonds. 3. Hydrogen Maleate. An ab initio and DFT Investigation. *Can. J. Chem.* **1997**, *75*, 1195-1202.

27.   Schwartz, B.; Drueckhammer, D. G., A Simple Method for Determining the Relative Strengths of Normal and Low-Barrier Hydrogen Bonds in Solution: Implications to Enzyme Catalysis. *J. Am. Chem. Soc.* **1995**, *117*, 11902-11905.

28.   Wilson, C. C.; Thomas, L. H.; Morrison, C. A., A Symmetric Hydrogen Bond Revisited: Potassium Hydrogen Maleate by Variable Temperature, Variable Pressure Neutron Diffraction and Plane-Wave DFT Methods. *Chem. Phys. Lett.* **2003**, *381*, 102-108.

29.   Hsu, B.; Schlemper, E. O., X-N Deformation Density Studies of the Hydrogen Maleate Ion and the Imidazolium Ion. *Acta Crystallogr. Sect. B* **1980**, *36*, 3017-3023.

30.   Fillaux, F.; Leygue, N.; Tomkinson, J.; Cousson, A.; Paulus, W., Structure and Dynamics of the Symmetric Hydrogen Bond in Potassium Hydrogen Maleate: A Neutron Scattering Study. *Chem. Phys.* **1999**, *244*, 387-403.

31.   Sequeira, A.; Rajagopal, H.; Gupta, M. P.; Vanhouteghem, F.; Lenstra, A. T. H.; Geise, H. J., Tetraaquabis(Hydrogen Maleato)Zinc(II) by Neutron Diffraction and Tetraaquabis(Hydrogen Maleato)Nickel(II) by High-Order X-Ray Diffraction. *Acta Crystallogr., Sect. C: Cryst. Struct. Commun.* **1992**, *48*, 1192-1197.

32. Barman, R. K.; Chakrabarty, R.; Das, B. K., Structure and Properties of Tetraaquabis(Hydrogenmaleato)Iron(II). *Polyhedron* **2002**, *21*, 1189-1195.

33. Sheldrick, G., A Short History of Shelx. *Acta Crystallogr. Sect. A* **2008**, *64*, 112-122.

34. Hakey, P. M.; Allis, D. G.; Ouellette, W.; Korter, T. M., Cryogenic Terahertz Spectrum of (+)-Methamphetamine Hydrochloride and Assignment Using Solid-State Density Functional Theory. *J. Phys. Chem. A* **2009**, *113*, 5119-5127.

35. Rice, A.; Jin, Y.; Ma, X. F.; Zhang, X. C.; Bliss, D.; Larkin, J.; Alexander, M., Terahertz Optical Rectification from 〈110〉 Zinc-Blende Crystals. *Appl. Phys. Lett.* **1994**, *64*, 1324-1326.

36. Wu, Q.; Litz, M.; Zhang, X. C., Broadband Detection Capability of Znte Electro-Optic Field Detectors. *Appl. Phys. Lett.* **1996**, *68*, 2924-2926.

37. Dovesi, R.; Orlando, R.; Erba, A.; Zicovich-Wilson, C. M.; Civalleri, B.; Casassa, S.; Maschio, L.; Ferrabone, M.; De La Pierre, M.; D'Arco, P.*, et al.*, CRYSTAL14: A Program for the *ab initio* Investigation of Crystalline Solids. *Int. J. Quantum Chem* **2014**, *114*, 1287-1317.

38. Becke, A. D., Density-Functional Thermochemistry. III. The Role of Exact Exchange. *J. Chem. Phys.* **1993**, *98*, 5648-5652.

39. Ruggiero, M. T.; Bardon, T.; Strlic, M.; Taday, P. F.; Korter, T. M., The Role of Terahertz Polariton Absorption in the Characterization of Crystalline Iron Sulfate Hydrates. *Phys. Chem. Chem. Phys.* **2015**, *17*, 9326-9334.

40. Krishnan, R.; Binkley, J. S.; Seeger, R.; Pople, J. A., Self-Consistent Molecular Orbital Methods. XX. A Basis Set for Correlated Wave Functions. *J. Chem. Phys.* **1980**, *72*, 650-654.

41. Mitin, A. V.; Baker, J.; Pulay, P., An Improved 6-31g* Basis Set for First-Row Transition Metals. *J. Chem. Phys.* **2003**, *118*, 7775-7782.

42. Noel, Y.; Zicovich-Wilson, C. M.; Civalleri, B.; D'Arco, P.; Dovesi, R., Polarization Properties of Zno and Beo: An *ab initio* Study through the Berry Phase and Wannier Functions Approaches. *Phys. Rev. B.* **2001**, *65*, 014111.

43. Frisch, M. J.; Trucks, G. W.; Schlegel, H. B.; Scuseria, G. E.; Robb, M. A.; Cheeseman, J. R.; Scalmani, G.; Barone, V.; Mennucci, B.; Petersson, G. A.*, et al.*, Gaussian 09, Revision B.01. Wallingford CT, 2009.

44. Gorelsky, S. I.; Lever, A. B. P., Electronic Structure and Spectra of Ruthenium Diimine Complexes by Density Functional Theory and Indo/S. Comparison of the Two Methods. *J. Organomet. Chem.* **2001**, *635*, 187-196.

45. Humphrey, W.; Dalke, A.; Schulten, K., Vmd: Visual Molecular Dynamics. *Journal of Molecular Graphics* **1996**, *14*, 33-38.

46. Lis, T., Structure of Manganese(II) Maleate Trihydrate, [Mn(C$_4$H$_2$O$_4$)].3H2O (I), and Reinvestigation of the Structure of Manganese(II) Hydrogen Maleate Tetrahydrate, [Mn(C$_4$H$_3$O$_4$)$_2$].4H$_2$O (II). *Acta Crystallogr., Sect. C: Cryst. Struct. Commun.* **1983**, *39*, 39-41.

47. Porollo, N. P.; Aliev, Z. G.; Dzhardimalieva, G. I.; Ivleva, I. N.; Uflyand, I. E.; Pomogailo, A. D.; Ovanesyan, N. S., Synthesis and Reactivity of Metal-Containing Monomers. *Russ. Chem. Bull.* **1997**, *46*, 362-370.

48. Eftekhari-Bafrooei, A.; Borguet, E., Effect of Hydrogen-Bond Strength on the Vibrational Relaxation of Interfacial Water. *J. Am. Chem. Soc.* **2010**, *132*, 3756-3761.

49.   Alexei, G.; Rajeev, A.; Olle, E., Balanced Crystal Orbital Overlap Population—a Tool for Analysing Chemical Bonds in Solids. *J. Phys.: Condens. Matter* **2003**, *15*, 7751.

50.   Gorelsky, S. I.; Basumallick, L.; Vura-Weis, J.; Sarangi, R.; Hodgson, K. O.; Hedman, B.; Fujisawa, K.; Solomon, E. I., Spectroscopic and DFT Investigation of [M{Hb(3,5-Ipr$_2$pz)$_3$}(SC$_6$F$_5$)] (M = Mn, Fe, Co, Ni, Cu, and Zn) Model Complexes: Periodic Trends in Metal-Thiolate Bonding. *Inorg. Chem.* **2005**, *44*, 4947-60.

CHAPTER 8: Exploring the Influence of Cation Identity on the Structures and Terahertz Spectra of Glutamic Acid Salts

8.1 Introduction

The relationship between metal-ligand interactions and bulk properties are often attributed to the size and charge of the metal cation, with many using the traditional point-charge model to describe complex interactions.[1-3] Recently there have been studies focused on providing a more concise description for physical observations, relating more fundamental electronic quantities such as spin density or *d*-orbital occupation to physical observables.[4-7] Such methods are important for gaining a more accurate understanding of the effects that govern the formation and characteristics of metal-containing systems, since many biological and pharmaceutical chemicals involve such materials.[8-11] One example is monosodium glutamate monohydrate (MSG), one of the most commercially produced compounds worldwide with an estimated yearly production of over one-million tons.[12-13] Given its prevalence, it is surprising that little data is available in the literature regarding its crystal structure and lattice dynamics.[14-15] Furthermore, there also exists a potassium analogue of MSG, monopotassium glutamate monohydrate (MPG), that crystallizes with a similar, but different, structure than MSG.[15-17] The existence of the two solids enables a comparative study into the role that metal cation size, charge, and electronic structure have on the bulk geometries and properties to be performed using a combination of X-ray diffraction and density functional theory (DFT) simulations.

First-principles calculations are powerful for the study of electronic effects because the calculated qualities are absolute and can be used to generate a number of dependent properties.[18-19] Theoretical simulations are convenient because they enable the determination of values that

would typically be difficult to measure experimentally, such as band structure[20-21] or atomic orbital overlap.[22-23] Two such analyses have been shown to be especially useful for the study of particular interactions between metal cations and ligands, known as the crystal orbital overlap population[23-24] (COOP) and crystal orbital Hamiltonian population[25-26] (COHP) methods. These two techniques are similar to the more conventional density of states (DOS) calculations, but instead of considering the contribution of a particular orbital or atom to the entire molecular (or crystalline) orbital, the COOP and COHP methods enable the study of a specific interaction between two selected sets of orbitals to be considered.[7] The two analyses are identical in formulation, with the only difference being the weighting of the interaction based on overlap matrix elements or Hamiltonian matrix elements, yielding a measure of the effective bond order and bond strength, for COOP and COHP respectively.

In order for calculated quantities to be credible they must be corroborated by experimental measurements in some way. Terahertz time-domain spectroscopy (THz-TDS) is a powerful technique for the study of molecular solids because the low-frequency vibrations are dependent on both the internal and external potential energy landscapes.[27-30] This means that any change in molecular structure or packing arrangement can be probed because it will result in a change in the bulk hypersurface. Thus, an accurate reproduction of the low-frequency vibrational spectrum by *ab initio* simulations implies that the potential energy surface is well reproduced by the theory, lending confidence to any related calculated parameters. Here, experimental X-ray diffraction and THz-TDS measurements are coupled with solid-state DFT calculations to investigate the role of metal cation identity on the structures of MSG and MPG.

8.2 Methods

8.2.1 Experimental

Both monosodium glutamate monohydrate (MSG) and monopotassium glutamate monohydrate (MPG) were purchased from Sigma-Aldrich ($\geq$ 98.0%) and used as received. Low-temperature (90 K) single-crystal XRD measurements were performed on a Bruker KAPPA APEX DUO diffractometer using monochromated Mo Kα radiation (λ = 0.71076 Å). The diffraction patterns were corrected for Lorentz and polarization effects, with absorption corrections made using SADABS.[31] The structures were solved using direct methods and were refined anisotropically using the SHELXTL software package.[32-33] Finally, the hydrogen positions were found from the residual electron density and all atoms were then refined isotropically.

The THz-TDS measurements were performed using a commercial Advantest TAS7500TS spectrometer. Broadband terahertz radiation was generated using an Advantest TAS1130 source module, which utilizes a lithium niobate ($LiNbO_3$) nonlinear crystal to generate Cherenkov-based radiation[34] with frequencies between 0.5-4.0 THz.[35-38] Detection was carried out using an Advantest TAS1230 detector module consisting of a photoconductive antenna. Samples were prepared for the THz-TDS experiments by mixing with polytetrafluoroethylene (PTFE) to a ~5% w/w concentration and subsequently pulverizing to homogenize the sample and reduce the potential for scattering effects.[39-40] Frequency-domain terahertz transmission spectra were obtained through Fourier transform of the time-domain waveform, and the terahertz absorption spectra presented here are a result of division of the transmission spectra by that of a PTFE blank.

All solid-state DFT simulations were performed using the CRYSTAL14 software package that incorporates periodic boundary conditions.[41] The range-corrected LC-ωPBE[42] hybrid density functional was coupled with the 6-311G(d,p)[43]/8-511G(d)[44] basis sets for nonmetals/metals. Atomic positions and lattice vectors were allowed to fully relax within the space group symmetry of the solid and were initiated using atomic positions taken from the experimental X-ray crystallographic data. The optimized structures were then used to perform the frequency and one-electron analyses. Vibrational eigenvectors and eigenvalues were calculated within the harmonic limit and the infrared-active intensities determined by the Berry phase method.[45-47] Convergence criteria were set to $\Delta E \leq 10^{-8}$ and 10^{-10} hartree for the optimization and frequency/one-electron calculations, respectively. The COOP and COHP analyses were performed using a developmental version of CRYSTAL,[7] and utilized a larger number of reciprocal space points for integration of the eigenvector data (1728 versus the 512 used for optimization and frequency calculations).

8.3 Results and Discussion

8.3.1 Structural Analysis

8.3.1.1 Monosodium Glutamate Monohydrate

The low-temperature structure of MSG obtained for this study is in general agreement with previously published results;[14] however it was found that the c-axis exhibits an uncommon expansion upon cooling. MSG crystallizes in the orthorhombic $P2_12_12_1$ space group, with lattice vectors of $a = 5.521$ Å, $b = 15.130$ Å, $c = 17.958$ Å, and $V = 1500.10$ Å^3. The unit cell contains two symmetry independent formula units ($Z' = 2$) producing a total of eight formula units ($Z=8$). The two glutamate zwitterions have very different geometries, with the planes defined by the carboxylate groups oriented nearly perpendicular and parallel to each other in the two molecules, respectively (**Figure 8-1**). The sodium cations generate drastically distorted octahedral coordination geometries with the surrounding molecules. One of the cations establishes two bonds with cocrystallized water molecules, and four bonds with three glutamate ions, with one glutamate having two oxygen atoms bound simultaneously. The other sodium cation also has two bonds with cocrystallized water, and four bonds to individual carboxylate oxygens (four total coordinated glutamate ions). The glutamate ions form parallel sheets in the crystallographic bc planes, with sodium coordination bonds connecting both intersheet and intrasheet glutamate ions, forming an infinite network throughout the bulk.

231
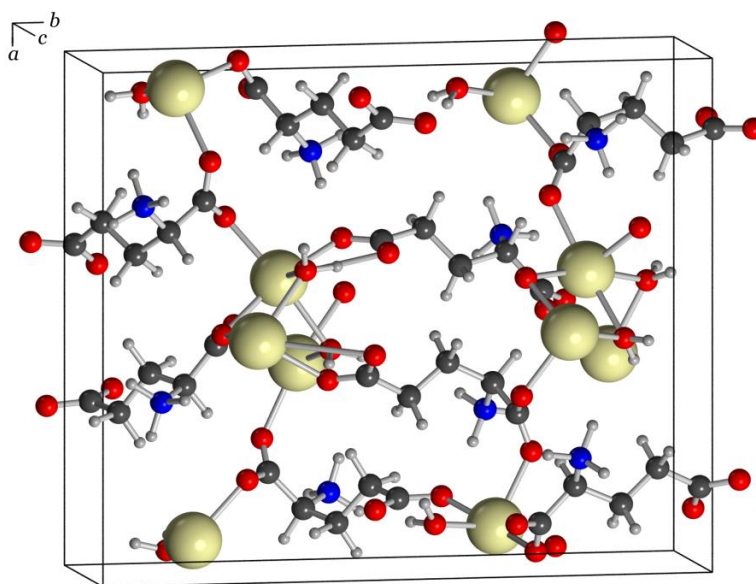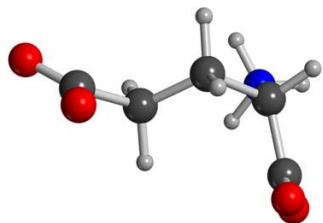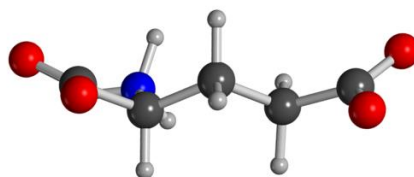
Figure 8-1. Unit cell of MSG (*i.*) and the two conformations of the glutamate ions (*ii.* and *iii.*).

8.3.1.2 Monopotassium Glutamate Monohydrate

Similar to MSG, the low-temperature structure of MPG is in agreement with previously published results with the exception again being a slight-expansion of the *a*-axis upon cooling.[17] MPG crystallizes in the orthorhombic $P2_12_12$ space group (**Figure 8-2**), with lattice vectors of *a* = 7.842 Å, *b* = 20.590 Å, *c* = 5.143 Å, and $V = 830.50$ Å^3. The unit cell contains four formula units ($Z = 4$), with one symmetry independent formula unit (with two potassium cations with half-occupancies in special symmetry positions) in the asymmetric unit ($Z' = 1$). The structure of the glutamate zwitterion is similar to the bent glutamate found in MSG (see **Figure 8-1**) and forms infinite polymeric chains along the *a*-axis via coordination bonds to the potassium cations. The two symmetry unique potassium cations exhibit drastically distorted octahedral coordination geometries, and both cations establish two bonds with cocrystallized water molecules and four bonds to four unique glutamate ions. These features result in an infinite network of sheets with the basic unit containing a central channel of potassium cations surrounded by four rows of glutamate zwitterions, and unlike MSG the neighboring sheets are not bound through coordination bonds.
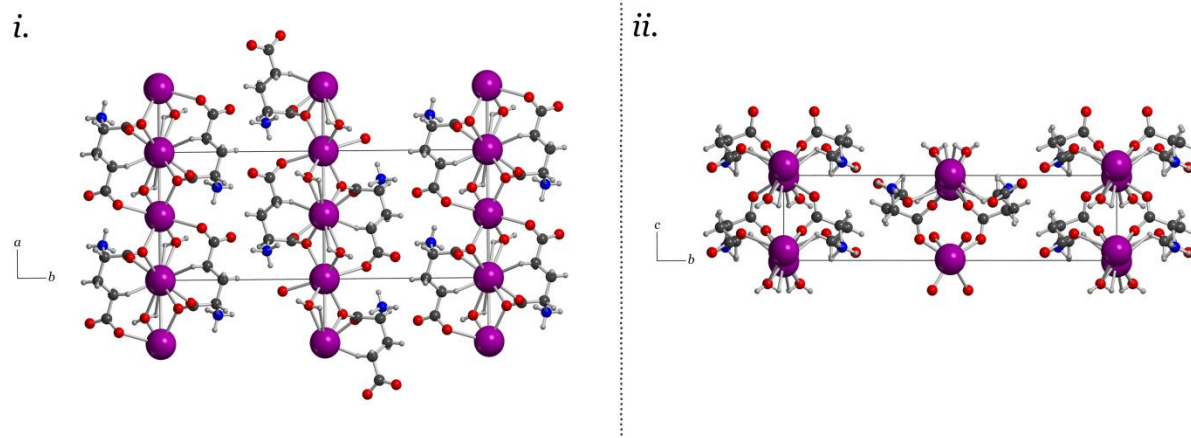
Figure 8-2. The experimental single-crystal X-ray diffraction packing arrangement of MPG viewed down the crystallographic *c* and *a* axes (i. and ii., respectively). The formation of sheets that are not covalently bonded to one another can be observed in both views.

8.3.2 Terahertz Time-Domain Spectroscopy

       The THz-TDS measurements of both MSG and MPG produced spectra with a large number of absorptions in the 0.5 – 4.0 THz frequency region (**Figure 3**). The spectrum of MSG has greater amount of resolvable features compared to MPG; likely due to the reduced symmetry of the system that enables more optically allowed infrared transitions. The contrast between the experimental THz-TDS results imply that the variations in packing arrangement are great enough to alter the potential energy surfaces governing formation of the two crystals. To further explore the possible energetic consequences of the differing geometries, a full vibrational analysis was performed for each solid, and the experimental spectra assigned (**Figure 8-3**).
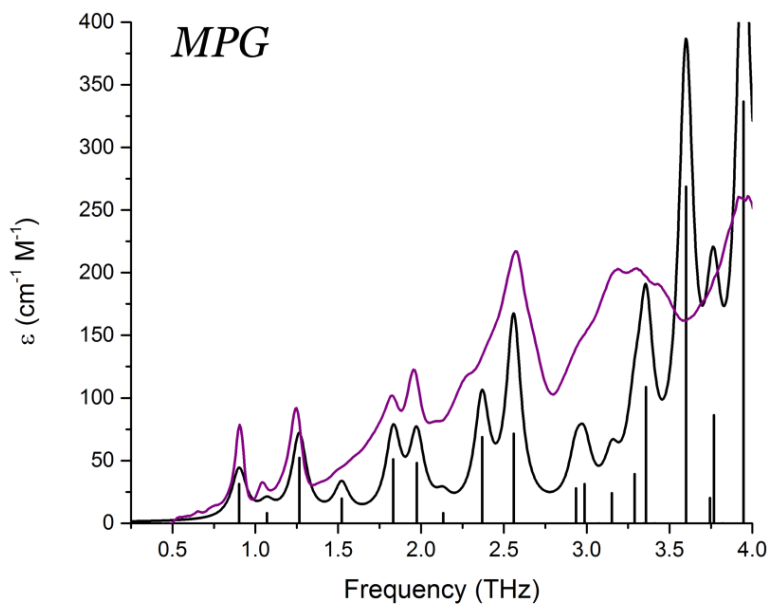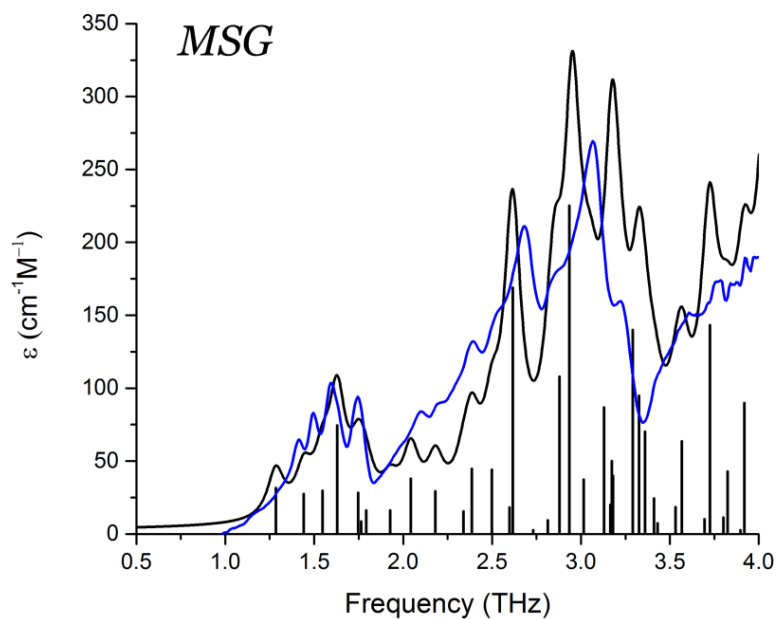
Figure 8-3. Experimental low-temperature THz-TD spectra of MSG (blue) and MPG (purple), and calculated vibrational spectra convolved using Lorentzian line shapes (black).

Visualization of the vibrational eigenvectors reveals that the two crystals have surprisingly similar mode-types. The motions in the terahertz region are primarily external translations and rotations of the individual molecular fragments, typically centered about the metal cation. The reduced symmetry of the MSG crystal permits a slightly more intricate mode-character than what is observed in MPG. Specifically, the symmetry unique dimers formed by two glutamate zwitterions and two sodium cations often exhibited concerted rotational and translational motions with different phase relationships within the dimer groups.

In MPG, the majority of the vibrational mode types are a result of glutamate-potassium sheet translations. Many modes involve motion of an entire plane (GLU-K-GLU) with respect to adjacent planes, but also included motion of only the glutamate-containing portion with respect to neighboring non-bonded sheets (-K-**GLU**⋯**GLU**-K-). There are also vibrations that involve translations of the potassium cations alone within the channels carved out by the glutamate ions. Overall, the MSG and MPG motions capture the various interactions present within the solid, namely ionic (potassium translations), coordination/covalent (potassium-glutamate translations), and London dispersion (adjacent glutamate motions). The accurate modeling of the experimental vibrational simulation indicates that the chosen density functional and basis set combination is effective for capturing these forces in the MPG and MSG crystals, and enables a more in depth analysis of the energetics governing their formation to be performed.

8.3.3 Orbital Analysis

Given the similarities between elements in the same group, it is interesting that only a ~25% increase in ionic radius between sodium and potassium generates the observed structural differences when crystallized with the same counter-ion. But as previous studies have shown it is not necessarily accurate to use such a general picture of atomic properties to explain observable traits. These changes must have origins in the electronic configurations of the different ions, which in turn dictate how the individual orbitals are able to interact with surrounding molecules.

In order to investigate the origin of the contrasting crystal structures of MSG and MPG COOP and COHP analyses were performed. The interaction between a single cation and a coordinated glutamate anion was explored in both MSG and MPG (**Figure 8-4**). In order to effectively compare the two systems all values discussed are in terms of bonding percentage, determined by dividing the integral of the positive region by the sum of the positive and negative integrals. The results (**Table 8-1**) showed that the interaction in both crystals is generally favorable. But when comparing the values obtained from the COOP and COHP curves (effective measures of bond order and bond energies, respectively) it was found that there is a significant decrease in bonding percentage between the two methods in MSG that is not realized in MPG. This can be interpreted in terms of the actual energies of the interactions, with the antibonding interactions in MSG more destabilizing than the bonding interactions are stabilizing.

To determine if this is caused by the packing arrangement of MSG or the specific cation identity, optimizations were performed where the cations were substituted with one another (potassium in place of sodium, and the inverse). Following full optimizations, the COOP and COHP curves were again generated for both crystals, and are presented in **Figure 8-5**. As one

would expect, the bonding ratio is drastically reduced in the substituted structures, an obvious indication that there is a definite correlation between cation identity and bulk structure. Closer inspection reveals that the same trend observed in the original crystals is observed in the substituted systems, except that now it is the MPG structure that shows the large deviation between the two methods. It is clear that this behavior is directly related to the sodium cation, and is not necessarily tied to the bulk geometry.

Table 8-1. Comparison of the COOP and COHP bonding percentages for the MSG and MPG crystals, as well as the substituted theoretical systems. The last column is the difference between the COOP and COHP bonding percentages.

	COOP	COHP	COOP-COHP
MSG	69.05	59.26	9.79
MPG	54.42	53.23	1.19
Substituted MSG	38.71	38.42	0.75
Substituted MPG	31.20	23.37	7.83
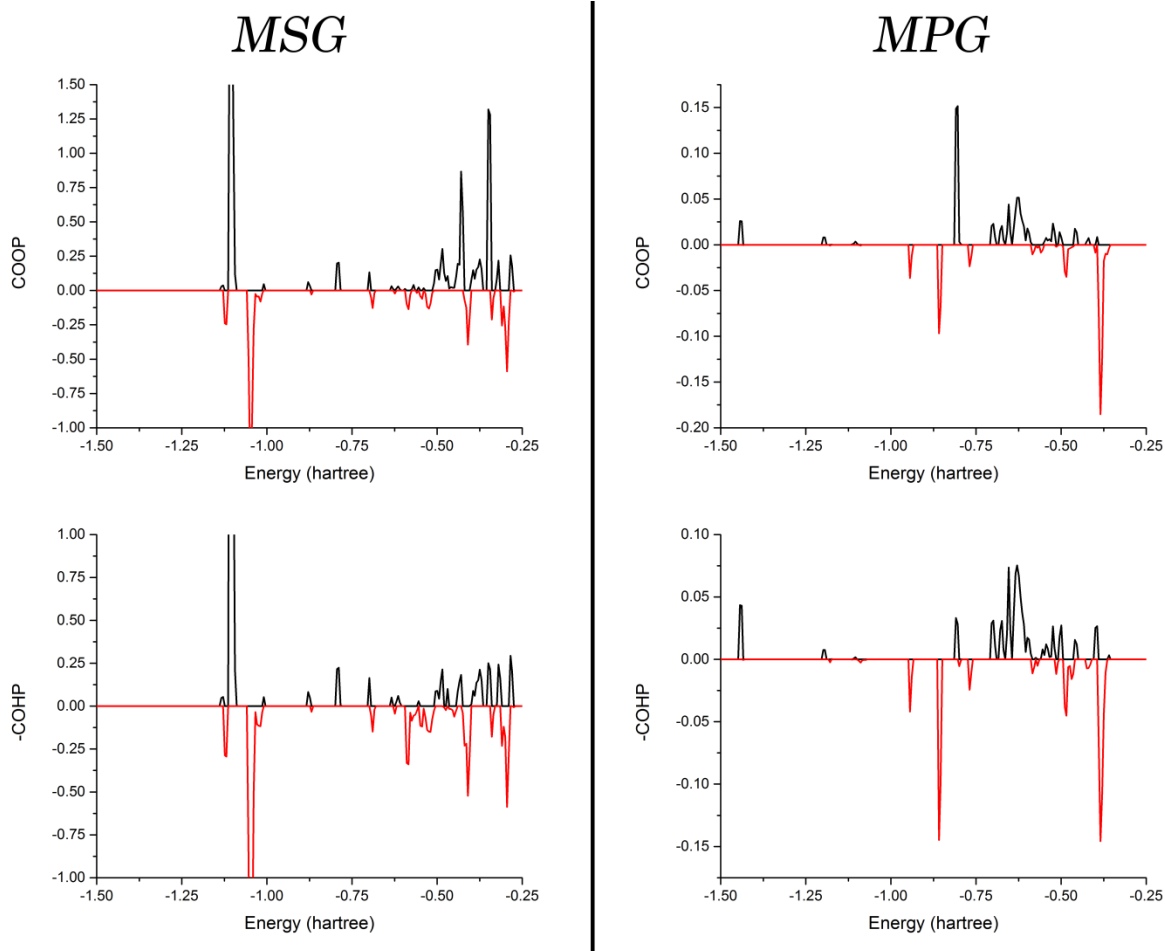
Figure 8-4. Generated COOP and COHP diagrams for the cation-glutamate interaction in MSG and KSG.
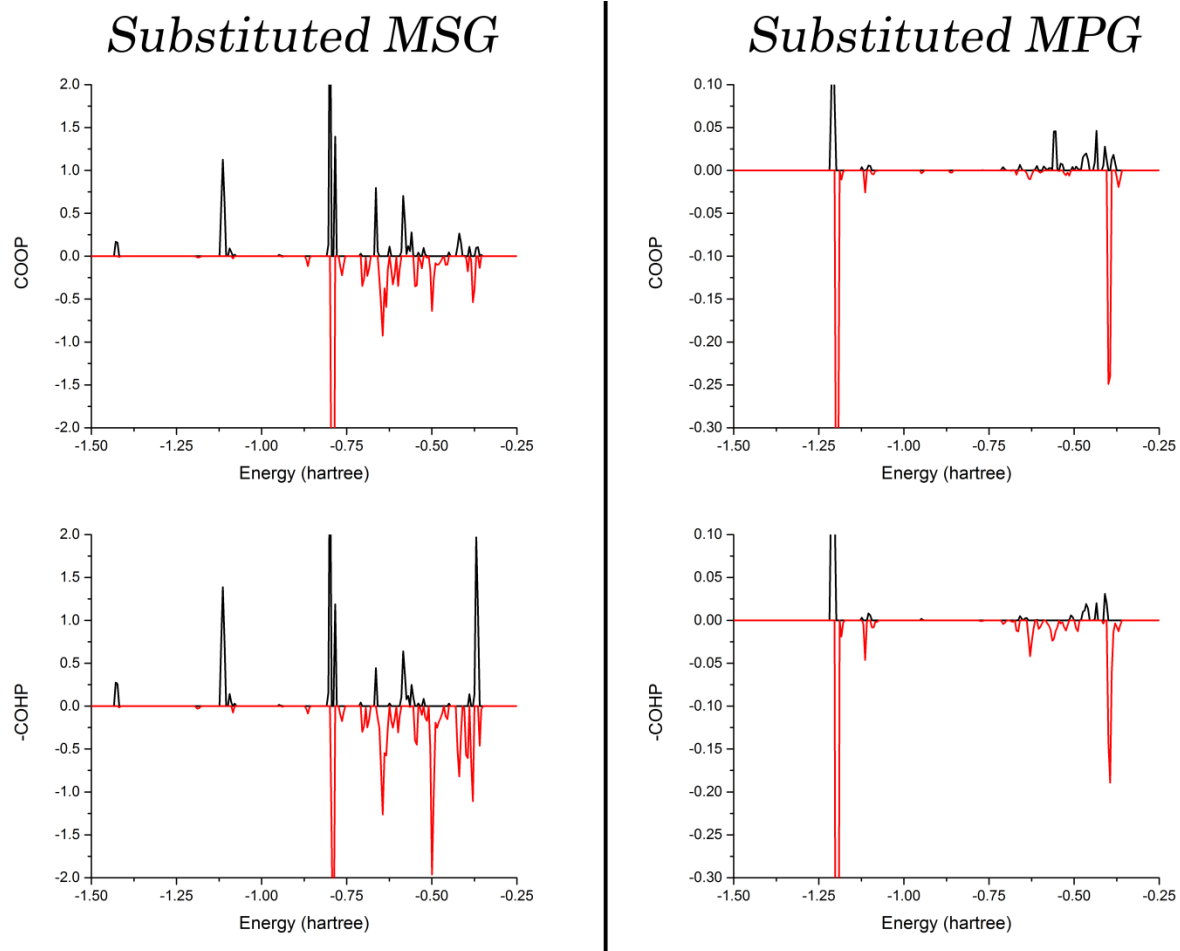
Figure 8-5. Generated COOP and COHP diagrams for the substituted MSG (containing potassium cations) and MPG (containing sodium cations) crystals.

8.4 Conclusions

While the one-electron analysis provided some details regarding the origin of the differing geometries between the MSG and MPG crystals, additional work is required to fully determine the exact orbitals responsible for the observed effects. However, it can be speculated that the accessibility of *d*-orbitals to potassium ions allows more flexibility for formation of hybrid orbitals that can minimize destabilizing interactions than what the sodium orbital configuration allows. The availability of low-lying states in potassium could also be more beneficial to its ionic size, as *d*-orbitals are more extended spatially than either *s*- or *p*-orbitals are. Future work will involve generating COOP and COHP diagrams for each individual atomic orbital, enabling discovery of the specific orbitals responsible for the observed behavior in MSG.

8.5 References

1.   Parish, R.; Platt, R., Studies in Mössbauer Spectroscopy. Part II. The Structures of Some Organotin Halides, and a Test of the Point-Charge Model. *Inorg. Chim. Acta* **1970**, *4*, 65-72.

2.   Baldoví, J. J.; Borrás-Almenar, J. J.; Clemente-Juan, J. M.; Coronado, E.; Gaita-Ariño, A., Modeling the Properties of Lanthanoid Single-Ion Magnets Using an Effective Point-Charge Approach. *Dalton Trans.* **2012**, *41*, 13705-13710.

3.   Kushkuley, B.; Stavrov, S. S., Theoretical Study of the Electrostatic and Steric Effects on the Spectroscopic Characteristics of the Metal-Ligand Unit of Heme Proteins. 2. Co Vibrational Frequencies, 17o Isotropic Chemical Shifts, and Nuclear Quadrupole Coupling Constants. *Biophys. J.* **1997**, *72*, 899.

4.   Cano, J.; Ruiz, E.; Alvarez, S.; Verdaguer, M., Spin Density Distribution in Transition Metal Complexes: Some Thoughts and Hints. *Comments Inorg. Chem.* **1998**, *20*, 27-56.

5.   Ruiz, E.; Cirera, J.; Alvarez, S., Spin Density Distribution in Transition Metal Complexes. *Coord. Chem. Rev.* **2005**, *249*, 2649-2660.

6.   Ruggiero, M. T.; Korter, T. M., The Crucial Role of Water in Shaping Low-Barrier Hydrogen Bonds. *Phys. Chem. Chem. Phys.* **2016**.

7.   Ruggiero, M. T.; Erba, A.; Orlando, R.; Korter, T. M., Origins of Contrasting Copper Coordination Geometries in Crystalline Copper Sulfate Pentahydrate. *Phys. Chem. Chem. Phys.* **2015**, *17*, 31023-31029.

8.   Okrasa, K.; Kazlauskas, R. J., Manganese-Substituted Carbonic Anhydrase as a New Peroxidase. *Chem. Eur. J.* **2006**, *12*, 1587-1596.

9.   Lindskog, S., Structure and Mechanism of Carbonic Anhydrase. *Pharmacology & Therapeutics* **1997**, *74*, 1-20.

10.   Delori, A.; Friščić, T.; Jones, W., The Role of Mechanochemistry and Supramolecular Design in the Development of Pharmaceutical Materials. *CrystEngComm* **2012**, *14*, 2350-2362.

11.   Horcajada, P.; Serre, C.; Maurin, G.; Ramsahye, N. A.; Balas, F.; Vallet-Regi, M.; Sebban, M.; Taulelle, F.; Férey, G., Flexible Porous Metal-Organic Frameworks for a Controlled Drug Delivery. *J. Am. Chem. Soc.* **2008**, *130*, 6774-6780.

12.   Ault, A., The Monosodium Glutamate Story: The Commercial Production of Msg and Other Amino Acids. *J. Chem. Educ.* **2004**, *81*, 347.

13.   Ikeda, M., Amino Acid Production Processes. In *Microbial Production of L-Amino Acids*, Springer: 2003; pp 1-35.

14.   Sano, C.; Nagashima, N.; Kawakita, T.; Iitaka, Y., Crystal and Molecular Structures of Monosodium L-Glutamate Monohydrate. *Anal. Sci.* **1989**, *5*, 121-122.

15.   Fedorov, M. V.; Goodman, J. M.; Schumm, S., To Switch or Not to Switch: The Effects of Potassium and Sodium Ions on A-Poly-L-Glutamate Conformations in Aqueous Solutions. *J. Am. Chem. Soc.* **2009**, *131*, 10854-10856.

16.   Schmidbaur, H.; Mikulcik, P.; Müller, G., Metal Ion Binding by Amino Acids. Potassium Hydrogen L-Glutamate Monohydrate K (L-GLUH)· H2O. *Chem. Ber.* **1990**, *123*, 1001-1004.

17.   Nagashima, N.; Sano, C.; Kawakita, T.; Iitaka, Y., Crystal Structure of Potassium L-Glutamate Monohydrate. *Anal. Sci.* **1992**, *8*, 115-117.

18.   Parr, R. G., *Density Functional Theory of Atoms and Molecules*; Springer, 1980.

19.   Connolly, J.; Williams, A., Density-Functional Theory Applied to Phase Transformations in Transition-Metal Alloys. *Phys. Rev. B.* **1983**, *27*, 5169.

20.   Piskunov, S.; Heifets, E.; Eglitis, R.; Borstel, G., Bulk Properties and Electronic Structure of Srtio 3, Batio 3, Pbtio 3 Perovskites: An ab initio HF/DFT Study. *Computational Materials Science* **2004**, *29*, 165-178.

21.   Setyawan, W.; Curtarolo, S., High-Throughput Electronic Band Structure Calculations: Challenges and Tools. *Computational Materials Science* **2010**, *49*, 299-312.

22.   Krapp, A.; Bickelhaupt, F. M.; Frenking, G., Orbital Overlap and Chemical Bonding. *Chemistry–A European Journal* **2006**, *12*, 9196-9216.

23.   Alexei, G.; Rajeev, A.; Olle, E., Balanced Crystal Orbital Overlap Population—a Tool for Analysing Chemical Bonds in Solids. *J. Phys.: Condens. Matter* **2003**, *15*, 7751.

24.   Hughbanks, T.; Hoffmann, R., Chains of Trans-Edge-Sharing Molybdenum Octahedra: Metal-Metal Bonding in Extended Systems. *J. Am. Chem. Soc.* **1983**, *105*, 3528-3537.

25.   Deringer, V. L.; Tchougréeff, A. L.; Dronskowski, R., Crystal Orbital Hamilton Population (COHP) Analysis as Projected from Plane-Wave Basis Sets. *J. Phys. Chem. A* **2011**, *115*, 5461-5466.

26.   Dronskowski, R.; Bloechl, P. E., Crystal Orbital Hamilton Populations (COHP): Energy-Resolved Visualization of Chemical Bonding in Solids Based on Density-Functional Calculations. *J. Phys. Chem* **1993**, *97*, 8617-8624.

27.   McIntosh, A. I.; Yang, B.; Goldup, S. M.; Watkinson, M.; Donnan, R. S., Terahertz Spectroscopy: A Powerful New Tool for the Chemical Sciences? *Chemical Society Reviews* **2012**, *41*, 2072-2082.

28. Smith, R. M.; Arnold, M. A., Terahertz Time-Domain Spectroscopy of Solid Samples: Principles, Applications, and Challenges. *Appl. Spectrosc. Rev.* **2011**, *46*, 636-679.

29. Zeitler, J. A.; Taday, P. F.; Newnham, D. A.; Pepper, M.; Gordon, K. C.; Rades, T., Terahertz Pulsed Spectroscopy and Imaging in the Pharmaceutical Setting - a Review. *J. Pharm. Pharmacol.* **2007**, *59*, 209-223.

30. Schmuttenmaer, C. A., Exploring Dynamics in the Far-Infrared with Terahertz Spectroscopy. *Chem. Rev.* **2004**, *104*, 1759-1780.

31. Bruker, S., Version 6.02 (Includes Xprep and SADABS). *Bruker AXS Inc., Madison, Wisconsin, USA* **1999**.

32. Sheldrick, G., A Short History of Shelx. *Acta Crystallogr. Sect. A* **2008**, *64*, 112-122.

33. Sheldrick, G., SHELXTL, Version 6.1; Bruker Analytical X-Ray Systems. *Inc.: Madison, WI* **1997**.

34. Zrelov, V. P. *Cherenkov Radiation in High-Energy Physics*; ERDA Div. Phys. Res.: 1973.

35. Yao, J.; Liu, P.; Xu, D.; Lv, Y.; Lv, D., Thz Source Based on Optical Cherenkov Radiation. *Science China Information Sciences* **2011**, *55*, 27-34.

36. Suizu, K.; Koketsu, K.; Shibuya, T.; Tsutsui, T.; Akiba, T.; Kawase, K., Extremely Frequency-Widened Terahertz Wave Generation Using Cherenkov-Type Radiation. *Opt. Express* **2009**, *17*, 6676-6681.

37. Theuer, M.; Torosyan, G.; Rau, C.; Beigang, R.; Maki, K.; Otani, C.; Kawase, K., Efficient Generation of Cherenkov-Type Terahertz Radiation from a Lithium Niobate Crystal with a Silicon Prism Output Coupler. *Appl. Phys. Lett.* **2006**, *88*, 071122.

38.   Auston, D.; Cheung, K.; Valdmanis, J.; Kleinman, D., Cherenkov Radiation from Femtosecond Optical Pulses in Electro-Optic Media. *Phys. Rev. Lett.* **1984**, *53*, 1555.

39.   Strachan, C. J.; Taday, P. F.; Newnham, D. A.; Gordon, K. C.; Zeitler, J. A.; Pepper, M.; Rades, T., Using Terahertz Pulsed Spectroscopy to Quantify Pharmaceutical Polymorphism and Crystallinity. *J. Pharm. Sci.* **2005**, *94*, 837-846.

40.   Walther, M.; Fischer, B. M.; Uhd Jepsen, P., Noncovalent Intermolecular Forces in Polycrystalline and Amorphous Saccharides in the Far Infrared. *Chem. Phys.* **2003**, *288*, 261-268.

41.   Dovesi, R.; Orlando, R.; Erba, A.; Zicovich-Wilson, C. M.; Civalleri, B.; Casassa, S.; Maschio, L.; Ferrabone, M.; De La Pierre, M.; D'Arco, P.*, et al.*, CRYSTAL14: A Program for the *ab initio* Investigation of Crystalline Solids. *Int. J. Quantum Chem* **2014**, *114*, 1287-1317.

42.   Weintraub, E.; Henderson, T. M.; Scuseria, G. E., Long-Range-Corrected Hybrids Based on a New Model Exchange Hole. *J. Chem. Theory Comput.* **2009**, *5*, 754-762.

43.   Krishnan, R.; Binkley, J. S.; Seeger, R.; Pople, J. A., Self-Consistent Molecular Orbital Methods. XX. A Basis Set for Correlated Wave Functions. *J. Chem. Phys.* **1980**, *72*, 650-654.

44.   Dovesi, R.; Roetti, C.; Freyria-Fava, C.; Prencipe, M.; Saunders, V. R., On the Elastic Properties of Lithium, Sodium and Potassium Oxide. An ab initio Study. *Chem. Phys.* **1991**, *156*, 11-19.

45.   Noel, Y.; Zicovich-Wilson, C. M.; Civalleri, B.; D'Arco, P.; Dovesi, R., Polarization Properties of Zno and Beo: An *ab initio* Study through the Berry Phase and Wannier Functions Approaches. *Phys. Rev. B.* **2001**, *65*, 014111.

46.   Pascale, F.; Zicovich-Wilson, C. M.; López Gejo, F.; Civalleri, B.; Orlando, R.; Dovesi, R., The Calculation of the Vibrational Frequencies of Crystalline Compounds and Its Implementation in the Crystal Code. *J. Comput. Chem.* **2004**, *25*, 888-897.

47.   Zicovich-Wilson, C. M.; Pascale, F.; Roetti, C.; Saunders, V. R.; Orlando, R.; Dovesi, R., Calculation of the Vibration Frequencies of A-Quartz: The Effect of Hamiltonian and Basis Set. *J. Comput. Chem.* **2004**, *25*, 1873-1881.

CHAPTER 9: Assignment of the Terahertz Spectra of Crystalline Copper Sulfate and Its Hydrates via Solid-State Density Functional Theory

The material contained within this chapter is published in the *Journal of Physical Chemistry A* (Ruggiero, M.T.; Bardon, T.; Strlič, M.; Taday, P.F.; Korter, T.M. *J. Phys. Chem. A* **2014.** *118*(43), 10101-10108). This article has been reproduced with permission from the American Chemical Society.
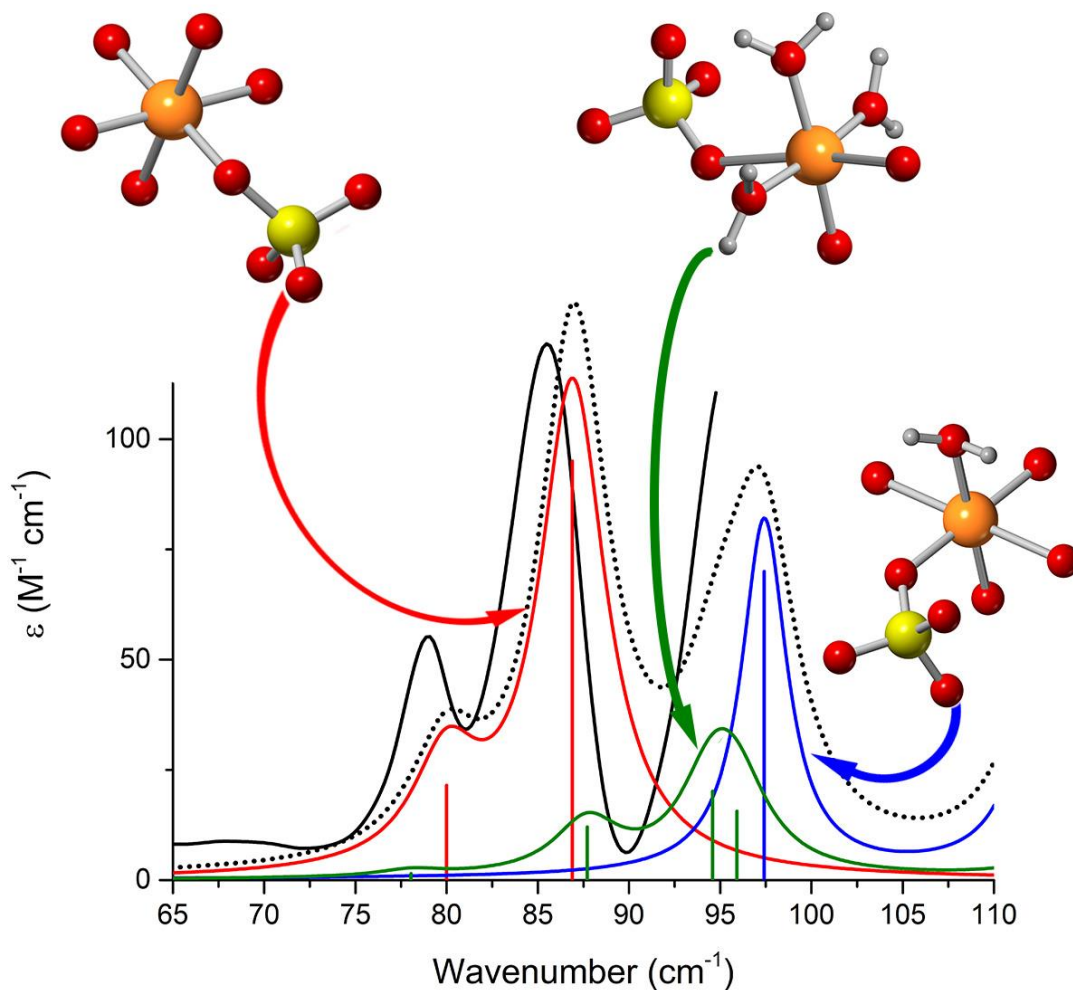
Abstract

Terahertz (THz) vibrational spectroscopy is a promising tool for the non-destructive and potentially non-invasive characterization of historical objects, which can provide information on the materials used for their production as well as identify and monitor their chemical degradation. Copper sulfate ($CuSO_4$) has drawn interest due to its inclusion in the preparation of iron gall inks found in historical artwork and documents. Copper sulfate rapidly forms hydrates which contribute to the formulation of these ink species, and may influence their corrosive nature. In this study, copper sulfate has been studied using a combination of THz time-domain spectroscopy, powder X-ray diffraction (PXRD), and solid-state density functional theory (DFT) in order to better understand the spectral absorbances in the THz region. The results have revealed that the THz spectrum of commercially available "anhydrous" copper sulfate results from the presence of not only the anhydrous form, but also the monohydrate ($CuSO_4 \cdot H_2O$) and trihydrate ($CuSO_4 \cdot 3H_2O$) forms. Complete assignment of the experimental spectrum was achieved through a comparison of density functionals and extensive investigation of the influence of basis set polarization functions on the bonding interactions, lattice parameters, and low-frequency motions in these crystalline solids.

9.1 Introduction

Terahertz (THz) vibrational spectroscopy has proven to be invaluable for characterizing organic molecules in the solid state[1-3] and has been used across multiple fields ranging from pharmaceutical manufacturing[4] to paper product inspection.[5-6] Moreover, coupling of terahertz spectroscopy with solid-state density functional theory (DFT) analyses provides a greatly enhanced understanding of intermolecular interactions and structure in solid materials.[7-9] In this study, copper sulfate and its hydrates are explored by terahertz spectroscopy and solid-state DFT, in order to better understand the nature of the lattice vibrations in these solids. The goal of this work is to achieve accurate and complete terahertz spectral assignments and enhance the analytical use of terahertz spectroscopy.

Due to the non-ionizing nature of terahertz radiation, it is an attractive alternative for investigating fragile historical artifacts.[10-11] Recent work has featured terahertz spectra of various ink species commonly found in historical documents.[10] Specifically, copper sulfate ($CuSO_4$) has been identified as a compound used in the preparation of iron gall inks[12] and has been found to influence their spectral signatures[10]. While copper sulfate exists in nature primarily as the pentahydrate form, there are actually four known species in total: anhydrous, monohydrate, trihydrate, and pentahydrate.[13-15] Given the chemical complexity of such an ostensibly simple compound, there exists a need in the conservation and heritage science fields to better understand the terahertz spectral signatures collected from ink inscriptions in historical documents and, ultimately, the roles of these various substances in historical inks.

Simulations of the properties of bulk metal systems are routinely performed using solid-state DFT methods,[16] yet little work has been done on the modeling of metal sulfate solids[17-18] like $CuSO_4$. Here, a careful investigation of density functional and basis set choices reveal that,

at least in the case of copper sulfate and its derivatives, metal sulfate structure and vibrational motion is highly sensitive to computational parameters. The results of this investigation provide several useful benefits including the development of computational methodologies for treating crystalline metal sulfate systems, definitive assignment of the terahertz spectrum of copper sulfate, and also new insights into the populations of the various hydrated copper sulfate species found in nature.

9.2 Methods

9.2.1 Experimental

Anhydrous copper sulfate was purchased from Sigma-Aldrich (≥99.99%) and used without further purification beyond dehydration. Bulk crystalline content was identified by powder X-ray diffraction (PXRD) measurements performed at 90 K (to mimic the temperature of the subsequent THz spectroscopic measurements) on a Bruker KAPPA APEX DUO diffractometer using monochromated Cu Kα radiation (λ = 1.5418 Å) with an APEX II CCD. Powder data was integrated using the Bruker APEX software package.[19] Calculated powder patterns were produced in Mercury[20] using published single-crystal X-ray diffraction data for anhydrous copper sulfate [21-23] and $CuSO_4 \cdot 3H_2O$ [24], and the powder neutron diffraction structure for $CuSO_4 \cdot H_2O$.[13]

Terahertz spectra were measured from 20 to 95 cm^{-1} with a custom time-domain terahertz spectrometer[25] utilizing an amplified femtosecond Ti:Sapphire near-infrared laser to generate and detect THz radiation via optical rectification[26-27] and free-space electrooptic sampling[28], respectively, in ZnTe crystals. Samples for terahertz spectroscopy were mixed with polytetrafluoroethylene (PTFE) with a w/w concentration of ~1.5% and pressed into 2mm thick freestanding pellets. The copper sulfate material was pulverized in a stainless steel ball mill prior to pelleting in order to homogenize the sample and reduce scattering.[29] Each terahertz waveform collection consisted of 32 averaged waveforms, with data recorded at a sample temperature of either 293 K (room temperature) or 77 K (liquid nitrogen). The total waveform was then Fourier transformed to create a frequency-domain transmission spectrum. Time-domain terahertz

waveforms were collected over a 32ps time window yielding ~ 1 cm^{-1} spectral resolution. The terahertz spectra shown here are in absorption units (ε, M^{-1}cm^{-1}) produced by taking the ratio of the sample spectra versus that of blank PTFE. The final terahertz spectra each consist of four separate data sets averaged together.

9.2.2 Computational

All solid-state simulations were carried out using the CRYSTAL09 software package.[30] Full geometry optimizations were performed with starting atomic positions from previously published crystallographic data[13, 21-22, 24] with an energy convergence criterion of 10^{-8} hartree. Lattice parameters were allowed to fully relax within the space group symmetry of the solids. The simulations utilized either the generalized gradient approximation (GGA) Perdew-Burke-Ernzerhof (PBE) [31] or the hybrid Becke-3-Lee-Yang-Parr (B3LYP)[32] density functional. Several basis sets were tested, including the Pettinger-Oliveria-Brewdow split-valence triple-ζ (pob-TZVP) basis set[33] and the split-valence double-ζ 6-31G basis set[34] with varying levels of polarization functions added. In the hydrated species, 6-31G(2d,p) was used for all non-metal atoms, including hydrogens. Vibrational analyses were then performed on the structurally optimized solids. Normal mode eigenvalues and eigenvectors were calculated within the harmonic approximation and infrared intensity data obtained through the Berry phase method.[35] The energy convergence limit was more stringent for frequency analyses and set at 10^{-10} hartree.

9.3 Results and Discussion

9.3.1 Powder X-ray Diffraction

The as-received anhydrous copper sulfate was first analyzed using PXRD to determine the bulk crystalline content, as well as to determine the degree of contamination by hydrated species. The PXRD pattern (**Figure 9-1**) revealed that the sample was mostly anhydrous copper sulfate, but with significant amounts of $CuSO_4 \cdot H_2O$ and $CuSO_4 \cdot 3H_2O$ present, at an approximate ratio of 7:2:1 ratio for the anhydrous, monohydrate, and trihydrate forms. No evidence of the common pentahydrate was detected. These populations were determined by scaling the single-crystal predicted powder patterns to best fit the experimental result by minimization of the residual resulting from subtraction of the predicted pattern from that observed (**Figure 9-2**). The presence of crystalline hydrates is not surprising given the hygroscopic nature of copper sulfate. However, these particular species coexisting, apparently contradicts the results of a recent neutron diffraction study which indicated that all of the anhydrous material would need to convert to the monohydrate before formation of the trihydrate could occur.[13] While the trihydrate is the smallest contributor to the observed PXRD pattern, several features can be identified (marked in **Figure 9-2**) that unambiguously identify its existence in the sample. The water content in the as-received $CuSO_4$ could be eliminated by simple heating, and a sample heated for 1 week at 473 K resulted in a PXRD pattern that only showed trace amounts of hydrates (**Appendix F**, **Figure F-1**).
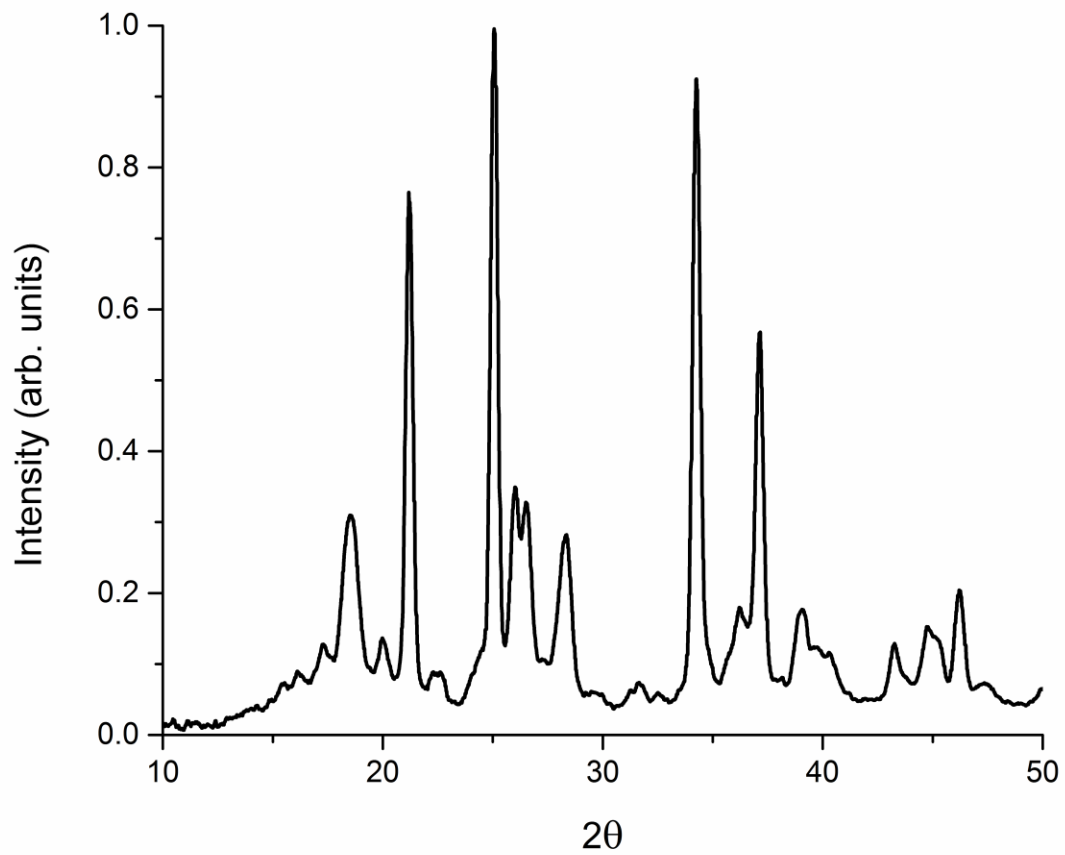
Figure 9-1. **Powder X-ray diffractogram (baseline corrected) of as-received copper sulfate.**
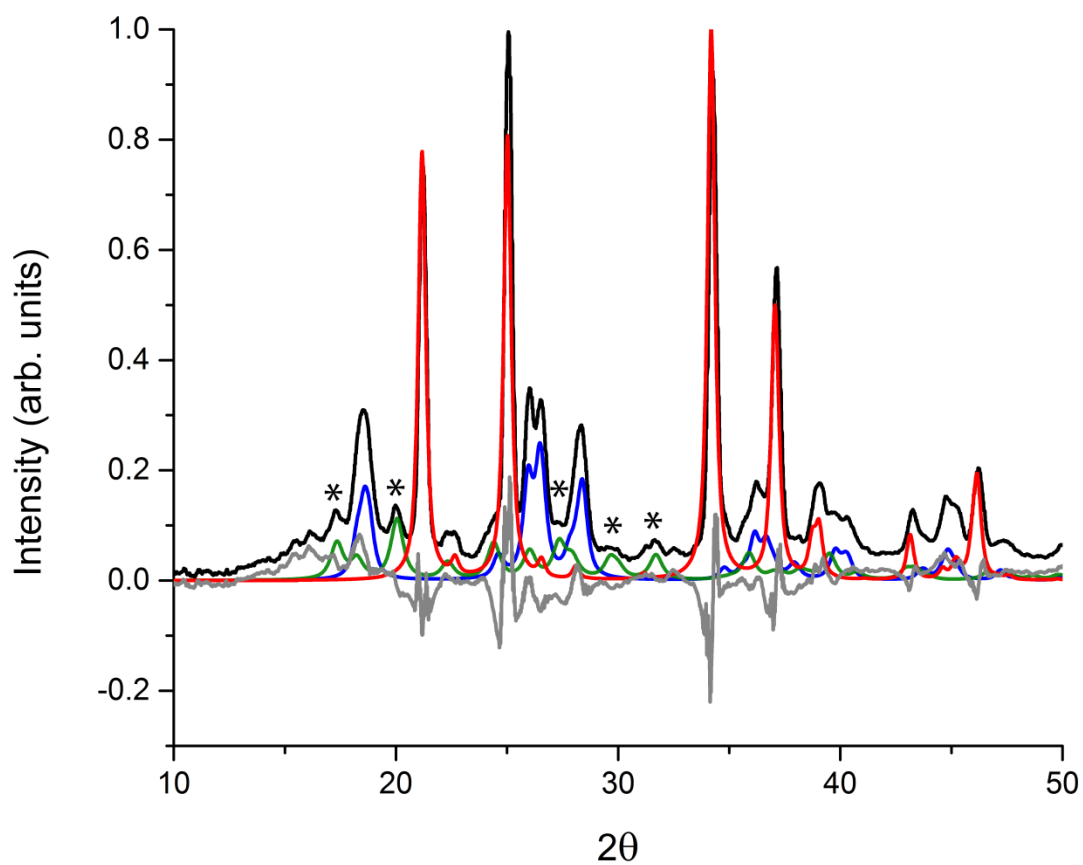
Figure 9-2. Comparison of the PXRD data for as-received copper sulfate with predicted PXRD diffractograms of $CuSO_4$ (red), $CuSO_4 \cdot H_2O$ (blue), and $CuSO_4 \cdot 3H_2O$ (green). The observed-minus-calculated residual (grey) is also shown. The most prominent features attributed to the trihydrate are denoted by asterisks (*).

9.3.2 Terahertz Spectroscopy

The experimental 293 K and 77 K terahertz spectra of the as-received anhydrous copper sulfate are shown in **Figure 9-3** and contain two well-defined peaks. These occur at 77.9 and 83.6 cm^{-1} at room temperature, and shift upon cooling to 78.9 and 85.3 cm^{-1}. The features narrow slightly and increase their maximum intensities once cooled, with average full-width half-maxima of 3.7 (293 K) and 3.3 cm^{-1} (77 K), though the strong low-temperature enhancement of the 83.6 cm^{-1} absorption strength is atypical (but reproducible). At both temperatures, a sharply rising absorption near the end of the spectral bandwidth (≥ 90 cm^{-1}) is observed, which corresponds to a partially resolved absorption feature and correlates with the previously reported terahertz spectrum of non-dried copper sulfate.[10] Upon drying, the ≥ 90 cm^{-1} absorption vanishes (see **Appendix F**, **Figure F-2**), indicating that the previously reported peak at 95 cm^{-1} is due to a hydrated species (either $CuSO_4 \cdot H_2O$ or $CuSO_4 \cdot 3H_2O$) in the sample. The terahertz spectra of copper sulfate has been previously reported, however the features attributed to the anhydrous species can be assigned to hydrated copper sulfate based on the current work.[36-37] It is also important to note that there is no discernible change in the intensity ratio of the two peaks at 78.9 cm^{-1} and 85.3 cm^{-1} between the as-received and dried samples, suggesting no significant underlying vibrational absorption originating from hydrates.
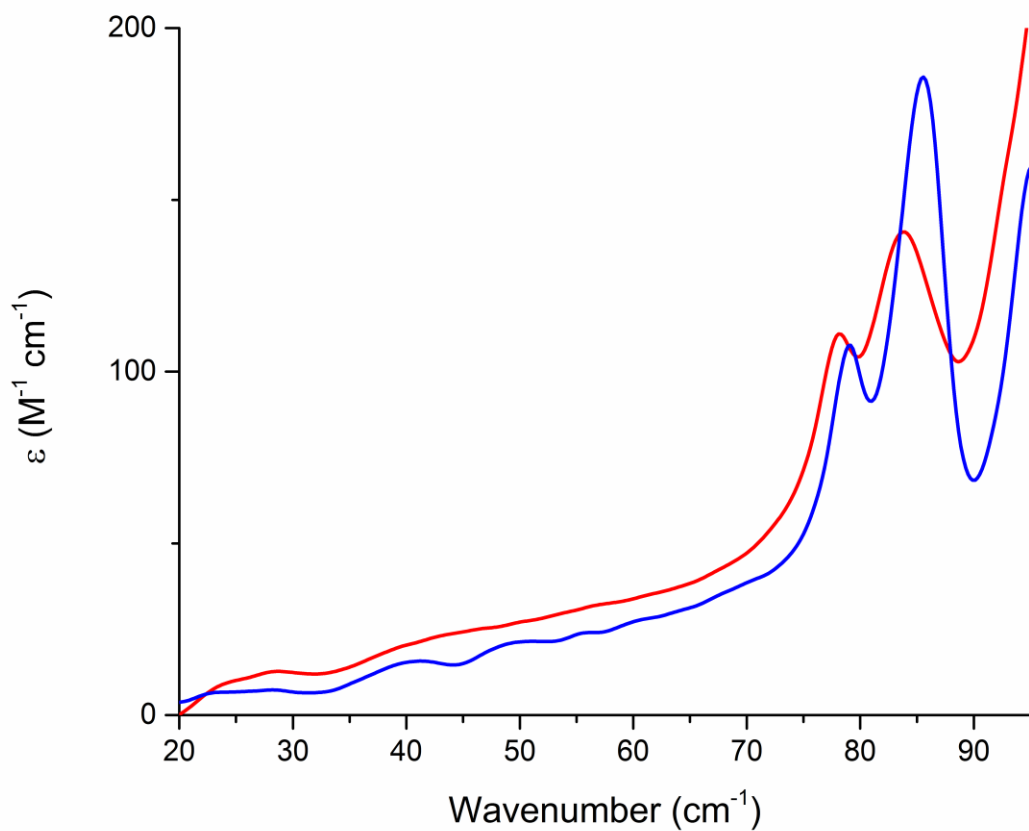
Figure 9-3. **298 K (red) and 77 K (blue) terahertz spectra of as-received copper sulfate.**

9.3.3 Computational Structural Analysis

9.3.3.1 Anhydrous Copper Sulfate

Initial solid-state DFT simulations focused on anhydrous copper sulfate and were performed using the PBE functional and the pob-TZVP basis set. The PBE functional was chosen based upon its general good performance[38] and the pob-TZVP basis set was selected because it was recently published specifically for use in solid-state calculations. Anhydrous copper sulfate crystallizes in the orthorhombic *Pnma* space group, with lattice dimensions of: $a = 8.409$ Å, $b = 6.709$ Å, $c = 4.833$ Å, $\alpha = \beta = \gamma = 90°$ (**Figure 9-4**). Four formula units comprise the unit cell ($Z = 4$) with one in the asymmetric unit. The copper cation adopts a Jahn-Teller distorted octahedral geometry with two elongated copper-oxygen bonds. The four copper atoms of the unit cell were set in an antiferromagnetic arrangement in accordance with previous low-temperature magnetic studies.[39] The PBE/pob-TZVP geometry optimization of $CuSO_4$ resulted in an unexpectedly large average sulfur-oxygen bond error of 5.51%, but performed well in predicting the experimentally observed distorted geometry about the metal cation, copper-oxygen bond distances, and overall lattice dimensions (**Table 9-1**). The unknown origin of the sulfur-oxygen bond error lead to the evaluation of several different functional and basis set combinations to determine a superior approach.
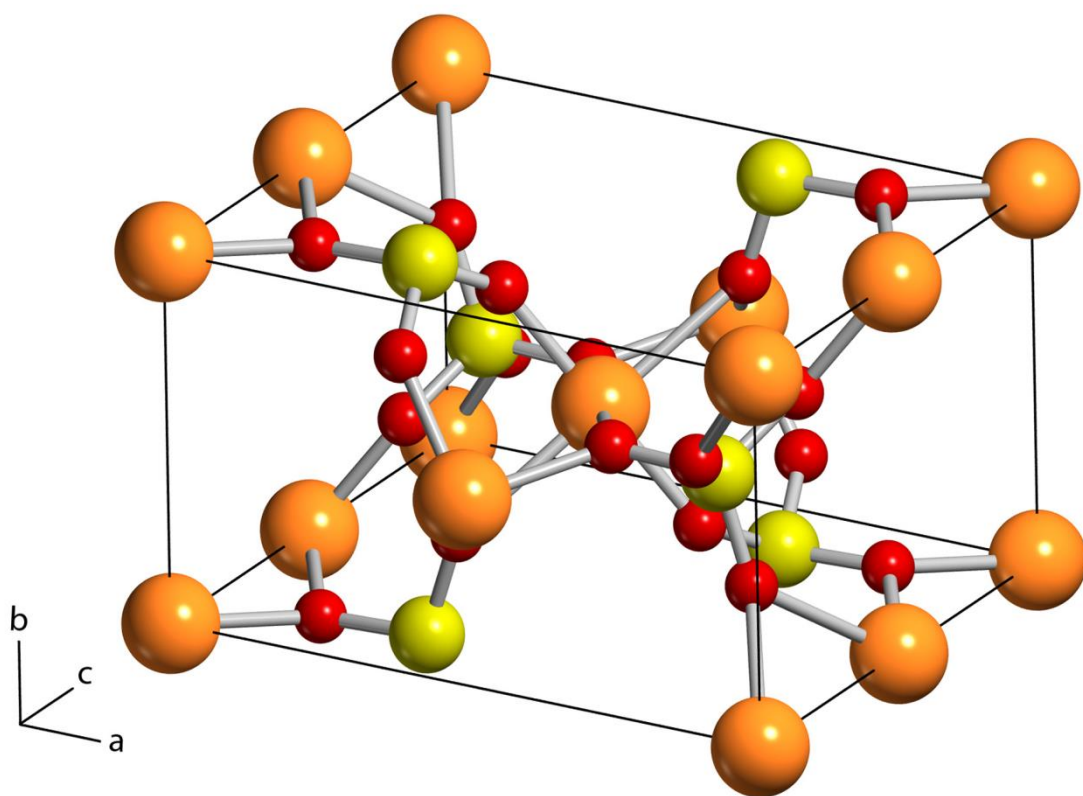
Figure 9-4. Experimental crystallographic unit cell of copper sulfate anhydrous (oxygen = red, sulfur = yellow, copper = orange).[22]

Table 9-1. Comparison of calculated anhydrous CuSO₄ structural parameters to experimental crystallographic data.[22] Listed values are absolute average percent deviations from experimental values. Bolded values indicate the minimum error in that column.

Basis Set		PBE				B3LYP			
Copper	Sulfur/Oxygen	S-O	Cu-O	Unit Cell	Average	S-O	Cu-O	Unit Cell	Average
pob-TZVP	pob-TZVP	5.51	**0.45**	1.90	2.47	4.14	0.42	1.10	1.89
6-31G(d)	6-31G(d)	3.64	0.64	1.07	1.78	2.34	**0.13**	1.26	1.24
	6-31G(2d)	2.39	0.63	**0.40**	**1.14**	1.06	0.18	**0.31**	**0.52**
	6-31G(3d)	**1.92**	0.94	1.43	1.43	**0.76**	1.12	1.62	1.17

The sensitivity of the calculated structure to basis set choice was investigated first, while keeping the PBE functional constant. The 6-31G(d) basis set was the first alternative chosen based on its computational efficiency (~2 times faster than pob-TZVP in these solids), wide accessibility, and has already been studied for use in transition metal compounds.[40] Also, for comparison purposes, its polarization extent is similar to the pob-TZVP basis set. However, the 6-31G(d) basis set was parameterized by utilizing gas-phase chemical data, and because of this, the unoccupied core sp-type orbital for copper is too diffuse for use in the solid state. Basis set functions with overly large spatial extents lead to false conducting states in periodic solid calculations. In order to correct this, the Gaussian exponent of the sp orbital was systematically varied between 0.10 and 0.60 (step-size of 0.05) with the goal being the determination of the lowest total electronic energy. Single-point energy calculations of the system frozen at the experimentally determined structure were evaluated at each exponent value, and a polynomial function fit to the energetic data distribution to locate the minimum. The optimized exponent was found to be 0.323590 (approximately eight times as large as the published value of 0.0473320) and did not lead to false conducting states. Utilizing this new sp-orbital exponent, the switch to 6-31G(d) on all atoms from pob-TZVP significantly reduced the average S-O bond error to 3.64% in the geometry optimizations, along with smaller improvements in the Cu-O bonds and lattice dimensions (**Table 9-1**).

Other studies have demonstrated that sulfur-oxygen bonds are highly sensitive to basis set choice, such as in the cases of gas-phase SO, SO_2, and SO_3.[41-42] The solid-state $CuSO_4$ system exhibited the same trend and addition of polarization functions to the sulfur and oxygen atoms greatly improved the average S-O bond errors, ultimately leading to an average S-O bond error of 1.92% with the 6-31G(3d) basis set. The influence of basis set choice on the structural

reproductions of crystalline $CuSO_4$ is detailed in **Table 9-1**. While additional polarization functions clearly improved the sulfur-oxygen bonds, switching from the 6-31G(2d) to 6-31G(3d) basis set yielded greater errors in the copper-oxygen bond distances as well as in the unit cell axes. The increase in the number of polarization functions does not result in the anticipated improvement in simulation quality from the increased basis set flexibility. The larger error from the additional polarization functions is due to poor parameterization of their Gaussian exponents for use in the solid state. In order to test this, a minimization of the total electronic energy by systematically varying the Gaussian exponent for each polarization function in the 6-31G(3d) basis set was performed, using the same procedure used for the copper *sp*-type orbital (optimized exponents available in the **Appendix F**). Subsequent PBE geometry optimizations with the optimized basis set decreased the total average error to 0.84%, now consistent with the anticipated improvements associated with the larger 6-31G(3d) basis set. However, the increased accuracy comes with significantly greater computational cost (~3 times slower than 6-31G(2d)). Given the modest structural improvement of 6-31G(3d) over 6-31G(2d) and the increased cost, the standard 6-31G(2d) basis set was selected as the best compromise between chemical accuracy and computational efficiency.

In order to determine the importance of polarization functions placed on copper, the 6-31G(2d) basis set was used for sulfur and oxygen, while the copper basis set was independently varied. The results listed in **Table 9-2** show that the average copper-oxygen bond changed very little with the different levels of polarization functions on copper, while the change in sulfur-oxygen bonds was even less ($\leq$ 0.04% deviation across basis sets, data not tabulated). This is attributed to the use of *f*-orbitals as polarization functions in the 6-31G(d) basis set for transition metals, which should have little spatial overlap and energetic coupling with the orbitals

responsible for bonding on the oxygen atoms. The widespread naming convention of 6-31G(d) is used here to represent a single polarization function added to the transition metal to maintain literature conformity, however a more descriptive nomenclature may be 6-31G(f). Beyond the standard 6-31G variations, the transition metal optimized m-6-31G(d) basis set[40] was also tested on the copper atom (with the aforementioned modification to the *sp* exponent). Surprisingly, the results were of lower quality as compared to the unmodified 6-31G(d) calculations, with errors 2.8 and 4.0 times greater with PBE and B3LYP, respectively. Because of these structural factors and the lower computational cost of smaller basis sets, 6-31G(d) was chosen as the most appropriate basis set to describe the copper atom.

Finally, to help determine if a particular atom type was the origin of the large error associated with the pob-TZVP basis set, calculations were performed where 6-31G(2d) was used for two of the elements while pob-TZVP was used for the third. The results of these geometry optimizations are shown in **Figure 9-5**. Use of pob-TZVP for sulfur has little effect on the lattice dimensions, but is clearly detrimental for the S-O bond lengths. The S-O bonds and lattice dimensions are both strongly influenced by the pob-TZVP basis set when used for oxygen. Thus, it appears as though pob-TZVP performs well for copper, but is less reliable for the other atoms in the $CuSO_4$ system, particularly oxygen.

Table 9-2. Average Cu-O bond errors and average unit cell parameter errors for simulated anhydrous CuSO₄.

Basis Set		PBE			B3LYP		
Copper	Sulfur/Oxygen	Cu-O	Unit Cell	Average	Cu-O	Unit Cell	Average
6-31G	6-31G(2d)	0.74	0.41	0.57	0.22	0.45	0.33
6-31G(d)		**0.63**	**0.40**	**0.51**	**0.18**	0.31	**0.24**
6-31G(2d)		0.72	0.44	0.58	0.38	**0.12**	0.25
m-6-31G(d)		1.21	1.62	1.41	0.88	1.14	1.01
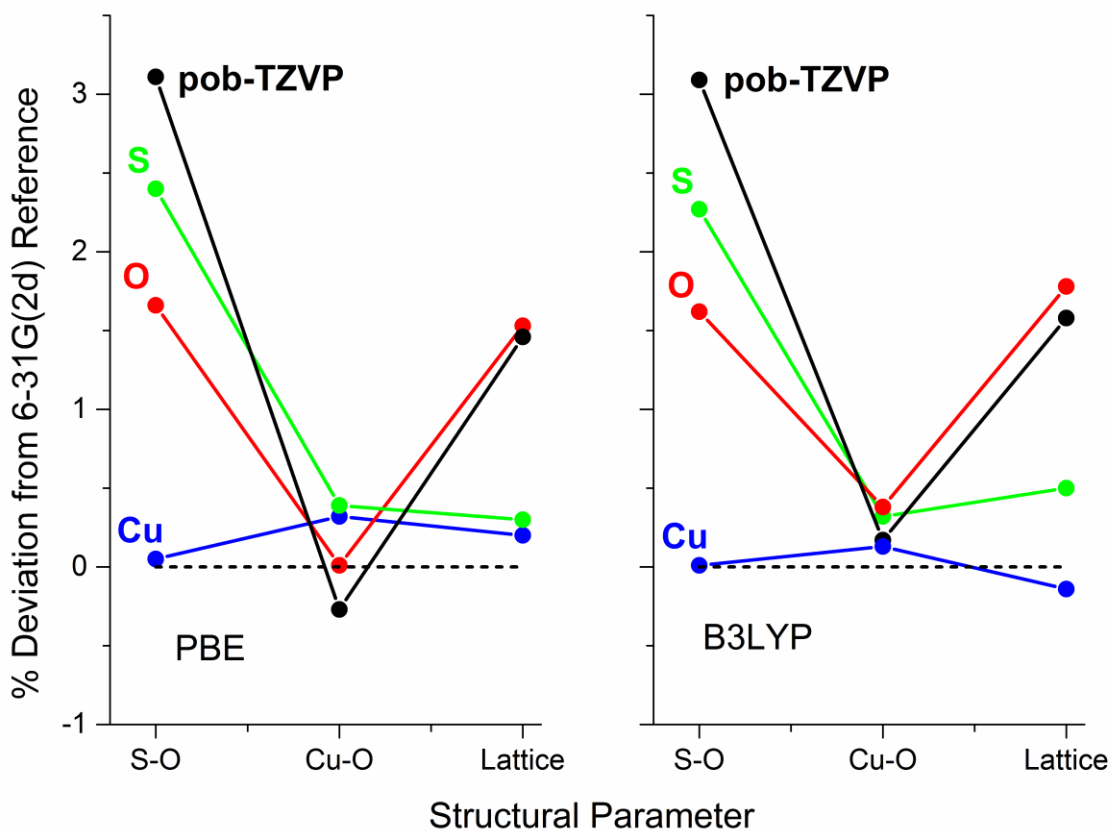
Figure 9-5 Effect of pob-TZVP usage on specific atom types shown through structural parameter changes. 6-31G(2d) on all atoms (dashed lines at 0 %) is set as the reference benchmark. The black trace shows the opposite extreme, with use of pob-TZVP on all atoms.

While the basis set dependence of the structural reproduction is clear, the choice of density functional is also critical. As seen in **Tables 9-1** and **9-2**, switching from the GGA-PBE functional to the hybrid-B3LYP functional, caused the average errors in the structural parameters to be greatly reduced. It is worthy to note that the same error trend related to basis set usage is observed when using either the GGA or hybrid functional. In light of these collective observations, B3LYP/6-31G(2d) (along with 6-31G(d) on copper) was determined to be the best performing functional/basis set combination. The success of B3LYP in providing the best structure for anhydrous $CuSO_4$ can be attributed to two factors. The capability of B3LYP for calculating accurate covalent bond distances has been well documented[43-46]. The success of B3LYP in predicting correct lattice parameters has also been reported[40], which in part is due to its better handling of long-range electrostatic interactions. In these ionic solids, which are dominated by electrostatic forces, B3LYP predicts more accurate copper-oxygen bonds and lattice parameters when compared to PBE. These structural improvements in $CuSO_4$ may be due to the B3LYP calculations predicting of a slightly greater charge disparity (~ 0.2 e) between the copper and oxygen atoms as compared to the GGA functional.

9.3.3.2 Copper Sulfate Hydrates

Single-crystal XRD data has been reported for $CuSO_4{\cdot}3H_2O$[24] , and therefore serves as a good test of the theoretical methods applied to hydrated $CuSO_4$. Copper sulfate trihydrate exhibits monoclinic *Cc* space group symmetry, with lattice dimensions of: $a = 5.592$ Å, $b = 13.029$ Å, $c = 7.341$ Å, $\beta = 97.05°$, $\alpha = \gamma = 90°$. The unit cell contains four formula units ($Z = 4$) with one in the asymmetric unit. As in the anhydrous form, the copper cation adopts a Jahn-

Teller distorted octahedral geometry with two elongated copper-oxygen bonds. Both PBE and B3LYP were used with the determined best basis set combination of 6-31G(d) on copper and 6-31G(2d,p) on sulfur, oxygen, and hydrogen. Full geometry optimizations produced bond errors that mimic the observed error trends in the geometry optimizations of the anhydrous form, with an overall average bond error of 2.11% and 0.63% for PBE and B3LYP, respectively. The lattice parameter errors in the trihydrate are also very similar to the anhydrous species, with an average error of 0.79% and 0.30% for PBE and B3LYP, respectively. These results (see **Appendix F** for details) and their consistency with the anhydrous $CuSO_4$ error trends provide confidence that the chosen basis set combination is appropriate for the $CuSO_4$ hydrates relevant to this study.

Only powder neutron diffraction data[13] is available for $CuSO_4 \cdot H_2O$, which provides accurate lattice parameters, but lacks the atomic precision of single-crystal X-ray diffraction experiments. Unfortunately, this limits its use in rigorously testing the theoretical methods for individual bond distance predictions. Copper sulfate monohydrate exhibits triclinic *P -1* space group symmetry, with lattice dimensions of: $a = 5.0401$ Å, $b = 5.1566$ Å, $c = 7.5691$ Å, $\alpha = 108.39°$, $\beta = 108.992°$, $\gamma = 90.4°$. The unit cell contains two formula units ($Z = 2$) with one in the asymmetric unit. As in the other $CuSO_4$ species, the copper cation adopts a Jahn-Teller distorted octahedral geometry. Full geometry optimizations were performed with both PBE and B3LYP using the same basis set combination as the trihydrate. While the calculated lattice parameters compare very well to experiment (0.72% and 0.66% deviations for PBE and B3LYP, respectively), the copper-oxygen and sulfur-oxygen predicted bond lengths differ significantly from the published data. These apparent errors are likely not due to limits of the applied theory, but rather are attributable to the uncertainty in the atomic positions from the powder neutron data. This conclusion is supported by the existing literature data for the related $CuSO_4 \cdot 3H_2O$

solid. Specifically, both powder neutron diffraction and single crystal X-ray diffraction results are available and yield lattice parameters that agree between experiments, but atomic positions that do not. As noted earlier, the $CuSO_4 \cdot 3H_2O$ calculated structure is in excellent agreement with the published single-crystal X-ray structure. These results imply that while the powder neutron diffraction experiment is well suited for determining lattice parameters, solid-state DFT is able to provide more accurate atomic positions in the absence of single-crystal measurements. The simulated powder patterns based on the calculated $CuSO_4 \cdot H_2O$ structure and based on the published neutron powder structure are essentially identical, which helps explain how the bond distance discrepancies were not identified previously. The improved atomic positions and lattice parameters for the calculated $CuSO_4 \cdot H_2O$ structure are available in **Appendix F**.

9.3.4 Computational Vibrational Analysis

9.3.4.1 Anhydrous Copper Sulfate

Initial vibrational simulations utilizing the pob-TZVP basis set on all atoms yielded only a single vibration in the ≤ 110 cm^{-1} spectral range, at 87.1 (PBE) and 92.4 cm^{-1} (B3LYP). This poor correlation with the experimental results again reveals that the pob-TZVP basis set is not a good choice for this system. More importantly, this result provides some reference as to what level of structural reproduction errors are acceptable when the goal is the simulation of terahertz spectra. Switching to the basis that yielded the best structure (6-31G(d) on copper, 6-31G(2d) on sulfur and oxygen) provided much improved simulated spectra that could be used to assign the observed terahertz absorption features. The calculated spectra are shown in **Figure 9-6** and have

271

been convolved with Lorentzian line shapes using the empirical full-width half-maximum value from the 77 K experimental spectrum. Although PBE and B3LYP both predict two vibrations in the sub-110 cm^{-1} range, the B3LYP simulation has a superior correlation with both the experimental positions and intensities. **Table 9-3** lists the assignments of the calculated frequencies and intensities. The two vibrations occurring in the anhydrous copper sulfate terahertz spectrum both involve significant motion of the copper cation. The lower-frequency motion (78.9 cm^{-1}) is a translation of the copper cations in the *a-b* crystallographic plane coupled with a simultaneous rotation of the sulfates about the *c*-axis. This results in an effective bending of the Cu-O-S angle that includes the Jahn-Teller elongated coordinated oxygens. The higher frequency motion (85.3 cm^{-1}) is a pure copper translation in the *a-c* plane which results in an anti-symmetric stretch of the copper-oxygen bond along the same elongated bond coordinate.

9.3.4.2 Copper Sulfate Monohydrate

The partially resolved feature at ≥ 90 cm^{-1} in the as-received anhydrous copper sulfate THz spectrum is attributed to contamination by water, as discussed. The simulation of the CuSO$_4$·H$_2$O terahertz spectrum was performed using both PBE and B3LYP with 6-31G(d) on copper and 6-31G(2d, p) on the other elements. The PBE simulation produced two vibrations in the spectral region below 110 cm^{-1} (82.0 and 104.1 cm^{-1}), while the B3LYP simulation predicted only a single vibration at 98.3 cm^{-1} in this same range. As observed in the anhydrous copper sulfate simulations, the PBE functional consistently underestimated the vibrational frequencies in these solids. For example, the lowest calculated vibration with PBE at 82.0 cm^{-1} correlates with the B3LYP-predicted vibration at 98.3 cm^{-1}. This particular motion involves copper translation in

the *a-c* plane coupled with simultaneous sulfate rotation about the *b*-axis, generally similar to the 78.9 cm^{-1} vibration in anhydrous CuSO$_4$. The results of the CuSO$_4$·H$_2$O simulations are shown in **Figure 9-6** and have been intensity scaled to reflect the relative anhydrous and hydrate populations in the powdered sample (as determined by PXRD).

9.3.4.3 Copper Sulfate Trihydrate

The PBE-based vibrational simulation of CuSO$_4$·3H$_2$O again predicts eigenvalues which are at lower energies than the B3LYP simulation, following the pattern of the anhydrous and monohydrate simulations. However, unlike the other solids, the normal mode energetic ordering is different between the two functionals (see **Table 9-3**), emphasizing the particular sensitivity of CuSO$_4$·3H$_2$O simulations to functional choice. The full list of correlated vibrational frequencies and the type of vibrational motions for all forms of copper sulfate is given in **Table 9-3**. While the majority of the terahertz vibrations in these solids involve copper translation with simultaneous rotation of the sulfates, CuSO$_4$·3H$_2$O also exhibits a weak translational mode at 72.7 cm^{-1}/79.9 cm^{-1} (PBE/B3LYP). The results of the trihydrate simulations (intensity scaled by its appropriate concentration) are shown in **Figure 9-6**. The PBE simulation incorrectly predicts normal modes with energies lower than the first experimental absorbance, which further justifies the use of B3LYP to provide a superior reproduction of the experimental frequencies and intensities in the experimental data.
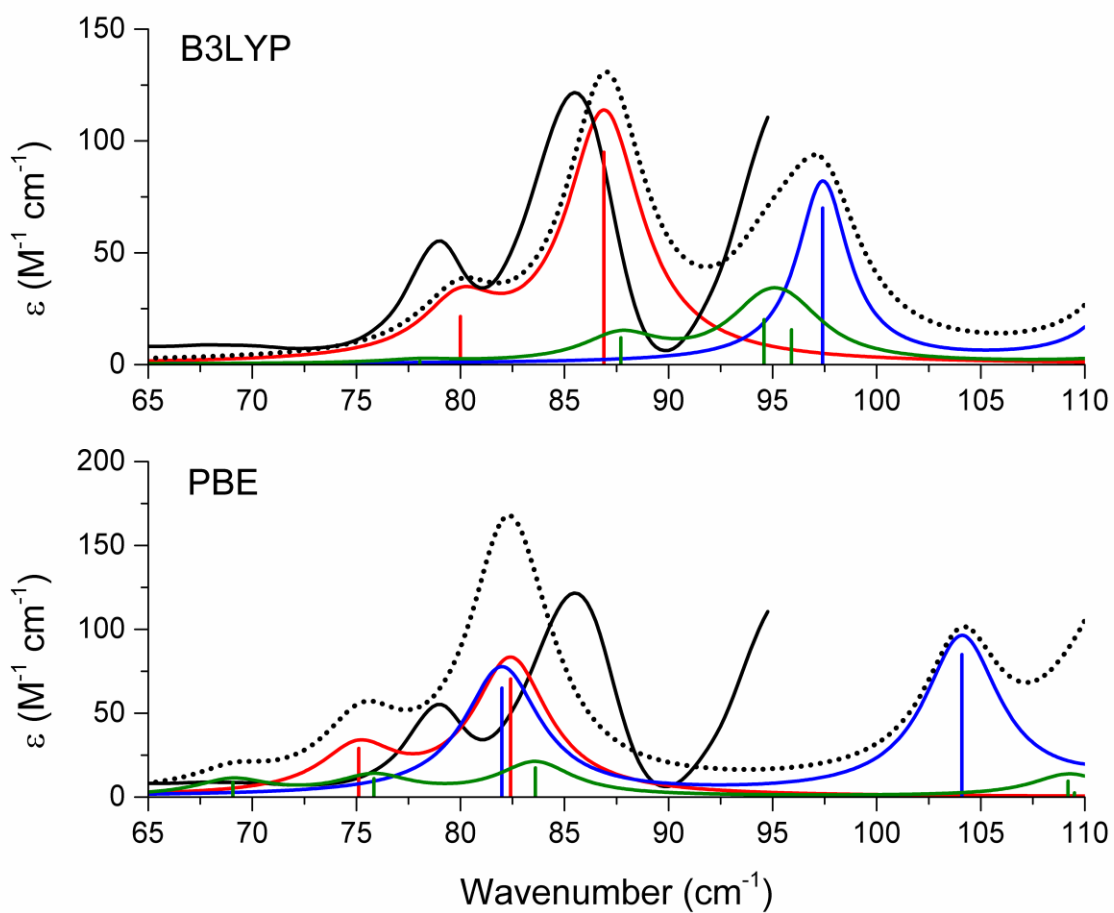
Figure 9-6. Comparison of the 77K terahertz spectrum of as-received copper sulfate (black), and the simulated vibrational spectra using B3LYP and PBE of $CuSO_4$ (red), $CuSO_4 \cdot H_2O$ (blue), and $CuSO_4 \cdot 3H_2O$ (green). The simulation intensities have each been scaled by their concentrations determined from PXRD. The dotted lines are linear combinations of all three simulations.

Table 9-3. List of correlated infrared-active vibrations (cm^{-1}) and infrared intensities (km/mol), and the motion descriptions for CuSO$_4$, CuSO$_4$·H$_2$O, and CuSO$_4$·3H$_2$O below 100 cm^{-1}. The experimental peak positions are 78.9 cm^{-1} and 85.3 cm^{-1}.

Form	PBE		B3LYP		Motion Type
	Freq	Int	Freq	Int	
Anhydrous	75.1	6.2	80.0	5.4	Copper translation in *a-b* plane and sulfate rotation about *c*.
	82.4	18.5	86.9	25.4	Copper translation in the *a-c* plane.
Monohydrate	82.0	34.8	97.4	25.1	Copper translation in the *a-c* plane and sulfate rotation about *b*.
Trihydrate	69.1	15.5	78.0	2.4	Copper translation in the *a-c* plane and sulfate rotation about *b*.
	72.7	0.7	79.9	0.1	Translation along *c*
	75.84	18.5	95.9	25.0	Copper translation along *b* and sulfate rotation about *c*.
	83.6	31.8	94.6	32.3	Copper translation in the *a-b* plane and sulfate rotation about *c*.
	87.0	1.0	87.7	19.3	Copper translation in the *b-c* plane and sulfate, sulfate rotation about *a*.

9.3.5 Calculated Thermodynamics of Hydration

      The success of the vibrational and structural simulations provides an opportunity to evaluate the Gibbs free energies (G) of each of the species to gain some insight into the hydration processes affecting solid-state $CuSO_4$. The free energies of crystalline anhydrous $CuSO_4$, $CuSO_4·H_2O$, $CuSO_4·3H_2O$, and a single gas-phase water molecule were calculated using B3LYP with 6-31G(d) on copper and 6-31G(2d,p) on all other atoms. The thermodynamic parameters were determined through evaluation of the canonical partition function.[47] Changes in free energy (ΔG) were calculated for three possible hydration routes:

$$CuSO_4 \text{ (s)} + H_2O \text{ (g)} \rightarrow CuSO_4·H_2O \text{ (s)} \quad \Delta G_{298K} = -49.08 \text{ kJ/mol}$$

$$CuSO_4·H_2O \text{ (s)} + 2H_2O \text{ (g)} \rightarrow CuSO_4·3H_2O \text{ (s)} \quad \Delta G_{298K} = -63.59 \text{ kJ/mol}$$

$$CuSO_4 + 3H_2O \text{ (g)} \rightarrow CuSO_4·3H_2O \text{ (s)} \quad \Delta G_{298K} = -112.67 \text{ kJ/mol}$$
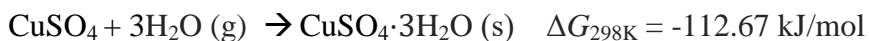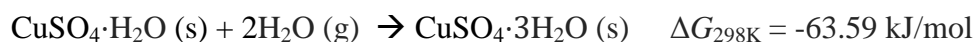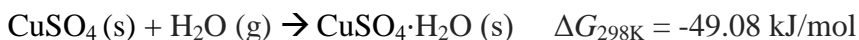
      All hydrated $CuSO_4$ species yielded negative ΔG values, indicating that at ambient pressure and temperature the formation of each is thermodynamically spontaneous. For completeness, the ΔG values were also checked at 90K (the same temperature as the terahertz and PXRD measurements), and no changes in spontaneity were found. The calculated thermodynamic data is in agreement with the PXRD-derived populations presented in this work, which showed significant amounts of all three hydrates coexisting. Interestingly, the anhydrous to trihydrate pathway has a $\Delta G_{298K} = -112.67$ kJ/mol, indicating that it is calculated to be even more thermodynamically favored than the anhydrous to monohydrate step in seeming contrast to previous reports[13]. It should be emphasized that the Gibbs free energies do not provide any

information about the hydration mechanisms, or the barriers that may exist along the formation

coordinates, but are valuable for evaluating the thermodynamic stability of various compounds

under specific conditions. Moreover, although the thermodynamic data does not preclude

formation of $CuSO_4 \cdot 3H_2O$, there is no information within the calculated ΔG values related to the

rates of hydration and this omission of kinetics may explain the differences in $CuSO_4$ hydrate

populations between research studies.

9.4 Conclusions

The terahertz spectrum of crystalline copper sulfate has been completely assigned using solid-state density functional theory. The identification of the chemical origins of the terahertz absorption features strengthens the use of terahertz spectroscopy for the analytical evaluation of metal sulfate samples that commonly occur in historical artwork and documents. Anhydrous copper sulfate, stored in typical laboratory conditions, contains a non-trivial amount of co-crystallized water existing as specific hydrates. A combination of terahertz spectroscopy, powder X-ray diffraction and solid-state theory were brought together to achieve a detailed picture of the chemical profile of the copper sulfate samples. Quantum mechanical simulations of the structures and vibrational motions of these materials provided important insights into the atomic-level details of these solids. The internal and external structure of anhydrous copper sulfate were found to be greatly dependent on the chosen functional and basis set combination. Use of the hybrid B3LYP functional with basis sets of 6-31G(d) on copper and 6-31G(2d, p) on all other atoms yielded excellent solid-state structures and terahertz vibrational frequencies and intensities. Solid-state theory has enabled the two terahertz features below 90 cm^{-1} to be assigned to anhydrous copper sulfate, with the absorption at 95 cm^{-1} originating primarily from $CuSO_4 \cdot H_2O$, though $CuSO_4 \cdot 3H_2O$ also absorbs in the same region. Additionally, Gibbs free energy analyses of the various species indicate that the hydrate formation processes are all spontaneous at ambient conditions, supporting the experimental observation of coexisting $CuSO_4$, $CuSO_4 \cdot H_2O$, and $CuSO_4 \cdot 3H_2O$.

9.5 Acknowledgements

Supporting Information (see APPENDIX F)

The calculated bond lengths, unit cell parameters (*a, b, c*, and angles where applicable), atomic positions for $CuSO_4$, $CuSO_4 \cdot H_2O$, and $CuSO_4 \cdot 3H_2O$, the PXRD and terahertz spectrum of dried $CuSO_4$, complete list of simulated vibrational frequencies, and optimized Gaussian exponents for 6-31G(3d). This material is available free of charge via the Internet at http://pubs.acs.org.

9.6 References

1.   King, M. D.; Buchanan, W. D.; Korter, T. M., Identification and Quantification of Polymorphism in the Pharmaceutical Compound Diclofenac Acid by Terahertz Spectroscopy and Solid-State Density Functional Theory. *Anal. Chem.* **2011**, *83*, 3786-3792.

2.   Williams, M. R. C.; True, A. B.; Izmaylov, A. F.; French, T. A.; Schroeck, K.; Schmuttenmaer, C. A., Terahertz Spectroscopy of Enantiopure and Racemic Polycrystalline Valine. *Phys. Chem. Chem. Phys.* **2011**, *13*, 11719-11730.

3.   Jepsen, P. U.; Clark, S. J., Precise Ab-Initio Prediction of Terahertz Vibrational Modes in Crystalline Systems. *Chem. Phys. Lett.* **2007**, *442*, 275-280.

4.   Shen, Y.-C., Terahertz Pulsed Spectroscopy and Imaging for Pharmaceutical Applications: A Review. *Int. J. Pharm.* **2011**, *417*, 48-60.

5.   Trafela, T.; Mizuno, M.; Fukunaga, K.; Strlič, M., Quantitative Characterisation of Historic Paper Using Thz Spectroscopy and Multivariate Data Analysis. *Appl. Phys. A* **2013**, *111*, 83-90.

6.   Banerjee, D.; von Spiegel, W.; Thomson, M. D.; Schabel, S.; Roskos, H. G., Diagnosing Water Content in Paper by Terahertz Radiation. *Opt. Express* **2008**, *16*, 9060-9066.

7.   King, M. D.; Korter, T. M., Effect of Waters of Crystallization on Terahertz Spectra: Anhydrous Oxalic Acid and Its Dihydrate. *J. Phys. Chem. A* **2010**, *114*, 7127-7138.

8.   Hakey, P. M.; Allis, D. G.; Hudson, M. R.; Ouellette, W.; Korter, T. M., Investigation of (1r,2s)-(−)-Ephedrine by Cryogenic Terahertz Spectroscopy and Solid-State Density Functional Theory. *ChemPhysChem* **2009**, *10*, 2434-2444.

9.   Delaney, S. P.; Pan, D.; Yin, S. X.; Smith, T. M.; Korter, T. M., Evaluating the Roles of Conformational Strain and Cohesive Binding in Crystalline Polymorphs of Aripiprazole. *Cryst. Growth Des.* **2013**, *13*, 2943-2952.

10.   Bardon, T.; May, R. K.; Taday, P. F.; Strlic, M., Systematic Study of Terahertz Time-Domain Spectra of Historically Informed Black Inks. *Analyst* **2013**, *138*, 4859-4869.

11.   Jackson, J. B.; Bowen, J.; Walker, G.; Labaune, J.; Mourou, G.; Menu, M.; Fukunaga, K., A Survey of Terahertz Applications in Cultural Heritage Conservation Science. *IEEE Trans. Terahertz Sci. Technol.* **2011**, *1*, 220-231.

12.   Kolar., J.; Strlič., M., *Iron Gall Inks: On Manufacture, Characterisation, Degradation and Stabilisation*; National and University Library: Ljubljana, Slovenia, 2006.

13.   Ting, V. P.; Henry, P. F.; Schmidtmann, M.; Wilson, C. C.; Weller, M. T., In Situ Neutron Powder Diffraction and Structure Determination in Controlled Humidities. *Chem. Commun.* **2009**, 7527-7529.

14.   Liu, D.; Ullman, F. G., Raman Spectrum of CuSO4 · 5h2o Single Crystal. *J. Raman Spectrosc.* **1991**, *22*, 525-528.

15.   White, R. L., Variable Temperature Infrared Study of Copper Sulfate Pentahydrate Dehydration. *Thermochim. Acta* **2012**, *528*, 58-62.

16.   Corà, F.; Alfredsson, M.; Mallia, G.; Middlemiss, D.; Mackrodt, W.; Dovesi, R.; Orlando, R., The Performance of Hybrid Density Functionals in Solid State Chemistry. In *Principles and Applications of Density Functional Theory in Inorganic Chemistry II*, Springer Berlin Heidelberg: 2004; Vol. 113, pp 171-232.

17.   Hudson, M. R.; Allis, D. G.; Ouellette, W.; Hakey, P. M.; Hudson, B. S., The Low-Temperature X-Ray Structure, Raman and Inelastic Neutron Scattering Vibrational

Spectroscopic Investigation of the Non-Centrosymmetric Amino Acid Salt Glycine Lithium Sulfate. *J. Mol. Struct.* **2009**, *934*, 138-144.

18.   Derzsi, M.; Stasiewicz, J.; Grochala, W., Crystal and Electronic Structures and High-Pressure Behavior of $AgSO_4$, a Unique Narrow Band Gap Antiferromagnetic Semiconductor: Lda(+U) Picture. *J Mol Model* **2011**, *17*, 2259-2264.

19.   Sheldrick, G., A Short History of Shelx. *Acta Crystallogr. Sect. A* **2008**, *64*, 112-122.

20.   Macrae, C. F.; Bruno, I. J.; Chisholm, J. A.; Edgington, P. R.; McCabe, P.; Pidcock, E.; Rodriguez-Monge, L.; Taylor, R.; van de Streek, J.; Wood, P. A., Mercury Csd 2.0 - New Features for the Visualization and Investigation of Crystal Structures. *J. Appl. Crystallogr.* **2008**, *41*, 466-470.

21.   Bacon G E, T. D. H., Neutron-Diffraction Studies of $CuSO_4*5(H_2O)$ and $CuSO_4*5(D_2o)$. Zeitschrift fur Kristallographie, 1975; Vol. 141, pp 330-341.

22.   Wildner, M.; Giester, G., Crystal Structure Refinements of Synthetic Chalcocyanite $(CuSO_4)$ and Zincosite $(ZnSO_4)$. *Mineralogy and Petrology* **1988**, *39*, 201-209.

23.   Szilagyi, R. K.; Frank, P.; DeBeer George, S.; Hedman, B.; Hodgson, K. O., High Covalence in CuSO4 and the Radicalization of Sulfate: An X-Ray Absorption and Density Functional Study. *Inorg. Chem.* **2004**, *43*, 8318-8329.

24.   Zahrobsky, R. F.; Baur, W. H., On the Crystal Chemistry of Salt Hydrates. V. The Determination of the Crystal Structure of $CuSO_4 • 3H_2O$ (Bonattite). *Acta Crystallogr. Sect. B* **1968**, *24*, 508-513.

25.   Hakey, P. M.; Allis, D. G.; Ouellette, W.; Korter, T. M., Cryogenic Terahertz Spectrum of (+)-Methamphetamine Hydrochloride and Assignment Using Solid-State Density Functional Theory. *J. Phys. Chem. A* **2009**, *113*, 5119-5127.

26. Rice, A.; Jin, Y.; Ma, X. F.; Zhang, X. C.; Bliss, D.; Larkin, J.; Alexander, M., Terahertz Optical Rectification from 〈110〉 Zinc-Blende Crystals. *Appl. Phys. Lett.* **1994**, *64*, 1324-1326.

27. Zhang, X. C.; Ma, X. F.; Jin, Y.; Lu, T. M.; Boden, E. P.; Phelps, P. D.; Stewart, K. R.; Yakymyshyn, C. P., Terahertz Optical Rectification from a Nonlinear Organic Crystal. *Appl. Phys. Lett.* **1992**, *61*, 3080-3082.

28. Wu, Q.; Litz, M.; Zhang, X. C., Broadband Detection Capability of Znte Electro-Optic Field Detectors. *Appl. Phys. Lett.* **1996**, *68*, 2924-2926.

29. Holden, J. R.; Dickinson, C. W., Crystal Structures of Three Solid Solution Phases of Ammonium Nitrate and Potassium Nitrate. *J. Phys. Chem* **1975**, *79*, 249-256.

30. Dovesi, R. O., R.; Civalleri, B.; Roetti, C.; Saunders, V. R.; Zicovich-Wilson, C. M. *CRYSTAL09*, University of Torino: Torino, 2009.

31. Perdew, J. P.; Ruzsinszky, A.; Csonka, G. I.; Vydrov, O. A.; Scuseria, G. E.; Constantin, L. A.; Zhou, X.; Burke, K., Restoring the Density-Gradient Expansion for Exchange in Solids and Surfaces. *Phys. Rev. Lett.* **2008**, *100*, 136406.

32. Becke, A. D., Density-Functional Thermochemistry. III. The Role of Exact Exchange. *J. Chem. Phys.* **1993**, *98*, 5648-5652.

33. Peintinger, M. F.; Oliveira, D. V.; Bredow, T., Consistent Gaussian Basis Sets of Triple-Zeta Valence with Polarization Quality for Solid-State Calculations. *J. Comput. Chem.* **2013**, *34*, 451-459.

34. Krishnan, R.; Binkley, J. S.; Seeger, R.; Pople, J. A., Self-Consistent Molecular Orbital Methods. Xx. A Basis Set for Correlated Wave Functions. *J. Chem. Phys.* **1980**, *72*, 650-654.

35.   Noel, Y.; Zicovich-Wilson, C. M.; Civalleri, B.; D'Arco, P.; Dovesi, R., Polarization

        Properties of Zno and Beo: An *ab initio* Study through the Berry Phase and Wannier

        Functions Approaches. *Phys. Rev. B.* **2001**, *65*, 014111.

36.   Fu, X.; Wu, H.; Xi, X.; Zhou, J., Molecular Rotation–Vibration Dynamics of Low-

        Symmetric Hydrate Crystal in the Terahertz Region. *J. Phys. Chem. A* **2013**, *118*, 333-

        338.

37.   Fu, X.; Yang, G.; Sun, J.; Zhou, J., Vibrational Spectra of Copper Sulfate Hydrates

        Investigated with Low-Temperature Raman Spectroscopy and Terahertz Time Domain

        Spectroscopy. *J. Phys. Chem. A* **2012**, *116*, 7314-7318.

38.   Cramer, C. J.; Truhlar, D. G., Density Functional Theory for Transition Metals and

        Transition Metal Chemistry. *Phys. Chem. Chem. Phys.* **2009**, *11*, 10757-10816.

39.   Wells, J. S.; Matarrese, L. M.; Sukle, D. J., Electron Spin Resonance in Single Crystals of

        Anhydrous Copper Sulfate. *J. Chem. Phys.* **1967**, *47*, 2259-2262.

40.   Mitin, A. V.; Baker, J.; Pulay, P., An Improved 6-31g* Basis Set for First-Row

        Transition Metals. *J. Chem. Phys.* **2003**, *118*, 7775-7782.

41.   Denis, P. A., Basis Set Requirements for Sulfur Compounds in Density Functional

        Theory: A Comparison between Correlation-Consistent, Polarized-Consistent, and

        Pople-Type Basis Sets. *J. Chem. Theory Comput.* **2005**, *1*, 900-907.

42.   Strömberg, A.; Wahlgren, U.; Pettersson, L.; Siegbahn, P. E. M., On the Role of 3d

        Orbitals in Sulfur. *Chem. Phys.* **1984**, *89*, 323-328.

43.   Momany, F. A.; Appell, M.; Strati, G.; Willett, J. L., B3LYP/6-311++G** Study of

        Monohydrates of A- and B-D-Glucopyranose: Hydrogen Bonding, Stress Energies, and

        Effect of Hydration on Internal Coordinates. *Carbohydrate Research* **2004**, *339*, 553-567.

44. Zicovich-Wilson, C. M.; Pascale, F.; Roetti, C.; Saunders, V. R.; Orlando, R.; Dovesi, R., Calculation of the Vibration Frequencies of A-Quartz: The Effect of Hamiltonian and Basis Set. *J. Comput. Chem.* **2004**, *25*, 1873-1881.

45. Ma, B.; Lii, J.-H.; Schaefer, H. F.; Allinger, N. L., Systematic Comparison of Experimental, Quantum Mechanical, and Molecular Mechanical Bond Lengths for Organic Molecules. *J. Phys. Chem* **1996**, *100*, 8763-8769.

46. Miao, R.; Jin, C.; Yang, G.; Hong, J.; Zhao, C.; Zhu, L., Comprehensive Density Functional Theory Study on Serine and Related Ions in Gas Phase: Conformations, Gas Phase Basicities, and Acidities. *J. Phys. Chem. A* **2005**, *109*, 2340-2349.

47. Zhuravlev, Y. N.; Korabel'nikov, D. V.; Aleinikova, M. V., Ab Initio Calculations of the Thermodynamic Parameters of Lithium, Sodium, and Potassium Oxides under Pressure. *Phys. Solid State* **2012**, *54*, 1518-1527.

CHAPTER 10: Uncovering the Terahertz Spectrum of Copper Sulfate Pentahydrate

The material contained within this chapter is published in the *Journal of Physical Chemistry A* (Ruggiero, M.T.; Korter, T.M. *J. Phys. Chem. A* **2016.** *120*(2), 227-232). This article has been reproduced with permission from the American Chemical Society.
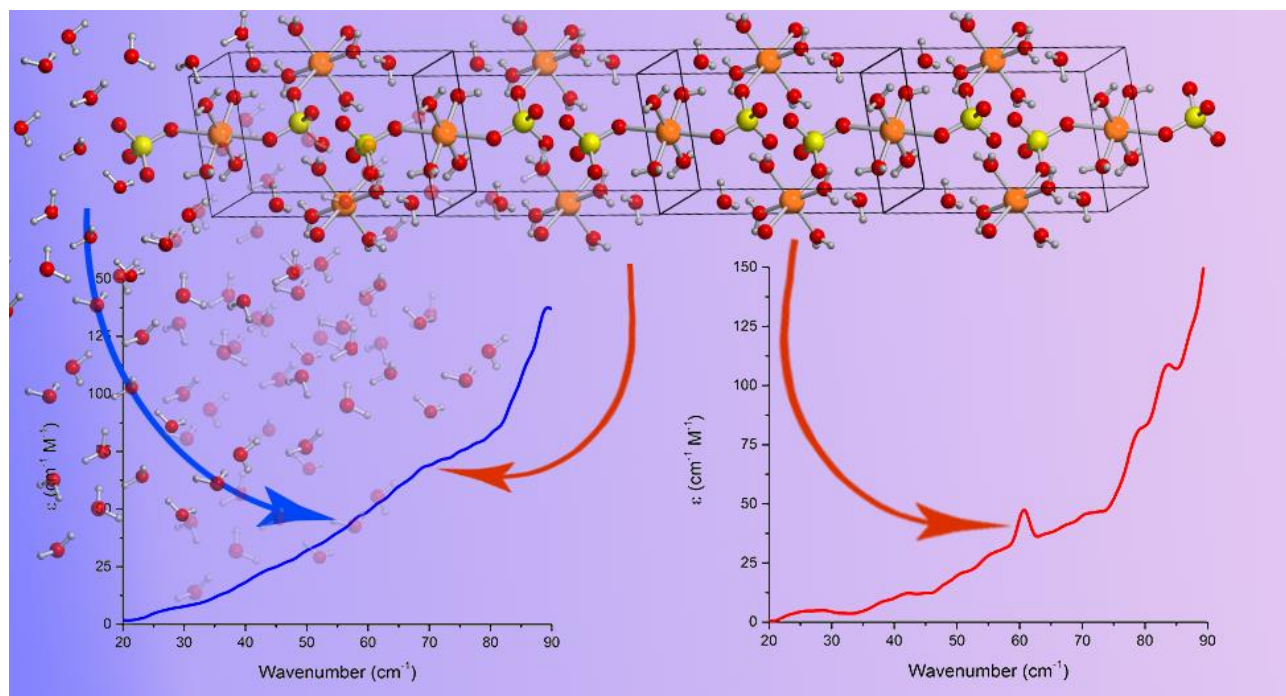
Abstract

Terahertz vibrational spectroscopy has evolved into a powerful tool for the detection and characterization of transition metal sulfate compounds, specifically for its ability to differentiate between various hydrated forms with high specificity. Copper(II) sulfate is one such system where multiple crystalline hydrates have had their terahertz spectra fully assigned, and the unique spectral fingerprints of the forms allows for characterization of multicomponent systems with relative ease. Yet the most commonly occurring form, copper(II) sulfate pentahydrate ($CuSO_4 \cdot 5H_2O$), has proven elusive due to the presence of a broad absorption across much of the terahertz region, making the unambiguous identification of its spectral signature difficult. Here it is shown that the sub-100 cm^{-1} spectrum of $CuSO_4 \cdot 5H_2O$ is obscured by absorption from adsorbed water, and that controlled drying reveals sharp underlying features. The crystalline composition of the samples was monitored in parallel by X-ray diffraction as a function of drying time, supporting the spectroscopic results. Finally, the terahertz spectrum of $CuSO_4 \cdot 5H_2O$ was fully assigned using solid-state density functional theory simulations, helping attribute the additional absorptions that appear after excessive drying to formation of $CuSO_4 \cdot 3H_2O$.

10.1 Introduction

Transition metal sulfates are common compounds with numerous applications.[1-5] These substances often contain varying levels of hydration, in terms of both co-crystallized and adsorbed water, which greatly alters the physical properties of the materials.[6-7] The extent of hydration is influenced by many factors, with temperature and humidity being the most critical.[8-10] The dynamic nature of these effects often results in samples that have a mixture of several hydration states, making it difficult to determine the contributions of the different hydrated forms with great accuracy.[10-12] Terahertz (far-infrared) spectroscopy has proven to be a valuable analytical tool for characterizing hydration content, not only because of its specific response to solid-state molecular arrangements and its non-destructive nature, but also due to its sensitivity to bulk water content.[12-14] Recently, terahertz spectroscopy has been used to investigate various transition metal sulfates, and it was shown to provide detailed information that complemented other methods such as X-ray diffraction.[10, 15] Because the low-frequency motions accessible by terahertz radiation are dependent on both internal *and* external structures, it provides a high level of reliability in detecting the presence of compounds that may be challenging to distinguish in the mid-infrared or even by diffraction methods.[16-17]

Terahertz spectroscopy of transition metal sulfates typically reveals well-resolved absorption features in the sub-100 cm^{-1} region.[10, 15] Considering copper(II) sulfate specifically, terahertz spectra of anhydrous copper(II) sulfate and two of its three known hydrates (monohydrate and trihydrate) have had their spectral absorptions identified and assigned.[10, 18] Unexpectedly, copper(II) sulfate pentahydrate ($CuSO_4 \cdot 5H_2O$) was found to deviate from the trend of the lower hydrates by exhibiting a broad rising absorption in the terahertz region, with only very weak features possibly being resolved on top of this base. The broad and essentially

featureless absorption spectrum of $CuSO_4 \cdot 5H_2O$ limits its analytical utility in terahertz spectroscopic sensing. This is unfortunate given that the pentahydrate is the most common copper(II) sulfate hydrate under typical conditions.[9, 19] Complicating the analysis is that copper sulfate(II) is known to readily form mixed hydrate samples, and that the isolation of one particular form is difficult to achieve.[9-10] Thus it is highly likely that a given sample of what may primarily be $CuSO_4 \cdot 5H_2O$ is actually contaminated by various hydrate species.

Solid-state density functional theory (DFT) calculations are an invaluable resource when studying multi-component systems.[20-24] The simulation of the vibrational spectrum of each individual compound allows for qualitative spectral deconvolution of mixed samples.[21, 23, 25] In the case of anhydrous $CuSO_4$, the DFT results enabled the recognition that the 'pure' sample actually contained detectable amounts of monohydrate and trihydrate species, which clearly altered the experimental terahertz spectrum.[10] Applying the same computational methods to $CuSO_4 \cdot 5H_2O$ enables the observed terahertz spectral results to be interpreted and reconciled with controlled dehydration experiments. Careful control of water content in the $CuSO_4 \cdot 5H_2O$ samples enables identification of the mechanisms responsible for the obscuring of its spectral signature. Ultimately, the combined experimental and theoretical results show that adsorbed surface water dominates the terahertz spectra of ambient condition samples, masking any discrete absorptions from the $CuSO_4 \cdot 5H_2O$ crystals.

10.2 Methods

10.2.1 Experimental

Anhydrous $CuSO_4$ (Sigma-Aldrich, ≥99.99%) was fully dissolved in deionized water until the solution was deep blue in color. The aqueous mixture was placed in a standard laboratory fume hood for one week, until all of the solvent evaporated. Large blue crystals of $CuSO_4 \cdot 5H_2O$ formed, and were immediately prepared for experimental measurements by pulverizing in a stainless steel ball mill. The resultant blue powder was either used in that state or placed in a calcium sulfate (Drierite) desiccator in order to remove excess water.

To confirm bulk crystalline content, powder X-ray diffraction (PXRD) was always performed in parallel with the terahertz measurements. The pulverized samples were dispersed in paraben oil, mounted using a MiTeGen MicroMount, and placed under a stream of liquid nitrogen (to mimic the conditions of the single-crystal[26] and terahertz measurements). The PXRD data was obtained using a Bruker KAPPA APEX DUO diffractometer, which contains an APEX II CCD system, using monochromatic Cu Kα radiation ($\lambda = 1.5418$ Å). The experimental PXRD patterns were compared to patterns calculated from the experimental single-crystal[26] data using the Mercury[27] software.

Terahertz vibrational spectra were obtained from 20-90 cm^{-1} at both room (298 K) and liquid-nitrogen (78 K) temperatures with a time-domain pulsed spectrometer.[28] Zinc telluride crystals were used to generate and detect terahertz pulses through optical rectification[29-30] and free-space electrooptic sampling[31], respectively. The spectrometer was continuously purged with dry air and the sample chamber held under vacuum in order to minimize absorption from atmospheric water. The samples were mixed with polytetrafluoroethylene (PTFE) and pressed

into pellets, with a final w/w concentration of ~2.5%. It is important to note that copper(II) sulfate is very hygroscopic and therefore sensitive to atmospheric water, but once dispersed in the PTFE matrix and pressed into a pellet the samples were stable for at least one week. Terahertz time-domain waveforms were collected by averaging 32 scans over a 32 ps window, and were subsequently Fourier transformed to create terahertz transmission spectra. Absorption units (ε, $M^{-1}cm^{-1}$, based on the concentration of crystallographic unit cells) were obtained by the division of a sample spectrum by a blank PTFE spectrum, and the presented spectra are a result of four averaged sample-blank data sets.

10.2.2 Theoretical

All solid-state DFT calculations were performed using the CRYSTAL14 software package[32]. Based on previous publications regarding metal-sulfate species,[10, 15, 26] the Becke-3-Lee-Yang-Parr (B3LYP)[33] density functional and the atom-centered 6-31G(d)/6-31G(2d,2p) basis sets[34] (copper/non-metals) were used for the simulations. Geometry optimizations were initialized with experimentally determined atomic positions, and were performed in the absence of any constraints other than the space group symmetry of the solid. Normal mode eigenvalues and eigenvectors were calculated from the optimized structure, using the central-difference numerical displacement method (two displacements per Cartesian axis, per atom). The infrared-active intensities were calculated using the Berry phase method.[35-37] The energy convergence criteria were set to $\Delta E < 10^{-8}$ and 10^{-10} hartree for the optimization and vibrational calculations, respectively.

10.3 Results and Discussion

10.3.1 Terahertz Spectroscopy

10.3.1.1 Initial Undried

The PXRD pattern (**Figure 10-1**) of the initially prepared $CuSO_4 \cdot 5H_2O$ material showed that the sample contained pure $CuSO_4 \cdot 5H_2O$, and no reflections from any additional crystalline species were present. The terahertz spectrum of this sample (**Figure 10-2a**) was entirely featureless, only exhibiting broad absorption in the 20-90 cm^{-1} spectral range. This type of observed broad absorption has previously been shown to be caused by contamination from water that is not incorporated into the crystalline lattice, but adsorbed to the particles.[13, 15]
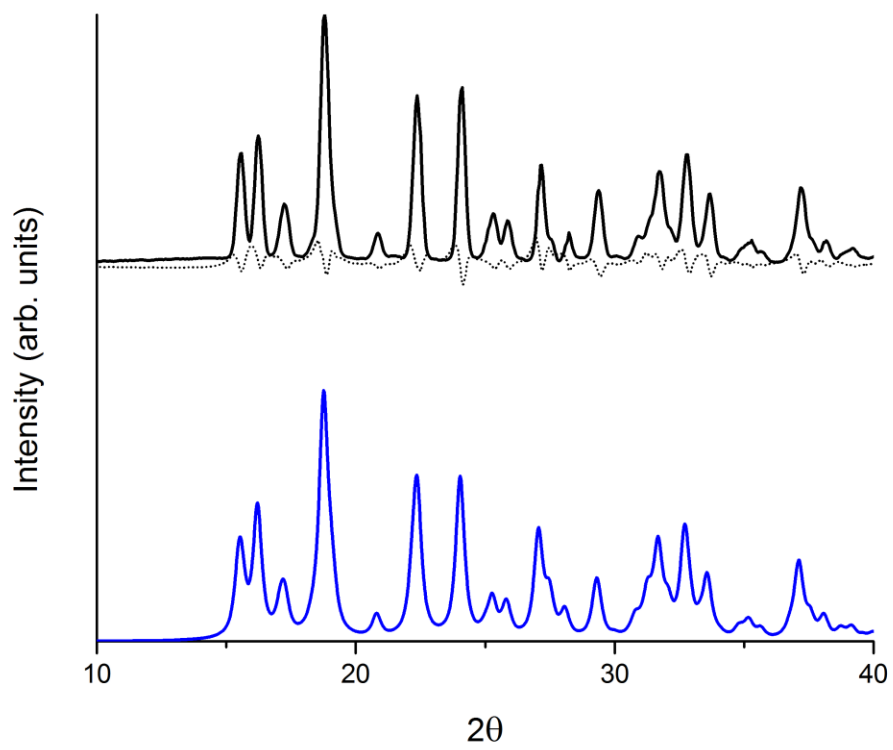
Figure 10-1. Experimental (black) and calculated (blue) PXRD patterns of CuSO$_4$·5H$_2$O.

The observed-minus-calculated residual is also shown (dotted trace).

10.3.1.2 Dried Six Hours

The $CuSO_4 \cdot 5H_2O$ powder was placed in a calcium sulfate desiccator for six hours in order to gently remove excess water from the sample. The sample lost 2.58 % of its original mass by the end of the drying period, but the PXRD pattern remained unchanged, indicating that only $CuSO_4 \cdot 5H_2O$ was present. It is important to note that the PXRD experiment accurately detects crystalline species present in samples, but provides no information regarding the amount of disordered adsorbed water. The terahertz spectrum of the corresponding sample is presented in **Figure 10-2b**. Similar to the undried terahertz spectrum, the dried sample exhibits a significant absorption which begins at ~20 cm^{-1} and steadily increases beyond the spectral bandwidth of the instrument. However upon drying, a resolvable absorption at 61.0 cm^{-1} appears with potential minor features between 75-90 cm^{-1}, but still contains significantly fewer features than previously reported.[18] The unchanged PXRD pattern, yet altered terahertz spectra and significant mass loss, show that unincorporated water must be present in the $CuSO_4 \cdot 5H_2O$ samples when stored under normal conditions (which makes copper sulfate a functional desiccant[38-40]) and highlights the sensitivity of terahertz spectroscopy to non-crystalline material.

10.3.1.3 Dried Twelve Hours

While the six-hour dried sample exhibited weak resolvable features, the terahertz spectrum still contained a broad absorption profile throughout the region, suggesting that unincorporated water was still present. The sample was placed into a desiccator for an additional six hours, resulting in a cumulative mass loss of 5.46%. The PXRD pattern of the dried sample

was again identical to the initial $CuSO_4 \cdot 5H_2O$ sample, indicating that no co-crystallized water was removed during the first twelve hours of drying. However the terahertz spectrum changed considerably between six and twelve hours of drying, with three additional features apparent at 71.4, 78.2 and 83.5 cm^{-1} (**Figure 10-2c**). Collectively, the changing terahertz spectrum, changing mass, but unchanged PXRD pattern further supports the hypothesis that the previously observed broad absorption originated from adsorbed water.

10.3.1.4 Dried Thirty Hours

In an attempt to remove any remaining adsorbed water, the sample was placed into the desiccator for an additional eighteen hours, after which the sample now experienced a cumulative total mass loss of 6.80%. The PXRD pattern of the newly dried sample now contained additional reflections that could not be assigned to $CuSO_4 \cdot 5H_2O$, but matched the pattern of $CuSO_4 \cdot 3H_2O$ (**Figure 10-3**). The presence of additional crystalline species resulted in the appearance of at least two new terahertz absorptions (**Figure 10-2d**), occurring at 76.6 and 87.2 cm^{-1}. The frequencies of these features correlate with the previously published vibrational analysis of $CuSO_4 \cdot 3H_2O$[10], confirming the identity of the contaminant indicated in the PXRD measurement.
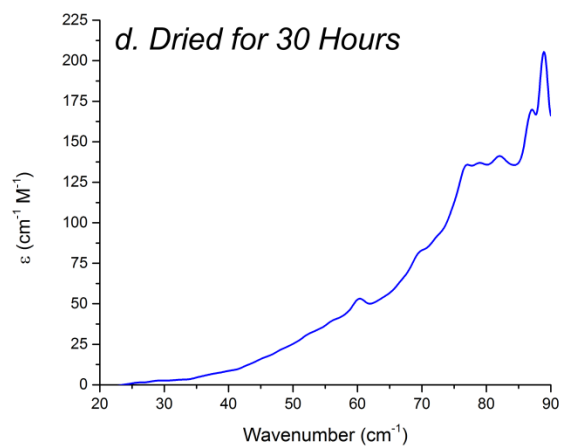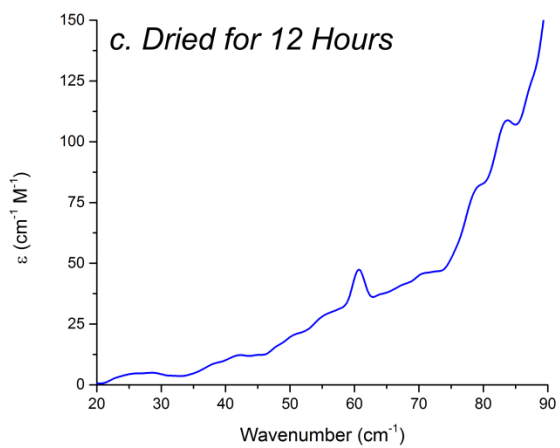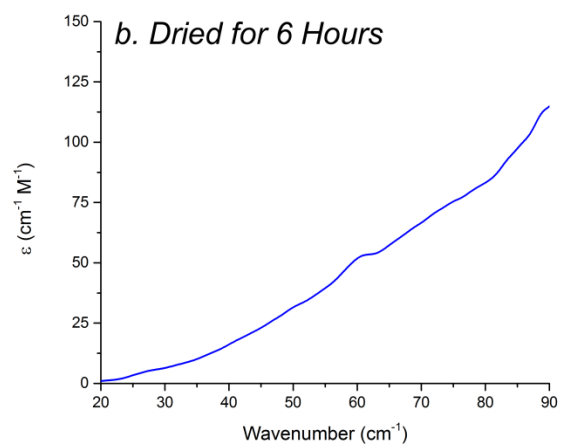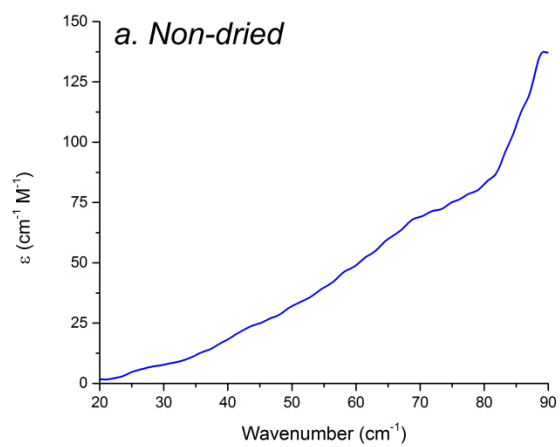
Figure 10-2. Terahertz spectra of CuSO₄·5H₂O after various drying intervals.
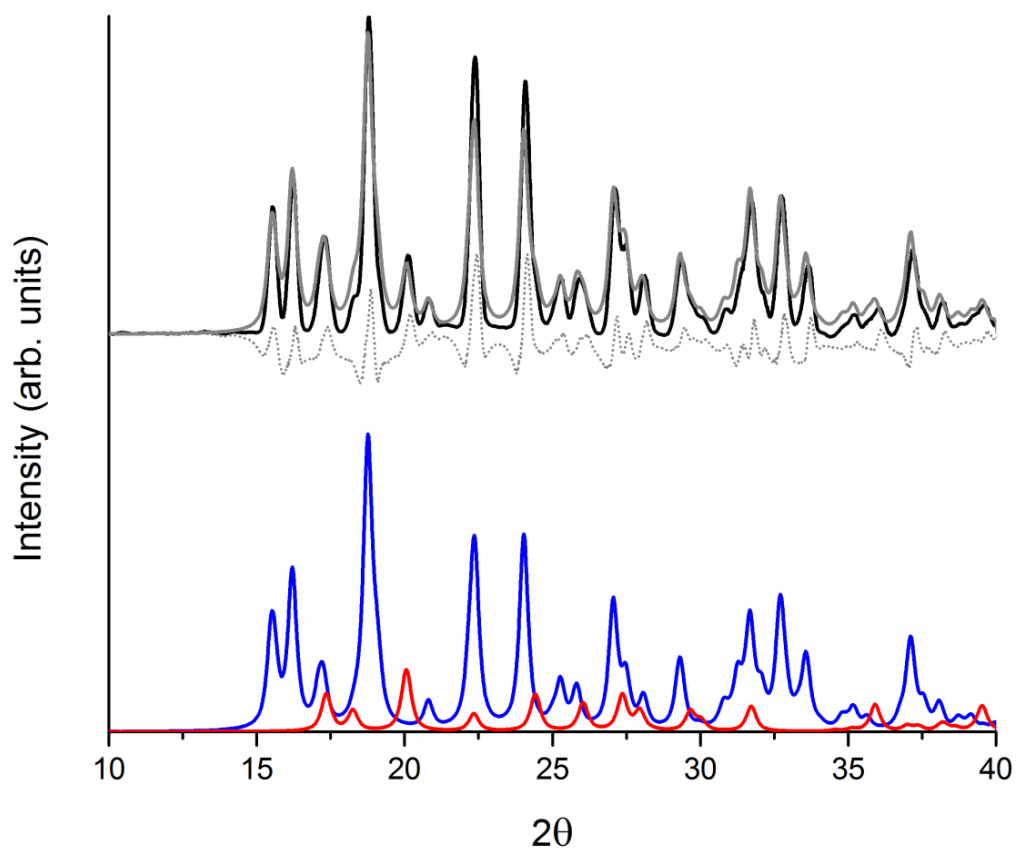
Figure 10-3. Dried (thirty hours) PXRD pattern (black) of CuSO₄·5H₂O. Contributions from CuSO₄·5H₂O (blue) and CuSO₄·3H₂O (red) are shown, along with their summed pattern (grey) and observed-minus-calculated residual (dotted).

10.3.2 Theoretical Analysis

10.3.2.1 Structural Details

The experimental low-temperature single-crystal XRD structure of $CuSO_4 \cdot 5H_2O$ has already been detailed in the literature, and will be discussed here only briefly.[26] Copper sulfate pentahydrate forms triclinic single crystals ($P\bar{1}$ space group symmetry) with lattice parameters of $a = 6.106$ Å, $b = 10.656$ Å, $c = 5.969$ Å, $\alpha = 77.332°$, $\beta = 82.433°$, $\gamma = 72.523°$, and $V = 360.548$ Å^3 (**Figure 10-4**). The unit cell contains four formula units ($Z=4$), and there are two symmetrically unique copper cations, resulting in two distinct coordination environments. The DFT geometry optimization accurately captures the internal and bulk structural details, with low absolute errors (0.69% and 0.45% for bond and unit cell dimension errors, respectively). The high quality structural reproductions form the basis for vibrational simulations of the crystalline solids.
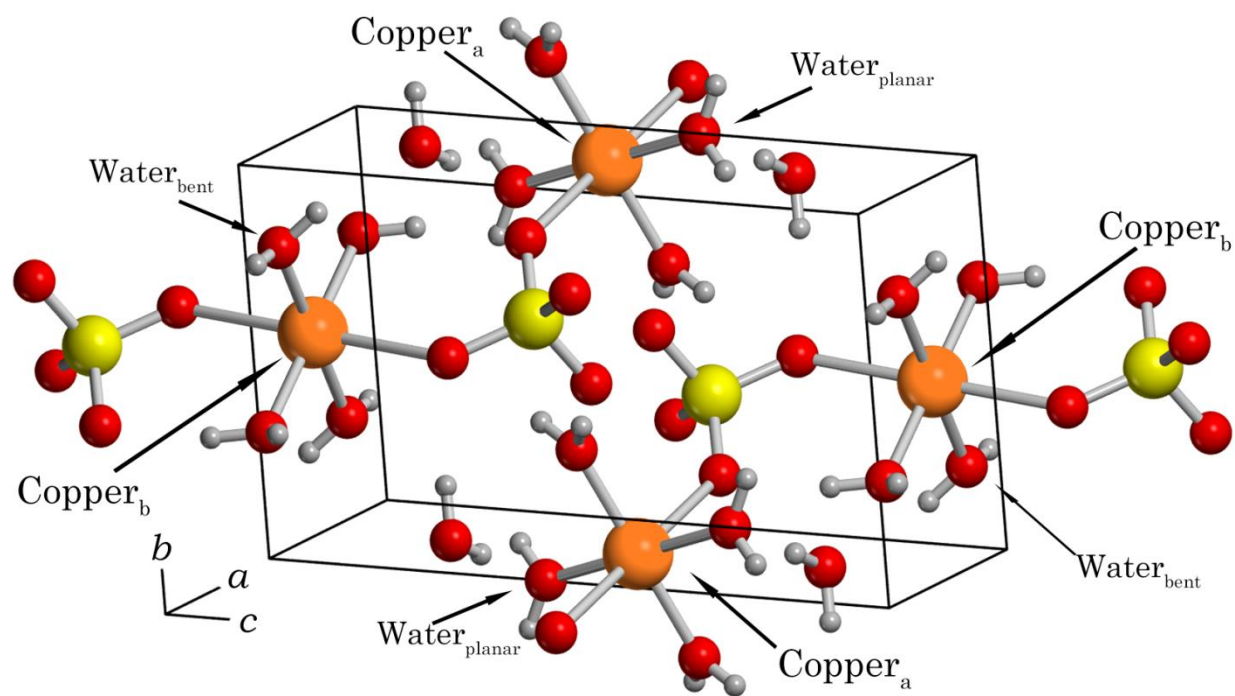
Figure 10-4. Fully optimized unit cell structure of CuSO$_4$·5H$_2$O, with the referenced atoms labeled.

10.3.2.2 Vibrational Simulations

The variability of the experimental terahertz spectra with increasing drying times adds complexity to the definitive assignment of the absorption features. Solid-state DFT calculations provide the tools necessary to arrive at this information, and help to elucidate the origins of the various absorptions in the $CuSO_4 \cdot 5H_2O$ terahertz spectra. The vibrational simulation shown in **Figure 10-5** is in good agreement with the experimental spectrum, and the prediction of multiple intense modes above 90 cm^{-1} provides an explanation for the sharply rising absorption beginning near 75 cm^{-1}. The calculated spectrum was convolved using Lorentzian line shapes, with the line width determined empirically from the experimental spectrum (FWHM = 3.3 cm^{-1}).

A full list describing the calculated normal modes and mode types is given in **Table 10-1**. All of the motions involve a significant amount of copper$_a$, copper$_b$, and water$_a$ motion, with a small subset also containing water$_b$ motion. The motion of individual water molecules inside of the crystal lattice showcases the utility of terahertz spectroscopy in probing particular non-bonded interactions, interactions that would typically be inaccessible using traditional spectroscopic techniques.
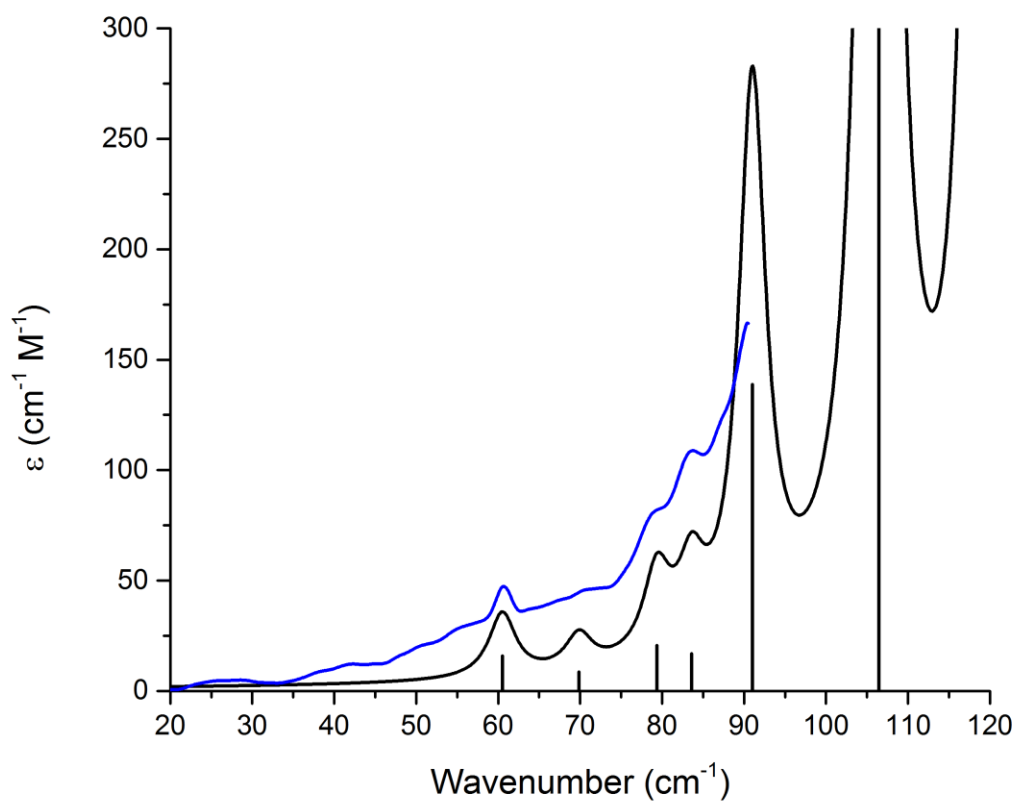
Figure 10-5. Twelve-hour dried terahertz spectrum of CuSO$_4$·5H$_2$O (blue) and solid-state simulated spectrum (black). The plot has been extended to 120 cm^{-1} to include the theoretically predicted modes outside of the experimental spectral bandwidth.

Table 10-1. Sub-120 cm^{-1} vibrational frequencies and mode types of crystalline

CuSO$_4$·5H$_2$O.

Calculated Frequency (cm^{-1})	Experimental Frequency (cm^{-1})	Mode type
60.5	60.9	Translation of copper cations with symmetric bending of each pair of water$_a$ (antisymmetric with respect to each other)
69.8	71.4	Translation of copper cations with symmetric bending of one pair of water$_a$ molecules
79.3	78.2	Translation of copper cations with water$_a$ umbrella motion and water$_{bent}$ scissor motion
83.5	83.5	Rotation of water$_{planar}$ and sulfate-oxygens about the remaining water$_a$-copper$_a$ axis
91.0	90.8	Antisymmetric translation of adjacent copper cations within the ribbon, with a copper$_a$-water$_a$ symmetric bend.
106.43	-	Antisymmetric translation of adjacent copper cations within the ribbon, with a copper$_b$-water$_{bent}$ symmetric bend.

The complete assignment of the spectral features in the terahertz frequency range for $CuSO_4 \cdot 5H_2O$ confirms that the additional features in the thirty-hour dried sample are due to the production of an additional compound. The PXRD result (**Figure 10-3**) clearly showed the existence of $CuSO_4 \cdot 3H_2O$, and that data was used to determine the relative concentrations of the two materials. This was accomplished by taking linear combinations of the PXRD patterns of the two hydrates (obtained using the experimental single-crystal XRD structures), and subsequently minimizing the observed-minus-calculated residual. Each individual PXRD pattern was multiplied by an intensity scaling coefficient and the absolute value of the residual was optimized as a function of the two coefficients. This method produced an accurate reproduction of the experimental PXRD pattern, with 24% of the sample found to be $CuSO_4 \cdot 3H_2O$, and the remainder being the pentahydrate. Conversion of this amount of $CuSO_4 \cdot 5H_2O$ to the trihydrate form corresponds to a mass loss of 3%, which is close to the measured value of 4% (mass loss between 12 and 30 hours).

Scaling the simulated mode intensities by the appropriate population values yielded a combined $CuSO_4 \cdot 5H_2O$ and $CuSO_4 \cdot 3H_2O$ terahertz spectrum (**Figure 10-6**) in good agreement with the experimental thirty-hour dried terahertz spectrum. Specifically, the two absorptions at 76.6 and 87.2 cm^{-1} that emerged after the prolonged drying period agree with the predicted $CuSO_4 \cdot 3H_2O$ vibrational simulation.[10] While weak compared to the very strong absorption of $CuSO_4 \cdot 5H_2O$, the inclusion of the $CuSO_4 \cdot 3H_2O$ simulation helps to explain the significant differences between the twelve-hour and thirty-hour spectra. The success of this binary fit helps highlight the use of terahertz spectroscopy as an analytical tool for the characterization of substances with mixed hydration states.
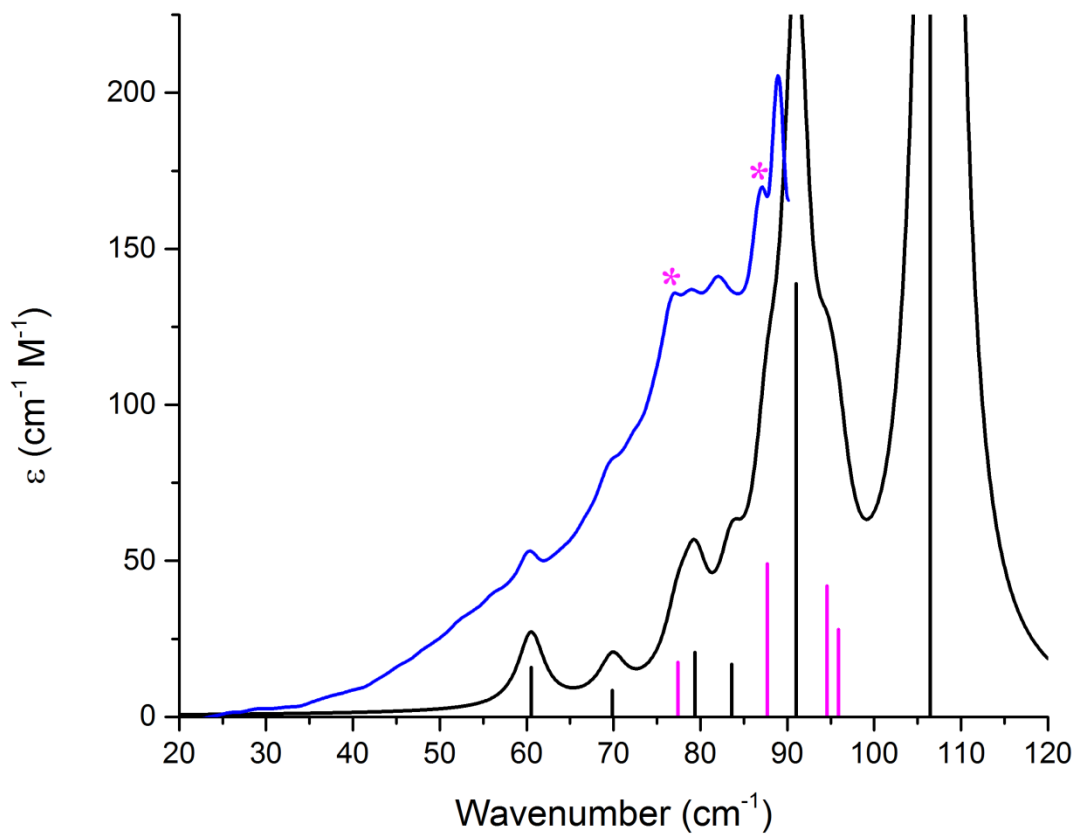
Figure 10-6. Thirty-hour dried terahertz spectrum of CuSO$_4$·5H$_2$O (blue) and simulated terahertz spectrum (purple) including contributions from both CuSO$_4$·5H$_2$O (black sticks) and CuSO$_4$·3H$_2$O (red sticks). Experimental trihydrate absorptions are marked with red asterisks (*). The line shape of the feature near 88.5 cm^{-1} is likely inaccurate since it occurs at the end of the instrument bandwidth.

10.4 Conclusions

The terahertz spectrum of pure crystalline copper(II) sulfate pentahydrate was obtained and the spectral features fully assigned using solid-state density functional theory calculations. Initially, the $CuSO_4 \cdot 5H_2O$ spectrum was obscured by a broad structureless absorption in the sub-100 cm^{-1} region. Through controlled drying and parallel powder X-ray diffraction measurements, the featureless absorption was unambiguously attributed to adsorbed water, and not to crystalline hydrates. The experimental terahertz spectra and diffraction data were supported by the observed mass losses in the dried material. It was found that dehydration of $CuSO_4 \cdot 5H_2O$ crystals must be done with great care, as the loss of cocrystallized water molecules is easily achieved by excessive drying times, resulting in the formation of the trihydrate species. The formation of $CuSO_4 \cdot 3H_2O$ was revealed by diffraction methods, and also resulted in the observation of new characteristic sharp absorption features in the terahertz spectrum of the sample. The results of this work demonstrate the sensitivity of terahertz spectroscopy to both cocrystallized and disordered water molecules, and emphasize its use as an analytical probe of hydration levels in hygroscopic materials.

10.5 Acknowledgements

10.6 References

1. Walsh, W.; Morberg, P.; Yu, Y.; Yang, J. L.; Haggard, W.; Sheath, P.; Svehla, M.; Bruce, W., Response of a Calcium Sulfate Bone Graft Substitute in a Confined Cancellous Defect. *Clin. Orthop. Relat. Res.* **2003**, *406*, 228-236.

2. Kelly, C. M.; Wilkins, R. M.; Gitelis, S.; Hartjen, C.; Watson, J. T.; Kim, P. T., The Use of a Surgical Grade Calcium Sulfate as a Bone Graft Substitute: Results of a Multicenter Trial. *Clin. Orthop. Relat. Res.* **2001**, *382*, 42-50.

3. Broughton, G., Calcium Sulfate Plasters. *Industrial & Engineering Chemistry* **1939**, *31*, 1002-1006.

4. Kolar, J.; Štolfa, A.; Strlič, M.; Pompe, M.; Pihlar, B.; Budnar, M.; Simčič, J.; Reissland, B., Historical Iron Gall Ink Containing Documents — Properties Affecting Their Condition. *Anal. Chim. Acta* **2006**, *555*, 167-174.

5. Salam, D.; El-Fadel, M., Mobility and Availability of Copper in Agricultural Soils Irrigated from Water Treated with Copper Sulfate Algaecide. *Water, Air, Soil Pollut.* **2008**, *195*, 3-13.

6. Konsta-Gdoutos, M. S.; Shah, S. P., Hydration and Properties of Novel Blended Cements Based on Cement Kiln Dust and Blast Furnace Slag. *Cem. Concr. Res.* **2003**, *33*, 1269-1276.

7. Zhao, L.-J.; Zhang, Y.-H.; Wei, Z.-F.; Cheng, H.; Li, X.-H., Magnesium Sulfate Aerosols Studied by Ftir Spectroscopy: Hygroscopic Properties, Supersaturated Structures, and Implications for Seawater Aerosols. *J. Phys. Chem. A* **2006**, *110*, 951-958.

8. Wang, A.; Freeman, J. J.; Jolliff, B. L.; Chou, I.-M., Sulfates on Mars: A Systematic Raman Spectroscopic Study of Hydration States of Magnesium Sulfates. *Geochim. Cosmochim. Acta* **2006**, *70*, 6118-6135.

9. Ting, V. P.; Henry, P. F.; Schmidtmann, M.; Wilson, C. C.; Weller, M. T., In Situ Neutron Powder Diffraction and Structure Determination in Controlled Humidities. *Chem. Commun.* **2009**, 7527-7529.

10. Ruggiero, M. T.; Bardon, T.; Strlič, M.; Taday, P. F.; Korter, T. M., Assignment of the Terahertz Spectra of Crystalline Copper Sulfate and Its Hydrates Via Solid-State Density Functional Theory. *J. Phys. Chem. A* **2014**, *118*, 10101-10108.

11. Singh, R. S.; Tewari, P.; Bourges, J. L.; Hubschman, J. P.; Bennett, D. B.; Taylor, Z. D.; Lee, H.; Brown, E. R.; Grundfest, W. S.; Culjat, M. O. In *Terahertz Sensing of Corneal Hydration*, Engineering in Medicine and Biology Society (EMBC), 2010 Annual International Conference of the IEEE, Aug. 31 2010-Sept. 4 2010; 2010; pp 3021-3024.

12. Suen, J. Y.; Tewari, P.; Taylor, Z. D.; Grundfest, W. S.; Lee, H.; Brown, E. R.; Culjat, M. O.; Singh, R. S., Towards Medical Terahertz Sensing of Skin Hydration. *Stud. Health Technol. Inform* **2009**, *142*, 364-368.

13. Balakrishnan, J.; Fischer, B. M.; Abbott, D., Sensing the Hygroscopicity of Polymer and Copolymer Materials Using Terahertz Time-Domain Spectroscopy. *Appl. Opt.* **2009**, *48*, 2262-2266.

14. Heyden, M.; Ebbinghaus, S.; Havenith, M., Terahertz Spectroscopy as a Tool to Study Hydration Dynamics. In *Encyclopedia of Analytical Chemistry*, John Wiley & Sons, Ltd: 2006.

15.   Ruggiero, M. T.; Bardon, T.; Strlic, M.; Taday, P. F.; Korter, T. M., The Role of Terahertz Polariton Absorption in the Characterization of Crystalline Iron Sulfate Hydrates. *Phys. Chem. Chem. Phys.* **2015**, *17*, 9326-9334.

16.   Kawase, K.; Ogawa, Y.; Watanabe, Y.; Inoue, H., Non-Destructive Terahertz Imaging of Illicit Drugs Using Spectral Fingerprints. *Opt. Express* **2003**, *11*, 2549-2554.

17.   Ho, L.; Pepper, M.; Taday, P., Terahertz Spectroscopy: Signatures and Fingerprints. *Nature Photon.* **2008**, *2*, 541-543.

18.   Fu, X.; Yang, G.; Sun, J.; Zhou, J., Vibrational Spectra of Copper Sulfate Hydrates Investigated with Low-Temperature Raman Spectroscopy and Terahertz Time Domain Spectroscopy. *J. Phys. Chem. A* **2012**, *116*, 7314-7318.

19.   Richardson, H. W., *Handbook of Copper Compounds and Applications*; CRC Press, 1997.

20.   Chen, J.; Chen, Y.; Zhao, H.; Bastiaans, G. J.; Zhang, X.-C., Absorption Coefficients of Selected Explosives and Related Compounds in the Range of 0.1-2.8 Thz. *Opt. Express* **2007**, *15*, 12060-12067.

21.   Strachan, C. J.; Taday, P. F.; Newnham, D. A.; Gordon, K. C.; Zeitler, J. A.; Pepper, M.; Rades, T., Using Terahertz Pulsed Spectroscopy to Quantify Pharmaceutical Polymorphism and Crystallinity. *J. Pharm. Sci.* **2005**, *94*, 837-846.

22.   Zeitler, J. A.; Newnham, D. A.; Taday, P. F.; Threlfall, T. L.; Lancaster, R. W.; Berg, R. W.; Strachan, C. J.; Pepper, M.; Gordon, K. C.; Rades, T., Characterization of Temperature-Induced Phase Transitions in Five Polymorphic Forms of Sulfathiazole by Terahertz Pulsed Spectroscopy and Differential Scanning Calorimetry. *J. Pharm. Sci.* **2006**, *95*, 2486-2498.

23. King, M. D.; Buchanan, W. D.; Korter, T. M., Identification and Quantification of Polymorphism in the Pharmaceutical Compound Diclofenac Acid by Terahertz Spectroscopy and Solid-State Density Functional Theory. *Anal. Chem.* **2011**, *83*, 3786-3792.

24. Zeitler, J. A.; Taday, P. F.; Newnham, D. A.; Pepper, M.; Gordon, K. C.; Rades, T., Terahertz Pulsed Spectroscopy and Imaging in the Pharmaceutical Setting-a Review. *J. Pharm. Pharmacol.* **2007**, *59*, 209-223.

25. Day, G. M.; Zeitler, J.; Jones, W.; Rades, T.; Taday, P., Understanding the Influence of Polymorphism on Phonon Spectra: Lattice Dynamics Calculations and Terahertz Spectroscopy of Carbamazepine. *J. Phys. Chem. B* **2006**, *110*, 447-456.

26. Ruggiero, M. T.; Erba, A.; Orlando, R.; Korter, T. M., Origins of Contrasting Copper Coordination Geometries in Crystalline Copper Sulfate Pentahydrate. *Phys. Chem. Chem. Phys.* **2015**, *17*, 31023-31029.

27. Macrae, C. F.; Bruno, I. J.; Chisholm, J. A.; Edgington, P. R.; McCabe, P.; Pidcock, E.; Rodriguez-Monge, L.; Taylor, R.; van de Streek, J.; Wood, P. A., Mercury Csd 2.0 - New Features for the Visualization and Investigation of Crystal Structures. *J. Appl. Crystallogr.* **2008**, *41*, 466-470.

28. Hakey, P. M.; Allis, D. G.; Ouellette, W.; Korter, T. M., Cryogenic Terahertz Spectrum of (+)-Methamphetamine Hydrochloride and Assignment Using Solid-State Density Functional Theory. *J. Phys. Chem. A* **2009**, *113*, 5119-5127.

29. Rice, A.; Jin, Y.; Ma, X. F.; Zhang, X. C.; Bliss, D.; Larkin, J.; Alexander, M., Terahertz Optical Rectification from 〈110〉 Zinc-Blende Crystals. *Appl. Phys. Lett.* **1994**, *64*, 1324-1326.

30. Zhang, X. C.; Ma, X. F.; Jin, Y.; Lu, T. M.; Boden, E. P.; Phelps, P. D.; Stewart, K. R.; Yakymyshyn, C. P., Terahertz Optical Rectification from a Nonlinear Organic Crystal. *Appl. Phys. Lett.* **1992**, *61*, 3080-3082.

31. Wu, Q.; Litz, M.; Zhang, X. C., Broadband Detection Capability of Znte Electro-Optic Field Detectors. *Appl. Phys. Lett.* **1995**, 2924.

32. Dovesi, R.; Orlando, R.; Erba, A.; Zicovich-Wilson, C. M.; Civalleri, B.; Casassa, S.; Maschio, L.; Ferrabone, M.; De La Pierre, M.; D'Arco, P.*, et al.*, CRYSTAL14: A Program for the *ab initio* Investigation of Crystalline Solids. *Int. J. Quantum Chem* **2014**, *114*, 1287-1317.

33. Becke, A. D., Density-Functional Thermochemistry. III. The Role of Exact Exchange. *J. Chem. Phys.* **1993**, *98*, 5648-5652.

34. Krishnan, R.; Binkley, J. S.; Seeger, R.; Pople, J. A., Self-Consistent Molecular Orbital Methods. XX. A Basis Set for Correlated Wave Functions. *J. Chem. Phys.* **1980**, *72*, 650-654.

35. Pascale, F.; Zicovich-Wilson, C. M.; López Gejo, F.; Civalleri, B.; Orlando, R.; Dovesi, R., The Calculation of the Vibrational Frequencies of Crystalline Compounds and Its Implementation in the Crystal Code. *J. Comput. Chem.* **2004**, *25*, 888-897.

36. Zicovich-Wilson, C. M.; Pascale, F.; Roetti, C.; Saunders, V. R.; Orlando, R.; Dovesi, R., Calculation of the Vibration Frequencies of A-Quartz: The Effect of Hamiltonian and Basis Set. *J. Comput. Chem.* **2004**, *25*, 1873-1881.

37. Noel, Y.; Zicovich-Wilson, C. M.; Civalleri, B.; D'Arco, P.; Dovesi, R., Polarization Properties of Zno and Beo: An *ab initio* Study through the Berry Phase and Wannier Functions Approaches. *Phys. Rev. B.* **2001**, *65*, 014111.

38.   Dover, M. V.; Marden, J. W., A Comparison of the Efficiency of Some Common Desiccants. *J. Am. Chem. Soc.* **1917**, *39*, 1609-1614.

39.   Trusell, F.; Diehl, H., Efficiency of Chemical Desiccants. *Anal. Chem.* **1963**, *35*, 674-677.

40.   Burfield, D. R.; Smithers, R. H., Desiccant Efficiency in Solvent Drying. 3. Dipolar Aprotic Solvents. *J. Org. Chem.* **1978**, *43*, 3966-3968.

CHAPTER 11: Origins of Contrasting Copper Coordination Geometries in Crystalline Copper Sulfate Pentahydrate

The material contained within this chapter is published in *Physical Chemistry Chemical Physics* (Ruggiero, M.T.; Erba, A.; Orlando, R.; Korter, T.M. *Phys. Chem. Chem. Phys.* **2015**. 17(46) 31023-31029) This article has been reproduced by permission of the PCCP Owner Societies.
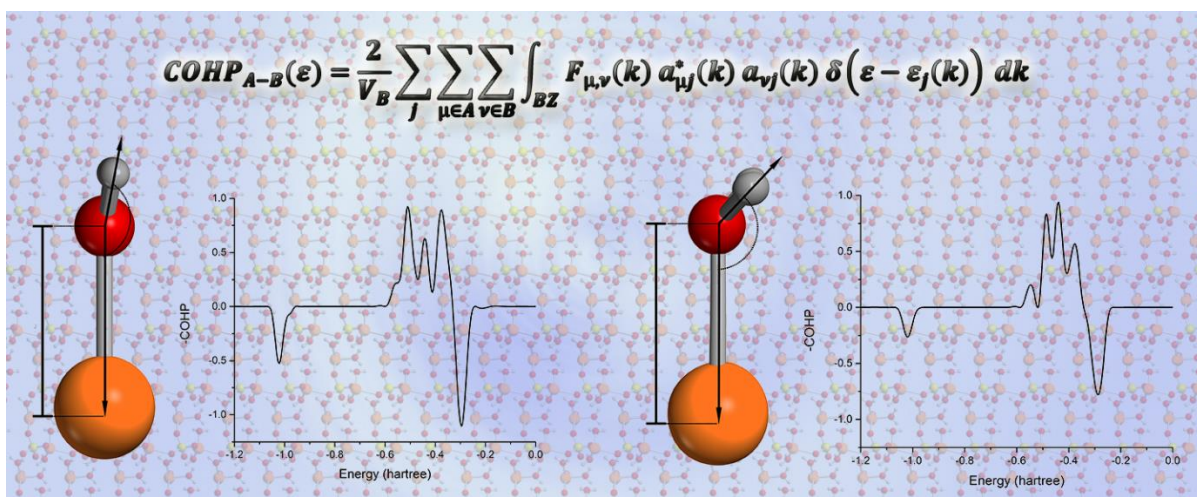
Abstract

Metal-aqua ion ($[M(H_2O)_n]^{X+}$) formation is a fundamental step in mechanisms that are central to enzymatic and industrial catalysis. Past investigations of such ions have yielded a wealth of information regarding their properties, however questions still exist involving the exact structures of these complexes. A prominent example of this is hexaaqua copper (II) ($[Cu(H_2O)_6]^{2+}$), with the solution versus gas-phase configurations under debate. The differences are often attributed to the intermolecular interactions between the bulk solvent and the aquated complex, resulting in structures stabilized by extended hydrogen-bonding networks. Yet solution phase systems are difficult to study due to the lack of atomic-level positional details. Crystalline solids are ideal models for comparative study, as they contain fixed structures that can be fully characterized using diffraction techniques. Here, crystalline copper sulfate pentahydrate ($CuSO_4 \cdot 5H_2O$), which contains two unique copper-water geometries, was studied in order to elucidate the origin of these contrasting hydrated metal environments. A combination of solid-state density functional theory and low-temperature X-ray diffraction was used to probe the electronic origins of this phenomenon. This was accomplished through implementation of crystal orbital overlap population and crystal orbital Hamiltonian population analyses into a developmental version of the CRYSTAL14 software. These new computational methods help highlight the delicate interplay between electronic structure and metal-water geometries.

11.1 Introduction

Metal-water interactions are key aspects of numerous chemical processes, especially those occurring throughout biology.[1-4] Despite their importance, description of metal-water coordination bonds beyond the traditional 'point-charge' model are not widely utilized, presumably due to the difficulty in studying such species.[5-7] This challenge is exemplified by the metal-water complexes that commonly form in aqueous solutions,[8-9] where discrepancies appear in the literature (both experimental and theoretical) concerning their characteristics.[10-13] One such species is hexaaqua-copper(II), whose solvent phase structure has been a subject of controversy, specifically regarding the orientation of the coordinated water molecules.[7, 9, 14-17] While not a direct probe of the solvated aqueous copper (II) cation, X-ray diffraction (XRD) studies of crystallized copper(II) hydrates can provide useful geometry information regarding the local environment around the metal cations with atomic precision. Investigation of crystalline solid-state samples enables rigorous study of both geometry and underlying electronic structure, leading to deeper understanding of their relationship.[18-21] In this study, copper sulfate pentahydrate ($CuSO_4 \cdot 5H_2O$) crystals were investigated using a combination of XRD and solid-state density functional theory (DFT) in order to accurately assess the synergistic roles that electronic structure and crystalline packing have on copper-water interactions.

In most crystalline solids, the individual molecules or formula units have the same internal geometries.[22-23] In some cases, two or more molecular configurations can exist concomitantly, presenting an opportunity to investigate how various packing interactions may lead to multiple unique structures within a single crystal.[24-25] Copper sulfate pentahydrate ($CuSO_4 \cdot 5H_2O$) is one such crystal, where two distinct copper cation coordination geometries

exist within the same solid.[26-29] The coordination of one copper cation is almost identical to the solution-phase structure, while the other is markedly different.[7, 14-16, 30] This has led to a detailed investigation of the copper-water interaction in the solid state, ultimately helping to clarify the origins of the dissimilar metal-water coordination configurations.

While evaluation of quantum mechanical phenomena, such as chemical bond strengths and electron occupations, may be possible using experimental techniques, the roots of these properties (*i.e.* molecular orbital structure) are difficult to examine experimentally.[31-34] Yet these aspects are of critical importance in determining the various physical properties of a material, such as molecular structure, electronic absorption and emission profiles, and catalytic potential.[35-39] Solid-state DFT has proven to be a powerful tool for the study of crystals containing transition metals, and enables direct investigation of these fundamental interactions.[40-41] The utilization of periodic boundary conditions in solid-state DFT permits the simulation of observable properties with greater accuracy as compared to isolated cluster calculations (when using the same level of theory), allowing for even subtle bulk effects to be captured.[42-43]

Typical vibrational or electronic density of states (DOS) calculations provide valuable insight into the electronic structure of solids, but they often lack the ability to characterize a specific bond within a material.[33, 44-45] In order to accomplish this, the atomic orbitals of interest can be projected onto the entire molecular or crystalline orbital, thus yielding insight into the contribution that a particular fragment has to the overall electronic structure.[46-47] However even this analysis is incomplete, as it does not take into account factors other than the extent of orbital occupation. Thus the crystal orbital overlap population (COOP) method was developed by Hoffman and Hughbanks to characterize single interactions in solids.[48] The COOP analysis is an analogue to DOS calculations, yet unlike the DOS scheme, the COOP method only considers

315

two discrete groups of atomic orbitals. This provides qualitative information regarding the specific bonding and antibonding components of a chemical bond, discerning the nature of specific electronic interactions. An extension of the COOP method is the crystal orbital Hamiltonian population (COHP), which partitions the band energies, rather than electron states, into bonding and antibonding regions.[17, 40, 49] Here, the COOP and COHP schemes were implemented into a development version of CRYSTAL14[42], marking the first time these methods have been included in a localized orbital software package

11.2 Methods

11.2.1 Experimental

Copper sulfate pentahydrate was prepared by dissolving anhydrous copper sulfate (Sigma-Aldrich, ≥ 99.99%) in deionized water and allowing the blue solution to evaporate under ambient conditions. After approximately one week, large blue crystals formed and single-crystal XRD measurements were taken to confirm them as being $CuSO_4 \cdot 5H_2O$. Low-temperature (90 K) single-crystal XRD measurements were done on a Bruker KAPPA APEX DUO diffractometer containing an APEX II CCD system using monochromatic Mo Kα radiation ($\lambda = 0.71076$ Å). The structures were solved using direct methods and refinements were performed with the SHELXTL software.[50] Upon identification of the heavy-atom positions, the structure was first refined using isotropic displacement parameters, followed with anisotropic parameters. The proton positions were assigned through the observed electron densities, and consequently refined isotropically.

11.2.2 Theoretical

A development version of the CRYSTAL14 software package was used to perform the solid-state DFT calculations. The same computational methodology previously developed for metal sulfate hydrates was adopted here[51-52], which makes use of the Becke-3-Lee-Yang-Parr (B3LYP)[53] density functional and the atom-centered 6-31G(d)/6-31G(2d,2p) basis set[54] for copper/non-metals. Geometry optimization was initiated with atomic coordinates taken from the

317

experimental crystallographic data. The entire solid-state structure, including atomic positions and lattice parameters, was allowed to relax with the only constraint being the space group symmetry of the solid. Solid-state COOP and COHP plots were calculated using CRYSTAL14. A finer k-point grid of 868 points was used for the COOP and COHP calculations (112 for optimizations). The energy convergence criteria were set to $\Delta E < 10^{-8}$ and 10^{-10} hartree for the optimization and one-electron calculations, respectively. Gas-phase COOP diagrams were created using Gaussian09[55] and the GaussSum[56] software packages.

11.3 Results and Discussion

11.3.1 Theoretical Background

The calculation of COOP and COHP diagrams in CRYSTAL14 was implemented for this study as an extension of the one-electron properties already included in this software.[57] Using localized basis sets is a common technique for gas and solvent phase calculations, but to replicate the band structure present in real solids, CRYSTAL14 uses symmetry and Bloch transformations to create periodic conditions. The overall schemes for these calculations are provided in various different sources, and a brief overview is provided here for completeness.[17, 49, 58-59]

The initial step in any calculation involving CRYSTAL14 is the building of the crystalline wavefunctions. First, the local atom-centered orbitals ($\varphi_\mu(r)$, with the angular part omitted for simplicity) are defined by the linear combination of Gaussian-type basis functions ($G(\alpha_i, r)$),

$$\varphi_\mu(r) = \sum_i d_i G(\alpha_i, r)$$
(11.1)

Where r represent the real space coordinates, d_i are the normalization coefficients, and α_i are the Gaussian exponents (both d_i and α_i are supplied in the input). The local atom-centered orbitals are then transformed into periodic Bloch functions ($\Phi_\mu(r; k)$) through multiplication by the phase factor $e^{ik\cdot\vec{g}}$,

$$\Phi_\mu(r; k) = \sum_g \varphi_\mu(r - g) e^{ik\cdot\vec{g}}$$
(11.2)

Where k is the reciprocal space coordinates and g are the set of all lattice vectors. The self-consistent field (SCF) scheme is then employed to minimize the total electronic energy in the matrix relation,

$$\mathbf{F}(k)\mathbf{A}(k) = \mathbf{S}(k)\mathbf{A}(k)\mathbf{E}(k) \tag{11.3}$$

Where $\mathbf{F}(k)$, $\mathbf{A}(k)$, $\mathbf{S}(k)$, and $\mathbf{E}(k)$ are the Fock, Bloch coefficient, overlap, and energy matricies, respectively. The Bloch coefficients $(a_{\mu,j})$ are then used to define the crystalline wavefunctions $(\Psi_j(r;k))$, with j indicating the crystalline orbital index.

$$\Psi_j(r;k) = \sum_{\mu} a_{\mu,j}(k)\Phi_\mu(r;k) \tag{11.4}$$

The crystalline orbitals (bands) are therefore evaluated at each k-point in reciprocal space, with the total k-point grid defined by the user at the onset of the calculation. The band structure for a particular crystal is then simply evaluated through interpolation of the eigenvalues of each band at different k-points. From this, the orbital (ρ_μ), atomic (ρ_A), and total DOS (ρ_{tot}) can be evaluated using the following relations:

$$\rho_\mu(\varepsilon) = \frac{2}{V_B}\sum_{j}\sum_{v}\int_{BZ} S_{\mu,v}(k)\, a_{\mu j}^*(k)\, a_{vj}(k)\ \delta\left(\varepsilon - \varepsilon_j(k)\right)\, dk \tag{11.5}$$

$$\rho_A(\varepsilon) = \sum_{\mu \in A} \rho_\mu(\varepsilon) \tag{11.6}$$

$$\boldsymbol{\rho_{tot}}(\boldsymbol{\varepsilon}) = \sum_{A} \boldsymbol{\rho_A}(\boldsymbol{\varepsilon}) \tag{11.7}$$

Where $\boldsymbol{V_B}$ is the volume of the first Brillouin zone, and $\boldsymbol{\varepsilon}$ is the energy. It is shown that the orbital DOS is simply the projection of a single atomic orbital onto the entire crystalline orbital, and thus is a measure of orbital contribution over a specified energy range. It is important to note that the diagonal elements of the overlap matrix $\boldsymbol{S}_{\mu,\mu}$ are included in the DOS calculation, which results in all values being ≥ 0. While the DOS calculation yields valuable data involving the contribution of an orbital or atom to the total electronic structure of the solid, it does not provide any information regarding the nature of the bond between two related orbitals, *i.e.* bond populations or the type of interaction (bonding or antibonding). This information can be obtained using the COOP and COHP methods, which are modifications of the DOS scheme.

$$\boldsymbol{COOP_{A-B}}(\boldsymbol{\varepsilon}) = \frac{2}{V_B} \sum_{j} \sum_{\mu \in A} \sum_{v \in B} \int_{BZ} \boldsymbol{S}_{\mu,v}(\boldsymbol{k}) \, \boldsymbol{a}^*_{\mu j}(\boldsymbol{k}) \, \boldsymbol{a}_{vj}(\boldsymbol{k}) \, \boldsymbol{\delta}\left(\boldsymbol{\varepsilon} - \boldsymbol{\varepsilon}_j(\boldsymbol{k})\right) \, \boldsymbol{dk} \tag{11.8}$$

$$\boldsymbol{COHP_{A-B}}(\boldsymbol{\varepsilon}) = \frac{2}{V_B} \sum_{j} \sum_{\mu \in A} \sum_{v \in B} \int_{BZ} \boldsymbol{F}_{\mu,v}(\boldsymbol{k}) \, \boldsymbol{a}^*_{\mu j}(\boldsymbol{k}) \, \boldsymbol{a}_{vj}(\boldsymbol{k}) \, \boldsymbol{\delta}\left(\boldsymbol{\varepsilon} - \boldsymbol{\varepsilon}_j(\boldsymbol{k})\right) \, \boldsymbol{dk} \tag{11.9}$$

Here, instead of projecting a single orbital onto all of the orbitals (as in the DOS equation), the orbitals of interest are only projected onto a subset of the crystalline orbitals belonging to groups *A* and *B* (diagonal elements are not considered), representing the chosen two fragments. In the COOP analysis, the density of states between the two fragments is weighted by the overlap matrix, partitioning the electronic states into bonding and antibonding regions. The COHP

321

equation is similar, but instead of electron states, the band structure is what is being partitioned, providing information regarding the bond energy (rather than bond order, as in the COOP case).

11.3.2 Structural Analysis

The structure of $CuSO_4 \cdot 5H_2O$ was redetermined at 90 K using single-crystal XRD (R=0.042), and the geometry described here is in agreement with previously reported structures.[26-29] The $CuSO_4 \cdot 5H_2O$ crystals form in the triclinic $P\overline{1}$ space group, and have lattice dimensions of: $a = 6.106$ Å, $b = 10.656$ Å, $c = 5.969$ Å, $\alpha = 77.332°$, $\beta = 82.433°$, $\gamma = 72.523°$, and V=360.548 Å^3. Four $CuSO_4 \cdot 5H_2O$ formula units make up the unit cell (Z=4) (**Figure 11-1**), with two formula unit halves in the asymmetric unit $[Cu(H_2O)_2SO_4Cu(H_2O)_2(H_2O)]$. Both symmetrically unique copper cations are in a distorted octahedral coordination environment. Each copper cation is coordinated by four equatorial water molecules (two symmetrically unique water molecules on each), and are bridged by sulfate anions bonded at the axial positions, forming infinite polymeric chains. The d^9 coppers display the characteristic Jahn-Teller distorted geometry, with the copper-sulfate axial bond elongated with respect to the four equatorial copper-water bonds.[60] The fifth co-crystallized water molecule forms two hydrogen bonds with the bridging oxygen atoms of the adjacent chains, and does not directly interact with the metal cations. The solid-state geometry optimization accurately represented the aforementioned structural features, with average errors in the bond lengths and unit cell parameters of 0.69% and 0.45%, respectively.
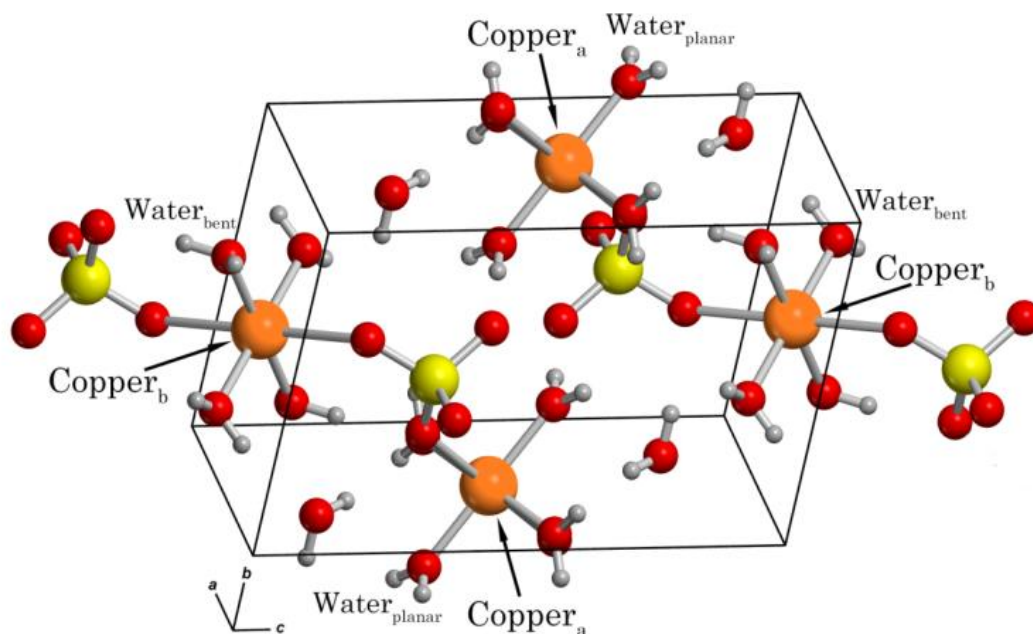
Figure 11-1. Experimental 90 K single-crystal X-ray diffraction structure of CuSO$_4$·5H$_2$O. The features of interest have been labeled for clarity.
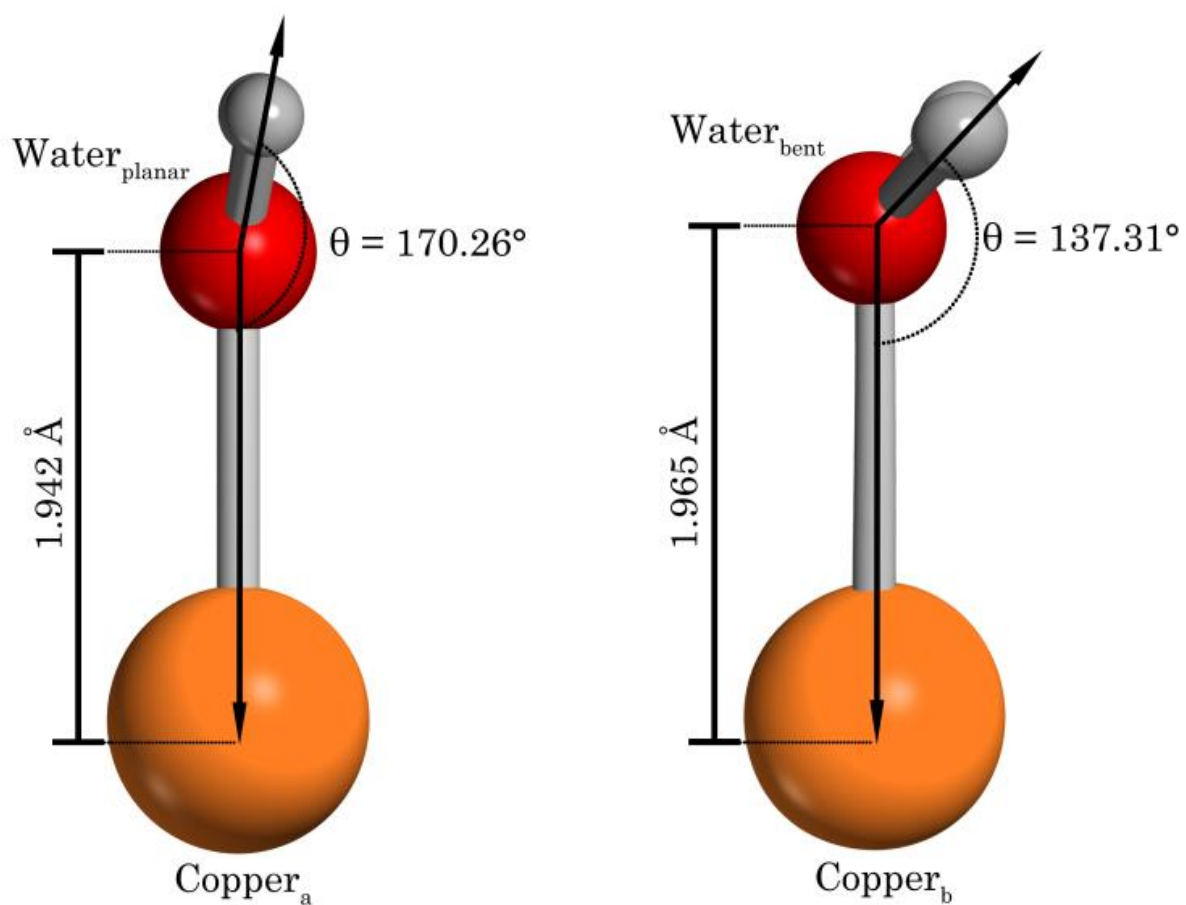
Figure 11-2. The two symmetrically unique copper cations, showing the different geometric arrangements of the coordinated water molecules.

The water molecules coordinated to the two symmetrically unique copper cations (copper$_a$ and copper$_b$, **Figures 11-1** and **11-2**) exist in two very different orientations. In the case of copper$_a$, the orientation of the coordinated water molecules results in the water hydrogens being nearly in the plane of the copper$_a$-water bond (water$_{planar}$). In contrast, the waters are tilted on copper$_b$, resulting in a bent geometry (water$_{bent}$). The copper-water bond lengths are also significantly different between the two symmetry unique metals, with an average experimental copper-water bond length of 1.942 Å and 1.965 Å for the copper$_a$-water$_{planar}$ and copper$_b$-water$_{bent}$ bonds, respectively. Both coordination types have water molecules maintaining two hydrogen bonds, with water$_{planar}$ hydrogen-bonded to the non-coordinated sulfate oxygen atoms and water$_{bent}$ hydrogen-bonded to the co-crystallized water and the coordinated sulfate oxygen atom. It is important to note that each copper cation has two symmetrically unique water molecules (four in total), and the tilting angle is consistent between the respective pairs.

11.3.3 Orbital Analysis

The existence of two types of copper-water geometries in the $CuSO_4 \cdot 5H_2O$ crystal is a phenomenon whose origins can be broadly explained by the solid-state packing arrangement that promotes different hydrogen bonding interactions for the different waters. However, the electronic interactions between the copper and coordinated waters must play a central role in governing the absolute orientations of the molecules in the structure. In fact, a gas-phase geometry optimization of an isolated $CuSO_4 \cdot 5H_2O$ results in a totally planar arrangement of the coordinated water molecules (in agreement with some previous gas and solution-phase studies[7, 14, 16, 30]), demonstrating that the crystalline environment causes the observed tilting of the waters.

Any structural deviations from the isolated-molecule calculation can be viewed as a strain, which results in a weakened copper-water$_{bent}$ bond, but this strain penalty must be offset by favorable cohesive interactions of the bulk solid for crystallization to occur.

The projected density of states for the copper-water interactions (**Figure 11-3**) revealed that the copper$_a$–water$_{planar}$ fragment contains a higher degree of occupied electronic states (increased electron density), compared to the corresponding copper$_b$-water$_{bent}$ pair, as determined by integration of the DOS (yielding the total states over the occupied energy range) (**Table 11-1**). While the DOS is acceptable for an overall picture of the electronic contribution of the atoms of interest to the overall crystalline bonds, it does not provide any fragment specific information regarding the type of interaction each occupied orbital is involved in exclusively within the chosen fragment. Greater detail into the nature of the copper-water chemical bonds is available by calculation of COOP and COHP diagrams. These analyses can be used to see the effect that changing coordination schemes have on the character of individual bonds and yield a complete description of the specific electronic interactions between the $CuSO_4 \cdot 5H_2O$ components.
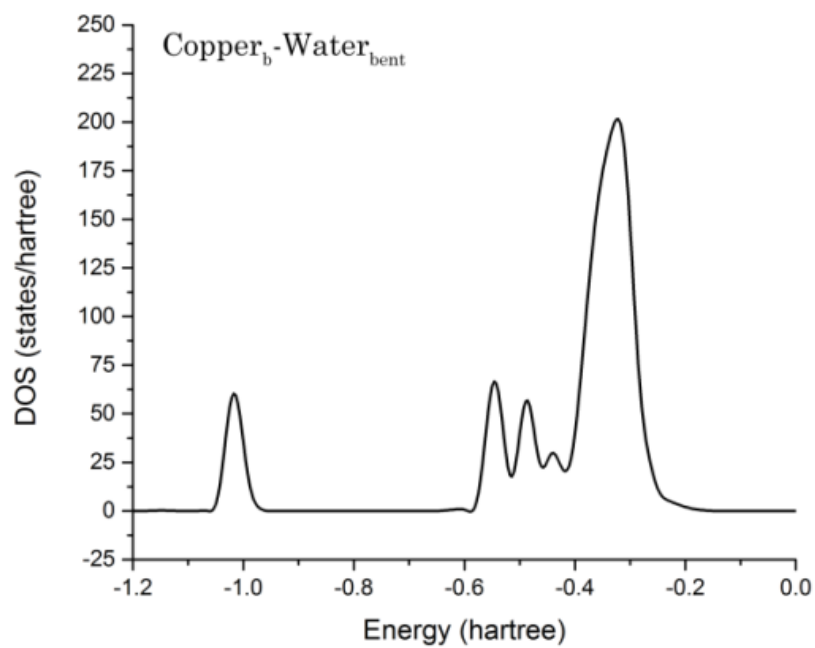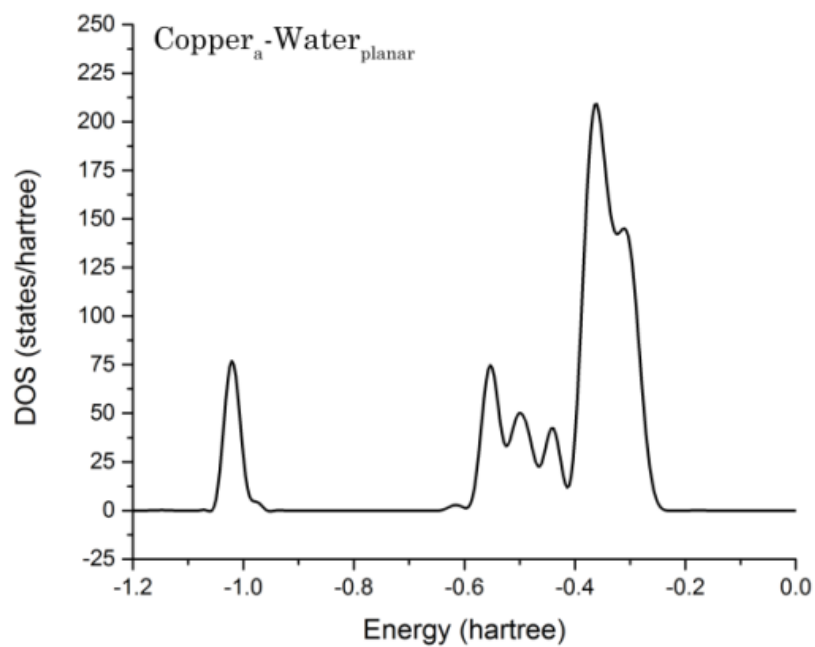
Figure 11-3. Electronic density of states (DOS) for the two copper-water fragment types in CuSO$_4$·5H$_2$O

To explore the role of crystalline environment on the $CuSO_4 \cdot 5H_2O$ structure, COOP diagrams were produced both in the gas phase (formula unit extracted from the optimized solid) and in the solid state using Gaussian09/GaussSum and CRYSTAL14, respectively, and are shown in **Figure 11-4**. In the case of the copper$_a$-water$_{planar}$ interaction, the solid-state and gas-phase COOP diagrams are in close agreement, especially in predicting the Fermi level of that particular bond. However in the case of the copper$_b$-water$_{bent}$ interaction, the two calculation methods differ noticeably, predominately in the prediction of the Fermi level and orbital energies. This result is not surprising when the solid-state copper-water coordination environments are taken into account, where the contrasting copper$_b$-water$_{bent}$ COOP calculations can be linked to water tilt angle. The fully relaxed gas-phase optimization of $CuSO_4 \cdot 5H_2O$ results in a planar orientation of the coordinated water-copper bond, implying limited strain exists in the packed copper$_a$-water$_{planar}$ arrangement, and ultimately meaning the gas-phase and solid-state COOP calculations should be in reasonable agreement. In the case of copper$_b$, the packing strain, which is presumably caused by the propensity of the structure to form hydrogen bonds, cannot be represented by a simple gas-phase calculation. Therefore the gas-phase model fails to accurately predict the electronic configuration of this purely solid-state geometry, leading to an inaccurate prediction of the Fermi level and slightly shifted orbital energies (compared to the solid-state calculated band energies).
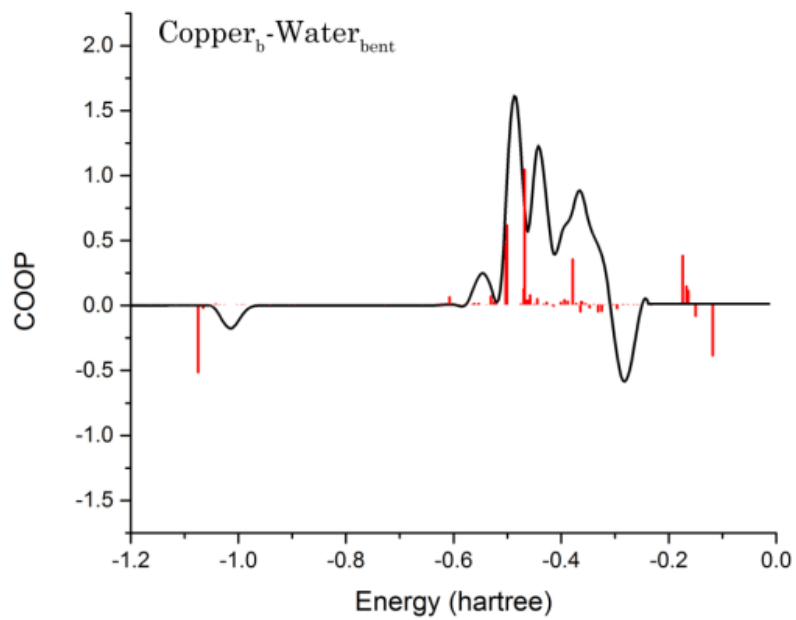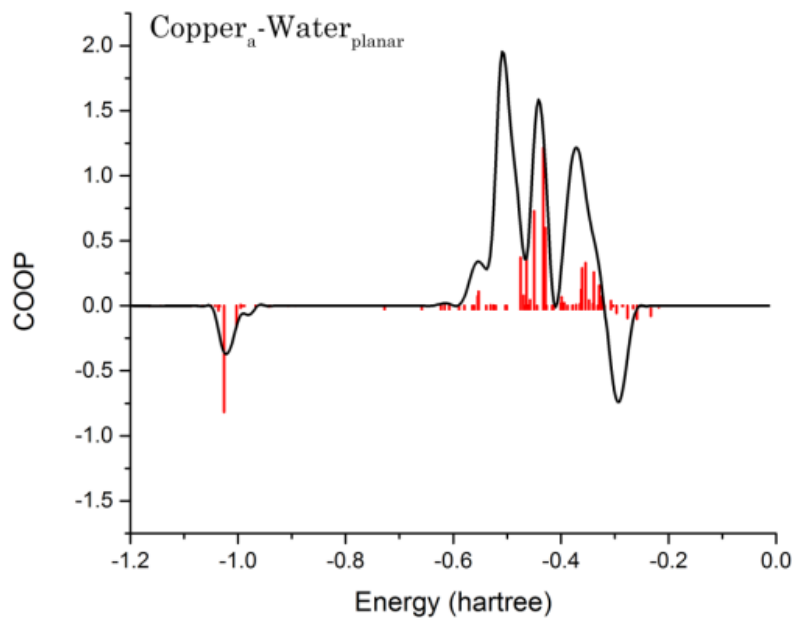
Figure 11-4. Solid (black) and gas-phase (red) COOP diagrams for the respective copper-water fragments in CuSO₄·5H₂O.

By integrating the positive and negative regions of the COOP plot, representing total bonding and antibonding populations, detail regarding the electronic arrangement of the two copper-water fragments can be obtained (**Table 11-1**). The total integrated COOP curve is an effective measure of bond order, and it is shown that the value obtained for the copper$_a$-water$_{planar}$ bond is higher than that of copper$_b$-water$_{bent}$. This phenomenon has been previously noted for other transition metal complexes, which showed that planar arrangements of water molecules around the metal cations promotes a stronger overlap.[7, 61] The overlap is decreased upon tilting of the water molecules, leading to a lower bond order. This effect is manifested in the copper-water bond lengths, where the copper$_a$-water$_{planar}$ bond is shorter than the corresponding copper$_b$-water$_{bent}$ bond.

Integration of the COHP diagram is a measure of bond strength (in units of energy), because this method partitions the *band energies* rather than the *electrons* (COOP). The COHP plots (**Figure 11-5**) are very similar to the COOP plots, and the same trend is observed when integrating the COOP diagram as when integrating the COHP plot. The calculated copper-water bond strengths (**Table 11-1**) are in good agreement with previously determined metal-water coordinated bond energies.[62] To confirm that the copper-water interaction strength varies due to intermolecular forces, COHP analyses were performed on the respective water molecules against the entire unit cell, excluding the copper cations. The integrated values were 229.76 and 252.49 kJ/mol for water$_{planar}$ and water$_{bent}$, respectively, showing that water$_{bent}$ is stabilized by external interactions (beyond the metal coordination) to a higher degree than water$_{planar}$. This, coupled with the hydrogen-bonding pattern, highlights the complex equilibrium that is established between electronic configuration, geometry, and external forces, and that the ultimate structure is dictated by the balance between all of these simultaneous factors.
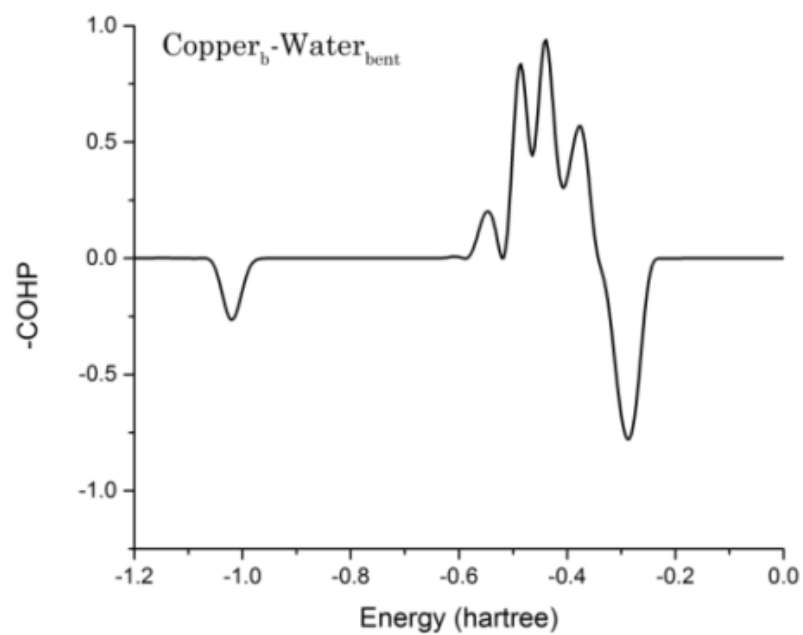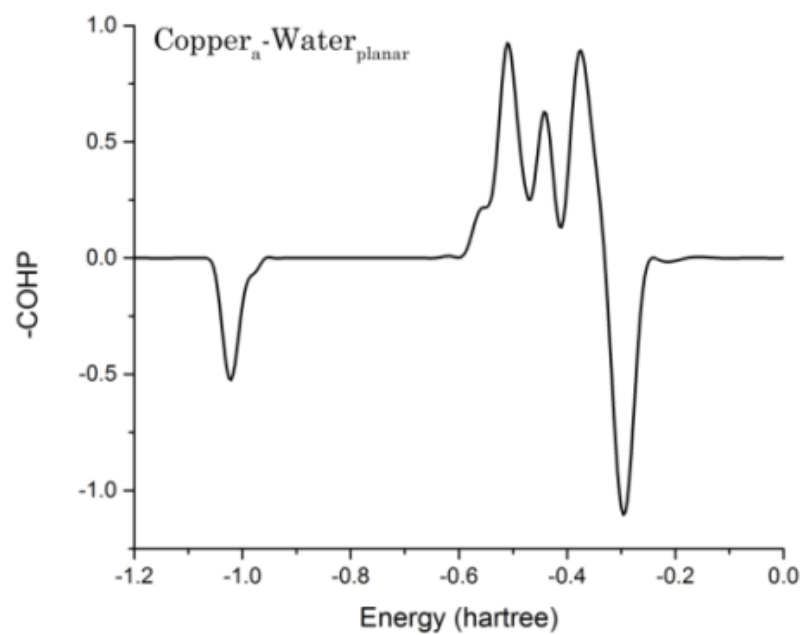
Figure 11-5. Solid-state COHP plots of CuSO₄·5H₂O. The negative of the values obtained from the COHP equation is presented by convention.

Table 11-1. Integrated DOS, COOP, and COHP values for the two copper-water interactions in CuSO$_4$·5H$_2$O. The DOS and COOP values are unitless, and the COHP values are in kJ/mol.

	Integrated DOS	Integrated COOP	Bonding Population	Antibonding Population	Integrated COHP	Bonding Energy	Antibonding Energy
copper$_a$-water$_{planar}$	28.135	0.323	0.404	0.081	-226.304	-411.318	185.015
copper$_b$-water$_{bent}$	26.416	0.275	0.333	0.058	-188.232	-328.096	139.854

11.3.4 Constant Volume Optimizations

The differing orientations of the coordinated water molecules have been shown to have an effect on the strength and nature of the chemical bond between the copper cation and each water molecule. The origin of these differences is attributed to packing induced strain, which causes water$_{bent}$ to sacrifice metal-ligand bonding energy in favor of other forces. In order to determine how large a role the solid-state packing has on the copper-water bonds, structural optimizations were performed where the unit cell volume was kept at fixed but increased values. The lattice parameters and atomic coordinates were allowed to fully relax, with the only constraint being preservation of the specified volume. The results shown in **Figure 11-6** reveal that the copper$_b$-water$_{bent}$ tilt angle is linearly dependent on unit cell volume, with the geometry approaching the gas-phase/solvent structure as the unit cell expands. Additionally, the water internal bond angle (H-O-H) increases with increasing unit cell volume as well, (108.15° to 109.25°) following the same trend as the tilt angle. This is indicative of an enhanced covalent bond between the copper and oxygen, which allows the H-O-H angle to open due to decreased electron density on the oxygen atom. In fact, both copper$_a$-water$_{planar}$ and copper$_b$-water$_{bent}$ exhibit a trend towards moving to perfectly planar tilt arrangements, as well as expansion of both water H-O-H bond angles with increasing unit cell volume, confirming that each copper coordination environment is sensitive to the crystalline packing strain.
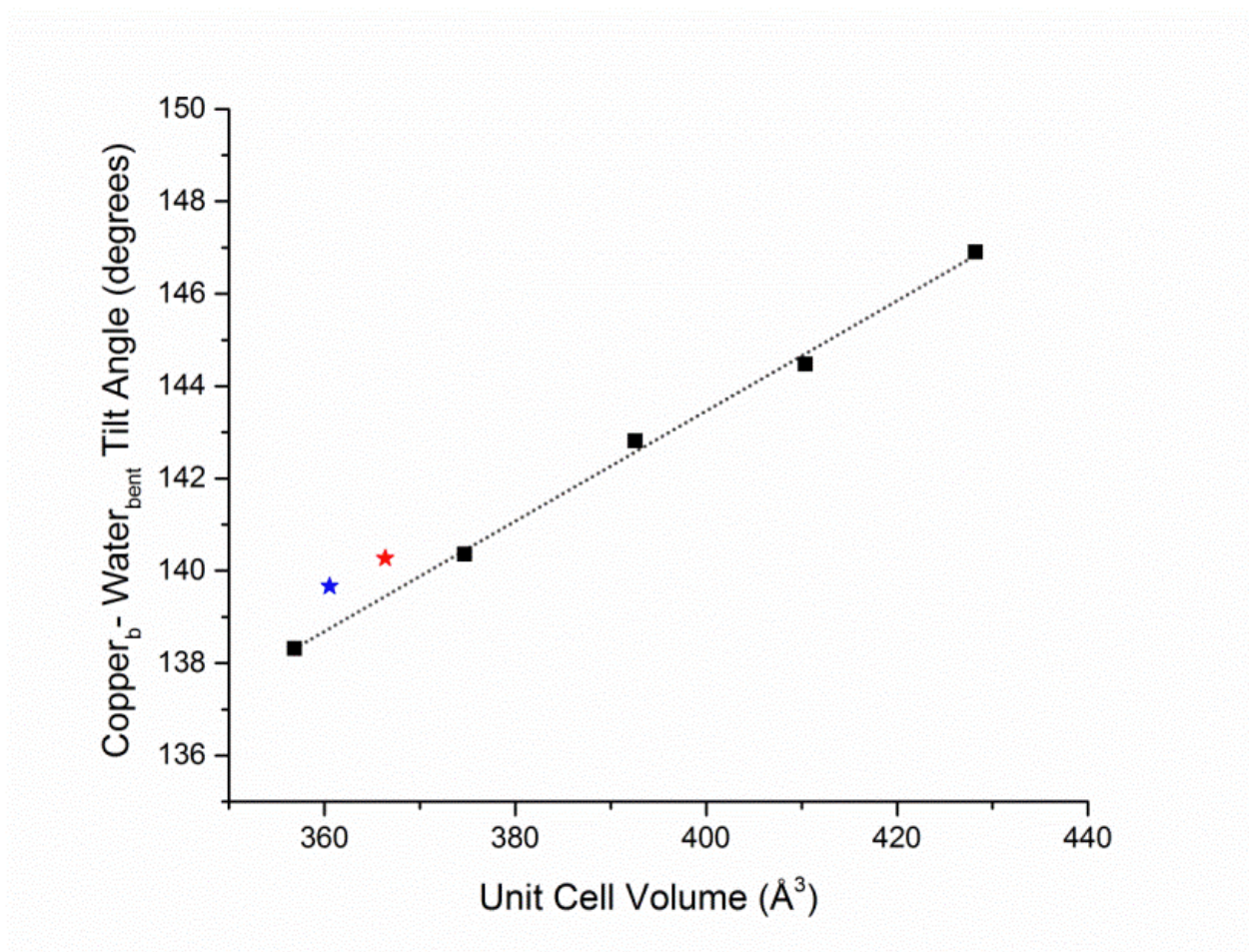
Figure 11-6. Effect of fixed-volume optimizations on the copper$_b$-water$_{bent}$ tilt angle. The dotted line represents a linear least-squared fit of the data points (R=99.74%). The experimental XRD (90 K) and neutron (298 K)[26] parameters are denoted by blue and red stars, respectively.

11.4 Conclusions

A detailed investigation was performed on the geometry and electronic structure of $CuSO_4 \cdot 5H_2O$ crystals, using solid-state DFT and experimental XRD measurements. While the traditional computational method of calculating a DOS plot provides useful insight into the overall characteristics of a solid, the slight differences between the DOS of two similar fragments within the solid often proves to be difficult to interpret. Implementation of COOP and COHP analyses into a developmental version of the CRYSTAL14 software package facilitated evaluation of particular interactions within the bulk. The enhanced specificity of these approaches yielded precise information concerning how molecular orbital occupations and overlaps influence the observed structural arrangements of atoms in the solid state. The COOP and COHP plots have the same basic shape (in terms of absolute values) as the DOS plot, however partitioning of data into bonding and antibonding regions enables the interactions to be described based on the specific local electronic environment. Integration of the COOP and COHP plots highlight that deviations from the copper-water gas-phase geometry results from decreased bond order and bond strength in the crystal, due to lessened orbital overlap between the two components.

Furthermore, orientations of the water$_{bent}$ molecules were found to be greatly influenced by the unit cell volume, showing that packing strain is the driving force in the observed structural trends. These packing interactions, largely characterized by the formation of hydrogen bonds between the water molecules, are analogous to the intermolecular forces acting upon aqueous hexaaqua-copper cations by the bulk solvent in aqueous solutions. The results are therefore

applicable to any condensed phase system involving aquated metal ions, where the equilibrium between internal and external factors dictates the final coordination arrangements.

11.5 Acknowledgements

11.6 References

1. Lauffer, R. B., Paramagnetic Metal Complexes as Water Proton Relaxation Agents for NMR Imaging: Theory and Design. *Chem. Rev.* **1987**, *87*, 901-927.

2. Andreini, C.; Bertini, I.; Cavallaro, G.; Holliday, G. L.; Thornton, J. M., Metal Ions in Biological Catalysis: From Enzyme Databases to General Principles. *J. Biol. Inorg. Chem.* **2008**, *13*, 1205-1218.

3. Yazaydın, A. O.; Benin, A. I.; Faheem, S. A.; Jakubczak, P.; Low, J. J.; Willis, R. R.; Snurr, R. Q., Enhanced CO_2 Adsorption in Metal-Organic Frameworks Via Occupation of Open-Metal Sites by Coordinated Water Molecules. *Chem. Mater.* **2009**, *21*, 1425-1430.

4. Haas, K. L.; Franz, K. J., Application of Metal Coordination Chemistry to Explore and Manipulate Cell Biology. *Chem. Rev.* **2009**, *109*, 4921-4960.

5. Nara, M.; Torii, H.; Tasumi, M., Correlation between the Vibrational Frequencies of the Carboxylate Group and the Types of Its Coordination to a Metal Ion: An Ab Initio Molecular Orbital Study. *J. Phys. Chem* **1996**, *100*, 19812-19817.

6. Ogasawara, H.; Brena, B.; Nordlund, D.; Nyberg, M.; Pelmenschikov, A.; Pettersson, L. G. M.; Nilsson, A., Structure and Bonding of Water on Pt(111). *Phys. Rev. Lett.* **2002**, *89*, 276102.

7. Bryantsev, V. S.; Diallo, M. S.; van Duin, A. C. T.; Goddard III, W. A., Hydration of Copper(II): New Insights from Density Functional Theory and the Cosmo Solvation Model. *J. Phys. Chem. A* **2008**, *112*, 9104-9112.

8. Reedijk, J., Metal-Ligand Exchange Kinetics in Platinum and Ruthenium Complexes. *Platinum Met. Rev.* **2008**, *52*, 2-11.

9.   van Duin, A. C.; Bryantsev, V. S.; Diallo, M. S.; Goddard, W. A.; Rahaman, O.; Doren, D. J.; Raymand, D.; Hermansson, K., Development and Validation of a Reaxff Reactive Force Field for Cu Cation/Water Interactions and Copper Metal/Metal Oxide/Metal Hydroxide Condensed Phases. *J. Phys. Chem. A* **2010**, *114*, 9507-9514.

10.   Jackson, V. E.; Felmy, A. R.; Dixon, D. A., Prediction of the Pka's of Aqueous Metal Ion +2 Complexes. *J. Phys. Chem. A* **2015**, *119*, 2926-2939.

11.   Crabtree, R. H., Multifunctional Ligands in Transition Metal Catalysis. *New J. Chem.* **2011**, *35*, 18-23.

12.   Seredyuk, V.; Vargalyuk, V., Estimation of Reliability of Quantum-Chemical Calculations of Electronic Transitions in Aqua Complexes of Transition Metals. *Russ. J. Electrochem.* **2008**, *44*, 1105-1112.

13.   Sala, X.; Maji, S.; Bofill, R.; García-Antón, J.; Escriche, L. s.; Llobet, A., Molecular Water Oxidation Mechanisms Followed by Transition Metals: State of the Art. *Acc. Chem. Res.* **2013**, *47*, 504-516.

14.   Liu, X.; Lu, X.; Jan Meijer, E.; Wang, R., Hydration Mechanisms of Cu2+: Tetra-, Penta- or Hexa-Coordinated? *Phys. Chem. Chem. Phys.* **2010**, *12*, 10801-10804.

15.   Frank, P.; Benfatto, M.; Qayyam, M.; Hedman, B.; Hodgson, K. O., A High-Resolution Xas Study of Aqueous Cu(II) in Liquid and Frozen Solutions: Pyramidal, Polymorphic, and Non-Centrosymmetric. *J. Chem. Phys.* **2015**, *142*, 084310.

16.   Xia, F.-F.; Yi, H.-B.; Zeng, D., Hydrates of Cu2+ and Cucl+ in Dilute Aqueous Solution: A Density Functional Theory and Polarized Continuum Model Investigation. *J. Phys. Chem. A* **2010**, *114*, 8406-8416.

17. Dronskowski, R.; Bloechl, P. E., Crystal Orbital Hamilton Populations (COHP): Energy-Resolved Visualization of Chemical Bonding in Solids Based on Density-Functional Calculations. *J. Phys. Chem* **1993**, *97*, 8617-8624.

18. Dovesi, R.; Orlando, R.; Civalleri, B.; Roetti, C.; Saunders, V. R.; Zicovich-Wilson, C. M., Crystal: A Computational Tool for the ab initio Study of the Electronic Properties of Crystals. *Z. Kristallogr.* **2005**, *220*, 571-573.

19. Cornil, J.; Calbert, J. P.; Brédas, J.-L., Electronic Structure of the Pentacene Single Crystal: Relation to Transport Properties. *J. Am. Chem. Soc.* **2001**, *123*, 1250-1251.

20. Zaanen, J.; Sawatzky, G.; Allen, J., Band Gaps and Electronic Structure of Transition-Metal Compounds. *Phys. Rev. Lett.* **1985**, *55*, 418.

21. Mérawa, M.; Llunell, M.; Orlando, R.; Gelize-Duvignau, M.; Dovesi, R., Structural, Electronic and Elastic Properties of Some Fluoride Crystals: An ab initio Study. *Chem. Phys. Lett.* **2003**, *368*, 7-11.

22. Wyckoff, R. W. G.; Wyckoff, R. W., *Crystal Structures*; Interscience New York, 1960; Vol. 1.

23. Piermarini, G. J.; Mighell, A. D.; Weir, C. E.; Block, S., Crystal Structure of Benzene II at 25 Kilobars. *Science* **1969**, *165*, 1250-1255.

24. Delaney, S. P.; Witko, E. M.; Smith, T. M.; Korter, T. M., Investigating Tautomeric Polymorphism in Crystalline Anthranilic Acid Using Terahertz Spectroscopy and Solid-State Density Functional Theory. *J. Phys. Chem. A* **2012**, *116*, 8051-8057.

25. Nangia, A., Conformational Polymorphism in Organic Crystals. *Acc. Chem. Res.* **2008**, *41*, 595-604.

26. Bacon G E, T. D. H., Neutron-Diffraction Studies of $CuSO_4*5(H_2O)$ and $CuSO_4*5(D_2o)$. Zeitschrift fur Kristallographie, 1975; Vol. 141, pp 330-341.

27. Beevers, C.; Lipson, H., The Crystal Structure of Copper Sulphate Pentahydrate, Cuso 4. 5h 2 O. *Proc. R. Soc. London, Ser. A* **1934**, 570-582.

28. Soda, G.; Chiba, T., Deuteron Magnetic Resonance Study of Cupric Sulfate Pentahydrate. *J. Chem. Phys.* **1969**, *50*, 439-455.

29. Baur, W.; Rolin, J., Salt Hydrates. Ix. The Comparison of the Crystal Structure of Magnesium Sulfate Pentahydrate with Copper Sulfate Pentahydrate and Magnesium Chromate Pentahydrate. *Acta Crystallogr. Sect. B: Struct. Sci.* **1972**, *28*, 1448-1455.

30. Breza, M.; Biskupič, S.; Kožíšek, J., On the Structure of Hexaaquacopper(II) Complexes. *J. Mol. Struct.* **1997**, *397*, 121-128.

31. Joly, Y.; Cabaret, D.; Renevier, H.; Natoli, C. R., Electron Population Analysis by Full-Potential X-Ray Absorption Simulations. *Phys. Rev. Lett.* **1999**, *82*, 2398.

32. Stewart, R. F., Electron Population Analysis with Generalized X-Ray Scattering Factors: Higher Multipoles. *J. Chem. Phys.* **1973**, *58*, 1668-1676.

33. Zhang, Y.; Tan, Y.-W.; Stormer, H. L.; Kim, P., Experimental Observation of the Quantum Hall Effect and Berry's Phase in Graphene. *Nature* **2005**, *438*, 201-204.

34. Blodgett Jr, A. J.; Spicer, W. E., Experimental Determination of the Density of States in Nickel. *Phys. Rev.* **1966**, *146*, 390.

35. Koga, N.; Morokuma, K., Ab Initio Molecular Orbital Studies of Catalytic Elementary Reactions and Catalytic Cycles of Transition-Metal Complexes. *Chem. Rev.* **1991**, *91*, 823-842.

36.   Suntivich, J.; May, K. J.; Gasteiger, H. A.; Goodenough, J. B.; Shao-Horn, Y., A Perovskite Oxide Optimized for Oxygen Evolution Catalysis from Molecular Orbital Principles. *Science* **2011**, *334*, 1383-1385.

37.   Tsirelson, V. G.; Ozerov, R. P., *Electron Density and Bonding in Crystals: Principles, Theory and X-Ray Diffraction Experiments in Solid State Physics and Chemistry*; Taylor & Francis, 1996.

38.   Kallies, B.; Meier, R., Electronic Structure of 3d [M(H2O)6]3+ Ions from Sciii to Feiii: A Quantum Mechanical Study Based on DFT Computations and Natural Bond Orbital Analyses. *Inorg. Chem.* **2001**, *40*, 3101-3112.

39.   Suzuki, H., *Electronic Absorption Spectra and Geometry of Organic Molecules: An Application of Molecular Orbital Theory*; Elsevier, 2012.

40.   Maintz, S.; Deringer, V. L.; Tchougréeff, A. L.; Dronskowski, R., Analytic Projection from Plane-Wave and PAW Wavefunctions and Application to Chemical-Bonding Analysis in Solids. *J. Comput. Chem.* **2013**, *34*, 2557-2567.

41.   Kulik, H. J.; Cococcioni, M.; Scherlis, D. A.; Marzari, N., Density Functional Theory in Transition-Metal Chemistry: A Self-Consistent Hubbard *U* Approach. *Phys. Rev. Lett.* **2006**, *97*, 103001.

42.   Dovesi, R.; Orlando, R.; Erba, A.; Zicovich-Wilson, C. M.; Civalleri, B.; Casassa, S.; Maschio, L.; Ferrabone, M.; De La Pierre, M.; D'Arco, P.*, et al.*, CRYSTAL14: A Program for the *ab initio* Investigation of Crystalline Solids. *Int. J. Quantum Chem* **2014**, *114*, 1287-1317.

43. Saunders, V. R.; Freyria-Fava, C.; Dovesi, R.; Salasco, L.; Roetti, C., On the Electrostatic Potential in Crystalline Systems Where the Charge Density Is Expanded in Gaussian Functions. *Mol. Phys.* **1992**, *77*, 629-665.

44. de Abajo, F. G.; Kociak, M., Probing the Photonic Local Density of States with Electron Energy Loss Spectroscopy. *Phys. Rev. Lett.* **2008**, *100*, 106804.

45. Lang, J.; Baer, Y.; Cox, P., Study of the 4f and Valence Band Density of States in Rare-Earth Metals. II. Experiment and Results. *J. Phys. F* **1981**, *11*, 121.

46. Schwarz, K., Partial Density of States Obtained from Apw Band Structure Calculations for Nbc and Nbn. *J. Phys. C* **1975**, *8*, 809.

47. Nolan, M.; Grigoleit, S.; Sayle, D. C.; Parker, S. C.; Watson, G. W., Density Functional Theory Studies of the Structure and Electronic Structure of Pure and Defective Low Index Surfaces of Ceria. *Surf. Sci.* **2005**, *576*, 217-229.

48. Hughbanks, T.; Hoffmann, R., Chains of Trans-Edge-Sharing Molybdenum Octahedra: Metal-Metal Bonding in Extended Systems. *J. Am. Chem. Soc.* **1983**, *105*, 3528-3537.

49. Deringer, V. L.; Tchougréeff, A. L.; Dronskowski, R., Crystal Orbital Hamilton Population (COHP) Analysis as Projected from Plane-Wave Basis Sets. *J. Phys. Chem. A* **2011**, *115*, 5461-5466.

50. Sheldrick, G., A Short History of Shelx. *Acta Crystallogr. Sect. A* **2008**, *64*, 112-122.

51. Ruggiero, M. T.; Bardon, T.; Strlič, M.; Taday, P. F.; Korter, T. M., Assignment of the Terahertz Spectra of Crystalline Copper Sulfate and Its Hydrates Via Solid-State Density Functional Theory. *J. Phys. Chem. A* **2014**, *118*, 10101-10108.

52. Ruggiero, M. T.; Bardon, T.; Strlic, M.; Taday, P. F.; Korter, T. M., The Role of Terahertz Polariton Absorption in the Characterization of Crystalline Iron Sulfate Hydrates. *Phys. Chem. Chem. Phys.* **2015**, *17*, 9326-9334.

53. Becke, A. D., Density-Functional Thermochemistry. III. The Role of Exact Exchange. *J. Chem. Phys.* **1993**, *98*, 5648-5652.

54. Krishnan, R.; Binkley, J. S.; Seeger, R.; Pople, J. A., Self-Consistent Molecular Orbital Methods. XX. A Basis Set for Correlated Wave Functions. *J. Chem. Phys.* **1980**, *72*, 650-654.

55. Frisch, M. J.; Trucks, G. W.; Schlegel, H. B.; Scuseria, G. E.; Robb, M. A.; Cheeseman, J. R.; Scalmani, G.; Barone, V.; Mennucci, B.; Petersson, G. A.*, et al.*, Gaussian 09, Revision B.01. Wallingford CT, 2009.

56. O'Boyle, N. M.; Tenderholt, A. L.; Langner, K. M., Cclib: A Library for Package-Independent Computational Chemistry Algorithms. *J. Comput. Chem.* **2008**, *29*, 839-845.

57. Casassa, S.; Erba, A.; Baima, J.; Orlando, R., Electron Density Analysis of Large (Molecular and Periodic) Systems: A Parallel Implementation. *J. Comput. Chem.* **2015**.

58. Alexei, G.; Rajeev, A.; Olle, E., Balanced Crystal Orbital Overlap Population—a Tool for Analysing Chemical Bonds in Solids. *J. Phys.: Condens. Matter* **2003**, *15*, 7751.

59. Pisani, C., *Quantum-Mechanical Ab-Initio Calculation of the Properties of Crystalline Materials*; Springer Berlin Heidelberg, 1996.

60. Bersuker, I. B., Modern Aspects of the Jahn−Teller Effect Theory and Applications to Molecular Problems. *Chem. Rev.* **2001**, *101*, 1067-1114.

61. Gorelsky, S. I.; Basumallick, L.; Vura-Weis, J.; Sarangi, R.; Hodgson, K. O.; Hedman, B.; Fujisawa, K.; Solomon, E. I., Spectroscopic and DFT Investigation of [M{Hb(3,5-Ipr$_2$pz)$_3$}(SC$_6$F$_5$)] (M = Mn, Fe, Co, Ni, Cu, and Zn) Model Complexes: Periodic Trends in Metal-Thiolate Bonding. *Inorg. Chem.* **2005**, *44*, 4947-60.

62. Labanowski, J. K.; Andzelm, J. W., *Density Functional Methods in Chemistry*; Springer Science & Business Media, 2012.

CHAPTER 12: The Role of Terahertz Polariton Absorption in the Characterization of Crystalline Iron Sulfate Hydrates

The material contained within this chapter is published in *Physical Chemistry Chemical Physics* (Ruggiero, M.T.; Bardon, T.; Strlič, M.; Taday, P.F.; Korter, T.M. *Phys. Chem. Chem. Phys.* **2016**. 17(14) 9326-9334) This article has been reproduced by permission of the PCCP Owner Societies.
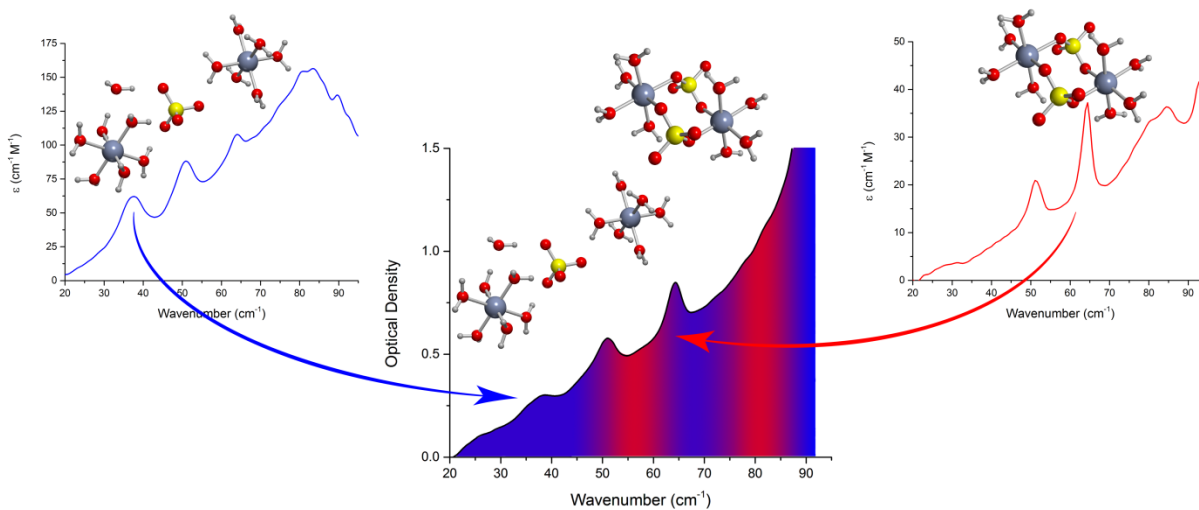
Abstract

Iron sulfate compounds have been used extensively to produce iron gall ink, a widely used writing ink in the western world from the 12th-20th centuries. Iron gall ink is well known to corrode writing supports, so detection of iron species is important for the preservation of historical artwork and documents. Iron(II) sulfate readily changes hydration states and oxidizes in ambient conditions, forming compounds that contribute to this deterioration. In this study, five forms of iron sulfate are characterized by terahertz spectroscopy and solid-state density functional theory (DFT). The results have revealed that the room temperature spectra of $FeSO_4$ $\cdot 7H_2O$ and $FeSO_4$ $\cdot 4H_2O$ are remarkably similar, differing by only a single absorption feature. The identifying terahertz spectra provide an unambiguous metric to determine the relative concentrations of the most common hydrates $FeSO_4$ $\cdot 7H_2O$ and $FeSO_4$ $\cdot 4H_2O$ in a mixed sample. Complete spectral assignments of these species were accomplished by quantum mechanical simulations, with the exception being a single anomalous feature at approximately 40 cm^{-1} in the heptahydrate. This peak is believed to be due to polariton absorption, brought about by the particular coordination structure of $FeSO_4$ $\cdot 7H_2O$ that results in a greater charge separation relative to the other iron sulfate crystals.

12.1 Introduction

The chemical flexibility of iron to exist in a variety of compounds results in difficulties with characterizing iron-containing samples.[1-2] Often seemingly simple systems involving iron become extremely complicated, with multiple coexisting oxidation and hydration states possible.[3-5] One such example is iron sulfate ($FeSO_4$), which has been used as an agricultural fertilizer, a nutritional supplement to treat iron deficiency anemia, and in inks and pigments.[6-7] Remarkably, $FeSO_4$ has been shown to have at least *thirteen* different fates depending on environmental conditions.[5] Iron sulfate naturally forms via the oxidation of pyrite and has been mined as 'vitriol', thus it was extensively available to prepare iron gall ink in medieval times.[7] Iron gall inks were widely used from the 12th-20th century due to its firm adherence to paper or parchment.[6] However, iron gall inks are corrosive and promote the degradation of the writing support over time, both in the parchment or paper sheet on which it was used on as well as sheets stored nearby.[8-10] Thus, the differentiation between corrosive and inert iron compounds in aged documents is extremely important for monitoring potential decay. However, current methods for determining iron content involve invasive techniques, such as using moist indicator strips which could damage already fragile documents. Terahertz (THz) spectroscopy is non-invasive, making it an ideal tool for the investigation of fragile documents and has previously been used to characterize complex samples containing many different chemical species, including those in historic inks.[11-14] Interpretation of the THz vibrational spectra of iron sulfate species could lead to a deeper understanding of the chemical composition and degradation paths of iron gall ink. Because there are no functional group specific absorption features in the terahertz region, every crystalline material has an identifying spectral fingerprint, even crystalline polymorphs of the

347

same compound.[15-17] This specificity allows for characterization of solid samples that complements other techniques such as X-ray diffraction (XRD).[18-19] Unlike XRD however, THz radiation is non-ionizing, and thus is an extremely attractive analytical tool for use with delicate samples, such as explosives and artwork.[20-23]

Combining THz spectroscopy with solid-state density functional theory (DFT) calculations allows for detailed interpretation of observed spectra and enhanced understanding of the intermolecular interactions in solid materials.[24-25] Copper (II) sulfate, also used for the production of ink species, intentionally or not, was recently completely characterized by THz spectroscopy and solid state DFT calculations.[26] The success of that work led to the present investigation of $FeSO_4$ and its hydrates. Iron sulfate heptahydrate is the most common (and most hydrated) form, but four species exist in total: anhydrous, monohydrate, tetrahydrate and heptahydrate.[27-32] There also exist numerous ferric (Fe^{3+}) sulfate species, as well as mixed ferrous-ferric sulfate species.[5, 33] Given this complexity, there exists a need for new characterization methods for investigating iron sulfate containing materials, especially in the conservation sciences.

In this work, Iron(II) sulfate is studied via terahertz (THz) spectroscopy, powder X-ray diffraction (PXRD), and solid state density functional theory (DFT) in order to further the analytical use of THz spectroscopy. Here, solid-state DFT calculations are performed on the four aforementioned hydrates of ferrous sulfate, as well as a ferric sulfate species, $Fe_2(SO_4)_3OH$ $\cdot 2H_2O$. The results of these simulations, coupled with the experimental THz spectra, provide a means for characterizing possible iron sulfate products in solid materials, and quantifying the amounts of the various species present

12.2 Methods

12.2.1 Experimental

Iron(II) sulfate heptahydrate ($\geq$ 99%) was purchased from Sigma Aldrich and recrystallized from an aqueous solution, which had a few drops of 6 M sulfuric acid added prior to dissolution.[34] The sample was left in ambient conditions for a few days forming large-green crystals of iron(II) sulfate heptahydrate, which were immediately used. Care must be taken when attempting to recrystallize any iron(II) species, since unintended oxidation readily occurs. For example, iron(III) sulfate hydroxide dihydrate formed as a red precipitant from an aqueous solution of iron(II) sulfate when too little sulfuric acid was added. Iron(II) sulfate tetrahydrate was synthesized by placing the heptahydrate in a calcium sulfate (Drierite) desiccator for 18 h, after which the sample visibly changed from green to gray. Iron(II) sulfate monohydrate was synthesized by heating the heptahydrate at 373 K in a nitrogen-purged vacuum oven for 24 h. The bulk crystalline content was confirmed for all samples through powder X-ray diffraction (PXRD) on a Bruker KAPPA APEX DUO diffractometer using monochromated Cu Kα radiation (λ = 1.5418 Å). Calculated powder patterns were produced from the published single-crystal X-ray data for all species.[27-32]

Terahertz spectra were obtained from 20-95 cm^{-1} on a custom terahertz time-domain spectrometer[35] based on an amplified femtosecond Ti:Sapphire near-infrared laser system. Terahertz radiation was generated and detected using zinc telluride crystals via optical rectification[36-37] and free space electro-optic sampling[38], respectively. The spectrometer was purged with dry air and the sample chamber placed under vacuum to minimize absorption from

atmospheric water. Samples were homogenously mixed and pulverized in a

polytetrafluoroethylene matrix with a w/w concentration of ~1.5% and pressed into 2 mm thick

pellets. It is important to note that once dispersed in the PTFE matrix and placed under vacuum,

the hydration levels of the samples were stable for at least 1 week. Thirty-two terahertz

waveforms were collected over a 32 ps time window and averaged at both 293 K and 78 K. The

resulting waveform was then treated with a Hanning window and Fourier transformed. The

frequency-domain spectra presented here are a ratio of the sample spectrum to the spectrum of

blank PTFE and are a result of four sample/blank averaged spectral data sets. The extinction

coefficient is reported in concentration of unit cells rather than individual molecules.

12.2.2 Computational

The CRYSTAL09 software package[39] was used for all solid-state simulations. All

calculations utilized the hybrid Becke-3-Lee-Yang-Parr (B3LYP)[40] density functional, coupled

with the 6-31G(d)/6-31G(2d,2p) basis set[41] for iron/non-metals. As previously reported, the

unoccupied *sp*-type orbital in the standard 6-31G basis set for transition metals is far too diffuse

for use in solid-state simulations.[26] Thus, the Gaussian exponent for iron was modified to

0.44698 using the same methodology used for copper sulfate. Both the atomic positions and

lattice vectors were fully optimized, with the published crystallographic data[27-32] serving as the

initial geometries. The energy convergence for geometry optimizations was set to $\Delta E < 10^{-8}$

hartree. After full optimization within the space group symmetry of the solid, the optimized

parameters were used to perform vibrational analyses. The vibrational modes were calculated

numerically within the harmonic approximation, with two displacements per Cartesian axis per

atom. The energy convergence for the vibrational simulation was set to $\Delta E < 10^{-10}$ hartree. The infrared intensities were calculated using the Berry phase method.[42] Optimized structural parameters and vibrational results are given to three and two decimal places of precision, respectively.

12.3 Results and Discussion

12.3.1 Terahertz Spectroscopy

12.3.1.1 Iron Sulfate Tetrahydrate (FeSO₄·4H₂O)

Iron sulfate heptahydrate (a green solid) would regularly change color when exposed to open air under normal laboratory conditions. This color change is indicative of an alteration in the hydration state with $FeSO_4 \cdot 7H_2O$ partially dehydrating in air to $FeSO_4 \cdot 4H_2O$, as measured by PXRD. A pure sample of $FeSO_4 \cdot 4H_2O$ was synthesized by placing $FeSO_4 \cdot 7H_2O$ in a desiccator for 18 h, with the final purity confirmed by PXRD (**Appendix H**). The room-temperature (298 K) and cold (78 K) terahertz spectra of $FeSO_4 \cdot 4H_2O$ are shown in **Figure 12-1.** The 298 K spectrum contains two clear absorption features at 51.4 and 64.3 cm^{-1}, with a broad absorption above 75 cm^{-1}. Upon cooling, two additional features at 81.3 and 89.0 cm^{-1} are resolved in the higher frequency region, and all of the features narrow slightly and shift to higher frequencies with an average full-width at half maximum (FWHM) of 5.2 cm^{-1} and 2.9 cm^{-1} at 298 and 78 K, respectively.
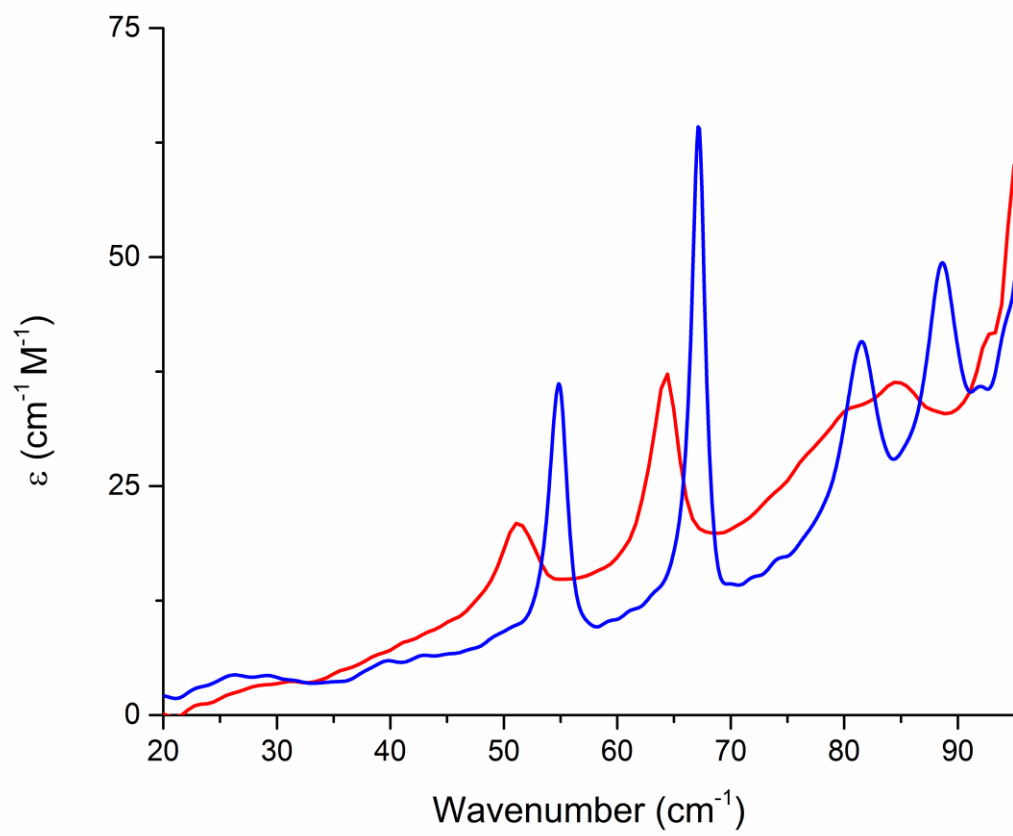
Figure 12-1. Terahertz spectra of FeSO$_4$ ·4H$_2$O at 298 K (red) and 78 K (blue).

12.3.1.2 Iron Sulfate Heptahydrate (FeSO$_4$ ·7H$_2$O)

Terahertz spectra were obtained of recrystallized iron sulfate heptahydrate immediately after formation, and are shown in **Figure 12-2.** The room temperature (298 K) spectrum shows three apparent absorption features at 36.90, 50.8 and 63.0 cm^{-1}, an unstructured absorption between 75-85 cm^{-1}, and a large rising baseline that is most likely due to condensed phase water that is unincorporated into the crystalline solid.[43] Unfortunately, any attempts to drive off this excess water to improve the baseline resulted in formation of the dehydrated FeSO$_4$ ·4H$_2$O form. Upon cooling, the features narrow, uncovering a well-defined absorption at 49.6 cm^{-1}, and increased resolution of the absorptions above 75 cm^{-1}. The features generally show the typical shift to higher frequencies with reduced temperature, with the obvious exception being the first feature, which shifts to a significantly lower frequency (~6 cm^{-1} shift). Red-shifting in this manner is uncommon, but has been reported in other crystalline solids such as sucrose.[44] However, the relative amount of shifting is unusual, with the average blue-shift being +6.3%, while the first absorption red-shifts by -15.6%, more than twice the shift of the rest of peaks. Terahertz spectra were also acquired at intermediate temperatures of 225 K and 150 K (**Appendix H**) and support the observation that while the two higher-frequency peaks monotonically blue-shift and sharpen as the temperature is lowered, the lower-frequency absorption red-shifts and sharpens much less than the other absorption features. Moreover, all unit cell axis of FeSO$_4$ ·7H$_2$O contract when cooled, with a total average contraction of -0.84%.[29, 45] The FWHM of the low-frequency absorption in FeSO$_4$ ·7H$_2$O is 5.9 cm^{-1} while the average FWHM of the remaining features is 3.1 cm^{-1}. It is important to note that the average

FWHM value of the heptahydrate spectrum, excluding the first absorption, closely matches the value obtained for $FeSO_4 \cdot 4H_2O$ (2.9 cm^{-1}).

In order to confirm that this unusual behavior was not a result of a solid-solid phase transition (to an unknown polymorph), powder X-ray diffraction measurements were taking at both room temperature and at 90 K. The powder patterns exhibited no change other than a slight shift induced by contraction of the unit cell from cooling, indicating that no phase transition was occurring.
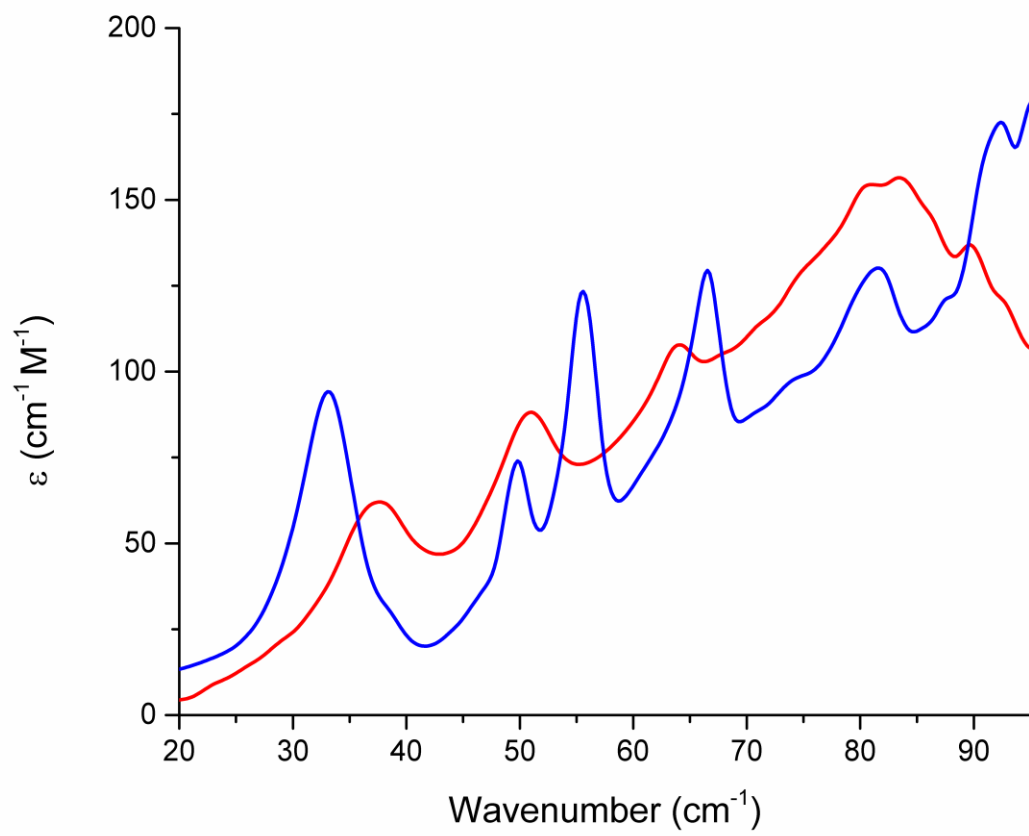
Figure 12-2. 298 K (red) and 78 K (blue) terahertz spectra of FeSO$_4$ ·7H$_2$O.

12.3.1.3 Quantitative Analysis of a Mixture of FeSO₄ ·7H₂O and FeSO₄ ·4H₂O

The room-temperature spectra of $FeSO_4 \cdot 7H_2O$ and $FeSO_4 \cdot 4H_2O$ are remarkably similar, however they are clearly identifiable by the presence of an extra feature in the heptahydrate at 39.0 cm^{-1}. These slight, but distinct differences in room-temperature terahertz absorption spectra allows for quantitative characterization of mixtures of the two hydrates. To demonstrate this, a sample was intentionally created containing an equimolar ratio of $FeSO_4 \cdot 7H_2O$ and $FeSO_4 \cdot 4H_2O$, with terahertz and PXRD measurements taken concurrently. The polynomial baseline-corrected 298 K terahertz spectrum of the mixture is shown in **Figure 12-3,** over the most relevant 30 to 70 cm^{-1} region**.** Relative concentrations were determined by scaling the room-temperature baseline corrected terahertz spectra of $FeSO_4 \cdot 7H_2O$ and $FeSO_4 \cdot 4H_2O$ individually, while minimizing the root-mean-squared deviation (RMSD) between the experimental mixture and the averaged individual spectra. This method resulted in a 57.3 : 42.7 ($\pm$ 1.4%) ratio of tetrahydrate to heptahydrate. The error was estimated by addition of the average absolute deviation in the residual to one species spectrum, and calculating the resulting difference between the new and the originally determined concentrations. This same method was employed for interpretation of the PXRD pattern, which resulted in a 55.5 : 44.5 ($\pm$ 4.7%) ratio of tetrahydrate to heptahydrate (**Appendix H**). The concentrations determined by the two methods are in good agreement, demonstrating terahertz spectroscopy to be a valuable technique for the non-destructive analytical characterization of mixed samples with performance that meets or exceeds PXRD.
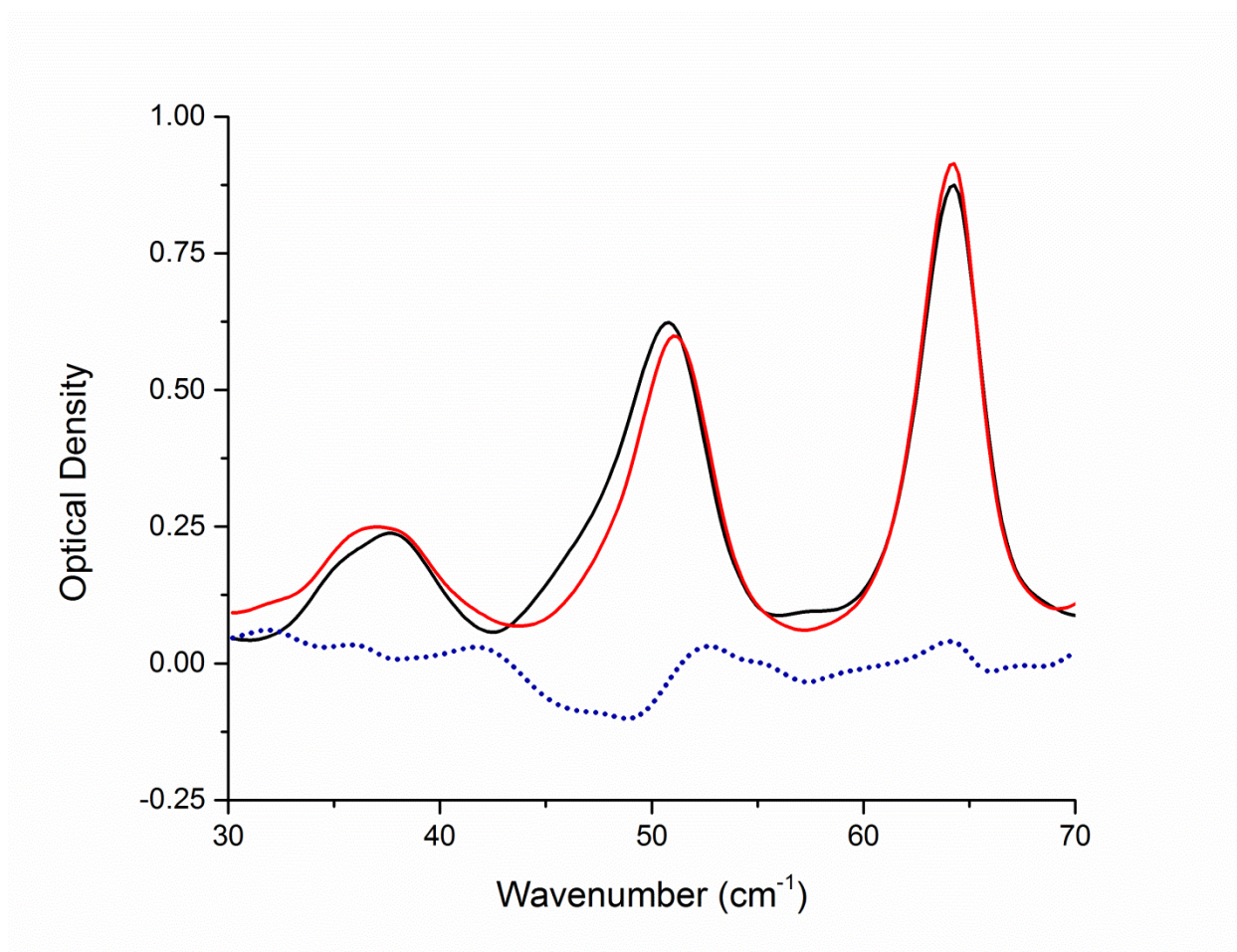
Figure 12-3. 298 K terahertz spectrum of a mixture of FeSO$_4$ ·7H$_2$O and FeSO$_4$ ·4H$_2$O (black), scaled average of the individual 298 K spectra of FeSO$_4$ ·7H$_2$O and FeSO$_4$ ·4H$_2$O (red) and the observed-calculated residual (dotted blue).

12.3.1.4 Contribution of Other Iron Species in the Terahertz Region

There are at least three other chemical species that could *potentially* contribute to the observed terahertz spectral features of an unpurified sample of iron sulfate under ambient conditions. The first being $FeSO_4 \cdot H_2O$, a stable hydrate that has been previously characterized by single-crystal XRD.[30, 32] Iron sulfate monohydrate was synthesized by drying the sample at 373K for 24 h in a nitrogen-purged vacuum oven. Another iron hydrate species that could be present is iron(III) sulfate hydroxide dihydrate. This was intentionally synthesized by dissolving $FeSO_4 \cdot 7H_2O$ in water without any addition of sulfuric acid, and collecting the orange precipitant. The synthesis of both species was confirmed by PXRD (**Appendix H**). Finally, anhydrous iron sulfate is known[31], however it is unlikely that it would influence the terahertz spectra due to the rapid hydration it undergoes when exposed to ambient atmosphere.[31] In fact, all attempts to synthesize and measure the PXRD pattern or the THz spectrum of anhydrous iron sulfate were unsuccessful.

Collectively, these various iron sulfate species are not factors in the terahertz spectra due to their unlikely existence under ambient conditions, but most importantly the aforementioned species have no infrared-active vibrations in the sub-100 cm^{-1} terahertz region. The lack of terahertz-frequency absorption was observed experimentally for $FeSO_4 \cdot H_2O$, and $Fe_2(SO_4)_3OH$ $\cdot 2H_2O$, but was only predicted computationally (*vide infra*) for the anhydrous species. Terahertz spectroscopic and PXRD data of $FeSO_4 \cdot H_2O$ and $Fe_2(SO_4)_3OH$, as well as predicted vibrational frequencies for all iron species studied, are available in **Appendix H**.

12.3.2 Computational Structural Analysis

12.3.2.1 Iron Sulfate Tetrahydrate (FeSO$_4$·4H$_2$O)

Based on previous metal-sulfate crystal work[26], the B3LYP density functional and 6-31G(d)/6-31G(2d,2p) (iron/non-metal) basis set was used for all solid-state DFT calculations. The initial crystalline geometry for FeSO$_4$ ·4H$_2$O was taken from single-crystal X-ray diffraction data.[27] Iron sulfate tetrahydrate crystallizes in the monoclinic P_12_1/n space group, with lattice dimensions: $a = 5.979$ Å, $b = 13.648$ Å, $c = 7.977$ Å, $\beta = 90.43°$ and four formula units in the unit cell ($Z = 4$). Many metal sulfates are known to adopt an antiferromagnetic electronic arrangement, and in the case of FeSO$_4$ ·4H$_2$O this gave an energetically favorable solution and thus was incorporated into the simulations.[46-48] In the bulk, two iron tetrahydrate complexes are bridged by two sulfate anions, forming a pseudo dimer (**Figure 12-4**). This configuration puts packing-induced conformational strain on the iron coordination environment which is evidenced by the distorted octahedral geometry at the iron. The optimization of FeSO$_4$ ·4H$_2$O produced an average bond error of 0.65% (**Table 12-1**), which is consistent with previous metal-sulfate structures reported utilizing the B3LYP/6-31G combination.[26] The full list of bond distances and errors are given in **Table 12-1**.
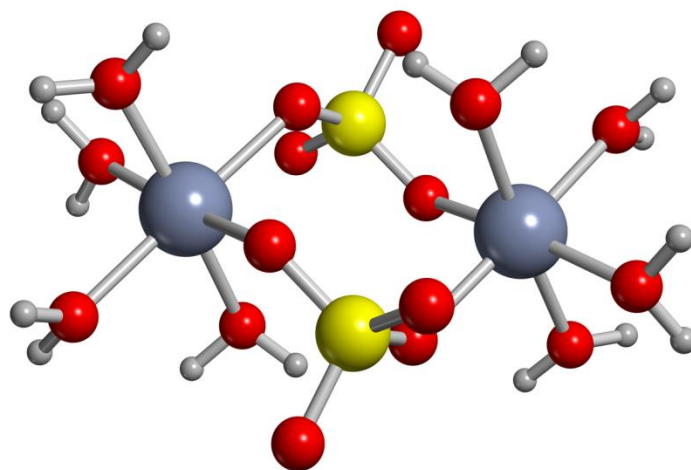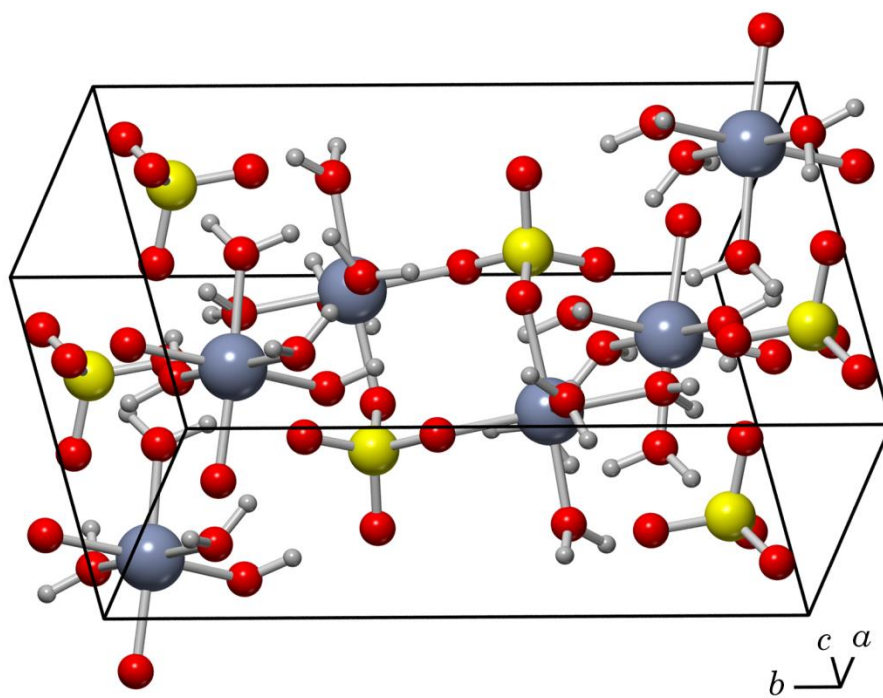
Figure 12-4. Iron(II) sulfate tetrahydrate unit cell and packing structure. The sulfate anions act as bridging ligands creating a pseudo dimer, shown separately for clarity.

Table 12-1. Average absolute percent errors for the different bond types in several iron sulfate species, as well as the overall average percent bond error.

Species	Fe-O$_{water}$	Fe-O$_{sulfur}$	S-O	Fe-O$_{Fe}$	Total Average
FeSO$_4$	-	1.33	4.90	4.53	4.44
FeSO$_4$ ·H$_2$O	0.58	0.56	1.15	-	0.80
FeSO$_4$ ·4H$_2$O	0.52	1.23	0.64	-	0.65
FeSO$_4$ ·7H$_2$O	1.05	-	1.15	-	1.09
Fe$_2$(SO$_4$)$_3$OH ·2H$_2$O	2.10	1.42	3.36	1.22	2.30

12.3.2.2 Iron Sulfate Heptahydrate (FeSO₄ ·7H₂O)

Iron sulfate heptahydrate crystallizes in the monoclinic $P2_1/c$ space group, with lattice dimensions: $a = 13.997$ Å, $b = 6.480$ Å, $c = 11.021$ Å, $\beta = 105.596°$ and four formula units in the unit cell ($Z = 4$).[29] In the bulk, the iron cation is completely coordinated by water, with an additional co-crystallized water molecule. The sulfate anion is centered between two adjacent aqua-iron complexes, and is stabilized by hydrogen bonds between the waters and the sulfate oxygen (**Figure 12-5**). In the case of $FeSO_4$ ·7H₂O, the iron geometry is nearly a perfect octahedron, with all octahedral bond angles within $1.5°$ of $90°$. These structural characteristics are again well reproduced by the simulations, with an average bond error of 1.09% (**Table 12-1**).

12.3.2.3 Iron Sulfate Monohydrate (FeSO₄ ·H₂O)

Iron sulfate monohydrate crystallizes in the monoclinic $C2/c$ space group, with lattice dimensions: $a = 7.078$ Å, $b = 7.549$ Å, $c = 7.773$ Å, $\beta = 118.65°$, with two formula units in the unit cell ($Z = 2$).[30, 32] The iron cation is coordinated by two water molecules and four sulfate anions, all of which act as bridging ligands forming an infinite network. The iron cation adopts a strained octahedral coordination environment due to the bridging ligands, similar to the tetrahydrate structure. The average bond distance error in the calculations is 0.80%, consistent with the other hydrated species (**Table 12-1**).
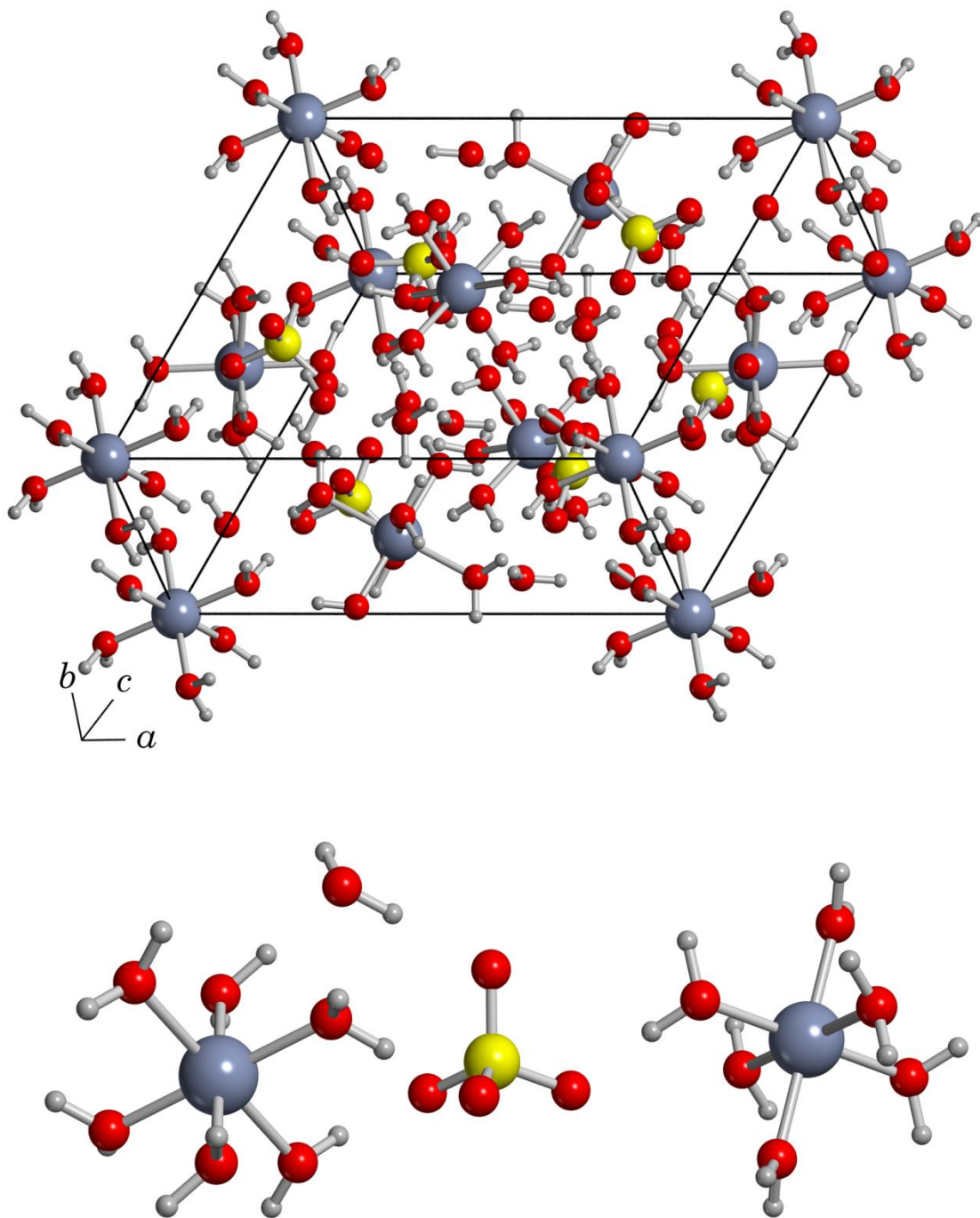
Figure 12-5. Iron(II) sulfate heptahydrate unit cell and packing structure. Two isolated coordinated iron cations are shown for clarity.

12.3.2.4 Anhydrous Iron Sulfate

While attempts at synthesizing anhydrous iron sulfate were unsuccessful, full geometry optimizations were still performed on this species. The structure produced by the solid-state DFT simulations (atomic positions and unit cell dimensions available **Appendix H**) appears to have very large errors associated with it (**Table 12-1**). However, the calculated structure is actually an improvement over the only reported anhydrous structure of $FeSO_4$. The structure published in 1970[31] from PXRD measurements had a confidence factor of 19.1% and sulfur-oxygen bonds that deviated greatly from other crystalline sulfates, indicating that the published structure was not entirely correct.[26-27, 29-32, 49-50] Anhydrous iron sulfate crystallizes in the orthorhombic *Cmcm* space group, with DFT predicted lattice dimensions: $a = 5.251$ Å, $b = 8.020$ Å, $c = 6.642$ Å, and contains two formula units in the unit cell ($Z = 2$). While the experimentally determined atomic positions were not accurate, the PXRD lattice dimensions should be reliable, and are found to be in good agreement with the predicted structure (total average deviation of 0.48%, not tabulated). The structure is isomorphic with anhydrous magnesium sulfate[51], and consists of a continuous network of iron cations in an octahedral environment coordinated by sulfate anions. The coordination environment of the metal is again slightly distorted due to the conformational strain induced by packing.

12.3.2.5 Iron(III) Sulfate Hydroxide Dihydrate (Fe₂(SO₄)₃OH ·2H₂O)

Iron(III) sulfate hydroxide dihydrate crystallizes in the monoclinic *P2₁/m* space group, with lattice dimensions: $a = 6.50$ Å, $b = 7.37$ Å, $c = 5.84$ Å, $\beta = 108.38°$ and contains two

formula units in the unit cell ($Z = 2$).[28] The structure consists of a continuous network of iron

cations in an octahedral environment coordinated by sulfate anions, as well as the hydronium ion

acting as a bridging ligand. As in the case of anhydrous iron sulfate, the literature structure for

$Fe_2(SO_4)_3OH \cdot 2H_2O$ shows some inconsistencies with other metal-sulfate structures, possibly due

to the XRD being done on twinned crystals.[28] The errors in the bonds containing oxygen appear

to be unusually large, but this may again be due to problems in the experimental structure

(confidence factor of 12%). However, the iron-sulfur distance is very well reproduced by solid-

state DFT (0.22% error, not tabulated) which is a result of both the iron and sulfur residing in

well-defined special positions. This causes their positions in the crystal to be completely

dependent on unit cell parameters which themselves match closely with the solid-state DFT

calculations (1.90% error, not tabulated) and are straightforward to obtain from XRD

measurements. Further value is added by the calculated structure since it provides hydrogen atom

positions, which are not included in the published data. The structure produced by the solid-state

DFT simulations is available in **Appendix H**.

12.3.3 Computational Vibrational Analysis

12.3.3.1 Iron Sulfate Tetrahydrate

The simulated terahertz spectrum of $FeSO_4 \cdot 4H_2O$ is shown in **Figure 12-6,** with the

calculated absorptions convolved with Lorentzian line shapes (FWHM = 2.95 cm^{-1}) determined

empirically from the measured spectrum. The simulation shown has been frequency scaled by

0.95, which results in an excellent frequency agreement with the experimental spectrum. The

intensities of the lowest two features appear to be slightly too intense, however the large

predicted feature at 98.19 cm^{-1} influences the intensities in the theoretical spectrum. The full list

of assigned mode types, including frequencies and intensities, is given in **Table 12-2**. The types

of motions encountered in the THz region can be exemplified by the two highest frequency

vibrations seen in $FeSO_4 \cdot 4H_2O$. The translation of the iron cation and its coordination sphere at

81.58 cm^{-1} results in a concerted rotation of the sulfate anion as the two 'rows' of iron cations

slide past one another, depicted in **Figure 12-7**. Beyond external vibrations, there is an internal

vibration that is equally well simulated at 91.62 cm^{-1} which is a torsion of a water-iron-water

group. The complete reproduction of these two motions, because they involve both internal and

external motions of $FeSO_4 \cdot 4H_2O$ crystal, provide further confidence in the theoretical methods

used for investigating the interatomic forces in transition metal sulfates. Good reproduction of

spectral features indicates that the curvature of the potential energy surface is correctly

represented by the applied computational model.
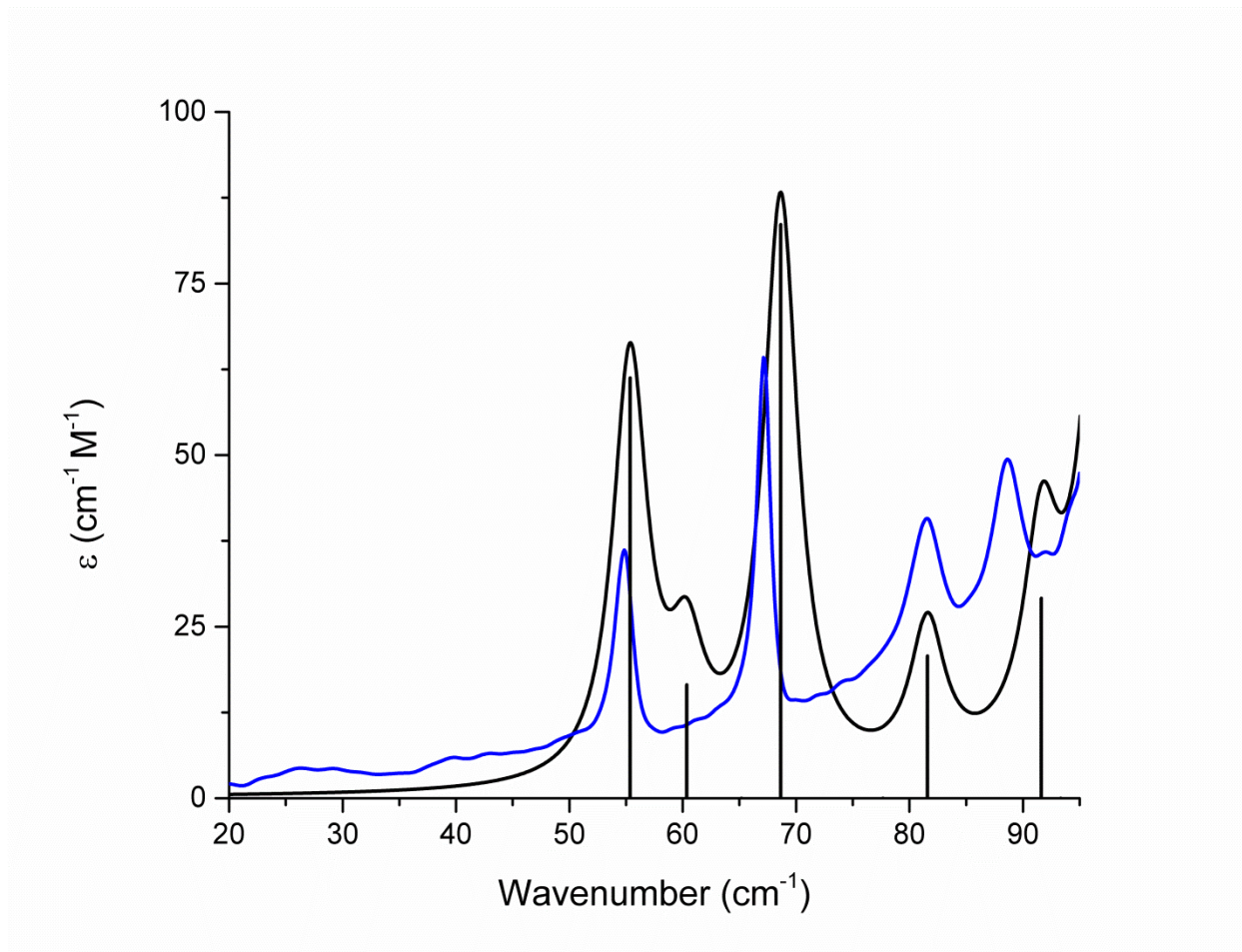
Figure 12-6. Solid-state DFT vibrational simulation (black) of iron sulfate tetrahydrate. The 78 K experimental spectra is shown in blue.

Table 12-2: Unscaled and scaled (x0.95) calculated frequencies (cm^{-1}), intensities (km mol^{-1}), and mode assignments of iron sulfate tetrahydrate.

Experimental	Simulated			
Frequency	Unscaled Freq	Scaled Freq	Intensity	Mode Type
51.4	58.27	55.36	8.75	translation in c
	63.53	60.36	2.36	rotation about c
64.3	72.25	68.64	11.94	translation in a
81.3	85.87	81.58	2.96	translation in a
89.0	96.44	91.62	4.16	water-iron-water torsion
	103.36	96.85	24.39	translation in c
	115.00	98.19	27.16	rotation about c
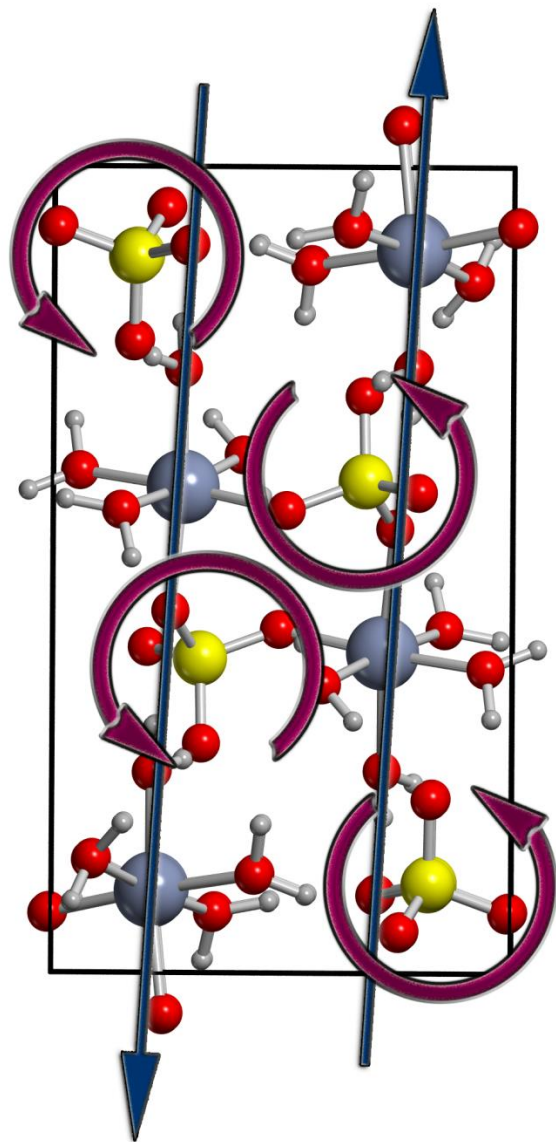
Figure 12-7. Eigenvector representation of the atomic displacements of the 81.58 cm^{-1} vibration in FeSO$_4$ · 4H$_2$O.

12.3.3.2 Iron Sulfate Heptahydrate

The vibrational simulation of $FeSO_4 \cdot 7H_2O$ is shown in **Figure 12-8**, along with the experimental 78 K THz spectrum with a polynomial baseline correction applied. The simulated spectrum has been scaled by 0.95, in the same way as $FeSO_4 \cdot 4H_2O$. While the simulation correctly reproduces both the frequency positions and absorption intensities of the majority of the experimental spectrum, the theory fails in predicting the low-frequency feature at 32.9 cm^{-1}. The normal-mode calculation yields no vibrations at all below 58.3 cm^{-1}, even considering both IR-allowed and IR-forbidden motions. Ignoring the lowest feature, the vibrations associated with iron sulfate heptahydrate are similar to the motions often associated with crystals composed of discrete molecules, due to the existence of largely independent species in the crystalline lattice. This is unlike the tetrahydrate species which forms extensive networks through bridging coordination interactions. The lower-frequency motions are primarily concerted translations of the aquated iron and water molecules, however because the center of mass must be preserved during vibrations, the sulfate anion rotates to maintain this condition. This type of motion is particularly interesting because even though the sulfate is not formally coordinated to the iron cation, the motions of the sulfate anions in both $FeSO_4 \cdot 7H_2O$ and $FeSO_4 \cdot 4H_2O$ are extremely similar, as shown in **Figure 12-9**. Internal motions also play an important role in this solid, with the three high-frequency features all involving iron-water torsions with no motion associated with the sulfate anion. As with $FeSO_4 \cdot 4H_2O$, both internal and external vibrations are well reproduced by the theoretical model. The full list of assigned mode types, including frequencies and intensities, is given in **Table 12-3.**
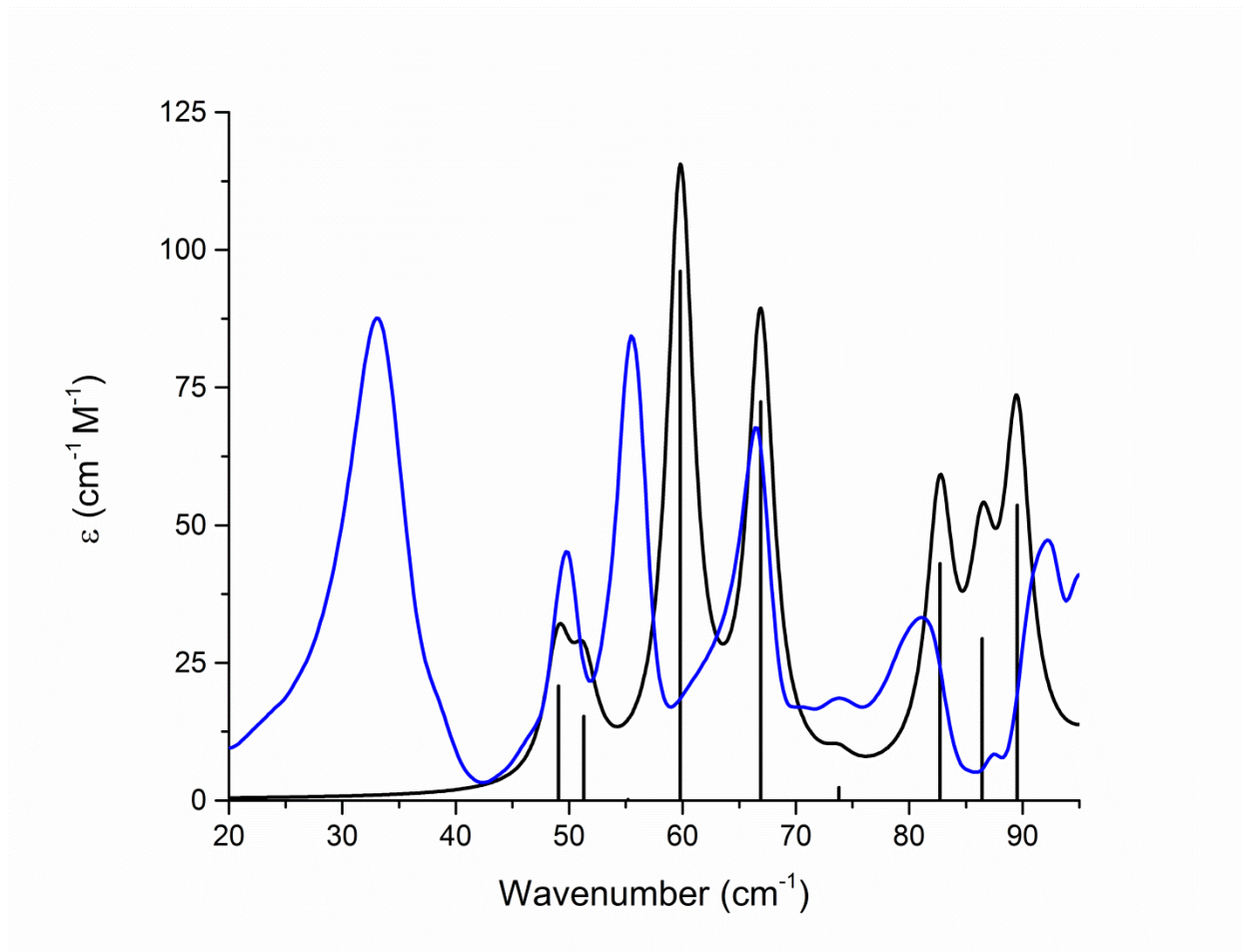
Figure 12-8. Simulated vibrational spectrum (black) and 78 K baseline corrected terahertz spectrum (blue) of iron sulfate heptahydrate.

Table 12-3. Unscaled and scaled (x0.95) calculated frequencies (cm^{-1}), intensities (km mol^{-1}), and mode assignments of iron sulfate heptahydrate.

Experimental	Simulated			
Frequency	Unscaled Freq	Scaled Freq	Intensity	Mode Type
49.6	51.63	49.04	2.60	translation in *b*
55.1	54.01	51.31	1.91	translation in *a*
	62.97	59.82	12.01	translation in *c*
65.9	70.42	66.89	9.05	translation in *b*
74.6	77.69	77.68	0.29	rotation about *c*
80.8	87.05	82.70	5.38	water-iron torsion
88.0	90.99	86.44	3.67	water-iron torsion
92.71	94.23	89.51	6.70	water-iron torsion
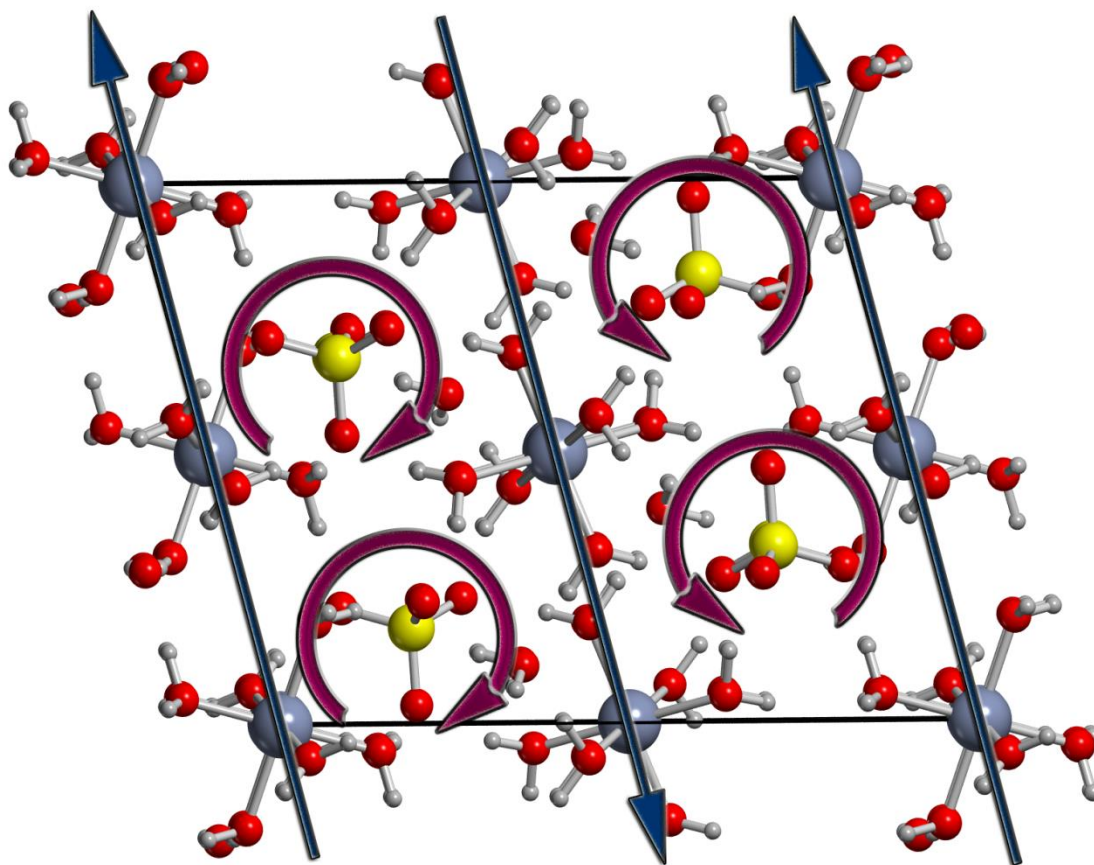
Figure 12-9. Eigenvector representation of the atomic displacements of the 59.82 cm^{-1} vibration in FeSO$_4$ ·7H$_2$O.

12.3.4 Origin of the Broad Absorption in Iron Sulfate Heptahydrate

The prominent and anomalously broad peak in the iron sulfate heptahydrate terahertz spectrum at 36.90 cm^{-1} was unable to be reproduced by the solid-state DFT simulations. The inability of the theoretical model, which in all other cases thus far has proven to be successful in reproducing all other features in the THz spectra of iron and copper sulfate hydrates[26], has led to the conclusion that the absorption is not due to simple Γ-point phonon dispersion. There exists no experimental evidence for typical causes of unexplainable absorption features, such as sample contamination or phase transitions. Additionally, the fact that neither $FeSO_4 \cdot H_2O$, $FeSO_4 \cdot 4H_2O$, nor $Fe(OH)SO_4 \cdot 2H_2O$ display any irregularities indicates that perhaps the unique structural arrangement of $FeSO_4 \cdot 7H_2O$ is important in explaining this unusual feature. In each species of iron sulfate, excluding the heptahydrate, the sulfate anion is directly coordinated to the iron cation. However in the case of the heptahydrate, the sulfate anion is relatively distant from the iron cation (41.7% more distant than in $FeSO_4 \cdot 4H_2O$). This increased separation of charge may lead to an environment that is the basis for long-range polariton excitations in the terahertz region[52], and could explain the otherwise unaccounted for feature in the iron sulfate heptahydrate spectrum.

The concept of polariton absorption has been utilized previous to explain the broad absorptions by lithium tantalate ($LiTaO_3$) in the 0.5-1.5 THz range, a result similar to that seen here.[53-56] While near- Γ avoided crossings are considered to be the cause of polariton absorptions, experimental evidence for such a process is difficult to obtain and the topic is still debated.[55, 57-60] Because polaritons are due to coupling of an optical phonon to a low-frequency electronic transition (occurring due to a charge induced quantum well[61]), the harmonic Γ-point

375

phonon analyses performed here would be unable to reproduce this phenomenon and thus would predict no absorption.[62] The *ab initio* calculation of such polaritons may be possible[62] but the use of supercells in the case of complex solids leads to extreme resource needs, with a simple 2x2x1 $FeSO_4 \cdot 7H_2O$ supercell requiring ~120 times more time to execute than a single unit cell calculation. Recently a solution to solving the dispersion relationship for polariton waves was found using classical mechanics by Dzedolik and Pereskokov, which was applied to cubic crystal systems.[63] While promising, the $FeSO_4 \cdot 7H_2O$ solid investigated here of significantly larger size and lower symmetry compared to the cubic systems, and the application of this method is unfortunately not immediately feasible. Despite the challenges associated with the rigorous calculation of polariton absorption in $FeSO_4 \cdot 7H_2O$, the available evidence strongly suggests this to be the origin of the broad absorption feature centered at 36.90 cm^{-1}. The possibility of such an absorption in this solid offers an exciting opportunity for aiding in the ongoing investigation of phonon dynamics in other complex ionic crystals.

12.4 Conclusions

Iron sulfate and its naturally occurring hydrates have been completely characterized by terahertz spectroscopy and solid-state density functional calculations. Iron gall inks have traditionally been created using $FeSO_4 \cdot 7H_2O$ under ambient conditions, however these inks are known to immediately rapidly degrade writing supports, often significantly reducing the expected lifetime of such documents. The use of terahertz spectroscopy to characterize a sample containing unknown amounts of iron sulfate species and provide quantative information regarding $FeSO_4 \cdot 4H_2O$ and $FeSO_4 \cdot 7H_2O$ mixtures strengthens its utility in the field of heritage science, where the hydration and oxidation states of iron sulfate is indicative of the corrosive potential of the ink. The rapid dehydration of $FeSO_4 \cdot 7H_2O$ to $FeSO_4 \cdot 4H_2O$ in dry atmospheres yields subtle spectral differences due to their room-temperature THz spectra being similar, yet they are different enough for analytical quantification of mixtures. In addition to the iron sulfate species that form the basis of the observed terahertz spectral features, other non-contributing related compounds were also investigated. Solid-state density functional theory optimized structures for anhydrous $FeSO_4$ and $Fe_2(SO_4)_3OH \cdot 2H_2O$ deviated from the structures available in the literature, yet in both cases the structures presented here provide a significant improvement in the atomic-level details of the crystals. Solid-state DFT calculations were also used to fully assign the spectrum of $FeSO_4 \cdot 4H_2O$, providing vital information about the vibrational motions occurring in the crystalline solid. In $FeSO_4 \cdot 7H_2O$, a full assignment was made, with the exception of a single absorption feature. This unusual low-frequency feature is hypothesized to be due to polaritons, arising from coupling of isolated electron charges with long range optical phonons. These polaritons are, by their nature, interactions occurring over multiple unit cells and

thus are not accessible by routine periodic boundary condition calculations, though resource intensive supercell calculations may lead to future assignment of the peak origin.

12.5 Acknowledgements

12.6 References

1. Castro, C. E., The Rapid Oxidation of Iron(II) Porphyrins by Alkyl Halides. A Possible Mode of Intoxication of Organisms by Alkyl Halides. *J. Am. Chem. Soc.* **1964**, *86*, 2310-2311.

2. Timothy, J. S., Redox Reactivity of Organically Complexed Iron(II) Species with Aquatic Contaminants. In *Aquatic Redox Chemistry*, American Chemical Society: 2011; Vol. 1071, pp 283-313.

3. Ponnamperuma, F. N.; Tianco, E. M.; Loy, T., Redox Equilibria in Flooded Soils: I. The Iron Hydroxide Systems. *Soil Science* **1967**, *103*, 374-382.

4. Flynn, C. M., Hydrolysis of Inorganic Iron(III) Salts. *Chem. Rev.* **1984**, *84*, 31-41.

5. Tosca, N. J.; McLennan, S. M.; Dyar, M. D.; Sklute, E. C.; Michel, F. M., Fe Oxidation Processes at Meridiani Planum and Implications for Secondary Fe Mineralogy on Mars. *Journal of Geophysical Research: Planets* **2008**, *113*, E05005.

6. Clark, R. J. H., Raman Microscopy: Application to the Identification of Pigments on Medieval Manuscripts. *Chemical Society Reviews* **1995**, *24*, 187-196.

7. Eastaugh, N.; Walsh, V.; Chaplin, T., Pigment Compendium. Routledge: Burlington, 2008.

8. Kolar, J.; Strlic, M., *Iron Gall Inks : On Manufacture, Characterisation, Degradation, and Stabilisation*; National and University Library: Ljubljana, 2006.

9. Zerdoun Bat-Yehouda, M., *Les Encres Noires Au Moyen Age (Jusqu'à 1600)*; Editions du Centre national de la recherche scientifique: Paris, 1983.

10.   Kolar, J.; Štolfa, A.; Strlič, M.; Pompe, M.; Pihlar, B.; Budnar, M.; Simčič, J.; Reissland, B., Historical Iron Gall Ink Containing Documents — Properties Affecting Their Condition. *Anal. Chim. Acta* **2006**, *555*, 167-174.

11.   Bardon, T.; May, R. K.; Taday, P. F.; Strlic, M., Systematic Study of Terahertz Time-Domain Spectra of Historically Informed Black Inks. *Analyst* **2013**, *138*, 4859-4869.

12.   Ueno, Y.; Rungsawang, R.; Tomita, I.; Ajito, K., Quantitative Measurements of Amino Acids by Terahertz Time-Domain Transmission Spectroscopy. *Anal. Chem.* **2006**, *78*, 5424-5428.

13.   Yuefang, H.; Hongjian, Z., Qualitative and Quantitative Detection of Pesticides with Terahertz Time-Domain Spectroscopy. *Microwave Theory and Techniques, IEEE Transactions on* **2010**, *58*, 2064-2070.

14.   Delaney, S. P.; Pan, D.; Yin, S. X.; Smith, T. M.; Korter, T. M., Evaluating the Roles of Conformational Strain and Cohesive Binding in Crystalline Polymorphs of Aripiprazole. *Cryst. Growth Des.* **2013**, *13*, 2943-2952.

15.   Ho, L.; Pepper, M.; Taday, P., Terahertz Spectroscopy: Signatures and Fingerprints. *Nat. Photon.* **2008**, *2*, 541-543.

16.   Allis, D. G.; Hakey, P. M.; Korter, T. M., The Solid-State Terahertz Spectrum of MDMA (Ecstasy) – a Unique Test for Molecular Modeling Assignments. *Chem. Phys. Lett.* **2008**, *463*, 353-356.

17.   Taday, P. F.; Bradley, I. V.; Arnone, D. D.; Pepper, M., Using Terahertz Pulse Spectroscopy to Study the Crystalline Structure of a Drug: A Case Study of the Polymorphs of Ranitidine Hydrochloride. *J. Pharm. Sci.* **2003**, *92*, 831-838.

18. Spurr, R. A.; Myers, H., Quantitative Analysis of Anatase-Rutile Mixtures with an X-Ray Diffractometer. *Anal. Chem.* **1957**, *29*, 760-762.

19. Taylor, J. C., Computer Programs for Standardless Quantitative Analysis of Minerals Using the Full Powder Diffraction Profile. *Powder Diffr.* **1991**, *6*, 2-9.

20. Kawase, K.; Ogawa, Y.; Watanabe, Y.; Inoue, H., Non-Destructive Terahertz Imaging of Illicit Drugs Using Spectral Fingerprints. *Opt. Express* **2003**, *11*, 2549-2554.

21. Jackson, J. B.; Mourou, M.; Whitaker, J. F.; Duling Iii, I. N.; Williamson, S. L.; Menu, M.; Mourou, G. A., Terahertz Imaging for Non-Destructive Evaluation of Mural Paintings. *Optics Communications* **2008**, *281*, 527-532.

22. Fukunaga, K.; Ogawa, Y.; Hayashi, S. i.; Hosako, I., Terahertz Spectroscopy for Art Conservation. *IEICE Electronics Express* **2007**, *4*, 258-263.

23. Abraham, E.; Younus, A.; Delagnes, J. C.; Mounaix, P., Non-Invasive Investigation of Art Paintings by Terahertz Imaging. *Appl. Phys. A* **2010**, *100*, 585-590.

24. Juliano, T. R.; King, M. D.; Korter, T. M., Evaluating London Dispersion Force Corrections in Crystalline Nitroguanidine by Terahertz Spectroscopy. *IEEE Trans. Terahertz Sci. Technol.* **2013**, *3*, 281-287.

25. Saito, S.; Inerbaev, T. M.; Mizuseki, H.; Igarashi, N.; Note, R.; Kawazoe, Y., Terahertz Phonon Modes of an Intermolecular Network of Hydrogen Bonds in an Anhydrous B-D-Glucopyranose Crystal. *Chem. Phys. Lett.* **2006**, *423*, 439-444.

26. Ruggiero, M. T.; Bardon, T.; Strlič, M.; Taday, P. F.; Korter, T. M., Assignment of the Terahertz Spectra of Crystalline Copper Sulfate and Its Hydrates Via Solid-State Density Functional Theory. *J. Phys. Chem. A* **2014**, *118*, 10101-10108.

27. Baur, W., Zur Kristallchemie Der Salzhydrate. Die Kristallstrukturen Von $Mgso_4 \bullet 4H_2O$ (Leonhardtit) Und $Feso_4 \bullet 4H_2O$ (Rozenit). *Acta Crystallographica* **1962**, *15*, 815-826.

28. Fanfani, L.; Nunzi, A.; Zanazzi, P. F., The Crystal Structure of Butlerite. *The American Minerologist* **1971**, *56*, 751-757.

29. Fronczek, F. R.; Collins, S. N.; Chan, J. Y., Refinement of Ferrous Sulfate Heptahydrate (Melanterite) with Low-Temperature Ccd Data. *Acta Crystallogr., Sect. E: Struct. Rep. Online* **2001**, *57*, i26-i27.

30. Pistorius, W. F. T., Lattice Constants of $Feso_4 \bullet H_2O$ (Artificial Szomolnokite) and $NiSO_4 \bullet H_2O$. *Bull. Soc. Chim. Belg.* **1960**, *69*, 570-574.

31. Saaras, D.; Coing-Boyat, J., Refinement of the Structure of α-$Feso_4$. *Bull. Soc. Chim. Fr.* **1970**, *93*, 190.

32. Wildner, M.; Giester, G., The Crystal Structures of Kieserite-Type Compounds. I. Crystal Structures of $Me(II)So_4 \bullet H_2O$ (Me = Mn,Fe,Co,Ni,Zn). *Neues Jahrb. Mineral.* **1991**, 296-306.

33. Marion, G. M.; Kargel, J. S.; Catling, D. C., Modeling Ferrous–Ferric Iron Chemistry with Application to Martian Surface Geochemistry. *Geochim. Cosmochim. Acta* **2008**, *72*, 242-266.

34. Makrides, A. C., Dissolution of Iron in Sulfuric Acid and Ferric Sulfate Solutions. *J. Electrochem. Soc.* **1960**, *107*, 869-877.

35. Hakey, P. M.; Allis, D. G.; Ouellette, W.; Korter, T. M., Cryogenic Terahertz Spectrum of (+)-Methamphetamine Hydrochloride and Assignment Using Solid-State Density Functional Theory. *J. Phys. Chem. A* **2009**, *113*, 5119-5127.

36. Rice, A.; Jin, Y.; Ma, X. F.; Zhang, X. C.; Bliss, D.; Larkin, J.; Alexander, M., Terahertz Optical Rectification from 〈110〉 Zinc-Blende Crystals. *Appl. Phys. Lett.* **1994**, *64*, 1324-1326.

37. Zhang, X. C.; Ma, X. F.; Jin, Y.; Lu, T. M.; Boden, E. P.; Phelps, P. D.; Stewart, K. R.; Yakymyshyn, C. P., Terahertz Optical Rectification from a Nonlinear Organic Crystal. *Appl. Phys. Lett.* **1992**, *61*, 3080-3082.

38. Wu, Q.; Litz, M.; Zhang, X. C., Broadband Detection Capability of Znte Electro-Optic Field Detectors. *Appl. Phys. Lett.* **1996**, *68*, 2924-2926.

39. Dovesi, R. O., R.; Civalleri, B.; Roetti, C.; Saunders, V. R.; Zicovich-Wilson, C. M. *CRYSTAL09*, University of Torino: Torino, 2009.

40. Becke, A. D., Density-Functional Thermochemistry. III. The Role of Exact Exchange. *J. Chem. Phys.* **1993**, *98*, 5648-5652.

41. Krishnan, R.; Binkley, J. S.; Seeger, R.; Pople, J. A., Self-Consistent Molecular Orbital Methods. XX. A Basis Set for Correlated Wave Functions. *J. Chem. Phys.* **1980**, *72*, 650-654.

42. Noel, Y.; Zicovich-Wilson, C. M.; Civalleri, B.; D'Arco, P.; Dovesi, R., Polarization Properties of Zno and Beo: An *ab initio* Study through the Berry Phase and Wannier Functions Approaches. *Phys. Rev. B.* **2001**, *65*, 014111.

43. Slocum, D. M.; Slingerland, E. J.; Giles, R. H.; Goyette, T. M., Atmospheric Absorption of Terahertz Radiation and Water Vapor Continuum Effects. *J. Quant. Spectrosc. Radiat. Transfer* **2013**, *127*, 49-63.

44.   Walther, M.; Fischer, B. M.; Uhd Jepsen, P., Noncovalent Intermolecular Forces in Polycrystalline and Amorphous Saccharides in the Far Infrared. *Chem. Phys.* **2003**, *288*, 261-268.

45.   Baur, W., On the Crystal Chemistry of Salt Hydrates. III. The Determination of the Crystal Structure of $FeSO_4.7H_2O$ (Melanterite). *Acta Crystallographica* **1964**, *17*, 1167-1174.

46.   Malinowski, P. J.; Derzsi, M.; Mazej, Z.; Jagličić, Z.; Gaweł, B.; Łasocha, W.; Grochala, W., Agiiso4: A Genuine Sulfate of Divalent Silver with Anomalously Strong One-Dimensional Antiferromagnetic Interactions. *Angew. Chem.* **2010**, *122*, 1727-1730.

47.   Paul, G.; Choudhury, A.; Sampathkumaran, E. V.; Rao, C. N. R., Organically Templated Mixed-Valent Iron Sulfates Possessing Kagomé and Other Types of Layered Networks. *Angew. Chem. Int. Ed.* **2002**, *41*, 4297-4300.

48.   Frazer, B.; Brown, P., Antiferromagnetic Structure of Crv and the Anhydrous Sulfates of Divalent Fe, Ni, and Co. *Phys. Rev.* **1962**, *125*, 1283-1291.

49.   Wildner, M.; Giester, G., Crystal Structure Refinements of Synthetic Chalcocyanite ($CuSO_4$) and Zincosite ($ZnSO_4$). *Mineralogy and Petrology* **1988**, *39*, 201-209.

50.   Zahrobsky, R. F.; Baur, W. H., On the Crystal Chemistry of Salt Hydrates. V. The Determination of the Crystal Structure of $CuSO_4 • 3H_2O$ (Bonattite). *Acta Crystallogr. Sect. B* **1968**, *24*, 508-513.

51.   Rentzeperis, P. J.; Soldatos, C. T., The Crystal Structure of the Anhydrous Magnesium Sulphate. *Acta Crystallographica* **1958**, *11*, 686-688.

52.   Cheung, K. P.; Auston, D. H., Excitation of Coherent Phonon Polaritons with Femtosecond Optical Pulses. *Phys. Rev. Lett.* **1985**, *55*, 2152-2155.

53. Cavalleri, A.; Wall, S.; Simpson, C.; Statz, E.; Ward, D. W.; Nelson, K. A.; Rini, M.; Schoenlein, R. W., Tracking the Motion of Charges in a Terahertz Light Field by Femtosecond X-Ray Diffraction. *Nature* **2006**, *442*, 664-666.

54. Bakker, H. J.; Hunsche, S.; Kurz, H., Observation of Thz Phonon-Polariton Beats in $LiTaO_3$. *Phys. Rev. Lett.* **1992**, *69*, 2823-2826.

55. Feurer, T.; Stoyanov, N. S.; Ward, D. W.; Vaughan, J. C.; Statz, E. R.; Nelson, K. A., Terahertz Polaritonics. *Annual Review of Materials Research* **2007**, *37*, 317-350.

56. Stoyanov, N. S.; Ward, D. W.; Feurer, T.; Nelson, K. A., Terahertz Polariton Propagation in Patterned Materials. *Nat. Mater.* **2002**, *1*, 95-98.

57. Bittner, B.; Scherm, M.; Schoedl, T.; Tyroller, T.; Schwarz, U. T.; Max, M., Phonon-Polariton Damping by Low-Frequency Excitations in Lithium Tantalate Investigated by Spontaneous and Stimulated Raman Scattering. *J. Phys.: Condens. Matter* **2002**, *14*, 9013.

58. Hushur, A.; Gvasaliya, S.; Roessli, B.; Lushnikov, S.; Kojima, S., Ferroelectric Phase Transition of Stoichiometric Lithium Tantalate Studied by Raman, Brillouin, and Neutron Scattering. *Phys. Rev. B.* **2007**, *76*, 064104.

59. Wiederrecht, G. P.; Dougherty, T. P.; Dhar, L.; Nelson, K. A.; Leaird, D. E.; Weiner, A. M., Explanation of Anomalous Polariton Dynamics in $LiTaO_3$. *Phys. Rev. B.* **1995**, *51*, 916-931.

60. Kojima, S.; Kitahara, H.; Nishizawa, S.; Takeda, M. W., Dielectric Properties of Ferroelectric Lithium Tantalate Crystals Studied by Terahertz Time-Domain Spectroscopy. *Japanese journal of applied physics* **2003**, *42*, 6238.

61.   Lee, Y.-S.; Tomaino, J. L.; Jameson, A. D.; Khitrova, G.; Gibbs, H. M.; Stroech, A.; Kira, M.; Koch, S. In *Interaction of Strong Terahertz Pulses with Exciton-Polaritons in Quantum-Well Microcavity*, CLEO:2011 - Laser Applications to Photonic Applications, Baltimore, Maryland, 2011/05/01; Optical Society of America: Baltimore, Maryland, 2011; p QMB2.

62.   Shluger, A. L.; Stoneham, A. M., Small Polarons in Real Crystals: Concepts and Problems. *J. Phys.: Condens. Matter* **1993**, *5*, 3049.

63.   Dzedolik, I. V.; Pereskokov, V., Variation of Spectral Properties of Dielectric Ionic Crystal in the Terahertz Range Due to the Polariton Absorption. *Appl. Opt.* **2014**, *53*, 3318-3327.

CHAPTER 13: Evaluation of Range-Corrected Density Functionals for the Simulation of Pyridinium-Containing Molecular Crystals

The material contained within this chapter is published in the *Journal of Physical Chemistry A* (Ruggiero, M.T.; Gooch, J.; Zubieta, J.; Korter, T.M. *J. Phys. Chem. A* **2016.** *In press.*). This article has been reproduced with permission from the American Chemical Society.
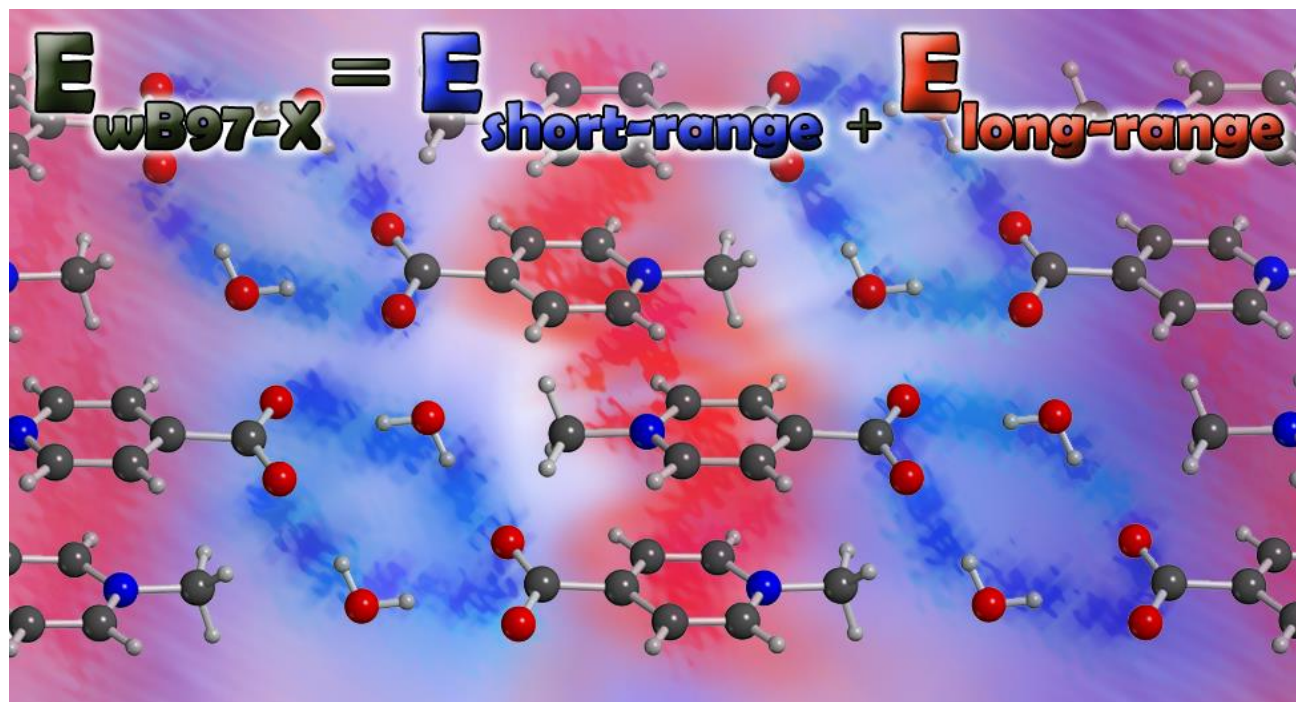
Abstract

The problem of non-local interactions in density functional theory calculations has in part been mitigated by the introduction of range-corrected functional methods. While promising solutions, the continued evaluation of range corrections in the structural simulations of complex molecular crystals is required to judge their efficacy in challenging chemical environments. Here, three pyridinium based crystals, exhibiting a wide range of intramolecular and intermolecular interactions, are used as benchmark systems for gauging the accuracy of several range-corrected density functional techniques. The computational results are compared to low-temperature experimental single-crystal X-ray diffraction and terahertz spectroscopic measurements, enabling the direct assessment of range correction in the accurate simulation of the potential energy surface minima and curvatures. Ultimately, the simultaneous treatment of both short- and long-range effects by the ωB97-X functional was found to be central to its rank as the top performer in reproducing the complex array of forces that occur in the studied pyridinium solids. These results demonstrate that while long-range corrections are the most commonly implemented range-dependent improvements to density functionals, short-range corrections are vital for the accurate reproduction of forces that rapidly diminish with distance, such as quadrupole-quadrupole interactions.

13.1 Introduction

Considerable work has been done to address the range-related problems, such as dissociation[1] and charge-transfer phenomena[2], found in density functional theory (DFT) calculations.[3-6] These studies have resulted in new classes of density functionals such as range-separated hybrids and meta-global gradient approximation (mGGA) forms.[7-11] These techniques are often evaluated on isolated molecular clusters[12-15], yet to judge their true universality and transferability, they must also be tested against solid materials where range effects dominate electronic and molecular structures.[16-18] Solid-state DFT calculations based on periodic boundary conditions offer a means for investigating the balance between intramolecular and intermolecular interactions within crystals, providing valuable insight.[19-22] While most range-modified approaches respond effectively to a specific problem (*i.e.* long-range electrostatic corrections), they often sacrifice accuracy in other areas thereby creating potential issues for complex solids where competition exists between numerous forces of varying ranges.[2, 8, 23-26] Here, the ability to capture both intramolecular and intermolecular forces in pyridinium-containing crystals is evaluated for several density functionals belonging to the GGA, hybrid, range-corrected, and mGGA classes.

Pyridinium carboxylates often form 1:1 or 2:1 complexes with various ions and acids, with their electronic configurations making them good proton acceptors.[27-29] The studied pyridine carboxylic acids (**Figure 13-1**) contain complex combinations of internal and external forces that determine the structures and affect the bulk physical properties of the solids. Although each crystal represents a unique geometry, they all contain an extensive set of generally similar interactions, including hydrogen bonding, ion-ion, π-stacking, and London

forces. Each contributes to differing degrees as a function of distance, making these solids excellent candidates for the evaluation of range-corrected DFT models. The results of the simulations are compared to experimental low-temperature single-crystal X-ray diffraction (XRD) and terahertz spectroscopic data, which are highly sensitive to the interactions within the solids and their accurate modelling signals a reliable density functional.[30-33] Crystallographic data is of clear importance since the packing of the components in the solid state is a direct consequence of the interaction energies within the crystals.[34-37] Low-frequency vibrational data adds greatly to the evaluation of DFT performance by providing information about the force constants governing the intermolecular coordinates in the crystal. The sub-100 cm^{-1} spectra are strongly influenced by intermolecular forces, providing a means for evaluating the calculation of potential energy surface curvatures and minima.[38-39] The combined experimental methods better highlight the strengths and weaknesses of the tested density functionals and their successful reproduction serve as a milestone for range-corrected DFT methodologies.
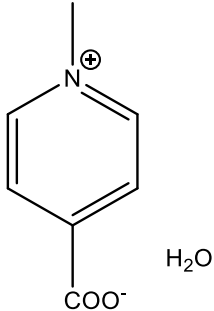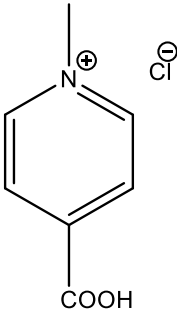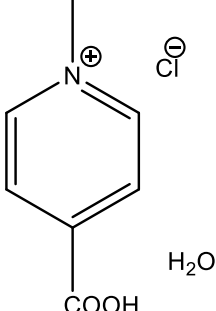
N-methyl-4-carboxylate pyridinium (inner-salt) monohydrate	N-methyl-4-carboxypyridinium chloride	N-methyl-4-carboxypyridinium chloride monohydrate
Me4CP·H₂O	Me4CP·Cl	Me4CP·Cl·H₂O

Figure 13-1. Skeletal structures and abbreviated naming for the three pyridinium crystals.

391

13.2 Methods

13.2.1 Synthetic Procedure

All carboxypyridinium salts were synthesized using methods derived from a previous publication.[40] All reagents were purchased from Alfa Aesar.

13.2.1.1 N-methyl-4-carboxylate pyridinium monohydrate (Me4CP·H$_2$O)

15 g of isonicotinic acid was dissolved in 70 mL of methanol and 13 mL of iodomethane and heated to 70° C for 48 h in a sealed tube, after which yellow crystals formed. The crystals were filtered and washed with acetone, then dried in ambient conditions for 1 h. The dried solid was dissolved in 20 mL of water and 5 mL of propylene oxide, and again sealed for 48 h. The organic layer was extracted with diethyl ether which was subsequently allowed to evaporate. Crystals of Me4CP·H$_2$O formed after approximately two days.

13.2.1.2 N-methyl-4-carboxypyridinium chloride (Me4CP·Cl)

The Me4CP·H$_2$O solid was dissolved in methanol with hydrochloric acid added to a concentration of 1 M. After a few days, large crystals of Me4CP·Cl formed that were suitable for single-crystal XRD measurements.

13.2.1.3 N-methyl-4-carboxypyridinium chloride monohydrate (Me4CP·Cl·H₂O)

The chloride salt was left open to standard laboratory conditions for 1 week, during which time atmospheric moisture (relative humidity of approximately 50-70 %) caused total conversion to the monohydrate chloride salt. The crystals underwent a visible appearance change, altering their habit from blocks to plates. Single-crystal XRD revealed the presence of cocrystallized water, and conversion of the bulk sample was confirmed using powder X-ray diffraction (PXRD pattern available in **Appendix I**).

13.2.2 Experimental

Low-temperature (90 K) single-crystal and powder XRD data for all compounds were collected on a Bruker KAPPA APEX DUO diffractometer equipped with an APEX II CCD system.[41] Single-crystal and powder collections utilized monochromatic Mo Kα radiation (λ = 0.71073 Å) and Cu Kα radiation (λ = 1.5418 Å), respectively. The data were corrected for Lorentz and polarization effects[42], with absorption corrections made using SADABS.[43] Structures were solved by direct methods, and refinements carried out using the SHELXTL crystallographic software.[44] Following assignment of all non-hydrogen atoms, the models were refined against F^2 first using isotropic and then using anisotropic thermal displacement parameters. The hydrogen atoms were introduced based on residual electron density and subsequently refined isotropically. Neutral atom scattering coefficients along with anomalous dispersion corrections were taken from the International Tables, Vol. C.[45] The structure of

Me4CP·Cl was twinned (non-merohedral) and the two domains were determined with the CELL_NOW software package.[46]

To prepare for terahertz spectroscopic experiments, the samples were pulverized with PTFE (w/w ~3 %) in a stainless steel ball mill and pressed into 13 mm x 2 mm pellets. To minimize absorption from atmospheric water[47-48], the spectrometer was continuously purged with dry air and the sample chamber held under constant vacuum. An amplified Ti:Sapphire pulsed laser system[49] and zinc telluride crystals were used to both generate and detect the terahertz radiation through optical rectification[50-51] and free-space electrooptic sampling[52], respectively. Thirty-two time-domain waveforms were acquired, averaged, and Fourier transformed to produce terahertz transmission spectra for each sample. Absorption spectra (ε, M^{-1}cm^{-1}, in terms of crystallographic unit cells) were obtained by division of the sample data set by that of a blank (pure PTFE), and the terahertz spectra shown are a result of four averaged absorption data sets.

13.2.3 Theoretical

The *ab initio* CRYSTAL14 code[53], which incorporates periodic boundary conditions, was used for all solid-state calculations. Geometry optimizations were performed using experimental single-crystal XRD positions as the initial atomic coordinates. The solids were allowed to fully relax with the only constraint being their space group symmetries. Vibrational normal mode eigenvalues and eigenvectors were calculated numerically within the harmonic limit, and infrared intensities were calculated using the Berry phase method.[54] The harmonic approximation has been proven effective for simulating the low-frequency vibrational spectra of various

solids.[55-57] The energy convergence criteria were set to $\Delta E < 10^{-8}$ and 10^{-10} hartree for the optimization and vibrational calculations, respectively.

A wide range of density functionals were used and evaluated, including generalized gradient approximation (GGA), hybrid, hybrid range-corrected, and hybrid meta-GGA classes. The GGA class was represented by the Perdew-Burke-Ernzerhof (PBE)[58] and the Beck-Lee-Yang-Parr (BLYP) functionals, where BLYP is a combination of the Becke B88[59] and Lee-Yang-Parr (LYP)[60] functionals for exchange and correlation, respectively. Hybrid functionals incorporating a constant amount of exact Hartree-Fock exchange were represented by the PBE0[61], B3LYP[62], and B97H[63-64] functionals, which are modifications of the PBE, BLYP and B97[63] functionals, respectively. A variety of range-corrected functionals, which are hybrid functionals parameterized by incorporating exact local and/or non-local Hartree-Fock exchange based on distance, were also tested. The PBE functional has been used as the foundation of three range-corrected functionals representing short (HSE06[65]), medium (HISS[66-67]), and long-range (LC-ωPBE[68]) correction limits. Two additional long-range corrected functionals, LC-ωBLYP[68] and ωB97[69], were also tested, along with one multi-range functional, ωB97-X[69], that contained exact exchange contributions in both the short and long-range limits. Finally, the hybrid meta-GGA class was represented by the M062X[70] functional, which was specifically formulated to handle non-covalent interactions and medium-range correlation effects.

London dispersion interactions were taken into account using the DFT-D* semi-empirical dispersion correction[71], with solid-state optimized radii values as determined by Civalleri *et al.*[72] The dispersion correction was included when using GGA and hybrid functionals (with s_6 coefficients set to 0.75 and 1.05, respectively), but was not included in the range-corrected or hybrid meta-GGA simulations due to their existing parameterizations for weak forces.[70] This

distinction was made because one goal of this work is to determine if range-corrected methods can deliver the same or better results as compared to dispersion-corrected techniques. However to gauge the impact of the *ex post* correction, test simulations were performed with HSE-06-D*, HISS-D* and LC-ωPBE-D* (see **Appendix I**). The atom-centered double-zeta 6-31G(d,p) basis set[73] was used for all atom types, balancing chemical accuracy with calculation time requirements. The influence of larger triple-zeta basis sets (6-311G(d,p) [74] and pob-TZVP[75]) on the structural errors was evaluated and it was found that the trends across functionals were preserved regardless of basis set size (see **Appendix I**). Due to the lack of significant improvements in calculation quality coupled with the drastically increased computational cost (approximate fivefold-increase in calculation time), the 6-31G(d,p) basis set was used for all simulations.

13.3 Results and Discussion

13.3.1 Experimental Structural Analysis

13.3.1.1 N-methyl-4-carboxylate pyridinium (inner-salt) monohydrate (Me4CP·H₂O)

The 90 K structure obtained for this work is in good agreement with the previous room-temperature structure[40]. Me4CP·H_2O crystallizes in the triclinic $P\bar{1}$ space group, with unit cell parameters of a = 6.726 Å, b = 7.612 Å, c = 7.708 Å, α = 72.223°, β = 72.141°, γ = 89.554°, and V = 356.135 Å³ (**Figure 13-2**). The unit cell contains two formula units (Z=2), with one symmetrically unique formula unit (Z'= 1). The pyridinium ring is zwitterionic, formally containing a negatively charged carboxylate group and a positively charged aromatic nitrogen atom. The co-crystallized water molecules form hydrogen bonds with carboxylate oxygens in adjacent planes, resulting in hydrogen-bonded dimers containing two stacked pyridinium rings and two water molecules. This hydrogen bonding network causes the carboxylate substituent to deviate from co-planarity with the ring, twisting by 11.48°.
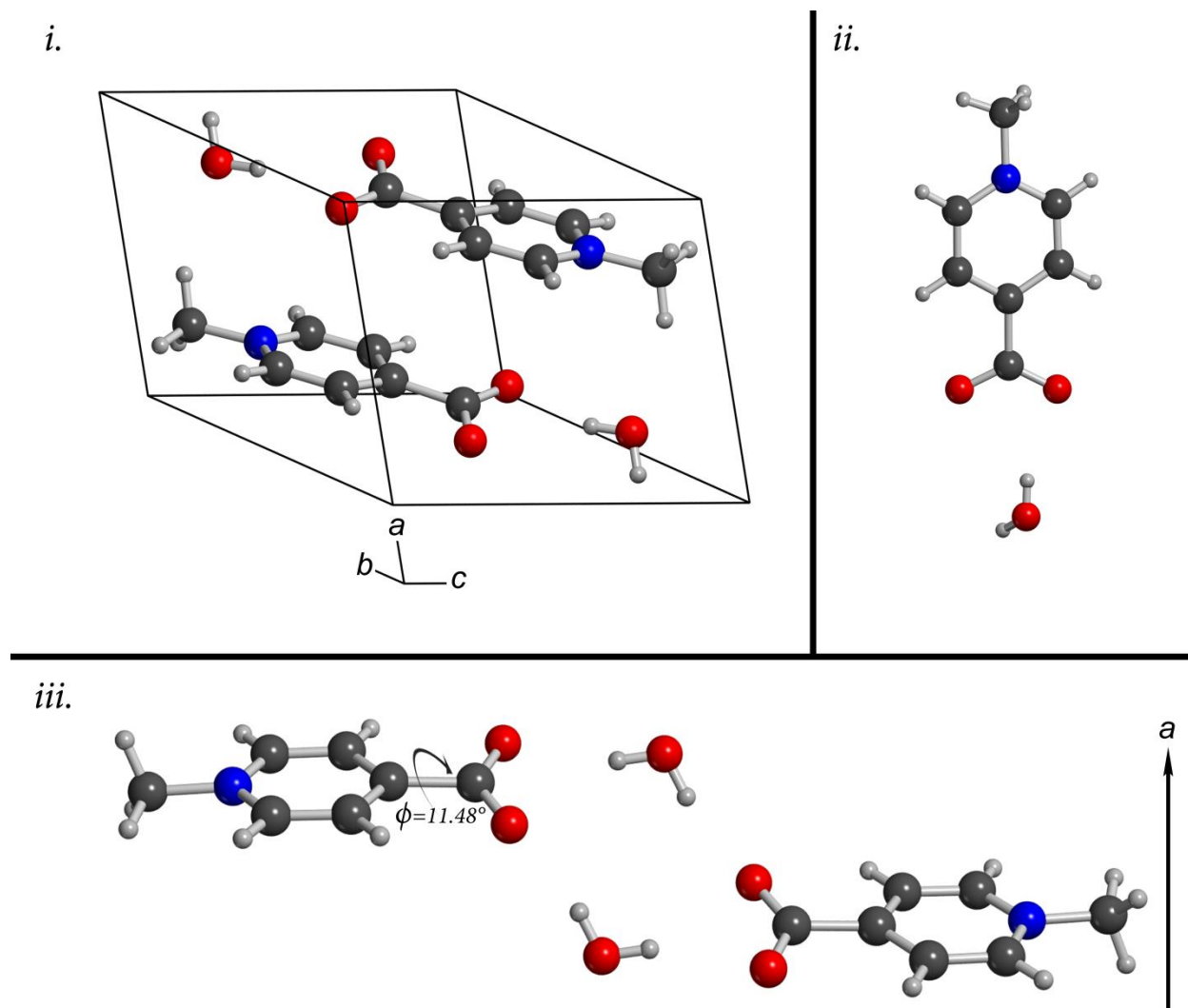
Figure 13-2. Experimental single-crystal XRD determined structure of Me4CP·H₂O (*i*), along with its formula unit (*ii*) and dimer structural unit (*iii*).

13.3.1.2 N-methyl-4-carboxypyridinium chloride (Me4CP·Cl)

The 90 K crystal structure of Me4CP·Cl was determined to be a new polymorph of the previously determined orthorhombic *Pnma* room-temperature structure[40]. The low-temperature variant is non-merohedrally twinned, crystallizing in the monoclinic *P 2₁/n* space group with lattice parameters of $a = 6.530$ Å, $b = 12.865$ Å, $c = 9.501$ Å, $\beta = 94.207°$, and $V = 796.016$ Å^3 (**Figure 13-3**). The structural changes of the phase transition are subtle, with only the *a*-axis and β-angle changing with any significance. The low-temperature structure reported here will be used for all analyses in this work.

The unit cell of **Me4CP·Cl** contains a symmetrically independent formula unit ($Z'=1$), with four units in the crystalline cell ($Z = 4$). Unlike the zwitterionic monohydrate, the pyridinium ring is cationic and is charge balanced by a chlorine anion. The chloride forms a hydrogen bond with the carboxyl substituent and an ionic bond with nitrogen atoms in adjacent planes, with the two interactions nearly perpendicular (95.15°). This causes the carboxyl groups to adopt a co-planar orientation with the rings, resulting in the formation of infinite parallel sheets.
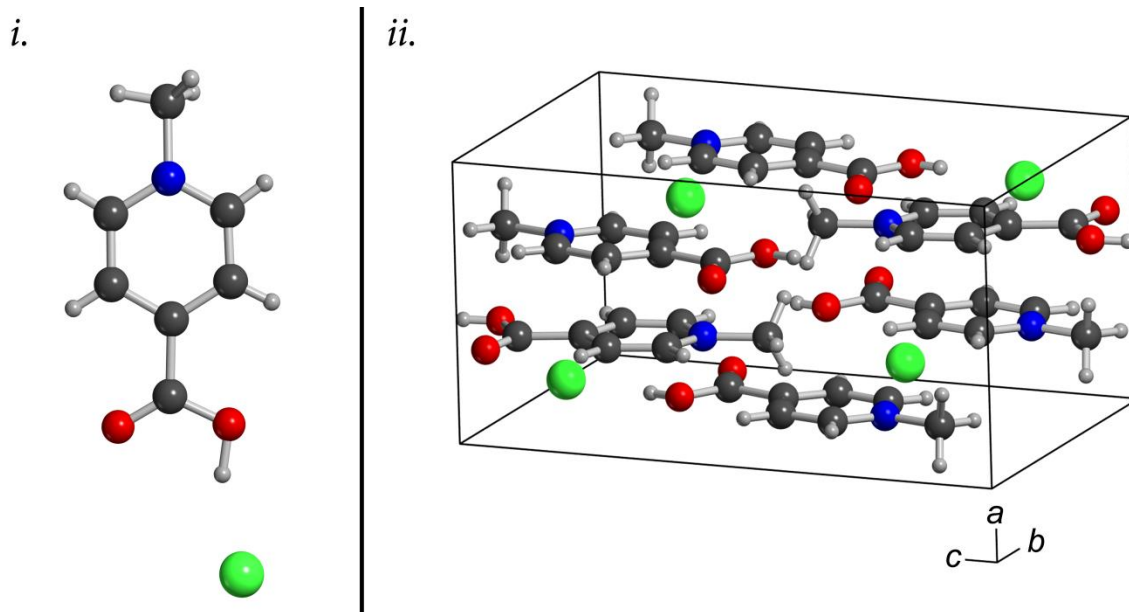
Figure 13-3. Formula unit (*i*) and experimental 90 K XRD crystal structure (*ii*) of Me4CP·Cl.

13.3.1.3 N-methyl-4-carboxypyridinium chloride monohydrate (Me4CP·Cl·H₂O)

The previously undetermined crystal structure of Me4CP·Cl·H$_2$O was obtained at 90 K. Me4CP·Cl·H$_2$O crystallizes in the monoclinic $P\,2_1/c$ space group, with lattice parameters of $a = 5.140$ Å, $b = 24.317$ Å, $c = 7.093$ Å, $\beta = 94.971°$, and $V = 883.160$ Å^3 (**Figure 13-4**). There are four formula units in the crystallographic cell ($Z=4$), with one symmetrically independent unit ($Z'=1$). The Me4CP·Cl·H$_2$O crystal combines structural features similar to those observed in the two aforementioned crystals. The carboxyl substituent is co-planar with the pyridinium ring, with the heavy atoms again forming parallel sheets in the (-102) miller plane. Each co-crystallized water forms two hydrogen bonds, one with the carboxyl group and the other involving the chlorine anion. The chlorine anion is almost directly below the positively charged nitrogen in an adjacent sheet. The combination of these multiple interaction types results in more complicated structural features in this crystal as compared to the other solid samples considered here.
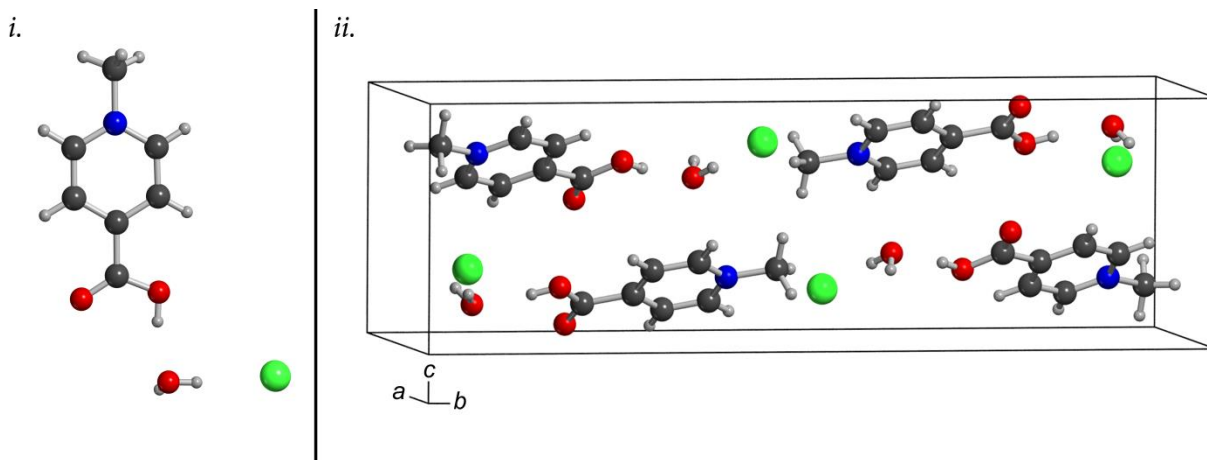
Figure 13-4. Formula unit (*i*) and experimental 90 K crystal structure (*ii*) of Me4CP·Cl·H₂O.

13.3.2 Theoretical Structural Results

The coexistence of a wide range of intramolecular and intermolecular forces in the pyridinium structures make them ideal benchmarks for evaluating the performance of computational methodologies. The crystalline geometries of each solid were fully optimized and all twelve functionals performed well with respect to the internal molecular geometries, with low errors in the heavy-atom covalent bond lengths and angles (**Figure 13-5**). This is highlighted with the best simulation yielding an overall average error in the covalent bond lengths of 0.15 % (LC-ωBLYP/Me4CP·H_2O), while the worst produced a 1.32 % error (PBE0-D*/Me4CP·Cl). Molecular dihedral angles are often the most difficult parameter to reproduce due to their dependence on internal and external factors[76-78], but in the case of the two chloride salts the errors in dihedrals are low and comparable to the bond and angle values. However in Me4CP·H_2O, the dihedral RMSD values are almost a factor of two greater than the hydrochloride salts. Closer inspection shows that the average dihedral errors are skewed by relatively large errors in the dihedral angle governing the carboxylate substituent, with some functionals deviating by more than 5° from the experimental value.
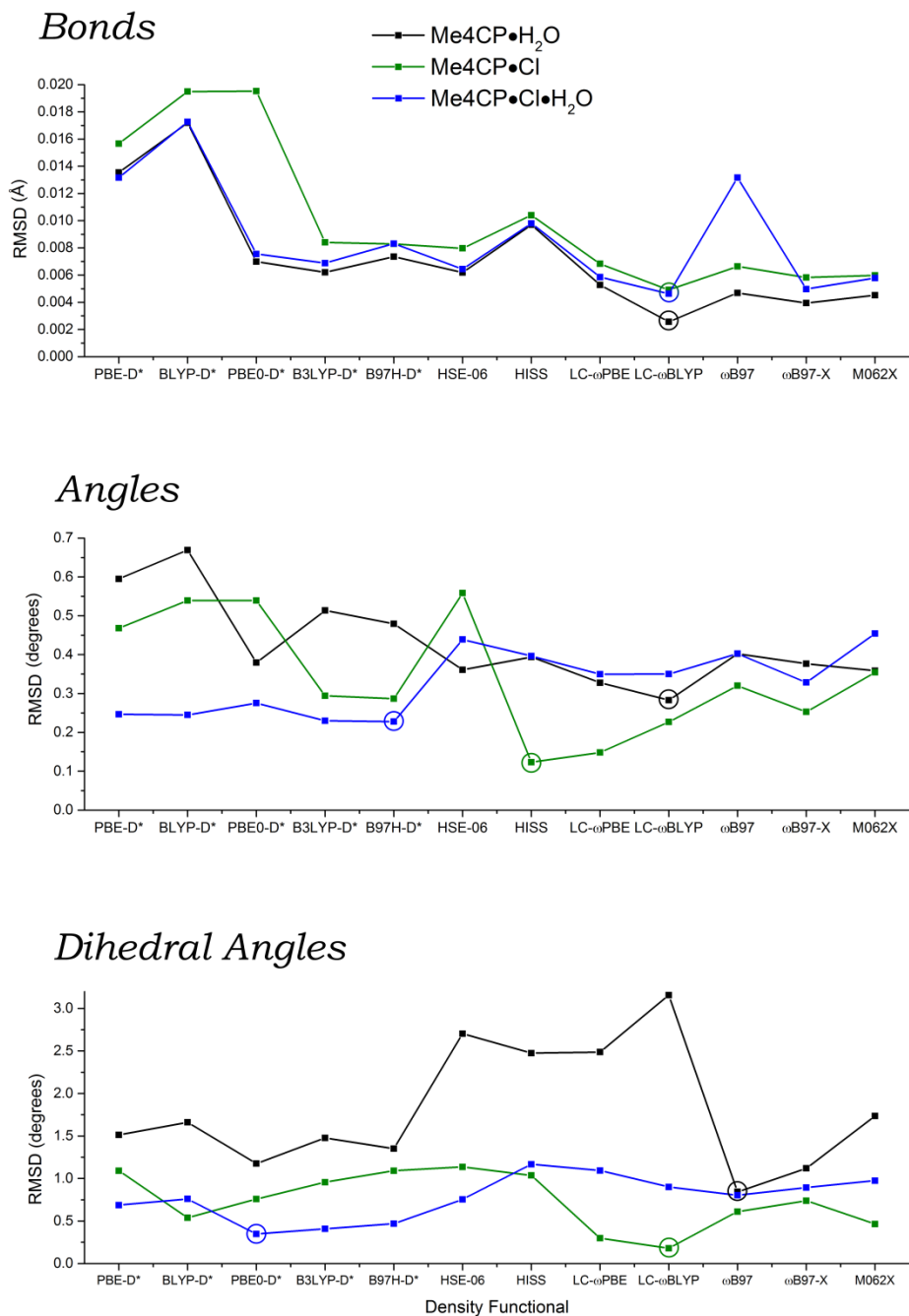
Figure 13-5: Heavy-atom covalent bond, angle, and dihedral angle root-mean-squared deviations (RMSD) for the three pyridinium solids (Me4CP·H$_2$O = black, Me4CP·Cl = green, Me4CP·Cl·H$_2$O = blue). Circles indicate the best performing functional for a given solid.

The good reproduction of internal geometries by all twelve functionals is not mirrored in the calculated crystalline packing parameters (**Figure 13-6**). While the errors in the internal structures are generally very consistent across the different functionals, the errors in lattice dimensions are not, with the overall best performance coming from the multi-range-corrected ωB97-X calculations (**Table 13-1**). This particular functional is unique among those tested in that it contains exact exchange at *both* short and long-range regions, as opposed to the other range-corrected functionals which address only one a single range. Because all three crystals experience generally similar external interactions (*i.e.* π-stacking), and the ωB97-X calculations were found to have the smallest errors, it is clear that the explicit treatment of short and long-range effects simultaneously is important for accurately capturing the balance between the array of forces present in complex materials.
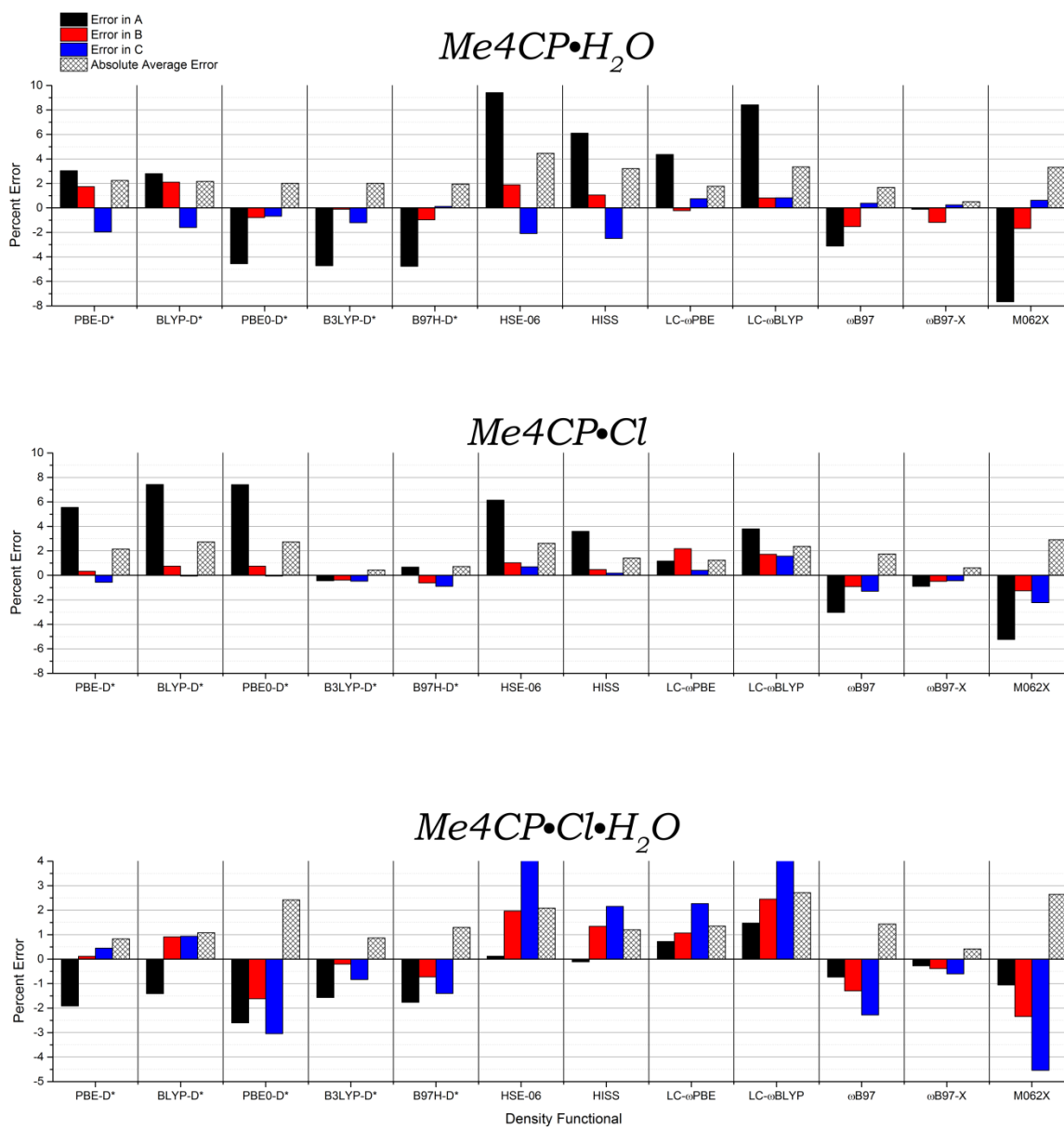
Figure 13-6: Calculated lattice parameter errors and average absolute errors for the three pyridinium solids.

Table 13-1. The best and worst performing functionals based on absolute average unit cell percent errors for the three pyridinium systems.

	Me4CP·H$_2$O		Me4CP·Cl		Me4CP·Cl·H$_2$O[a]	
Best	ωB97-X	0.514 %	ωB97-X	0.418 %	B3LYP	0.432 %
Worst	HSE06	4.464 %	LC-ωBLYP	2.714 %	M062X	2.908 %

[a]ωB97-X is the second best performing functional for Me4CP·Cl·H$_2$O, with an average error of 0.607 %

The range-corrected variants of the PBE functional, which has been modified to contain short (HSE06), medium (HISS), and long-range (LC-ωPBE) corrections, enables the effect of local versus nonlocal exchange contributions to be systematically evaluated. Compared to the pure PBE-D* results, HSE06 provides an improvement in the side-to-side separation between molecules within each sheet over LC-ωPBE (the *b* and *a* axes in Me4CP·Cl and Me4CP·Cl·H_2O, respectively, see **Figure 13-5**). Because these particular coordinates are dominated by a mixture of London dispersion[79] and quadrupole-quadrupole interactions[80-82], which have $1/r^6$ and $1/r^5$ dependencies, respectively, the short-range correction is able to appropriately represent them since their importance rapidly diminishes with distance. However this functional performs poorly in the simulation of axes where π-stacking is important (see **Figure 13-5**). Because the layer separation is influenced primarily by electrostatic forces, having $1/r$ or $1/r^3$ dependencies, long-range corrections are necessary to accurately model these interactions. It is important to note that further advanced functionals that incorporate more sophisticated dispersion corrections, could more accurately describe these interactions; however these techniques are not yet broadly available.[83-85] Given the nature of the forces in these solids and their relative importance, it is appropriate that the long-range LC-ωPBE functional has the best overall performance amongst the PBE family of range-corrected functionals. However, the increased weighting of the long-range region in LC-ωPBE does lead to decreased accuracy in the short-range limit, further indicating the reasons behind the exceptional performance seen in the ωB97-X calculations.

13.3.3 Vibrational Analysis

The low errors produced by ωB97-X indicate that the minimum of the potential energy surface was accurately located in the geometry simulations, but provides no data regarding the accuracy of the surface curvature or the charge distributions within these systems. Such information can be accessed by comparison of simulated vibrational spectra with experimentally measured terahertz spectra. The normal mode frequencies and infrared intensities of each solid were calculated using ωB97-X, and the simulated spectra compared with experiment (**Figure 13-7**). In the particular case of Me4CP·H$_2$O, the lowest frequency optically-allowed vibration was predicted to occur at 97.32 cm^{-1} (outside the instrument bandwidth), and thus omitted from this analysis.

The simulated spectra are in excellent agreement with the experimental results, considering both the frequencies and intensities of the absorptions. To demonstrate the sensitivity of the terahertz spectra to density functional choice and structural simulations, the vibrational spectra of the two crystals were also calculating using PBE-D*, a method commonly employed.[86-87] In the case of Me4CP·Cl, for which PBE-D* had large errors in both the *a* and *c* axes, the predicted frequencies are in poor agreement with the experimental spectrum. However, the intensities are comparable, meaning that the charge distribution (which is based largely on internal structure) is reasonably well modelled. In the Me4CP·Cl·H$_2$O crystals, where the PBE-D* optimizations resulted in lower unit cell errors, the correlation between experiment and theory is much better. This highlights the sensitivity of both the simulation of low-frequency vibrational spectra and experimental terahertz spectroscopic measurements to both external and

internal potential energy surfaces, and that both must be well accounted for by the applied theory in order to arrive at results that correlate well with experimental observations.
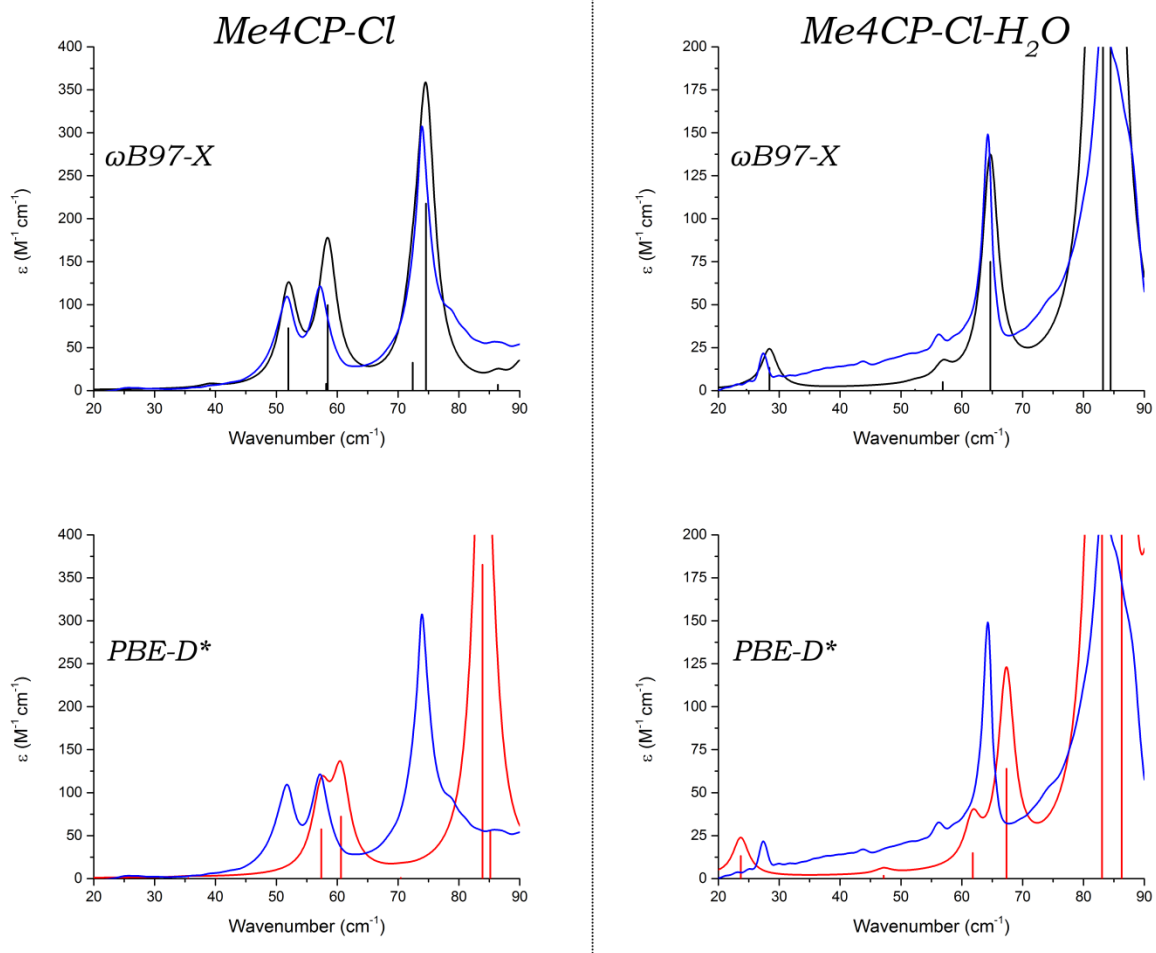
Figure 13-7. Experimental terahertz spectra (blue) and simulated ωB97-X (black) and PBE-D* (red) vibrational spectra for two pyridinium crystals. Simulated spectra were convolved with Lorentzian lineshapes using empirical fits. The slight feature at 75 cm^{-1} in Me4CP·Cl·H$_2$O is due to minor Me4CP·Cl contamination.

13.4 Conclusions

Density functional theory calculations are an effective method for investigating the multiple interactions within molecular crystals, yet non-local effects have proven to be difficult to reproduce by common functionals. Numerous methods for rectifying these shortcomings have been proposed and used with success, but the introduction of range-corrected functionals show the greatest promise. Pyridinium carboxylate crystals were used as benchmark systems to examine the performance of a range of density functionals on recreating the complex forces present in these solids. Functionals belonging to the GGA, hybrid, range-corrected hybrid, and meta-GGA classes were tested, with the results showing that all methods accurately reproduce internal molecular structures, but many fail when modelling external interactions. It was shown that the range-corrected ωB97-X functional, which contains both short and long-range corrections, is the best choice for these types of crystals. Finally, the popular PBE-D* functional and the ωB97-X functional were both used to simulate the vibrational spectra of the crystals, with the results showing that ωB97-X was in better agreement with experiment than the PBE-D* functional. The excellent correlation between experiment and theory (both structural and vibrational) indicates that ωB97-X is the best choice when calculating the properties of pyridinium-containing solids that contain a variety of intermolecular forces that have differing range dependencies.

13.5 Acknowledgements

Supporting Information (see APPENDIX I)

The experimental powder X-ray diffraction pattern of Me4CP·Cl·H_2O. This material is available free of charge via the Internet at http://pubs.acs.org. CCDC 1437511-1437513 contain supplemental crystallographic data for this paper. These data can be obtained free of charge from the Cambridge Crystallographic Data Centre via http://www.ccdc.ac.uk/data_request/cif.

13.6 References

1. Bally, T.; Sastry, G. N., Incorrect Dissociation Behavior of Radical Ions in Density Functional Calculations. *J. Phys. Chem. A* **1997**, *101*, 7923-7925.

2. Dreuw, A.; Weisman, J. L.; Head-Gordon, M., Long-Range Charge-Transfer Excited States in Time-Dependent Density Functional Theory Require Non-Local Exchange. *J. Chem. Phys.* **2003**, *119*, 2943-2946.

3. Tsuneda, T.; Hirao, K., Long-Range Correction for Density Functional Theory. *Wiley Interdiscip. Comput. Mol. Sci.* **2014**, *4*, 375-390.

4. Grimme, S., Semiempirical GGA-Type Density Functional Constructed with a Long-Range Dispersion Correction. *J. Comput. Chem.* **2006**, *27*, 1787-1799.

5. Tawada, Y.; Tsuneda, T.; Yanagisawa, S.; Yanai, T.; Hirao, K., A Long-Range-Corrected Time-Dependent Density Functional Theory. *J. Chem. Phys.* **2004**, *120*, 8425-8433.

6. Ángyán, J. G.; Gerber, I. C.; Savin, A.; Toulouse, J., Van Der Waals Forces in Density Functional Theory: Perturbational Long-Range Electron-Interaction Corrections. *Phys. Rev. A* **2005**, *72*, 012510.

7. Refaely-Abramson, S.; Baer, R.; Kronik, L., Fundamental and Excitation Gaps in Molecules of Relevance for Organic Photovoltaics from an Optimally Tuned Range-Separated Hybrid Functional. *Phys. Rev. B.* **2011**, *84*, 075144.

8. Gerber, I. C.; Ángyán, J. G.; Marsman, M.; Kresse, G., Range Separated Hybrid Density Functional with Long-Range Hartree-Fock Exchange Applied to Solids. *J. Chem. Phys.* **2007**, *127*, 054101.

9.   Tao, J.; Perdew, J. P.; Staroverov, V. N.; Scuseria, G. E., Climbing the Density Functional Ladder: Nonempirical Meta-Generalized Gradient Approximation Designed for Molecules and Solids. *Phys. Rev. Lett.* **2003**, *91*, 146401.

10.   Goerigk, L.; Grimme, S., Efficient and Accurate Double-Hybrid-Meta-GGA Density Functionals—Evaluation with the Extended GMTKN30 Database for General Main Group Thermochemistry, Kinetics, and Noncovalent Interactions. *J. Chem. Theory Comput.* **2011**, *7*, 291-309.

11.   Peverati, R.; Truhlar, D. G., Improving the Accuracy of Hybrid Meta-GGA Density Functionals by Range Separation. *J. Phys. Chem. Lett.* **2011**, *2*, 2810-2817.

12.   Vydrov, O. A.; Scuseria, G. E., Assessment of a Long-Range Corrected Hybrid Functional. *J. Chem. Phys.* **2006**, *125*, 234109.

13.   Song, J.-W.; Tokura, S.; Sato, T.; Watson, M. A.; Hirao, K., An Improved Long-Range Corrected Hybrid Exchange-Correlation Functional Including a Short-Range Gaussian Attenuation (LCgau-BOP). *J. Chem. Phys.* **2007**, *127*, 154109.

14.   Yanai, T.; Tew, D. P.; Handy, N. C., A New Hybrid Exchange–Correlation Functional Using the Coulomb-Attenuating Method (CAM-B3LYP). *Chem. Phys. Lett.* **2004**, *393*, 51-57.

15.   Song, J.-W.; Watson, M. A.; Nakata, A.; Hirao, K., Core-Excitation Energy Calculations with a Long-Range Corrected Hybrid Exchange-Correlation Functional Including a Short-Range Gaussian Attenuation (LCgau-BOP). *J. Chem. Phys.* **2008**, *129*, 184113.

16.   York, D. M.; Darden, T. A.; Pedersen, L. G., The Effect of Long-Range Electrostatic Interactions in Simulations of Macromolecular Crystals: A Comparison of the Ewald and Truncated List Methods. *J. Chem. Phys.* **1993**, *99*, 8345-8348.

17. Rhee, M.; Zbib, H. M.; Hirth, J. P.; Huang, H.; Rubia, T. d. l., Models for Long-/Short-Range Interactions and Cross Slip in 3d Dislocation Simulation of Bcc Single Crystals. *Modell. Simul. Mater. Sci. Eng.* **1998**, *6*, 467.

18. Domb, C.; Dalton, N. W., Crystal Statistics with Long-Range Forces: I. The Equivalent Neighbour Model. *Proc. Phys. Soc.* **1966**, *89*, 859.

19. Witko, E. M.; Buchanan, W. D.; Korter, T. M., The Importance of London Dispersion Forces in Crystalline Magnesium Nitrate Hexahydrate. *Inorg. Chim. Acta* **2012**, *389*, 176-182.

20. Usvyat, D.; Yin, C.; Wälz, G.; Mühle, C.; Schütz, M.; Jansen, M., Phase Transition in GeF_2 Driven by Change of Type of Intermolecular Interaction. *Phys. Rev. B.* **2012**, *86*, 054102.

21. Dikundwar, A. G.; Row, T. N. G., Evidence for the "Amphoteric" Nature of Fluorine in Halogen Bonds: An Instance of Cl···F Contact. *Cryst. Growth Des.* **2012**, *12*, 1713-1716.

22. van Eijck, L.; Johnson, M. R.; Kearley, G. J., Intermolecular Interactions in Bithiophene as a Model for Polythiophene. *J. Phys. Chem. A* **2003**, *107*, 8980-8984.

23. Körzdörfer, T.; Sears, J. S.; Sutton, C.; Brédas, J.-L., Long-Range Corrected Hybrid Functionals for Π-Conjugated Systems: Dependence of the Range-Separation Parameter on Conjugation Length. *J. Chem. Phys.* **2011**, *135*, 204107.

24. Rohrdanz, M. A.; Martins, K. M.; Herbert, J. M., A Long-Range-Corrected Density Functional That Performs Well for Both Ground-State Properties and Time-Dependent Density Functional Theory Excitation Energies, Including Charge-Transfer Excited States. *J. Chem. Phys.* **2009**, *130*, 054112.

25. Song, J.-W.; Tsuneda, T.; Sato, T.; Hirao, K., Calculations of Alkane Energies Using Long-Range Corrected DFT Combined with Intramolecular Van Der Waals Correlation. *Org. Lett.* **2010**, *12*, 1440-1443.

26. Jacquemin, D.; Perpète, E. A.; Scalmani, G.; Frisch, M. J.; Kobayashi, R.; Adamo, C., Assessment of the Efficiency of Long-Range Corrected Functionals for Some Properties of Large Compounds. *J. Chem. Phys.* **2007**, *126*, 144105.

27. Godzisz, D.; Ilczyszyn, M. M.; Ilczyszyn, M., Classification and Nature of Hydrogen Bonds to Betaine. X-Ray, ^{13}C CP MAS and IR Description of Low Barrier Hydrogen Bonds. *J. Mol. Struct.* **2002**, *606*, 123-137.

28. Rudert, R.; Schulz, B.; Reck, G.; Vollhardt, D.; Kriwanek, J., N-N-Alkyl N,N-Dimethylammonioacetic Acid Bromides: The First Complete Series of Crystal and Molecular Structure Determinations of an Amphiphilic Compound with Alkyl Chain Lengths N = 1 ,..., 16. *Acta Crystallogr. Sect. B: Struct. Sci.* **2000**, *56*, 124-131.

29. Szafran, M.; Kowalczyk, I.; Katrusiak, A.; Dega-Szafran, Z., X-Ray and B3LYP Structures and Vibrational Spectra of Pyridine Betaine Perchlorate Monohydrate and Conformation of $\geq N^+CH_2COO$ Moiety in Crystalline Betaines. *J. Mol. Struct.* **2003**, *651-653*, 621-634.

30. Walther, M.; Fischer, B. M.; Uhd Jepsen, P., Noncovalent Intermolecular Forces in Polycrystalline and Amorphous Saccharides in the Far Infrared. *Chem. Phys.* **2003**, *288*, 261-268.

31. Fischer, B.; Hoffmann, M.; Helm, H.; Modjesch, G.; Jepsen, P. U., Chemical Recognition in Terahertz Time-Domain Spectroscopy and Imaging. *Semicond. Sci. Technol.* **2005**, *20*, S246.

32. Taday, P. F., Applications of Terahertz Spectroscopy to Pharmaceutical Sciences. *Phil. Trans. R. Soc. A* **2004**, *362*, 351-364.

33. Siegrist, K.; Bucher, C. R.; Mandelbaum, I.; Hight Walker, A. R.; Balu, R.; Gregurick, S. K.; Plusquellic, D. F., High-Resolution Terahertz Spectroscopy of Crystalline Trialanine: Extreme Sensitivity to B-Sheet Structure and Cocrystallized Water. *J. Am. Chem. Soc.* **2006**, *128*, 5764-5775.

34. King, M. D.; Blanton, T. N.; Misture, S. T.; Korter, T. M., Prediction of the Unknown Crystal Structure of Creatine Using Fully Quantum Mechanical Methods. *Cryst. Growth Des.* **2011**, *11*, 5733-5740.

35. Kihara, T.; Koba, S., Crystal Structures and Intermolecular Forces of Rare Gases. *J. Phys. Soc. Jpn.* **1952**, *7*, 348-354.

36. Tasumi, M.; Shimanouchi, T., Crystal Vibrations and Intermolecular Forces of Polymethylene Crystals. *J. Chem. Phys.* **1965**, *43*, 1245-1258.

37. R. Desiraju, G., Designer Crystals: Intermolecular Interactions, Network Structures and Supramolecular Synthons. *Chem. Commun.* **1997**, 1475-1482.

38. Schmuttenmaer, C. A., Exploring Dynamics in the Far-Infrared with Terahertz Spectroscopy. *Chem. Rev.* **2004**, *104*, 1759-1780.

39. Zeitler, J. A.; Taday, P. F.; Newnham, D. A.; Pepper, M.; Gordon, K. C.; Rades, T., Terahertz Pulsed Spectroscopy and Imaging in the Pharmaceutical Setting - a Review. *J. Pharm. Pharmacol.* **2007**, *59*, 209-223.

40. Szafran, M.; Koput, J.; Dega-Szafran, Z.; Katrusiak, A., X-Ray and ab initio Studies of the Structure and Vibrational Spectra of 4-Carboxy-1-Methylpyridinium Chloride. *J. Mol. Struct.* **2006**, *797*, 66-81.

41. *Apex2, Data Collection Software*, Version 2011.8-0; Bruker-AXS Inc.: Madison, WI, 2011, 2011.

42. *Saint Plus, Data Reduction Software*, Version 6.45A; Bruker-AXS Inc.: Madison, WI 2013, 2013.

43. Sheldrick, G., SADABS. University of Göttingen, Germany Program for Empirical Absorption Correction of Area Detector Data: 1996.

44. Sheldrick, G., SHELXTL, Version 6.1; Bruker Analytical X-Ray Systems. *Inc.: Madison, WI* **1997**.

45. Wilson, A.; Geist, V., International Tables for Crystallography. Volume C: Mathematical, Physical and Chemical Tables. *Crystal Research and Technology* **1993**, *28*, 110-110.

46. Sheldrick, G., Cell_Now. *Bruker AXS, Madison* **2003**.

47. Ruggiero, M. T.; Bardon, T.; Strlic, M.; Taday, P. F.; Korter, T. M., The Role of Terahertz Polariton Absorption in the Characterization of Crystalline Iron Sulfate Hydrates. *Phys. Chem. Chem. Phys.* **2015**, *17*, 9326-9334.

48. Ruggiero, M. T.; Erba, A.; Orlando, R.; Korter, T. M., Origins of Contrasting Copper Coordination Geometries in Crystalline Copper Sulfate Pentahydrate. *Phys. Chem. Chem. Phys.* **2015**, *17*, 31023-31029.

49. Hakey, P. M.; Allis, D. G.; Ouellette, W.; Korter, T. M., Cryogenic Terahertz Spectrum of (+)-Methamphetamine Hydrochloride and Assignment Using Solid-State Density Functional Theory. *J. Phys. Chem. A* **2009**, *113*, 5119-5127.

50. Rice, A.; Jin, Y.; Ma, X. F.; Zhang, X. C.; Bliss, D.; Larkin, J.; Alexander, M., Terahertz Optical Rectification from 〈110〉 Zinc-Blende Crystals. *Appl. Phys. Lett.* **1994**, *64*, 1324-1326.

51. Zhang, X. C.; Ma, X. F.; Jin, Y.; Lu, T. M.; Boden, E. P.; Phelps, P. D.; Stewart, K. R.; Yakymyshyn, C. P., Terahertz Optical Rectification from a Nonlinear Organic Crystal. *Appl. Phys. Lett.* **1992**, *61*, 3080-3082.

52. Wu, Q.; Litz, M.; Zhang, X. C., Broadband Detection Capability of Znte Electro-Optic Field Detectors. *Appl. Phys. Lett.* **1995**, 2924.

53. Dovesi, R.; Orlando, R.; Erba, A.; Zicovich-Wilson, C. M.; Civalleri, B.; Casassa, S.; Maschio, L.; Ferrabone, M.; De La Pierre, M.; D'Arco, P.*, et al.*, CRYSTAL14: A Program for the *ab initio* Investigation of Crystalline Solids. *Int. J. Quantum Chem* **2014**, *114*, 1287-1317.

54. Noel, Y.; Zicovich-Wilson, C. M.; Civalleri, B.; D'Arco, P.; Dovesi, R., Polarization Properties of Zno and Beo: An *ab initio* Study through the Berry Phase and Wannier Functions Approaches. *Phys. Rev. B.* **2001**, *65*, 014111.

55. Ryder, M. R.; Civalleri, B.; Bennett, T. D.; Henke, S.; Rudić, S.; Cinque, G.; Fernandez-Alonso, F.; Tan, J.-C., Identifying the Role of Terahertz Vibrations in Metal-Organic Frameworks: From Gate-Opening Phenomenon to Shear-Driven Structural Destabilization. *Phys. Rev. Lett.* **2014**, *113*, 215502.

56. Jepsen, P. U.; Clark, S. J., Precise Ab-Initio Prediction of Terahertz Vibrational Modes in Crystalline Systems. *Chem. Phys. Lett.* **2007**, *442*, 275-280.

57.   Delaney, S. P.; Pan, D.; Galella, M.; Yin, S. X.; Korter, T. M., Understanding the Origins of Conformational Disorder in the Crystalline Polymorphs of Irbesartan. *Cryst. Growth Des.* **2012**, *12*, 5017-5024.

58.   Perdew, J. P.; Burke, K.; Ernzerhof, M., Generalized Gradient Approximation Made Simple. *Phys. Rev. Lett.* **1996**, *77*, 3865-3868.

59.   Becke, A. D., Density-Functional Exchange-Energy Approximation with Correct Asymptotic Behavior. *Phys. Rev. A* **1988**, *38*, 3098-3100.

60.   Lee, C.; Yang, W.; Parr, R. G., Development of the Colle-Salvetti Correlation-Energy Formula into a Functional of the Electron Density. *Phys. Rev. B.* **1988**, *37*, 785-789.

61.   Adamo, C.; Barone, V., Toward Reliable Density Functional Methods without Adjustable Parameters: The PBE0 Model. *J. Chem. Phys.* **1999**, *110*, 6158-6170.

62.   Becke, A. D., Density-Functional Thermochemistry. III. The Role of Exact Exchange. *J. Chem. Phys.* **1993**, *98*, 5648-5652.

63.   Becke, A. D., Density-Functional Thermochemistry. V. Systematic Optimization of Exchange-Correlation Functionals. *J. Chem. Phys.* **1997**, *107*, 8554-8560.

64.   Hamprecht, F. A.; Cohen, A. J.; Tozer, D. J.; Handy, N. C., Development and Assessment of New Exchange-Correlation Functionals. *J. Chem. Phys.* **1998**, *109*, 6264-6271.

65.   Krukau, A. V.; Vydrov, O. A.; Izmaylov, A. F.; Scuseria, G. E., Influence of the Exchange Screening Parameter on the Performance of Screened Hybrid Functionals. *J. Chem. Phys.* **2006**, *125*, 224106.

66.   Henderson, T. M.; Izmaylov, A. F.; Scuseria, G. E.; Savin, A., The Importance of Middle-Range Hartree-Fock-Type Exchange for Hybrid Density Functionals. *J. Chem. Phys.* **2007**, *127*, 221103.

67.   Henderson, T. M.; Izmaylov, A. F.; Scuseria, G. E.; Savin, A., Assessment of a Middle-Range Hybrid Functional. *J. Chem. Theory Comput.* **2008**, *4*, 1254-1262.

68.   Weintraub, E.; Henderson, T. M.; Scuseria, G. E., Long-Range-Corrected Hybrids Based on a New Model Exchange Hole. *J. Chem. Theory Comput.* **2009**, *5*, 754-762.

69.   Chai, J.-D.; Head-Gordon, M., Systematic Optimization of Long-Range Corrected Hybrid Density Functionals. *J. Chem. Phys.* **2008**, *128*, 084106.

70.   Zhao, Y.; Truhlar, D. G., The M06 Suite of Density Functionals for Main Group Thermochemistry, Thermochemical Kinetics, Noncovalent Interactions, Excited States, and Transition Elements: Two New Functionals and Systematic Testing of Four M06-Class Functionals and 12 Other Functionals. *Theor. Chem. Acc.* **2008**, *120*, 215-241.

71.   Grimme, S., Accurate Description of Van Der Waals Complexes by Density Functional Theory Including Empirical Corrections. *J. Comput. Chem.* **2004**, *25*, 1463-1473.

72.   Civalleri, B.; Zicovich-Wilson, C. M.; Valenzano, L.; Ugliengo, P., B3LYP Augmented with an Empirical Dispersion Term (B3LYP-D*) as Applied to Molecular Crystals. *CrystEngComm* **2008**, *10*, 405-410.

73.   Hariharan, P. C.; Pople, J. A., The Influence of Polarization Functions on Molecular Orbital Hydrogenation Energies. *Theoret. Chim. Acta* **1973**, *28*, 213-222.

74.   Krishnan, R.; Binkley, J. S.; Seeger, R.; Pople, J. A., Self-Consistent Molecular Orbital Methods. XX. A Basis Set for Correlated Wave Functions. *J. Chem. Phys.* **1980**, *72*, 650-654.

75. Peintinger, M. F.; Oliveira, D. V.; Bredow, T., Consistent Gaussian Basis Sets of Triple-Zeta Valence with Polarization Quality for Solid-State Calculations. *J. Comput. Chem.* **2013**, *34*, 451-459.

76. Malmstrom, M. C.; Cordes, A. W., The Crystal and Molecular Structure of Phenothiazine-10-Propionitrile. The Effect of Crystal Packing on the Dihedral Angle of Phenothiazine Heterocycles. *J. Heterocycl. Chem.* **1973**, *10*, 715-720.

77. Brock, C. P.; Minton, R. P., Systematic Effects of Crystal-Packing Forces: Biphenyl Fragments with Hydrogen Atoms in All Four Ortho Positions. *J. Am. Chem. Soc.* **1989**, *111*, 4586-4593.

78. London, R. E.; Wingad, B. D.; Mueller, G. A., Dependence of Amino Acid Side Chain ^{13}C Shifts on Dihedral Angle: Application to Conformational Analysis. *J. Am. Chem. Soc.* **2008**, *130*, 11097-11105.

79. Lin, I. C.; von Lilienfeld, O. A.; Coutinho-Neto, M. D.; Tavernelli, I.; Rothlisberger, U., Predicting Noncovalent Interactions between Aromatic Biomolecules with London-Dispersion-Corrected DFT. *J. Phys. Chem. B* **2007**, *111*, 14346-14354.

80. Williams, J. H., The Molecular Electric Quadrupole Moment and Solid-State Architecture. *Acc. Chem. Res.* **1993**, *26*, 593-598.

81. Meyer, E. A.; Castellano, R. K.; Diederich, F., Interactions with Aromatic Rings in Chemical and Biological Recognition. *Angew. Chem. Int. Ed.* **2003**, *42*, 1210-1250.

82. Waters, M. L., Aromatic Interactions in Model Systems. *Curr. Opin. Chem. Biol.* **2002**, *6*, 736-741.

83. Reilly, A. M.; Tkatchenko, A., Van Der Waals Dispersion Interactions in Molecular Materials: Beyond Pairwise Additivity. *Chemical Science* **2015**, *6*, 3289-3301.

84.   Kronik, L.; Tkatchenko, A., Understanding Molecular Crystals with Dispersion-Inclusive

        Density Functional Theory: Pairwise Corrections and Beyond. *Acc. Chem. Res.* **2014**, *47*,

        3208-3216.

85.   Reilly, A. M.; Tkatchenko, A., Understanding the Role of Vibrations, Exact Exchange,

        and Many-Body Van Der Waals Interactions in the Cohesive Properties of Molecular

        Crystals. *J. Chem. Phys.* **2013**, *139*, 024705.

86.   Juliano, T. R.; King, M. D.; Korter, T. M., Evaluating London Dispersion Force

        Corrections in Crystalline Nitroguanidine by Terahertz Spectroscopy. *IEEE Trans.

        Terahertz Sci. Technol.* **2013**, *3*, 281-287.

87.   King, M. D.; Buchanan, W. D.; Korter, T. M., Application of London-Type Dispersion

        Corrections to the Solid-State Density Functional Theory Simulation of the Terahertz

        Spectra of Crystalline Pharmaceuticals. *Phys. Chem. Chem. Phys.* **2011**, *13*, 4250-4259.

CHAPTER 14: Measuring the Elasticities of Poly-L-Proline Helices with Terahertz Spectroscopy

Abstract

The rigidity of poly-L-proline is an important contributor to the stability of many protein secondary structures where it has been shown to strongly influence bulk flexibilities. Here, experimental Young's moduli of the two known poly-L-proline helical forms, right-handed all-*cis* (form I) and left-handed all-*trans* (form II), were determined using an approach combining terahertz time-domain spectroscopy, X-ray diffraction, and solid-state density functional theory. Contrary to expectations, the helices were found to be considerably less rigid than many other natural and synthetic polymers, as well as differing greatly from each other, having Young's moduli of 4.9 and 10.6 GPa for forms I and II, respectively.

The ability of a protein to maintain proper secondary structure[1-4] is reflected in its elasticity,[5-6] which represents the tendency of the system to structurally deform under external forces. Several studies have invoked elasticity to explain the origins of observed protein properties, including structural stability,[7-8] mechanical strength,[9-10] and catalytic activity.[11-12] Despite the great relevance of elasticity, its quantification in large biomolecules has proven to be an elusive goal due to the difficulties associated with measuring stress-strain curves of these materials.[13-14] Common methods for studying protein flexibility include X-ray crystallography and nuclear magnetic resonance,[15-18] but neither is able to provide specific values for the elastic parameters and only general inferences can be drawn. To overcome experimental limitations, several indirect approaches have been developed that attempt to relate amino acid sequences in various domains to bulk elasticity, but these often rely on simple empirical data (*i.e.* packing density and intermolecular contacts), rather than actual stress-strain probe measurements.[11, 19-22] A promising alternative experimental technique is vibrational spectroscopy because it offers the advantage of being able to probe the stress (energy) and resulting strain (motion) of particular vibrational modes.[23-24] A drawback is that traditional vibrational methods (*e.g.* mid-infrared spectroscopy[25]) probe only the motions localized to individual bonds. This may yield elastic information about the specific bond, but does not provide knowledge of the sample in its entirety. Therefore, different types of vibrations must be considered.

Terahertz time-domain spectroscopy (THz-TDS) is a powerful tool for accessing the sub-150 cm^{-1} vibrational modes that involve large-amplitude global molecular motions.[26] These low-frequency motions include both external (rotations and translations) and internal (torsions) vibrations of condensed-phase sample components, meaning both the bulk and localized stress-strain relationships can be simultaneously explored. The vibrational force constants determined

426

via THz-TDS are a direct measure of the elastic properties of the studied material, yielding immediately useful elastic constants such as Young's modulus through classical relationships to Hooke's law. This approach is used here to characterize the two helical conformations of the poly-L-proline polypeptide and evaluate its rigidity as compared to other polymers.

Poly-L-proline, a component of collagen,[27] is considered to be a rigid peptide sequence often found in proteins where it is believed to add mechanical stability to secondary structures.[28-30] Proline is unique amongst naturally occurring amino acids as the only residue able to readily form both *cis*- and *trans*-configurations about its peptide bond linkages,[31-32] permitting two different helical structures to exist for poly-L-proline.[33] The all-*cis* right-handed helix (Form I, **PP-I**) is tightly wound[34], while the all-*trans* left-handed helix (Form II, **PP-II**) adopts a less dense geometry (**Figure 14-1**).[35] The availability of these similar, yet fundamentally different, polyproline helices makes them excellent choices for exploring the connection between molecular structure, low-frequency vibrational motions, and bulk elastic constants.

While the rigidity of poly-L-proline chains has been explored within protein structures[30], no studies of the actual elasticity have been performed. This dearth of information is in part due to the lack of atomic-level structural data for either helix. Here, the terahertz vibrations of PP-I and PP-II are assigned and analyzed using structures determined from a combination of experimental powder X-ray diffraction (PXRD) and solid-state density functional theory (ss-DFT) calculations. Collectively, these techniques enable quantification of the elastic properties of this large biopolymer.

PP-I

d_{cavity} = 4.08 Å
d_{helix} = 9.55 Å

10-residue repeat
d_{repeat} = 18.93 Å
pitch = 6.31 Å/turn
Φ = -72.78°
Ψ = 164.60°

PP-II

d_{helix} = 7.36 Å

3-residue repeat
d_{repeat} = 9.60 Å
pitch = 9.60 Å/turn
Φ = -82.51°
Ψ = 161.25°
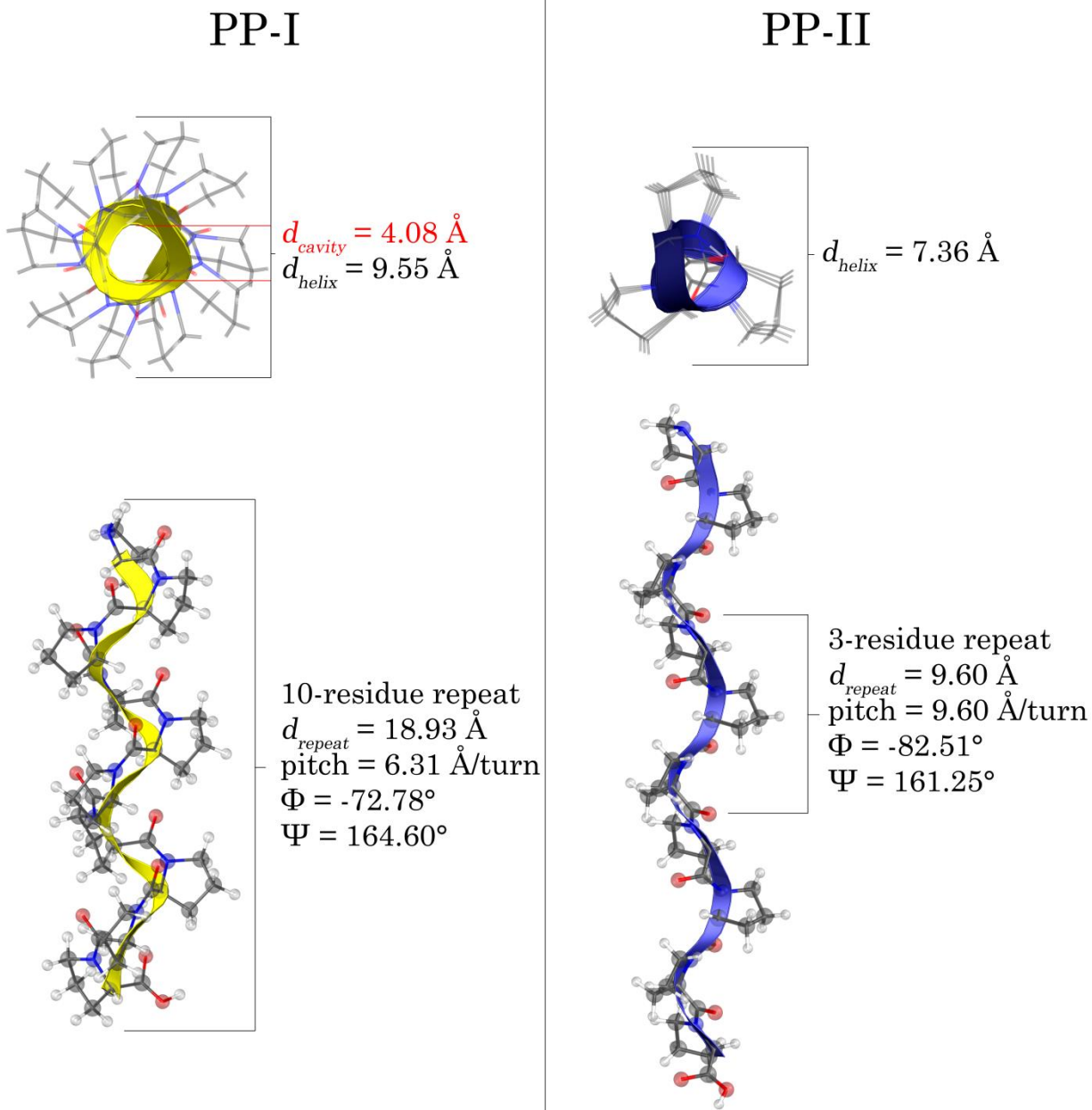
Figure 14-1. Structures of ten-residue fragments of the poly-L-proline isomers (PP-I and PP-II). The distance per crystallographic repeat (d_{repeat}), pitch (distance per helical turn), the two Ramachandran angles (ϕ and Ψ), as well as the diameter of the helix and cavity (for PP-I only, not applicable to PP-II) determined using ss-DFT calculations are provided.

The low-temperature (78 K) THz-TDS vibrational spectra (**Figure 14-2**) of solid PP-I

and PP-II (experimental details available in **Appendix J**) were acquired over a 20-150 cm^{-1} (0.6-

4.5 THz, 7.6 GHz resolution) spectral window using a Cherenkov-radiation based source,[36]

permitting features to be identified beyond the reach of more commonly available instruments.[37-

38] The THz-TDS spectra of both samples contain distinct features that are specific to the

conformation of each poly-L-proline helix and also to the three-dimensional arrangement of the

helices in the solid-state. The analysis of the vibrational data began with full redeterminations of

the complete crystal structures of both PP-I and PP-II.
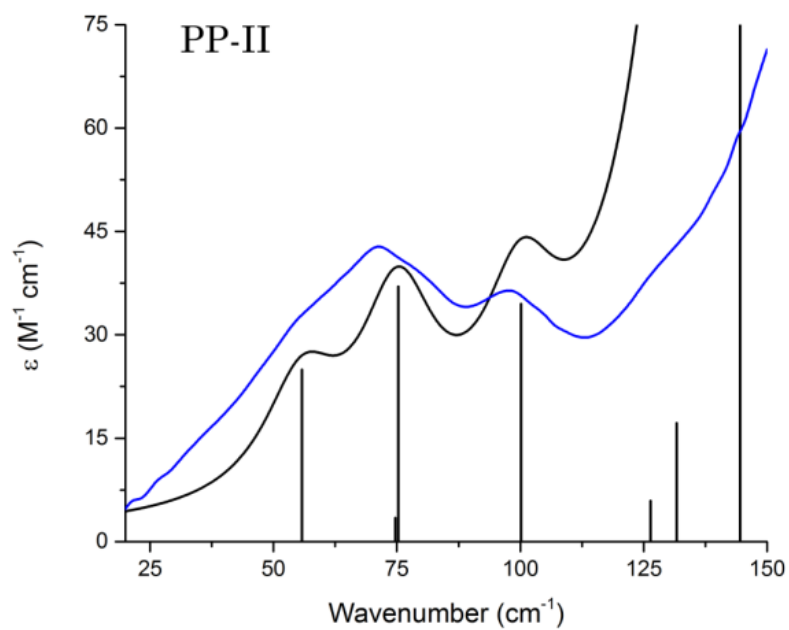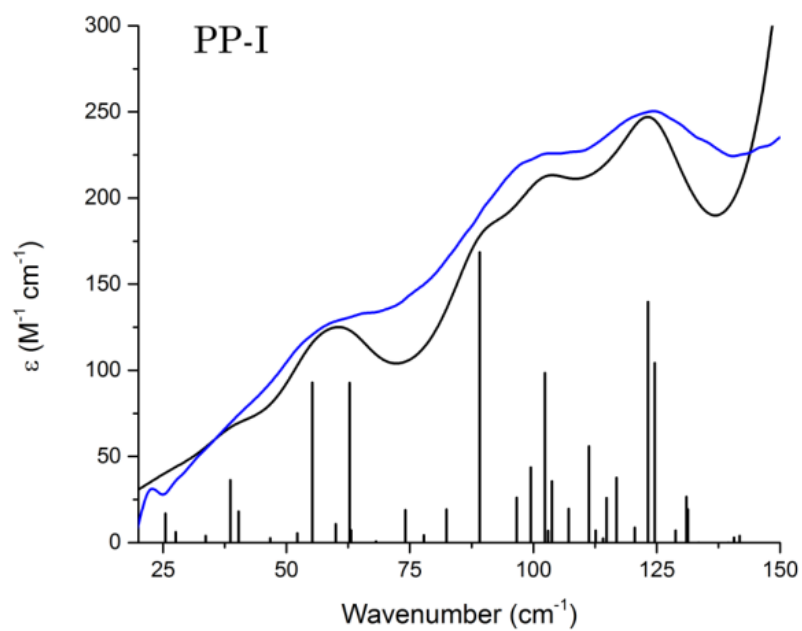
Figure 14-2. Low-temperature (78 K) THz-TDS spectra of PP-I and PP-II (blue), overlaid with simulated vibrational spectra (black).

Powder X-ray diffraction measurements were performed on both samples (**Figure 14-3**), and revealed numerous Bragg reflections unique to each solid, surpassing the quality of those previously reported. [34-35] Despite the high-quality PXRD patterns, such data alone was not sufficient for a complete structural determination with atomic precision and utilization of computational methods was necessary to arrive at detailed solutions.

In the case of PP-I, initial crystal structures were constructed using the previously published interatomic distances and angles[34], but with the solid-state packing arrangements and strand orientations varied (details provided in **Appendix J**). After full ss-DFT optimization the PP-I crystal was found to have monoclinic $P2_1$ symmetry in agreement with estimates made by Shmueli and Traub (**Figure 14-4**).[39] The unit cell contains a single all-*cis* polyproline helix that makes three complete turns over the course of 10 residues, with the helical axis corresponding to the crystallographic *b*-axis. This arrangement results in an infinite matrix of neighboring helices oriented parallel to each other and extending throughout the entire crystalline solid.

The structure of PP-II is similar to that reported previously,[35] but with the most obvious advancement being inclusion of hydrogen atom positions. PP-II crystallizes in the hexagonal $P3_2$ space group, and similar to the PP-I structure, the unit cell contains a single all-*trans* helix with three proline residues corresponding to a single helical turn (**Figure 14-4**). The PP-II helices are arranged parallel to each other in order to minimize void space, but the more extended PP-II helix enables more efficient packing than PP-I, thereby maximizing London dispersion interactions. This is particularly important because both poly-L-proline structures lack any hydrogen bond donors, meaning that the inter-helix interactions are due entirely to London dispersion and dipolar forces.
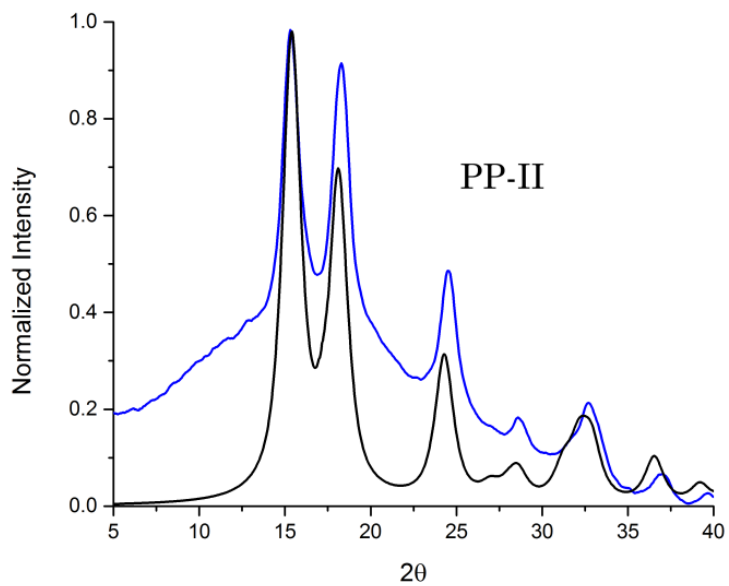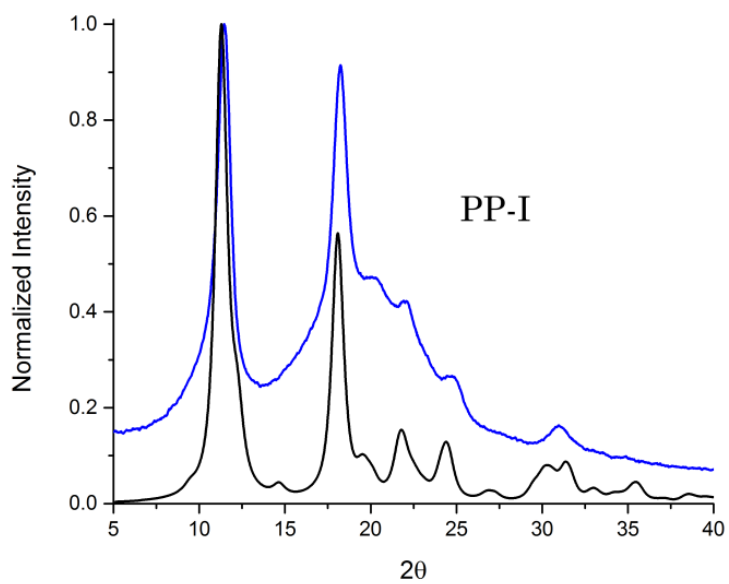
Figure 14-3. Experimental (blue) and calculated (black) PXRD patterns of the two forms of solid-state polyproline.

	PP-I		PP-II
Monoclinic	$a = 6.643$ Å	Hexagonal	$a = b = 6.643$ Å
$P2_1$	$b = 18.927$ Å	$P3_2$	$c = 9.601$ Å
	$c = 9.203$ Å		
	$\beta = 59.278°$		
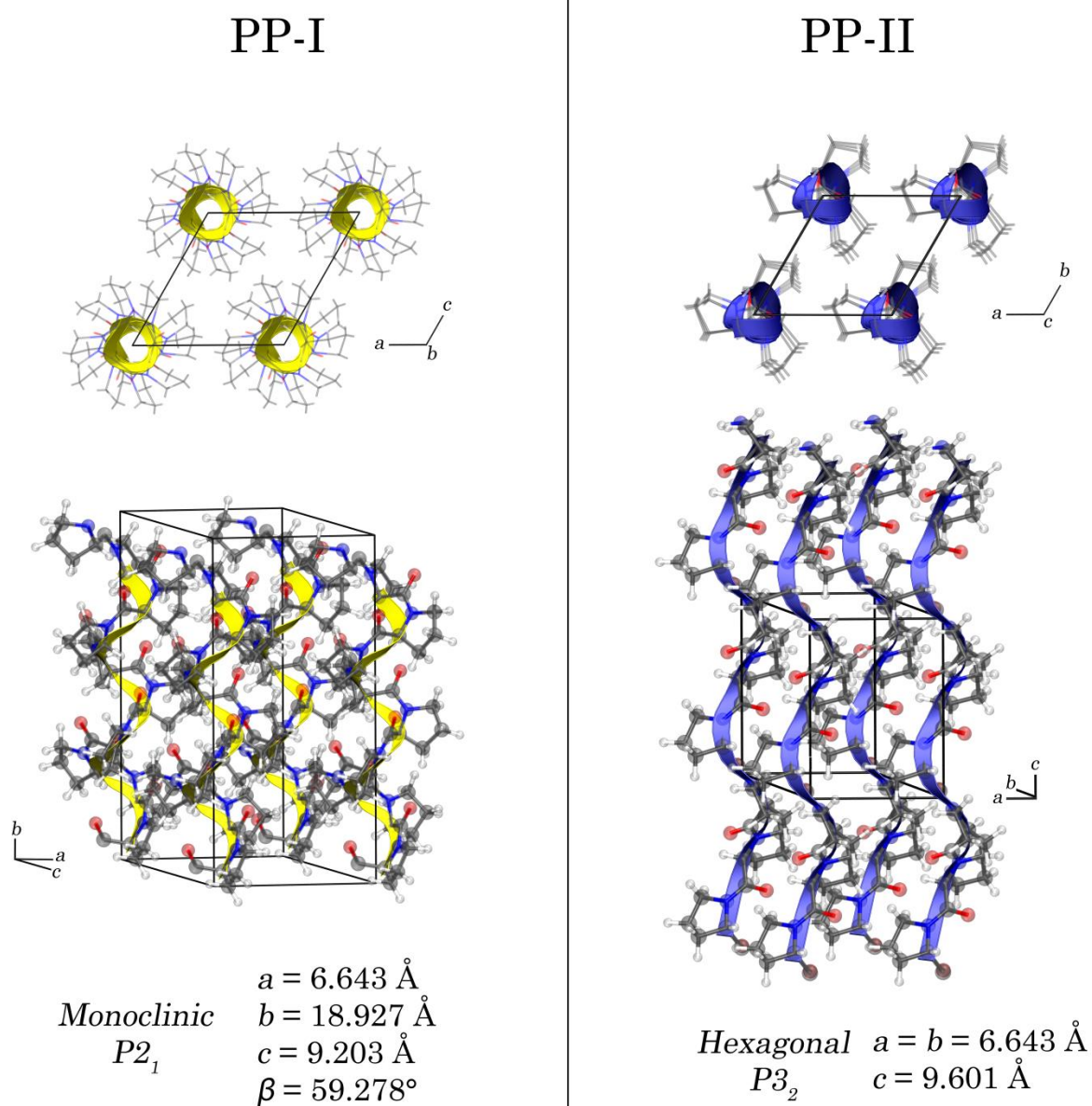
Figure 14-4. Solid-state packing structures (two views) and crystallographic parameters of PP-I and PP-II.

433

With the two poly-L-proline structures completely solved, calculation of the vibrational eigenvectors and eigenvalues could be performed, enabling assignment of specific modes for determination of the elastic properties of the helices. Considering PP-II first, where the higher crystalline symmetry results in a lower number of IR-active vibrational modes, a clear correlation between experiment and theory can be observed (**Figure 14-2**, bottom). The lower symmetry of PP-I results in a far greater number of IR-active vibrational modes and a higher spectral density in the low-frequency region, but the major contributing modes can still be assigned. The sub-150 cm^{-1} vibrational motions of both forms, determined by visualization of the eigenvector displacements, are primarily rotations and torsions of the pyrrolidine rings resulting in complex spring-like elongation and contraction of the helix (**Figure 14-5**). Specifically, the 68.15 cm^{-1} mode (exp. 66.6 cm^{-1}) in PP-I and the 100.10 cm^{-1} mode in PP-II (exp. 98.1 cm^{-1}) are most representative of the prototypical helical compression-extension motion, making them prime candidates for Young's modulus determination via the vibrational force constants.

Compression   Expansion
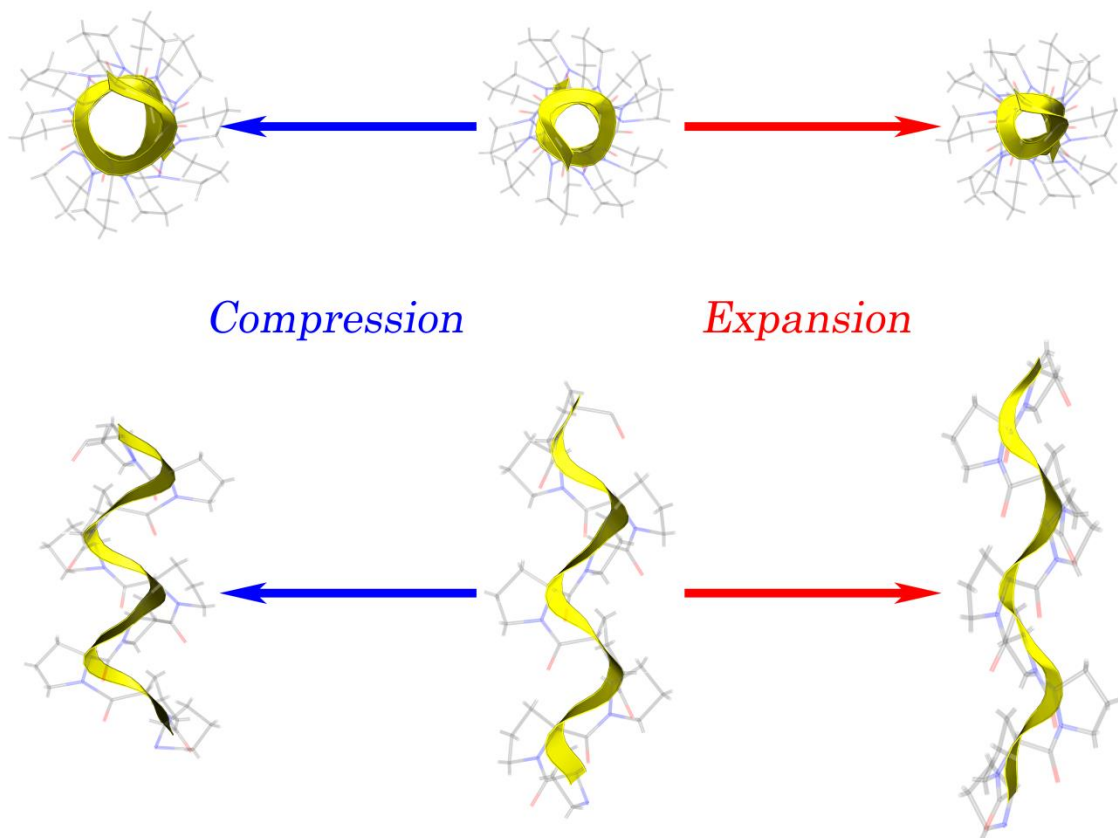
Figure 5. Visualization of the eigenvector displacements of the 68.15 cm^{-1} (exp. 66.6 cm^{-1}) vibration in PP-I showing the observed spring-type motion.

Young's modulus (Y) is used to describe the rigidity of solids, with a higher value indicative of a more rigid structure ($Y_{rubber} \approx 0.01$ GPa,[40] $Y_{iron\ bar} \approx 200$ GPa[41]). The equation for Young's modulus relates the stress (σ) to the strain (ε), and is commonly calculated from the slope of an experimental stress-strain curve,

$$Y = \frac{\sigma}{\varepsilon} = \frac{FL_0}{A_0 \Delta L} \tag{14.1}$$

where F is the force exerted on the material, L_0 and A_0 are the equilibrium length and area of the material, respectively, and ΔL is the change in equilibrium length of the sample. It becomes clear that rearranging the equation for Young's modulus results in a form of Hooke's law,

$$F = \overbrace{\frac{YA_0}{L_0} \Delta L}^{Stress-Strain} = \overbrace{k \Delta L}^{Hooke's\ Law} \tag{14.2}$$

$$\therefore\ k = \frac{YA_0}{L_0} \tag{14.3}$$

which is a valid assumption when considering small stresses and strains.[42] The connection between Hooke's law and Young's modulus can be leveraged through vibrational spectroscopy, since it relates the vibrational frequency (ν) of a harmonic oscillator with a reduced mass (μ), to an analogue of the classical force constant force constant (k),

$$\nu = \frac{1}{2\pi} \sqrt{\frac{k}{\mu}} = \frac{1}{2\pi} \sqrt{\frac{YA_0}{L_0} \frac{1}{\mu}} \tag{14.4}$$

The low-frequency motions accessible by THz-TDS are large-amplitude vibrations of the entire bulk structure, and therefore can be used to determine Young's modulus for the solid.

Using the observed terahertz frequencies and calculated μ values, the experimental force constants could be determined for the two assigned spring modes, ultimately yielding the Young's moduli of the different polyproline helices (**Table 14-1**). The elastic properties of the two polyproline helices were verified computationally using fully *ab initio* methods (not via vibrational force constants).[43-45] The results (**Table 14-1**) show that the values for Young's moduli calculated entirely from first principles are in very good agreement with those determined using the experimental terahertz vibrational frequencies. Additionally, as an independent check of the applied theory, the Young's modulus of crystalline polyethylene was calculated using the same methods, and the results ($Y = 14.63$ GPa) matched well with previously published literature data[46] ($Y = 15.8$ GPa).

Contrary to literature suggestions,[47-49] the elasticity results indicate that poly-L-proline is actually considerably less rigid than many other common polymeric materials[46, 50-53], although it is more rigid than poly-L-alanine (**Table 14-2**).[54] The significantly different rigidities of the two forms of poly-L-proline, with PP-II having a ~96% larger Young's modulus than PP-I, is due to the differences in the peptide bond geometries between the two structures. The near orthogonal orientation of the *cis*-peptide bond with respect to the helical axis in PP-I means that any change in it leads to a large alteration in the overall helical length. This was confirmed computationally by comparing the geometries of the two helices after manually increasing the helical axes from their equilibrium lengths by 10 %, and subsequently allowing the structures to relax within the constraint of fixed helical length. The results showed that both the covalent bond lengths and dihedral angles were distorted in PP-I (average absolute change per Å of distortion of 0.002 Å

and 2.678°, respectively) by a much smaller degree than PP-II (average absolute change per Å of distortion of 0.024 Å and 13.08°, respectively), despite the same relative change in helical length. Additionally, the calculations provided some insight into the energy required for conversion of the more stable PP-II structure into the PP-I form (ΔG_{298K} = 4.39 kJ/mol per residue). The 10% elongation of the PP-II helix and concomitant dihedral angle changes resulted in an energy increase within the polypeptide of 10.02 kJ/mol per Å of distortion, serving as a preliminary indicator of the barrier opposing the formation of PP-I. These results are consistent with previous studies of the poly-L-proline transformation that found large activation energy barriers to exist along the conversion coordinate.[33, 55]

The measurement of biopolymer elasticity through a combined approach of THz-TDS experiments coupled with ss-DFT simulations, enables quantification of molecular rigidities to be achieved in a relatively straightforward way. This methodology has yielded the previously unmeasured Young's moduli of the widespread poly-L-proline polypeptide in both helical forms and revealed them to be considerably more elastic than expected, prompting contemplation of their role as an analytical standard for rigidity. Ultimately, the reliable quantification of biomolecular elasticities promotes complete understanding of protein stability factors and the mechanism associated with structural change.

Table 14-1. Vibrational frequencies (cm^{-1}), force constants (N/m), reduced mass (Da), and Young's moduli (GPa) determined from the terahertz data and first principles calculations of PP-I and PP-II crystals.

	Experimental			Calculated				Elastic Calculation
	$\tilde{\nu}$	k^a	Y	$\tilde{\nu}$	k	μ	Y	Y
PP-I	66.6	1.9	4.9 ± 0.2	68.15	1.94	7.08	5.04	5.06
PP-II	98.1	3.8	9.6 ± 0.1	100.11	3.91	6.62	9.82	10.57

^{a}Derived using calculated μ values.

Table 14-2. List of Young's moduli for crystalline polymeric systems

Polymer	Young's Modulus (GPa)
Poly-L-alanine[54]	2.4 – 2.9
Polyproline Form I[a]	4.9 ± 0.2
Polyproline Form II[a]	9.6 ± 0.1
Poly(methyl methacrylate) Single Helix[50]	11
Polyethylene[46]	15.8
Poly(methyl methacrylate) Double Helix[50]	19
Collagen[52]	21
Cellulose[53]	25
Poly-L-glycine[51, 56]	42

[a]This work.

References

1.   Richards, F. M.; Kundrot, C. E., Identification of Structural Motifs from Protein Coordinate Data: Secondary Structure and First-Level Supersecondary Structure*. *Proteins: Struct., Funct., Bioinf.* **1988**, *3*, 71-84.

2.   Wright, P. E.; Dyson, H. J., Intrinsically Unstructured Proteins: Re-Assessing the Protein Structure-Function Paradigm. *J. Mol. Biol.* **1999**, *293*, 321-331.

3.   Chiti, F.; Dobson, C. M., Protein Misfolding, Functional Amyloid, and Human Disease. *Annu. Rev. Biochem.* **2006**, *75*, 333-366.

4.   Drummond, D. A.; Wilke, C. O., Mistranslation-Induced Protein Misfolding as a Dominant Constraint on Coding-Sequence Evolution. *Cell* **2008**, *134*, 341-352.

5.   Urry, D. W., Entropic Elastic Processes in Protein Mechanisms. I. Elastic Structure Due to an Inverse Temperature Transition and Elasticity Due to Internal Chain Dynamics. *J. Protein Chem.* **1988**, *7*, 1-34.

6.   Gosline, J.; Lillie, M.; Carrington, E.; Guerette, P.; Ortlepp, C.; Savage, K., Elastic Proteins: Biological Roles and Mechanical Properties. *Phil. Trans. R. Soc. B* **2002**, *357*, 121-132.

7.   Tskhovrebova, L.; Trinick, J.; Sleep, J.; Simmons, R., Elasticity and Unfolding of Single Molecules of the Giant Muscle Protein Titin. *Nature* **1997**, *387*, 308-312.

8.   Labeit, S.; Kolmerer, B., Titins: Giant Proteins in Charge of Muscle Ultrastructure and Elasticity. *Science* **1995**, *270*, 293.

9.   Tatham, A. S.; Shewry, P. R., Comparative Structures and Properties of Elastic Proteins. *Phil. Trans. R. Soc. B* **2002**, *357*, 229-234.

10. Zheng, W.; Doniach, S., A Comparative Study of Motor-Protein Motions by Using a Simple Elastic-Network Model. *PNAS* **2003**, *100*, 13253-13258.

11. Schlessinger, A.; Rost, B., Protein Flexibility and Rigidity Predicted from Sequence. *Proteins: Struct., Funct., Bioinf.* **2005**, *61*, 115-126.

12. Jacobs, D. J.; Kuhn, L. A.; Thorpe, M. F., Flexible and Rigid Regions in Proteins. In *Rigidity Theory and Applications*, Thorpe, M. F.; Duxbury, P. M., Eds. Springer US: 2002; pp 357-384.

13. Wenger, M. P. E.; Bozec, L.; Horton, M. A.; Mesquida, P., Mechanical Properties of Collagen Fibrils. *Biophys. J.* **2007**, *93*, 1255-1263.

14. Iwamoto, S.; Kai, W.; Isogai, A.; Iwata, T., Elastic Modulus of Single Cellulose Microfibrils from Tunicate Measured by Atomic Force Microscopy. *Biomacromolecules* **2009**, *10*, 2571-2576.

15. Bahadur, P.; Sastry, N., *Principles of Polymer Science*; Alpha Science Int'l Ltd., 2005.

16. Berjanskii, M.; Wishart, D. S., NMR: Prediction of Protein Flexibility. *Nat. Protocols* **2006**, *1*, 683-688.

17. Ishima, R.; Torchia, D. A., Protein Dynamics from NMR. *Nat. Struct. Mol. Biol.* **2000**, *7*, 740-743.

18. Pelikan, M.; Hura, G. L.; Hammel, M., Structure and Flexibility within Proteins as Identified through Small Angle X-Ray Scattering. *General Physiology and Biophysics* **2009**, *28*, 174-189.

19. Knowles, T. P.; Fitzpatrick, A. W.; Meehan, S.; Mott, H. R.; Vendruscolo, M.; Dobson, C. M.; Welland, M. E., Role of Intermolecular Forces in Defining Material Properties of Protein Nanofibrils. *Science* **2007**, *318*, 1900-1903.

20.   Chen, K.; Kurgan, L. A.; Ruan, J., Prediction of Flexible/Rigid Regions from Protein Sequences Using K-Spaced Amino Acid Pairs. *BMC Structural Biology* **2007**, *7*, 1-13.

21.   Jacobs, D. J.; Rader, A. J.; Kuhn, L. A.; Thorpe, M. F., Protein Flexibility Predictions Using Graph Theory. *Proteins: Struct., Funct., Bioinf.* **2001**, *44*, 150-165.

22.   Carlson, H. A.; McCammon, J. A., Accommodating Protein Flexibility in Computational Drug Design. *Mol. Pharmacol.* **2000**, *57*, 213-218.

23.   Miyagawa, H.; Sato, C.; Mase, T.; Drown, E.; Drzal, L. T.; Ikegami, K., Transverse Elastic Modulus of Carbon Fibers Measured by Raman Spectroscopy. *Mat. Sci. Eng. A-Struct.* **2005**, *412*, 88-92.

24.   Lee, J.-U.; Yoon, D.; Cheong, H., Estimation of Young's Modulus of Graphene by Raman Spectroscopy. *Nano Lett.* **2012**, *12*, 4444-4448.

25.   Stuart, B., Infrared Spectroscopy. In *Kirk-Othmer Encyclopedia of Chemical Technology*, John Wiley & Sons, Inc.: 2000.

26.   Beard, M. C.; Turner, G. M.; Schmuttenmaer, C. A., Terahertz Spectroscopy. *J. Phys. Chem. B* **2002**, *106*, 7146-7159.

27.   Gratzer, W.; Rhodes, W.; Fasman, G., Optical Properties of the Poly-L-Proline and Collagen Helices. *Biopolymers* **1963**, *1*, 319-330.

28.   Adzhubei, A. A.; Sternberg, M. J. E.; Makarov, A. A., Polyproline-II Helix in Proteins: Structure and Function. *J. Mol. Biol.* **2013**, *425*, 2100-2132.

29.   Arora, P. S.; Ansari, A. Z.; Best, T. P.; Ptashne, M.; Dervan, P. B., Design of Artificial Transcriptional Activators with Rigid Poly-L-Proline Linkers. *J. Am. Chem. Soc.* **2002**, *124*, 13067-13071.

30.   Ma, K.; Kan, L.-s.; Wang, K., Polyproline II Helix Is a Key Structural Motif of the Elastic Pevk Segment of Titin. *Biochemistry* **2001**, *40*, 3427-3438.

31.   Swenson, C. A.; Formanek, R., Infrared Study of Poly-L-Proline in Aqueous Solution. *J. Phys. Chem* **1967**, *71*, 4073-4077.

32.   Wedemeyer, W. J.; Welker, E.; Scheraga, H. A., Proline Cis−Trans Isomerization and Protein Folding†. *Biochemistry* **2002**, *41*, 14637-14644.

33.   Shi, L.; Holliday, A. E.; Shi, H.; Zhu, F.; Ewing, M. A.; Russell, D. H.; Clemmer, D. E., Characterizing Intermediates Along the Transition from Polyproline I to Polyproline II Using Ion Mobility Spectrometry-Mass Spectrometry. *J. Am. Chem. Soc.* **2014**, *136*, 12702-12711.

34.   Traub, W.; Shmueli, U., Structure of Poly-L-Proline I. *Nature* **1963**, *198*, 1165-1166.

35.   Arnott, S.; Dover, S., The Structure of Poly-L-Proline II. *Acta Crystallogr. Sect. B: Struct. Sci.* **1968**, *24*, 599-601.

36.   Yao, J.; Liu, P.; Xu, D.; Lv, Y.; Lv, D., Thz Source Based on Optical Cherenkov Radiation. *Science China Information Sciences* **2011**, *55*, 27-34.

37.   Rice, A.; Jin, Y.; Ma, X. F.; Zhang, X. C.; Bliss, D.; Larkin, J.; Alexander, M., Terahertz Optical Rectification from 〈110〉 Zinc-Blende Crystals. *Appl. Phys. Lett.* **1994**, *64*, 1324-1326.

38.   Di, L.; Yi, H. In *Comparison of Terahertz Antennas*, Antennas and Propagation, 2006. EuCAP 2006. First European Conference on, 6-10 Nov. 2006; 2006; pp 1-5.

39.   Engel, J. In *Conformational Transitions of Poly-L-Proline and Poly-(L-Prolyl-Glycyl-L-Proline)*, Conformation of Biopolymers: Papers Read at an International Symposium Held at the University of Madras, 18-21 January 1967, Academic Press: 1967; p 483.

40. Ismail, H.; Suryadiansyah, Thermoplastic Elastomers Based on Polypropylene/Natural Rubber and Polypropylene/Recycle Rubber Blends. *Polym. Test.* **2002**, *21*, 389-395.

41. Benito, J. A.; Jorba, J.; Manero, J. M.; Roca, A., Change of Young's Modulus of Cold-Deformed Pure Iron in a Tensile Test. *Metall. Mater. Trans. A*, *36*, 3317-3324.

42. Sokolnikoff, I. S.; Specht, R. D., *Mathematical Theory of Elasticity*; McGraw-Hill New York, 1956; Vol. 83.

43. Perger, W. F.; Criswell, J.; Civalleri, B.; Dovesi, R., Ab-Initio Calculation of Elastic Constants of Crystalline Systems with the Crystal Code. *Comput. Phys. Commun.* **2009**, *180*, 1753-1759.

44. Erba, A.; Mahmoud, A.; Orlando, R.; Dovesi, R., Elastic Properties of Six Silicate Garnet End Members from Accurate ab initio Simulations. *Phys. Chem. Miner.* **2013**, *41*, 151-160.

45. Erba, A.; Ferrabone, M.; Baima, J.; Orlando, R.; Rérat, M.; Dovesi, R., The Vibration Properties of the (N,0) Boron Nitride Nanotubes from ab initio Quantum Chemical Simulations. *J. Chem. Phys.* **2013**, *138*, 054906.

46. Odajima, A.; Maeda, T., Calculation of the Elastic Constants and the Lattice Energy of the Polyethylene Crystal. *J. Polym. Sci. C Polym. Lett.* **1967**, *15*, 55-74.

47. Schuler, B.; Lipman, E. A.; Steinbach, P. J.; Kumke, M.; Eaton, W. A., Polyproline and the "Spectroscopic Ruler" Revisited with Single-Molecule Fluorescence. *PNAS* **2005**, *102*, 2754-2759.

48. Best, R. B.; Merchant, K. A.; Gopich, I. V.; Schuler, B.; Bax, A.; Eaton, W. A., Effect of Flexibility and Cis Residues in Single-Molecule Fret Studies of Polyproline. *PNAS* **2007**, *104*, 18964-18969.

49.   Ungar-Waron, H.; Gurari, D.; Hurwitz, E.; Sela, M., Role of a Rigid Polyproline Spacer Inserted between Hapten and Carrier in the Induction of Anti-Hapten Antibodies and Delayed Hypersensitivity. *Eur. J. Immunol.* **1973**, *3*, 201-205.

50.   Urbanek, S.; Tashiro, K.; Kitayama, T.; Hatada, K., Crystallite Modulus of Double-Stranded Helices of Isotactic Poly(Methyl Methacrylate): The X-Ray Measurement and the Theoretical Calculation. *Polymer* **1999**, *40*, 3345-3351.

51.   Nakamura, H.; Go, N., Conformational Energy Analysis and Mechanical Properties of Polyglycine II. *Int. J. Pept. Protein Res.* **1985**, *25*, 232-237.

52.   Cusack, S.; Miller, A., Determination of the Elastic Constants of Collagen by Brillouin Light Scattering. *J. Mol. Biol.* **1979**, *135*, 39-51.

53.   Eichhorn, S. J.; Young, R. J., The Young's Modulus of a Microcrystalline Cellulose. *Cellulose*, *8*, 197-207.

54.   Adamovic, I.; Mijailovich, S. M.; Karplus, M., The Elastic Properties of the Structurally Characterized Myosin II S2 Subdomain: A Molecular Dynamics and Normal Mode Analysis. *Biophys. J.* **2008**, *94*, 3779-3789.

55.   Moradi, M.; Babin, V.; Roland, C.; Darden, T. A.; Sagui, C., Conformations and Free Energy Landscapes of Polyproline Peptides. *PNAS* **2009**, *106*, 20746-20751.

56.   Enomoto, S.; Krimm, S., Elastic Moduli of Helical Polypeptide Chain Structures. *Biophys. J.* **1962**, *2*, 317-326.

CHAPTER 15: Examination of L-Glutamic Acid Polymorphs by Solid-State Density Functional Theory and Terahertz Spectroscopy

Abstract

The ability of L-glutamic acid to crystallize in two different forms has long been the subject of study due to its commercial importance. While a solvent-mediated phase transformation between the α and β polymorphs is the prevailing theory, recent reports indicate a thermal solid-solid transformation between the two may be possible. However, determining accurate thermodynamic stabilities of these crystals has been challenging. Here, new low-temperature single-crystal X-ray diffraction data coupled with solid-state density functional theory simulations have enabled a detailed description to be achieved for the energetic parameters governing the stabilization of the two L-glutamic acid solids. The temperature-dependent Gibbs free energy curves show that α-glutamic acid is the preferred form at low-temperatures (< 222 K) and the β form being most stable at ambient temperatures. Terahertz time-domain spectroscopy was utilized to evaluate the quality of the intermolecular force modeling, as well as to provide characteristic low-frequency spectral data that can be used for quantification of polymorph mixtures or crystal growth monitoring.

15.1 Introduction

L-Glutamic acid is one of the most commercially produced amino acids, with an estimated worldwide annual production of two billion kilograms.[1-4] The majority is utilized in the food additive industry for the synthesis of monosodium glutamate (MSG).[5-6] The morphology of crystalline glutamic acid is of particular interest because the differing crystallite shapes of the two known polymorphs directly impact their industrial usage.[7-9] In a manufacturing setting, the α polymorph (α-GLU) is preferred because it is easier to separate from the crystallization solution and easier to handle mechanically than the *β* polymorph (*β*-GLU) where the *β*-crystal habit often results in higher water retention and gelatinization.[7, 10-11] Given the need to promote and maintain the crystal growth of one polymorph over the other, the energetics and mechanism of the α-GLU/*β*-GLU acid phase transformation have been topics of debate over several decades.[12-14] The difficulty in studying the two glutamic acid polymorphs lies in the tendency of α-GLU to readily convert to *β*-GLU if left in solution for even a few hours, a behavior that promotes the idea of a solvent-mediated phase transformation.[15-16] This has made obtaining high-quality crystals for structural analysis challenging, and even when single crystals of α-GLU are grown, they are often contaminated by domains of *β*-GLU that grow both inside[17] and on the surface[18-23] of the α-GLU crystallites. In this study, pure crystals of both forms were grown, and their structures completely solved using single-crystal X-ray diffraction (SCXRD), yielding the first reported low-temperature crystal structures of these polymorphs.

The availability of new structural data facilitated an in-depth investigation of the two glutamic acid polymorphs using solid-state density functional theory (DFT) calculations, with the goal being a complete electronic and thermodynamic description of the energies associated

with the α-GLU/β-GLU phase transition. The specific question to be answered is if α-GLU and β-GLU are enantiotopically related as recently suggested by thermal studies,[13] or is the long-believed solvent-mediated transformation mechanism correct.[15, 17-18, 22] The numerous energetic factors contributing to the polymorph stabilities will be presented, such as molecular conformation and intermolecular cohesion, but with particular focus on the origins of the intermolecular forces. Ultimately, the roles of all these components together will be considered in terms of the temperature dependency of the Gibbs free energies of α and β-GLU and how their relationship helps elucidate the observed polymorph stabilities.

Terahertz time-domain spectroscopy (THz-TDS) was also utilized in this study in two capacities. First, THz-TDS of molecular crystals is a well-established method for identifying the characteristic spectral signatures of solid-state polymorphs[24-27] and thus the work presented here provides a new means for the rapid detection of the presence of the α and β forms in industrial mixtures. Secondly, as the vibrational modes accessible by terahertz radiation are dependent on both the internal conformation and external packing arrangement of the molecules in the solid state, THz-TDS provides an excellent test of the computational models.[28-29] This is especially important here, where the evaluation of the relative stabilities of the crystalline polymorphs is of central interest and the accurate modelling of the interactions between molecules is crucial.[30-31] Experimental THz-TDS data for both α-GLU and β-GLU were obtained and assigned using solid-state DFT, highlighting the utility of a combined experimental and theoretical investigation for providing a more complete picture of the energetics associated with polymorphic phase transformations.

15.2 Methods

15.2.1 Experimental

15.2.1.1 Polymorph Synthesis

Monosodium-L-glutamate monohydrate and L-tyrosine were both purchased from Sigma-Aldrich ($\geq$ 98.0% purity). The α-GLU form was synthesized using a combination of several previously published methods.[17-18, 32] To produce a homogenous microcrystalline sample suitable for powder X-ray diffraction (PXRD) and terahertz spectroscopy, 5 g of monosodium-L-glutamate monohydrate was dissolved in 50 mL of distilled water and placed in an ice bath, to which 2 mL of 12 M hydrochloric acid was added dropwise while stirring to minimize any temperature increases from the exothermic formation of the hydronium ions. The mixture was left undisturbed for 5 minutes, followed by the addition of 1 mL of hydrochloric acid that was slowly added as the zwitterionic glutamic acid solid precipitated out of solution. The solution was allowed to rest for an additional 5 minutes, and was then filtered and washed using deionized water, yielding pure α-glutamic acid (confirmed by PXRD). Crystals suitable for single-crystal X-ray diffraction (SCXRD) were grown by dissolving the newly synthesized α-GLU in deionized water at 80°C and adding a small amount of L-tyrosine (~2 x 10^{-3} M), followed by immediately placing the solution in a refrigerator (~2°C). Large crystals of α-GLU formed within a few hours, but after complete evaporation of the solvent a small fraction of β-GLU could be observed by PXRD.

A similar method was employed to synthesize *β*-GLU, but unlike in the α-GLU

synthesis, the hydrochloric acid was added at once without the use of an ice bath. The crystals

were again filtered, and redissolved in water at room temperature, and the solution was allowed

to evaporate over the course of several days. This produced a homogenous sample of *β*-GLU that

contained large crystals suitable for SCXRD.

15.2.1.2 X-ray Diffraction

X-ray diffraction studies were performed on a Bruker KAPPA APEX DUO

diffractometer equipped with an APEX II CCD using monochromated Cu Kα radiation (λ =

1.5418 Å) for PXRD and Mo Kα radiation (λ = 0.71076 Å) for SCXRD.[33] The SCXRD data

were corrected for Lorentz and polarization effects[34], and absorption corrections were made

using SADABS.[35-36] The structures were solved using direct methods with the SHELXTL

software.[37] Upon identification of all non-hydrogen atoms, the models were refined

anisotropically. All hydrogen positions were determined based on residual electron density,

followed by isotropic refinement of the entire structure.

15.2.1.3 Terahertz Time-Domain Spectroscopy

Terahertz time-domain spectra were obtained using a commercial Advantest TAS7500TS

spectrometer. Terahertz radiation was produced using an Advantest TAS1130 source module,

which made use of a lithium niobate nonlinear crystal to generate Cherenkov-radiation in the

0.5-4.0 THz range.[38-40] Detection of the terahertz pulse was performed by an Advantest

TAS1230 detector module containing a photoconductive antenna.[41-42] Samples were prepared for THz-TDS by pulverizing the sample in a polytetrafluoroethylene (PTFE) matrix (~ 5% w/w), and then pressing into pellets. The frequency-domain absorption spectra presented in this work are a result of Fourier transforming the time-domain spectra followed by division by the spectra of a blank PTFE sample.

15.2.2 Theoretical

Solid-state DFT simulations were performed using the *ab initio* CRYSTAL14 software package,[43] which utilizes periodic boundary conditions to impose the translational symmetry found in real crystals. The generalized gradient approximation (GGA) Perdew-Burke-Ernzerhof (PBE) density functional[44] was combined with the split-valence triple-ζ 6-311G(d,p) basis set.[45] For completeness, the Becke-3-Lee-Yang-Parr[46] (B3LYP) hybrid functional was used initially to check relative polymorph energies, and the results were consistent between functionals. London dispersion forces were accounted for using the DFT-D3 correction developed by Grimme, a method that explicitly calculates the C6 dispersion coefficients iteratively based on the structure and electronics of the particular system.[47] Geometry optimizations were performed using the experimental atomic positions as starting coordinates, and the entire structure (including lattice vectors) was allowed to relax. The optimized structures were then used for vibrational analyses, with infrared intensities calculated using the Berry phase method.[48] The energy convergence criteria were set to $\Delta E \leq 10^{-8}$ and 10^{-10} hartree for the optimization and frequency calculations, respectively.

15.3 Results and Discussion

15.3.1 Structural Results

15.3.1.1 α-L-Glutamic Acid (α-GLU)

The low-temperature structure of α-GLU was determined using SCXRD at 90 K and is in general agreement with previously published room-temperature structures.[49-50] The α-GLU crystals form in the orthorhombic $P2_12_12_1$ space group, with lattice dimensions of $a = 7.012$ Å, $b = 8.762$ Å, $c = 10.273$ Å, and $V = 631.17$ Å^3 (**Figure 15-1**). The unit cell is constructed from one symmetry independent glutamic acid ($Z' = 1$), resulting in four zwitterionic α-GLU molecules per cell ($Z = 4$) and providing a derived density of $1.548 \frac{g}{cm^3}$. Each α-GLU zwitterion forms four hydrogen bonds with neighboring molecules, three originating from the amino group and bonding to two adjacent carboxylate oxygens and the carbonyl oxygen, and one from the carboxyl OH bonding to an neighboring carboxylate as well (three total H $\cdots$ COO$^-$ bonds and one H $\cdots$ COOH bond). The latter hydrogen bond is uniquely strong (though not of the low-barrier variety), with inter-oxygen spacing of only 2.579 Å and O-H distances of 0.912 Å and 1.677 Å for the covalent and non-covalent bonds, respectively. The theoretical simulations accurately reproduce these structural features, with the average absolute errors in the covalent bond distances and lattice vectors being 0.40 % and 0.47 %, respectively.
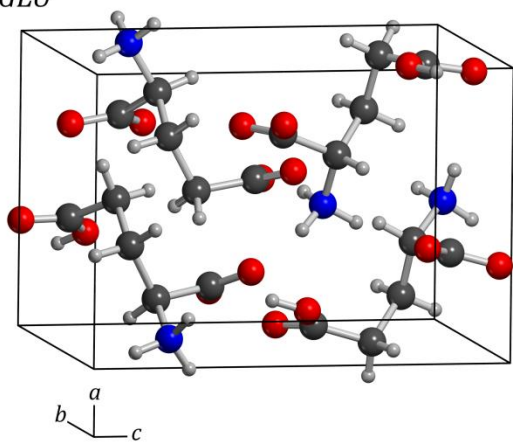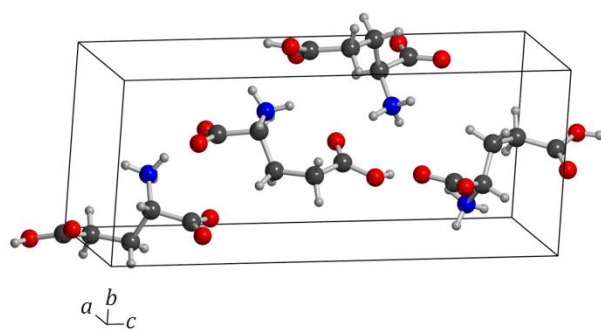
Figure 15-1. Experimental SCXRD determined structures of α-GLU (left) and β-GLU (right).

15.3.1.2 β-L-Glutamic Acid (β-GLU)

The SCXRD structure of β-GLU was redetermined at 90 K, and is in good agreement with the previously reported room-temperature structure.[51] Like α-GLU, β-GLU crystallizes in the orthorhombic $P2_12_12_1$ space group (**Figure 15-1)** and contains one symmetry independent molecule (Z'=1), leading to a total of four molecules in the crystallographic cell (Z=4). The unit cell has lattice dimensions of $a = 5.139$ Å, $b = 6.879$ Å, $c = 17.246$ Å, and $V = 609.72$ Å^3, yielding a derived density of $1.603 \frac{g}{cm^3}$. The largest difference between the two polymorphs is in the orientation of the carboxylate group with respect to the carbon backbone. In β-GLU the carboxylate group follows the nearly linear arrangement of the other carbon atoms, having a dihedral angle of 8.70°. However in α-GLU, the carboxylate group is skewed out of the plane of the carbon backbone, exhibiting a 59.26° dihedral angle **(Figure 15-2)**. Moreover, the hydrogen bonding structure in β-GLU is more favorable, with each zwitterion accepting five bonds. Both carboxylate oxygens receive two hydrogen bonds, with one accepting two from the amino group and the other accepting one from the amino group as well as the carboxyl group. In turn, the double-bonded carboxyl oxygen accepts a single hydrogen bond from an adjacent amino group. The solid-state DFT optimized structure of β-GLU is an excellent reproduction of the experimental structure, with average absolute errors in the covalent bond distances and lattice vectors of 0.50 % and 0.52 %, respectively.
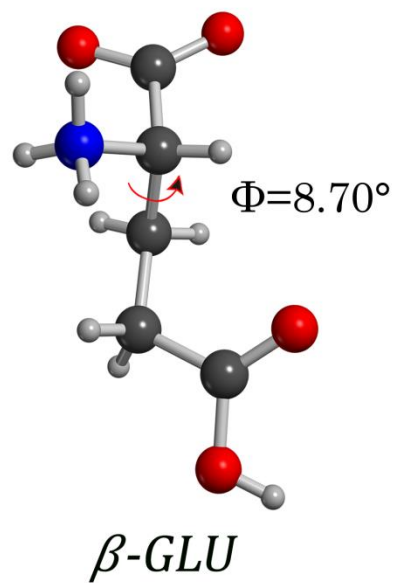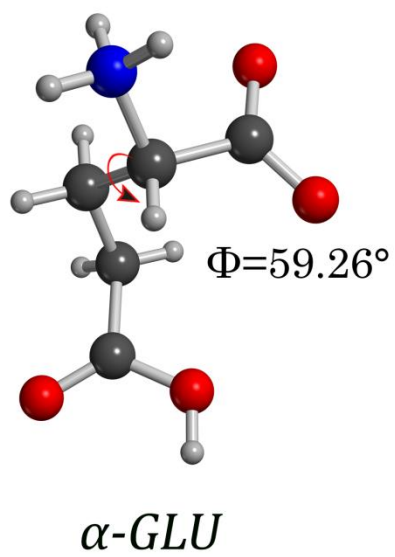
Figure 15-2. The molecular conformations of L-glutamic acid in the α and β polymorphs with the dihedral angles noted in the text indicated by curved arrows.

15.3.2 Terahertz Time-Domain Spectroscopy

The ability of THz-TDS to differentiate between polymorphic forms makes it a powerful technique for studying the two L-glutamic acid crystals. The terahertz spectra shown in **Figure 15-3** were obtained at 100 K, and both samples exhibit a number of sharp resolvable features in the 0.5-4 THz region. The spectrum of β-GLU contains a noticeably increasing baseline and minor asymmetry in the absorption occurring at 1.25 THz, both indicative of Christensen effect scattering,[52-53] but the distinct β-GLU spectral pattern is clear. Despite the common difficulty of mixed samples, the α-GLU sample showed no contamination from β-GLU as evidenced by the absence of any features in the α-GLU spectra below 1.5 THz. The unique spectral fingerprints of the different crystals demonstrates the utility of THz-TDS for polymorph detection, but also the high number of well-resolved absorptions makes them valuable benchmarks for gauging the accuracy of the theoretical model beyond any structural reproduction.

The low-frequency vibrational spectra were simulated using the solid-state DFT optimized crystal structures and the excellent correlation with experiment can be seen in **Figure 15-3**. The simulations agree in terms of both frequency and intensity indicating that the potential energy curvatures and atomic charge distributions were equally well modelled. The types of vibrational modes in this region (determined through visualization of the eigenvector displacements) are similar between the two crystals. The motions are primarily external librations and internal torsions, with a majority of the atomic movement centered on the carboxyl(ate) groups (full mode list provided in **Appendix K**). The occurrence of a large number of terahertz torsional motions is likely due to the flexibility of the carbon backbone, where little energetic penalty exists for hindered rotation about the single-bonds.
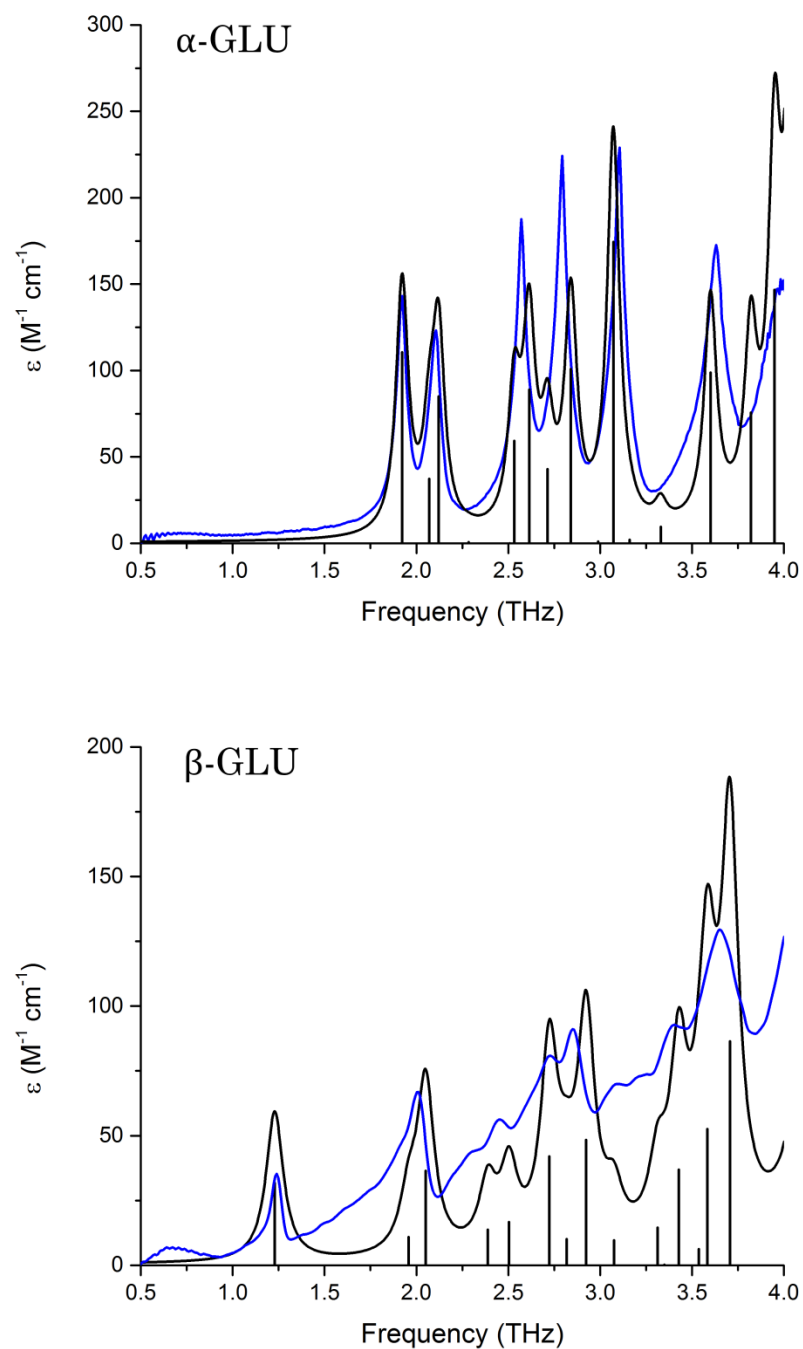
Figure 15-3. Experimental 100 K THz-TDS of α-GLU and *β*-GLU (blue) and solid-state DFT simulated spectra (black). The simulated spectra have been convolved using a Lorentzian lineshapes with full-width at half-maxima of 96 GHz and 114 GHz for α-GLU and *β*-GLU, respectively.

15.3.3 Energetics of the Two Glutamic Acid Polymorphs

15.3.3.1 Gibbs Free Energy Curves

The accurate simulation of the crystal structures and vibrational spectra of the L-glutamic acid polymorphs lends confidence to the computational investigation of their thermodynamic behavior, specifically the Gibbs free energies. The calculated Gibbs free energy curves (**Figure 15-4**), show that α-GLU is the more stable form at absolute zero by 1.17 kJ/mol. A predicted phase transition occurs at 222 K, so that β-GLU becomes the more stable at 298 K by 0.60 kJ/mol. These results are consistent with the observation of the preferential growth of α-GLU at lower temperatures,[9] yet in contrast with a recent report claiming a possible solid-solid α-β phase transition at temperatures near the melting point (~450 K). However that study conceded that numerous processes were likely occurring simultaneously, and that the discovery of a new phase transition was not conclusive.
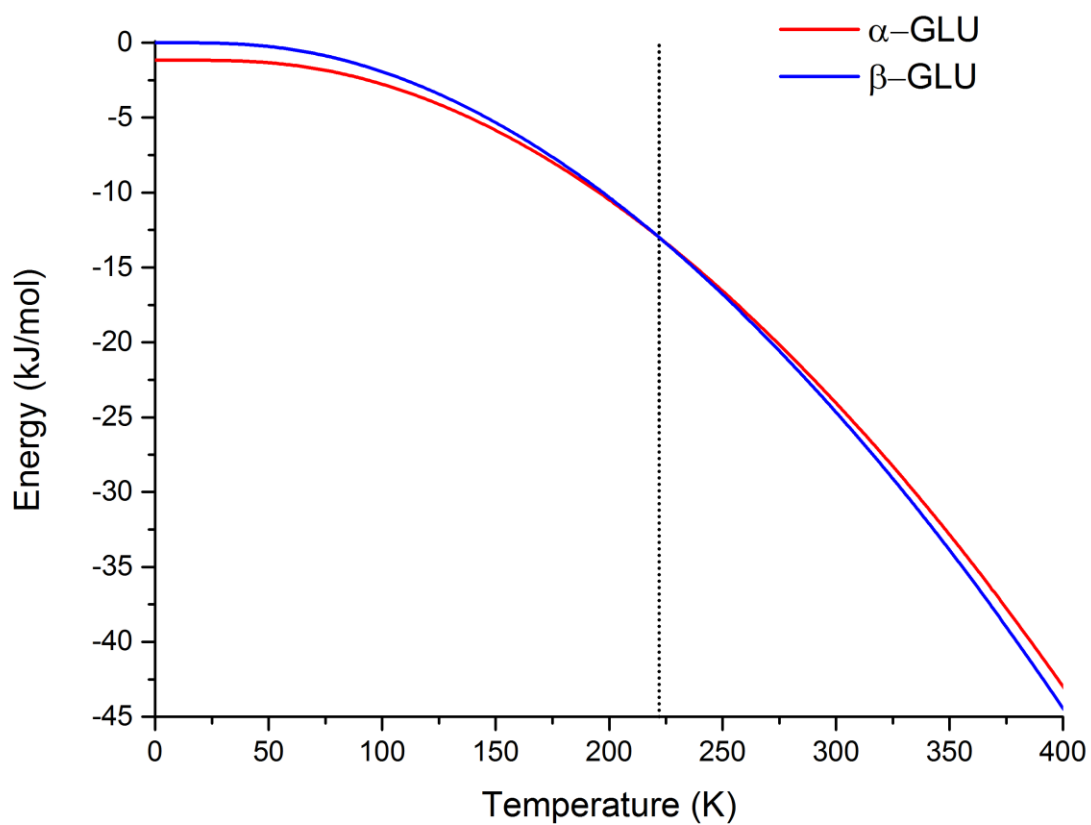
Figure 15-4. Simulated Gibbs free energy curves for α-GLU (blue) and *β*-GLU (red) relative to the 0 K energy of α-GLU. The phase transition temperature is indicated by the dotted line (222 K).

15.3.3.2 Deconstruction of the Electronic Energies

The most surprising result of the relative polymorph stabilities is that the α form is more stable than the β form at the zero-Kelvin limit. The DFT calculations enable a more complete description of the electronic energies to be performed by deconstructing the total energy into its various components, including the molecular conformational and cohesion energies, but also contributions specifically from London dispersion forces. It is important to note that all energies provided throughout this discussion are in terms of a single L-glutamic acid molecule and have been corrected for basis set superposition error, which was found to be relatively small and nearly equal (~20 kJ/mol, $\Delta E_{BSSE}^{\alpha-\beta} = 0.22$ kJ/mol) in the two glutamic acid crystals.

Considering the packing arrangements of the two polymorphs, specifically the higher density and enhanced hydrogen bonding of β-GLU, it might be expected to be the more stable of the two polymorphs. However, when considering the DFT-calculated electronic energy alone (no London dispersion energy corrections), α-GLU is favored by 8.23 kJ/mol compared to β-GLU. This is partially due to α-GLU being comprised of molecules of lower conformational energy. A single molecule extracted from the optimized α-GLU crystal was found to be 3.97 kJ/mol lower in energy than one extracted from β-GLU. In terms of intermolecular energy contributions, the calculated electronic cohesion energy is in favor of α-GLU by 4.26 kJ/mol, in seeming contrast to the structural analysis that revealed a greater amount of hydrogen bonding in the β-GLU crystal. The other factors beyond hydrogen bonding that must be considered in the cohesion energy are dipole-dipole interactions, and this was investigated by calculating the dipole moments of isolated molecules, again extracted from the optimized solids.[54] The results of those calculations showed that while the dipole moment magnitude in β-GLU molecules was larger

than those in α-GLU (12.03 and 9.31 Debye, respectively), the orientations of the nearby dipoles in the bulk with respect to each other are more favorable in α-GLU. The individual dipole moment vectors are arranged directly head-to-tail between adjacent molecules, and the neighboring sheets formed by the α-GLU molecules are oriented in an antiparallel manner, maximizing stabilization. The efficient organization of the dipoles in the α-GLU solid is sufficient to overcome its less favorable hydrogen bonding scheme (as compared to β-GLU), leading to the observed values for cohesion energy.

The inclusion of London dispersion energy into the simulations greatly alters the intermolecular potential energy landscape, as β-GLU experiences a larger amount of stabilization from them than α-GLU does. The higher density of β-GLU leads to a cohesion energy that is 1.14 kJ/mol more stable than α-GLU. Furthermore, the relative difference in total electronic energy is reduced from 8.23 kJ/mol to 3.69 kJ/mol (without and with dispersion energies, respectively) in favor of α-GLU, providing some insight into the origin of the observed properties of the two crystals.

15.4 Conclusions

While these energetic values provide no information regarding the specific transformation mechanisms or kinetics, the results can be used to help explain some of the observations made of the α-GLU/β-GLU crystal growth and interconversion. It is accepted that the two polymorphs are unable to undergo a solid-state phase transition, in seeming contrast with the ss-DFT simulations that show they should be enantiotropic, from a purely energetic point of view. The majority of reported techniques for synthesizing α-GLU involve rapid crystallization, often relying on supersaturation or precipitation. This can be broadly interpreted using the energetic conclusions drawn here, as the lower conformational energy found for α-GLU molecules likely represents a structure that is closer to the preferred of L-glutamic acid in solution. But as nucleation begins, the greater amount of external stabilization offered by London dispersion forces in crystals of β-GLU offsets the conformational stability of α-GLU, promoting its formation. This hypothesis can then explain the well-known observation of β-GLU forming both inside and on surface of α-GLU crystallites. Overall these molecular crystals represent the commonly encountered balance established between conformational and cohesive stabilities, and are another example of how the competition between the two factors dictates the ultimate crystalline geometry.

15.5 References

1. Sano, C., History of Glutamate Production. *The American Journal of Clinical Nutrition* **2009**, *90*, 728S-732S.

2. Shyamkumar, R.; Moorthy, I. M. G.; Ponmurugan, K.; Baskar, R., Production of L-Glutamic Acid with Corynebacterium Glutamicum (Ncim 2168) and Pseudomonas Reptilivora (Ncim 2598): A Study on Immobilization and Reusability. *Avicenna Journal of Medical Biotechnology* **2014**, *6*, 163-168.

3. Jyothi, A. N.; Sasikiran, K.; Nambisan, B.; Balagopalan, C., Optimisation of Glutamic Acid Production from Cassava Starch Factory Residues Using Brevibacterium Divaricatum. *Process Biochem.* **2005**, *40*, 3576-3579.

4. Leuchtenberger, W.; Huthmacher, K.; Drauz, K., Biotechnological Production of Amino Acids and Derivatives: Current Status and Prospects. *Appl. Microbiol. Biotechnol.* **2005**, *69*, 1-8.

5. Ault, A., The Monosodium Glutamate Story: The Commercial Production of Msg and Other Amino Acids. *J. Chem. Educ.* **2004**, *81*, 347.

6. Izumi, Y.; Chibata, I.; Itoh, T., Production and Utilization of Amino Acids. *Angewandte Chemie International Edition in English* **1978**, *17*, 176-183.

7. Sugita, Y.-h., Polymorphism of L-Glutamic Acid Crystals and Inhibitory Substance for Β-Transition in Beet Molasses. *Agricultural and Biological Chemistry* **1988**, *52*, 3081-3085.

8. Kitamura, M., Controlling Factors and Mechanism of Polymorphic Crystallization. *Cryst. Growth Des.* **2004**, *4*, 1153-1159.

9.   Kitamura, M., Polymorphism in the Crystallization of L-Glutamic Acid. *J. Cryst. Growth* **1989**, *96*, 541-546.

10.   Mougin, P.; Wilkinson, D.; Roberts, K. J., In Situ Measurement of Particle Size During the Crystallization of L-Glutamic Acid under Two Polymorphic Forms: Influence of Crystal Habit on Ultrasonic Attenuation Measurements. *Cryst. Growth Des.* **2002**, *2*, 227-234.

11.   Di Profio, G.; Curcio, E.; Ferraro, S.; Stabile, C.; Drioli, E., Effect of Supersaturation Control and Heterogeneous Nucleation on Porous Membrane Surfaces in the Crystallization of L-Glutamic Acid Polymorphs. *Cryst. Growth Des.* **2009**, *9*, 2179-2186.

12.   Helmdach, L.; Feth, M. P.; Ulrich, J., Integration of Process Analytical Technology Tools in Pilot-Plant Setups for the Real-Time Monitoring of Crystallizations and Phase Transitions. *Organic Process Research & Development* **2013**, *17*, 585-598.

13.   Wu, H.; Reeves-McLaren, N.; Jones, S.; Ristic, R. I.; Fairclough, J. P. A.; West, A. R., Phase Transformations of Glutamic Acid and Its Decomposition Products. *Cryst. Growth Des.* **2010**, *10*, 988-994.

14.   Bouchoucha, M.; Jaber, M.; Onfroy, T.; Lambert, J.-F.; Xue, B., Glutamic Acid Adsorption and Transformations on Silica. *J. Phys. Chem. C* **2011**, *115*, 21813-21825.

15.   Chowdhury, A. U.; Dettmar, C. M.; Sullivan, S. Z.; Zhang, S.; Jacobs, K. T.; Kissick, D. J.; Maltais, T.; Hedderich, H. G.; Bishop, P. A.; Simpson, G. J., Kinetic Trapping of Metastable Amino Acid Polymorphs. *J. Am. Chem. Soc.* **2014**, *136*, 2404-2412.

16.   Kitamura, M., Morphological Change Mechanism of A-L-Glutamic Acid with Inclusion of L-Phenylalanine. In *Separation and Purification by Crystallization*, American Chemical Society: 1997; Vol. 667, pp 83-91.

17. Cashell, C.; Corcoran, D.; Hodnett, B. K., Effect of Amino Acid Additives on the Crystallization of L-Glutamic Acid. *Cryst. Growth Des.* **2005**, *5*, 593-597.

18. Schöll, J.; Bonalumi, D.; Vicum, L.; Mazzotti, M.; Müller, M., In Situ Monitoring and Modeling of the Solvent-Mediated Polymorphic Transformation of L-Glutamic Acid. *Cryst. Growth Des.* **2006**, *6*, 881-891.

19. Cornel, J.; Lindenberg, C.; Mazzotti, M., Experimental Characterization and Population Balance Modeling of the Polymorph Transformation of L-Glutamic Acid. *Cryst. Growth Des.* **2009**, *9*, 243-252.

20. Kee, N. C. S.; Tan, R. B. H.; Braatz, R. D., Selective Crystallization of the Metastable A-Form of L-Glutamic Acid Using Concentration Feedback Control. *Cryst. Growth Des.* **2009**, *9*, 3044-3051.

21. Ferrari, E. S.; Davey, R. J., Solution-Mediated Transformation of A to B L-Glutamic Acid: Rate Enhancement Due to Secondary Nucleation. *Cryst. Growth Des.* **2004**, *4*, 1061-1068.

22. Cashell, C.; Corcoran, D.; Hodnett, B. K., Secondary Nucleation of the B-Polymorph of L-Glutamic Acid on the Surface of α-Form Crystals. *Chem. Commun.* **2003**, 374-375.

23. Rusin, M.; Ewan, B. C. R.; Ristic, R. I., The Glycine-Stimulated Nucleation and Solution-Mediated Polymorphic Transformation of L-Glutamic Acid. *CrystEngComm* **2013**, *15*, 2192-2196.

24. Strachan, C. J.; Taday, P. F.; Newnham, D. A.; Gordon, K. C.; Zeitler, J. A.; Pepper, M.; Rades, T., Using Terahertz Pulsed Spectroscopy to Quantify Pharmaceutical Polymorphism and Crystallinity. *J. Pharm. Sci.* **2005**, *94*, 837-846.

25.   Zeitler, J. A.; Taday, P. F.; Newnham, D. A.; Pepper, M.; Gordon, K. C.; Rades, T.,
        Terahertz Pulsed Spectroscopy and Imaging in the Pharmaceutical Setting - a Review. *J.
        Pharm. Pharmacol.* **2007**, *59*, 209-223.

26.   Taday, P. F.; Bradley, I. V.; Arnone, D. D.; Pepper, M., Using Terahertz Pulse
        Spectroscopy to Study the Crystalline Structure of a Drug: A Case Study of the
        Polymorphs of Ranitidine Hydrochloride. *J. Pharm. Sci.* **2003**, *92*, 831-838.

27.   Chakkittakandy, R.; Corver, J. A. W. M.; Planken, P. C. M., Terahertz Spectroscopy to
        Identify the Polymorphs in Freeze-Dried Mannitol. *J. Pharm. Sci.* **2010**, *99*, 932-940.

28.   Ruggiero, M. T.; Gooch, J.; Zubieta, J.; Korter, T. M., Evaluation of Range-Corrected
        Density Functionals for the Simulation of Pyridinium-Containing Molecular Crystals. *J.
        Phys. Chem. A* **2016**.

29.   Ruggiero, M. T.; Korter, T. M., The Crucial Role of Water in Shaping Low-Barrier
        Hydrogen Bonds. *Phys. Chem. Chem. Phys.* **2016**.

30.   Delaney, S. P.; Pan, D.; Galella, M.; Yin, S. X.; Korter, T. M., Understanding the Origins
        of Conformational Disorder in the Crystalline Polymorphs of Irbesartan. *Cryst. Growth
        Des.* **2012**, *12*, 5017-5024.

31.   King, M. D.; Buchanan, W. D.; Korter, T. M., Identification and Quantification of
        Polymorphism in the Pharmaceutical Compound Diclofenac Acid by Terahertz
        Spectroscopy and Solid-State Density Functional Theory. *Anal. Chem.* **2011**, *83*, 3786-
        3792.

32.   Garti, N.; Zour, H., The Effect of Surfactants on the Crystallization and Polymorphic
        Transformation of Glutamic Acid. *J. Cryst. Growth* **1997**, *172*, 486-498.

33.   *Apex2, Data Collection Software*, Version 2011.8-0; Bruker-AXS Inc.: Madison, WI, 2011, 2011.

34.   *Saint Plus, Data Reduction Software*, Version 6.45A; Bruker-AXS Inc.: Madison, WI 2013, 2013.

35.   Sheldrick, G., SADABS. University of Göttingen, Germany Program for Empirical Absorption Correction of Area Detector Data: 1996.

36.   Wilson, A.; Geist, V., International Tables for Crystallography. Volume C: Mathematical, Physical and Chemical Tables. *Crystal Research and Technology* **1993**, *28*, 110-110.

37.   Sheldrick, G., SHELXTL, Version 6.1; Bruker Analytical X-Ray Systems. *Inc.: Madison, WI* **1997**.

38.   Lee, Y.-S.; Meade, T.; Perlin, V.; Winful, H.; Norris, T. B.; Galvanauskas, A., Generation of Narrow-Band Terahertz Radiation Via Optical Rectification of Femtosecond Pulses in Periodically Poled Lithium Niobate. *Appl. Phys. Lett.* **2000**, *76*, 2505-2507.

39.   Theuer, M.; Torosyan, G.; Rau, C.; Beigang, R.; Maki, K.; Otani, C.; Kawase, K., Efficient Generation of Cherenkov-Type Terahertz Radiation from a Lithium Niobate Crystal with a Silicon Prism Output Coupler. *Appl. Phys. Lett.* **2006**, *88*, 071122.

40.   Suizu, K.; Koketsu, K.; Shibuya, T.; Tsutsui, T.; Akiba, T.; Kawase, K., Extremely Frequency-Widened Terahertz Wave Generation Using Cherenkov-Type Radiation. *Opt. Express* **2009**, *17*, 6676-6681.

41.   Kono, S.; Tani, M.; Gu, P.; Sakai, K., Detection of up to 20 Thz with a Low-Temperature-Grown Gaas Photoconductive Antenna Gated with 15 Fs Light Pulses. *Appl. Phys. Lett.* **2000**, *77*, 4104-4106.

42.   Cai, Y.; Brener, I.; Lopata, J.; Wynn, J.; Pfeiffer, L.; Stark, J. B.; Wu, Q.; Zhang, X. C.; Federici, J. F., Coherent Terahertz Radiation Detection: Direct Comparison between Free-Space Electro-Optic Sampling and Antenna Detection. *Appl. Phys. Lett.* **1998**, *73*, 444-446.

43.   Dovesi, R.; Orlando, R.; Erba, A.; Zicovich-Wilson, C. M.; Civalleri, B.; Casassa, S.; Maschio, L.; Ferrabone, M.; De La Pierre, M.; D'Arco, P.*, et al.*, CRYSTAL14: A Program for the *ab initio* Investigation of Crystalline Solids. *Int. J. Quantum Chem* **2014**, *114*, 1287-1317.

44.   Perdew, J. P.; Burke, K.; Ernzerhof, M., Generalized Gradient Approximation Made Simple. *Phys. Rev. Lett.* **1996**, *77*, 3865-3868.

45.   Krishnan, R.; Binkley, J. S.; Seeger, R.; Pople, J. A., Self-Consistent Molecular Orbital Methods. XX. A Basis Set for Correlated Wave Functions. *J. Chem. Phys.* **1980**, *72*, 650-654.

46.   Becke, A. D., Density-Functional Thermochemistry. III. The Role of Exact Exchange. *J. Chem. Phys.* **1993**, *98*, 5648-5652.

47.   Grimme, S.; Antony, J.; Ehrlich, S.; Krieg, H., A Consistent and Accurate ab initio Parametrization of Density Functional Dispersion Correction (DFT-D) for the 94 Elements H-Pu. *J. Chem. Phys.* **2010**, *132*, 154104.

48.   Noel, Y.; Zicovich-Wilson, C. M.; Civalleri, B.; D'Arco, P.; Dovesi, R., Polarization

        Properties of Zno and Beo: An *ab initio* Study through the Berry Phase and Wannier

        Functions Approaches. *Phys. Rev. B.* **2001**, *65*, 014111.

49.   Hirayama, N.; Shirahata, K.; Ohashi, Y.; Sasada, Y., Structure of α Form of L-Glutamic

        Acid. A−B Transition. *Bull. Chem. Soc. Jpn.* **1980**, *53*, 30-35.

50.   Lehmann, M.; Nunes, A., A Short Hydrogen Bond between near Identical Carboxyl

        Groups in the A-Modification of L-Glutamic Acid. *Acta Crystallogr. Sect. B: Struct. Sci.*

        1980, *36*, 1621-1625.

51.   Lehmann, M. S.; Koetzle, T. F.; Hamilton, W. C., Precision Neutron Diffraction

        Structure Determination of Protein and Nucleic Acid Components. Viii: The Crystal and

        Molecular Structure of the B-Form of the Amino Acidl-Glutamic Acid. *Journal of*

        Crystal and Molecular Structure, *2*, 225-233.

52.   Franz, M.; Fischer, B. M.; Walther, M., The Christiansen Effect in Terahertz Time-

        Domain Spectra of Coarse-Grained Powders. *Appl. Phys. Lett.* **2008**, *92*, 021107.

53.   Christiansen, C., Untersuchungen Über Die Optischen Eigenschaften Von Fein

        Vertheilten Körpern. *Annalen der Physik* **1884**, *259*, 298-306.

54.   Frisch, M. J.; Trucks, G. W.; Schlegel, H. B.; Scuseria, G. E.; Robb, M. A.; Cheeseman,

        J. R.; Scalmani, G.; Barone, V.; Mennucci, B.; Petersson, G. A.*, et al.*, Gaussian 09,

        Revision B.01. Wallingford CT, 2009.

APPENDIX A: Terahertz Disorder-Localized Rotational Modes and Lattice Vibrational Modes in the Orientationally-Disordered and Ordered Phases of Camphor

Abstract

The temperature-dependent terahertz spectra of the partially-disordered and ordered phases of camphor ($C_{10}H_{16}O$) are measured using terahertz time-domain spectroscopy. In its partially-disordered phases, a low-intensity, extremely broad resonance is found and is characterized using both a phenomological approach and an approach based on *ab initio* solid-state DFT simulations. These two descriptions are consistent and stem from the same molecular origin for the broad resonance: the disorder-localized rotational correlations of the camphor molecules. In its completely ordered phase(s), multiple lattice phonon modes are measured and are found to be consistent with those predicted using solid-state DFT simulations.

A.1 Introduction

The room temperature bulk condensed phase of camphor, a bicyclic chiral molecule with the general formula $C_{10}H_{16}O$, is considered a plastic-crystal (PC) due to the presence of translational order and orientational disorder: disorder which arises from the dynamic rotation of the translationally-fixed molecules, i.e. a rotor phase.[1] This rotational disorder is characteristic of both the crystals containing only right or left-handed enantiomers (homochiral) and of a crystal with a 1:1 mixture of both enantiomers (racemic).[2] The similar phase behavior of racemic and homochiral camphor diverges at lower temperatures. Homochiral camphor undergoes a first-order solid-solid phase transition at T_{PC-OC}=244K into an orientationally-ordered crystal (OC).[3] Conversely, racemic camphor, at T_{PC-GC}=190–210K, undergoes a higher-order transition into a glassy-crystal (GC) phase where its orientational disorder is 'frozen-in', i.e. the molecules in its orthorhombic unit cell are each frozen into one of 4 fixed orientations, and the orientation of each molecule is random with respect to that of its neighbors.[4] Therefore, camphor is a rich molecular system that consists of multiple condensed phases with varying permutations of partial disorder and complete order.

Terahertz time-domain spectroscopy (THz-TDS) is uniquely suited to probe the properties of its partially-disordered and ordered phases. It has provided valuable insight into many other disordered materials, such as polymers,[5] glasses,[6-8] and liquids.[9-11] In addition, dynamics universal to disordered materials, including disordered-induced coupling of localized vibrational modes to photons,[12] the Poley peak in liquids,[13] and the Boson peak in amorphous solids,[14] are known to occur in the far-IR and THz range. On the other hand, THz-TDS is also an excellent tool for probing ordered molecular crystals, which often exhibit infrared-active lattice

vibrational modes in this spectral range.[15-18] In camphor, neutron scattering measurements of its orientationally-disordered phases have already revealed a curious excess feature in its phonon density of states in the range of 25 to 100 cm-1 (0.75 – 3.0 THz).[19] Additionally, Raman[20] and far-IR[21] studies of homochiral camphors' low-T OC phase(s) have revealed multiple resonance features in the range from 30 to 80 cm^{-1} (0.9-2.4 THz). However, no attempt has been made to assign these features to their specific molecular origins. Therefore, THz-TDS of racemic and homochiral camphor, coupled with solid-state DFT simulations, has the potential to provide valuable fundamental insight into the ordered and partially-disordered phases of this complex soft condensed matter system.

In this study we present the temperature-dependent THz spectra of racemic (RS($\pm$)) and homochiral (R(+) & S(-)) camphor, from frequencies of 0.2 to 2.70 THz and temperatures from 12 K to 340 K. In the orientationally-disordered phases of these three materials, their spectra are virtually indistinguishable, exhibiting a very broad, low intensity absorption peak. In racemic camphor (RS($\pm$)), this feature persists through a solid-solid phase transition into its low-T orientationally-disordered GC phase. This is an indication that the origin of the broad absorption feature is related to the presence of disorder and not to dynamical reorientations, which freeze out upon cooling from the PC rotor phase to the GC phase. We characterize the broad feature using both a phenomological and an *ab initio* approach. In contrast, homochiral camphors' (R(+) or S(-)) low-T OC spectra exhibit multiple lattice phonon modes typical of ordered molecular crystals. These modes are compared and assigned to those predicted using rigorous solid-state density functional theory (DFT) simulations.
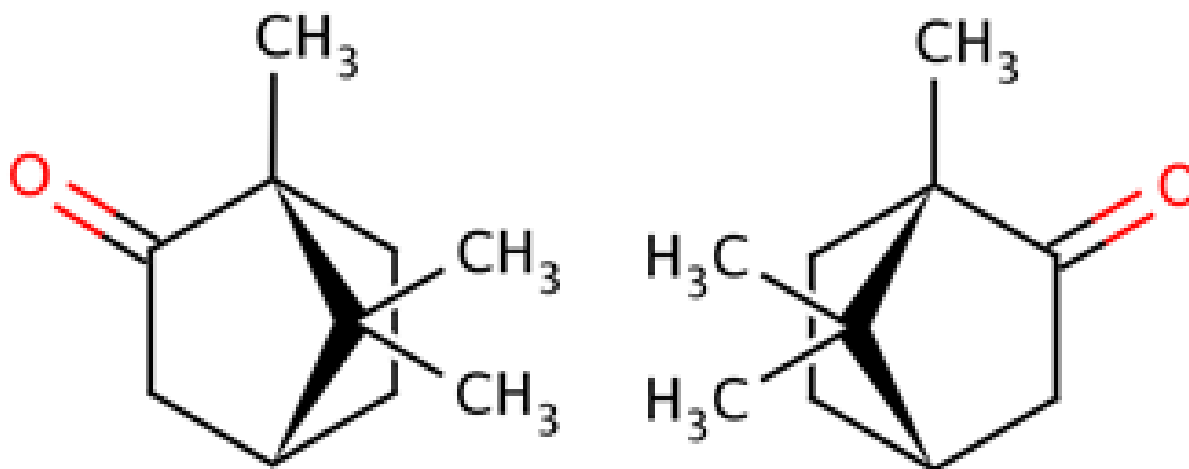
Figure A-1. R(+) (left) and S(-) (right) camphor.

A.2 Experimental details and theory

Homochiral and racemic camphor samples were obtained from Sigma-Aldrich chemicals with purities of 98% for R(+), 99% for S(-), and 96% for RS(±) and used without further purification. The individual molecular structures of the enantiomers are shown in **Fig. A-1**. The initially opaque, soft polycrystalline solids are hand-pressed into transparent discs in the center of Teflon ring spacers, with inner diameters of 4 mm and thicknesses of 600 μm, 300 μm, and 100 μm. The thickness of the Teflon spacers sets the optical path length of the measurements. Two thick (2 mm) high-resistivity Si wafers are placed over the exposed faces of the camphor and Teflon discs, to serve as both windows and thermal contacts for efficient temperature control. The prepared samples are then mounted inside a Cryo-Industries RC-102 cryostat, positioned so the sample rests in the focal plane of the THz beam. THz transients are generated using a custom GaAs photoconductive switch which is gated by 80 fs optical (800 nm) pulses from a Ti:sapphire oscillator, and are measured using electro-optic sampling using a 1 mm thick ZnTe crystal.[22] The THz beam is quasi-optically collimated and focused through the cryostat and the sample using pairs of off-axis parabolic mirrors and Si lenses, respectively. To eliminate water vapor absorption, the entire THz beam path is purged with dry N_2. In order to obtain the sample's indices of refraction, $n(\nu)$, and absorption coefficients, $\alpha(\nu)$, the ratio of the Fourier transforms of the time-domain waveforms transmitted through the sample and through an empty cell reference, i.e. the transmission function, is inverted using the thick-film approximation[23] or numerically solved using the Newton-Raphson method.[24] Theoretical fits to the measured spectra were performed using the OriginPro software package which utilizes the Levenberg-Marquardt algorithm.

The solid-state simulations were performed with the CRYSTAL09 software package.[25] Geometry optimizations were performed with energy convergence criterion of 10^{-8} hartree, and the starting atomic positions were taken from the published crystallographic data. While low temperature synchrotron powder X-ray diffraction experiments have been performed on the homochiral species,[3] yielding reliable atomic positions, only disordered powder X-ray diffraction data for the racemic species exists in the literature.[4] The disorder associated with the racemic species led to four possible ordered crystallographic arrangements in the *Cc* space group, and simulations were performed on each form individually. The simulations were performed with the generalized gradient approximation (GGA) Perdew-Burke-Ernzerhof (PBE)[26] density functional. The split-valence double-ζ 6-31G(d,p) basis set was used for all atomic species.[27] Grimme's semi-empirical D-2 London-dispersion correction[28] was used, with the modified van der Waals radii[29] and the s_6 scaling factor set to 0.50. The simulations of the vibrational spectra were performed within the harmonic approximation using the optimized atomic positions, and infrared intensity data was obtained through the Berry phase method.[30] The energy convergence for the frequency analyses was set to 10^{-10} hartree.

A.3 Results and discussion

A.3.1 Terahertz spectra

Plotted in **Fig. A-2** are $n(\nu)$ and $\alpha(\nu)$ for racemic and homochiral camphor in their PC phases at T = 294 K, and in the GC phase (racemic) and OC phase(s) (homochiral) at T = 12 K. At room temperature their spectra are virtually indistinguishable, displaying a very broad absorption peak with a center frequency, ν_c, of approximately 36 cm^{-1} (1.1 THz). However, upon cooling through their respective solid-solid phase transitions, racemic and homochiral camphors' spectra become strikingly different. Racemic camphor retains the very broad absorption feature, which shifts continuously to higher frequencies at lower T's. It also becomes slightly asymmetric, with a steeper high frequency wing. Conversely, homochiral camphors' low-T spectra exhibit at least five Lorentzian-like peaks. Considering that the sample at this temperature is orientationally and translationally ordered,[3] these can be attributed a priori to lattice vibrational modes, i.e., phonons. The apparent differences in the absorption intensity between the two homochiral samples are due to inconsistencies in sample quality.
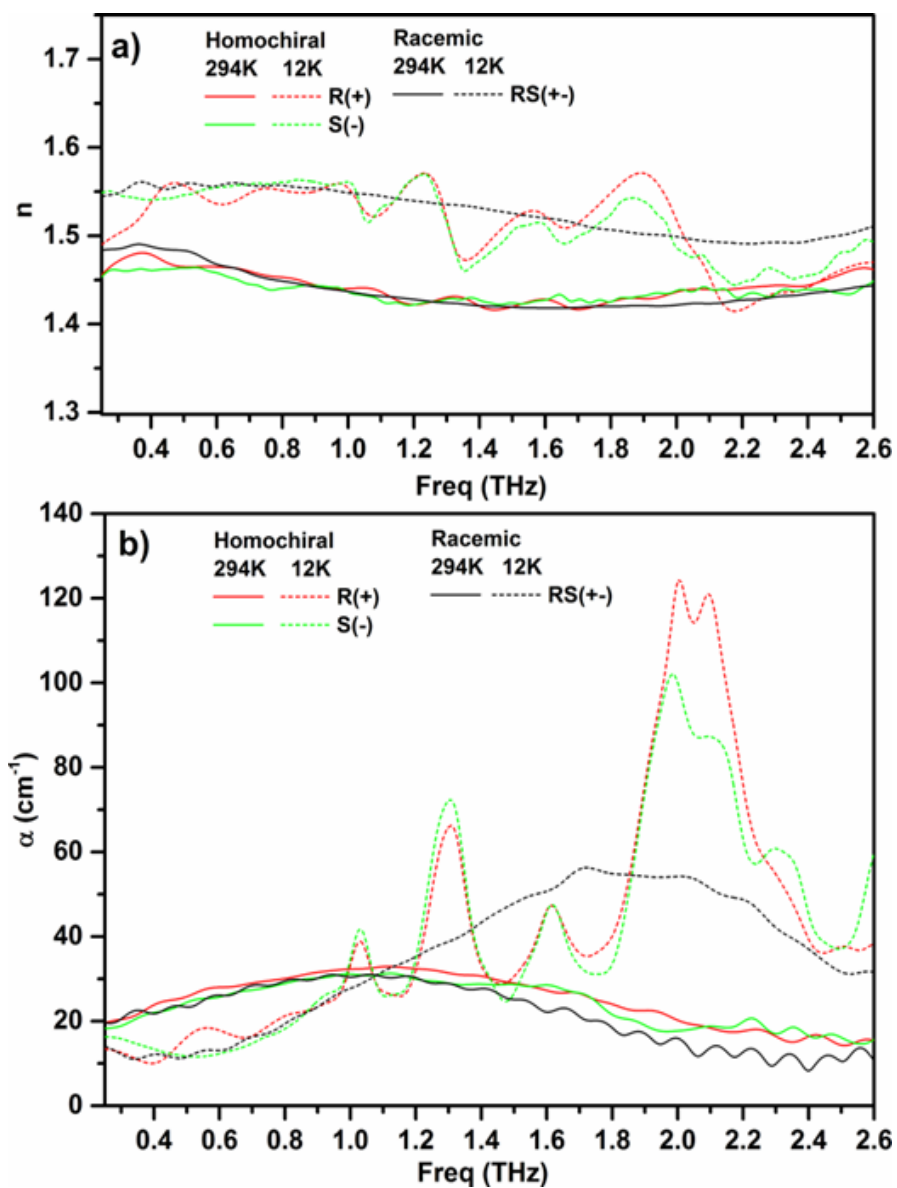
Fig A-2. a) *n*(ν) **and b)** α(ν) **for the racemic (black) and homochiral (red, green) camphor samples at T=294K (solid) and T=12K (dashed).**

A.3.2 Temperature-dependence of the absorption features

In **Fig. A-3(a)** and **(b),** the center frequencies, ν_c, of the broad absorption feature and of the five most prominent lattice phonon modes are plotted vs. T. The mean ν_c's of the broad absorption feature red-shift with increasing T (**Fig. A-3(a)**). There is significant error in the mean ν_c's between different samples and T's, not surprising given its extremely broad linewidth. Given this uncertainty, racemic camphor's GC to PC phase transition around T~190K is virtually imperceptible in the T-dependence of the ν_c's. However, the phase transition can clearly be distinguished in the temperature-dependent index of refraction (**Fig. A-3(a)** inset). The change in its $\delta n/\delta T$ around T~195K is a clear indication of the GC-PC phase transition, similar to the glass transitions observed in polymers.[5] The phonon modes in the low-T OC phase(s) of homochiral camphor also red-shift with increasing T, typical of lattice modes that are anharmonic[31] (**Fig**. **A-3(b)**). The modes are qualitatively consistent with those observed in the previously cited Raman[20] and far-IR[21] studies. Above T~140K the two higher frequency modes near 66 cm^{-1} (2 THz) become nearly indistinguishable due to significant broadening, resulting in the increased scatter in their measured ν_c's. The appearances or disappearances of the prominent phonon modes at T~235 K in the homochiral camphor samples are consistent with their previously cited phase behavior. Above T~235 K, the ν_c's of the broad features in the racemic and homochiral samples are indistinguishable. Curiously, upon heating or cooling racemic camphor through T~40 K a repeatable discontinuity in the broad absorption feature's ν_c also appears. This significant shift also coincides with a small discontinuity in $n(\nu)$, usually taken as an indication of a phase transition.[32] However, a previous low-T thermodynamic study shows no sign of a phase transition at this temperature.[33] This discrepancy may be due to a difference in

experimental pressures; in this experiment the pressure surrounding the sample is $<10^{-3}$ mbar ($<10^{-5}$ atm), while in the cited reference the stated pressure is 10^5 Pa (0.986 atm). Given the very complex phase diagram of camphor, with at least nine different polymorphs when varying the pressure and temperature,[34] it is possible that this feature near 40 K indicates another as-yet-unidentified low-T, low-P polymorph.
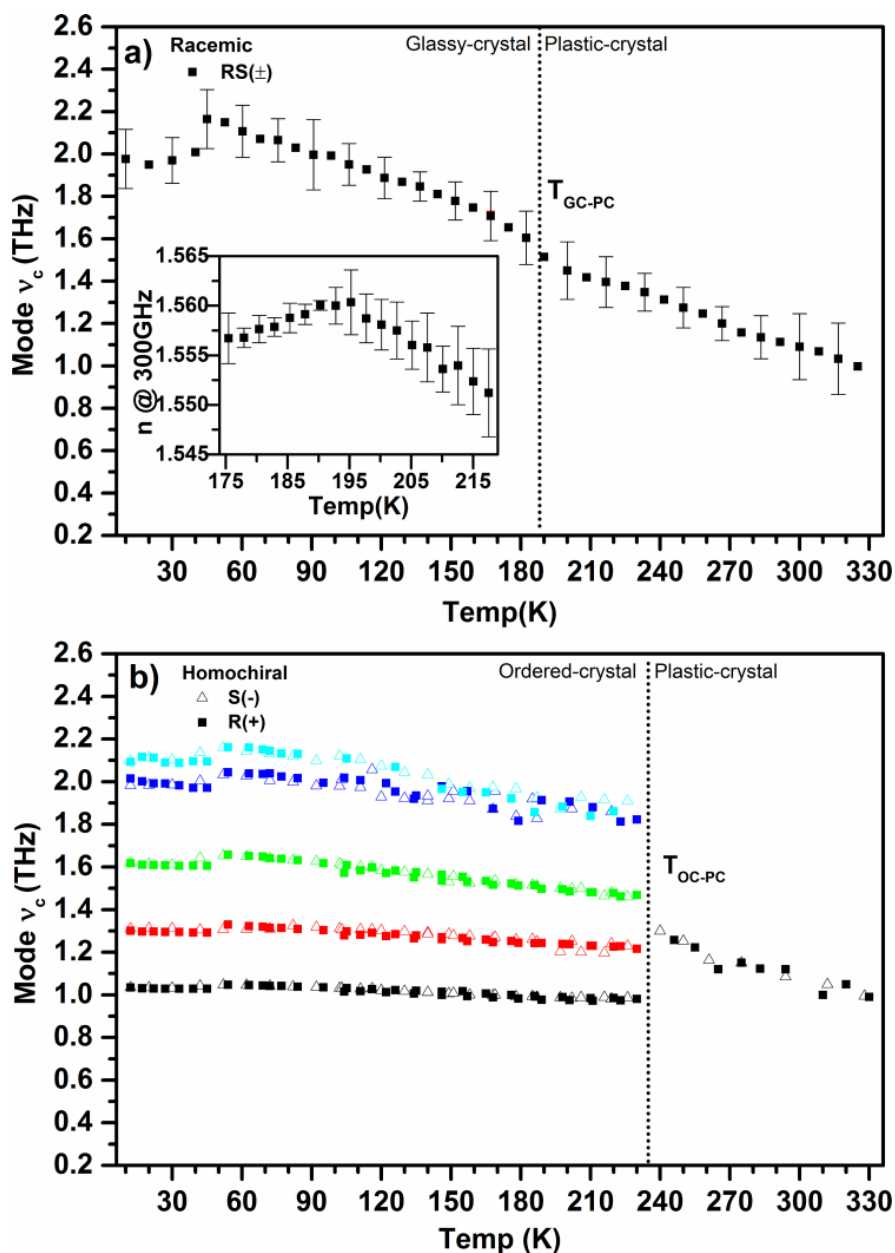
Fig A-3. a) Plot of the mean center frequencies, v_c, vs. T of the broad absorption feature for 3 different racemic (RS±) camphor samples. Inset of a): Mean refractive indices, n, at 300GHz vs. T, showing the glass transition at T~190-200K. b) The v_c's of the five most prominent phonon modes in the homochiral camphor samples (100µm thick, R(+) and S(-)) for their OC phases (<235K) and the v_c's of the broad absorption features in their PC phases (>235K). Approximate phase transition T's are demarcated with the dotted lines.

A.3.3 Origin of the OC phase absorption features

Plotted in **Fig. 4** is a representative OC phase spectrum of a 300 μm thick homochiral (S(-)) sample at T=100 K, along with the vibrational modes predicted via solid-state DFT simulations. Despite homochiral camphor's complex low-T structure [3], the simulations reproduce a spectrum very similar to the experiment, predicting 15 IR-active modes with relative intensities comparable to the experimental values. When the modes are convolved with Lorentzians, using the predicted IR intensities and mode-independent FWHM linewidths of 100 GHz, the theoretical absorption spectrum closely resembles the measured one. The slightly lower experimental intensities are probably due to the quality of the samples (polycrystalline vs. oriented single crystals) and, potentially, the presence of residual orientationally-disorder domains after cooling below T_{PC-OC}. Given the large number of predicted modes it can be difficult to unambiguously assign them to their experimental counterparts. The predicted modes, IR intensities, and their corresponding molecular motion are given in **Table A-1**.
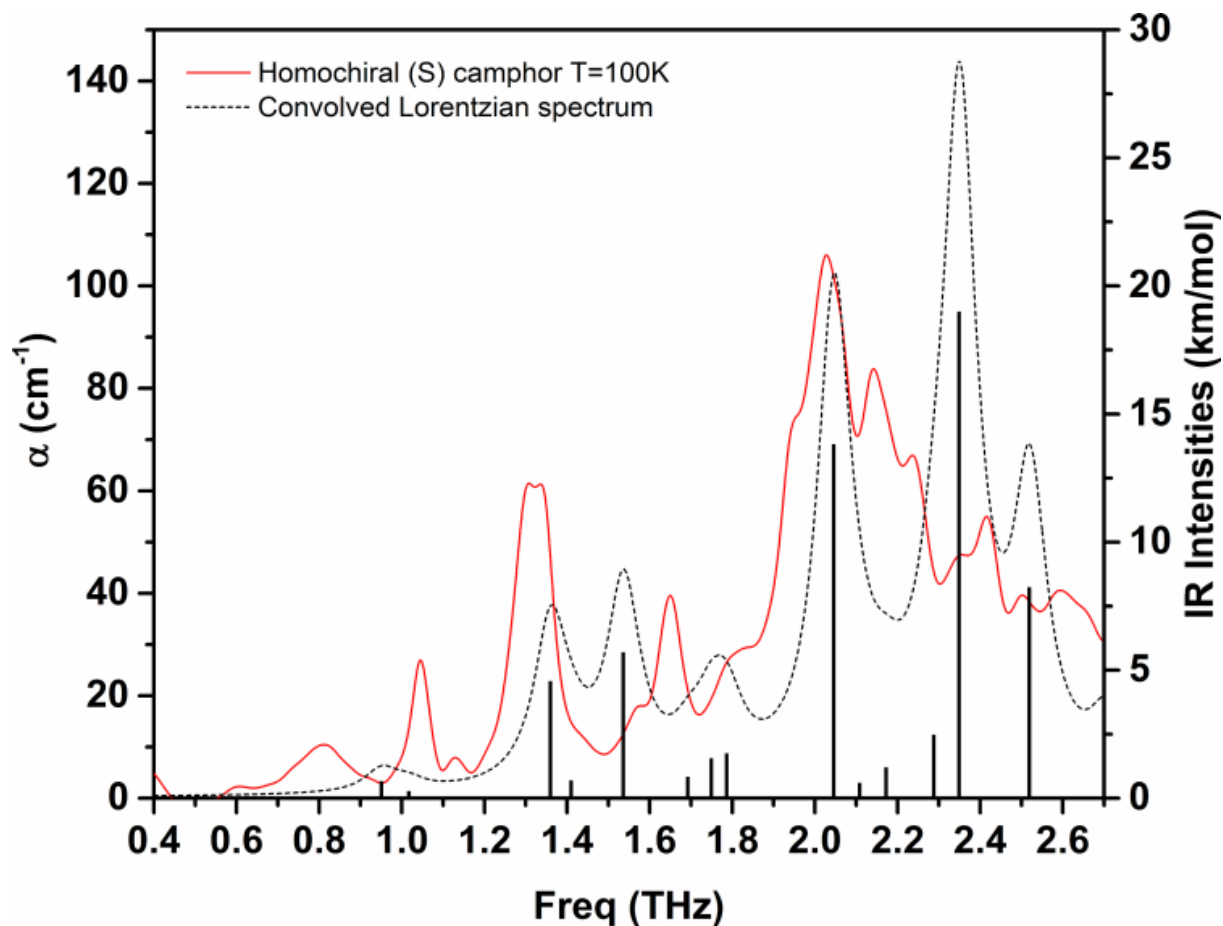
Figure A-4. Comparison of the measured 100K homochiral (S(-)) spectrum (red line) with the convolved Δυ=100GHz Lorentzian spectrum using the predicted mode frequencies and intensities (black dotted line). The mode IR intensities are also plotted (columns, right scale). The measured spectrum has been offset by -17cm^{-1} to zero.

Table A-1. DFT predicted mode frequencies, IR intensities, and assignments for homochiral camphor in its OC phase.

Frequency (THz)	Wavenumber (cm^{-1})	Intensity (km mol^{-1})	Motion
0.9505	31.706	0.65	rotation about c
1.017	33.9264	0.26	translation in c
1.359	45.3489	4.56	rotation about a
1.409	47.0282	0.68	rotation about a
1.536	51.2386	5.68	rotation about c
1.692	56.4552	0.82	rotation about b
1.748	58.339	1.54	rotation about c
1.786	59.5829	1.74	translation in b
2.045	68.2232	13.81	rotation about a
2.108	70.3267	0.58	rotation about b
2.172	72.457	1.19	rotation about c
2.287	76.3069	2.46	rotation about c
2.348	78.3521	18.98	rotation about a
2.510	84.02	8.22	rotation about a
2.704	90.2	1.84	rotation about c

A.3.4 Origin of the PC and GC phase absorption feature

The origin of the broad absorption feature in both racemic and homochiral camphors' room-T PC phases and in racemic camphor's low-T GC phase is of particular interest. Its persistence through racemic camphor's PC-to-GC phase transition would seem to preclude the possibility of attributing it to long-range phonon mode(s) since, in addition to the presence of orientational disorder in both phases, the structure of the PC and GC phases are not equivalent; its PC phases have a hexagonal unit cell,[2] while its GC phase unit cell is orthorhombic.[4] Additionally, earlier dielectric measurements have shown a Debye relaxation time of ~20 ps or slower at room temperature for the PC phase.[35-37] This would result in a resonance outside of our accessible frequency window, and moreover it is not observed in racemic camphor's low-T GC phase. Therefore the measured absorption feature can not be attributed to the same Debye reorientational process observed in the dielectric studies. The dynamic process behind the measured THz feature is more than an order of magnitude faster; hence it must arise from a different molecular origin. To explore its origin, we take two approaches. The first is a phenomological approach which stems from the characterization of completely disordered materials, including polar and non-polar liquids. The second is a computational approach which relies upon ab initio DFT simulations of four possible permutations of racemic camphor's GC phase unit cell.

To phenomologically characterize dipolar correlations in condensed phase disordered materials in the far-IR range, Mori's continued fraction formalism is often used.[38] This approach stems from the generalized Langevin equation and the dipole correlation function, and has been

used to characterize the far-IR absorption (the so-called Poley peak) in non-dipolar liquids[39,40] and, more recently, a Boson peak in the rotor-phases of n-alkanes.[32] Past investigations of other orientationally-disordered PC's, such as tertiary butyl-chloride[41] and methyl-chloroform,[42] have suggested their far-IR spectra can be attributed to short-range correlated vibrations similar to the origin of the Poley peak in liquids, even in these cases where there is complete translational order but orientational disorder. The Poley peak's physical origin has been attributed to gyroscopic orientational oscillations (librations) of a molecule's permanent and/or induced dipole moment. In a simple itinerant oscillator model, the frequency of this libration is proportional to that of a rigid rotor, $(kT/I)^{1/2}$.[43] Camphor has a non-zero dipole moment,[44] so these dipolar librations could couple to the probing THz radiation. Using this approach, the experimental observables, $n(\omega)$ and $\alpha(\omega)$, can be related to the second order expansion of the Mori memory kernel using[13,38]:

$$(1) \qquad \alpha(\omega)n(\omega) = \frac{\Delta\varepsilon}{c} \frac{\gamma K_1 K_2}{\gamma^2\left(K_1 - \omega^2\right) + \omega^2\left(\omega^2 - K_1 - K_2\right)^2}$$

Ideally, the parameter K_1 can be related to dipolar angular momentum while K_2 and γ can be related to the amplitude and damping constant of the intermolecular torque correlation decay function, $K_2(t) = K_2 e^{-\gamma t}$.

Plotted in **Fig. A-5** are the fits of Eq. 1 to a few representative spectra, with their frequencies normalized by camphor's symmetric top rigid rotor frequencies, $(2kT/I)^{1/2}$.[45] With the known values of $\Delta\varepsilon(T)^{35}$ and K_1, K_2, and γ as free parameters, the fits of Eq. 1 to racemic camphor's low-T GC phase (T<190K) spectra are satisfactory; it reproduces the measured spectra well in the region of the peaks but deviates on their low frequency wings. However, Eq. 1

begins to fail for T>190K, demonstrated by the less than satisfactory fits of the T=195K and T=294K spectra in **Figure A-5**. With inclusion of an additional $n(0)\alpha(0)$ additive offset parameter, the higher-T PC phase spectra can also be satisfactorily reproduced. Physically, this offset, which increases as T increases, can be attributed to the encroaching high-frequency wing of camphor's PC phase Debye relaxation.[35-37] Plotted in the inset are the extracted parameters K_1, K_2, and γ from the fits over the entire range of T's. The two intermolecular torque correlation parameters K_2 and γ remain relatively constant in racemic camphor's low-T GC phase, but then begin to decrease and slowly increase, respectively, as T approaches and passes T_{GC-PC}. The parameter K_1, with the exceptions of the anomalous and expected phase transitions, decreases approximately linearly with T. We can qualitatively compare our normalized fit parameters (normalized using $(2kT/I)^{1/2}$ for γ and $(2kT/I)$ for K_1, K_2) to the results of Davies and Evans[13] for several different molecules in their bulk liquid phases (**Fig. A-6 (b)**). Interestingly, camphor's K_2 parameters in its GC and PC phases (practically equivalent to each other) are almost an order of magnitude smaller compared to the liquids, i.e. relative to the liquids its mean squared intermolecular torque is initially more weakly correlated, which is reasonable given its translational order. The K_1 and γ parameters are comparable to the liquids in its PC phase (T=294) but are an order of magnitude less in its low-T GC phase (T=12K), corresponding to a significant decrease in both the dipolar angular momentum and in the damping of the correlations. Hence with reduced temperature its rotational/librational dynamics are slowed and remain correlated for a longer period of time. From γ, the lifetime of these correlation are ~0.2 ps and ~0.06 ps in its GC (T=12K) and PC (T=294K) phases, respectively. The satisfactory fits of the spectra to Eq. 1 support the hypothesis that the broad feature originates from correlated dipolar motion, following the correlation function derived in Davies and Evans.[13]
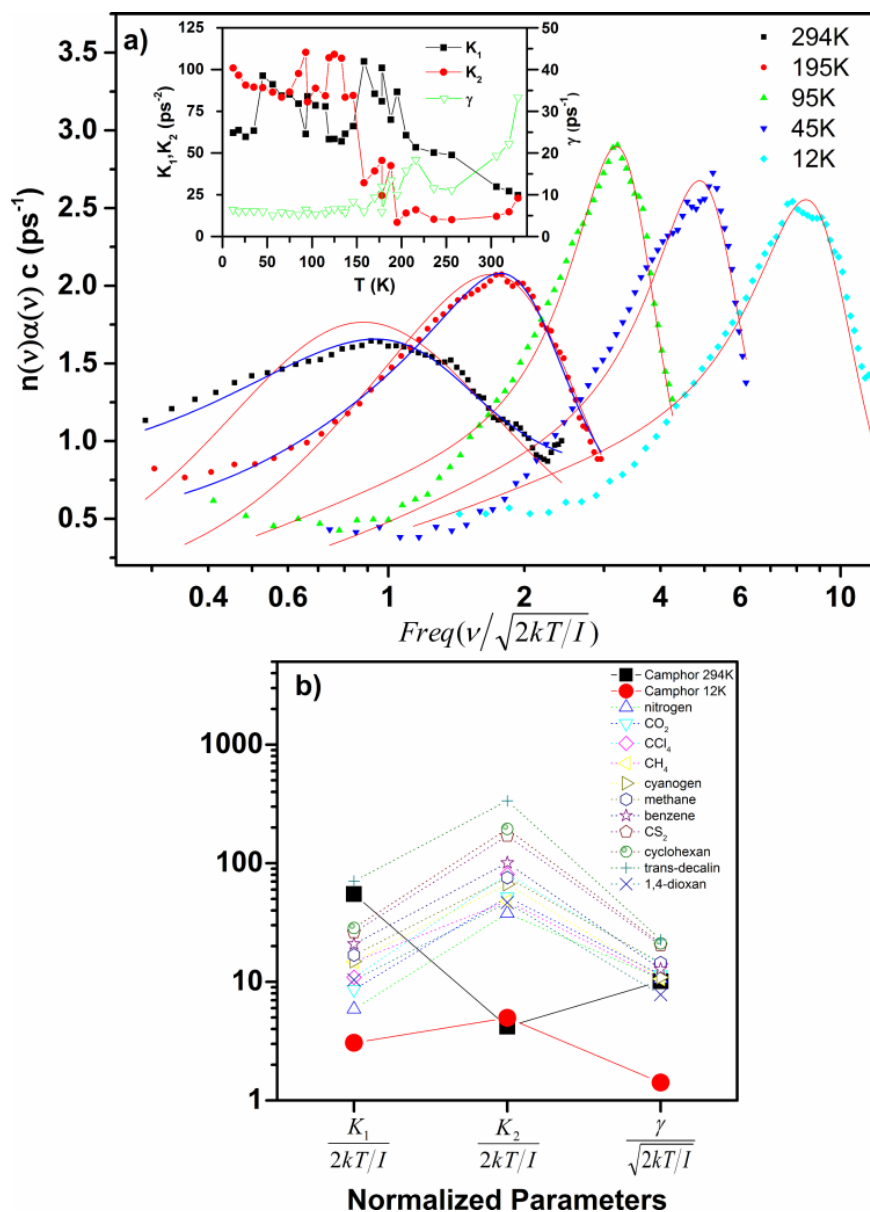
Figure A-5. a) The combined, $n(\nu)\alpha(\nu)c$, spectra of racemic camphor plotted vs. their reduced frequencies at a few different T's. Fits to Eq. 1 (red lines) and Eq. 1 with the Debye relaxation offset (blue lines) are also plotted. Inset: The extracted fit parameters K_1, K_2 and γ vs. T. b) Normalized fit parameters compared to the normalized parameters of several liquids from the work of Davies and Evans.[13]

As an alternative approach to analyzing the broad absorption feature, we can use *ab initio* density functional theory. We simulate the four known polymorphs of racemic camphor's GC phase unit cells, treating each as a separate orientationally-ordered single-crystal. The simulations of each of the separate polymorphs predict the presence of ≤8 IR-active modes in this spectral range. Since each unit cell in the sample contains randomly oriented molecules representing one of these four possible orientations, it is reasonable to assume that the measured spectrum could be predicted by superposing the four independently calculated spectra. The superimposed modes of the four 'single-crystal' polymorphs are plotted in **Fig. A-6** along with the spectrum of the 600 μm thick racemic camphor sample at T=100 K. The modes from the different polymorphs, which group together in the spectrum with similar ν_c's, arise from identical molecular rotations about their crystallographic axes. In order of increasing frequency, the predicted modes correspond to the following rotations: about *a*, about *b*, about *c*, about *a*, in *bc* plane, in *ab* plane, about *abc*, and about *b*. The theoretical rotational modes, superimposed in the same spectrum, physically represent a theoretical polycrystal which consists of extended orientationally-ordered single crystal domains of camphor's four simulated GC polymorphs. In reality, however, camphor's orientational disorder is much more homogeneously distributed. This increased nano-scale disorder relative to the theoretical polycrystal would manifest itself in the experimental spectra through broadening of the mode linewidths, $\Delta \upsilon$. With this in mind, we convolve the modes with Lorentzians using their predicted IR intensities and equal $\Delta \upsilon$'s of 20 cm^{-1}. This theoretical spectrum is plotted in **Fig. 6** along with a representative experimental spectrum. In this case the predicted modes can closely mimic the experimental spectrum when significant broadening is included. With $\Delta \upsilon$'s of 20 cm^{-1} (0.6 THz), we can make an order of magnitude estimate of the coherence length of the vibrations contributing to the broad spectral

feature. A FWHM linewidth of 0.6 THz corresponds to a lifetime of ~0.3 ps. Using the speed of sound in camphene (~1500 m/s) (a similar plastic-crystal),[46] this lifetime correspond to a coherence length of only ~0.4 nm, which is roughly the size of a single camphor molecule. If the broad feature does originate from the superposition of these predicted 'single-crystal' modes, the extreme broadening in the experimental spectra is undoubtedly a result of racemic camphor's inherent orientational disorder. We have confirmed experimentally that this disorder is intrinsic to the sample by annealing a racemic crystal at T_{GC-PC} for 144 hrs. In spite of the annealing process, no change was observed in its low-T spectra.
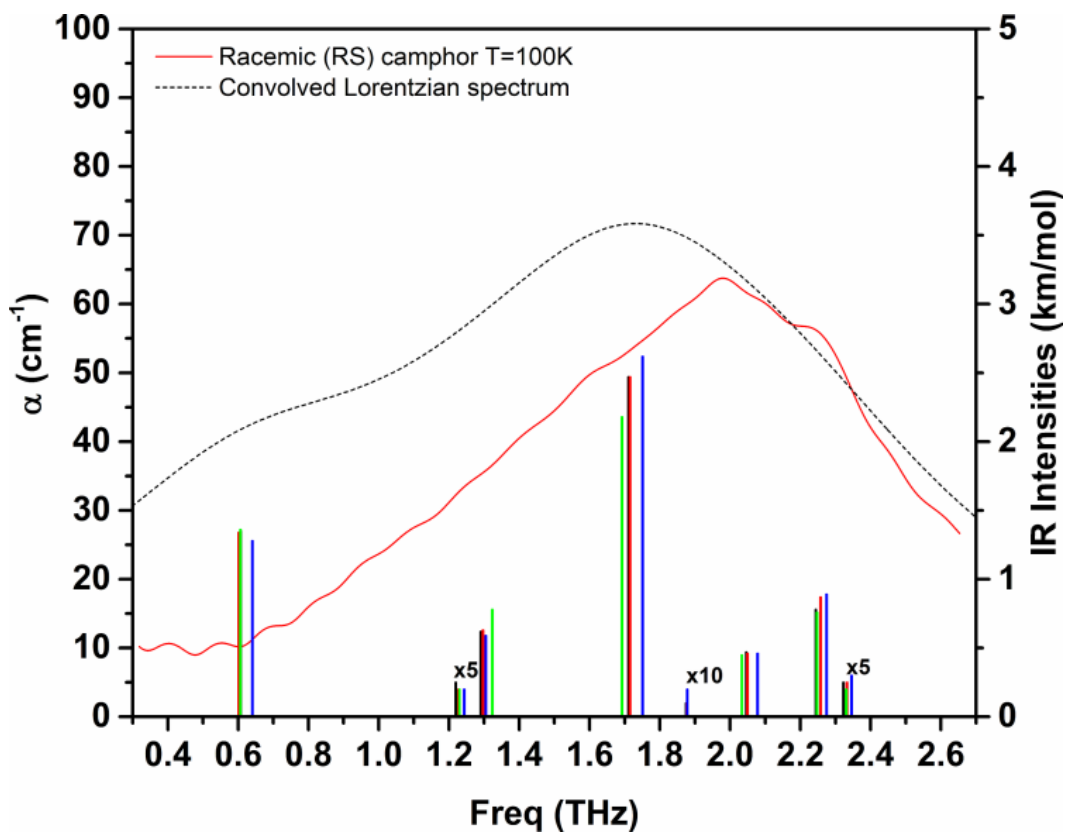
Figure A-6. The measured absorption spectrum of a 600µm racemic camphor sample at T=100K (red line) plotted with the combined spectrum using the DFT predicted modes from its four GC phase 'single-crystal' unit cells (each broadened using a Lorentzian with a broadening factor of $\Delta\upsilon$=600GHz) (black dotted line). Also plotted are the mode IR intensities for all four unit cells (columns, right scale).

A.4 Conclusions

In the partially-disordered phases of this soft matter, both the phenomological and computational approach characterize the behavior of its THz absorption spectrum. In both cases, we are led to the same conclusion for the molecular origin: the correlated rotation/libration of the molecules. Both approaches also lead to nearly the same estimated lifetime for these correlations of about 0.2-0.3 ps. This time constant is nearly two orders of magnitude faster than previously characterized Debye processes in this material, suggesting a different molecular origin. Since the dynamics are disorder-localized and purely rotational, they can persist through the PC to GC phase transition despite the different structures and the 'freezing-in' of its dynamic orientational disorder. The intermediary nature of the disorder in the PC and GC phases of camphor pose an interesting question concerning what terminology to use to label this broad feature. It is tempting to label it as a Poley or Boson peak, given the satisfactory fits to Equation 1, the evidence for disorder-localized modes, and the past studies of disordered solids and other PC's. It has been suggested both the Boson peak and Poley peak arise from the same underlying molecular origin.[47] Both labels, however, have historically only been used for the anomalous far-IR peaks found in amorphous solids and liquids. In addition, the Boson peak has traditionally been described as an excess in the Debye acoustic vibrational density of states, modes which normally would not couple to optical excitations. However, it is well known that the presence of disorder breaks down the selection rules preventing far-IR optical excitation of acoustic modes[12] and studies have shown that the Boson peak can consist of both acoustic and/or non-acoustic contributions.[48-50] And, indeed, a similar far-IR feature in ortho-carborane, another orientationally-disordered molecular PC, has been labeled as a Boson peak, with its origin

attributed to the coupling of IR-active phonon-like modes to localized vibrational modes.[51] While it may be presumptuous to label camphor's THz range broad absorption feature as a Boson peak or Poley peak, it certainly could be their analogue in this partially-disordered molecular system.

A.5 Acknowledgements

A.6 References

1   J. N. Sherwood, (Ed.) *The Plastically Crystalline State*; John Wiley and Sons: New York, 1979.

2   Mjojo, C. C. *J. Chem. Soc. Faraday Trans 2* 1979, 75, 692.

3   Brunelli, M.; Fitch, A. N.; Mora, A. J., *J. Sol. St. Chem.* 2002, 163, 253.

4   Mora, A. J.; Fitch, A.N. *J. Sol. St. Chem.* 1997, 134, 211.

5   S. Wietzke, C. Jansen, T. Jung, M. Reuter, B. Baudrit, M. Bastian, S. Chatterjee, and M. Koch, *Opt. Express.* 2009, 17, 19006-19014.

6   Zalkovskij, M.; Zoffmann C.B.; Novitsky, A.; Malureanu, R.; Savastru, D.; Popescu, A.; Jepsen, P.U.; Lavrinenko, A. V., *App. Phys. Lett.* 2012, 100, 031901.

7   Podzorov, A.; Gallot, G*., Chem. Phys. Lett.* 2010, 495,46.

8   Naftaly, M.; Miles, R. E., *J. Appl. Phys.* 2007, 102, 043517.

9   Thrane, L.; Jacobsen, R. H.; Jepsen, P. U.; Keiding, S. R., *Chem. Phys. Lett.* 1995, 240, 330.

10   Laib, P; Mittleman, D.M., *J. Infrared Milli. Terahz. Waves* 2010, 31, 1015.

11   Kindt, J. T.; Schmuttenmaer, C.A., *J. Phys. Chem.* 1996, 100, 10373.

12   Taraskin, S.N.; Simdyankin, S.I.; Elliot, S.R.; Neilson, J.R.; Lo, T.,*. Phys. Rev. Lett.* 2006, 97, 055504.

13   Davies, G. J.; Evans, M*., J. Chem. Soc., Faraday Trans. 2* 1976, 72, 1194.

14   Phillips, W. A. *Amorphous solids: low-temperature properties*. Springer: New York. 1981.

15   Allis, D. G.; Prokhorova, D. A.; Korter T. M., *J. Phys. Chem. A* 2006, 110, 1951-1959.

16   Kawase, K.; Ogawa, Y.; Watanabe, Y.; Inoue, H. , *Opt. Express* 2003, 11, 2549.

17   Jepsen, P. U.; Clark, S. J., *Chem. Phys. Lett.* 2007, 442, 275.

18   Nickel D. V.; Delaney, S.P; Bian, H.; Zheng, J.; Korter, T.M.; Mittleman, D. M., *J. Phys. Chem. A* 2014, 118, 2442-2446.

19   Holderna-Natkaniec, K.; Natkaniec, I.; Habrylo, S.; Mayer, J., *Physica B.* 1994, 194-196, 369-370.

20   Wilkinson, G.R.; Medina, J.A.; Sherman, W.F., *J. Ram. Spec.* 1981, 10, 155.

21   Ramnarine, R.; Sherman, W.F.; Wilkinson, G.R., *Infr. Phys.* 1981, 21, 391.

22   Wu, Q.; Zhang, X. C., *Appl. Phys. Lett.* 1995, 67, 3523.

23   Lee, Y.S. *Principles of Terahertz Science and Technology*; Springer: New York, 2009.

24   Garcia, A. J. *Numerical Methods for Physics*; Prentice Hall: New Jersey, 2000.

25   Dovesi, R. O., R.; Civalleri, B.; Roetti, C.; Saunders, V. R.; Zicovich-Wilson, C. M. Crystal09, University of Torino: Torino, 2009.

26   Perdew, J. P.; Ruzsinszky, A.; Csonka, G. I.; Vydrov, O. A.; Scuseria, G. E.; Constantin, L. A.; Zhou, X.; Burke, K., *Phys. Rev. Lett.* 2008, 100, 136406.

27   Krishnan, R.; Binkley, J. S.; Seeger, R.; Pople, J. A., *J. Chem. Phys.* 1980, 72, 650-654.

28   Grimme, S., *J. Comput. Chem.* 2004, 25, 1463-1473.

29   Civalleri, B.; Zicovich-Wilson, C. M.; Valenzano, L.; Ugliengo, P., *CrystEngComm* 2008, 10, 405-410.

30   Noel, Y.; Zicovich-Wilson, C. M.; Civalleri, B.; D'Arco, P.; Dovesi, R., *Phys. Rev. B.* 2001, 65, 014111.

31   Dexheimer, S. *Terahertz Spectroscopy: Principles and Applications.* CRC: Boca Raton, 2008.

32   Laib, J. P.; Nickel, D. V.; Mittleman, D. M. *Chem. Phys. Lett.* 2010, 493, 279.

33   Nagumo, T.; Matsuo, T.; Suga, H. *Thermochimica Acta* 1989, 139, 121.

34   Bridgeman, P. W. *The Physics of High Pressure*; G. Bell and Sons: London, 1958.

35   Williams, D.E.; Smyth, C. R., *J. Am. Chem. Soc.* 1962, 84, 1808.

36   Rossiter, V., *J. Phys. C: Solid State Phys.* 1972 5, 1969.

37   Clement, C.; Davies, *Trans. Faraday Soc.*, 1962, 58, 1718.

38   Prigogine, I.; Rice, S.A Eds. *Advances in Chemical Physic Volume LVIs*; John Wiley and

   Sons: 1984.

39   Pederson, J. E.; Keiding, S.R., *IEEE J. Quant. Elec.* 1992, 28, 2518.

40   Flanders, B. N.; Cheville, R. A.; Grischowsky, D.; Scherer, N. F., *J. Phys. Chem.* 1996,

   100, 11824.

41   Brot, C.; Lassier, B.; Chantry G.W.; Gebbie, H.A., *Spectrochim. Acta* 1967, 24, 295.

42   Lassier, B.; Brot, C.; Chantry, G.W.; Gebbie, H.A., *Chem. Phys. Lett.* 1969, 3,96.

43   Hill, N.E., *Proc. Phys. Soc.* 1963, 82, 723.

44   Kisiel, Z.; Desyatnyk, O.; Bialkowska-Jaworska, E.; Pszczolkowski, L., *Phys. Chem.*

   Chem. Phys. 2003, 5, 820.

45   Jauquet, M.; Laszlo, P., *Chem. Phys. Lett.* 1972, 15, 600.

46   Green, J.R.; Scheie, C.E., *J. Phys. Chem. Sol.* 1967, 28, 383.

47   Johari, G.P., *J. Non-Crys. Sol.* 2002, 307-310, 114.

48   Ruffle, B.; Parshin, D.a.; Courtens, E.; Vacher, R., *Phys. Rev. Lett.* 2008, 100, 015501.

49   Hehlen, B.; Courtens, E.; Vacher, R.; Yamanaka, A.; Kataoka, M.; Inoue, K., *Phys. Rev.*

   Lett. 2008, 100, 015501.

50   Duval, E.; Mermet, A.; Saviot, L., *Phys Rev. B* 2007, 75, 024201.

51 Lunkenheimer, P.; Loidl, A., *J. Non-Cryst. Sol.* 2006, 352, 4556.

APPENDIX B: Investigation of the Terahertz Vibrational Modes of ZIF-8 and ZIF-90 with Terahertz Time-Domain Spectroscopy

Abstract

We present experimental and computational evidence that gate-opening modes for zeolitic imidazole frameworks can be observed at terahertz frequencies. Our work highlights the critical importance to correctly optimise the crystal structure prior to computational lattice dynamics analysis. The results support the hypothesis that the low energy vibrational modes do indeed play a significant role in host–guest interactions for ZIFs, such as gas loading.

Zeolitic imidazolate frameworks (ZIFs) are a subclass of the metal–organic framework (MOF) family which comprise tetrahedral metal centres bridged by imidazolate linkers with topologies similar to zeolites.[1,2] In order to tune the properties of ZIFs, the metal cations can be varied between Zn^{2+}, Li^+ and B^{3+}, while various functional groups can be added on the imidazolate linkers.[1,3,4] Due to their relatively high thermal and chemical stability, ZIFs have been heavily studied for applications in gas storage,[5] separations,[6] and catalysis.[7] While ZIFs are crystalline solids, some of them (*e.g.* ZIF-4, ZIF-7 and ZIF-8) have flexible molecular structures which lead to concerted 'swing' motions of the imidazole linkers and changes in the windows or cage structures.[8–11] This has been associated with changes in the accessibility of the pores, making these motions crucial to the molecular adsorption properties of these ZIFs. However, despite the important applications of ZIFs, the fundamental lattice dynamics of these structures have not been fully revealed.

A recent study combined the use of computational methods, inelastic neutron scattering and infra-red spectroscopy to study the lattice dynamics of several different ZIFs.[12] The terahertz frequency region was marked as an area of great interest as *ab initio* quantum mechanical calculations predicted a number of soft modes, pore breathing, and gate-opening motions for ZIF-4, ZIF-7 and ZIF-8 falling in the frequency region below 3 THz. Inelastic neutron scattering experiments were performed to probe the terahertz modes of these ZIFs. However, while the experimental spectra matched qualitatively with the simulated spectra in the crucial <3 THz region, there was insufficient resolution of the spectral features at these frequencies to match conclusively the experimental and simulated spectra. Furthermore, the density functional theory (DFT) simulations of ZIF-8 in the aforementioned study were performed using an imposed reduced crystalline symmetry structure due to the occurrence of imaginary modes in the

vibrational calculation. While this method apparently yielded an accurate simulation in the mid-IR region, there is evidence that the simulations deviate from experiment below 3 THz.

Terahertz time-domain spectroscopy (THz-TDS) has been used extensively to study the chemical and structural properties of a variety of systems,[13] ranging from molecular crystals,[14,15] to amorphous solids,[16,17] liquids[18,19] and proteins.[20] It has shown sufficient spectral resolution to differentiate between crystalline polymorphs, as well as probe phase transitions in disordered crystals, and study dynamics in amorphous solids. Due to the non-destructive nature of the technique, spectra across a wide range of temperatures can be readily acquired, allowing for temperature-induced changes in spectral response to be investigated. Given the initial suggestions that swing and gate-opening motions in ZIFs fall within the terahertz frequency region,[12] THz-TDS is used here to probe the terahertz vibrational modes of two ZIFs with the sodalite (SOD) structure: ZIF-8 and ZIF-90. These two systems are particularly interesting due to the swing effect that occurs during the adsorption of small molecules at low and medium relative pressures, respectively, and the opening of the narrow windows around 3.4 Å diameter. The fundamental understanding of flexibility of MOFs is key for the application of these materials in industrial separation. We then performed revised *ab initio* quantum mechanical calculations for comparison with the experimental data.

ZIF-8 and ZIF-90 were prepared using previously reported methods.[21,22] 15–60 mg of the respective ZIF sample was mixed with 360 mg of high-density polyethylene and compressed under 2 tons of force for 3 minutes to form approximately 3 mm thick pellets of 13 mm diameter for the THz-TDS measurements. Variable temperature THz-TDS measurements were performed using previously employed equipment and methodology in the range of 0.2 to 2.4 THz (60 mg sample)[23] and using an Advantest TAS7500TS in the range 0.5 to 4.5 THz (15 mg sample).

Solid-state DFT calculations were performed using the CRYSTAL14[24] software package, which makes use of periodic boundary conditions to replicate the crystalline nature of the studied materials. The recently implemented M06-2X meta-hybrid exchange correlation functional,[25] designed for use with transition metal containing systems, was coupled with the split-valence double-zeta 6-31G(d,p) basis set[26] for all calculations. Vibrational normal mode eigenvectors and eigenvalues were determined numerically within the harmonic approximation based on fully geometry optimised solids.[27,28] Infrared intensities were calculated using the Berry Phase method.[29]

The terahertz spectrum of ZIF-8 at 90 K shows a weak feature at 1.51 THz, a strong feature at 1.95 THz, several weak features between 2.5 THz and 3.3 THz, as well as a very strong feature at 3.9 THz (**Fig**. **B-1a‡**); while the spectrum of ZIF-90 at 80 K shows weak and spectrally poorly resolved features at 0.76 and 2.34 THz, and a feature developing at 2.47 THz (**Fig. B-1b**). The simulated spectrum of ZIF-8, which was calculated from the optimised cubic structure (a = 17.038 Å), is an excellent match to the experimental spectrum. It is important to note that unlike the previous simulations, the result shown here was optimised within the experimentally determined space group[8,30] (cubic *I-43m*) and did not produce any imaginary frequencies. The literature structure of ZIF-90 exhibits significant disorder and geometrical distortion on account of the imposed *I-43m* crystallographic symmetry. To produce a chemically feasible model, the published structure was expanded to space group *P*1, and the duplicate atoms of the aldehyde groups were deleted. The structure optimised without constraints resulted in a final monoclinic structure in space group $P2_1$ with symmetrised unit-cell parameters a = 17.612 Å, b = 17.256 Å, c = 16.923 Å, β = 90.046°, V = 5143.395 Å^3. The distortions from numerous

higher-symmetry space groups are slight, which suggests that the material could adopt a complex domain-type structure.
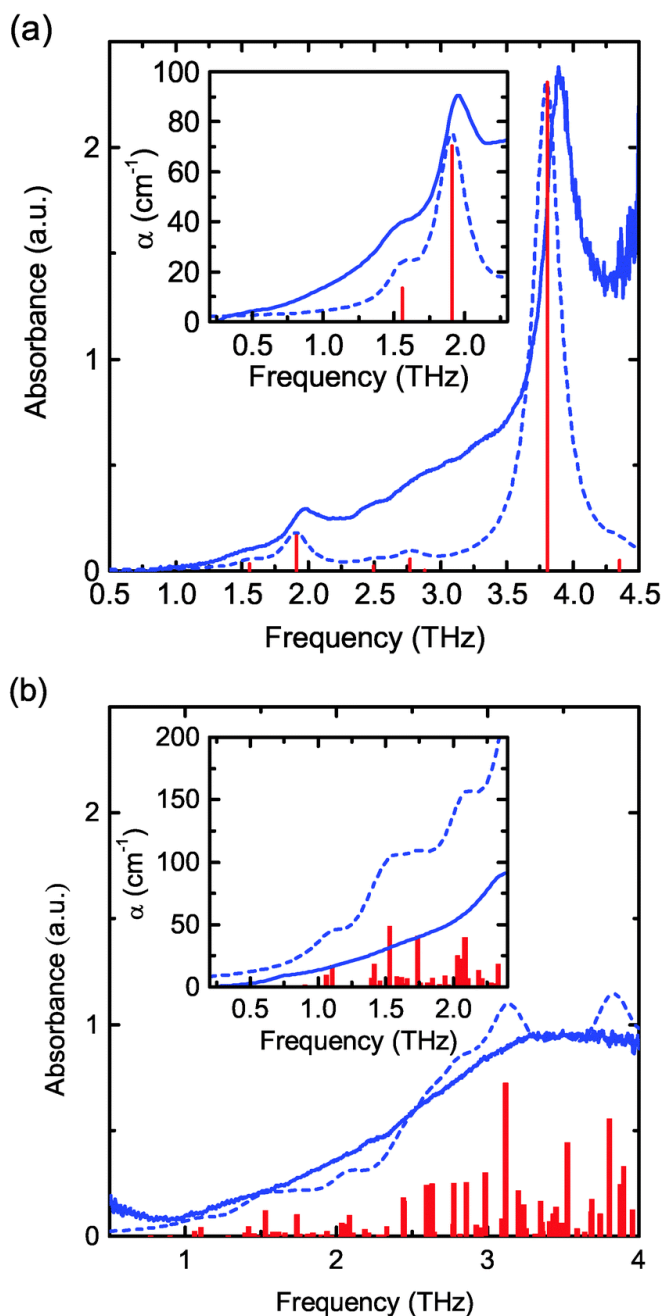
Fig. B-1 Experimental and simulated terahertz spectra of (a) ZIF-8 (at 90 K) and (b) ZIF-90 (at 80 K). Solid lines represent experimental spectra and dashed lines represent simulated spectra. Red bars indicate frequencies and intensities of the individual calculated terahertz modes. The inset plots highlight the respective low frequency spectra of the absorption coefficient as acquired using higher concentration sample pellets.

Analysis of the predicted terahertz vibrational modes in both ZIF-8 and ZIF-90 show that they mostly involve shearing and torsional motions of the imidazolate linkers, and not the rotational motions required for gate opening. However, the strong vibrational mode predicted for ZIF-8 at 1.89 THz, as well as the vibrational modes at 1.13 and 1.31 THz predicted for ZIF-90 result from rotational motions of the linkers, which suggests that they could be the crucial gate-opening motions. The motion of the predicted mode at 3.82 THz in ZIF-8 is primarily a bending of the two imidizolate ligands about the metal coordination bond, which ultimately results in a breathing-type mode of the MOF cavity.

Powder X-ray diffraction (PXRD) was carried out on ZIF-8 and ZIF-90 to confirm their structures. The PXRD pattern for ZIF-8 matched well with the published structure[31,32] under both ambient conditions and when the sample was placed under vacuum at 298 K. The PXRD pattern for ZIF-90 under ambient conditions is similar to that of ZIF-8, but the Bragg peaks show different relative intensities. The differences are not attributable to any preferred orientation effect, since they were reproducible between several samples, and furthermore, become similar to those seen in ZIF-8 (**ESI**,† **Fig. S1**) when the sample is placed under vacuum. This suggests that there may be some guest loading in ZIF-90 under ambient conditions. It has been found that water uptake in ZIF-90 is over 30 times higher than that in ZIF-8 at water activities above 0.413 due to the adsorption site in the aldehyde group from the imidazole ring compared to the 2-methylimidazole from ZIF-8.[33] A coarse model with water introduced into the voids in the ZIF-90 structure reproduced this change in Bragg intensities (see **ESI**,† and **Fig. S2** and **S3**), and hence, it is foreseeable that water molecules are adsorbed in ZIF-90 under ambient conditions. Variable temperature THz-TDS measurements were performed on ZIF-90 in order to investigate further the possibility of guest loading. Below 220 K, minor variations in the spectra are

observed. However, the terahertz absorption across the entire frequency range probed increases significantly between 220 and 250 K. Above 250 K, the terahertz absorption then decreases, returning to the original level at 280 K and beyond (**Fig. B-2**). This trend is consistently seen when the measurements are repeated on the same sample.
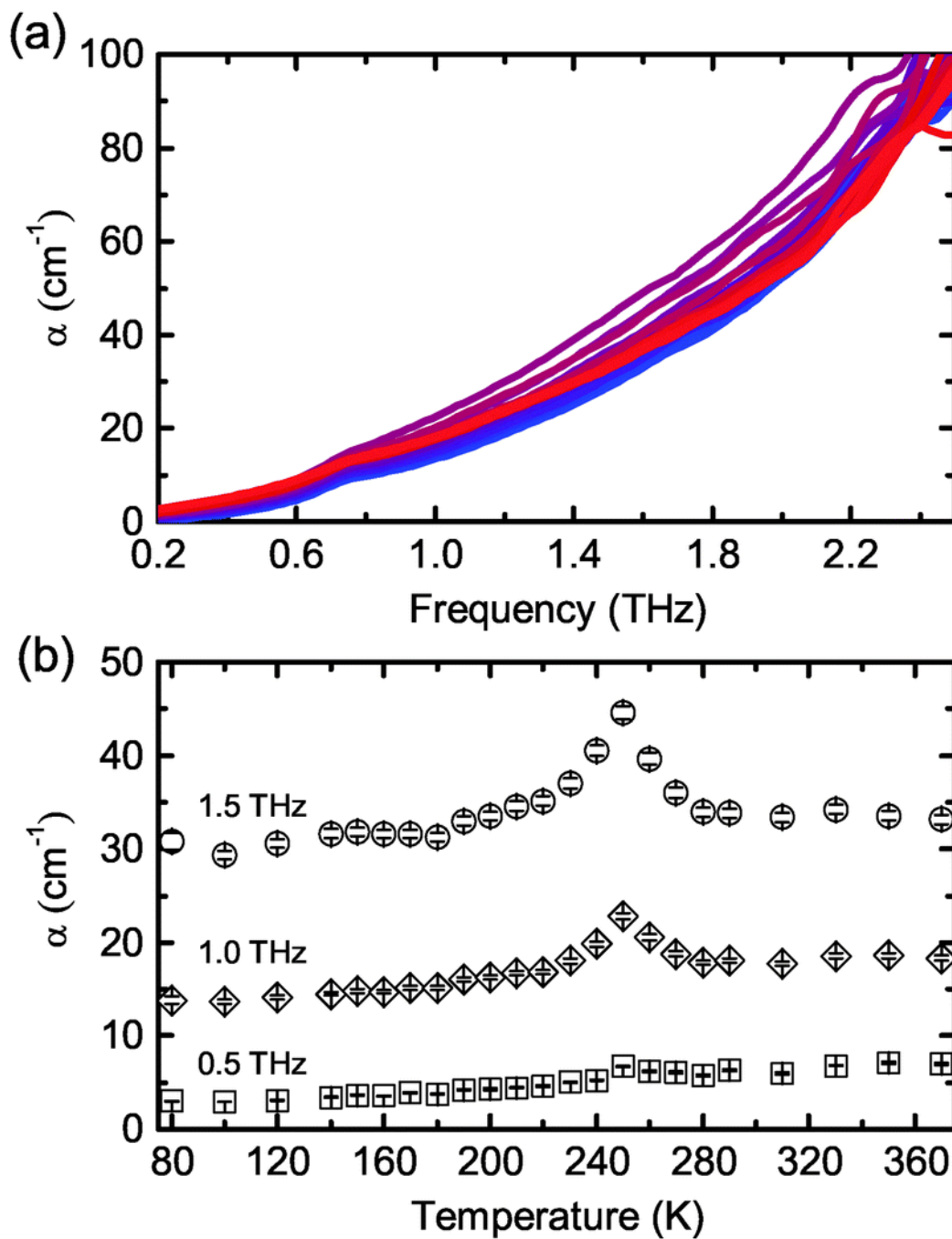
Fig. B-2 (a) Terahertz spectra of ZIF-90 from 80 (blue) – 370 (red) K. (b) Terahertz absorption coefficients at 0.5 (squares), 1.0 (diamonds) and 1.5 (circles) THz. Error bars indicate standard deviation over 3 experimental runs.

Given the affinity of ZIF-90 for water, it is possible that some residual water molecules are present in the pores, which freeze when cooled rapidly to 80 K prior to the acquisition of the spectra. Liquid water has very strong terahertz absorption which increases monotonously with frequency. However, crystalline ice has much weaker terahertz absorption, with negligible absorption below 1 THz and small but increasing absorption above 1.3 THz due to a phonon mode centred at 3 THz.[34,35] As the temperature is raised above 220 K, it is possible that the ice begins to melt to give liquid water and this causes the increase in terahertz absorption which is more significant at higher frequencies. Although this is lower than the expected melting point of water, previous reports have found that confinement of organic molecules in porous materials result in melting point depression[36] and changes in the physical state[37] due to the interaction of adsorbates with the microporosity.[38] Above 250 K, the drop in absorption coefficient can be attributed to the evaporation of the liquid water from the pores under prolonged exposure to vacuum conditions which are applied during the variable temperature THz-TDS measurements. This would be consistent with the changes in Bragg intensities seen in the PXRD data at 298 K when placed under vacuum. The absorption returns to the same levels as those below 200 K since ice has negligible contributions to the terahertz absorption, so the ice-loaded and empty ZIF-90 should have similar absorption levels. The fact that this trend can be reproduced multiple times with the same sample suggests that some adsorption of water in ZIF-90 occurs spontaneously under ambient conditions.

In the sample of ZIF-8 we observed that the strong vibrational feature that is observed around 2 THz appears very broad and low in intensity in the spectrum at 80 K. Upon heating to 90 K it red-shifts to slightly lower frequency and sharpens up (**Fig**. **B-3**). The red-shift ceases at around 120 K and the feature shifts to slightly higher frequencies upon further heating (see inset

in **Fig**. **B-3**). The very strong mode at just below 4 THz appears unaffected by the change in temperature between 80 and 90 K. We cannot explain this behaviour comprehensively at this point but speculate that the change in vibrational features might be indicative of a change in disorder in the structure of ZIF-8 that is associated with the vibrational mode around 2 THz. Further work is required to better understand this behaviour.
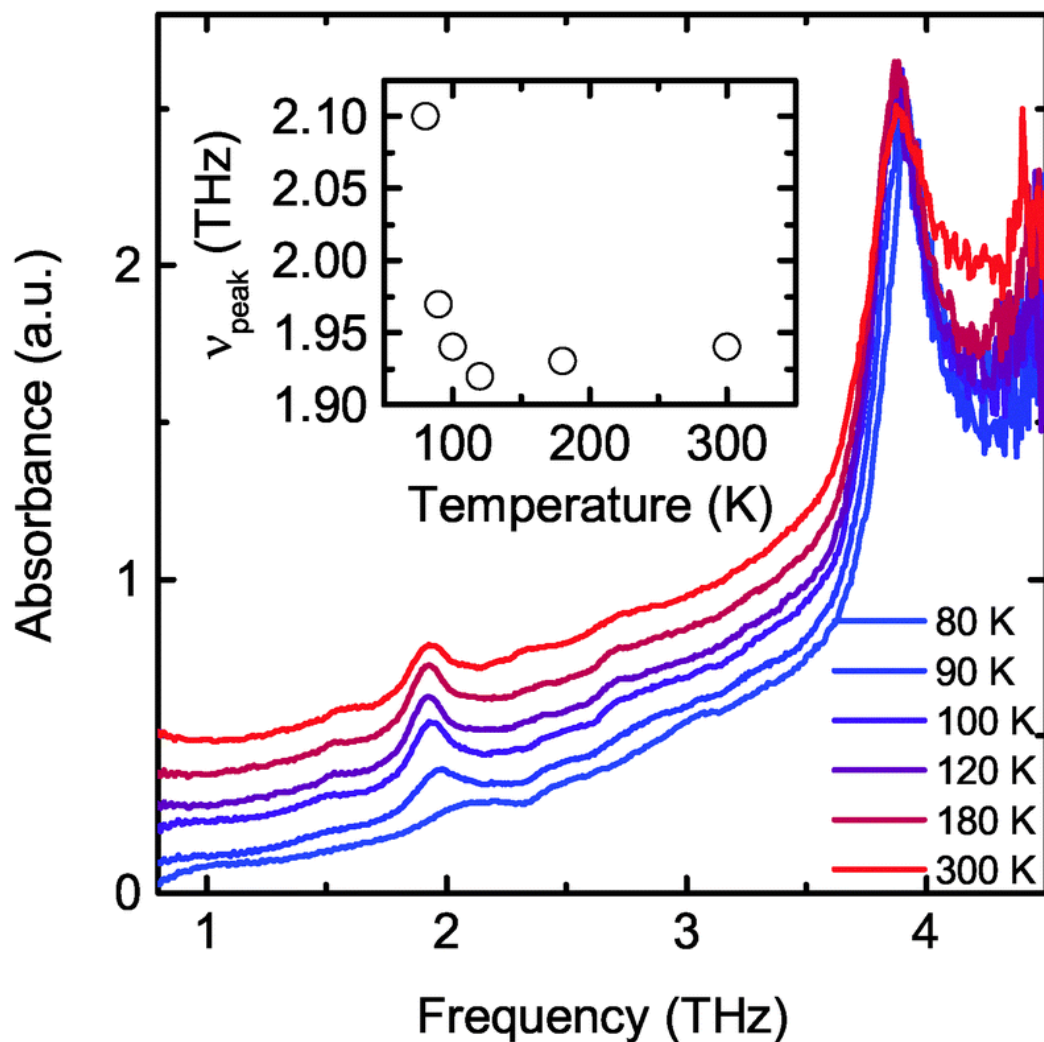
Fig. B-3 Experimental spectra of ZIF-8 acquired at temperatures between 80 and 300 K. Spectra are offset by 0.1 a.u. with increasing temperature from 80 K (bottom) to 300 K (top). The peak frequency of the lowest frequency spectral feature is plotted as a function of temperature in the inset plot to highlight the unusual shift behaviour of this vibrational mode.

In this paper, the terahertz spectrum of ZIF-8 is investigated with a combination of THz-TDS and *ab initio* quantum mechanical calculations. The use of THz-TDS allows for a well resolved spectrum to be obtained, while revised quantum mechanical calculations proved to be an excellent match for the experimental data. These methods were then extended to ZIF-90 and a reasonable match was also obtained between the experimental and calculated spectra. Closer analysis shows terahertz vibrational modes at 1.89 THz in ZIF-8 and 1.13 and 1.31 THz in ZIF-90 which involve rotational motions of the imidazolate linkers and hence may be the key gate-opening, swing effect motions in these systems. Subsequent PXRD experiments found unusual behaviour in ZIF-90 which could be related to guest loading under ambient conditions. Variable temperature THz-TDS spectra showed significant differences in the 220–280 K temperature range. The spike in absorption and subsequent decrease to the original levels suggest the presence of adsorbed water in ZIF-90 stored under ambient conditions, which is first frozen as ice, then liquefies and subsequently vaporises.

These results demonstrate the utility of THz-TDS in the study of ZIFs and provide further evidence that the crucial gate-opening vibrations in ZIFs lie at terahertz frequencies. Furthermore, variable temperature THz-TDS is shown to be sensitive to host–guest interactions in ZIFs. This demonstrates the potential of the technique in studying such interactions in ZIFs, which will have direct applications in gas and drug loading in these systems.

References

1. K. S. Park, Z. Ni, A. P. Coˆte´, J. Y. Choi, R. Huang, F. J. Uribe-Romo, H. K. Chae, M. O'Keeffe and O. M. Yaghi, Proc. Natl. Acad. Sci. U. S. A., 2006, 103, 10186–10191.

2. X. C. Huang, Y. Y. Lin, J.-P. Zhang and X.-M. Chen, Angew. Chem., Int. Ed., 2006, 45, 1557 1559.

3. J. Zhang, T. Wu, C. Zhou, S. Chen, P. Feng and X. Bu, Angew. Chem., Int. Ed., 2009, 48, 2542–2545.

4. T. Wu, J. Zhang, C. Zhou, L. Wang, X. Bu and P. Feng, J. Am. Chem. Soc., 2009, 131, 6111–6113.

5. A. Phan, C. J. Doonan, F. J. Uribe-Romo, C. B. Knobler, M. O'Keeffe and O. M. Yaghi, Acc. Chem. Res., 2009, 43, 58–67.

6. K. Li, D. H. Olson, J. Seidel, T. J. Emge, H. Gong, H. Zeng and J. Li, J. Am. Chem. Soc., 2009, 131, 10368–10369.

7. H.-L. Jiang, B. Liu, T. Akita, M. Haruta, H. Sakurai and Q. Xu, J. Am. Chem. Soc., 2009, 131, 11302–11303.

8. D. Fairen-Jimenez, S. A. Moggach, M. T. Wharmby, P. A. Wright, S. Parsons and T. Du¨ren, J. Am. Chem. Soc., 2011, 133, 8900–8902.

9. C. Gu¨cu¨yener, J. van den Bergh, J. Gascon and F. Kapteijn, J. Am. Chem. Soc., 2010, 132, 17704–17706.

10. D. Fairen-Jimenez, R. Galvelis, A. Torrisi, A. D. Gellan, M. T. Wharmby, P. A. Wright, C. Mellot-Draznieks and T. Du¨ren, J. Mater. Chem., 2012, 41, 10752–10762.

11. M. T. Wharmby, S. Henke, T. D. Bennett, S. R. Bajpe, I. Schwedler, S. P. Thompson, F. Gozzo, P. Simoncic, C. Mellot-Draznieks, H. Tao, Y. Yue and A. K. Cheetham, Angew. Chem., Int. Ed., 2015, 54, 6447–6451.

12. M. R. Ryder, B. Civalleri, T. D. Bennett, S. Henke, S. Rudic, G. Cinque, F. Fernandez Alonso and J.-C. Tan, Phys. Rev. Lett., 2014, 113, 215502.

13. E. P. J. Parrott and J. A. Zeitler, Appl. Spectrosc., 2015, 69, 1–25.

14. J. Sibik, M. J. Sargent, M. Franklin and J. A. Zeitler, Mol. Pharmaceutics, 2014, 11, 1326 1334.

15. E. P. J. Parrott, N. Y. Tan, R. Hu, J. A. Zeitler, B. Z. Tang and E. Pickwell-MacPherson, Mater. Horiz., 2014, 1, 251.

16 J. Sibik, E. Y. Shalaev and J. A. Zeitler, Phys. Chem. Chem. Phys., 2013, 15, 11931–11942.

17. J. Sibik, S. R. Elliott and J. A. Zeitler, J. Phys. Chem. Lett., 2014, 5, 1968–1972.

18. R. Li, C. D'Agostino, J. McGregor, M. D. Mantle, J. A. Zeitler and L. F. Gladden, J. Phys. Chem. B, 2014, 118, 10156–10166.

19. N. Y. Tan, R. Li, P. Bra¨uer, C. D'Agostino, L. F. Gladden and J. A. Zeitler, Phys. Chem. Chem. Phys., 2015, 17, 5999–6008.

20. S. Ebbinghaus, S. Kim, M. Heyden, X. Yu, U. Heugen, M. Gruebele, D. Leitner and M. Havenith, Proc. Natl. Acad. Sci. U. S. A., 2007, 104, 20749–20752.

21. F. K. Shieh, S. C. Wang, S. Y. Leo and K. C. W. Wu, Chem. – Eur. J., 2013, 19, 11139–11142.

22. K. Kida, M. Okita, K. Fujita, S. Tanaka and Y. Miyake, CrystEngComm, 2013, 15, 1794–1801.

23. N. Y. Tan and J. A. Zeitler, Mol. Pharmaceutics, 2015, 12, 810–815.

24. R. Dovesi, R. Orlando, A. Erba, C. M. Zicovich Wilson, B. Civalleri, S. Casassa, L. Maschio, M. Ferrabone, M. De La Pierre, P. D'Arco, Y. Noe¨l, M. Causa`, M. Re´rat and B. Kirtman, Int. J. Quantum Chem., 2014, 114, 1287–1317.

25. Y. Zhao and D. G. Truhlar, Theor. Chem. Acc., 2007, 120, 215–241.

26. P. C. Hariharan and J. A. Pople, Theor. Chim. Acta, 1973, 28, 213–222.

27. F. Pascale, C. M. Zicovich Wilson, F. Lo´pez Gejo, B. Civalleri, R. Orlando and R. Dovesi, J. Comput. Chem., 2004, 25, 888–897.

28. C. M. Zicovich Wilson, F. Pascale, C. Roetti, V. R. Saunders, R. Orlando and R. Dovesi, J. Comput. Chem., 2004, 25, 1873–1881.

29. Y. Noel, C. M. Zicovich Wilson, B. Civalleri, P. D'Arco and R. Dovesi, Phys. Rev. B: Condens. Matter Mater. Phys., 2001, 65, 014111.

30. O. Shekhah, R. Swaidan, Y. Belmabkhout, M. du Plessis, T. Jacobs, L. J. Barbour, I. Pinnau and M. Eddaoudi, Chem. Commun., 2014, 50, 2089–2092.

31. H. Bux, F. Liang, Y. Li, J. Cravillon, M. Wiebcke and J. Caro, J. Am. Chem. Soc., 2009, 131, 16000–16001.

32. H. Bux, C. Chmelik, J. M. van Baten, R. Krishna and J. Caro, Adv. Mater., 2010, 22, 4741 4743.

33. K. Zhang, R. P. Lively, M. E. Dose, A. J. Brown, C. Zhang, J. Chung, S. Nair, W. J. Koros and R. R. Chance, Chem. Commun., 2013, 49, 3245–3247.

34. K. D. Mo¨ller and W. G. Rothschild, Far-infrared spectroscopy, Wiley-VCH Verlag, 1971.

35. V. I. Gaiduk and D. S. F. Crothers, J. Mol. Liq., 2006, 128, 145–160.

36. C. L. Jackson and G. B. McKenna, J. Chem. Phys., 1990, 93, 9002–9011.

37. D. Fairen-Jimenez, F. Carrasco-Marn, D. Djurado, F. Bley, F. Ehrburger-Dolle and C. Moreno-Castilla, J. Phys. Chem. B, 2006, 110, 8681–8688.

38. D. Fairen-Jimenez, N. A. Seaton and T. Du¨ren, Langmuir, 2010, 26, 14694–14699.

PXRD patterns for ZIF-8 and ZIF-90 (298 K, CuK☐ radiation)
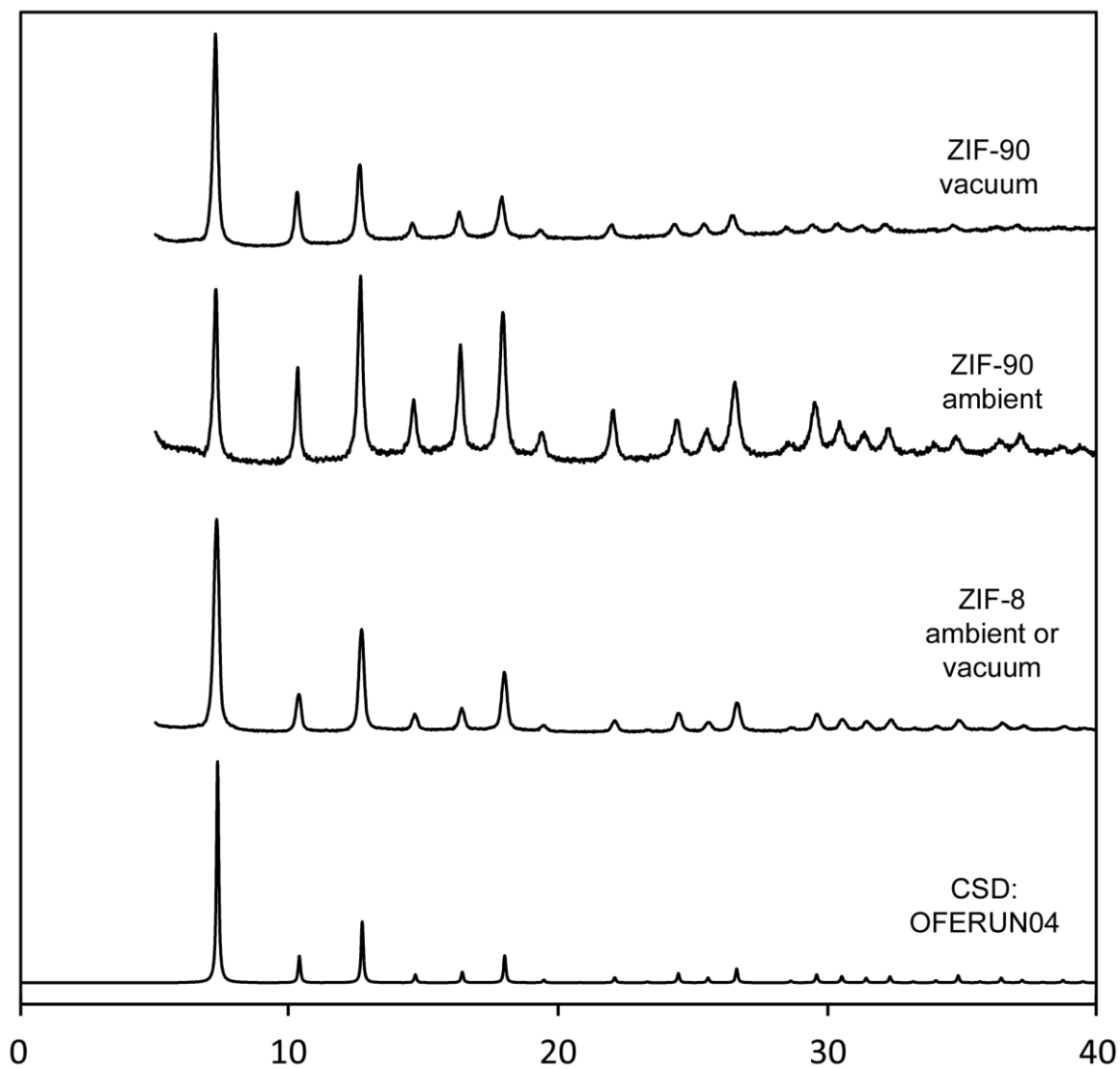
Figure S1. Powder X-ray diffraction (PXRD) patterns for simulated ZIF-90S1 and experimental ZIF-8 and ZIF-90 at vacuum and ambient conditions.

PXRD: variation in relative intensities for ZIF-90

The changes in the observed relative intensities for the Bragg peaks in the PXRD pattern of ZIF-90 under ambient conditions and under vacuum are attributed to water adsorption/desorption.

A coarse model illustrating the consistency of this interpretation was prepared as follows:

(1) The crystal structure of the empty framework was extracted from the Cambridge Structural Database (refcode: OFERUN04; Zhu *et al.*, 2012).

(2) The structure in space group I–43m was expanded to I1 (*i.e.* all non-translational symmetry elements were removed).

(3) O atoms were placed at positions corresponding to a dodecahedron around the unit-cell origin, with O…O edges ≈ 2.5 Å (radius of enclosing sphere = 3.5 Å). The I-centring places a dodecahedron also in the void at (½,½,½).
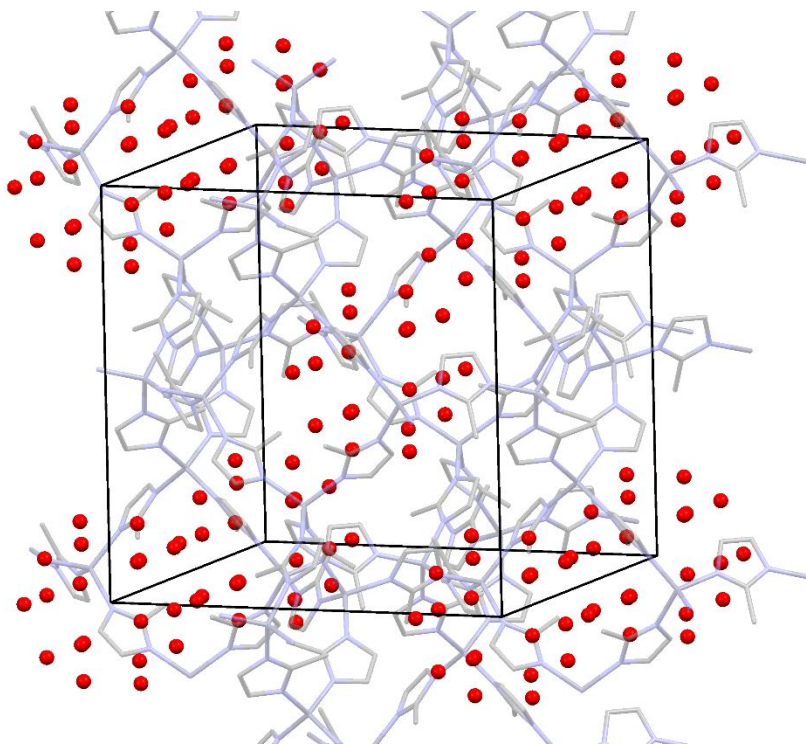
Figure S2. Crystalline model for ZIF-90, grey and blue, with adsorbed water molecules, red spheres.

This model is not chemically or energetically rigorous – it is only intended to create a reasonable electron density distribution in the voids of ZIF-90.

The simulated PXRD pattern shows changes in the relative intensities of the Bragg peaks compared to the empty ZIF-90 structure, which correspond to those seen by experiment.
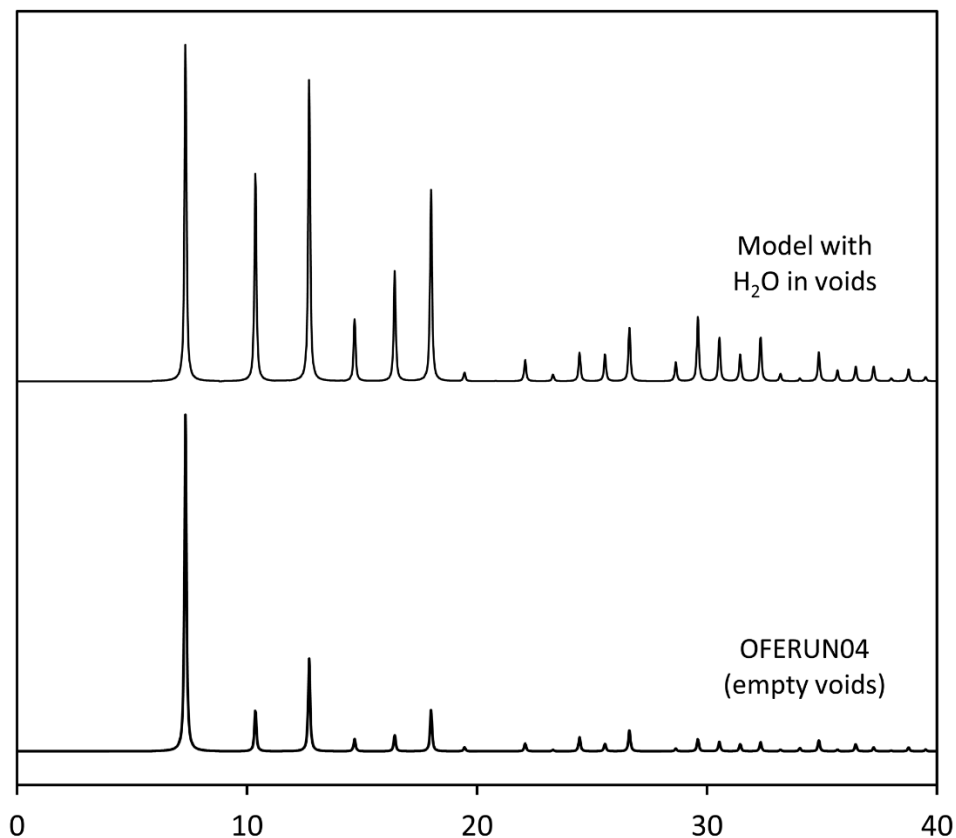
Figure S3. Powder X-ray diffraction (PXRD) patterns for simulated empty ZIF-90 and water adsorbed ZIF-90, and experimental ZIF-90 at ambient conditions. Note the changes in the relative intensities.

APPENDIX C: Piezo-Optic Tensor of Crystals from Quantum-Mechanical Calculations

Abstract

An automated computational strategy is devised for the *ab initio* determination of the full fourth-rank piezo-optic tensor of crystals belonging to any space group of symmetry. Elastic stiffness and compliance constants are obtained as numerical first derivatives of analytical energy gradients with respect to the strain and photo-elastic constants as numerical derivatives of analytical dielectric tensor components, which are in turn computed through a Coupled-Perturbed-Hartree-Fock/Kohn-Sham (CPHF/KS) approach, with respect to the strain. Both point and translation symmetry are exploited at all steps of the calculation, within the framework of periodic boundary conditions. The scheme is applied to the determination of the full set of ten symmetry-independent piezo-optic constants of calcium tungstate $CaWO_4$, which have recently been experimentally reconstructed. Present calculations unambiguously determine the absolute sign (positive) of the π_{61} constant, confirm the reliability of 6 out of 10 experimentally determined constants and provide new, more accurate values for the remaining 4 constants.

C.1 Introduction

Several optical properties of anisotropic media are related to birefringence or double refraction. It is indeed well-known that two plane polarized electro-magnetic waves, with two distinct velocities *v*, may in general be propagated through a crystal with the same propagation direction. The *c/v* ratio for each wave (*c* being the speed of light) is referred to as the refractive index for that wave and can be derived for any propagation direction from the so-called optical *indicatrix*: an ellipsoid oriented along the principal axes of the dielectric tensor ϵ and whose semi-axes give the principal refractive indices of the system.[1] It follows that any change in the shape, size, and orientation of the indicatrix results in the modification/modulation of the optical properties of a crystal. Such changes can be induced by electric fields, strains and stresses giving rise to the electro-optic, elasto-optic (i.e., photo-elastic), and piezo-optic effects, respectively.

In particular, the piezo-optic effect (measuring the variation of the dielectric tensor components as induced by an applied stress) has proven to be an effective tool for mapping 2D and 3D mechanical stresses through stress tensor-field tomography.[2,3] Furthermore, such an effect is extremely relevant to the field of optoelectronics where the search for highly efficient electro-optic and piezo-optic materials is experiencing a great interest in recent years due to their applications as photo-elastic modulators of light polarization and as components of many devices related to acousto-optic light modulators, deflectors, tunable spectral filters, etc.[4–11] The piezo-optic and photo-elastic responses of a crystal are quite anisotropic even for high-symmetry systems. In order to accurately optimize the orientation of a crystal, which maximizes the efficiency of the acousto-optic transformation, absolute values, and signs of all non-zero elements

of the fourth-rank elastic $\mathbb{C}$, compliance $\mathbb{S}$, photo-elastic p, and piezo-optic π tensors have to be determined, which is not a trivial task (see below), especially for low-symmetry crystals.[10,12,13]

From an experimental point of view, photo-elastic constants could be measured through acousto-optic methods. Within the phenomenological theory of Brillouin scattering, for instance, photo-elastic constants are given in terms of the intensities of Brillouin components.[14,15] Acousto-optic methods, however, are unable to uniquely determine all signs of the photo-elastic constants, particularly so for low-symmetry crystals.[4,12] The full set of independent piezo-optic constants can be measured for crystals of any symmetry via the combination of optical interferometry and polarization-optical techniques (once the elastic compliances are known).[12,16–18] Still, this approach requires a large number of measurements to be performed on a large number of crystalline samples (properly cut to specific orientations). In their fundamental work of 2005, Andrushchak *et al.*[12] derived the minimum set of samples and measurements necessary to determine the whole piezo-optic tensor for all crystal families: 57 measurements on 16 samples are required to determine the 36 independent components of a triclinic crystal, 29 measurements on 8 samples for the 20 independent components of a monoclinic crystal, 14 measurements on 6 samples for the 10 independent components of tetragonal crystals belonging to the 4, -4, or 4/*m* classes, just to name a few. Even small errors in the sample cut preparation or in the alignment of the whole optical setup may result in large errors in the piezo-optic constants determination (see the detailed analysis on the possible sources of inaccuracies given by Krupych *et al.* in Ref. 16). Furthermore, the interferometric method is known to provide a somewhat poor description of so-called *rotating* piezo-optical constants (those which correspond to a rotation of the optical indicatrix under mechanical stress); a conoscopic method has recently been devised to determine such constants more accurately.[19]

In this paper we present a general, fully automated scheme for the theoretical *ab initio* calculation of the fourth-rank piezo-optic tensor π of crystals belonging to any space group symmetry, which requires the simultaneous determination of the elastic stiffness and compliance tensors and of the photo-elastic tensor. The scheme adopts periodic-boundary conditions, fully exploits both point and translational symmetries at all steps,[20–23] is based on the evaluation of analytical energy gradients with respect to both atomic coordinates and lattice parameters[24–27] and utilizes the analytical Coupled-Perturbed-Hartree-Fock/Kohn-Sham (CPHF/KS) method to compute static and electric field frequency-dependent optical (i.e., dielectric) properties of crystals.[28–30] We have implemented the present scheme into a development version of the public Crystal14 program,[31,32] taking advantage of the many recent developments made to the algorithms for the evaluation of strain-related tensorial properties (elastic, piezoelectric, photo-elastic) of crystals.[33–38]

The proposed scheme is first described in detail and then applied to the determination of the piezo-optic tensor of tetragonal calcium tungstate, $CaWO_4$, which belongs to the scheelite family of minerals. This is a promising material for acousto-optic modulators and its full set of piezo-optic (and photo-elastic) constants has been experimentally determined only quite recently.[13,17–19] An explicit investigation is performed on the effect of adopting several functionals of density functional theory (DFT) belonging to three rungs of the so-called "Jacob's ladder"[39] (namely, a local-density approximation, a generalized-gradient approximation, and a couple of global hybrids), and on the electric field frequency-dependence of all computed dielectric, piezo-optic, and photo-elastic properties. Our calculations allow us to confirm the experimentally measured values of a sub-set of the 10 independent piezo-optic and photo-elastic constants of $CaWO_4$ and, on the contrary, to point-out large discrepancies in the determination of

the others and to provide a complete description of the anisotropic stress-optical response of this crystal.

C.2 Theory and Methods

C.2.1 Stress-related Tensorial Properties of Crystals and their Symmetry Features

The stress-strain relation for an anisotropic crystal is given by the generalized Hooke's law:

$$\sigma_{ij} = C_{ijkl}\eta_{kl} \quad (1)$$

which relates the second-rank stress tensor σ to the second-rank pure strain tensor η through the 81 elastic stiffness constants C_{ijkl} that constitute the fourth-rank elastic tensor $\mathbb{C}$. In the above expression, i, j, k, l are Cartesian indices. As both σ and η are symmetric tensors, the number of their independent components reduces from 9 to 6, and those of $\mathbb{C}$ accordingly from 81 to 36. As a consequence, Voigt's notation can be used, which introduces a mapping between pairs of Cartesian indices and Voigt's indices running from 1 to 6: $v, u = 1, \ldots, 6$ where $1 = xx$, $2 = yy$, $3 = zz$, $4 = yz$, $5 = xz$ and $6 = xy$:[1]

$$\sigma_v = C_{vu}\eta_u \; and \; \eta_u = S_{vu}\sigma_u \quad (2)$$

where the fourth-rank elastic tensor has been given a 6 x 6 matrix representation and where $S = \mathbb{C}^{-1}$ represents the so-called elastic compliance tensor. To second-order in the strain, the

elastic constants can be defined as second energy density derivatives with respect to pairs of strains:

$$C_{vu} = \frac{1}{V} \frac{\partial^2 E}{(\partial \eta_u \partial \eta_v)} \quad (3)$$

being V the volume of the crystal cell. From Equation (3), the equivalence $C_{vu} \equiv C_{uv}$ is evident, which makes the 6×6 $\mathbb{C}$ matrix symmetric and reduces the number of its independent components to 21. Neumann's principle, which states that any physical property of a crystal must exhibit at least the same point-symmetry of the crystal, can be exploited to further reduce the number of independent components by imposing the invariance ($\mathbb{C}^R = \mathbb{C}$) of the fourth-rank elastic tensor to the action of any point-symmetry operator $\hat{R}\hat{R}$ of the point-group to which the crystal belongs,

$$C^R_{ijkl} = r_{ip} r_{jq} r_{ks} r_{lt} C_{pqst}, \quad (4)$$

where r is the 3 x 3 Cartesian matrix representation of the symmetry operator $\hat{R}$ and Einstein's notation is used according to which repeated indices are meant to be summed. By imposing the invariance of C with respect to all the symmetry operators of the $4/m$ class of the tetragonal crystal system to which $CaWO_4$ belongs, the following shape of the elastic tensor is obtained, for instance:

$$
C = \begin{pmatrix}
C_{11} & C_{12} & C_{13} & 0 & 0 & C_{16} \\
C_{12} & C_{11} & C_{13} & 0 & 0 & -C_{16} \\
C_{13} & C_{13} & C_{33} & 0 & 0 & 0 \\
0 & 0 & 0 & C_{44} & 0 & 0 \\
0 & 0 & 0 & 0 & C_{44} & 0 \\
C_{16} & -C_{16} & 0 & 0 & 0 & C_{66}
\end{pmatrix} . \quad (5)
$$

In the present implementation, elastic constants in Equation (3) are computed as numerical first-derivatives of analytical energy gradients.[33,40]

The variation of the components of the inverse dielectric tensor ϵ^{-1} as induced by strain is given by the strain-optical coefficients (*i.e.* elements of the fourth-rank Pockels' elasto-optic or photo-elastic tensor **p**): Δ

$$
\Delta \epsilon^{-1}_{ij} = p_{ijkl} \, \eta_{kl} \quad (6)
$$

As both the inverse dielectric tensor ϵ^{-1} and the pure strain tensor η are symmetric, Voigt's notation can be adopted also in this case so that the photo-elastic tensor p can be given a 6□6 matrix representation as for the elastic tensor. Photo-elastic constants can then be derived according to: δ

$$
p_{vu} = \frac{\delta \epsilon^{-1}_{v}}{\delta \eta_{u}} \, , \, , (7)
$$

where, in the present scheme, the derivative with respect to the strain is evaluated numerically while the dielectric tensor ($\epsilon = 1 + 4\pi\alpha/V$) analytically from the polarizability α determined through the CPHF/KS method (for a closed-shell system),[31]

$$\alpha_{ij} = -\frac{1}{n_k} = \sum_k^{BZ} \Re\{Tr(C^{k'} \Omega^{k,i} C^k U^{k,j} n)\} \quad (8)$$

where n_k is the number of k points in the first Brillouin Zone (BZ) and n is the diagonal occupation matrix whose elements are 2 for occupied orbitals and 0 otherwise. Here $U^{k,j}$ is an anti-Hermitian block off-diagonal matrix that relates the unperturbed coefficient matrix C^k, to the corresponding first-order perturbed matrix, $C^{k,j} = C^k U^{k,j}$, which gives the linear (first-order) response to the electric field perturbation represented by the matrix $\Omega^{k,i}$. The off-diagonal blocks of $U^{k,j}$ depend not only on $\Omega^{k,j}$ but also on the first-order perturbed density matrix (through the two-electron terms in the Hamiltonian) which, in turn, depends upon $U^{k,j}$. Hence, a self-consistent solution of the CPHF/KS equations is required.

As recalled in the introduction, the dielectric tensor ϵ determines the optical indicatrix of the crystal. For cubic crystals the indicatrix is a sphere. For hexagonal, tetragonal (as $CaWO_4$) and trigonal crystals (optically *uniaxial*), the indicatrix is an ellipsoid of revolution about the principal symmetry axis of the system (also called *optic axis*). The section of the indicatrix perpendicular to the optic axis is a circle whose radius n_o is the *ordinary* refractive index of the system while the section perpendicular to any other direction is an ellipse whose semi-axes are n_o and n_e, the

latter being the *extraordinary* refractive index. Calcium tungstate is said to be an optically *positive* crystal as $n_e > n_o$. The birefringence of a material can be defined as ($\partial = n_e - n_o$).

Given stress-strain relation (2), the fourth-rank piezo-optic tensor π (whose elements are the stress-optical coefficients π_{vu}) can be obtained from the photo-elastic p and elastic $\mathbb{C}$ ones as[1]

$$\pi = p\,S \quad \text{and conversely} \quad p = \pi\,C \quad (9)$$

At variance with the elastic C and compliance S tensors, p and π are not symmetric (*i.e.* in general $p_{vu} \neq p_{uv}$ and $\pi_{vu} \neq \pi_{uv}$. It follows that the number of symmetry-independent components to be determined for the stress-optical and strain-optical tensors is generally larger than for the elastic tensors. The invariance of the piezo-optic tensor with respect to all the point-symmetry operators $\hat{R}$ of the crystal has to be imposed ($\pi^R = \pi$) without the constraint of being symmetric:

$$\pi^R_{ijkl} = r_{ip}\,r_{jq}\,r_{ks}\,r_{lt}\,\pi_{pqst} \quad .(10)$$

For instance, a triclinic crystal has 36 independent piezo-optic coefficients, with the number of unique values decreasing with increasing symmetry. In the case of $CaWO_4$ (tetragonal $4/m$), the shape of the piezo-optic tensor is:

$$\pi = \begin{pmatrix} \pi_{11} & \pi_{12} & \pi_{13} & 0 & 0 & \pi_{16} \\ \pi_{12} & \pi_{11} & \pi_{13} & 0 & 0 & -\pi_{16} \\ \pi_{31} & \pi_{31} & \pi_{33} & 0 & 0 & 0 \\ 0 & 0 & 0 & \pi_{44} & \pi_{45} & 0 \\ 0 & 0 & 0 & -\pi_{45} & \pi_{44} & 0 \\ \pi_{61} & -\pi_{61} & 0 & 0 & 0 & \pi_{66} \end{pmatrix}. \tag{11}$$

The piezo-optic coefficients π_{vu} where both v, $u = 1, 2, 3$ describe the connection between the principal refractive indices and the normal stresses and are referred to as *principal* coefficients. Coefficients π_{vu} where $v = 1, 2, 3$ and $u = 4, 5, 6$ relate the principal refractive indices to shear stresses and are called *shifting* coefficients. Piezo-optic coefficients where $v = 4, 5, 6$ correspond to the rotation of the optical indicatrix and are called *rotating* or *rotating-shifting* coefficients depending on whether $u = 1, 2, 3$ or $u = 4, 5, 6$, respectively.[3] Photo-elastic constants p_{vu} are dimensionless while piezo-optic π_{vu} ones are generally expressed in units of Brewsters, where $1 \text{ Br} = 10^{-12} \text{ Pa}^{-1} = 1 \text{ TPa}^{-1}$.

C.2.2 The Automated Algorithm

One of the specific features of the present scheme for the evaluation of the piezo-optic fourth-rank tensor of crystals of any symmetry is its fully automated character, which requires a "one-shot" calculation of elastic, dielectric and photo-elastic constants, and their combination. Such a scheme involves the efficient integration of several fundamental algorithms, such as analytic energy gradients, geometry optimizations for the relaxation of atomic positions within strained and unstrained configurations, and CPHF/KS self-consistent-field procedures. As for elastic, piezoelectric, and photo-elastic constants, piezo-optic ones can also be decomposed into purely electronic "clamped-ion" and nuclear "internal-strain" contributions where the latter measures the piezo-optic effect due to the nuclear relaxation induced by strain,[41,42] which is

527

accounted for by optimizing the atomic positions within the strained cell. Experimental measurements of the static dielectric and piezo-optic response properties of crystals should refer to the limit of infinite electric-field wavelength λ. Practically, they are performed at finite values of λ, which are expected to correspond to sufficiently high frequencies of the applied electric field to make nuclear contributions negligible, but not high enough for promoting electronic excitations. These two constraints are such that the adopted values of λ often do not correspond to the $\lambda \to \infty$ limit of the static CPHF/KS calculations. In the present implementation, we take advantage of recent developments on the evaluation of "dynamic" dielectric properties of solids[31,43,44] to explicitly investigate the effect of λ on computed piezo-optic constants.

The resulting algorithm can be sketched as follows: (i) the starting crystal structure is fully optimized at the selected level of theory; (ii) cell gradients are computed on the optimized unstrained configuration as well as the equilibrium dielectric tensor (which is then inverted) with the CPHF/KS scheme (by default $\lambda = \infty$); (iii) a full symmetry analysis is performed in order to determine the non-null independent elastic and piezo-optic constants. The minimal set of independent deformations to be applied, out of a maximum of six, is also found; (iv) a given deformation is selected and the corresponding residual symmetry determined; for each deformation, N_s strained configurations are defined according to a strain amplitude a (by default, $N_s = 2$, corresponding to one "expanded" and one "contracted" configuration with a strain amplitude $a = 0.015$, i.e., a deformation of 1.5% with respect to the unstrained lattice); (v) for each strained configuration, atomic positions are relaxed (default option) or not depending on whether one wants to go beyond or not the "clamped-ion" approximation; cell gradients and dielectric tensor of the strained configurations are computed; (vi) cell gradients and inverse dielectric tensors along a given deformation are fitted with singular-value-decomposition

528

routines, their derivatives determined numerically and the corresponding elastic and photo-elastic constants obtained; (vii) once all independent deformations have been considered and all independent elastic and photo-elastic constants determined, full elastic and photo-elastic tensors are built based on the symmetry analysis performed at the beginning, the elastic tensor is inverted and the piezo-optic constants obtained by combining the photo-elastic with the compliance tensors.

C.2.3 Computational Setup

The algorithm described in Section II B has been implemented into a development version of the CRYSTAL14 program,[31] which adopts a basis set of localized Gaussian-type functions (GTF). An all-electron basis set has been adopted for describing O and Ca atoms, which consists in a 6-31G($2d$) contraction and a 6-31G(d) contraction of GTFs, respectively. The large-core effective pseudo-potential derived by Hay and Wadt has been chosen for tungsten, which leaves only the $5d$ and $6sp$ valence electrons to be explicitly described. A split-valence basis set has been adopted, composed of two independent, single Gaussian sp shells, and a 3-1G contraction for d electrons.[45] Four different formulations of exchange-correlation DFT functional are considered: the local-density approximation (LDA), SVWN functional,[46,47] the generalized-gradient approximation (GGA), PBE[48] functional, and hybrid B3LYP[49] and PBE0[50] functionals. Thresholds controlling the accuracy of Coulomb and exchange series are set to 8, 8, 8, 8, 16.[32] Reciprocal space is sampled using a Monkhorst-Pack mesh with a shrinking factor of 6 for the primitive cell of $CaWO_4$, corresponding to 36 independent k-points in the irreducible portion of the Brillouin zone. A pruned grid with 1454 radial and 99 angular points is used to calculate the DFT exchange-correlation contribution through numerical integration of the electron density

over the unit cell volume.[32] The self-consistent field convergence on energy was set to a value of 10^{-8} hartree for all geometry optimizations.3 Results and Discussion

Before discussing stress- or strain-induced anisotropic responses (elasticity, photo-elasticity, piezo-optics) of calcium tungstate, $CaWO_4$, we briefly comment on the description provided by different classes of DFT functionals of equilibrium structural, elastic, electronic, and dielectric properties. **Table C-1** reports such properties as computed with four functionals (SVWN, PBE, B3LYP, and PBE0), belonging to three rungs of "Jacob's ladder," along with their experimental counterparts. Experimental values for lattice parameters a and c, and fractional coordinates (x, y, z) of the oxygen atom in general position are taken from the single-crystal X-ray study by Hazen et al.[51] Voigt's upper bound to the bulk modulus K_V is defined in terms of the elastic constants as

$$K_V = \frac{1}{9}[2C_{11} + C_{33} + 2(C_{12} + 2C_{13})] .$$ (12)

The experimental value reported in the table (89.4 GPa) refers to 0 K and has been derived from the extrapolated elastic constants measured in the temperature range 4.2–300 K by Farley and Saunders;[52] note that computed values also refer to 0 K but neglect zero-point motion effects which, on the contrary, are included in the experimental counterpart. Ordinary n_o and extraordinary n_e refractive indices, and the corresponding birefringence $\delta = n_e - n_o$ are taken from Bond[53] and from Houston et al.[54] and correspond to an electric field wavelength $\lambda = 2500$ nm, while theoretical values refer to the $\lambda \to \infty$ limit (see below for a theoretical investigation of the dispersion of refractive indices with λ).

Table C-1: Lattice parameters *a* and *c* (in Å), fractional coordinates (x,y,z) of the oxygen atom in general position, Voigt bulk modulus K_V (in GPa), electronic band gap E_g (in eV), ordinary n_o and extraordinary n_e refractive indices, and birefringence ∂ of CaWO$_4$. Computed values, as obtained with four functionals, are compared with experimental data from Refs. 51-54.

	a	*c*	*x*	*y*	*z*	K_V	E_g	n_o	n_e	∂
SVWN	5.158	11.210	0.237	0.093	0.038	108.6	3.6	1.878	1.908	0.030
PBE	5.221	11.660	0.239	0.103	0.041	85.2	3.7	1.806	1.823	0.017
B3LYP	5.277	11.649	0.236	0.105	0.042	86.1	5.8	1.725	1.732	0.007
PBE0	5.241	11.516	0.236	0.102	0.041	90.4	6.2	1.736	1.747	0.011
Exp.	5.243	11.374	0.241	0.099	0.039	89.4	-	1.872	1.885	0.013

From inspection of **Table C-1**, it is seen that, as expected, the simple LDA functional significantly underestimates the cell size (a by 1.6% and c by 1.4%), overestimates the bulk modulus (by almost 20 GPa, corresponding to about 22%), describes a relatively narrow electronic band gap of 3.6 eV (here a reliable experimental reference is not available), and largely overestimates the birefringence δ (by more than a factor of 2). The generalized-gradient PBE functional provides a slightly better description of the lattice parameters, underestimating a by 0.4% and overestimating c by 2%, a similar description of the electronic band-gap (3.7 eV) but significantly improves upon LDA in the description of the bulk modulus (with an underestimation of about 4.5%) and of the birefringence. Hybrid functionals provide the best overall description of all considered properties, with PBE0 slightly outperforming B3LYP. Indeed, PBE0 gives an excellent description of the a lattice parameter (with a deviation smaller than 0.04%), only slightly overestimating the c one (by 1.2%), reliably describes the optical anisotropy of the system (with a δ of 0.011 with respect to the experimental value of 0.013) and provides an excellent description of the elasticity of the system, with a bulk modulus of 90.4 GPa with respect to the experimental value of 89.4 GPa; an overestimation by about 1% is perfectly compatible with the reduction of the bulk modulus that would be induced by the neglected zero-point motion and that could be evaluated by quasi-harmonic calculations.[55–59] As expected, hybrid functionals describe a significantly larger gap E_g (5.8–6.2 eV) than local-density and generalized-gradient approximations. All functional give a good description of the atomic positions within the cell.

C.3.1 The Elastic Response

As recalled in Section II A, a prerequisite to a reliable description of the piezo-optics of a crystal is a good calculation of its anisotropic elastic response. In **Table C-2**, we report the seven symmetry-independent elastic stiffness C_{vu} and compliance S_{vu} constants of tetragonal $CaWO_4$. The shape of the full fourth-rank elastic tensor for this system is given in Equation (5). In the table, the elastic constants are reported as computed with four DFT functionals and compared with two experimental determinations (one at room temperature and one extrapolated down to 0 K from data collected in the 4.2–300 K temperature range).[52] As expected from the overall structural description given in **Table C-1**, the LDA functional is seen to systematically overestimate the C_{vu} and underestimate the S_{vu} constants. The PBE generalized-gradient functional tends to slightly underestimate the elastic stiffness constants C_{vu} while hybrid functionals (more so PBE0 than B3LYP) do provide a satisfactory description of low-temperature elastic constants. As the experimental piezo-optic constants were measured at room temperature, it is interesting to illustrate the effect of temperature on the measured elastic constants. From inspection of the table, we can see that passing from 0 K to 300 K the absolute values of all C_{vu} constants are systematically reduced by about 4% (a converse increase of about 4% of S_{vu} constants is observed).

Table C-2. Symmetry-independent elastic stiffness C_{vu} and compliance S_{vu} constants of tetragonal CaWO$_4$, as computed with four different DFT functionals and compared to experimental data from Farley and Saunders [52] as measured at 300 K and extrapolated to 0 K.

| | Elastic stiffness constants (GPa) | | | | | | Elastic compliance constants (Br ≡ TPa−1) | | | | | | | |
	C_{11}	C_{12}	C_{13}	C_{33}	C_{44}	C_{66}	C_{16}	S_{11}	S_{12}	S_{13}	S_{33}	S_{44}	S_{66}	S_{16}
SVWN	185.7	86.03	68.08	161.9	51.6	59.45	−20.29	8.16	−3.50	−1.96	7.83	19.38	19.54	3.98
PBE	150.2	63.74	53.71	124	41.6	49.57	−13.77	9.33	−3.36	−2.59	10.3	24.04	22.13	3.52
B3LYP	156.7	60.9	52.39	131.4	44.27	51.78	−13.07	8.45	−2.76	−2.27	9.42	22.59	20.74	2.83
PBE0	161.7	67.05	54.68	137.7	45.63	54.17	−15.85	8.56	−3.16	−2.14	8.97	21.91	20.46	3.43
Expt. 0 K	150.6	65.89	59.06	135.7	35.58	47.75	−17.22	9.94	−3.89	−2.64	9.67	28.11	24.54	4.99
Expt. 300 K	143.9	63.5	56.17	130.2	33.61	45.07	−16.35	10.45	−4.15	−2.71	10.02	29.75	26.03	5.3

A better insight into the description provided by different DFT functionals of the anisotropy of the elastic response of a crystal can be achieved by analyzing directional elastic properties, such as directional seismic wave velocities (i.e., the velocities with which elastic waves do propagate within a crystal along different crystallographic directions). From a fundamental point of view, within the elastic continuum model, the velocity of propagation of a seismic wave traveling along any general crystallographic direction represented by unit wave-vector qˆqˆ, can be obtained from the elastic tensor via Christoffel's equation, which can be given an eigenvalues/ eigenvectors form as follows:[8,60]

$$A^q U = V^2 U \quad and \quad A_{jk}^{\hat{q}} = \frac{1}{p} \sum_{il} \hat{q}_i \, C_{ijkl} \hat{q}_l \quad (13)$$

where $A_{jk}^{\hat{q}}$ is Christoffel's matrix, p the crystal density, $i,j,k,l = x,y,z$ represent Cartesian directions, $\hat{q}_i$ is the i-th element of the unit vector $\hat{q}$, V is a 3 x 3 diagonal matrix whose three elements give the acoustic velocities and U = ($\hat{u}_1,\hat{u}_2,\hat{u}_3$) is the eigenvector 3 x 3 matrix where each column represents the polarization $\hat{u}$ of the corresponding eigenvalue. The three acoustic wave velocities, also referred to as seismic velocities, can be labeled as quasi-longitudinal v_p, slow quasi-transverse v_{s1} and fast quasi-transverse v_{s2}, depending on the polarization direction $\hat{u}$ with respect to wave-vector $\hat{q}$.[61] From directional seismic wave velocities, fundamental aspects of the elastic anisotropy of a crystal, such as shear-wave birefringence and azimuthal anisotropy, can be fruitfully discussed. These data are reported in **Figure C-1** as computed with the four DFT

functionals. We observe that: i) the four functionals provide a similar overall description of the directional elastic properties of $CaWO_4$; ii) the crystallographic direction of maximum longitudinal propagation velocity is found between the [110] and the [010] ones while the minimum longitudinal velocity is along the [001] direction; iii) the direction of maximum propagation velocity of transverse waves is found between the [100] and [110] ones while the minimum is between the [110] and [010] ones; iv) the basal *ab* plane is found to be more anisotropic than the vertical *ac* plane; v) LDA provides the largest anisotropy, B3LYP the smallest while PBE and PBE0 give a similar and intermediate description of the elastic anisotropy.
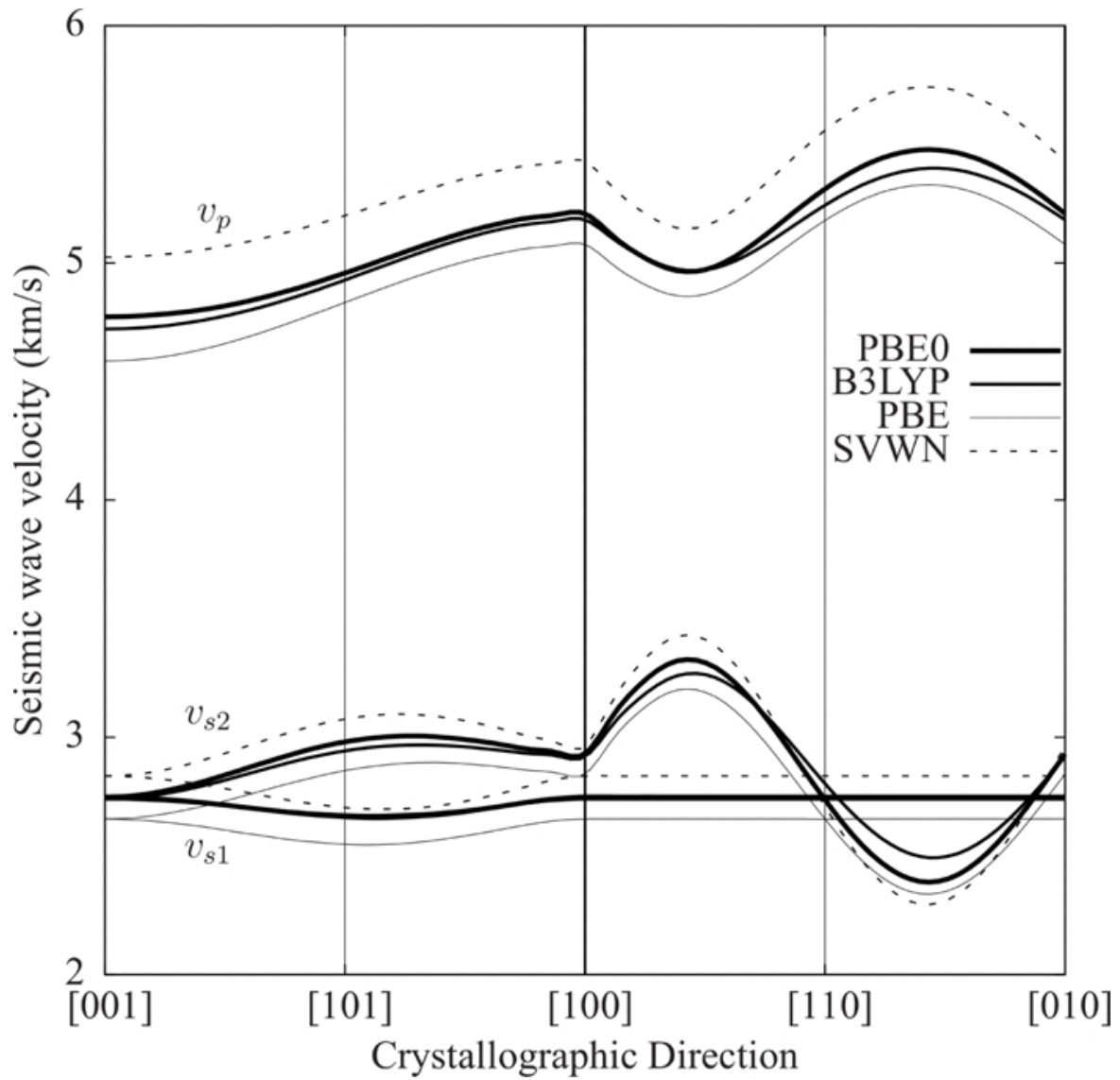
Figure C-1: Directional seismic wave velocities of tetragonal CaWO$_4$ as computed with four different DFT functionals.

C.3.2 Photo-elastic and Piezo-optic Response

We can now compare theoretically calculated with experimentally determined stress-optical π_{vu} and strain-optical p_{vu} constants of calcium tungstate. However, before doing so, it is worth illustrating how these two sets of data are obtained:

- Theoretically, strain-optical (photo-elastic) constants are determined as numerical derivatives of the inverse of the dielectric tensor with respect to an applied strain according to equation (7). Stress-optical constants are then obtained through the computed elastic compliance constants ($\pi = p\,S$);

- Experimentally, mechanical stresses are measured on five differently cut samples;[18] previously experimentally determined elastic compliances[52] S_{vu} and refractive indices[62] n_o and n_e are then used to solve a set of equations that provide stress-optical π_{vu} constants. Strain-optical constants are determined by combining these stress-optical constants with the elastic stiffness ones C_{vu} previously experimentally measured ($p = \pi\,C$).

Let us stress that if on the one hand the theoretical determination of p_{vu} and π_{vu} constants is achieved with a single calculation within a homogeneous computational setup, on the other hand experimental determinations of such properties require a rather complex combination of measurements of different quantities (mechanical stresses, elastic constants, refractive indices) on different samples, which are generally performed in different studies, by different groups, in different conditions, and, above all, with different accuracies. Bearing these considerations in mind, in **Table C-3** we report the ten symmetry-independent strain- and stress-optical constants (see equation (11) for the shape of the fourth-rank p and π tensors) as computed with the four DFT functionals and as compared with available experimental determinations. The full set of

piezo-optic π_{vu} constants has recently been reported by Mytsyk *et al.*[18] where just the sign of the

π_{61} constant could not be determined while its absolute value was reported to be $\pi_{61}=|0.16|$ Br.

Demyanyshyn *et al.*[13] have then coupled such constants to the elastic stiffness ones to determine

the photo-elastic p_{vu} constants: due to the uncertainty on the sign of the π_{61} constant, two photo-

elastic constants, p_{61} and p_{66}, were not uniquely determined (for $\pi_{61}=-0.16$ Br they got

$p_{61}=-0.001$ and $p_{66}=-0.018$, while for $\pi_{61}=+0.16$ Br they obtained $p_{61}=0.025$ and $p_{66}=-0.031$).

Table C-3. Photoelastic p_{vu} and piezo-optic π_{vu} symmetry-independent constants of CaWO$_4$ as computed with four different DFT functionals and as experimentally determined by Mytsyk and co-workers (see text for details). [13,17–19] Depending on the sign of the π_{61} constant (experimentally ill-determined), different experimental values of p_{61} and p_{66} are found (values in parentheses correspond to $\pi_{61} = -0.16$ Br while the others to $\pi_{61} = 0.16$ Br).

						Photoelastic constants					
	p_{11}	p_{12}	p_{13}	p_{31}	p_{33}	p_{44}	p_{45}	p_{16}	p_{61}	p_{66}
SVWN	0.154	0.15	0.263	0.254	0.201	0.018	−0.018	0.051	0.029	−0.071
PBE	0.157	0.175	0.249	0.256	0.226	0.018	−0.017	0.022	0.026	−0.058
B3LYP	0.152	0.194	0.24	0.264	0.208	0.009	−0.017	0.019	0.026	−0.050
PBE0	0.177	0.185	0.255	0.265	0.229	0.014	−0.019	0.032	0.025	−0.055
Expt.	0.4	−0.02	0.24	0.25	0.21	0.011	−0.06	−0.27	0.025	−0.031
										(−0.001)	(−0.018)
					Piezo-optic constants (Br ≡ TPa−1)						
	π_{11}	π_{12}	π_{13}	π_{31}	π_{33}	π_{44}	π_{45}	π_{16}	π_{61}	π_{66}
SVWN	0.417	−0.035	1.467	0.788	0.578	0.352	−0.345	1.006	0.058	−1.151
PBE	0.308	0.387	1.706	0.946	1.001	0.436	−0.404	0.43	0.128	−1.104
B3LYP	0.256	0.622	1.48	1.03	0.759	0.202	−0.384	0.283	0.149	−0.896
PBE0	0.495	0.367	1.508	0.938	0.922	0.318	−0.409	0.637	0.1	−0.964
Expt.	1.86	−0.60	1.52	1.02	1.01	0.33	−1.77	−5.64	|0.16|	−0.63

Regarding the effect of DFT functional on such computed properties, from **Table C-3** we see that: i) the computed values of p_{vu} constants obtained with all functionals are rather consistent with each other, particularly so if generalized-gradient (PBE) and hybrid (B3LYP and PBE0) functionals are considered (LDA providing slightly deviating results for some constants, such as p_{12}, p_{13}, p_{16} and p_{66}); ii) a similar trend is also observed for π_{vu} constants where LDA deviates more from the other functionals due to its poorer description of the elastic compliance constants; furthermore, given the different description of elastic constants provided by PBE, B3LYP and PBE0, larger differences (never exceeding a factor of 2.2 in the worst cases, though) are found on predicted piezo-optic constants by these functionals; iii) given the overall better description of elastic constants (see **Table C-2**) and refractive indices (see **Table C-1**), hybrid functionals are expected to constitute the best choice for the calculation of these properties and to provide the most reliable results.

In order to compare computed constants with experimentally derived ones, let us group the 10 symmetry-independent components of both the photo-elastic and piezo-optic tensors into two sub-sets: a first sub-set contains the x_{13}, x_{31}, x_{33}, x_{44}, x_{61} and x_{66} constants while the second sub-set contains the x_{11}, x_{12}, x_{45} and x_{16} ones, where x can be either p or π. For the first sub-set, which contains 6 constants, considering how delicate both the calculation and the experimental determination of these constants are, the agreement between computed and experimental values is very satisfactory, particularly so if hybrid functionals are considered, as expected. Such a good agreement is a strong evidence of the accuracy of both the experimental reconstruction of these constants and the automated computational strategy here devised. Present calculations allow for the ambiguous determination of the sign of the π_{61} constant, which is indeed found to be positive by all functionals. Furthermore we find that by taking the positive sign of this constant,

the experimental values of the p_{61} (0.025) and p_{66} (-0.031) constants are also found to be in much better agreement with present calculations. The small residual deviations between computed and experimental constants for this set might be due to either the neglect of thermal effects on computed elastic properties (which, however, is expected to be rather small: about 4% as noticed above) or the finite value of the electric-field wavelength used in the experiments versus the $\lambda = \infty$ of the calculations (see Section IIIC for an explicit investigation of such effect).

The situation is completely different when the second sub-set of 4 constants is considered. In this case, indeed, there is little agreement between computed and experimentally derived values, with very large differences on both absolute values and signs. Given that all computed constants are obtained with the same numerical accuracy, we have to deduce that the experimental reconstruction of these four constants is not as reliable as it was for the other six. On the contrary, present calculations do provide a complete, homogeneous set of all of the ten symmetry-independent photo-elastic and piezo-optic constants of $CaWO_4$.
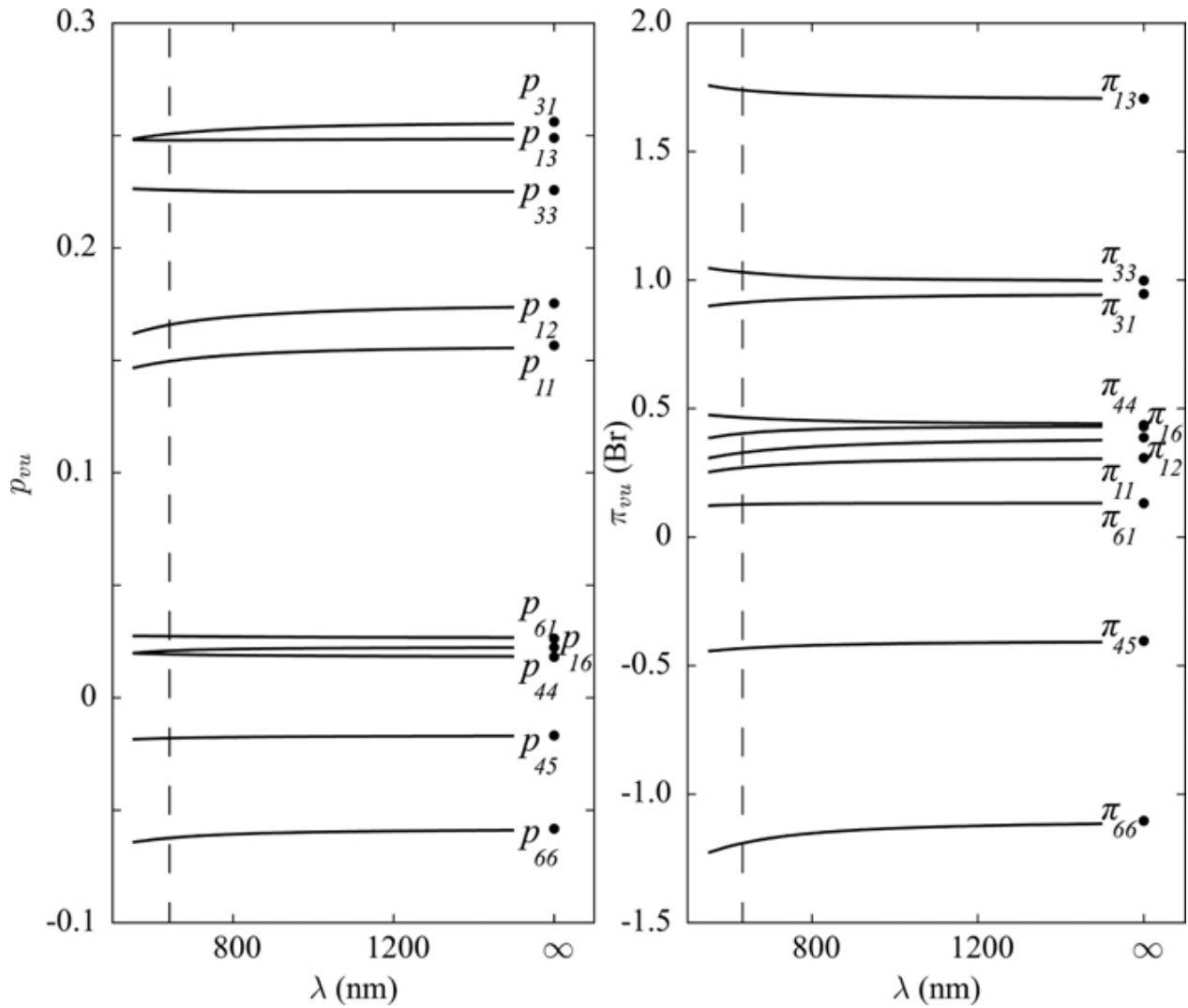
Figure C-2: Dependence on electric field wavelength □ of computed photo-elastic p_{vu} and piezo-optic π_{vu} constants of CaWO$_4$. The dashed vertical lines mark the experimental wavelength (λ =633 nm) used in the determination of the constants reported in Table C-3. Values obtained with the PBE functional. Computed values for $\lambda = \infty$ are represented by full circles

C.3.3 Effect of the Electric Field Wavelength

As mentioned at the end of Section III B, experimental measurements of optical properties of crystals are performed using a finite value of the wavelength λ of the electric field, whereas theoretical calculations generally refer to the $\lambda = \infty$ case. For instance, all of the experimental photo-elastic and piezo-optic constants of calcium tungstate reported in **Table C-3** correspond to $\lambda = 633$ nm. One might wonder if some of the discrepancies between computed and experimentally derived constants could be ascribed to such an issue. Electric field frequency dependent optical properties of crystals can be computed with a "dynamical" formulation of the CPHF/KS approach.[31,43,44] The present algorithm for the calculation of photo-elastic and piezo-optic tensors has been generalized to such a case too. In **Figure C-2**, we report computed p_{vu} and π_{vu} constants of CaWO$_4$ (just at the PBE level as similar trends are observed also for other functionals) as a function of λ in the range 500–1500 nm (continuous lines) while static values obtained at $\lambda = \infty$ are given as full circles. A dashed vertical line marks the $\lambda = 633$ nm value. We can clearly see that the dispersion of all computed stress-optical and strain-optical constants with λ is relatively small (i.e., their values change by just few percents passing from $\lambda = \infty$ to 633 nm). As regards photo-elastic constants, p_{11} and p_{12} show the largest dispersion, followed by p_{31} and p_{66} while the other constants are almost flat. Piezo-optic constants show a slightly larger dispersion, π_{66} exhibiting the largest among them. Overall, given the small variations of all constants, the electric field frequency dispersion can be ruled out as a possible reason for the large inconsistency of computed and experimental constants of the second sub-set discussed in Section III B.

C.4 Conclusions

A computational strategy has been devised and implemented in a fully-automated fashion for the quantum-mechanical prediction of piezo-optic fourth-rank tensors of crystals belonging to any space group of symmetry. This strategy is based on the simultaneous determination of elastic and photo-elastic tensors. A Coupled-Perturbed-Hertree-Fock/Kohn-Sham approach is used to compute the dielectric tensor of strained and unstrained configurations both in the static (infinite electric field wavelength) and dynamic (finite wavelength) cases. Both point and translation symmetry are fully exploited thus drastically reducing the number of independent components to be determined and the computational cost of all steps of the calculation.

The scheme has been applied to the $CaWO_4$ calcium tungstate crystal and the full set of 10 symmetry-independent photo-elastic and piezo-optic constants has been determined using four different formulations of the exchange-correlation functional within the density-functional-theory. Present results validate a sub-set of 6 experimentally reconstructed symmetry-independent constants (x_{13}, x_{31}, x_{33}, x_{44}, x_{61} and x_{66}, being x either the photo-elastic tensor p or the piezo-optic tensor π) and provide more reliable values for a second sub-set of 4 constants (x_{11}, x_{12}, x_{45} and x_{16}).

C.5 References

1. J. F. Nye, Physical Properties of Crystals (Oxford University Press, Oxford, 1957).

2. H.-J. Weber, Phys. Rev. B 51, 12209 (1995).

3. O. Krupych, V. Savaryn, A. Krupych, I. Klymiv, and R. Vlokh, Appl. Opt. 52, 4054 (2013).

4. T. S. Narasimhamurty, Photoelastic and Electrooptic Properties of Crystals (Plenum, 1981).

5 I. Slezinger, A. Alievskaya, and Y. Mironov, Meas. Tech. 28, 1059 (1985).

6. J. Badoz, M. Billardon, J. C. Canit, and M. F. Russel, J. Opt. 8, 373 (1977).

7. J. C. Kemp, J. Opt. Soc. Am. 59, 950 (1969).

8. B. A. Auld, Acoustic Fields and Waves in Solids (Krieger Publishing Company, Malabar, Florida, 1973).

9. J. Xu and R. Stroud, Acousto-Optic Devices: Principles, Design, and Applications

(Wiley, 1992).

10. A. S. Andrushchak, B. G. Mytsyk, H. P. Laba, O. V. Yurkevych, I. M. Solskii, A. V. Kityk, and B. Sahraoui, J. Appl. Phys. 106, 073510 (2009).

11. B. G. Mytsyk, A. S. Andrushchak, N. M. Demyanyshyn, Y. P. Kost', A. V. Kityk, P. Mandracci, and W. Schranz, Appl. Opt. 48, 1904 (2009).

12. A. Andrushchak, Y. Bobitski, M. Kaidan, B. Mytsyk, A. Kityk, and W. Schranz, Opt. Laser Technol. 37, 319 (2005).

13. N. M. Demyanyshyn, B. G. Mytsyk, Y. P. Kost, I. M. Solskii, and O. M. Sakharuk, Appl. Opt. 54, 2347 (2015).

14. H. Z. Cummins and P. E. Schoen, in Laser Handbook, edited by F. T. Arecchi and E. O. Schulz-Dubois (North-Holland Publishing Company, Amsterdam, 1972), p. 1029.

15. D. Landheer, H. E. Jackson, R. A. McLaren, and B. P. Stoicheff, Phys. Rev. B 13, 888 (1976).

16. O. Krupych, V. Savaryn, and R. Vlokh, Appl. Opt. 53, B1 (2014).

17. B. Mytsyk, N. Demyanyshyn, A. Andrushchak, Y. Kost', O. Parasyuk, and A. Kityk, Opt. Mater. 33, 26 (2010).

18. B. Mytsyk, Ya. P. Kost', N. Demyanyshyn, A. Andrushchak, and I. Solskii, Crystallogr. Rep. 60, 130 (2015).

19. B. Mytsyk, Y. Kost, N. Demyanyshyn, V. Gaba, and O. Sakharuk, Opt. Mater. 39, 69 (2015).

20. R. Dovesi, Int. J. Quantum Chem. 29, 1755 (1986).

21. C. Zicovich-Wilson and R. Dovesi, Int. J. Quantum Chem. 67, 299 (1998).

22. C. Zicovich-Wilson and R. Dovesi, Int. J. Quantum Chem. 67, 311 (1998).

23. R. Orlando, M. D. L. Pierre, C. M. Zicovich-Wilson, A. Erba, and R. Dovesi, J. Chem. Phys. 141, 104108 (2014).

24. K. Doll, N. M. Harrison, and V. R. Saunders, Int. J. Quantum Chem. 82, 1 (2001).

25. K. Doll, Comput. Phys. Commun. 137, 74 (2001).

26. K. Doll, R. Dovesi, and R. Orlando, Theor. Chem. Acc. 112, 394 (2004).

27. K. Doll, R. Dovesi, and R. Orlando, Theor. Chem. Acc. 115, 354 (2006).

28. M. Ferrero, M. Rérat, R. Orlando, and R. Dovesi, J. Comput. Chem. 29, 1450 (2008).

29. M. Ferrero, M. Rérat, R. Orlando, and R. Dovesi, J. Chem. Phys. 128, 014110 (2008).

30. M. Ferrero, M. Rérat, B. Kirtman, and R. Dovesi, J. Chem. Phys. 129, 244110 (2008).

31. R. Dovesi, R. Orlando, A. Erba, C. M. Zicovich-Wilson, B. Civalleri, S. Casassa, L. Maschio, M. Ferrabone, M. De La Pierre, Ph. D'Arco et al., Int. J. Quantum Chem. 114, 1287 (2014).

32. R. Dovesi, V. R. Saunders, C. Roetti, R. Orlando, C. M. Zicovich-Wilson, F. Pascale, K. Doll, N. M. Harrison, B. Civalleri, I. J. Bush et al., CRYSTAL14 User's Manual, Università di Torino, Torino, 2014, http://www.crystal.unito.it.

33. A. Erba, A. Mahmoud, R. Orlando, and R. Dovesi, Phys. Chem. Miner. 41, 151 (2014).

34. A. Erba, A. Mahmoud, D. Belmonte, and R. Dovesi, J. Chem. Phys. 140, 124703 (2014).

35. A. Erba, K. E. El-Kelany, M. Ferrero, I. Baraille, and M. Rérat, Phys. Rev. B 88, 035102 (2013).

36. K. E. El-Kelany, P. Carbonnière, A. Erba, and M. Rérat, J. Phys. Chem. C 119, 8966 (2015).

37. A. Erba, M. Ferrabone, J. Baima, R. Orlando, M. Rérat, and R. Dovesi, J. Chem. Phys. 138, 054906 (2013).

38. A. Erba and R. Dovesi, Phys. Rev. B 88, 045121 (2013).

39. J. P. Perdew and K. Schmidt, AIP Conf. Proc. 577, 1 (2001).

40. W. F. Perger, J. Criswell, B. Civalleri, and R. Dovesi, Comput. Phys. Commun. 180, 1753 (2009).

41G. Saghi-Szabo, R. E. Cohen, and H. Krakauer, Phys. Rev. Lett. 80, 4321

(1998).

42. A. Dal Corso, M. Posternak, R. Resta, and A. Baldereschi, Phys. Rev. B 50, 10715 (1994).

43. L. Bernasconi, S. Tomic, M. Ferrero, M. Rérat, R. Orlando, R. Dovesi, and N. M. Harrison, Phys. Rev. B 83, 195325 (2011).

44. A. Ferrari, R. Orlando, and M. Rérat, J. Chem. Theor. Comput. 11(7), 3245–3258 (2015).

45. F. Corá, A. Patel, N. M. Harrison, R. Dovesi, and C. R. A. Catlow, J. Am. Chem. Soc. 118, 12174 (1996).

46. J. C. Slater, Phys. Rev. 81, 385 (1951).

47. S. H. Vosko, L. Wilk, and M. Nusair, Can. J. Phys. 58, 1200 (1980).

48. J. P. Perdew, K. Burke, and M. Ernzerhof, Phys. Rev. Lett. 77, 3865 (1996).

49. A. D. Becke, J. Chem. Phys. 98, 5648 (1993).

50. C. Adamo and V. Barone, J. Chem. Phys. 110, 6158 (1999).

51. R. M. Hazen, L. W. Finger, and J. W. Mariathasan, J. Phys. Chem. Solids 46, 253 (1985).

52. J. Farley and G. Saunders, Solid State Commun. 9, 965 (1971).

53. W. L. Bond, J. Appl. Phys. 36, 1674 (1965).

54. T. W. Houston, L. F. Johnson, P. Kisliuk, and D. J. Walsh, J. Opt. Soc. Am. 53, 1286 (1963).

55. A. Erba, J. Chem. Phys. 141, 124115 (2014).

56. A. Erba, M. Shahrokhi, R. Moradian, and R. Dovesi, J. Chem. Phys. 142, 044114 (2015).

57. A. Erba, J. Maul, R. Demichelis, and R. Dovesi, Phys. Chem. Chem. Phys. 17, 11670 (2015).

58. A. Erba, J. Maul, M. De La Pierre, and R. Dovesi, J. Chem. Phys. 142, 204502 (2015).

59. A. Erba, J. Maul, M. Itou, R. Dovesi, and Y. Sakurai, Phys. Rev. Lett. 115, 117402 (2015).

60. M. J. P. Musgrave, Crystal Acoustics (Holden-Day, San Francisco, California, 1970).

61. B. B. Karki, L. Stixrude, and R. M. Wentzcovitch, Rev. Geophys. 39, 507,

62. T. A. Davis and K. Vedam, J. Opt. Soc. Am. 58, 1446 (1968).

APPENDIX D: Chapter 7 Supporting Information

CONTENTS:

Results

Table D-1. Single crystal XRD determined $Water_a$ tilt angle and O_{far}-H_{mal} bond distances.

Table D-2. Experimental THz linewidths for the MMT series.

Figure D-1. Experimental and calculated THz vibrational spectra of MnMT.

Figure D-2. Experimental and calculated THz vibrational spectra of FeMT.

Figure D-3. Experimental and calculated THz vibrational spectra of CoMT.

Figure D-4. Experimental and calculated THz vibrational spectra of NiMT.

Figure D-5. Experimental and calculated THz vibrational spectra of ZnMT.

Figure D-6. Mass-dependence of MnMT vibrational frequency.

Table D-2. Calculated O_{far}-H_{mal}-O_{near} stretching frequencies.

Figure D-7. MnMT COOP diagram.

Figure D-8. FeMT COOP diagram.

Figure D-9. CoMT COOP diagram.

Figure D-10. NiMT COOP diagram.

Figure D-11. ZnMT COOP diagram.

D.1 Additional Structural Results

All five MMT species are isomorphic and crystallize in the triclinic $P\bar{1}$ space group, and contain a single formula unit in the unit cell (Z=1) (**Figure 1**). The original literature structure of MnMT[1] indicated it to be completely isomorphic with ZnMT.[1-2] However, that data was found to be inaccurate by a later report, where the authors determined that the β angle was incorrect.[3] The structure obtained for this work confirmed these observations.

The unit cell parameters and heavy-atom positions of the redetermined structures are in good agreement with the available literature data.[1-2, 4-5] An exception is CoMT, for which the literature structure contains multiple errors that are resolved by the high-quality diffraction data obtained here.[6] The DFT geometry optimizations yielded excellent agreement with the experimental structure. For example, the average error in the ZnMT non-hydrogen covalent bond distances is 0.44% (with respect to the low-temperature X-ray structure). Of particular note is the correct modeling of the maleate C-O bond distances (average error of 0.36%). This indicates that the proper single and double bond character of the carboxylate groups has been achieved by the simulation, meaning the hydrogen atom position in the LBHB is also accurate.

While the heavy-atom positions are in agreement there exist systematic differences in the covalent bond lengths involving hydrogen, particular when comparing the ZnMT neutron diffraction structure to the XRD determined structure,[2] but this variation is attributable to the imprecise nature of XRD for measuring hydrogen positions. Considering the X-H covalent bonds, only ZnMT has been studied using neutron diffraction and therefore is the only structure available with precise hydrogen positions to serve as a benchmark. The average error in the calculated ZnMT X-H bond distances are small (2.0%) when compared to the neutron data,

meaning the simulations provide reliable hydrogen positional data.[2] Given the high quality of the simulations, all discussed bond distances and angles involving hydrogen atoms refer to the solid-state DFT optimized positions.

The pair of water$_a$ molecules exhibits significant tilting in ZnMT that is not present in MnMT. The angle of this tilt is defined by the angle between the line connecting the metal and water$_a$-oxygen, and the line bisector of the water$_a$ H-O-H angle. In MnMT, the water$_a$ tilt is 8.875°, with an O_{near}-O_{water_a} bond distance of 3.09 Å and an O_{near}···H-O_{water_a} angle of 102.47°, while in ZnMT these values are 41.602°, 2.78 Å, and 140.17°, respectively (Table 1). The experimental water$_a$ tilt angles are also provided in Table 1, and while calculated values differ slightly, the trends are very similar. The average deviation in the calculated tilt angles is ~8°, which is less than the differences between the individual species. The second subtle deviation is observed in the LBHB of the maleate ligand, with MnMT exhibiting a slightly longer O_{far}-H bond than in ZnMT (**Table D-1**).

Table D-1. Single crystal XRD determined water$_a$ tilt angles and $O_{far} - H_{mal}$ bond distances for the MMT series.

Species	Experimental Water$_a$ Tilt Angle (°)	Experimental O_{far}-H_{mal} Distance (Å)
MnMT	14.16	1.17
FeMT	17.25	1.00
CoMT	22.46	1.04
NiMT	37.57	0.97
ZnMT	31.49	1.02

D.2 Terahertz Spectroscopic Results

The terahertz and calculated low frequency vibrational spectra are provided in **Figures D-(1-5)**. The simulated spectra have been convolved using Lorentzian lineshapes using empirical full-width half-maxima (FWHM) **(Table D-2)**. The lowest-frequency terahertz motion involves an antisymmetric translation of the metal cation and coordinated water molecules, with simultaneous rotation of the maleate ligands. The higher-frequency motion involves a rotation of the maleate ligands with concurrent bending of all four coordinated metal-water bonds (animations of the motions have been uploaded as .avi files). As first approximations, the observed frequency trends could be caused by mass or radius changes from the different metal cations, and both of these factors were explored. The metal mass dependence of the vibrational modes was examined by utilizing MnMT as a model system and substituting the manganese cation mass with the masses of the other four metal cations, then re-evaluating the eigenvalues of the mass-weighted Hessian matrix. The result (**Figure D-6**) showed that increasing the mass of the metal cation decreases the vibrational frequencies, as expected from the $\frac{1}{\sqrt{reduced\ mass}}$ dependence. However, the actual experimental frequencies increase significantly with increasing metal mass. The influence of different metal sizes was investigated by performing a geometry optimization of ZnMT while fixing the unit cell volume to that of the MnMT crystal (volumes of 313.95 and 357.13 $\mathring{A}^3$ for ZnMT and MnMT, respectively), but allowing all lattice parameters, angles, and atomic positions to relax within this constraint. The resulting structure did not yield any significant changes, and the position of H_{mal} and $water_a$ remained consistent with the unconstrained optimization. The vibrations obtained from this expanded volume test were at slightly lower frequencies than the original simulation, but the calculated shift was not nearly as much as the measured shift. For the first vibrational mode, a shift of -0.77 cm^{-1} was provided

from the expanded volume test, only 16% of the -4.79 cm^{-1} shift observed experimentally. These results indicate that metal mass and ionic radii can influence the terahertz vibrations, but they do not play a dominating role.

The dependence of the terahertz features on the water$_a$ tilt angle also provides a possible explanation for the varying FWHM of the absorptions in the experimental spectra **(Table D-2)**. It has been shown that the vibrational lifetime (and thus, spectral linewidth) of the modes is inversely proportional to hydrogen bonding strength.[7] The linearity of the hydrogen bond geometry between water$_a$ and O$_{near}$ is directly related to the water$_a$ rotation angle, with the furthest from linear (weakest) in MnMT and closest to linear (strongest) in NiMT. Therefore it can be surmised that the increasing linewidths are a result of stronger hydrogen bonding networks.

Table 2. Experimental THz linewidths for the MMT series.

Species	Average THz Linewidth
MnMT	3.28
FeMT	3.58
CoMT	3.52
NiMT	6.95
ZnMT	4.92
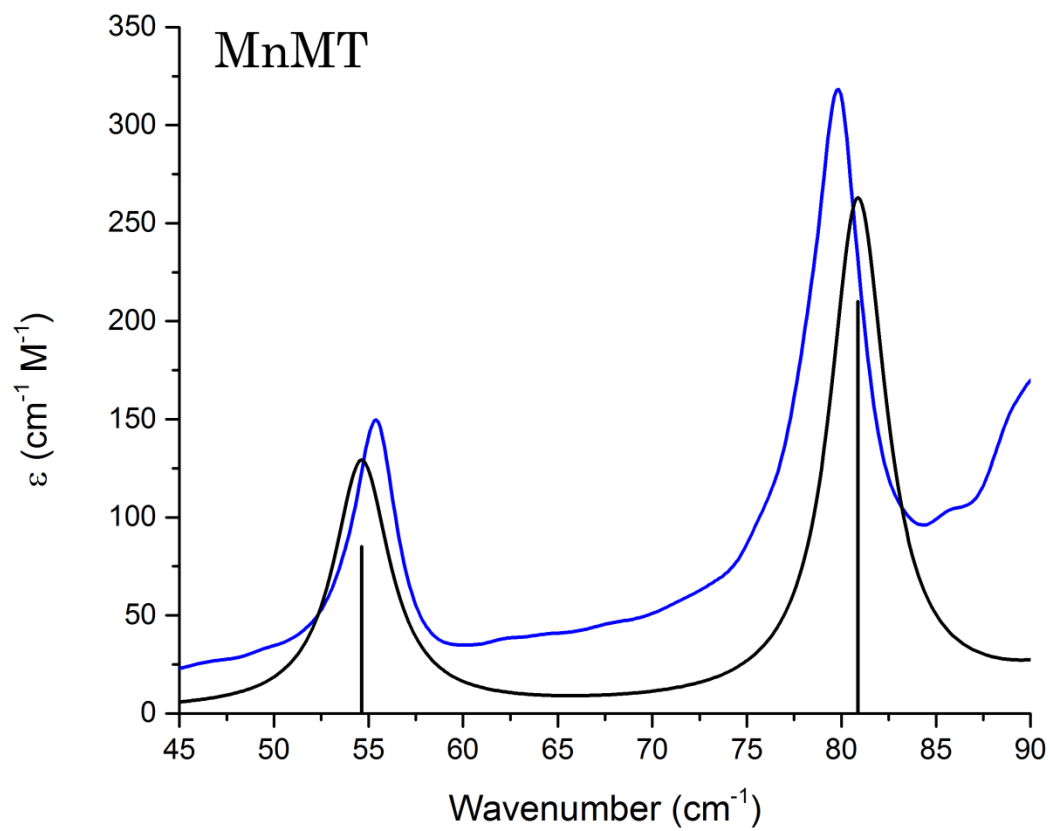
Figure D-1. Experimental and calculated THz vibrational spectra of MnMT.
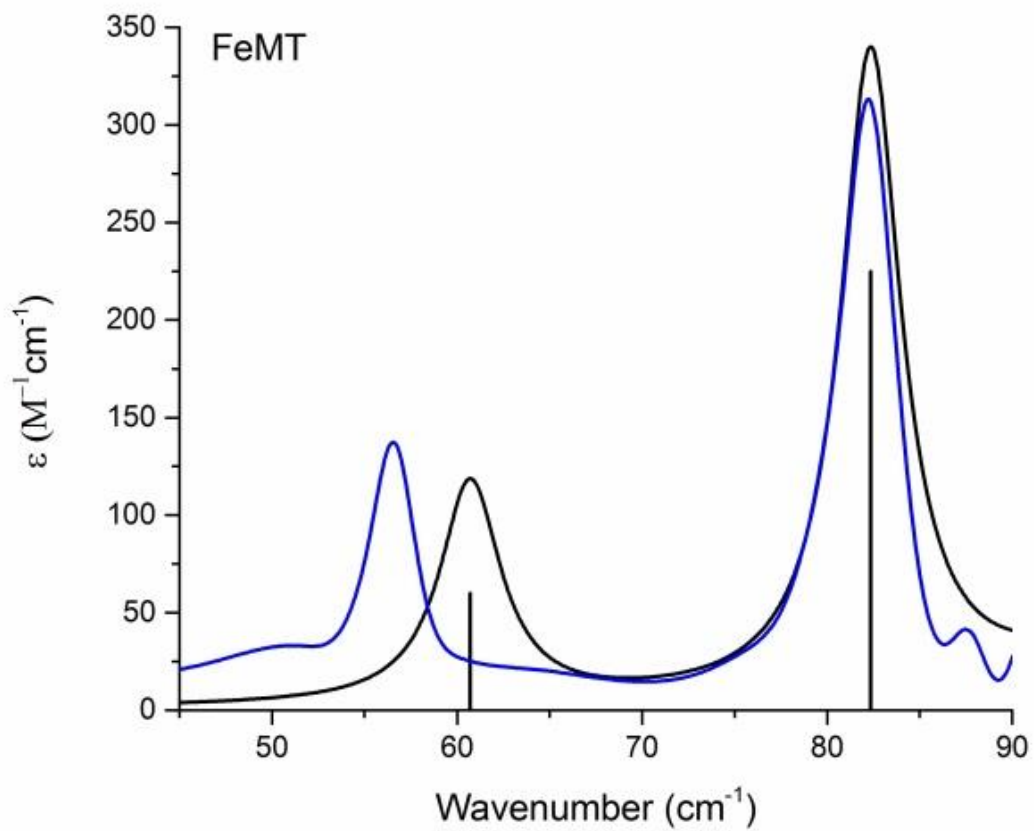
Figure D-2. Experimental and calculated THz vibrational spectra of FeMT
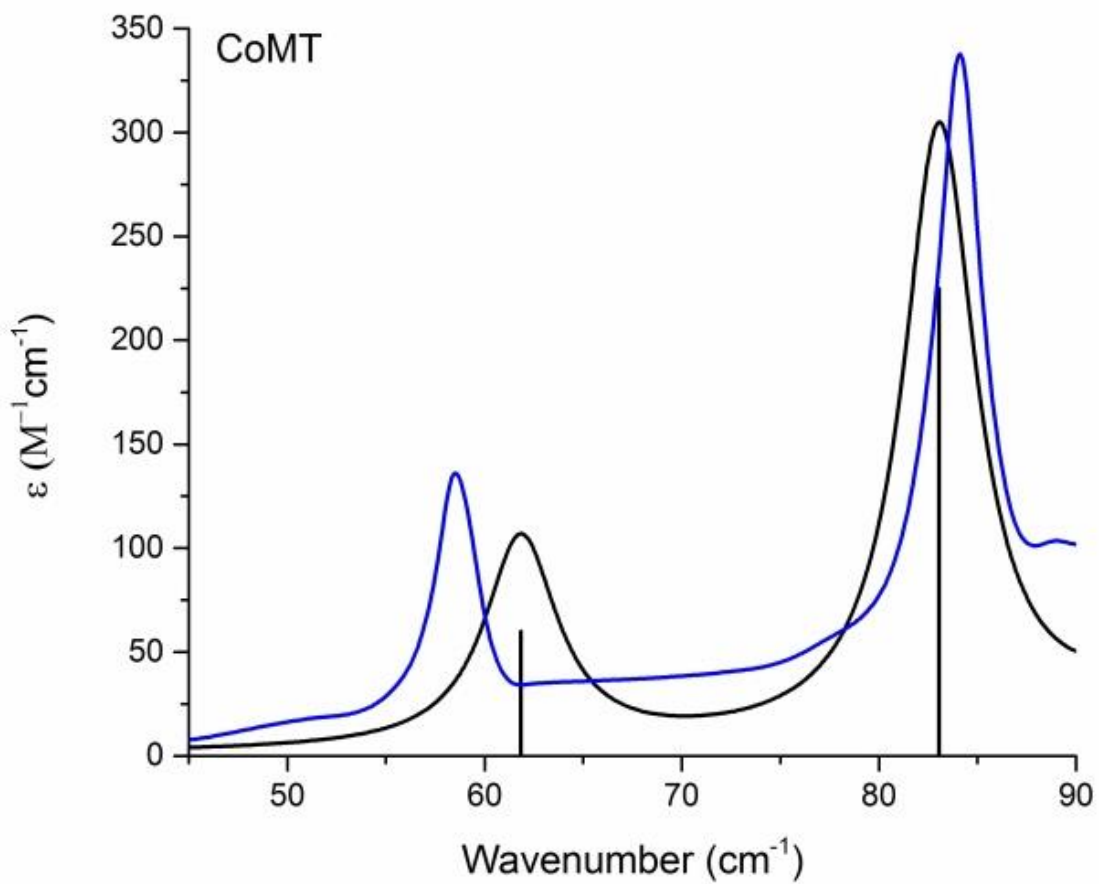
Figure D-3. Experimental and calculated THz vibrational spectra of CoMT
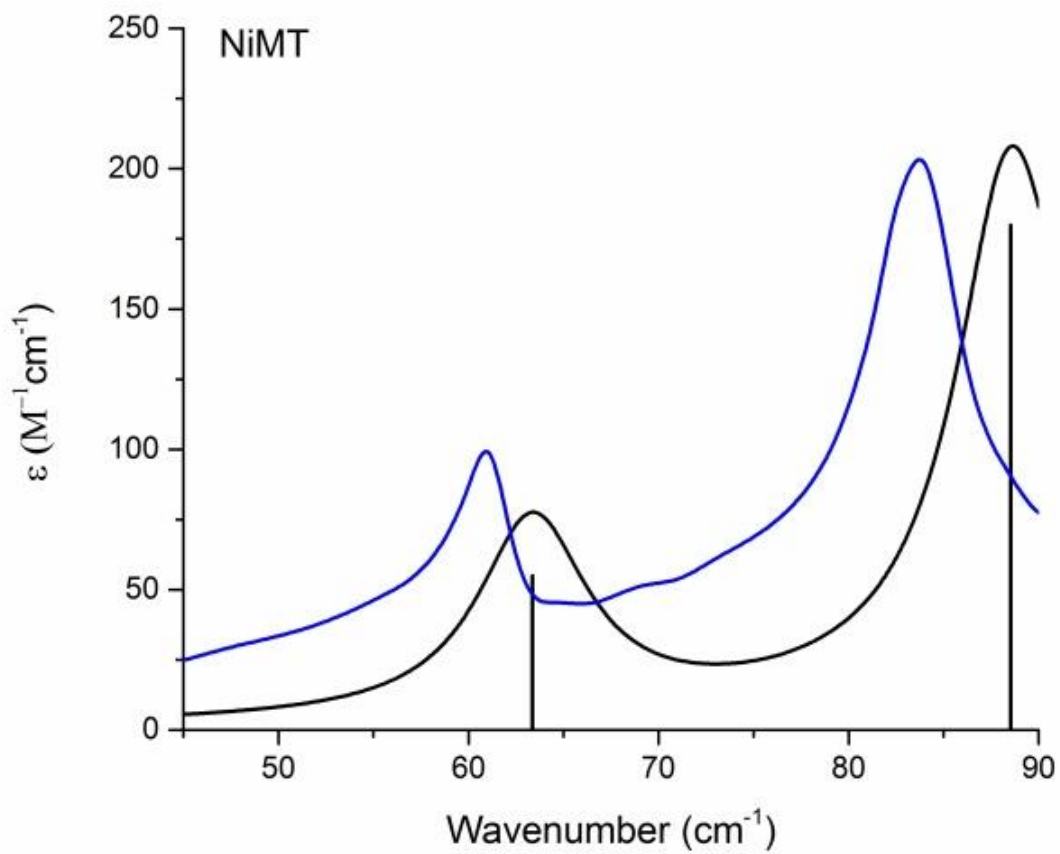
Figure D-4. Experimental and calculated THz vibrational spectra of NiMT
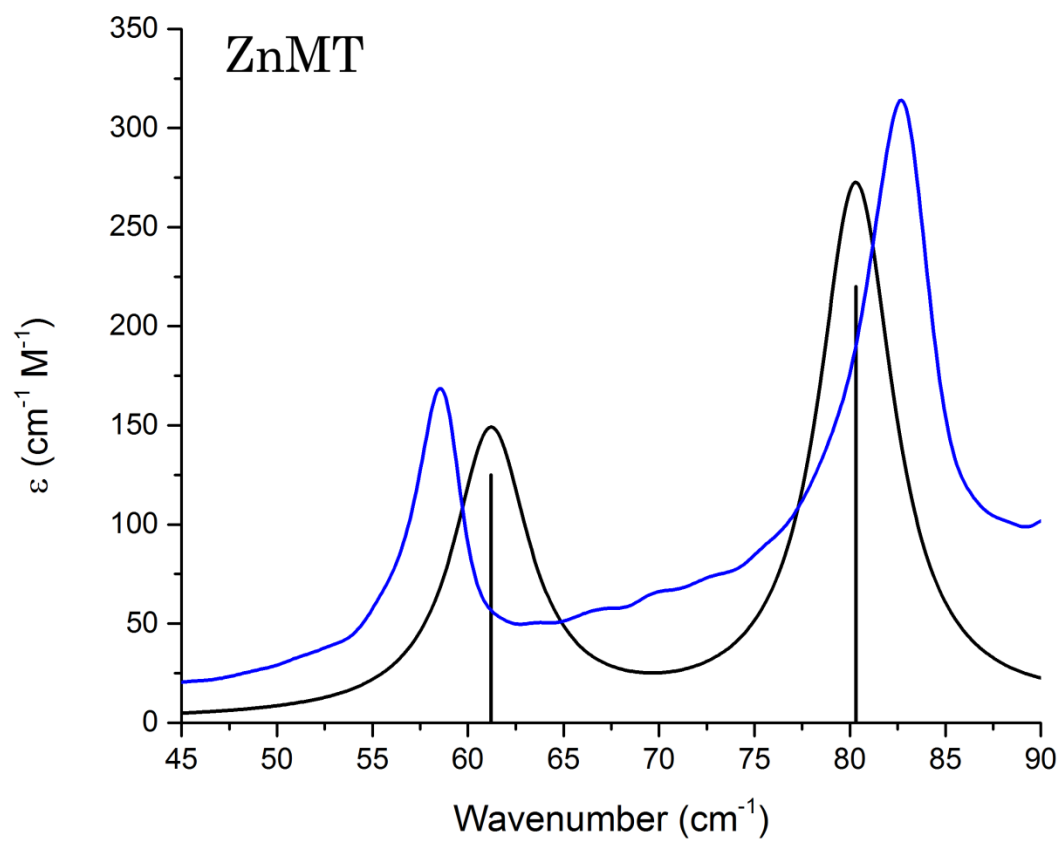
Figure D-5. Experimental and calculated THz vibrational spectra of ZnMT
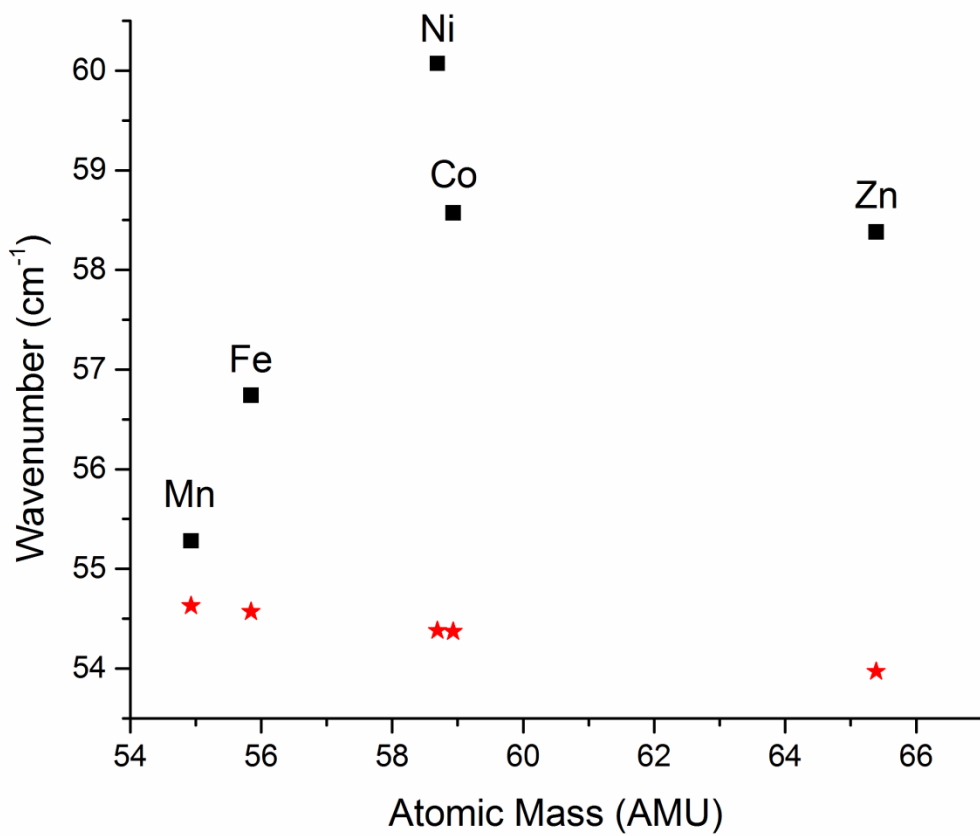
Figure D-6. Calculated and experimental mass-dependence on vibrational frequency of MnMT

Table D-2. Calculated O_{far}-H_{mal}-O_{near} stretching frequencies.

Species	Frequency (cm^{-1})
MnMT	1958.78
FeMT	2172.10
CoMT	2346.12
NiMT	2441.26
ZnMT	2417.86

D.3 Molecular Orbital Analyses

The solid-state optimized atomic positions were used as the basis for non-periodic calculations, where the isolated system under study was defined as a single crystallographic unit cell (Z=1): a metal cation, two maleate anions, and four water molecules. Rigid structures were used since all attempts to optimize the metal maleate formula units in the gas phase resulted in the loss of the solid-state structural features, even when clusters of up to nine formula units were tested. The isolated calculations were used to produce molecular orbitals, state densities, and the overlap matrices for every orbital present in the metal maleates, permitting detailed analysis of the spatial distribution of the electron density in each system.

A full analysis of the metal-water$_a$ orbital overlap matrix was performed with specific attention given to the d-orbitals (the predominant variable across the transition metal series). To aid in the determination of the role of the individual metal d-orbitals involved in each molecular orbital, a Mulliken population analysis was also done for each species.[8-11] In agreement with the visual inspection of the molecular orbitals, the net overlap between the two species decreases as the metal-water$_a$ angle increases. While total orbital overlap is useful for characterizing the metal-water$_a$ interaction, it does not necessarily provide information regarding the specific populations of the molecular orbitals, such as bonding or antibonding character. In order to account for this, the overlap matrix elements must be weighted by the respective occupations of the molecular orbitals. This method is commonly referred to crystal orbital overlap population (COOP) analysis, and has been used in the past to characterize the interactions between fragments in molecular species.

The COOP analyses (**Figures D-(7-11)**) provide detailed pictures regarding the nature of the chemical bond between the metals and water$_a$. For example, if only the orbital overlap was considered, MnMT and ZnMT would appear to be non-interacting because the bonding and antibonding interactions are equal, which is a result of the lack of crystal field stabilization energy typically attributed to d^5 and d^{10} metal-ligand interactions. However in the COOP diagrams, it is clearly shown that ZnMT and MnMT contain a larger proportion of bonding versus antibonding populations. In keeping with this approach, the total amount of bonding and antibonding populations were determined for each MMT by integration of the positive and negative regions of the COOP diagrams, respectively.

The antibonding population only slightly increases when moving from MnMT to FeMT, while there is a large increase in the total bonding population. This can be attributed to the increased overlap as well as the addition of an electron to the favorable d_{xz} orbital. This is further evidenced by the appearance of a positive peak on the FeMT COOP diagram. This peak disappears upon switching to CoMT, indicating that the next electron (added to one of the degenerate d_{xy} or d_{yz} orbitals) is involved in antibonding interactions. This causes water$_a$ to tilt and ultimately results in relatively no change between the water$_a$-metal bond populations found in FeMT and CoMT.
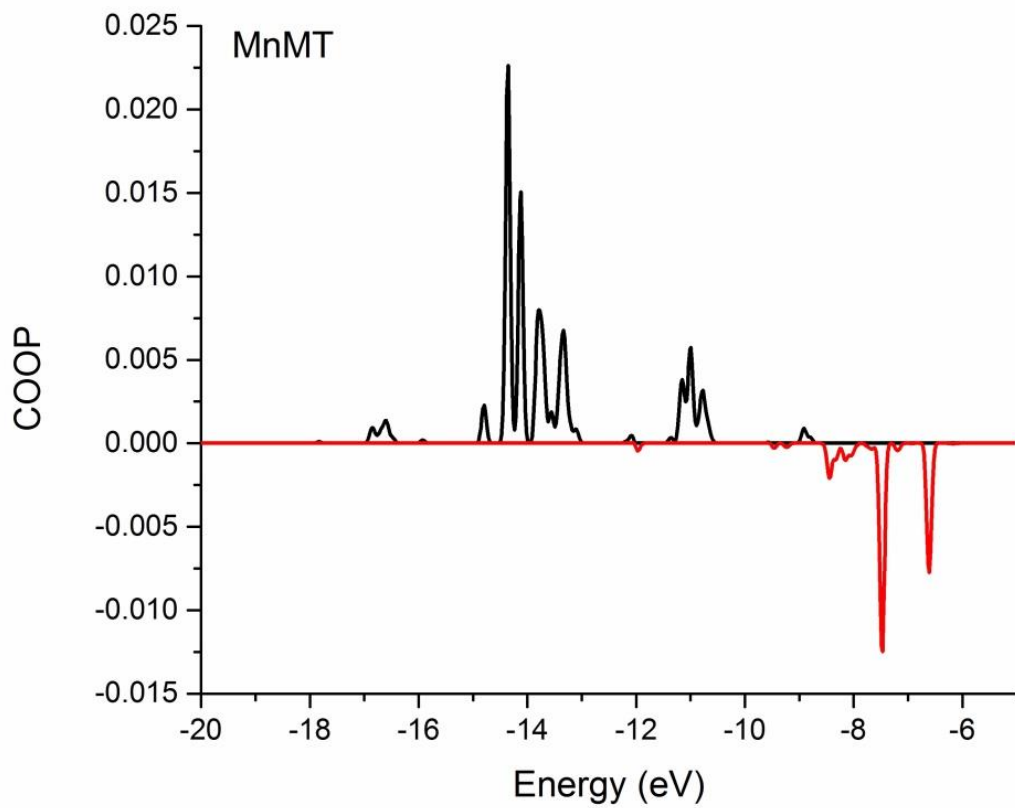
Figure D-7. MnMT COOP diagram.
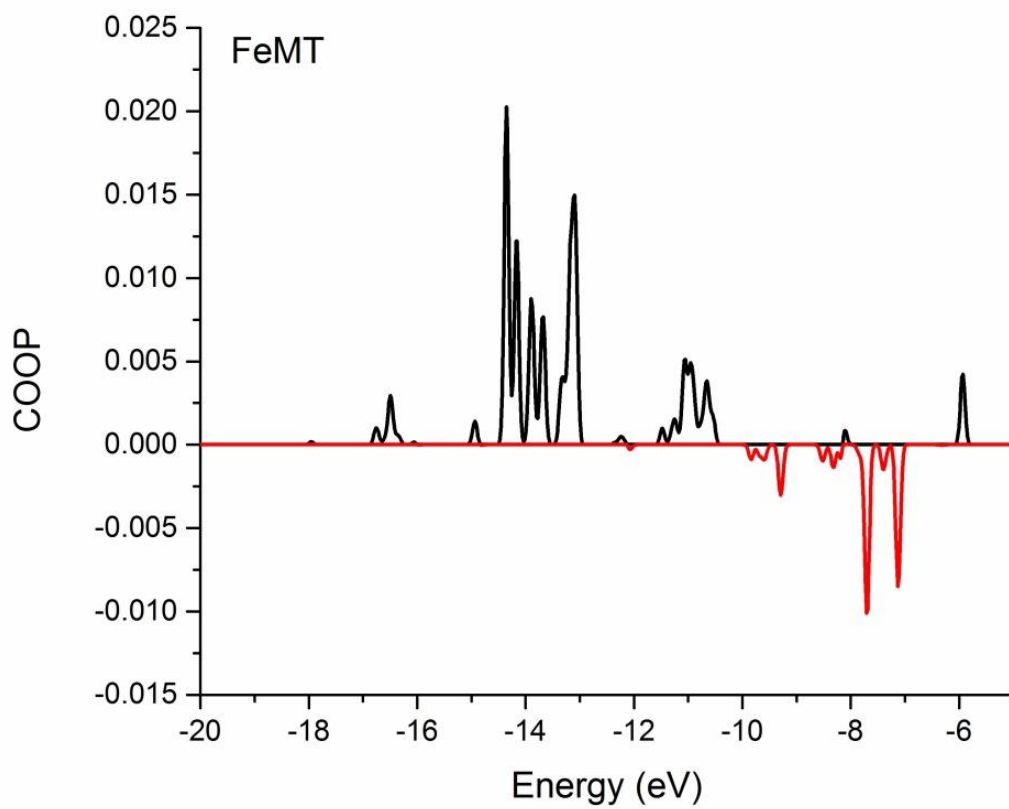
Figure D-8. FeMT COOP diagram.
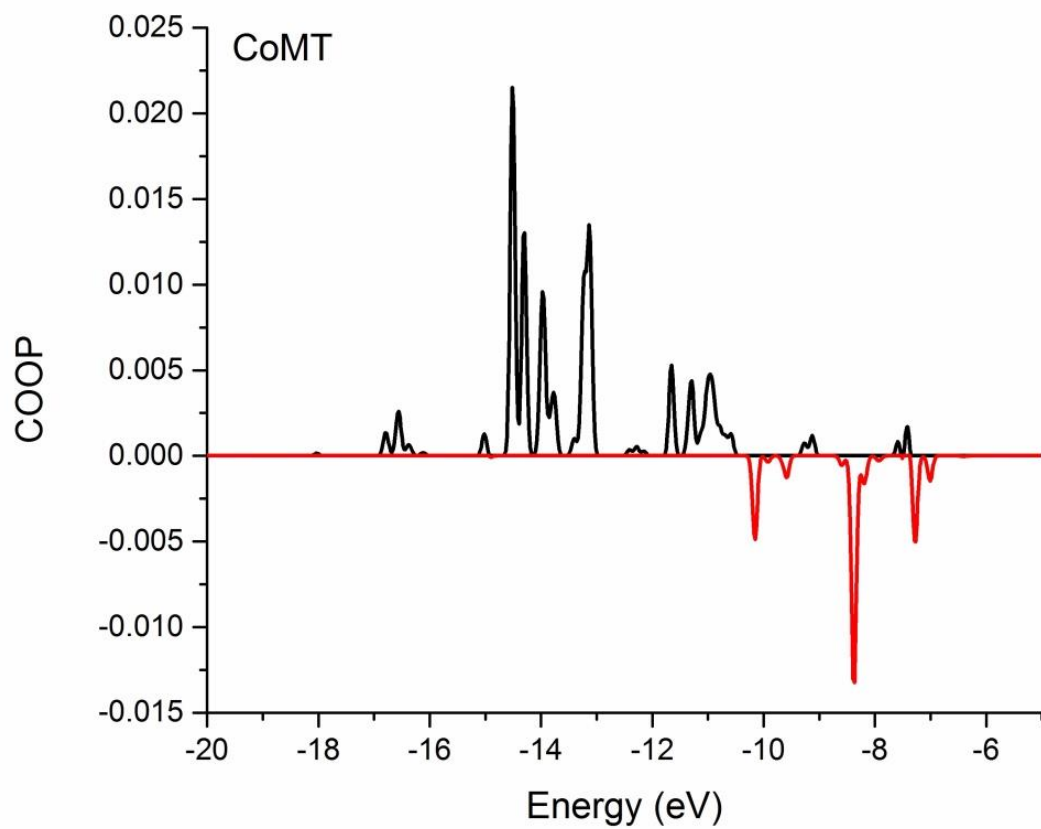
Figure 9. CoMT COOP diagram.
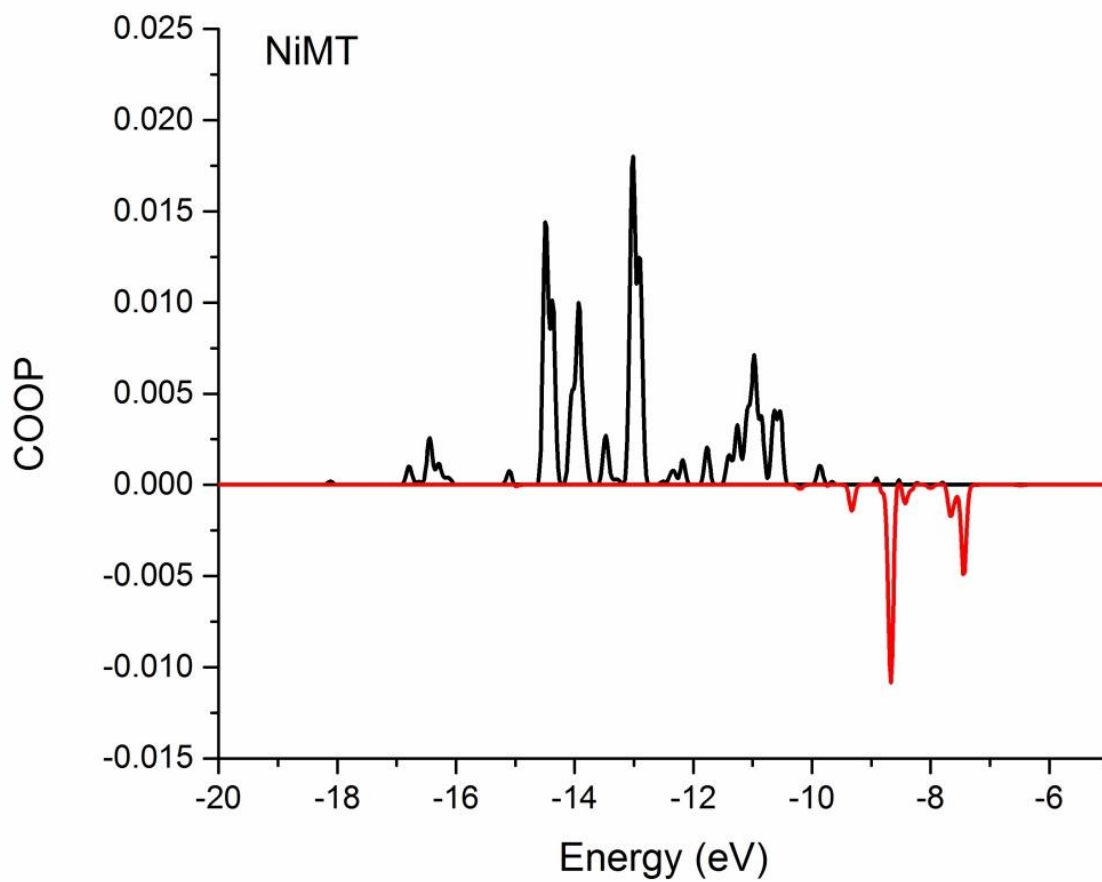
Figure D-10. NiMT COOP diagram.
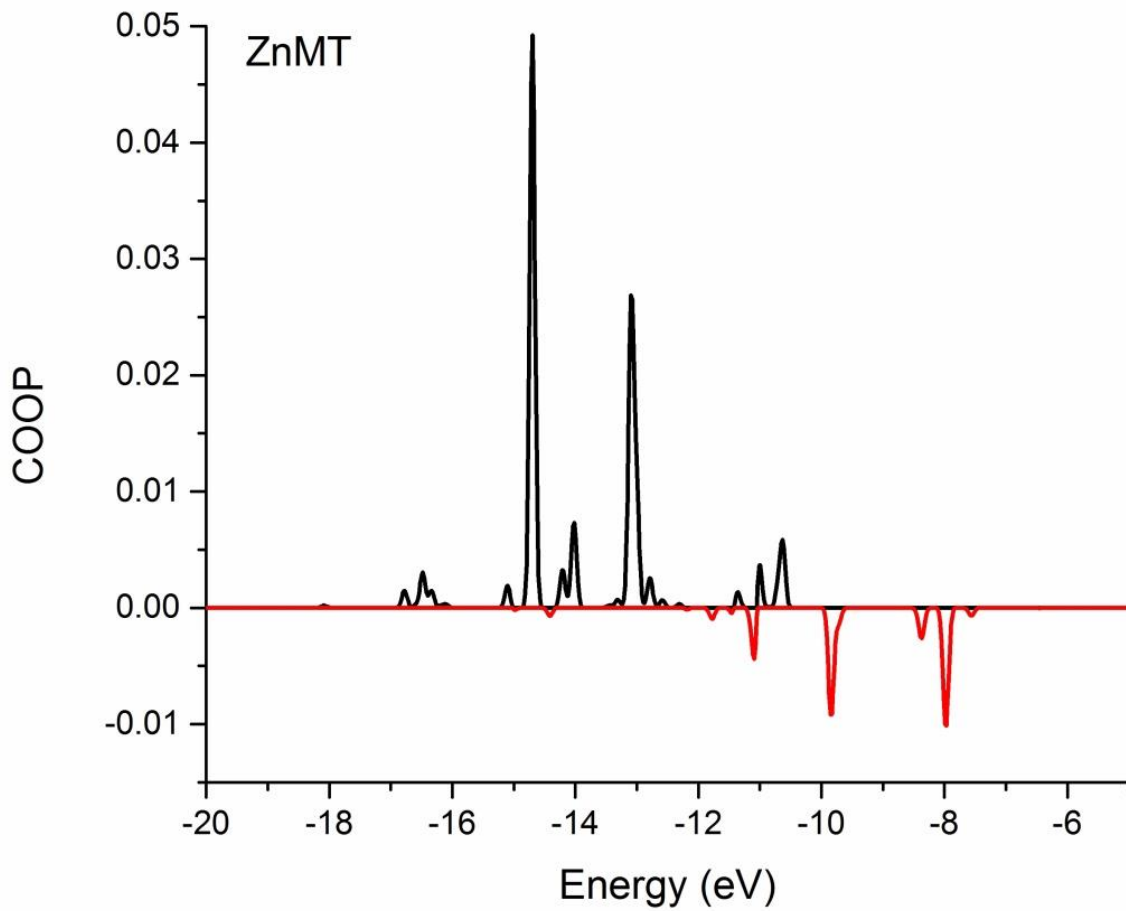
Figure D-11. ZnMT COOP diagram.
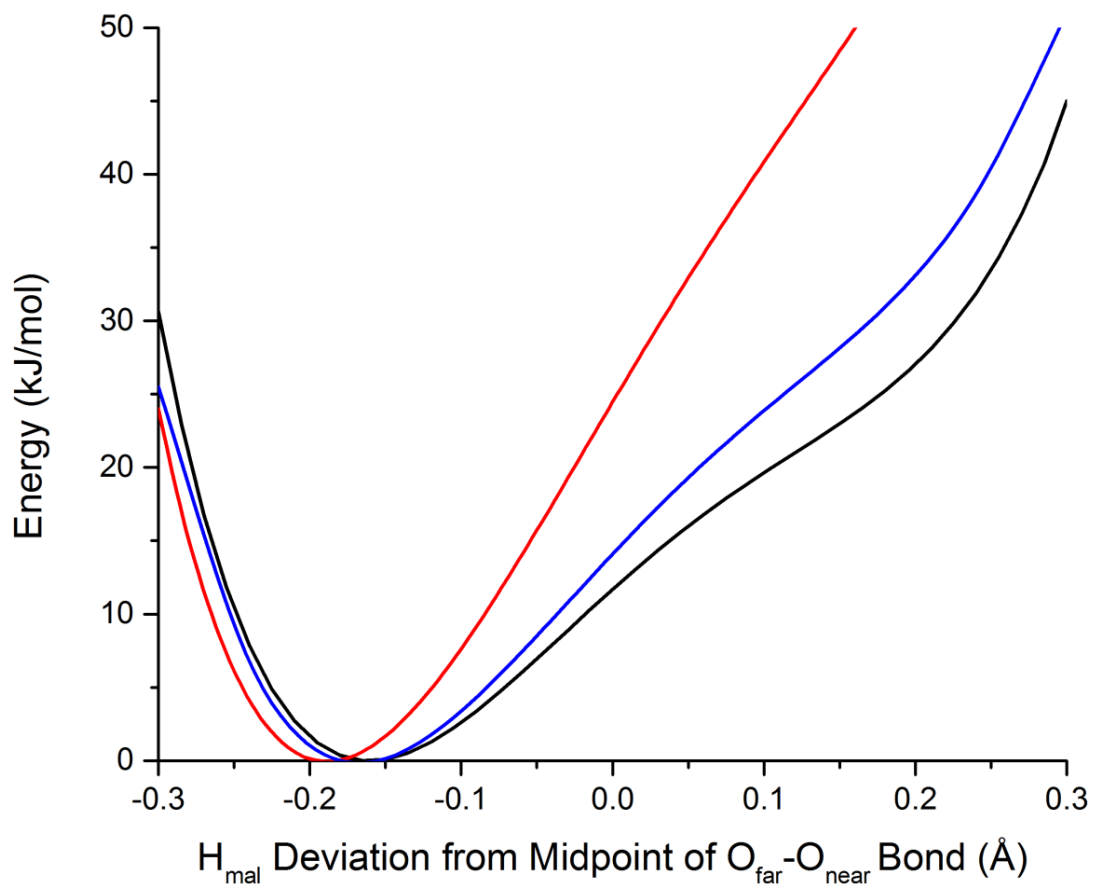
Figure D-12. H$_{mal}$ potential of ZnMT (black), ZnMT without water$_b$ (blue), and ZnMT without water$_a$ (red).

D.4 References

1. Gupta, M. P.; Mahanta, B., Tetraaquabis(Hydrogenmaleato)Manganese(II), [Mn(C$_4$H$_3$O$_4$)$_2$(H$_2$O)$_4$]. *Cryst. Struct. Commun.* **1978**, *7*, 179-82.

2. Sequeira, A.; Rajagopal, H.; Gupta, M. P.; Vanhouteghem, F.; Lenstra, A. T. H.; Geise, H. J., Tetraaquabis(Hydrogen Maleato)Zinc(II) by Neutron Diffraction and Tetraaquabis(Hydrogen Maleato)Nickel(II) by High-Order X-Ray Diffraction. *Acta Crystallogr., Sect. C: Cryst. Struct. Commun.* **1992**, *48*, 1192-1197.

3. Lis, T., Structure of Manganese(II) Maleate Trihydrate, [Mn(C$_4$H$_2$O$_4$)].3H2O (I), and Reinvestigation of the Structure of Manganese(II) Hydrogen Maleate Tetrahydrate, [Mn(C$_4$H$_3$O$_4$)$_2$].4H$_2$O (II). *Acta Crystallogr., Sect. C: Cryst. Struct. Commun.* **1983**, *39*, 39-41.

4. Barman, R. K.; Chakrabarty, R.; Das, B. K., Structure and Properties of Tetraaquabis(Hydrogenmaleato)Iron(II). *Polyhedron* **2002**, *21*, 1189-1195.

5. Gupta, M. P.; Geise, H. J.; Lenstra, A. T. H., Tetraaquabis(Hydrogen Maleato)Nickel(II), [Ni(C4H3O4)2(H2O)4]. *Acta Crystallogr., Sect. C: Cryst. Struct. Commun.* **1984**, *40*, 1152-1154.

6. Porollo, N. P.; Aliev, Z. G.; Dzhardimalieva, G. I.; Ivleva, I. N.; Uflyand, I. E.; Pomogailo, A. D.; Ovanesyan, N. S., Synthesis and Reactivity of Metal-Containing Monomers. *Russ. Chem. Bull.* **1997**, *46*, 362-370.

7. Eftekhari-Bafrooei, A.; Borguet, E., Effect of Hydrogen-Bond Strength on the Vibrational Relaxation of Interfacial Water. *J. Am. Chem. Soc.* **2010**, *132*, 3756-3761.

8. Mulliken, R. S., Electronic Population Analysis on Lcao–Mo Molecular Wave Functions. I. *J. Chem. Phys.* **1955**, *23*, 1833-1840.

9.   Csizmadia, I. G., Theory and Practice of Mo Calculations on Organic Molecules. . *Int. J. Quantum Chem* **1978**, *13*, 159-159.

10.   Baerends, E. J.; Ellis, D. E.; Ros, P., A Theoretical Study of the Interaction of Ethylene with Transition Metal Complexes. *Theoret. Chim. Acta* **1972**, *27*, 339-354.

11.   Hillier, I. H.; Saunders, V. R., Ab Initio Molecular Orbital Calculations of Transition Metal Complexes. *Mol. Phys.* **1971**, *22*, 1025-1034.

D.7 Experimental CIF Files

data_MnMT

_audit_creation_method   SHELXL-2014/6

_chemical_name_systematic   ?

_chemical_name_common   ?

_chemical_melting_point   ?

_chemical_formula_moiety   ?

_chemical_formula_sum

 'C8 H14 Mn O12'

_chemical_formula_weight   357.13

loop_

 _atom_type_symbol

 _atom_type_description

 _atom_type_scat_dispersion_real

 _atom_type_scat_dispersion_imag

 _atom_type_scat_source

 'C' 'C'   0.0033   0.0016

 'International Tables Vol C Tables 4.2.6.8 and 6.1.1.4'

 'H' 'H'   0.0000   0.0000

 'International Tables Vol C Tables 4.2.6.8 and 6.1.1.4'

 'O' 'O'   0.0106   0.0060

 'International Tables Vol C Tables 4.2.6.8 and 6.1.1.4'

'Mn' 'Mn'   0.3368   0.7283

'International Tables Vol C Tables 4.2.6.8 and 6.1.1.4'

_space_group_crystal_system   triclinic

_space_group_IT_number   2

_space_group_name_H-M_alt   'P -1'

_space_group_name_Hall   '-P 1'

_shelx_space_group_comment

;

The symmetry employed for this shelxl refinement is uniquely defined

by the following loop, which should always be used as a source of

symmetry information in preference to the above space-group names.

They are only intended as comments.

;

loop_

 _space_group_symop_operation_xyz

'x, y, z'

'-x, -y, -z'

_cell_length_a   5.2823(2)

_cell_length_b   7.3398(3)

_cell_length_c   9.3651(3)

_cell_angle_alpha   109.765(2)

_cell_angle_beta   *105.152(2)*

_cell_angle_gamma   *92.454(2)*

_cell_volume   *326.37(2)*

_cell_formula_units_Z   *1*

_cell_measurement_temperature   *90(2)*

_cell_measurement_reflns_used   *?*

_cell_measurement_theta_min   *?*

_cell_measurement_theta_max   *?*

_exptl_crystal_description   *Block*

_exptl_crystal_colour   *colorless*

_exptl_crystal_density_meas   *?*

_exptl_crystal_density_method   *?*

_exptl_crystal_density_diffrn   *1.817*

_exptl_crystal_F_000   *183*

_exptl_transmission_factor_min   *0.6799*

_exptl_transmission_factor_max   *0.7504*

_exptl_crystal_size_max   *0.20*

_exptl_crystal_size_mid   *0.18*

_exptl_crystal_size_min   *0.07*

_exptl_absorpt_coefficient_mu   *1.076*

_shelx_estimated_absorpt_T_min   *?*

_shelx_estimated_absorpt_T_max   *?*

_exptl_absorpt_correction_type   *multi-scan*

_exptl_absorpt_process_details   *'SADABS V2012/1 (Bruker AXS Inc.)'*

_diffrn_ambient_temperature   90(2)

_diffrn_radiation_wavelength   0.71073

_diffrn_radiation_type   MoK\a

_diffrn_radiation_source   'fine-focus sealed tube'

_diffrn_radiation_monochromator   graphite

_diffrn_measurement_device_type   'Bruker APEX-II CCD'

_diffrn_measurement_method   '\f and \w scans'

_diffrn_detector_area_resol_mean ?

_diffrn_reflns_number   14510

_diffrn_reflns_av_unetI/netI   0.0105

_diffrn_reflns_av_R_equivalents   0.0276

_diffrn_reflns_limit_h_min   -6

_diffrn_reflns_limit_h_max   6

_diffrn_reflns_limit_k_min   -8

_diffrn_reflns_limit_k_max   8

_diffrn_reflns_limit_l_min   -10

_diffrn_reflns_limit_l_max   10

_diffrn_reflns_theta_min   2.417

_diffrn_reflns_theta_max   24.407

_diffrn_reflns_theta_full   25.242

_diffrn_measured_fraction_theta_max   1.000

_diffrn_measured_fraction_theta_full 0.909

_diffrn_reflns_Laue_measured_fraction_max   1.000

_diffrn_reflns_Laue_measured_fraction_full 0.909

_diffrn_reflns_point_group_measured_fraction_max 1.000

_diffrn_reflns_point_group_measured_fraction_full 0.909

_reflns_number_total   1075

_reflns_number_gt   1012

_reflns_threshold_expression   'I > 2\s(I)'

_reflns_Friedel_coverage   0.000

_reflns_Friedel_fraction_max   .

_reflns_Friedel_fraction_full   .

_reflns_special_details
;
Reflections were merged by SHELXL according to the crystal

class for the calculation of statistics and refinement.

_reflns_Friedel_fraction is defined as the number of unique

Friedel pairs measured divided by the number that would be

possible theoretically, ignoring centric projections and

systematic absences.
;

_computing_data_collection   'Bruker APEX2 (Bruker, 2011)'

_computing_cell_refinement   'SAINT V8.30C (Bruker AXS Inc., 2013)'

_computing_data_reduction   'SAINT V8.30C (Bruker AXS Inc., 2013)'

_computing_structure_solution   'SHELXL-2013 (Sheldrick, 2013)'

_computing_structure_refinement   'SHELXL-2013 (Sheldrick, 2013)'

_computing_molecular_graphics   'CrystalMaker (Palmer, 2010)'

_computing_publication_material   'Bruker SHELXTL (Bruker, 2011)'

_refine_special_details   ?

_refine_ls_structure_factor_coef Fsqd

_refine_ls_matrix_type   full

_refine_ls_weighting_scheme   calc

_refine_ls_weighting_details

'w=1/[\s^2^(Fo^2^)+(0.0188P)^2^+0.1699P] where P=(Fo^2^+2Fc^2^)/3'

_atom_sites_solution_primary   ?

_atom_sites_solution_secondary   ?

_atom_sites_solution_hydrogens   difmap

_refine_ls_hydrogen_treatment   refall

_refine_ls_extinction_method   none

_refine_ls_extinction_coef   .

_refine_ls_number_reflns   1075

_refine_ls_number_parameters   125

_refine_ls_number_restraints   0

_refine_ls_R_factor_all   0.0185

_refine_ls_R_factor_gt   0.0166

_refine_ls_wR_factor_ref   0.0421

_refine_ls_wR_factor_gt   0.0411

_refine_ls_goodness_of_fit_ref   1.067

_refine_ls_restrained_S_all   1.067

_refine_ls_shift/su_max   0.000

_refine_ls_shift/su_mean   0.000

loop_

_atom_site_label

_atom_site_type_symbol

_atom_site_fract_x

_atom_site_fract_y

_atom_site_fract_z

_atom_site_U_iso_or_equiv

_atom_site_adp_type

_atom_site_occupancy

_atom_site_site_symmetry_order

_atom_site_calc_flag

_atom_site_refinement_flags_posn

_atom_site_refinement_flags_adp

_atom_site_refinement_flags_occupancy

_atom_site_disorder_assembly

_atom_site_disorder_group

Mn01 Mn 0.5000 0.5000 1.0000 0.01275(11) Uani 1 2 d S . P . .

O002 O 0.8269(2) 0.36186(17) 1.10178(13) 0.0163(2) Uani 1 1 d . . . . .

O003 O 0.65084(19) 0.44009(14) 0.79083(11) 0.0166(2) Uani 1 1 d . . . . .

O004 O 0.7460(2) 0.77361(16) 1.07949(15) 0.0191(2) Uani 1 1 d . . . . .

O005 O 0.1621(2) 0.04001(16) 0.33326(12) 0.0227(3) Uani 1 1 d . . . . .

O006 O 0.2898(2) 0.02409(15) 0.12344(12) 0.0208(2) Uani 1 1 d . . . . .

O007 O 0.3051(2) 0.23071(16) 0.61467(12) 0.0216(3) Uani 1 1 d . . . . .

C008 C 0.3298(3) 0.0885(2) 0.26845(17) 0.0152(3) Uani 1 1 d . . . . .

C009 C 0.5811(3) 0.2222(2) 0.37068(17) 0.0165(3) Uani 1 1 d . . . . .

C00A C 0.6666(3) 0.3181(2) 0.52747(17) 0.0162(3) Uani 1 1 d . . . . .

C00B C 0.5316(3) 0.3291(2) 0.65127(17) 0.0140(3) Uani 1 1 d . . . . .

H1 H 0.722(4) 0.842(3) 1.027(3) 0.040(6) Uiso 1 1 d . . . . .

H2 H 0.840(4) 0.838(3) 1.164(3) 0.038(6) Uiso 1 1 d . . . . .

H3 H 0.980(4) 0.420(3) 1.130(2) 0.034(5) Uiso 1 1 d . . . . .

H4 H 0.825(4) 0.257(3) 1.041(3) 0.036(6) Uiso 1 1 d . . . . .

H5 H 0.224(5) 0.125(4) 0.470(3) 0.084(9) Uiso 1 1 d . . . . .

H6 H 0.690(3) 0.237(2) 0.313(2) 0.020(4) Uiso 1 1 d . . . . .

H7 H 0.833(4) 0.393(3) 0.570(2) 0.023(4) Uiso 1 1 d . . . . .

loop_

 _atom_site_aniso_label

 _atom_site_aniso_U_11

 _atom_site_aniso_U_22

 _atom_site_aniso_U_33

 _atom_site_aniso_U_23

 _atom_site_aniso_U_13

 _atom_site_aniso_U_12

Mn01 0.01179(16) 0.01409(17) 0.01237(17) 0.00459(13) 0.00408(12) 0.00017(12)

O002 0.0141(6) 0.0159(6) 0.0165(6) 0.0032(5) 0.0042(4) 0.0010(4)

O003 0.0160(5) 0.0189(5) 0.0114(5) 0.0020(4) 0.0034(4) -0.0007(4)

O004 0.0212(6) 0.0187(6) 0.0130(6) 0.0058(5) -0.0006(5) -0.0055(5)

O005 0.0195(6) 0.0292(6) 0.0133(6) 0.0028(5) 0.0030(4) -0.0075(5)

O006 0.0307(6) 0.0176(6) 0.0106(5) 0.0031(4) 0.0037(5) -0.0020(4)

O007 0.0168(5) 0.0303(6) 0.0127(5) 0.0022(5) 0.0049(4) -0.0065(5)

C008 0.0188(7) 0.0128(7) 0.0145(8) 0.0055(6) 0.0044(6) 0.0045(6)

C009 0.0174(7) 0.0179(8) 0.0160(8) 0.0060(6) 0.0081(6) 0.0028(6)

C00A 0.0127(7) 0.0170(8) 0.0168(8) 0.0039(6) 0.0042(6) -0.0010(6)

C00B 0.0143(7) 0.0143(7) 0.0133(7) 0.0052(6) 0.0033(6) 0.0035(6)

_geom_special_details

;

All esds (except the esd in the dihedral angle between two l.s. planes)

are estimated using the full covariance matrix. The cell esds are taken

into account individually in the estimation of esds in distances, angles

and torsion angles; correlations between esds in cell parameters are only

used when they are defined by crystal symmetry. An approximate (isotropic)

treatment of cell esds is used for estimating esds involving l.s. planes.

;

loop_

 _geom_bond_atom_site_label_1

 _geom_bond_atom_site_label_2

 _geom_bond_distance

 _geom_bond_site_symmetry_2

 _geom_bond_publ_flag

Mn01 O004 2.1296(11) . ?

Mn01 O004 2.1296(11) 2_667 ?

Mn01 O002 2.2047(10) 2_667 ?

Mn01 O002 2.2047(10) . ?

Mn01 O003 2.2201(9) 2_667 ?

Mn01 O003 2.2201(9) . ?

O002 H3 0.83(2) . ?

O002 H4 0.79(2) . ?

O003 C00B 1.2548(17) . ?

O004 H1 0.81(2) . ?

O004 H2 0.79(2) . ?

O005 C008 1.2961(18) . ?

O005 H5 1.16(3) . ?

O006 C008 1.2327(17) . ?

O007 C00B 1.2706(18) . ?

O007 H5 1.26(3) . ?

C008 C009 1.494(2) . ?

C009 C00A 1.335(2) . ?

C009 H6 0.913(17) . ?

C00A C00B 1.494(2) . ?

C00A H7 0.929(18) . ?

*loop_*

 _geom_angle_atom_site_label_1

 _geom_angle_atom_site_label_2

 _geom_angle_atom_site_label_3

 _geom_angle

 _geom_angle_site_symmetry_1

 _geom_angle_site_symmetry_3

_geom_angle_publ_flag

O004 Mn01 O004 180.0 . 2_667 ?

O004 Mn01 O002 87.23(5) . 2_667 ?

O004 Mn01 O002 92.77(5) 2_667 2_667 ?

O004 Mn01 O002 92.77(5) . . ?

O004 Mn01 O002 87.23(5) 2_667 . ?

O002 Mn01 O002 180.00(4) 2_667 . ?

O004 Mn01 O003 97.30(4) . 2_667 ?

O004 Mn01 O003 82.70(4) 2_667 2_667 ?

O002 Mn01 O003 87.92(4) 2_667 2_667 ?

O002 Mn01 O003 92.08(4) . 2_667 ?

O004 Mn01 O003 82.70(4) . . ?

O004 Mn01 O003 97.30(4) 2_667 . ?

O002 Mn01 O003 92.08(4) 2_667 . ?

O002 Mn01 O003 87.92(4) . . ?

O003 Mn01 O003 180.0 2_667 . ?

Mn01 O002 H3 117.9(14) . . ?

Mn01 O002 H4 110.2(15) . . ?

H3 O002 H4 107(2) . . ?

C00B O003 Mn01 126.27(9) . . ?

Mn01 O004 H1 119.9(15) . . ?

Mn01 O004 H2 130.7(15) . . ?

H1 O004 H2 108(2) . . ?

C008 O005 H5 111.9(13) . . ?

C00B O007 H5 112.0(12) . . ?

O006 C008 O005 121.63(13) . . ?

O006 C008 C009 118.56(13) . . ?

O005 C008 C009 119.79(13) . . ?

C00A C009 C008 130.64(14) . . ?

C00A C009 H6 117.5(10) . . ?

C008 C009 H6 111.8(10) . . ?

C009 C00A C00B 129.85(14) . . ?

C009 C00A H7 117.8(10) . . ?

C00B C00A H7 112.3(10) . . ?

O003 C00B O007 122.22(12) . . ?

O003 C00B C00A 117.03(12) . . ?

O007 C00B C00A 120.75(13) . . ?

_refine_diff_density_max   0.204

_refine_diff_density_min   -0.188

_refine_diff_density_rms   0.040

#===END

data_FeMT

_audit_creation_method   SHELXL-2014/6

_chemical_name_systematic   ?

_chemical_name_common   ?

_chemical_melting_point   ?

_chemical_formula_moiety   ?

_chemical_formula_sum

 'C8 H14 Fe O12'

_chemical_formula_weight   358.04

loop_

 _atom_type_symbol

 _atom_type_description

 _atom_type_scat_dispersion_real

 _atom_type_scat_dispersion_imag

 _atom_type_scat_source

 'C' 'C'   0.0033   0.0016

 'International Tables Vol C Tables 4.2.6.8 and 6.1.1.4'

 'H' 'H'   0.0000   0.0000

 'International Tables Vol C Tables 4.2.6.8 and 6.1.1.4'

 'O' 'O'   0.0106   0.0060

 'International Tables Vol C Tables 4.2.6.8 and 6.1.1.4'

 'Fe' 'Fe'   0.3463   0.8444

 'International Tables Vol C Tables 4.2.6.8 and 6.1.1.4'

_space_group_crystal_system   triclinic

_space_group_IT_number   2

_space_group_name_H-M_alt   'P -1'

_space_group_name_Hall   '-P 1'

_shelx_space_group_comment

;

The symmetry employed for this shelxl refinement is uniquely defined
by the following loop, which should always be used as a source of
symmetry information in preference to the above space-group names.
They are only intended as comments.

;

loop_
 _space_group_symop_operation_xyz
 'x, y, z'
 '-x, -y, -z'

_cell_length_a   5.2115(2)

_cell_length_b   7.3307(3)

_cell_length_c   9.2529(4)

_cell_angle_alpha   109.019(2)

_cell_angle_beta   105.339(2)

_cell_angle_gamma   92.530(2)

_cell_volume   318.98(2)

_cell_formula_units_Z   1

_cell_measurement_temperature   90(2)

_cell_measurement_reflns_used   ?

_cell_measurement_theta_min   ?

_cell_measurement_theta_max   ?

_exptl_crystal_description   block

_exptl_crystal_colour   yellow

_exptl_crystal_density_meas   ?

_exptl_crystal_density_method   ?

_exptl_crystal_density_diffrn   1.864

_exptl_crystal_F_000   184

_exptl_transmission_factor_min   0.6832

_exptl_transmission_factor_max   0.7479

_exptl_crystal_size_max   0.24

_exptl_crystal_size_mid   0.11

_exptl_crystal_size_min   0.07

_exptl_absorpt_coefficient_mu   1.248

_shelx_estimated_absorpt_T_min   ?

_shelx_estimated_absorpt_T_max   ?

_exptl_absorpt_correction_type   multi-scan

_exptl_absorpt_process_details   'SADABS V2012/1 (Bruker AXS Inc.)'

_exptl_absorpt_special_details   ?

_diffrn_ambient_temperature   90(2)

_diffrn_radiation_wavelength   0.71073

_diffrn_radiation_type   MoK\a

_diffrn_radiation_source   'fine-focus sealed tube'

_diffrn_radiation_monochromator graphite

_diffrn_measurement_device_type 'Bruker APEX-II CCD'

_diffrn_measurement_method   '\f and \w scans'

_diffrn_detector_area_resol_mean ?

_diffrn_reflns_number   30234

_diffrn_reflns_av_unetI/netI   0.0345

_diffrn_reflns_av_R_equivalents   0.0536

_diffrn_reflns_limit_h_min   -9

_diffrn_reflns_limit_h_max   9

_diffrn_reflns_limit_k_min   -13

_diffrn_reflns_limit_k_max   13

_diffrn_reflns_limit_l_min   -16

_diffrn_reflns_limit_l_max   16

_diffrn_reflns_theta_min   2.437

_diffrn_reflns_theta_max   40.022

_diffrn_reflns_theta_full   25.242

_diffrn_measured_fraction_theta_max   0.985

_diffrn_measured_fraction_theta_full 1.000

_diffrn_reflns_Laue_measured_fraction_max   0.985

_diffrn_reflns_Laue_measured_fraction_full   1.000

_diffrn_reflns_point_group_measured_fraction_max   0.985

_diffrn_reflns_point_group_measured_fraction_full 1.000

_reflns_number_total   3913

_reflns_number_gt   3357

_reflns_threshold_expression   'I > 2\s(I)'

_reflns_Friedel_coverage   0.000

_reflns_Friedel_fraction_max   .

_reflns_Friedel_fraction_full   .

_reflns_special_details

;

Reflections were merged by SHELXL according to the crystal

class for the calculation of statistics and refinement.

_reflns_Friedel_fraction is defined as the number of unique

Friedel pairs measured divided by the number that would be

possible theoretically, ignoring centric projections and

systematic absences.

;

_computing_data_collection   'Bruker APEX2 (Bruker, 2011)'

_computing_cell_refinement   'SAINT V8.30C (Bruker AXS Inc., 2013)'

_computing_data_reduction   'SAINT V8.30C (Bruker AXS Inc., 2013)'

_computing_structure_solution   'SHELXL-2013 (Sheldrick, 2013)'

_computing_structure_refinement   'SHELXL-2013 (Sheldrick, 2013)'

_computing_molecular_graphics   'CrystalMaker (Palmer, 2010)'

_computing_publication_material   'Bruker SHELXTL (Bruker, 2011)'

_refine_special_details   ?

_refine_ls_structure_factor_coef Fsqd

_refine_ls_matrix_type   full

_refine_ls_weighting_scheme   calc

_refine_ls_weighting_details

'w=1/[\s^2^(Fo^2^)+(0.0356P)^2^+0.0682P] where P=(Fo^2^+2Fc^2^)/3'

_atom_sites_solution_primary   ?

_atom_sites_solution_secondary   ?

_atom_sites_solution_hydrogens   difmap

_refine_ls_hydrogen_treatment   refall

_refine_ls_extinction_method   none

_refine_ls_extinction_coef   .

_refine_ls_number_reflns   3913

_refine_ls_number_parameters   125

_refine_ls_number_restraints   0

_refine_ls_R_factor_all   0.0494

_refine_ls_R_factor_gt   0.0374

_refine_ls_wR_factor_ref   0.0757

_refine_ls_wR_factor_gt   0.0715

_refine_ls_goodness_of_fit_ref   1.089

_refine_ls_restrained_S_all   1.089

_refine_ls_shift/su_max   0.000

_refine_ls_shift/su_mean   0.000

loop_

 _atom_site_label

 _atom_site_type_symbol

 _atom_site_fract_x

 _atom_site_fract_y

 _atom_site_fract_z

 _atom_site_U_iso_or_equiv

_atom_site_adp_type

_atom_site_occupancy

_atom_site_site_symmetry_order

_atom_site_calc_flag

_atom_site_refinement_flags_posn

_atom_site_refinement_flags_adp

_atom_site_refinement_flags_occupancy

_atom_site_disorder_assembly

_atom_site_disorder_group

Fe01 Fe 0.5000 0.5000 0.0000 0.00855(5) Uani 1 2 d S . P . .

O002 O 0.17720(13) 0.63679(10) -0.09859(8) 0.01160(11) Uani 1 1 d . . . . .

O003 O 0.74629(15) 0.76480(11) 0.07585(9) 0.01329(12) Uani 1 1 d . . . . .

O004 O 0.35109(13) 0.56021(10) 0.20507(8) 0.01203(11) Uani 1 1 d . . . . .

O005 O 0.83957(15) 0.96188(12) 0.66623(9) 0.01745(14) Uani 1 1 d . . . . .

O006 O 0.69823(14) 0.77287(12) 0.38291(9) 0.01694(14) Uani 1 1 d . . . . .

O007 O 0.70346(16) 0.97873(11) 0.87655(8) 0.01576(13) Uani 1 1 d . . . . .

C008 C 0.66828(18) 0.91217(13) 0.73082(10) 0.01099(13) Uani 1 1 d . . . . .

C009 C 0.47135(17) 0.67211(13) 0.34583(10) 0.01005(13) Uani 1 1 d . . . . .

C00A C 0.33286(18) 0.67884(14) 0.46937(11) 0.01230(14) Uani 1 1 d . . . . .

C00B C 0.41687(18) 0.77514(13) 0.62823(11) 0.01232(14) Uani 1 1 d . . . . .

H1 H 0.833(4) 0.827(3) 0.162(3) 0.041(6) Uiso 1 1 d . . . . .

H2 H 0.719(4) 0.835(3) 0.023(2) 0.025(4) Uiso 1 1 d . . . . .

H3 H 0.179(4) 0.742(3) -0.038(2) 0.031(5) Uiso 1 1 d . . . . .

H4 H 0.028(4) 0.582(3) -0.125(2) 0.027(4) Uiso 1 1 d . . . . .

H5 H 0.165(4) 0.597(3) 0.427(2) 0.024(4) Uiso 1 1 d . . . . .

H6 H 0.305(3) 0.761(2) 0.6885(18) 0.014(3) Uiso 1 1 d . . . . .

H7 H 0.778(6) 0.893(4) 0.547(4) 0.077(9) Uiso 1 1 d . . . . .

*loop_*

 _atom_site_aniso_label

 _atom_site_aniso_U_11

 _atom_site_aniso_U_22

 _atom_site_aniso_U_33

 _atom_site_aniso_U_23

 _atom_site_aniso_U_13

 _atom_site_aniso_U_12

Fe01 0.00718(7) 0.01020(8) 0.00823(8) 0.00267(6) 0.00299(5) 0.00089(5)

O002 0.0091(2) 0.0122(3) 0.0122(3) 0.0028(2) 0.0029(2) 0.0011(2)

O003 0.0144(3) 0.0128(3) 0.0099(3) 0.0035(2) 0.0006(2) -0.0033(2)

O004 0.0106(2) 0.0148(3) 0.0081(3) 0.0011(2) 0.0025(2) -0.0004(2)

O005 0.0143(3) 0.0234(4) 0.0094(3) 0.0009(3) 0.0026(2) -0.0066(3)

O006 0.0120(3) 0.0246(4) 0.0098(3) 0.0009(3) 0.0037(2) -0.0061(2)

O007 0.0230(3) 0.0140(3) 0.0081(3) 0.0021(2) 0.0039(2) -0.0007(2)

C008 0.0130(3) 0.0107(3) 0.0087(3) 0.0031(3) 0.0026(3) 0.0019(3)

C009 0.0094(3) 0.0118(3) 0.0087(3) 0.0029(3) 0.0031(2) 0.0017(3)

C00A 0.0098(3) 0.0156(4) 0.0101(3) 0.0024(3) 0.0037(3) -0.0005(3)

C00B 0.0125(3) 0.0142(4) 0.0098(3) 0.0026(3) 0.0048(3) 0.0006(3)

_geom_special_details

;

All esds (except the esd in the dihedral angle between two l.s. planes)

are estimated using the full covariance matrix. The cell esds are taken

into account individually in the estimation of esds in distances, angles

and torsion angles; correlations between esds in cell parameters are only

used when they are defined by crystal symmetry. An approximate (isotropic)

treatment of cell esds is used for estimating esds involving l.s. planes.

;

*loop_*

_geom_bond_atom_site_label_1

_geom_bond_atom_site_label_2

_geom_bond_distance

_geom_bond_site_symmetry_2

_geom_bond_publ_flag

Fe01 O003 2.0793(7) . ?

Fe01 O003 2.0793(7) 2_665 ?

Fe01 O002 2.1450(7) . ?

Fe01 O002 2.1450(7) 2_665 ?

Fe01 O004 2.1589(7) 2_665 ?

Fe01 O004 2.1590(6) . ?

O002 H3 0.79(2) . ?

O002 H4 0.797(19) . ?

O003 H1 0.78(2) . ?

O003 H2 0.805(19) . ?

O004 C009 1.2603(11) . ?

O005 C008 1.2970(11) . ?

O005 H7 1.01(3) . ?

O006 C009 1.2667(11) . ?

O006 H7 1.42(3) . ?

O007 C008 1.2339(11) . ?

C008 C00B 1.4937(13) . ?

C009 C00A 1.4943(12) . ?

C00A C00B 1.3441(13) . ?

C00A H5 0.947(18) . ?

C00B H6 0.931(16) . ?

loop_

 _geom_angle_atom_site_label_1

 _geom_angle_atom_site_label_2

 _geom_angle_atom_site_label_3

 _geom_angle

 _geom_angle_site_symmetry_1

 _geom_angle_site_symmetry_3

 _geom_angle_publ_flag

O003 Fe01 O003 180.0 . 2_665 ?

O003 Fe01 O002 87.38(3) . . ?

O003 Fe01 O002 92.62(3) 2_665 . ?

O003 Fe01 O002 92.62(3) . 2_665 ?

O003 Fe01 O002 87.38(3) 2_665 2_665 ?

O002 Fe01 O002 180.0 . 2_665 ?

O003 Fe01 O004 82.74(3) . 2_665 ?

O003 Fe01 O004 97.26(3) 2_665 2_665 ?

O002 Fe01 O004 93.13(3) . 2_665 ?

O002 Fe01 O004 86.87(3) 2_665 2_665 ?

O003 Fe01 O004 97.26(3) . . ?

O003 Fe01 O004 82.74(3) 2_665 . ?

O002 Fe01 O004 86.87(3) . . ?

O002 Fe01 O004 93.13(3) 2_665 . ?

O004 Fe01 O004 180.0 2_665 . ?

Fe01 O002 H3 110.6(14) . . ?

Fe01 O002 H4 118.0(13) . . ?

H3 O002 H4 106.3(19) . . ?

Fe01 O003 H1 127.8(16) . . ?

Fe01 O003 H2 119.8(13) . . ?

H1 O003 H2 109(2) . . ?

C009 O004 Fe01 126.57(6) . . ?

C008 O005 H7 110.6(17) . . ?

C009 O006 H7 110.5(12) . . ?

O007 C008 O005 121.71(9) . . ?

O007 C008 C00B 118.10(8) . . ?

O005 C008 C00B 120.17(8) . . ?

O004 C009 O006 122.64(8) . . ?

O004 C009 C00A 116.30(8) . . ?

O006 C009 C00A 121.06(8) . . ?

C00B C00A C009 129.67(8) . . ?

C00B C00A H5 117.1(11) . . ?

C009 C00A H5 113.2(11) . . ?

C00A C00B C008 130.31(8) . . ?

C00A C00B H6 118.4(10) . . ?

C008 C00B H6 111.3(9) . . ?

_refine_diff_density_max   1.178

_refine_diff_density_min   -0.446

_refine_diff_density_rms   0.103

#===END

data_CoMT

_audit_creation_method   SHELXL-2014/6

_chemical_name_systematic   ?

_chemical_name_common   ?

_chemical_melting_point   ?

_chemical_formula_moiety   ?

_chemical_formula_sum

'C8 H14 Co O12'

_chemical_formula_weight   361.12

loop_

_atom_type_symbol

_atom_type_description

_atom_type_scat_dispersion_real

_atom_type_scat_dispersion_imag

_atom_type_scat_source

'C' 'C'   0.0033   0.0016

'International Tables Vol C Tables 4.2.6.8 and 6.1.1.4'

'H' 'H'   0.0000   0.0000

'International Tables Vol C Tables 4.2.6.8 and 6.1.1.4'

'Co' 'Co'   0.3494   0.9721

'International Tables Vol C Tables 4.2.6.8 and 6.1.1.4'

'O' 'O'   0.0106   0.0060

'International Tables Vol C Tables 4.2.6.8 and 6.1.1.4'

_space_group_crystal_system   triclinic

_space_group_IT_number   2

_space_group_name_H-M_alt   'P -1'

_space_group_name_Hall   '-P 1'

_shelx_space_group_comment

;

The symmetry employed for this shelxl refinement is uniquely defined

by the following loop, which should always be used as a source of

symmetry information in preference to the above space-group names.

They are only intended as comments.

;

loop_

 _space_group_symop_operation_xyz

 'x, y, z'

 '-x, -y, -z'

_cell_length_a   5.1742(3)

_cell_length_b   7.2742(4)

_cell_length_c   9.2053(5)

_cell_angle_alpha   108.809(2)

_cell_angle_beta   105.003(2)

_cell_angle_gamma   92.409(3)

_cell_volume   313.79(3)

_cell_formula_units_Z   1

_cell_measurement_temperature   90(2)

_cell_measurement_reflns_used   ?

_cell_measurement_theta_min   ?

_cell_measurement_theta_max   ?

_exptl_crystal_description   block

_exptl_crystal_colour   pink

_exptl_crystal_density_meas   ?

_exptl_crystal_density_method   ?

_exptl_crystal_density_diffrn   1.911

_exptl_crystal_F_000   185

_exptl_transmission_factor_min   0.6994

_exptl_transmission_factor_max   0.7476

_exptl_crystal_size_max   0.24

_exptl_crystal_size_mid   0.16

_exptl_crystal_size_min   0.09

_exptl_absorpt_coefficient_mu   1.434

_shelx_estimated_absorpt_T_min   ?

_shelx_estimated_absorpt_T_max   ?

_exptl_absorpt_correction_type   multi-scan

_exptl_absorpt_process_details   'SADABS V2012/1 (Bruker AXS Inc.)'

_diffrn_ambient_temperature   90(2)

_diffrn_radiation_wavelength   0.71073

_diffrn_radiation_type   MoK\a

_diffrn_radiation_source   'fine-focus sealed tube'

_diffrn_radiation_monochromator   graphite

_diffrn_measurement_device_type   'Bruker APEX-II CCD'

_diffrn_measurement_method   '\f and \w scans'

_diffrn_detector_area_resol_mean ?

_diffrn_reflns_number   55628

_diffrn_reflns_av_unetI/netI   0.0257

_diffrn_reflns_av_R_equivalents 0.0551

_diffrn_reflns_limit_h_min   -10

_diffrn_reflns_limit_h_max   10

_diffrn_reflns_limit_k_min   -14

_diffrn_reflns_limit_k_max   14

_diffrn_reflns_limit_l_min   -18

_diffrn_reflns_limit_l_max   18

_diffrn_reflns_theta_min   2.441

_diffrn_reflns_theta_max   46.633

_diffrn_reflns_theta_full   25.242

_diffrn_measured_fraction_theta_max   0.983

_diffrn_measured_fraction_theta_full 1.000

_diffrn_reflns_Laue_measured_fraction_max   0.983

_diffrn_reflns_Laue_measured_fraction_full   1.000

_diffrn_reflns_point_group_measured_fraction_max   0.983

_diffrn_reflns_point_group_measured_fraction_full 1.000

_reflns_number_total   5537

_reflns_number_gt   4888

_reflns_threshold_expression   'I > 2\s(I)'

_reflns_Friedel_coverage   0.000

_reflns_Friedel_fraction_max   .

_reflns_Friedel_fraction_full   .

_reflns_special_details

;

Reflections were merged by SHELXL according to the crystal

class for the calculation of statistics and refinement.

_reflns_Friedel_fraction is defined as the number of unique

Friedel pairs measured divided by the number that would be

possible theoretically, ignoring centric projections and

systematic absences.

;

_computing_data_collection   *'Bruker APEX2 (Bruker, 2011)'*

_computing_cell_refinement   *'SAINT V8.30C (Bruker AXS Inc., 2013)'*

_computing_data_reduction   *'SAINT V8.30C (Bruker AXS Inc., 2013)'*

_computing_structure_solution   *'SHELXL-2013 (Sheldrick, 2013)'*

_computing_structure_refinement   *'SHELXL-2013 (Sheldrick, 2013)'*

_computing_molecular_graphics   *'CrystalMaker (Palmer, 2010)'*

_computing_publication_material   *'Bruker SHELXTL (Bruker, 2011)'*

_refine_special_details   *?*

_refine_ls_structure_factor_coef Fsqd

_refine_ls_matrix_type   *full*

_refine_ls_weighting_scheme   *calc*

_refine_ls_weighting_details

'w=1/[\s^2^(Fo^2^)+(0.0271P)^2^+0.0398P] where P=(Fo^2^+2Fc^2^)/3'

_atom_sites_solution_primary   *?*

_atom_sites_solution_secondary   *?*

_atom_sites_solution_hydrogens   *difmap*

_refine_ls_hydrogen_treatment   *refall*

_refine_ls_extinction_method   *none*

_refine_ls_extinction_coef   *.*

_refine_ls_number_reflns   *5537*

_refine_ls_number_parameters   125

_refine_ls_number_restraints   0

_refine_ls_R_factor_all   0.0362

_refine_ls_R_factor_gt   0.0269

_refine_ls_wR_factor_ref   0.0597

_refine_ls_wR_factor_gt   0.0565

_refine_ls_goodness_of_fit_ref   1.069

_refine_ls_restrained_S_all   1.069

_refine_ls_shift/su_max   0.000

_refine_ls_shift/su_mean   0.000

*loop_*

_atom_site_label

_atom_site_type_symbol

_atom_site_fract_x

_atom_site_fract_y

_atom_site_fract_z

_atom_site_U_iso_or_equiv

_atom_site_adp_type

_atom_site_occupancy

_atom_site_site_symmetry_order

_atom_site_calc_flag

_atom_site_refinement_flags_posn

_atom_site_refinement_flags_adp

_atom_site_refinement_flags_occupancy

_atom_site_disorder_assembly

_atom_site_disorder_group

Co01 Co 0.5000 0.5000 1.0000 0.00851(2) Uani 1 2 d S . P . .

O002 O 0.17818(9) 0.63439(6) 0.89772(5) 0.01171(6) Uani 1 1 d . . . . .

O003 O 0.74730(9) 0.75861(6) 1.07512(5) 0.01276(7) Uani 1 1 d . . . . .

O004 O 0.64212(9) 0.43911(6) 0.79495(5) 0.01186(6) Uani 1 1 d . . . . .

O005 O 0.15729(10) 0.03710(8) 0.33240(6) 0.01689(8) Uani 1 1 d . . . . .

O006 O 0.29579(10) 0.22438(8) 0.61678(6) 0.01641(8) Uani 1 1 d . . . . .

O007 O 0.29912(11) 0.02123(7) 0.12209(5) 0.01560(7) Uani 1 1 d . . . . .

C008 C 0.33166(11) 0.08760(8) 0.26820(6) 0.01109(7) Uani 1 1 d . . . . .

C009 C 0.52345(10) 0.32694(8) 0.65430(6) 0.01001(7) Uani 1 1 d . . . . .

C00A C 0.66460(11) 0.32137(8) 0.53052(7) 0.01183(8) Uani 1 1 d . . . . .

C00B C 0.58296(11) 0.22520(8) 0.37125(6) 0.01212(8) Uani 1 1 d . . . . .

H1 H 0.177(3) 0.737(2) 0.9600(19) 0.030(3) Uiso 1 1 d . . . . .

H2 H 0.029(3) 0.579(2) 0.8753(17) 0.025(3) Uiso 1 1 d . . . . .

H3 H 0.824(4) 0.818(3) 1.164(2) 0.042(4) Uiso 1 1 d . . . . .

H4 H 0.717(3) 0.831(2) 1.0243(19) 0.033(4) Uiso 1 1 d . . . . .

H5 H 0.833(3) 0.404(2) 0.5742(17) 0.026(3) Uiso 1 1 d . . . . .

H6 H 0.700(3) 0.2441(18) 0.3128(15) 0.017(3) Uiso 1 1 d . . . . .

H7 H 0.215(5) 0.111(3) 0.456(3) 0.076(7) Uiso 1 1 d . . . . .

loop_

_atom_site_aniso_label

_atom_site_aniso_U_11

_atom_site_aniso_U_22

_atom_site_aniso_U_33

_atom_site_aniso_U_23

_atom_site_aniso_U_13

_atom_site_aniso_U_12

Co01 0.00807(4) 0.00976(4) 0.00734(4) 0.00235(3) 0.00260(3) 0.00003(3)

O002 0.01028(14) 0.01220(15) 0.01177(15) 0.00290(12) 0.00331(12) 0.00109(11)

O003 0.01426(16) 0.01215(15) 0.00934(14) 0.00268(12) 0.00117(12) -0.00278(12)

O004 0.01138(15) 0.01399(15) 0.00805(13) 0.00119(11) 0.00290(11) -0.00070(12)

O005 0.01445(17) 0.0222(2) 0.00945(15) 0.00096(14) 0.00298(13) -0.00620(14)

O006 0.01267(16) 0.0228(2) 0.00985(15) 0.00105(14) 0.00398(13) -0.00614(14)

O007 0.0227(2) 0.01393(16) 0.00796(14) 0.00188(12) 0.00369(14) -0.00126(14)

C008 0.01314(18) 0.01080(17) 0.00855(16) 0.00268(14) 0.00275(14) 0.00108(14)

C009 0.00956(17) 0.01157(17) 0.00830(16) 0.00255(13) 0.00279(13) 0.00077(13)

C00A 0.01036(17) 0.01436(19) 0.00950(17) 0.00199(14) 0.00383(14) -0.00080(14)

C00B 0.01251(18) 0.01388(19) 0.00945(17) 0.00243(15) 0.00462(15) -0.00006(15)

_geom_special_details

;

All esds (except the esd in the dihedral angle between two l.s. planes)

are estimated using the full covariance matrix. The cell esds are taken

into account individually in the estimation of esds in distances, angles

and torsion angles; correlations between esds in cell parameters are only

used when they are defined by crystal symmetry. An approximate (isotropic)

treatment of cell esds is used for estimating esds involving l.s. planes.

;

*loop_*

_geom_bond_atom_site_label_1

_geom_bond_atom_site_label_2

_geom_bond_distance

_geom_bond_site_symmetry_2

_geom_bond_publ_flag

Co01 O003 2.0384(4) . ?

Co01 O003 2.0384(4) 2_667 ?

Co01 O004 2.1229(4) . ?

Co01 O004 2.1229(4) 2_667 ?

Co01 O002 2.1292(4) . ?

Co01 O002 2.1292(4) 2_667 ?

O002 H1 0.780(16) . ?

O002 H2 0.798(15) . ?

O003 H3 0.775(18) . ?

O003 H4 0.807(16) . ?

O004 C009 1.2587(7) . ?

O005 C008 1.2986(7) . ?

O005 H7 1.05(2) . ?

O006 C009 1.2699(7) . ?

O006 H7 1.38(2) . ?

O007 C008 1.2359(7) . ?

C008 C00B 1.4941(8) . ?

C009 C00A 1.4956(7) . ?

C00A C00B 1.3456(8) . ?

C00A H5 0.950(15) . ?

C00B H6 0.942(13) . ?

loop_

 _geom_angle_atom_site_label_1

 _geom_angle_atom_site_label_2

 _geom_angle_atom_site_label_3

 _geom_angle

 _geom_angle_site_symmetry_1

 _geom_angle_site_symmetry_3

 _geom_angle_publ_flag

O003 Co01 O003 180.0 . 2_667 ?

O003 Co01 O004 83.294(18) . . ?

O003 Co01 O004 96.707(18) 2_667 . ?

O003 Co01 O004 96.706(18) . 2_667 ?

O003 Co01 O004 83.294(18) 2_667 2_667 ?

O004 Co01 O004 180.000(10) . 2_667 ?

O003 Co01 O002 88.688(19) . . ?

O003 Co01 O002 91.312(19) 2_667 . ?

O004 Co01 O002 91.464(18) . . ?

O004 Co01 O002 88.536(17) 2_667 . ?

O003 Co01 O002 91.311(19) . 2_667 ?

O003 Co01 O002 88.688(19) 2_667 2_667 ?

O004 Co01 O002 88.536(17) . 2_667 ?

O004 Co01 O002 91.464(18) 2_667 2_667 ?

O002 Co01 O002 180.0 . 2_667 ?

Co01 O002 H1 108.9(12) . . ?

Co01 O002 H2 116.2(10) . . ?

H1 O002 H2 104.2(15) . . ?

Co01 O003 H3 124.5(13) . . ?

Co01 O003 H4 119.2(11) . . ?

H3 O003 H4 110.2(16) . . ?

C009 O004 Co01 127.66(4) . . ?

C008 O005 H7 110.9(13) . . ?

C009 O006 H7 111.0(10) . . ?

O007 C008 O005 121.65(5) . . ?

O007 C008 C00B 118.06(5) . . ?

O005 C008 C00B 120.27(5) . . ?

O004 C009 O006 122.87(5) . . ?

O004 C009 C00A 116.19(5) . . ?

O006 C009 C00A 120.94(5) . . ?

C00B C00A C009 129.78(5) . . ?

C00B C00A H5 117.6(9) . . ?

C009 C00A H5 112.6(9) . . ?

C00A C00B C008 130.28(5) . . ?

C00A C00B H6 116.8(8) . . ?

C008 C00B H6 112.9(8) . . ?

_refine_diff_density_max   0.819

_refine_diff_density_min   -0.893

_refine_diff_density_rms   0.087

#===END

data_NiMT

_audit_creation_method   SHELXL-2014/6

_chemical_name_systematic   ?

_chemical_name_common   ?

_chemical_melting_point   ?

_chemical_formula_moiety   ?

_chemical_formula_sum

 'C8 H14 Ni O12'

_chemical_formula_weight   360.90

loop_

 _atom_type_symbol

 _atom_type_description

 _atom_type_scat_dispersion_real

 _atom_type_scat_dispersion_imag

 _atom_type_scat_source

 'C' 'C'   0.0033   0.0016

 'International Tables Vol C Tables 4.2.6.8 and 6.1.1.4'

 'H' 'H'   0.0000   0.0000

'International Tables Vol C Tables 4.2.6.8 and 6.1.1.4'

'O' 'O'   0.0106   0.0060

'International Tables Vol C Tables 4.2.6.8 and 6.1.1.4'

'Ni' 'Ni'   0.3393   1.1124

'International Tables Vol C Tables 4.2.6.8 and 6.1.1.4'

_space_group_crystal_system   triclinic

_space_group_IT_number   2

_space_group_name_H-M_alt   'P -1'

_space_group_name_Hall   '-P 1'

_shelx_space_group_comment

;

The symmetry employed for this shelxl refinement is uniquely defined

by the following loop, which should always be used as a source of

symmetry information in preference to the above space-group names.

They are only intended as comments.

;

loop_

 _space_group_symop_operation_xyz

'x, y, z'

'-x, -y, -z'

_cell_length_a   5.1420(3)

_cell_length_b   7.2793(4)

_cell_length_c   9.1121(5)

_cell_angle_alpha   108.025(3)

_cell_angle_beta   105.191(3)

_cell_angle_gamma   92.140(3)

_cell_volume   310.38(3)

_cell_formula_units_Z   1

_cell_measurement_temperature   90(2)

_cell_measurement_reflns_used   ?

_cell_measurement_theta_min   ?

_cell_measurement_theta_max   ?

_exptl_crystal_description   block

_exptl_crystal_colour   green

_exptl_crystal_density_meas   ?

_exptl_crystal_density_method   ?

_exptl_crystal_density_diffrn   1.931

_exptl_crystal_F_000   186

_exptl_transmission_factor_min   0.6158

_exptl_transmission_factor_max   0.7479

_exptl_crystal_size_max   0.22

_exptl_crystal_size_mid   0.14

_exptl_crystal_size_min   0.10

_exptl_absorpt_coefficient_mu   1.631

_shelx_estimated_absorpt_T_min   ?

_shelx_estimated_absorpt_T_max   ?

_exptl_absorpt_correction_type   multi-scan

_exptl_absorpt_correction_T_min   ?

_exptl_absorpt_correction_T_max   ?

_exptl_absorpt_process_details   'SADABS V2012/1 (Bruker AXS Inc.)'

_diffrn_ambient_temperature   90(2)

_diffrn_radiation_wavelength   0.71073

_diffrn_radiation_type   MoK\a

_diffrn_radiation_source   'fine-focus sealed tube'

_diffrn_radiation_monochromator   graphite

_diffrn_measurement_device_type 'Bruker APEX-II CCD'

_diffrn_measurement_method   '\f and \w scans'

_diffrn_reflns_number   24601

_diffrn_reflns_av_unetI/netI   0.0353

_diffrn_reflns_av_R_equivalents   0.0525

_diffrn_reflns_limit_h_min   -9

_diffrn_reflns_limit_h_max   9

_diffrn_reflns_limit_k_min   -13

_diffrn_reflns_limit_k_max   12

_diffrn_reflns_limit_l_min   -16

_diffrn_reflns_limit_l_max   16

_diffrn_reflns_theta_min   2.454

_diffrn_reflns_theta_max   40.061

_diffrn_reflns_theta_full   25.242

_diffrn_measured_fraction_theta_max   0.978

_diffrn_measured_fraction_theta_full 1.000

_diffrn_reflns_Laue_measured_fraction_max   0.978

_diffrn_reflns_Laue_measured_fraction_full 1.000

_diffrn_reflns_point_group_measured_fraction_max 0.978

_diffrn_reflns_point_group_measured_fraction_full 1.000

_reflns_number_total   3783

_reflns_number_gt   3346

_reflns_threshold_expression   'I > 2\s(I)'

_reflns_Friedel_coverage   0.000

_reflns_Friedel_fraction_max   .

_reflns_Friedel_fraction_full   .

_reflns_special_details
;
Reflections were merged by SHELXL according to the crystal

class for the calculation of statistics and refinement.

_reflns_Friedel_fraction is defined as the number of unique

Friedel pairs measured divided by the number that would be

possible theoretically, ignoring centric projections and

systematic absences.
;

_computing_data_collection   'Bruker APEX2 (Bruker, 2011)'
_computing_cell_refinement   'SAINT V8.30C (Bruker AXS Inc., 2013)'

_computing_data_reduction   'SAINT V8.30C (Bruker AXS Inc., 2013)'

_computing_structure_solution   'SHELXL-2013 (Sheldrick, 2013)'

_computing_structure_refinement   'SHELXL-2013 (Sheldrick, 2013)'

_computing_molecular_graphics   'CrystalMaker (Palmer, 2010)'

_computing_publication_material   'Bruker SHELXTL (Bruker, 2011)'

_refine_special_details   ?

_refine_ls_structure_factor_coef Fsqd

_refine_ls_matrix_type   full

_refine_ls_weighting_scheme   calc

_refine_ls_weighting_details

'w=1/[\s^2^(Fo^2^)+(0.0379P)^2^+0.0413P] where P=(Fo^2^+2Fc^2^)/3'

_atom_sites_solution_primary   ?

_atom_sites_solution_secondary   ?

_atom_sites_solution_hydrogens   difmap

_refine_ls_hydrogen_treatment   refall

_refine_ls_extinction_method   none

_refine_ls_extinction_coef   .

_refine_ls_number_reflns   3783

_refine_ls_number_parameters   125

_refine_ls_number_restraints   0

_refine_ls_R_factor_all   0.0398

_refine_ls_R_factor_gt   0.0321

_refine_ls_wR_factor_ref   0.0751

_refine_ls_wR_factor_gt   0.0722

_refine_ls_goodness_of_fit_ref   1.068

_refine_ls_restrained_S_all   1.068

_refine_ls_shift/su_max   0.000

_refine_ls_shift/su_mean   0.000

loop_

_atom_site_label

_atom_site_type_symbol

_atom_site_fract_x

_atom_site_fract_y

_atom_site_fract_z

_atom_site_U_iso_or_equiv

_atom_site_adp_type

_atom_site_occupancy

_atom_site_site_symmetry_order

_atom_site_calc_flag

_atom_site_refinement_flags_posn

_atom_site_refinement_flags_adp

_atom_site_refinement_flags_occupancy

_atom_site_disorder_assembly

_atom_site_disorder_group

Ni01 Ni 0.5000 0.5000 1.0000 0.01037(5) Uani 1 2 d S . P . .

O002 O 0.81718(13) 0.36536(11) 1.09924(9) 0.01332(11) Uani 1 1 d . . . . .

O003 O 0.24621(14) 0.24889(10) 0.92567(9) 0.01358(11) Uani 1 1 d . . . . .

O004 O 0.64126(13) 0.44094(10) 0.79827(8) 0.01331(11) Uani 1 1 d . . . . .

O005 O 0.31091(16) 0.02039(11) 0.12443(9) 0.01787(13) Uani 1 1 d . . . . .

O006 O 0.15838(15) 0.04084(12) 0.33365(9) 0.02007(14) Uani 1 1 d . . . . .

O007 O 0.29730(15) 0.22468(12) 0.62066(9) 0.01891(14) Uani 1 1 d . . . . .

C008 C 0.33799(18) 0.08928(13) 0.27003(11) 0.01321(14) Uani 1 1 d . . . . .

C009 C 0.52374(16) 0.32813(13) 0.65780(10) 0.01166(13) Uani 1 1 d . . . . .

C00A C 0.66582(17) 0.32388(14) 0.53321(11) 0.01404(14) Uani 1 1 d . . . . .

C00B C 0.58722(18) 0.22774(14) 0.37385(11) 0.01428(14) Uani 1 1 d . . . . .

H1 H 0.828(4) 0.406(3) 0.576(2) 0.025(4) Uiso 1 1 d . . . . .

H2 H 0.708(3) 0.241(2) 0.3165(19) 0.015(3) Uiso 1 1 d . . . . .

H3 H 0.203(4) 0.192(3) 0.833(3) 0.041(6) Uiso 1 1 d . . . . .

H4 H 0.280(4) 0.174(3) 0.974(2) 0.024(4) Uiso 1 1 d . . . . .

H5 H 0.204(6) 0.107(4) 0.449(4) 0.068(8) Uiso 1 1 d . . . . .

H6 H 0.959(4) 0.423(3) 1.118(2) 0.029(5) Uiso 1 1 d . . . . .

H7 H 0.816(4) 0.262(3) 1.034(3) 0.033(5) Uiso 1 1 d . . . . .

*loop_*

_atom_site_aniso_label

_atom_site_aniso_U_11

_atom_site_aniso_U_22

_atom_site_aniso_U_33

_atom_site_aniso_U_23

_atom_site_aniso_U_13

_atom_site_aniso_U_12

Ni01 0.00737(6) 0.01285(7) 0.00936(7) 0.00216(5) 0.00198(5) -0.00096(4)

O002 0.0096(2) 0.0148(3) 0.0140(3) 0.0031(2) 0.0029(2) 0.0003(2)

O003 0.0130(3) 0.0134(3) 0.0110(3) 0.0016(2) 0.0016(2) -0.0026(2)

O004 0.0106(2) 0.0165(3) 0.0097(3) 0.0012(2) 0.0020(2) -0.0012(2)

O005 0.0231(3) 0.0175(3) 0.0099(3) 0.0015(2) 0.0038(2) -0.0016(2)

O006 0.0153(3) 0.0271(4) 0.0116(3) -0.0004(3) 0.0030(2) -0.0078(2)

O007 0.0128(3) 0.0273(4) 0.0117(3) 0.0008(2) 0.0035(2) -0.0080(2)

C008 0.0137(3) 0.0133(3) 0.0107(3) 0.0026(3) 0.0022(3) 0.0007(2)

C009 0.0095(3) 0.0139(3) 0.0103(3) 0.0029(2) 0.0022(2) 0.0005(2)

C00A 0.0102(3) 0.0175(4) 0.0123(3) 0.0022(3) 0.0033(3) -0.0019(3)

C00B 0.0127(3) 0.0169(4) 0.0118(3) 0.0026(3) 0.0041(3) -0.0009(3)

_geom_special_details

;

All esds (except the esd in the dihedral angle between two l.s. planes)

are estimated using the full covariance matrix. The cell esds are taken

into account individually in the estimation of esds in distances, angles

and torsion angles; correlations between esds in cell parameters are only

used when they are defined by crystal symmetry. An approximate (isotropic)

treatment of cell esds is used for estimating esds involving l.s. planes.

;

*loop_*

_geom_bond_atom_site_label_1

_geom_bond_atom_site_label_2

_geom_bond_distance

_geom_bond_site_symmetry_2

_geom_bond_publ_flag

Ni01 O003 2.0237(7) 2_667 ?

Ni01 O003 2.0237(7) . ?

Ni01 O004 2.0798(7) . ?

Ni01 O004 2.0798(7) 2_667 ?

Ni01 O002 2.0816(7) 2_667 ?

Ni01 O002 2.0816(7) . ?

O002 H6 0.78(2) . ?

O002 H7 0.80(2) . ?

O003 H3 0.78(2) . ?

O003 H4 0.799(19) . ?

O004 C009 1.2589(11) . ?

O005 C008 1.2318(11) . ?

O006 C008 1.3024(12) . ?

O006 H5 0.97(3) . ?

O007 C009 1.2679(11) . ?

O007 H5 1.47(3) . ?

C008 C00B 1.4937(13) . ?

C009 C00A 1.4961(13) . ?

C00A C00B 1.3432(13) . ?

C00A H1 0.923(18) . ?

C00B H2 0.929(16) . ?

*loop_*

_geom_angle_atom_site_label_1

_geom_angle_atom_site_label_2

_geom_angle_atom_site_label_3

_geom_angle

_geom_angle_site_symmetry_1

_geom_angle_site_symmetry_3

_geom_angle_publ_flag

O003 Ni01 O003 180.0 2_667 . ?

O003 Ni01 O004 82.93(3) 2_667 . ?

O003 Ni01 O004 97.07(3) . . ?

O003 Ni01 O004 97.07(3) 2_667 2_667 ?

O003 Ni01 O004 82.93(3) . 2_667 ?

O004 Ni01 O004 180.0 . 2_667 ?

O003 Ni01 O002 89.74(3) 2_667 2_667 ?

O003 Ni01 O002 90.26(3) . 2_667 ?

O004 Ni01 O002 92.29(3) . 2_667 ?

O004 Ni01 O002 87.71(3) 2_667 2_667 ?

O003 Ni01 O002 90.26(3) 2_667 . ?

O003 Ni01 O002 89.74(3) . . ?

O004 Ni01 O002 87.71(3) . . ?

O004 Ni01 O002 92.29(3) 2_667 . ?

O002 Ni01 O002 180.00(3) 2_667 . ?

Ni01 O002 H6 112.4(14) . . ?

Ni01 O002 H7 108.0(15) . . ?

H6 O002 H7 106(2) . . ?

Ni01 O003 H3 116.0(16) . . ?

Ni01 O003 H4 118.6(13) . . ?

H3 O003 H4 109(2) . . ?

C009 O004 Ni01 127.52(6) . . ?

C008 O006 H5 112.6(17) . . ?

C009 O007 H5 112.3(11) . . ?

O005 C008 O006 121.47(8) . . ?

O005 C008 C00B 118.19(8) . . ?

O006 C008 C00B 120.33(8) . . ?

O004 C009 O007 123.21(8) . . ?

O004 C009 C00A 115.92(7) . . ?

O007 C009 C00A 120.87(8) . . ?

C00B C00A C009 130.00(8) . . ?

C00B C00A H1 117.9(11) . . ?

C009 C00A H1 112.1(11) . . ?

C00A C00B C008 130.49(8) . . ?

C00A C00B H2 117.1(10) . . ?

C008 C00B H2 112.3(10) . . ?

_refine_diff_density_max   1.004

_refine_diff_density_min   -0.971

_refine_diff_density_rms   0.104

#===END

data_ZnMT

_audit_creation_method   SHELXL-2014/6

_chemical_name_systematic   ?

_chemical_name_common   ?

_chemical_melting_point   ?

_chemical_formula_moiety   ?

_chemical_formula_sum

 'C8 H14 O12 Zn'

_chemical_formula_weight   367.56

loop_

 _atom_type_symbol

 _atom_type_description

 _atom_type_scat_dispersion_real

 _atom_type_scat_dispersion_imag

 _atom_type_scat_source

 'C' 'C'   0.0033   0.0016

 'International Tables Vol C Tables 4.2.6.8 and 6.1.1.4'

 'H' 'H'   0.0000   0.0000

 'International Tables Vol C Tables 4.2.6.8 and 6.1.1.4'

 'O' 'O'   0.0106   0.0060

 'International Tables Vol C Tables 4.2.6.8 and 6.1.1.4'

 'Zn' 'Zn'   0.2839   1.4301

 'International Tables Vol C Tables 4.2.6.8 and 6.1.1.4'

_space_group_crystal_system   triclinic

_space_group_IT_number   2

_space_group_name_H-M_alt   'P -1'

_space_group_name_Hall   '-P 1'

_shelx_space_group_comment

;

The symmetry employed for this shelxl refinement is uniquely defined

by the following loop, which should always be used as a source of

symmetry information in preference to the above space-group names.

They are only intended as comments.

;

loop_

 _space_group_symop_operation_xyz

 'x, y, z'

 '-x, -y, -z'

_cell_length_a   5.1749(2)

_cell_length_b   7.2736(3)

_cell_length_c   9.1901(4)

_cell_angle_alpha   108.304(2)

_cell_angle_beta   105.213(2)

_cell_angle_gamma   92.434(2)

_cell_volume   313.95(2)

_cell_formula_units_Z   1

_cell_measurement_temperature   90(2)

_cell_measurement_reflns_used   ?

_cell_measurement_theta_min   ?

_cell_measurement_theta_max   ?

_exptl_crystal_description   block

_exptl_crystal_colour   colorless

_exptl_crystal_density_meas   ?

_exptl_crystal_density_method   ?

_exptl_crystal_density_diffrn   1.944

_exptl_crystal_F_000   188

_exptl_transmission_factor_min   0.6641

_exptl_transmission_factor_max   0.7482

_exptl_crystal_size_max   0.30

_exptl_crystal_size_mid   0.16

_exptl_crystal_size_min   0.08

_exptl_absorpt_coefficient_mu   2.023

_shelx_estimated_absorpt_T_min   ?

_shelx_estimated_absorpt_T_max   ?

_exptl_absorpt_correction_type   multi-scan

_exptl_absorpt_process_details   'SADABS V2012/1 (Bruker AXS Inc.)'

_diffrn_ambient_temperature   90(2)

_diffrn_radiation_wavelength   0.71073

_diffrn_radiation_type   MoK\a

_diffrn_radiation_source   'fine-focus sealed tube'

_diffrn_radiation_monochromator   graphite

_diffrn_measurement_device_type   'Bruker APEX-II CCD'

_diffrn_measurement_method   '\f and \w scans'

_diffrn_detector_area_resol_mean ?

_diffrn_reflns_number   34723

_diffrn_reflns_av_unetI/netI   0.0154

_diffrn_reflns_av_R_equivalents   0.0275

_diffrn_reflns_limit_h_min   -9

_diffrn_reflns_limit_h_max   9

_diffrn_reflns_limit_k_min   -13

_diffrn_reflns_limit_k_max   13

_diffrn_reflns_limit_l_min   -17

_diffrn_reflns_limit_l_max   17

_diffrn_reflns_theta_min   2.440

_diffrn_reflns_theta_max   41.471

_diffrn_reflns_theta_full   25.242

_diffrn_measured_fraction_theta_max   0.985

_diffrn_measured_fraction_theta_full 1.000

_diffrn_reflns_Laue_measured_fraction_max   0.985

_diffrn_reflns_Laue_measured_fraction_full   1.000

_diffrn_reflns_point_group_measured_fraction_max   0.985

_diffrn_reflns_point_group_measured_fraction_full 1.000

_reflns_number_total   4197

_reflns_number_gt   3997

_reflns_threshold_expression   'I > 2\s(I)'

_reflns_Friedel_coverage   0.000

_reflns_Friedel_fraction_max   .

_reflns_Friedel_fraction_full   .

_reflns_special_details

;

Reflections were merged by SHELXL according to the crystal

class for the calculation of statistics and refinement.

_reflns_Friedel_fraction is defined as the number of unique

Friedel pairs measured divided by the number that would be

possible theoretically, ignoring centric projections and

systematic absences.

;

_computing_data_collection   'Bruker APEX2 (Bruker, 2011)'

_computing_cell_refinement   'SAINT V8.30C (Bruker AXS Inc., 2013)'

_computing_data_reduction   'SAINT V8.30C (Bruker AXS Inc., 2013)'

_computing_structure_solution   'SHELXL-2013 (Sheldrick, 2013)'

_computing_structure_refinement   'SHELXL-2013 (Sheldrick, 2013)'

_computing_molecular_graphics   'CrystalMaker (Palmer, 2010)'

_computing_publication_material   'Bruker SHELXTL (Bruker, 2011)'

_refine_special_details   ?

_refine_ls_structure_factor_coef Fsqd

_refine_ls_matrix_type   full

_refine_ls_weighting_scheme   calc

_refine_ls_weighting_details

'w=1/[\s^2^(Fo^2^)+(0.0353P)^2^+0.0490P] where P=(Fo^2^+2Fc^2^)/3'

_atom_sites_solution_primary   ?

_atom_sites_solution_secondary   ?

_atom_sites_solution_hydrogens   difmap

_refine_ls_hydrogen_treatment   refall

_refine_ls_extinction_method   none

_refine_ls_extinction_coef   .

_refine_ls_number_reflns   4197

_refine_ls_number_parameters   125

_refine_ls_number_restraints   0

_refine_ls_R_factor_all   0.0290

_refine_ls_R_factor_gt   0.0260

_refine_ls_wR_factor_ref   0.0630

_refine_ls_wR_factor_gt   0.0616

_refine_ls_goodness_of_fit_ref   1.145

_refine_ls_restrained_S_all   1.145

_refine_ls_shift/su_max   0.001

_refine_ls_shift/su_mean   0.000

loop_

 _atom_site_label

 _atom_site_type_symbol

 _atom_site_fract_x

_atom_site_fract_y

_atom_site_fract_z

_atom_site_U_iso_or_equiv

_atom_site_adp_type

_atom_site_occupancy

_atom_site_site_symmetry_order

_atom_site_calc_flag

_atom_site_refinement_flags_posn

_atom_site_refinement_flags_adp

_atom_site_refinement_flags_occupancy

_atom_site_disorder_assembly

_atom_site_disorder_group

Zn01 Zn 0.5000 0.5000 1.0000 0.01019(3) Uani 1 2 d S . P . .

O002 O 0.82089(10) 0.36413(8) 1.10097(6) 0.01213(8) Uani 1 1 d . . . . .

O003 O 0.24869(11) 0.24330(8) 0.92469(6) 0.01317(8) Uani 1 1 d . . . . .

O004 O 0.64524(10) 0.43994(8) 0.79507(6) 0.01256(8) Uani 1 1 d . . . . .

O005 O 0.29916(12) 0.22537(10) 0.61804(7) 0.01735(10) Uani 1 1 d . . . . .

O006 O 0.15844(12) 0.04008(10) 0.33339(7) 0.01798(10) Uani 1 1 d . . . . .

O007 O 0.30331(13) 0.02100(9) 0.12367(7) 0.01662(9) Uani 1 1 d . . . . .

C008 C 0.52645(12) 0.32772(9) 0.65501(7) 0.01047(9) Uani 1 1 d . . . . .

C009 C 0.33433(13) 0.08868(9) 0.26928(8) 0.01166(9) Uani 1 1 d . . . . .

C00A C 0.58515(13) 0.22593(10) 0.37203(8) 0.01280(10) Uani 1 1 d . . . . .

C00B C 0.66666(13) 0.32218(10) 0.53098(8) 0.01257(9) Uani 1 1 d . . . . .

H1 H 0.196(4) 0.185(3) 0.841(2) 0.030(4) Uiso 1 1 d . . . . .

H2 H 0.280(4) 0.167(3) 0.970(2) 0.027(4) Uiso 1 1 d . . . . .

H3 H 0.818(4) 0.262(2) 1.035(2) 0.024(4) Uiso 1 1 d . . . . .

H4 H 0.966(3) 0.419(2) 1.1255(19) 0.020(3) Uiso 1 1 d . . . . .

H5 H 0.223(5) 0.110(4) 0.454(3) 0.062(7) Uiso 1 1 d . . . . .

H6 H 0.696(3) 0.242(2) 0.3139(19) 0.019(3) Uiso 1 1 d . . . . .

H7 H 0.831(3) 0.406(2) 0.576(2) 0.023(4) Uiso 1 1 d . . . . .

*loop_*

 _atom_site_aniso_label

 _atom_site_aniso_U_11

 _atom_site_aniso_U_22

 _atom_site_aniso_U_33

 _atom_site_aniso_U_23

 _atom_site_aniso_U_13

 _atom_site_aniso_U_12

Zn01 0.00954(4) 0.01129(5) 0.01054(5) 0.00388(3) 0.00403(3) 0.00118(3)

O002 0.01082(17) 0.01284(18) 0.01242(19) 0.00343(15) 0.00384(14) 0.00177(14)

O003 0.01488(19) 0.01255(19) 0.00978(18) 0.00237(15) 0.00205(14) -0.00182(15)

O004 0.01227(18) 0.01513(19) 0.00827(17) 0.00119(14) 0.00326(14) 0.00014(15)

O005 0.01373(19) 0.0243(3) 0.01054(19) 0.00108(17) 0.00485(15) -0.00571(18)

O006 0.0160(2) 0.0237(3) 0.00962(19) 0.00064(17) 0.00361(16) -0.00596(18)

O007 0.0251(2) 0.0147(2) 0.00812(18) 0.00175(15) 0.00478(17) -0.00051(18)

C008 0.0104(2) 0.0119(2) 0.0089(2) 0.00263(16) 0.00352(16) 0.00146(16)

C009 0.0145(2) 0.0111(2) 0.0088(2) 0.00270(17) 0.00328(17) 0.00185(17)

C00A 0.0136(2) 0.0145(2) 0.0102(2) 0.00268(18) 0.00537(18) 0.00065(18)

C00B 0.0111(2) 0.0154(2) 0.0102(2) 0.00218(18) 0.00440(17) -0.00042(18)

_geom_special_details

;

All esds (except the esd in the dihedral angle between two l.s. planes)

are estimated using the full covariance matrix. The cell esds are taken

into account individually in the estimation of esds in distances, angles

and torsion angles; correlations between esds in cell parameters are only

used when they are defined by crystal symmetry. An approximate (isotropic)

treatment of cell esds is used for estimating esds involving l.s. planes.

;

loop_

 _geom_bond_atom_site_label_1

 _geom_bond_atom_site_label_2

 _geom_bond_distance

 _geom_bond_site_symmetry_2

 _geom_bond_publ_flag

Zn01 O003 2.0411(5) 2_667 ?

Zn01 O003 2.0411(5) . ?

Zn01 O002 2.1217(5) 2_667 ?

Zn01 O002 2.1218(5) . ?

Zn01 O004 2.1346(5) 2_667 ?

Zn01 O004 2.1346(5) . ?

O002 H3 0.796(18) . ?

O002 H4 0.776(16) . ?

O003 H1 0.724(18) . ?

O003 H2 0.792(19) . ?

O004 C008 1.2582(8) . ?

O005 C008 1.2689(8) . ?

O005 H5 1.41(3) . ?

O006 C009 1.2983(9) . ?

O006 H5 1.02(3) . ?

O007 C009 1.2352(8) . ?

C008 C00B 1.4950(9) . ?

C009 C00A 1.4925(9) . ?

C00A C00B 1.3458(9) . ?

C00A H6 0.908(17) . ?

C00B H7 0.940(17) . ?

*loop_*

_geom_angle_atom_site_label_1

_geom_angle_atom_site_label_2

_geom_angle_atom_site_label_3

_geom_angle

_geom_angle_site_symmetry_1

_geom_angle_site_symmetry_3

_geom_angle_publ_flag

O003 Zn01 O003 180.0 2_667 . ?

O003 Zn01 O002 89.10(2) 2_667 2_667 ?

O003 Zn01 O002 90.90(2) . 2_667 ?

O003 Zn01 O002 90.90(2) 2_667 . ?

O003 Zn01 O002 89.10(2) . . ?

O002 Zn01 O002 180.0 2_667 . ?

O003 Zn01 O004 96.97(2) 2_667 2_667 ?

O003 Zn01 O004 83.03(2) . 2_667 ?

O002 Zn01 O004 87.78(2) 2_667 2_667 ?

O002 Zn01 O004 92.22(2) . 2_667 ?

O003 Zn01 O004 83.03(2) 2_667 . ?

O003 Zn01 O004 96.97(2) . . ?

O002 Zn01 O004 92.21(2) 2_667 . ?

O002 Zn01 O004 87.78(2) . . ?

O004 Zn01 O004 180.0 2_667 . ?

Zn01 O002 H3 107.1(13) . . ?

Zn01 O002 H4 116.7(12) . . ?

H3 O002 H4 106.3(17) . . ?

Zn01 O003 H1 122.0(15) . . ?

Zn01 O003 H2 120.3(13) . . ?

H1 O003 H2 105.1(19) . . ?

C008 O004 Zn01 127.20(4) . . ?

C008 O005 H5 109.6(11) . . ?

C009 O006 H5 109.1(15) . . ?

O004 C008 O005 122.92(6) . . ?

O004 C008 C00B 116.21(6) . . ?

O005 C008 C00B 120.86(6) . . ?

O007 C009 O006 121.67(6) . . ?

O007 C009 C00A 118.10(6) . . ?

O006 C009 C00A 120.21(6) . . ?

C00B C00A C009 130.39(6) . . ?

C00B C00A H6 117.9(10) . . ?

C009 C00A H6 111.7(10) . . ?

C00A C00B C008 129.92(6) . . ?

C00A C00B H7 119.0(10) . . ?

C008 C00B H7 111.0(10) . . ?

_refine_diff_density_max   1.666

_refine_diff_density_min   -0.641

_refine_diff_density_rms   0.099

APPENDIX E: Chapter 8 Supporting Information

Contents

Experimental MSG and MPG CIF files (page 634 and 643, respectively).

E.1 MSG CIF

data_MSG_EXPERIMENTAL_STRUCTURE

_audit_creation_method   SHELXL-2014/6

_chemical_name_systematic   ?

_chemical_name_common   ?

_chemical_melting_point   ?

_chemical_formula_moiety   ?

_chemical_formula_sum

'C5 H10 N Na O5'

_chemical_formula_weight   187.13

loop_

_atom_type_symbol

_atom_type_description

_atom_type_scat_dispersion_real

_atom_type_scat_dispersion_imag

_atom_type_scat_source

'C' 'C'   0.0033   0.0016

'International Tables Vol C Tables 4.2.6.8 and 6.1.1.4'

'H' 'H'   0.0000   0.0000

'International Tables Vol C Tables 4.2.6.8 and 6.1.1.4'

'N' 'N'   0.0061   0.0033

'International Tables Vol C Tables 4.2.6.8 and 6.1.1.4'

'O' 'O'   0.0106   0.0060

'International Tables Vol C Tables 4.2.6.8 and 6.1.1.4'

'Na' 'Na'   0.0362   0.0249

'International Tables Vol C Tables 4.2.6.8 and 6.1.1.4'

_space_group_crystal_system   orthorhombic

_space_group_IT_number   19

_space_group_name_H-M_alt   'P 21 21 21'

_space_group_name_Hall   'P 2ac 2ab'

_shelx_space_group_comment

;

The symmetry employed for this shelxl refinement is uniquely defined

by the following loop, which should always be used as a source of

symmetry information in preference to the above space-group names.

They are only intended as comments.

;

loop_

_space_group_symop_operation_xyz

'x, y, z'

'-x+1/2, -y, z+1/2'

'-x, y+1/2, -z+1/2'

'x+1/2, -y+1/2, -z'

_cell_length_a   5.5212(15)

_cell_length_b   15.130(4)

_cell_length_c   17.958(5)

_cell_angle_alpha   90

_cell_angle_beta   90

_cell_angle_gamma   90

_cell_volume   1500.1(7)

_cell_formula_units_Z   8

_cell_measurement_temperature   95(2)

_cell_measurement_reflns_used   ?

_cell_measurement_theta_min   ?

_cell_measurement_theta_max   ?

_exptl_crystal_description   Block

_exptl_crystal_colour   Colorless

_exptl_crystal_density_meas   ?

_exptl_crystal_density_method   ?

_exptl_crystal_density_diffrn   1.657

_exptl_crystal_F_000   784

_exptl_transmission_factor_min   ?

_exptl_transmission_factor_max   ?

_exptl_crystal_size_max   0.10

_exptl_crystal_size_mid   0.07

_exptl_crystal_size_min   0.06

_exptl_absorpt_coefficient_mu   0.193

_shelx_estimated_absorpt_T_min   ?

_shelx_estimated_absorpt_T_max   ?

_exptl_absorpt_correction_type   multi-scan

_exptl_absorpt_process_details   'SADABS V2012/1 (Bruker AXS Inc.)'

_diffrn_ambient_temperature   90(2)

_diffrn_radiation_wavelength   0.71073

_diffrn_radiation_type   MoK\a

_diffrn_radiation_source   'fine-focus sealed tube'

_diffrn_radiation_monochromator   graphite

_diffrn_measurement_device_type   'Bruker APEX-II CCD'

_diffrn_measurement_method   '\f and \w scans'

_diffrn_detector_area_resol_mean ?

_diffrn_reflns_number   7599

_diffrn_reflns_av_unetI/netI   0.0509

_diffrn_reflns_av_R_equivalents   0.0838

_diffrn_reflns_limit_h_min   -5

_diffrn_reflns_limit_h_max   4

_diffrn_reflns_limit_k_min   -13

_diffrn_reflns_limit_k_max   13

_diffrn_reflns_limit_l_min   -16

_diffrn_reflns_limit_l_max   16

_diffrn_reflns_theta_min   1.760

_diffrn_reflns_theta_max   18.877

_diffrn_reflns_theta_full   25.242

_diffrn_measured_fraction_theta_max   1.000

_diffrn_measured_fraction_theta_full 0.452

_diffrn_reflns_Laue_measured_fraction_max   1.000

_diffrn_reflns_Laue_measured_fraction_full   0.452

_diffrn_reflns_point_group_measured_fraction_max   1.000

_diffrn_reflns_point_group_measured_fraction_full 0.431

_reflns_number_total   1174

_reflns_number_gt   1011

_reflns_threshold_expression   'I > 2\s(I)'

_reflns_Friedel_coverage   0.617

_reflns_Friedel_fraction_max   1.000

_reflns_Friedel_fraction_full   0.402

_reflns_special_details

;

Reflections were merged by SHELXL according to the crystal

class for the calculation of statistics and refinement.

_reflns_Friedel_fraction is defined as the number of unique

Friedel pairs measured divided by the number that would be

possible theoretically, ignoring centric projections and

systematic absences.

;

_computing_data_collection   'Bruker APEX2 (Bruker, 2011)'

_computing_cell_refinement   'SAINT V8.30C (Bruker AXS Inc., 2013)'

_computing_data_reduction   'SAINT V8.30C (Bruker AXS Inc., 2013)'

_computing_structure_solution   'SHELXL-2013 (Sheldrick, 2013)'

_computing_structure_refinement   'SHELXL-2013 (Sheldrick, 2013)'

_computing_molecular_graphics   'CrystalMaker (Palmer, 2010)'

_computing_publication_material   'Bruker SHELXTL (Bruker, 2011)'

_refine_special_details   ?

_refine_ls_structure_factor_coef Fsqd

_refine_ls_matrix_type   full

_refine_ls_weighting_scheme   calc

_refine_ls_weighting_details

'w=1/[\s^2^(Fo^2^)+(0.0344P)^2^] where P=(Fo^2^+2Fc^2^)/3'

_atom_sites_solution_primary   ?

_atom_sites_solution_secondary   ?

_atom_sites_solution_hydrogens   difmap

_refine_ls_hydrogen_treatment   refall

_refine_ls_extinction_method   none

_refine_ls_extinction_coef   .

_refine_ls_abs_structure_details

;

Flack x determined using 364 quotients $[(I+)-(I-)]/[(I+)+(I-)]$

(Parsons, Flack and Wagner, Acta Cryst. B69 (2013) 249-259).

639

;

_refine_ls_abs_structure_Flack   0.5(9)

_chemical_absolute_configuration ?

_refine_ls_number_reflns   1174

_refine_ls_number_parameters   297

_refine_ls_number_restraints   0

_refine_ls_R_factor_all   0.0429

_refine_ls_R_factor_gt   0.0312

_refine_ls_wR_factor_ref   0.0669

_refine_ls_wR_factor_gt   0.0623

_refine_ls_goodness_of_fit_ref   1.008

_refine_ls_restrained_S_all   1.008

_refine_ls_shift/su_max   0.681

_refine_ls_shift/su_mean   0.013

loop_

 _atom_site_label

 _atom_site_type_symbol

 _atom_site_fract_x

 _atom_site_fract_y

 _atom_site_fract_z

 _atom_site_U_iso_or_equiv

 _atom_site_adp_type

 _atom_site_occupancy

 _atom_site_site_symmetry_order

_atom_site_calc_flag

_atom_site_refinement_flags_posn

_atom_site_refinement_flags_adp

_atom_site_refinement_flags_occupancy

_atom_site_disorder_assembly

_atom_site_disorder_group

Na01 Na -0.0523(6) 0.4244(2) 0.17960(16) 0.0184(11) Uani 1 1 d . . . . .

Na02 Na 1.0670(6) 0.4316(2) 0.67529(16) 0.0183(11) Uani 1 1 d . . . . .

O003 O -0.4073(19) 0.4352(6) 0.1037(4) 0.020(2) Uani 1 1 d . . . . .

O004 O 0.6625(11) 0.4915(3) 0.2645(3) 0.0166(15) Uani 1 1 d . . . . .

O005 O 0.8914(16) 0.3912(4) 0.9858(3) 0.017(2) Uani 1 1 d . . . . .

O006 O 1.4584(9) 0.2211(4) 0.7638(3) 0.0181(15) Uani 1 1 d . . . . .

O007 O 0.2705(11) 0.4525(3) 0.2556(3) 0.0169(15) Uani 1 1 d . . . . .

O008 O 1.1459(11) 0.3518(4) 1.0785(4) 0.0168(17) Uani 1 1 d . . . . .

O009 O 0.8763(11) 0.3480(4) 0.5845(4) 0.0153(17) Uani 1 1 d . . . . .

O00A O 1.1186(17) 0.3923(4) 0.4924(3) 0.019(2) Uani 1 1 d . . . . .

O00B O 1.4326(16) 0.4371(5) 0.6109(4) 0.021(2) Uani 1 1 d . . . . .

O00C O 1.1357(11) 0.3133(3) 0.7586(3) 0.0173(16) Uani 1 1 d . . . . .

N00D N 1.7182(17) 0.3225(6) 0.8548(5) 0.015(2) Uani 1 1 d . . . . .

N00E N 0.3011(17) 0.3255(6) 0.3584(5) 0.018(3) Uani 1 1 d . . . . .

C00F C 1.4817(18) 0.3593(6) 0.8278(5) 0.013(3) Uani 1 1 d . . . . .

C00G C 0.482(2) 0.4442(6) 0.2814(4) 0.011(2) Uani 1 1 d . . . . .

C00H C 0.5309(19) 0.3698(6) 0.3366(5) 0.017(3) Uani 1 1 d . . . . .

C00I C 1.270(2) 0.3258(7) 0.9518(5) 0.011(3) Uani 1 1 d . . . . .

C00J C 0.674(2) 0.4013(6) 0.4044(6) 0.016(3) Uani 1 1 d . . . . .

C00K C 1.350(2) 0.2912(7) 0.7793(4) 0.016(2) Uani 1 1 d . . . . .

C00L C 1.330(2) 0.3949(7) 0.8930(5) 0.016(3) Uani 1 1 d . . . . .

C00M C 1.091(2) 0.3588(6) 1.0102(6) 0.015(3) Uani 1 1 d . . . . .

C00N C 0.739(2) 0.3294(7) 0.4589(6) 0.017(3) Uani 1 1 d . . . . .

C00O C 0.929(2) 0.3599(6) 0.5164(6) 0.014(3) Uani 1 1 d . . . . .

H1 H 1.403(18) 0.307(4) 0.978(4) 0.00(3) Uiso 1 1 d . . . . .

H2 H 1.206(14) 0.266(5) 0.924(4) 0.02(2) Uiso 1 1 d . . . . .

H3 H 1.167(17) 0.418(5) 0.871(4) 0.03(3) Uiso 1 1 d . . . . .

H4 H 1.399(14) 0.441(5) 0.916(4) 0.00(3) Uiso 1 1 d . . . . .

H5 H 1.81(2) 0.348(6) 0.902(6) 0.06(4) Uiso 1 1 d . . . . .

H6 H 1.846(17) 0.325(6) 0.814(5) 0.05(3) Uiso 1 1 d . . . . .

H7 H 1.699(14) 0.270(5) 0.866(4) 0.00(3) Uiso 1 1 d . . . . .

H8 H -0.29(3) 0.418(10) 0.058(9) 0.20(8) Uiso 1 1 d . . . . .

H9 H -0.51(2) 0.418(9) 0.092(7) 0.08(7) Uiso 1 1 d . . . . .

H10 H 0.31(2) 0.246(8) 0.376(6) 0.11(4) Uiso 1 1 d . . . . .

H12 H 0.242(15) 0.360(5) 0.394(4) 0.00(3) Uiso 1 1 d . . . . .

H13 H 0.813(15) 0.283(5) 0.435(4) 0.01(3) Uiso 1 1 d . . . . .

H14 H 0.583(18) 0.307(4) 0.485(4) 0.00(2) Uiso 1 1 d . . . . .

H15 H 0.815(17) 0.436(6) 0.386(4) 0.03(3) Uiso 1 1 d . . . . .

H16 H 0.589(13) 0.451(5) 0.429(4) 0.00(2) Uiso 1 1 d . . . . .

H17 H 0.634(13) 0.325(5) 0.307(4) 0.02(3) Uiso 1 1 d . . . . .

H19 H 1.561(14) 0.413(5) 0.606(4) 0.00(3) Uiso 1 1 d . . . . .

H18 H 1.34(2) 0.429(7) 0.574(5) 0.06(5) Uiso 1 1 d . . . . .

H20 H 1.508(13) 0.410(5) 0.794(3) 0.00(2) Uiso 1 1 d . . . . .

H11 H 0.207(15) 0.319(5) 0.323(4) 0.00(3) Uiso 1 1 d . . . . .

E.2 Experimental MPG CIF

data_MPG_EXPERIMENTAL_CIF

_audit_creation_method   SHELXL-2014/6

_chemical_name_systematic   ?

_chemical_name_common   ?

_chemical_melting_point   ?

_chemical_formula_moiety   ?

_chemical_formula_sum

 'C5 H10 K N O5'

_chemical_formula_weight   203.24

loop_

 _atom_type_symbol

 _atom_type_description

 _atom_type_scat_dispersion_real

 _atom_type_scat_dispersion_imag

 _atom_type_scat_source

 'C' 'C'   0.0033   0.0016

 'International Tables Vol C Tables 4.2.6.8 and 6.1.1.4'

 'H' 'H'   0.0000   0.0000

 'International Tables Vol C Tables 4.2.6.8 and 6.1.1.4'

 'N' 'N'   0.0061   0.0033

 'International Tables Vol C Tables 4.2.6.8 and 6.1.1.4'

'O' 'O' 0.0106 0.0060

'International Tables Vol C Tables 4.2.6.8 and 6.1.1.4'

'K' 'K' 0.2009 0.2494

'International Tables Vol C Tables 4.2.6.8 and 6.1.1.4'

_space_group_crystal_system   orthorhombic

_space_group_IT_number   18

_space_group_name_H-M_alt   'P 21 21 2'

_space_group_name_Hall   'P 2 2ab'

_shelx_space_group_comment

;

The symmetry employed for this shelxl refinement is uniquely defined

by the following loop, which should always be used as a source of

symmetry information in preference to the above space-group names.

They are only intended as comments.

;

loop_
 _space_group_symop_operation_xyz
'x, y, z'
'-x, -y, z'
'-x+1/2, y+1/2, -z'
'x+1/2, -y+1/2, -z'

_cell_length_a   7.8423(2)

_cell_length_b   20.5904(6)

_cell_length_c   5.1432(2)

_cell_angle_alpha   90

_cell_angle_beta   90

_cell_angle_gamma   90

_cell_volume   830.50(5)

_cell_formula_units_Z   4

_cell_measurement_temperature   95(2)

_cell_measurement_reflns_used   ?

_cell_measurement_theta_min   ?

_cell_measurement_theta_max   ?

_exptl_crystal_description   Block

_exptl_crystal_colour   Colorless

_exptl_crystal_density_meas   ?

_exptl_crystal_density_method   ?

_exptl_crystal_density_diffrn   1.625

_exptl_crystal_F_000   424

_exptl_transmission_factor_min   ?

_exptl_transmission_factor_max   ?

_exptl_crystal_size_max   0.14

_exptl_crystal_size_mid   0.11

_exptl_crystal_size_min   0.09

_exptl_absorpt_coefficient_mu   0.624

_shelx_estimated_absorpt_T_min   ?

_shelx_estimated_absorpt_T_max   ?

_exptl_absorpt_correction_type   multi-scan

_exptl_absorpt_process_details   'SADABS V2012/1 (Bruker AXS Inc.)'

_diffrn_ambient_temperature   90(2)

_diffrn_radiation_wavelength   0.71073

_diffrn_radiation_type   MoK\a

_diffrn_radiation_source   'fine-focus sealed tube'

_diffrn_radiation_monochromator   graphite

_diffrn_measurement_device_type   'Bruker APEX-II CCD'

_diffrn_measurement_method   '\f and \w scans'

_diffrn_detector_area_resol_mean ?

_diffrn_reflns_number   15941

_diffrn_reflns_av_unetI/netI   0.0400

_diffrn_reflns_av_R_equivalents   0.0454

_diffrn_reflns_limit_h_min   -12

_diffrn_reflns_limit_h_max   12

_diffrn_reflns_limit_k_min   -33

_diffrn_reflns_limit_k_max   23

_diffrn_reflns_limit_l_min   -8

_diffrn_reflns_limit_l_max   8

_diffrn_reflns_theta_min   1.978

_diffrn_reflns_theta_max   35.030

_diffrn_reflns_theta_full   25.242

_diffrn_measured_fraction_theta_max 0.999

_diffrn_measured_fraction_theta_full 1.000

_diffrn_reflns_Laue_measured_fraction_max   0.999

_diffrn_reflns_Laue_measured_fraction_full 1.000

_diffrn_reflns_point_group_measured_fraction_max   0.998

_diffrn_reflns_point_group_measured_fraction_full 0.997

_reflns_number_total   3678

_reflns_number_gt   3246

_reflns_threshold_expression   'I > 2\s(I)'

_reflns_Friedel_coverage   0.714

_reflns_Friedel_fraction_max   0.996

_reflns_Friedel_fraction_full   0.993

_reflns_special_details

;

Reflections were merged by SHELXL according to the crystal

class for the calculation of statistics and refinement.

_reflns_Friedel_fraction is defined as the number of unique

Friedel pairs measured divided by the number that would be

possible theoretically, ignoring centric projections and

systematic absences.

;

_computing_data_collection   'Bruker APEX2 (Bruker, 2011)'

_computing_cell_refinement   'SAINT V8.30C (Bruker AXS Inc., 2013)'

_computing_data_reduction   'SAINT V8.30C (Bruker AXS Inc., 2013)'

_computing_structure_solution   'SHELXL-2013 (Sheldrick, 2013)'

_computing_structure_refinement   'SHELXL-2013 (Sheldrick, 2013)'

_computing_molecular_graphics   'CrystalMaker (Palmer, 2010)'

_computing_publication_material   'Bruker SHELXTL (Bruker, 2011)'

_refine_special_details   ?

_refine_ls_structure_factor_coef Fsqd

_refine_ls_matrix_type   full

_refine_ls_weighting_scheme   calc

_refine_ls_weighting_details

'w=1/[\s^2^(Fo^2^)+(0.0438P)^2^+0.0722P] where P=(Fo^2^+2Fc^2^)/3'

_atom_sites_solution_primary   ?

_atom_sites_solution_secondary   ?

_atom_sites_solution_hydrogens   difmap

_refine_ls_hydrogen_treatment   refall

_refine_ls_extinction_method   none

_refine_ls_extinction_coef   .

_refine_ls_abs_structure_details

;

Flack x determined using 1269 quotients [(I+)-(I-)]/[(I+)+(I-)]

(Parsons, Flack and Wagner, Acta Cryst. B69 (2013) 249-259).

;

_refine_ls_abs_structure_Flack   -0.001(18)

_chemical_absolute_configuration ?

_refine_ls_number_reflns   3678

_refine_ls_number_parameters   150

_refine_ls_number_restraints   0

_refine_ls_R_factor_all   0.0433

_refine_ls_R_factor_gt   0.0352

_refine_ls_wR_factor_ref   0.0791

_refine_ls_wR_factor_gt   0.0762

_refine_ls_goodness_of_fit_ref   1.012

_refine_ls_restrained_S_all   1.012

_refine_ls_shift/su_max   0.000

_refine_ls_shift/su_mean   0.000

loop_

 _atom_site_label

 _atom_site_type_symbol

 _atom_site_fract_x

 _atom_site_fract_y

 _atom_site_fract_z

 _atom_site_U_iso_or_equiv

 _atom_site_adp_type

 _atom_site_occupancy

 _atom_site_site_symmetry_order

 _atom_site_calc_flag

 _atom_site_refinement_flags_posn

 _atom_site_refinement_flags_adp

 _atom_site_refinement_flags_occupancy

_atom_site_disorder_assembly

_atom_site_disorder_group

K001 K 0.5000 0.5000 0.01328(9) 0.01190(9) Uani 1 2 d S T P . .

K002 K 0.0000 0.5000 0.88840(10) 0.01397(10) Uani 1 2 d S T P . .

O003 O 0.27724(16) 0.55393(6) 0.6494(3) 0.0121(2) Uani 1 1 d . . . . .

O004 O 0.90594(17) 0.62786(7) 0.6852(3) 0.0167(3) Uani 1 1 d . . . . .

O005 O 0.20535(19) 0.45164(8) 1.2742(3) 0.0174(3) Uani 1 1 d . . . . .

O006 O 0.32095(19) 0.59184(7) 0.2492(3) 0.0163(3) Uani 1 1 d . . . . .

O007 O 0.83222(19) 0.71591(7) 0.9057(3) 0.0205(3) Uani 1 1 d . . . . .

N1 N 0.22342(19) 0.67482(8) 0.8435(3) 0.0109(3) Uani 1 1 d . . . . .

C009 C 0.7959(2) 0.66439(9) 0.7896(4) 0.0114(3) Uani 1 1 d . . . . .

C00A C 0.3008(2) 0.59922(8) 0.4887(3) 0.0097(3) Uani 1 1 d . . . . .

C00B C 0.5009(3) 0.69042(7) 0.6113(3) 0.0117(2) Uani 1 1 d . . . . .

C00C C 0.6091(2) 0.64376(9) 0.7732(4) 0.0122(3) Uani 1 1 d . . . . .

C00D C 0.3133(2) 0.66905(8) 0.5902(3) 0.0095(3) Uani 1 1 d . . . . .

H1 H 0.172(4) 0.4204(15) 1.361(7) 0.029(8) Uiso 1 1 d . . . . .

H2 H 0.227(4) 0.4847(19) 1.353(8) 0.046(10) Uiso 1 1 d . . . . .

H3 H 0.605(3) 0.5995(12) 0.695(5) 0.009(5) Uiso 1 1 d . . . . .

H4 H 0.577(4) 0.6426(14) 0.956(6) 0.024(7) Uiso 1 1 d . . . . .

H5 H 0.511(4) 0.7337(11) 0.689(5) 0.013(5) Uiso 1 1 d . . . . .

H6 H 0.539(3) 0.6927(12) 0.433(5) 0.014(6) Uiso 1 1 d . . . . .

H7 H 0.109(4) 0.6643(13) 0.816(6) 0.021(7) Uiso 1 1 d . . . . .

H8 H 0.266(4) 0.6428(18) 0.983(7) 0.035(9) Uiso 1 1 d . . . . .

H9 H 0.229(4) 0.7167(17) 0.915(7) 0.028(8) Uiso 1 1 d . . . . .

H10 H 0.257(3) 0.6973(14) 0.467(6) 0.014(6) Uiso 1 1 d . . . . .

650

APPENDIX F: Chapter 9 Supporting Information.

List of Tables

Table F.13 Experimental[1] and calculated bond lengths (Å) of $CuSO_4 \cdot 3H_2O$ using PBE and B3LYP with 6-31G(d) on copper and hydrogen and 6-31G(2d) on sulfur and oxygen.

Table F.14 Experimental[2] and calculated unit cell dimensions (Å, degrees) of $CuSO_4 \cdot 3H_2O$ using PBE and B3LYP with 6-31G(d) on copper and hydrogen and 6-31G(2d) on sulfur and oxygen.

Table F.15 Experimental[3] and calculated unit cell dimensions (Å, degrees) of $CuSO_4 \cdot H_2O$ using PBE and B3LYP with 6-31G(d) on copper and hydrogen and 6-31G(2d) on sulfur and oxygen.

Table F.16 Calculated anhydrous $CuSO_4$ atomic positions (in fractional coordinates) using B3LYP with 6-31G(d) on copper and 6-31G(2d) on sulfur and oxygen. The space group is *Pnma* and a=8.40456, b=7.71152, c=4.86126 and α=β=γ=90°.

Table F.17 Calculated $CuSO_4 \cdot H_2O$ atomic positions (in fractional coordinates) using B3LYP with 6-31G(d) on copper and hydrogen and 6-31G(2d) on sulfur and oxygen. The space group is *P-1* and a=8. 50241, b= 5.19702, c= 7.63583and α= 109.975° β= 108.061° γ= 89.012°.

Table F.18 Calculated $CuSO_4 \cdot 3H_2O$ atomic positions (in fractional coordinates) using B3LYP with 6-31G(d) on copper and hydrogen and 6-31G(2d) on sulfur and oxygen. The space group is *Cc* and a=5.57873, b= 13.01883, c= 7.37945and α =γ=90°, β= 96.166°.

Table F.19 Calculated B3LYP vibrational frequencies (cm^{-1}), real intensities (km mol^{-1}) and symmetry labels of $CuSO_4$

Table F.20 Calculated B3LYP vibrational frequencies (cm^{-1}), real intensities (km mol^{-1}) and symmetry labels of $CuSO_4 \cdot H_2O$

Table F.21 Calculated B3LYP vibrational frequencies (cm^{-1}), real intensities (km mol^{-1}) and symmetry labels of $CuSO_4 \cdot 3H_2O$

Table F.22 Optimized 6-31G(3d) polarization functions for sulfur and oxygen.

List of Figures

Supporting Information References

1.   Wildner, M.; Giester, G., Crystal Structure Refinements of Synthetic Chalcocyanite ($Cuso_4$) and Zincosite ($Znso_4$). *Mineralogy and Petrology* **1988**, *39*, 201-209.
2.   Zahrobsky, R. F.; Baur, W. H., On the Crystal Chemistry of Salt HydrateF. V. The Determination of the Crystal Structure of $Cuso4.3h2o$ (Bonattite). *Acta Crystallogr. Sect. B* **1968**, *24*, 508-513.
3.   Ting, V. P.; Henry, P. F.; Schmidtmann, M.; Wilson, C. C.; Weller, M. T., In Situ Neutron Powder Diffraction and Structure Determination in Controlled HumiditieF. *Chem. Commun.* **2009**, 7527-7529.

Table F.1 Experimental[1] and calculated bond lengths (Å) of anhydrous $CuSO_4$ using PBE with different basis setF. With the exception of pob-TZVP (where all elements are modeled with pob-TZVP), copper is modeled with 6-31G(d).

Literature		pob-TZVP		6-31G(d)		6-31G(2d)		6-31G(3d)	
Bond	Length	Bond Length	% Error	Bond Length	% Error	Bond Length	% Error	Bond Length	% Error
Cu1-O1	2.37	2.38	0.21	2.37	-0.24	2.36	-0.72	2.41	1.64
Cu1-O2	2.05	2.05	-0.16	2.02	-1.53	2.03	-1.15	2.05	0.10
Cu1-O3	1.92	1.94	0.99	1.92	0.16	1.92	-0.01	1.94	1.08
S1-O1	1.45	1.53	5.17	1.50	3.01	1.48	1.92	1.47	1.29
S1-O2	1.52	1.61	5.85	1.59	4.46	1.57	3.08	1.56	2.65
S1-O3	1.47	1.55	5.50	1.52	3.45	1.50	2.18	1.49	1.82

Table F.2 Experimental[1] and calculated unit cell dimensions (Å) of anhydrous $CuSO_4$ using PBE with different basis setF. With the exception of pob-TZVP (where all elements are modeled with pob-TZVP) copper is modeled with 6-31G(d).

Literature		POB		6-31G(d)		6-31G(2d)		6-31G(3d)	
Axis	Length	Length	% Error	Length	% Error	Length	% Error	Length	% Error
a	8.41	8.59	2.19	8.38	-0.31	8.38	-0.31	8.45	0.45
b	6.71	6.69	-0.24	6.72	0.17	6.68	-0.50	6.75	0.68
c	4.83	4.91	1.60	4.93	1.94	4.87	0.80	4.92	1.71

Table F.3 Experimental[1] and calculated bond lengths (Å) of anhydrous $CuSO_4$ using B3LYP with different basis setF. With the exception of pob-TZVP (where all elements are modeled with pob-TZVP) copper is modeled with 6-31G(d).

Literature		POB		6-31G(d)		6-31G(2d)		6-31G(3d)	
Bond	Length	Bond Length	% Error	Bond Length	% Error	Bond Length	% Error	Bond Length	% Error
Cu1-O1	2.37	2.38	0.47	2.38	0.14	2.37	-0.24	2.42	2.15
Cu1-O2	2.05	2.06	0.29	2.05	-0.15	2.05	-0.13	2.07	0.78
Cu1-O3	1.92	1.93	0.49	1.92	0.09	1.91	-0.18	1.92	0.42
S1-O1	1.45	1.51	4.13	1.49	2.15	1.47	0.90	1.46	0.34
S1-O2	1.52	1.58	3.97	1.56	2.49	1.54	1.22	1.54	1.05
S1-O3	1.47	1.53	4.32	1.50	2.37	1.48	1.06	1.48	0.89

Table F.4 Experimental[1] and calculated unit cell dimensions (Å) of anhydrous $CuSO_4$ using B3LYP with different basis setF. With the exception of pob-TZVP (where all elements are modeled with pob-TZVP) copper is modeled with 6-31G(d).

Literature		POB		6-31G(d)		6-31G(2d)		6-31G(3d)	
Axis	Length	Length	% Error	Length	% Error	Length	% Error	Length	% Error
a	8.41	8.58	2.01	8.44	0.31	8.40	-0.05	8.45	0.53
b	6.71	6.74	0.46	6.76	0.81	6.71	0.04	6.78	1.12
c	4.83	4.89	1.19	4.90	1.39	4.86	0.58	4.91	1.57

Table F.5 Experimental[1] and calculated bond lengths (Å) of anhydrous $CuSO_4$ using PBE with 6-31G(2d) on sulfur and oxygen, while the basis set on copper was varied.

	Literature	6-31G		6-31G(2d)		m-6-31G(d)	
Bond	Length	Bond Length	% Error	Bond Length	% Error	Bond Length	% Error
Cu1-O1	2.37	2.35	-0.76	2.35	-0.91	2.40	1.18
Cu1-O2	2.05	2.03	-0.90	2.02	-1.24	2.06	0.42
Cu1-O3	1.92	1.93	0.54	1.92	0.01	1.96	2.05
S1-O1	1.45	1.48	1.99	1.48	1.91	1.48	1.91
S1-O2	1.52	1.57	3.07	1.57	3.04	1.57	3.14
S1-O3	1.47	1.50	2.16	1.50	2.16	1.50	2.22

Table F.6 Experimental[1] and calculated unit cell dimensions (Å) of anhydrous $CuSO_4$ using PBE with 6-31G(2d) on sulfur and oxygen, while the basis set on copper was varied.

	Literature	6-31G		6-31G(2d)		m-6-31G(d)	
Axis	Length	Length	% Error	Length	% Error	Length	% Error
a	8.41	8.40	-0.11	8.38	-0.35	8.47	0.77
b	6.71	6.68	-0.37	6.67	-0.54	6.75	0.63
c	4.83	4.87	0.82	4.87	0.72	4.92	1.82

Table F.7 Experimental[1] and calculated bond lengths (Å) of anhydrous $CuSO_4$ using B3LYP with 6-31G(2d) on sulfur and oxygen, while the basis set on copper was varied.

Literature		6-31G		6-31G(2d)		m-6-31G(d)	
Bond	Length	Bond Length	% Error	Bond Length	% Error	Bond Length	% Error
Cu1-O1	2.37	2.37	-0.24	2.36	-0.40	2.41	1.43
Cu1-O2	2.05	2.05	0.07	2.04	-0.21	2.06	0.49
Cu1-O3	1.92	1.92	0.35	1.91	-0.15	1.93	0.73
S1-O1	1.45	1.47	0.95	1.47	0.91	1.46	0.69
S1-O2	1.52	1.54	1.26	1.54	1.19	1.55	1.58
S1-O3	1.47	1.48	1.04	1.48	1.04	1.48	1.16

Table F.8 Experimental[1] and calculated unit cell dimensions (Å) of anhydrous $CuSO_4$ using B3LYP with 6-31G(2d) on sulfur and oxygen, while the basis set on copper was varied.

Literature		6-31G		6-31G(2d)		m-6-31G(d)	
Axis	Length	Length	% Error	Length	% Error	Length	% Error
a	8.41	8.42	0.12	8.40	-0.10	8.44	0.43
b	6.71	6.72	0.14	6.71	-0.02	6.75	0.68
c	4.83	4.86	0.64	4.86	0.53	4.91	1.53

Table F.9 Experimental[1] and calculated bond lengths (Å) of anhydrous $CuSO_4$ using PBE with pob-TZVP on one element and 6-31G(2d) on the otherF.

Literature		Cu-pob-TZVP		S-pob-TZVP		O-pob-TZVP	
Bond	Length	Bond Length	% Error	Bond Length	% Error	Bond Length	% Error
Cu1-O1	2.37	2.35	-1.05	2.34	-1.58	2.40	1.08
Cu1-O2	2.05	2.01	-1.71	2.02	-1.37	2.04	-0.33
Cu1-O3	1.92	1.92	0.37	1.91	-0.39	1.93	0.77
S1-O1	1.45	1.48	1.86	1.52	4.56	1.50	3.45
S1-O2	1.52	1.57	3.28	1.60	5.12	1.60	4.81
S1-O3	1.47	1.50	2.18	1.54	4.70	1.52	3.90

Table F.10 Experimental[1] and calculated unit cell dimensions (Å) of anhydrous $CuSO_4$ using PBE with pob-TZVP on one element and 6-31G(2d) on the otherF.

Literature		Cu-pob-TZVP		S-pob-TZVP		O-pob-TZVP	
Axis	Length	Length	% Error	Length	% Error	Length	% Error
a	8.41	8.36	-0.60	8.47	0.69	8.52	1.30
b	6.71	6.66	-0.69	6.67	-0.65	6.71	-0.02
c	4.83	4.86	0.58	4.87	0.79	4.96	2.63

Table F.11 Experimental[1] and calculated bond lengths (Å) of anhydrous $CuSO_4$ using B3LYP with pob-TZVP on one element and 6-31G(2d) on the otherF.

Literature		Cu-pob-TZVP		S-pob-TZVP		O-pob-TZVP	
Bond	Length	Bond Length	% Error	Bond Length	% Error	Bond Length	% Error
Cu1-O1	2.37	2.36	-0.68	2.35	-0.94	2.41	1.35
Cu1-O2	2.05	2.04	-0.31	2.04	-0.37	2.06	0.34
Cu1-O3	1.92	1.91	-0.14	1.91	-0.42	1.92	0.21
S1-O1	1.45	1.47	0.86	1.50	3.42	1.49	2.41
S1-O2	1.52	1.54	1.22	1.57	3.12	1.57	2.89
S1-O3	1.47	1.48	1.10	1.52	3.41	1.51	2.73

Table F.12 Experimental[1] and calculated unit cell dimensions (Å) of anhydrous $CuSO_4$ using B3LYP with pob-TZVP on one element and 6-31G(2d) on the otherF.

Literature		Cu-pob-TZVP		S-pob-TZVP		O-pob-TZVP	
Axis	Length	Length	% Error	Length	% Error	Length	% Error
a	8.41	8.39	-0.22	8.48	0.86	8.51	1.20
b	6.71	6.71	-0.03	6.70	-0.06	6.75	0.68
c	4.83	4.84	0.19	4.86	0.66	4.94	2.19

Table F.13 Experimental[1] and calculated bond lengths (Å) of $CuSO_4 \cdot 3H_2O$ using PBE and B3LYP with 6-31G(d) on copper and hydrogen and 6-31G(2d) on sulfur and oxygen.

Literature		PBE		B3LYP	
Bond	Length	Bond Length	% Error	Bond Length	% Error
Cu1-Owat1	1.96	1.94	-0.87	1.95	-0.36
Cu1-Owat2	1.98	1.97	-0.56	1.97	-0.25
Cu1-Owat3	1.97	1.97	-0.05	1.97	0.00
Cu1-O1	2.45	2.49	1.63	2.47	0.78
Cu1-O2	2.40	2.35	-2.13	2.35	-2.00
Cu1-O3	1.94	1.94	0.05	1.95	0.41
S1-O1	1.48	1.54	4.07	1.49	0.61
S1-O2	1.46	1.51	3.51	1.49	2.47
S1-O3	1.49	1.54	3.23	1.52	1.88
S1-O4	1.47	1.51	2.59	1.49	1.29

Table F.14 Experimental[2] and calculated unit cell dimensions (Å, degrees) of $CuSO_4 \cdot 3H_2O$ using PBE and B3LYP with 6-31G(d) on copper and hydrogen and 6-31G(2d) on sulfur and oxygen.

Literature		PBE		B3LYP	
Axis	Length	Length	% Error	Length	% Error
a	5.59	5.50	-1.66	5.58	-0.24
b	13.03	13.11	0.63	13.02	-0.08
c	7.34	7.36	0.21	7.38	0.52
Angle		Angle	% Error	Angle	% Error
β	97.05	96.24	-0.83	96.17	-0.91

Table F.15 Experimental[3] and calculated unit cell dimensions (Å, degrees) of $CuSO_4 \cdot H_2O$ using PBE and B3LYP with 6-31G(d) on copper and hydrogen and 6-31G(2d) on sulfur and oxygen.

Literature		PBE		B3LYP	
Axis	Length	Length	% Error	Length	% Error
a	5.04	5.01	-0.51	5.02	-0.32
b	5.16	5.18	0.53	5.20	0.78
c	7.57	7.65	1.13	7.64	0.88
Angle		Angle	% Error	Angle	% Error
α	108.39	110.46	1.91	109.98	1.46
β	108.99	108.24	-0.69	108.06	-0.85
γ	90.40	88.31	-2.32	89.01	-1.54

Table F.16 Calculated anhydrous $CuSO_4$ atomic positions (in fractional coordinates) using B3LYP with 6-31G(d) on copper and 6-31G(2d) on sulfur and oxygen. The space group is *Pnma* and a=8.40456, b=7.71152, c=4.86126 and α=β=γ=90°.

Atom Type	x	y	z
Cu	0.00000	0.00000	0.00000
Cu	-0.50000	0.00000	-0.50000
S	0.18210	0.25000	0.45060
O	0.12838	0.25000	-0.26224
O	0.36537	0.25000	0.43749
O	0.13123	0.06519	0.30856
O	0.36877	-0.06519	-0.19144

Table F.17 Calculated $CuSO_4 \cdot H_2O$ atomic positions (in fractional coordinates) using B3LYP with 6-31G(d) on copper and hydrogen and 6-31G(2d) on sulfur and oxygen. The space group is *P-1* and a=8. 50241, b= 5.19702, c= 7.63583and α= 109.975° β= 108.061° γ= 89.012°.

Atom Type	x	y	z
Cu	0.00000	0.00000	0.00000
Cu	0.50000	-0.50000	-0.50000
S	-0.39059	-0.08213	0.24028
O	-0.25656	-0.17601	0.08328
O	0.29529	-0.16481	0.14671
O	-0.33713	0.22367	0.33082
O	-0.28486	-0.21821	0.38536
O	0.14782	0.45240	0.27383
H	-0.00950	-0.47202	0.31857
H	0.18749	-0.42551	0.20800

Table F.18 Calculated $CuSO_4 \cdot 3H_2O$ atomic positions (in fractional coordinates) using B3LYP with 6-31G(d) on copper and hydrogen and 6-31G(2d) on sulfur and oxygen. The space group is *Cc* and a=5.57873, b= 13.01883, c= 7.37945and α =γ=90°, β= 96.166°.

Atom Type	x	y	z
Cu	-0.00414	-0.13273	0.49759
S	0.25221	0.11368	0.41461
O	0.14800	0.16662	0.24077
O	0.31861	-0.19723	0.04753
O	0.46695	0.05323	0.37517
O	0.06824	-0.04480	-0.01710
O	-0.17245	-0.13050	0.24868
O	-0.31525	0.09076	0.07718
O	0.28098	-0.19183	0.40731
H	-0.08777	-0.10440	0.14753
H	-0.24425	-0.19695	0.21356
H	-0.34985	0.08379	0.20459
H	-0.38645	0.02913	0.01216
H	0.43419	-0.16738	0.46976
H	0.29448	-0.18950	0.27505

Table F.19 Calculated B3LYP vibrational frequencies (cm^{-1}), real intensities (km mol^{-1}) and symmetry labels of $CuSO_4$

Frequency	Intensity	Symmetry
80.0	5.4	AU
80.5	0.1	AU
86.9	25.4	BU
127.3	0.0	AU
128.3	56.1	BU
140.0	213.8	AU
152.8	0.0	AU
162.2	205.5	BU
169.1	4.1	BU
190.1	54.7	BU
195.1	0.2	AU
202.3	164.1	BU
225.3	198.7	AU
231.4	215.9	BU
240.6	0.1	AU
244.9	21.0	BU
266.9	92.2	AU
327.6	255.5	AU
342.6	239.6	BU
358.5	0.0	AU
391.4	256.1	BU
484.1	59.3	BU
487.3	54.3	BU
488.2	0.0	AU
488.8	102.2	AU
554.5	235.5	BU
554.8	45.8	AU
583.2	193.0	AU
589.0	38.1	BU
680.9	700.3	BU
702.3	0.0	AU
879.3	3174.1	AU
895.5	135.8	BU
1024.8	1780.2	AU
1025.7	519.8	BU
1089.4	3370.6	BU
1110.3	0.8	AU
1139.0	3980.6	BU

| 1155.3 | 0.8 | AU |

Table F.20 Calculated B3LYP vibrational frequencies (cm^{-1}), real intensities (km mol^{-1}) and symmetry labels of $CuSO_4 \cdot H_2O$

Frequency	Intensity	Symmetry
97.4	25.1	AG
113.0	22.5	AU
133.5	64.7	AU
149.1	118.9	AU
178.4	27.7	AU
201.3	64.2	AU
242.3	59.8	AU
276.9	42.1	AU
298.0	326.1	AU
323.3	85.8	AU
345.9	73.5	AU
413.8	11.4	AU
429.3	55.2	AU
508.4	291.2	AU
539.9	190.3	AU
576.5	159.6	AU
605.5	115.0	AU
663.1	270.2	AU
875.4	1249.3	AU
954.7	495.8	AU
964.8	733.6	AU
1031.5	970.3	AU
1075.9	1840.9	AU
1137.8	1560.9	AU
1673.9	464.0	AU
3330.2	3080.5	AU
3574.8	1813.3	AU

Table F.21 Calculated B3LYP vibrational frequencies (cm^{-1}), real intensities (km mol^{-1}) and symmetry labels of CuSO$_4$·3H$_2$O

Frequency	Intensity	Symmetry
79.9	0.1	A
87.7	19.3	A
94.6	32.3	A
95.9	25.0	A
115.1	13.4	A
116.8	5.2	A
136.3	52.7	A
145.6	39.8	A
147.6	55.4	A
150.8	3.6	A
151.1	25.8	A
167.9	12.1	A
179.2	34.4	A
180.8	52.1	A
203.4	159.6	A
205.8	12.4	A
228.9	75.7	A
229.9	17.8	A
244.2	48.8	A
249.4	3.3	A
260.6	10.7	A
262.5	114.7	A
291.8	11.5	A
295.1	162.4	A
307.1	3.5	A
307.5	44.6	A
394.8	1.9	A
402.3	84.7	A
411.0	0.9	A
428.6	10.1	A
447.5	3.4	A
450.8	22.3	A
480.9	16.3	A
482.4	7.9	A
484.3	11.7	A
495.5	1.0	A
536.7	50.9	A
562.3	2.7	A

564.4	48.2	A
571.0	196.6	A
588.6	4.4	A
595.2	79.1	A
611.3	374.4	A
618.7	219.2	A
627.4	149.2	A
640.6	43.0	A
702.4	879.9	A
744.3	537.8	A
754.2	80.4	A
758.5	609.2	A
785.0	83.2	A
813.5	632.3	A
826.6	109.8	A
842.1	7.1	A
861.1	43.2	A
877.3	233.5	A
946.9	148.8	A
951.1	598.2	A
954.3	3.1	A
968.7	216.1	A
1004.8	305.3	A
1009.5	650.5	A
1025.4	1234.3	A
1054.3	152.4	A
1095.7	493.3	A
1101.2	722.3	A
1118.9	516.2	A
1122.6	386.4	A
1644.1	111.0	A
1652.1	2.2	A
1675.9	312.3	A
1684.1	107.4	A
1708.7	6.5	A
1709.2	128.2	A
3191.7	1554.9	A
3222.7	2608.0	A
3366.3	1824.4	A
3371.7	17.3	A
3389.9	7119.6	A

3397.6	154.1	A
3425.5	473.5	A
3460.7	7.4	A
3526.6	2387.6	A
3532.1	55.7	A
3587.4	885.4	A
3609.0	1143.0	A

Table F.22 Optimized 6-31G(3d) polarization functions for sulfur and oxygen.

Element	First Exponent	Second Exponent	Third Exponent
Oxygen	5.6021	0.8213	0.2427
Sulfur	2.9988	0.6102	0.1065
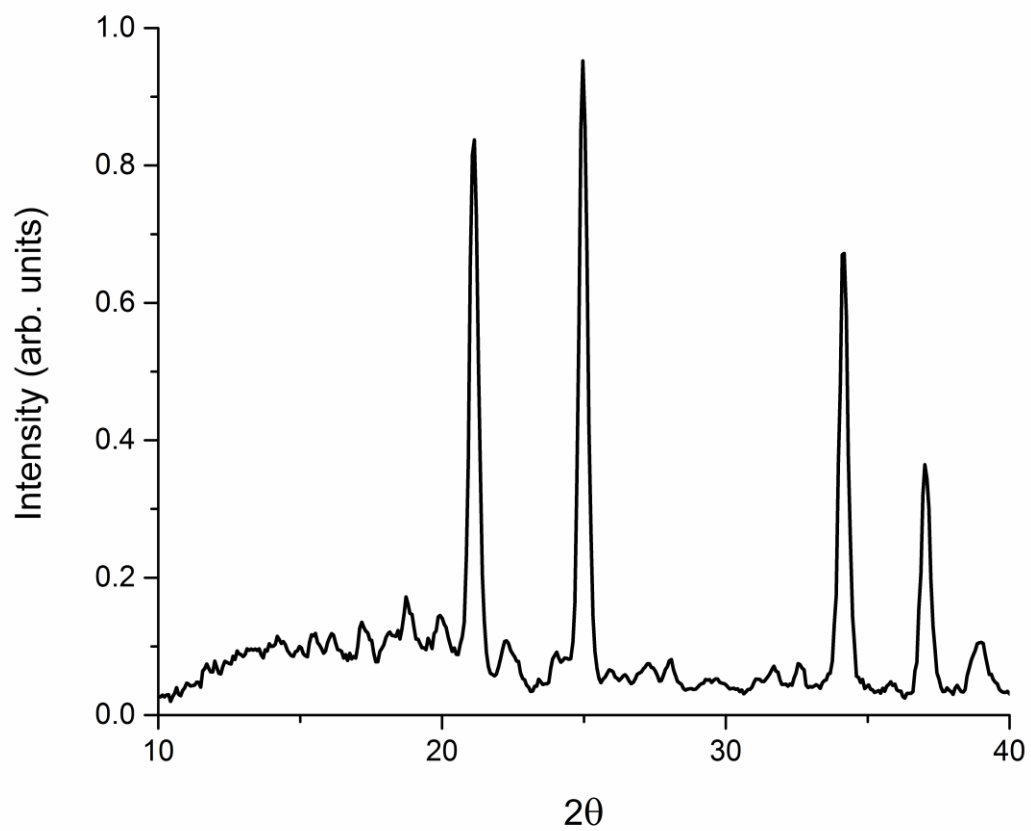
Figure F.1. Powder X-ray diffraction pattern of copper sulfate after 1 week of drying at 473K.
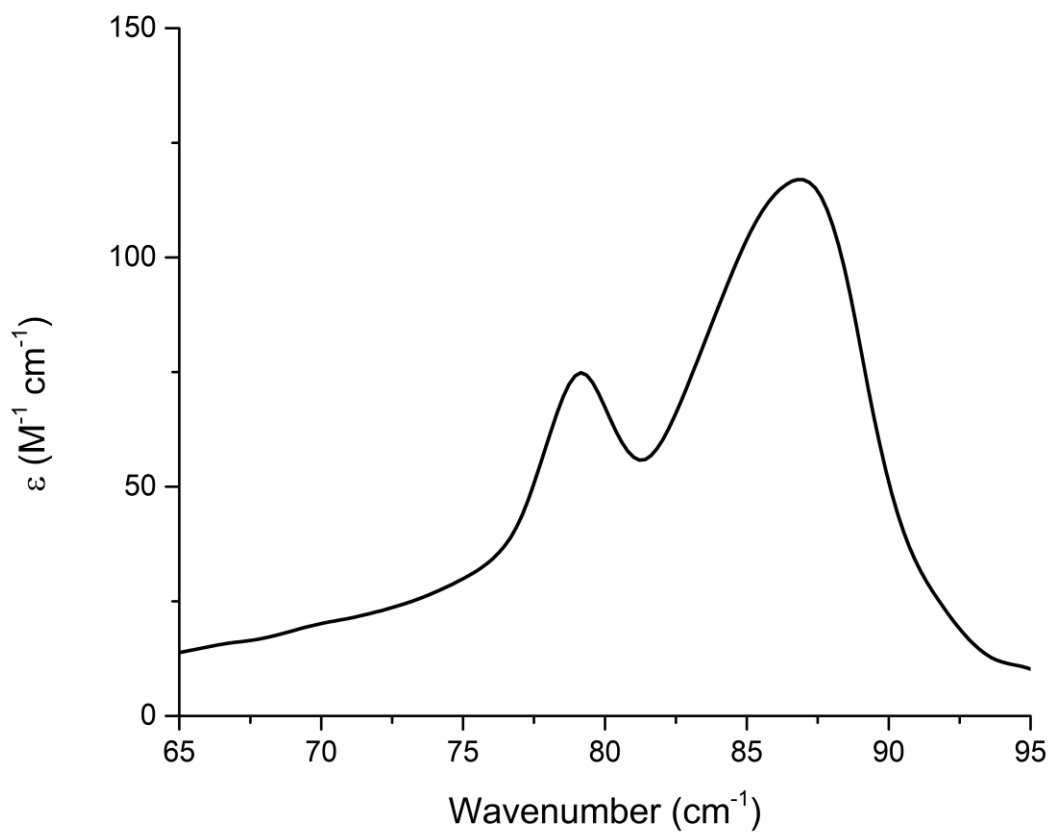
Figure F.2 Terahertz spectrum (77 K) of anhydrous copper sulfate after drying for 1 week.
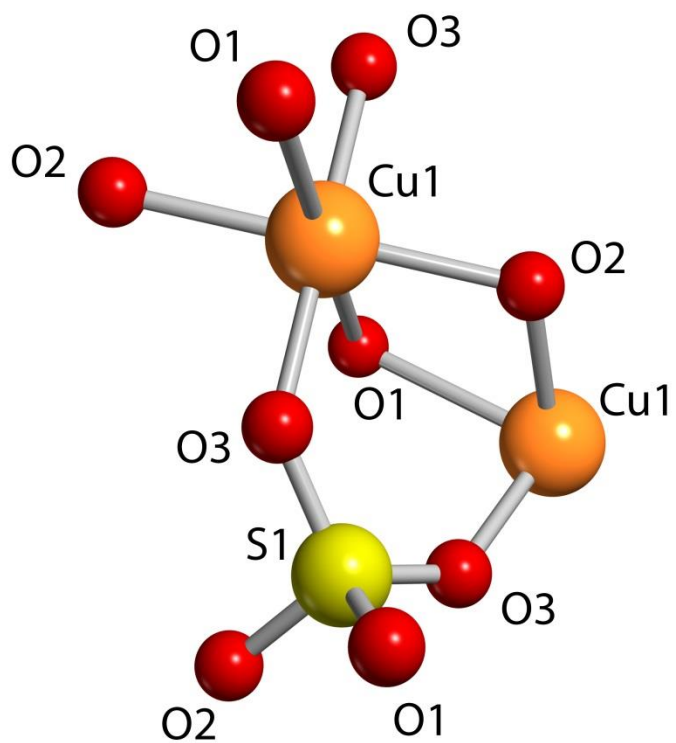
Figure F.3 Labeling scheme for anhydrous $CuSO_4$ used for bond length data.
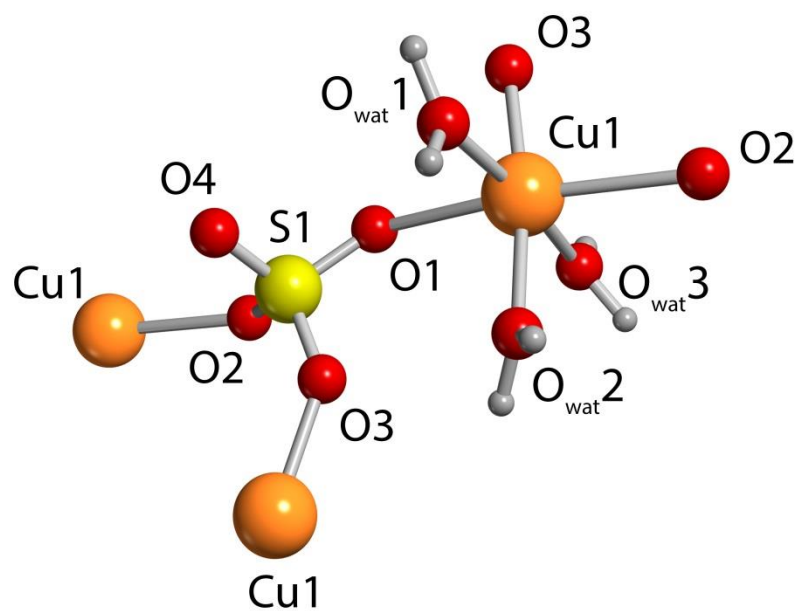
Figure F.4 Labeling scheme for $CuSO_4 \cdot 3H_2O$ used for bond length data.

Table C-1: Experimental single-crystal XRD fractional atomic coordinates for CuSO₄·5H₂O. The crystals have $P\overline{1}$ space group symmetry, and lattice dimensions of: a = 6.106 Å, b = 10.656 Å, c = 5.969 Å, α = 77.332°, β = 82.433°, γ = 72.523°, and V=360.548 Å³

Atom	X/A	Y/B	Z/C
Cu	0.5000	1.0000	0.5000
Cu	0.5000	0.5000	1.0000
S	0.8741	0.5140	0.7140
O	0.7032	0.7469	0.6832
O	0.4804	1.2569	0.5826
O	0.7955	1.0345	0.4056
H	0.8400	1.1540	0.3820
H	0.9110	0.9250	0.3920
O	0.8257	0.4056	0.8488
O	0.3491	0.7900	0.8822
O	0.3522	0.3159	0.9257
H	0.2870	0.2300	0.9790
H	0.2600	0.3800	0.8690
O	1.1154	0.5431	0.6999
O	0.8632	0.3620	0.6264
O	0.1299	0.0679	0.1244
H	0.1650	-0.0760	0.1300
H	0.1940	0.0860	0.1840
H	0.3570	1.3420	0.6120
H	0.5830	1.2990	0.5920
H	0.2290	0.8150	0.8760
H	0.4290	0.8020	0.8070

APPENDIX H: Chapter 12 Supporting Information

List of Figures

Figure H.1. Experimental (black) and calculated (red) PXRD of $FeSO_4 \cdot 4H_2O$.

Figure H.2. Terahertz spectra of $FeSO_4 \cdot 7H_2O$ taken at 225 K (red) and 150 K (blue).

Figure H.3. Experimental PXRD of an $FeSO_4 \cdot 7H_2O$ and $FeSO_4 \cdot 4H_2O$ mixture (black), linear combination of the two individual patterns (red) and the difference (blue).

Figure H.4. Experimental (black) and calculated (red) PXRD of $FeSO_4 \cdot 7H_2O$.

Figure H.5. Experimental (black) and calculated (red) PXRD of $FeSO_4 \cdot 4H_2O$.

Figure H.6. Experimental (black) and calculated (red) PXRD of $Fe_2(SO_4)_3OH \cdot 2H_2O$.

Figure H.7. Terahertz spectrum of $FeSO_4 \cdot H_2O$ taken at 77 K.

Figure H.8. Terahertz spectrum of $Fe_2(SO_4)_3OH \cdot 2H_2O$ at 77 K.

Figure H.9. 78 K terahertz spectrum of $FeSO_4 \cdot 4H_2O$ with standard deviation in the absorption shown.

List of Tables

Table H.1. Simulated IR-active vibrational frequencies (cm^{-1}) and intensities ($km\ mol^{-1}$) of anhydrous $FeSO_4$.

Table H.2. Simulated IR-active vibrational frequencies (cm^{-1}) and intensities ($km\ mol^{-1}$) of $FeSO_4 \cdot H_2O$.

Table H.3. Simulated IR-active vibrational frequencies (cm^{-1}) and intensities ($km\ mol^{-1}$) of $FeSO_4 \cdot 4H_2O$.

Table H.4. Simulated IR-active vibrational frequencies (cm^{-1}) and intensities ($km\ mol^{-1}$) of $FeSO_4 \cdot 7H_2O$.

Table H.5. Simulated IR-active vibrational frequencies (cm^{-1}) and intensities ($km\ mol^{-1}$) of $Fe_2(SO_4)_3OH \cdot 2H_2O$.

Table H.6. Solid-state DFT optimized atomic positions of anhydrous $FeSO_4$, which crystallizes *Cmcm*, with lattice parameters a = 5.251 Å, b = 8.020 Å, c = 6.642 Å.

Table H.7. Solid-state DFT optimized atomic positions of $Fe_2(SO_4)_3OH \cdot 2H_2O$, which crystallizes *P2₁/m*, with lattice parameters a = 6.826 Å, b = 7.404 Å, c = 5.809 Å, β =90.254°.

Figure H.1. Experimental (black) and calculated (red) PXRD of $FeSO_4 \cdot 4H_2O$.

Figure H.2. Terahertz spectra of $FeSO_4 \cdot 7H_2O$ taken at 225 K (red) and 150 K (blue).

Figure H.3. Experimental PXRD of an $FeSO_4 \cdot 7H_2O$ and $FeSO_4 \cdot 4H_2O$ mixture (black), linear combination of the two individual patterns (red) and the difference (blue).

Figure H.4. Experimental (black) and calculated (red) PXRD of $FeSO_4 \cdot 7H_2O$.

Figure H.5. Experimental (black) and calculated (red) PXRD of $FeSO_4 \cdot 4H_2O$.

Figure H.6. Experimental (black) and calculated (red) PXRD of $Fe_2(SO_4)_3OH \cdot 2H_2O$.

Figure H.7. Terahertz spectrum of $FeSO_4 \cdot H_2O$ taken at 77 K.

Figure H.8. Terahertz spectrum of $Fe_2(SO_4)_3OH \cdot 2H_2O$ at 77 K.

Figure H.9. 78 K terahertz spectrum of $FeSO_4 \cdot 4H_2O$ with standard deviation in the absorption shown.

Table H.1. Simulated IR-active vibrational frequencies (cm^{-1}) and intensities ($km\ mol^{-1}$) of anhydrous $FeSO_4$.

Frequency	Intensity
136.89	0.06
150.15	108.13
157.41	41.93
191.81	146.45
209.69	413.13
227.76	0.08
245.50	177.13
305.82	239.99
343.84	205.31
471.56	85.16
472.56	0.00
584.42	83.47
587.20	149.13
663.45	252.24
942.36	268.15
978.20	2179.02
1095.32	1744.22
1142.05	1562.27

Table H.2. Simulated IR-active vibrational frequencies (cm^{-1}) and intensities (km mol^{-1}) of $FeSO_4$ ·H_2O.

Frequency	Intensity
121.63	7.14
127.52	40.94
165.68	130.80
178.83	40.36
191.74	24.47
229.45	226.35
235.39	176.87
277.29	615.90
303.30	52.85
306.78	125.88
325.34	27.15
329.17	90.45
426.25	0.09
527.57	47.17
586.41	300.91
608.21	112.09
613.05	691.31
708.16	231.31
886.72	1954.31
943.45	35.10
961.57	268.56
1042.18	598.61
1086.05	1564.54
1140.22	1759.60
1617.19	167.13
3428.36	1385.50
3449.11	3867.82

Table H.3. Simulated IR-active vibrational frequencies (cm^{-1}) and intensities (km mol^{-1}) of FeSO$_4$ ·4H$_2$O.

Frequncy	Intensity
58.27	8.75
63.54	2.36
68.62	0.00
72.25	11.94
81.75	0.00
85.87	2.96
96.44	4.16
98.26	0.00
101.95	0.00
103.36	24.39
108.00	0.00
115.00	27.16
119.47	4.55
120.56	0.00
123.95	0.00
129.67	0.10
131.77	162.59
132.07	0.20
135.90	48.91
139.19	0.00
147.83	0.01
148.56	94.71
148.72	40.45
153.24	18.68
153.73	0.33
156.94	22.73
158.05	0.01
158.64	0.01
160.54	154.88
164.09	0.00
164.85	0.02
172.12	200.30
173.02	0.01
174.70	3.62
177.39	0.01
184.95	2.17

185.55	39.80
189.46	244.79
189.50	0.01
190.78	0.23
193.94	100.20
195.22	43.78
196.41	0.02
201.05	250.94
206.06	0.00
208.54	0.02
216.17	0.01
218.10	68.23
219.91	0.81
225.32	0.00
228.24	0.01
228.74	5.57
230.60	67.03
236.90	0.00
238.23	0.01
247.24	376.19
247.36	111.03
249.00	0.00
250.15	0.07
250.46	3.54
255.04	27.13
260.36	47.34
261.31	0.01
267.79	137.70
270.35	0.01
310.22	0.23
311.47	85.87
313.29	3.61
314.57	23.30
358.53	192.21
364.82	0.01
369.39	0.04
370.34	0.02
374.04	69.38
377.05	2.41
377.89	141.38
378.69	0.05

407.80	39.68
412.78	46.22
413.06	1.59
417.90	0.02
442.82	80.24
443.42	19.32
443.56	192.75
445.71	0.04
459.59	0.00
462.81	35.24
463.08	542.67
472.00	15.61
476.51	0.00
478.12	244.04
478.59	0.15
497.09	0.01
516.63	0.03
522.85	7.37
524.98	767.98
528.23	19.76
556.30	0.16
567.73	666.68
569.73	1.77
571.63	971.77
585.43	84.33
586.41	0.22
588.80	0.01
590.39	213.03
590.99	45.16
591.48	362.87
592.91	0.01
594.80	0.23
596.33	1075.58
598.56	0.04
598.95	0.03
601.47	132.97
605.93	430.52
610.95	0.03
613.53	0.02
629.26	100.41
639.28	1947.07

648.56	0.01
649.95	175.51
659.46	0.10
677.16	0.00
688.79	0.39
697.07	159.71
712.53	0.01
714.89	140.08
716.47	474.71
718.04	49.79
728.06	0.20
742.49	116.20
748.12	0.01
757.09	191.48
765.37	81.73
769.95	0.29
783.31	44.52
789.89	449.15
792.07	0.92
794.98	0.39
802.97	86.60
805.27	2.95
812.47	47.66
821.32	0.07
822.92	0.08
831.79	4.45
842.55	270.18
871.90	0.00
880.77	97.08
890.40	0.03
893.57	48.76
949.03	11.97
950.05	0.14
950.53	85.36
951.22	0.00
1033.66	3578.84
1034.61	81.23
1046.34	0.00
1048.40	0.02
1073.95	0.00
1082.00	0.03

1085.56	865.60
1087.54	3199.14
1123.55	1827.06
1129.91	0.00
1138.02	25.98
1163.39	0.00
1618.29	0.01
1622.71	370.79
1623.85	3.03
1629.62	92.16
1645.85	415.58
1653.31	0.01
1656.64	50.83
1666.72	0.33
1667.42	181.88
1671.43	12.64
1676.89	278.12
1678.56	0.02
1681.08	0.00
1684.82	538.74
1749.67	0.00
1749.89	0.00
3451.20	4285.27
3452.21	11.22
3459.34	2445.12
3467.56	0.05
3533.42	472.93
3535.08	60.81
3535.19	452.70
3536.23	280.11
3549.86	719.34
3554.76	3537.25
3556.28	10.23
3559.88	61.73
3614.00	0.30
3614.18	0.00
3619.50	386.88
3623.02	2915.85
3623.71	0.00
3623.98	6.44
3639.95	1595.83

3641.58	0.06
3642.35	876.95
3646.76	12.04
3655.39	541.48
3659.75	6647.16
3706.42	0.50
3709.33	1024.14
3714.87	2606.74
3729.42	0.96
3787.12	1576.44
3791.10	516.00
3796.34	0.26
3807.43	0.03

Table H.4. Simulated IR-active vibrational frequencies (cm^{-1}) and intensities (km mol^{-1}) of $FeSO_4$ $\cdot 7H_2O$.

Frequency	Intensity
51.63	2.60
54.01	1.91
58.09	0.00
62.97	12.01
70.42	9.05
77.69	0.29
87.05	5.38
90.99	3.67
94.23	6.70
103.00	0.06
109.62	35.94
117.65	1.80
118.49	3.23
125.94	77.26
128.72	20.09
131.48	43.09
135.02	143.00
140.27	94.72
142.37	140.68
149.56	12.14
149.57	57.79
155.37	73.05
157.17	1.15
163.32	1.73
163.72	51.46
163.93	85.14
173.06	9.38
174.45	39.05
177.59	0.86
185.89	52.44
187.18	96.88
190.82	3.16
192.47	5.05
202.64	11.64

204.30	137.31
205.90	2.30
206.95	56.83
221.09	31.12
222.45	315.06
235.00	221.42
238.31	45.98
239.85	78.91
246.75	65.47
250.43	79.54
262.45	33.93
279.89	120.71
284.71	21.69
286.29	74.52
290.52	147.35
298.66	83.47
301.37	0.09
307.41	21.81
317.90	59.65
351.89	23.85
356.65	361.90
384.57	39.05
389.65	122.21
403.25	11.66
405.51	120.80
417.25	146.14
423.99	168.07
434.84	7.23
437.43	74.16
453.63	38.49
456.67	21.44
461.98	116.88
463.30	6.78
477.16	783.35
483.65	74.48
488.61	257.46
504.28	167.44
557.75	499.76
565.85	26.57
570.34	1098.79
573.70	42.10

577.70	117.63
585.06	104.38
594.71	218.94
599.18	393.71
599.24	595.47
602.77	703.03
607.10	64.62
614.63	766.13
629.19	145.38
642.01	501.69
654.19	594.41
675.60	85.43
676.96	279.35
692.66	196.83
700.06	34.49
717.91	545.30
723.31	91.51
728.64	155.93
737.81	375.96
751.26	587.76
761.66	224.89
762.50	1173.24
768.99	578.21
776.59	239.45
783.91	88.77
790.56	103.20
808.21	807.26
819.11	208.71
842.04	36.72
844.01	37.67
853.56	346.83
864.26	49.37
885.62	226.40
891.01	235.66
896.29	5.32
910.77	187.14
935.94	28.88
938.30	223.05
954.82	877.21
966.33	722.25
1029.70	2865.38

1032.94	20.97
1053.21	192.58
1069.10	1343.64
1071.91	1346.03
1079.19	1.31
1116.24	1482.03
1123.68	940.77
1602.89	53.07
1604.50	311.04
1657.53	72.43
1660.32	482.53
1678.17	265.68
1680.85	16.67
1694.46	67.09
1694.47	55.63
1701.06	23.90
1705.03	223.49
1705.05	100.49
1707.90	167.71
1735.99	289.78
1737.16	97.56
3304.97	5063.57
3319.87	2273.69
3400.38	114.00
3414.15	6948.60
3461.74	931.49
3463.44	10.13
3477.20	5618.75
3480.08	355.64
3514.32	4109.33
3518.63	4162.44
3537.70	6155.89
3543.87	528.38
3548.73	2073.99
3561.39	23.70
3591.22	2400.28
3591.75	1103.93
3594.35	292.36
3594.52	47.16
3609.49	7691.99
3612.09	106.18

3615.76	3215.99
3622.41	323.70
3666.19	503.79
3667.18	1119.07
3680.34	1279.37
3681.46	2585.53
3712.15	2875.65
3714.40	649.02

Table H.5. Simulated IR-active vibrational frequencies (cm^{-1}) and intensities (km mol^{-1}) of Fe$_2$(SO$_4$)$_3$OH·2H$_2$O.

Frequency	Intensity
109.33	16.97
127.94	0.31
138.42	60.39
159.18	110.57
164.11	104.01
174.80	128.52
180.97	82.28
209.85	224.33
244.69	169.78
250.86	12.10
271.10	91.62
294.69	190.06
302.67	269.31
327.93	293.12
433.73	73.11
436.00	16.00
445.62	218.70
471.61	906.30
476.27	209.25
484.40	0.26
524.67	877.07
537.29	527.26
580.01	270.89

590.22	228.46
651.00	0.58
705.51	32.25
723.42	168.13
794.30	833.24
835.60	47.66
909.68	106.28
925.47	2398.45
963.04	268.88
1033.67	334.01
1058.23	2600.35
1128.62	1453.04
1672.50	22.54
1713.74	383.75
3400.72	1816.96
3447.43	3091.65
3453.35	5598.98
3538.55	4434.23
3802.21	342.48

Table H.6. Solid-state DFT optimized atomic positions of anhydrous FeSO$_4$, which crystallizes *Cmcm*, with lattice parameters a = 5.251 Å, b = 8.020 Å, c = 6.642 Å.

	a	b	c
Fe	0.000	0.000	0.000
Fe	0.000	0.000	-0.500
S	0.000	0.350	0.250
O	0.000	0.250	0.064
O	0.000	-0.250	-0.436
O	-0.265	-0.040	0.250

Table H.7. Solid-state DFT optimized atomic positions of $Fe_2(SO_4)_3OH \cdot 2H_2O$, which crystallizes $P2_1/m$, with lattice parameters $a = 6.826$ Å, $b = 7.404$ Å, $c = 5.809$ Å, $\beta = 90.254°$.

	a	b	c
Fe	0.000	0.000	0.000
O	0.180	0.085	0.251
O	0.230	-0.026	-0.222
H	-0.345	0.403	0.174
H	-0.278	-0.421	0.309
S	0.305	0.250	0.285
O	0.378	0.250	-0.475
O	0.468	0.250	0.117
O	0.049	-0.250	0.115
H	0.136	-0.250	0.247
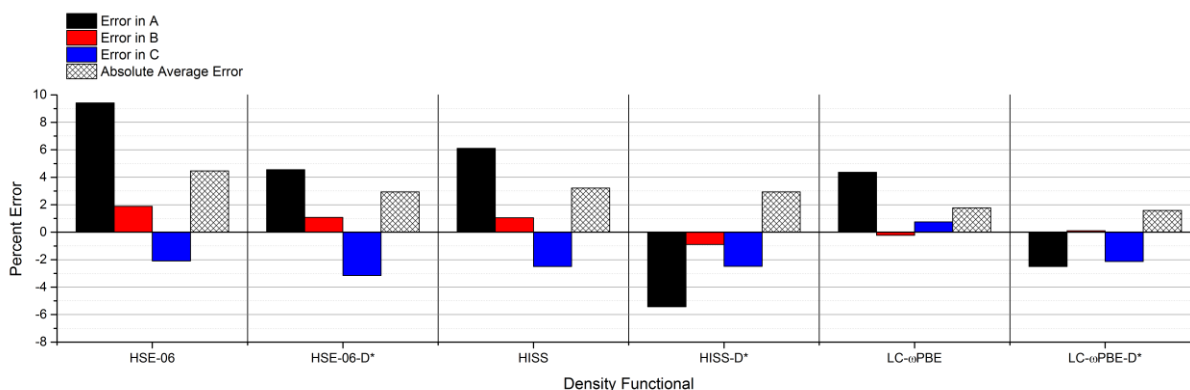
Figure I.1. Effect of including dispersion corrections into the geometry optimization of Me4CP·H$_2$O using the PBE-family of range-corrected functionals.
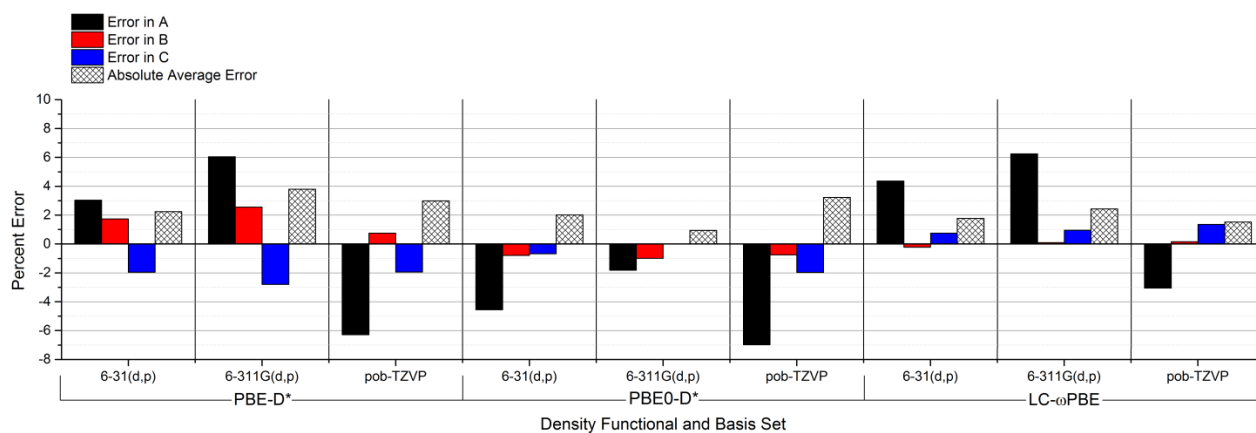
Figure I.2. The role of increased basis set size on the geometry optimization of Me4CP·H$_2$O using the PBE-family of functionals (PBE-D*, PBE0-D*, LC-ωPBE).
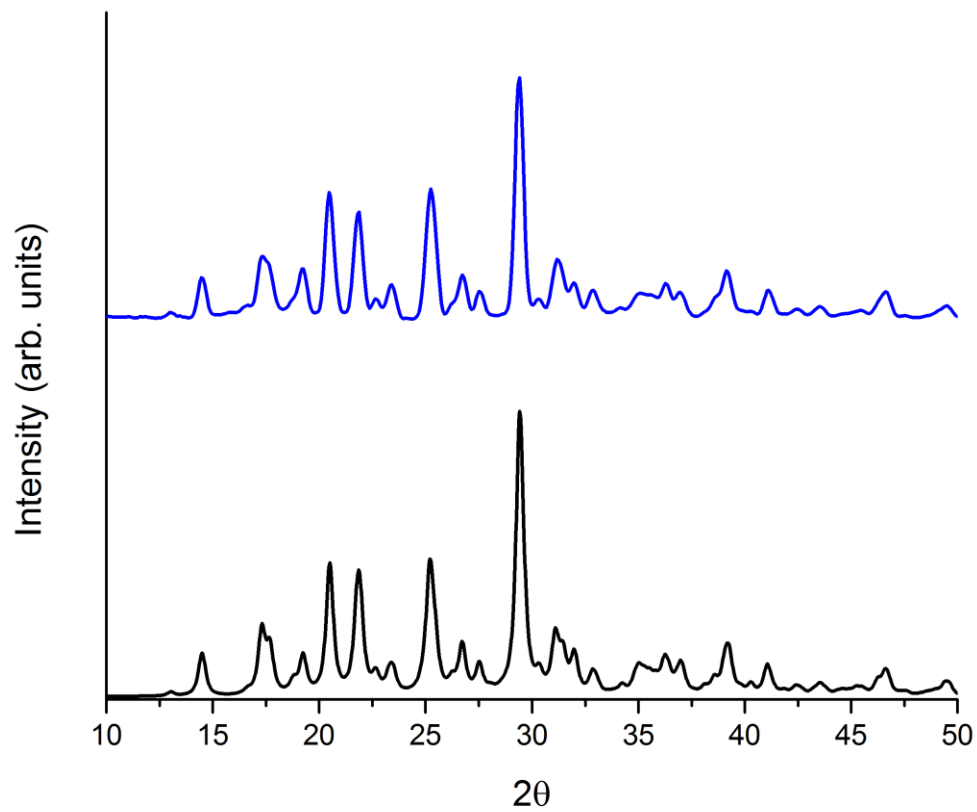
Figure I.3. Experimental 90 K (blue) and simulated (black) powder X-ray diffraction patterns of Me4CP·Cl·H₂O.

APPENDIX J: Chapter 14 Supporting Information.

J.1 Experimental Methods

Powder X-ray diffraction (PXRD) measurements were performed using a Bruker KAPPA APEX DUO diffractometer equipped with a CCD detector. Data was acquired at 90 K using monochromated Cu Kα radiation (λ = 1.54056 Å). The diffraction patters were created using the Bruker APEX2 software package.[1]

Poly-L-proline was purchased from Sigma Aldrich (1 kDa – 10 kDa), and the initial PXRD patterns showed evidence of a largely amorphous material. PP-I was synthesized by dissolving the polyproline in a 1:9 formic acid to *n*-propanol solution and allowing the mixture to stand for three days, after which an equal volume of diethyl ether was added and subsequently allowed to evaporate. Upon evaporation, ethanol was added and the solution was stirred under gentle heating, resulting in obtaining microcrystalline PP-I. PP-II was synthesized by dissolving polyproline in a 1:3 formic acid to water mixture, and allowing the solution to evaporate while stirring.

Samples were prepared for terahertz spectroscopy by mixing poly-L-proline with polytetrafluoroethylene (PTFE, ~3.5 % w/w) and pressing into13mm diameter pellets. The terahertz absorption spectra were obtained using a commercial Advantest TAS7500TS spectrometer in the 20-150 cm^{-1} range. The broadband terahertz radiation was generated using an Advantest TAS1130 source module that contained a lithium niobate ($LiNbO_3$) nonlinear crystal, and was detected using an Advantest TAS1230 detector module.

The quantum mechanical simulations were performed using a developmental version of the CRYSTAL14 software package.[2] The all-electron split-valence double-ζ def2-SVP[3] basis set and Becke-3-Lee-Yang-Parr[4] (B3LYP) hybrid density functional were employed for all calculations. London dispersion forces were modeled using the DFT-D3 dispersion method,[5] and basis set superposition error (BSSE) was dynamically accounted for through the geometrical counterpoise (gCP) scheme.[6] Vibrational normal mode eigenvectors and eigenvalues were calculated numerically within the harmonic approximation, and infrared intensities were determined using the Berry phase method.[7-9] The energy convergence criteria were set to $\Delta E \leq 10^{-8}$ and 10^{-10} hartree for the optimization and frequency calculations, respectively.

J.2 PP-I Structure Determination Details

The structure of PP-I was determined by first building initial models using the previously published interatomic distances and angles,[10] followed by arranging the resulting helices in various configurations. The proposed geometry solutions were optimized using solid-state DFT without symmetry constraints, other than the translational symmetry of the periodic model. Upon complete relaxation, only two structures were energetically feasible, with the major difference between them being the parallel or antiparallel arrangements of neighboring polyproline helices as packed in the crystals. The polyproline strands exhibit a net dipole oriented along the helical axis, and while an antiparallel orientation of the adjacent dipoles may suggest a more stable crystal structure, the large diameter of the helices negates a large portion of that stabilization energy. The preference for the all-parallel arrangement is related to it being able to pack together more efficiently, leading to a larger stabilization by London dispersion forces. Beyond energies,

the calculated PXRD patterns of the two potential forms showed that the parallel structure was clearly in superior agreement with the experimental PXRD pattern (**Figure J.1**).
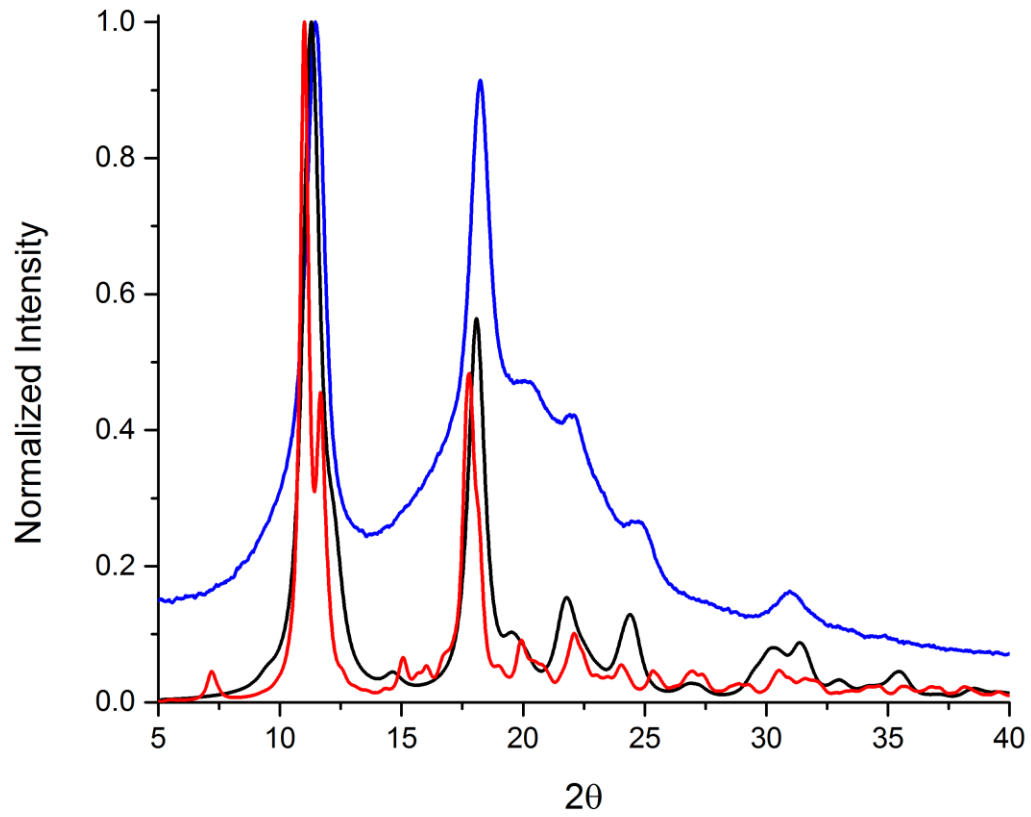
Figure J.1. Experimental PXRD pattern of PP-I (blue) with the accurate helical orientation (black) and incorrect orientation (red) patterns shown.

J.3 Gibbs Free Energy Curves

The solid-state vibrational calculations can be used to determine the temperature-dependent Gibbs free energy curves for the two forms, with the intersection of the two curves representing the transition temperature for phase stability. Plots of the Gibbs free energy for the two poly-L-proline helices are shown in **Figure J.2**, and the crossing temperature was found to be 557.39 K, nearly identical (yet slightly higher) to the experimentally determined decomposition temperature of polyproline (553 K). This result is consistent with the two forms not being able to undergo isomerization in the solid-state, and that such change is only accessible via solution phase processes. However those studies also found that these barriers could be lowered through external stabilization by solvent interactions, specifically related to the PP-II geometry offering greater hydrogen bond acceptor accessibility compared to the tightly wound PP-I.[11] Here, the energy analysis showed that PP-I is stabilized internally to a larger degree than PP-II by London dispersion forces (~16% larger London dispersion energies than PP-II) while PP-II is stabilized greater externally by both dispersion and dipole-dipole interactions (~6% and 17%, respectively).
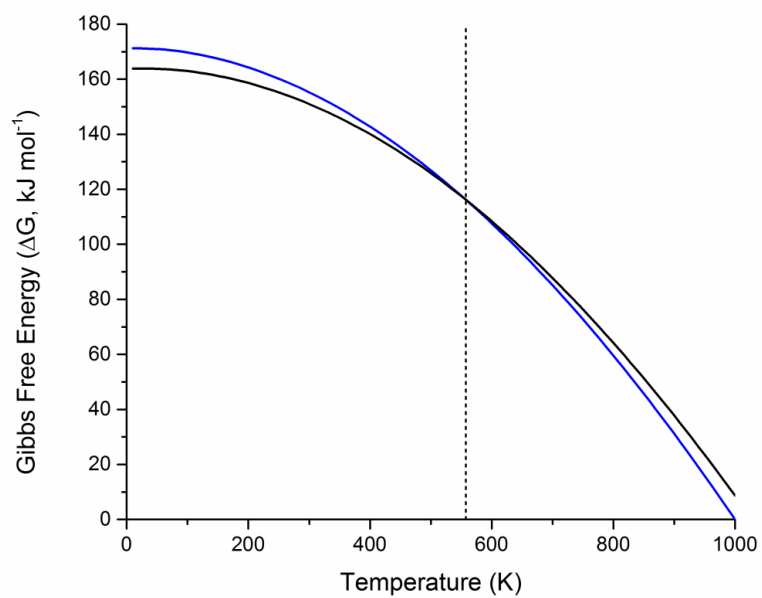
Figure J.2. Gibbs free energy curves for PP-I and PP-II (blue and black, respectively). The dashed line represents the temperature where the two curves intersect.
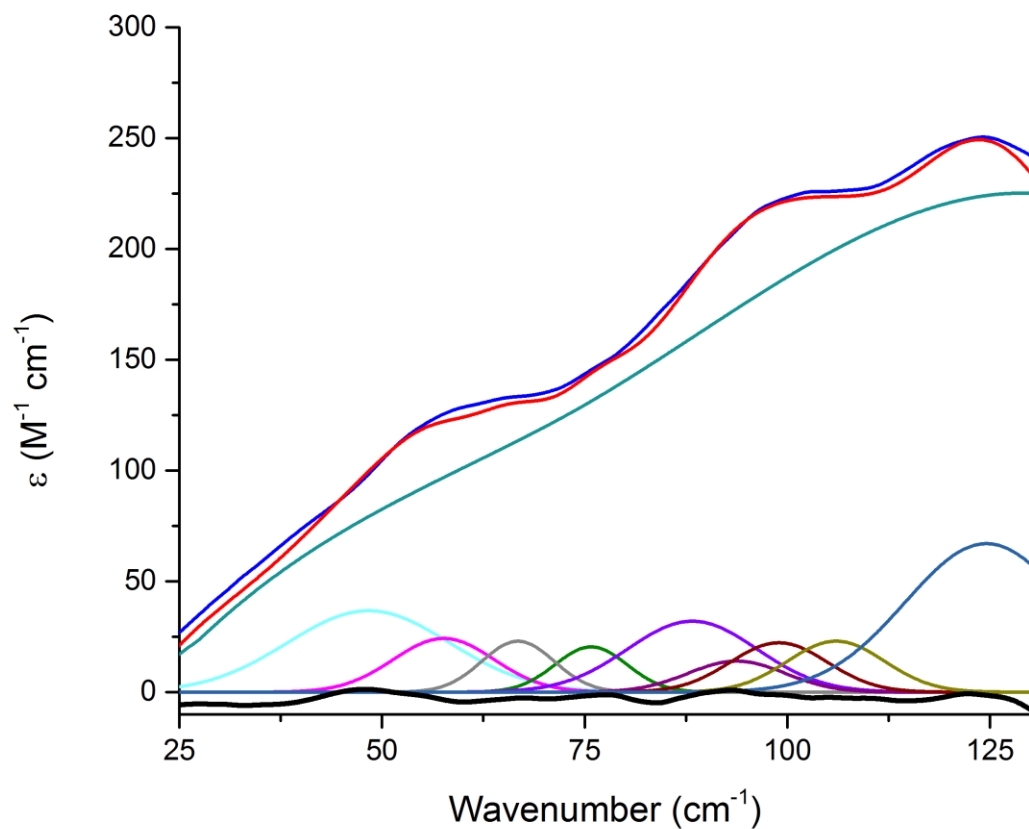
Figure J.3. Spectral deconvolution result of PP-I. The experimental spectrum (blue), result of calculated fit (red), baseline (green), observed-minus-calculated residual (black) and primitive functions (remainder) are shown.
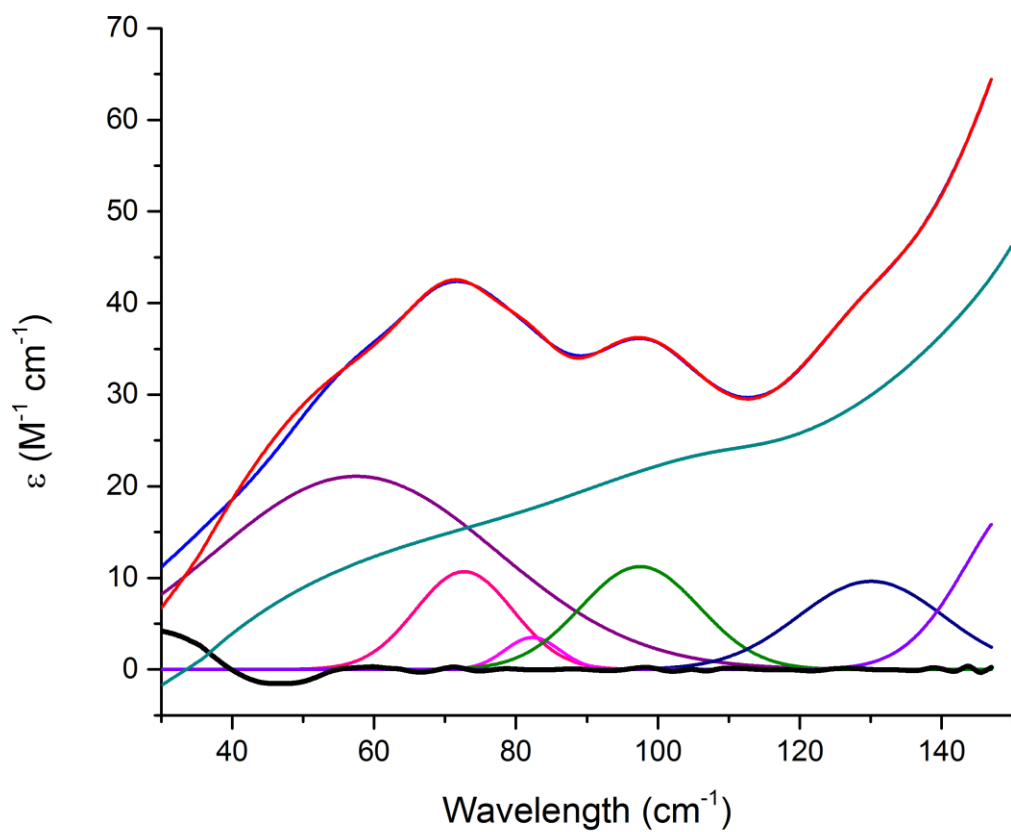
Figure J.4. Spectral deconvolution result of PP-II. The experimental spectrum (blue), result of calculated fit (red), baseline (green), observed-minus-calculated residual (black) and primitive functions (remainder) are shown.

Table J.1 Frequencies (cm^{-1}) of the observed absorptions in the spectra of PP-I and PP-II.

PP-I	PP-II
26.3	72.7
30.7	82.3
48.3	98.1
57.6	130.1
66.6	152.4
75.8	
77.2	
88.3	
93.7	
99.0	
106.0	

Table J.2. DFT-calculated frequencies (cm^{-1}) and intensities (km/mol) for PP-I and PP-II.

PP-I		PP-II	
Frequency	Intensity	Frequency	Intensity
9.41	0.01	55.75	11.35
18.26	0.89	74.67	1.55
25.43	5.60	75.24	16.83
27.57	2.02	100.10	15.67
33.59	1.28	126.35	2.68
38.59	12.07	131.68	7.82
40.30	6.01	144.49	240.40
46.73	0.86	170.75	0.85
52.19	1.81	190.25	0.22
55.24	30.94	191.24	11.49
59.96	3.58	226.10	2.84
62.78	30.90	260.22	7.59
63.06	2.34		
68.15	0.20		
74.01	0.01		
74.06	6.29		
77.78	1.40		
82.37	6.38		
89.09	56.16		
96.61	8.68		
99.48	14.50		
102.33	32.79		
103.00	2.28		
103.72	11.83		
107.12	6.53		
111.23	18.62		
112.60	2.29		
114.10	0.80		
114.80	8.60		
116.84	12.54		
120.51	2.89		
123.18	46.57		
124.60	34.75		
128.82	2.31		
131.02	8.84		
131.31	6.38		
133.43	0.01		
139.52	0.01		

140.63	0.98		
141.77	1.29		
158.37	122.28		

J.5 References

(1)   Version 2011.8-0 ed.; Bruker-AXS Inc.: Madison, WI, 2011, 2011.

(2)   Dovesi, R.; Orlando, R.; Erba, A.; Zicovich-Wilson, C. M.; Civalleri, B.; Casassa, S.; Maschio, L.; Ferrabone, M.; De La Pierre, M.; D'Arco, P.*et al. Int. J. Quantum Chem* **2014**, *114*, 1287.

(3)   Weigend, F.; Ahlrichs, R. *Phys. Chem. Chem. Phys.* **2005**, *7*, 3297.

(4)   Becke, A. D. *J. Chem. Phys.* **1993**, *98*, 5648.

(5)   Grimme, S.; Antony, J.; Ehrlich, S.; Krieg, H. *J. Chem. Phys.* **2010**, *132*, 154104.

(6)   Brandenburg, J. G.; Alessio, M.; Civalleri, B.; Peintinger, M. F.; Bredow, T.; Grimme, S. *J. Phys. Chem. A* **2013**, *117*, 9282.

(7)   Noel, Y.; Zicovich-Wilson, C. M.; Civalleri, B.; D'Arco, P.; Dovesi, R. *Phys. Rev. B.* **2001**, *65*, 014111.

(8)   Pascale, F.; Zicovich-Wilson, C. M.; López Gejo, F.; Civalleri, B.; Orlando, R.; Dovesi, R. *J. Comput. Chem.* **2004**, *25*, 888.

(9)   Zicovich-Wilson, C. M.; Pascale, F.; Roetti, C.; Saunders, V. R.; Orlando, R.; Dovesi, R. *J. Comput. Chem.* **2004**, *25*, 1873.

(10)   Traub, W.; Shmueli, U. *Nature* **1963**, *198*, 1165.

(11)   Moradi, M.; Babin, V.; Roland, C.; Darden, T. A.; Sagui, C. *PNAS* **2009**, *106*, 20746.

J.6 PP-I CIF

data_PPF1

_symmetry_cell_setting   monoclinic

_symmetry_space_group_name_H-M   'P 21'

_symmetry_Int_Tables_number   4

loop_

_symmetry_equiv_pos_site_id

_symmetry_equiv_pos_as_xyz

1 x,y,z

2 -x,1/2+y,-z

_cell_length_a   9.14900228

_cell_length_b   18.92718359

_cell_length_c   9.20299131

_cell_angle_alpha   90.000000

_cell_angle_beta   59.278284

_cell_angle_gamma   90.000000

_cell_volume   1369.98

loop_

_atom_site_label

_atom_site_type_symbol

_atom_site_fract_x

_atom_site_fract_y

_atom_site_fract_z

C C 0.8276375452806 0.43245863269917 1.07427969807817

C C 1.1671727700399 0.2364208856348 0.998002896864204

C C 0.94135138124756 0.0363137301487 0.91112132967896

C C 1.05480162801772 0.3304200868807 0.8175092825812

C C 0.8730866036357 0.1408632077258 1.1801370574150

C C 0.90449522689719 0.44795530467499 0.8832043727942

C C 1.01309923830554 0.2569669674838 1.1726234188941

C C 1.1357585082993 0.0501762507332 0.8196365371131

C C 1.2138516564414 0.3482577722380 0.8297272650316

C C 0.8240883632562 0.1553606442864 1.04477703981188

O O 0.8779139810799 0.504364611227709 0.8337901888258

O O 1.007357712829828 0.3147227104041 1.2375942732200

O O 1.19723170758393 0.1055625213712 0.7413537947221

O O 1.2940622773011 0.40336516104575 0.7691227599336

O O 0.7576595269640 0.2119922932710 1.04396415182152

N N 0.992661556528396 0.3943396426017 0.7761453666150

N N 0.8894273811567 0.2076293616559 1.2527616798926

N N 0.7665455606165 0.4976236786232 1.1746557427575

N N 1.2630678468038 0.2993546429568 0.90427209694193

N N 0.8481418128764 0.1026705815847 0.93494018386091

C C 1.09923473109778 0.2821139015106 0.6644808310625

C C 0.7235817463467 0.1037425832480 1.3355964993496

C C 0.6621439692241 0.3885630271675 1.1420186974714

C C 1.3011050899917 0.1946003686335 1.01896032453379

C C 0.8942787845655 -0.007419581428498 0.7981922966570

C C 1.1686404704888 0.3342757636982 0.5157098721598

C C 0.6097269827730 0.1659329580773 1.4397686440886

C C 0.5277699333729 0.4457483447857 1.1813635139110

C C 1.4075526005321 0.2530739961393 1.03693073969087

C C 0.8763183854358 0.04925265902031 0.6884910550431

C C 1.06257757039571 0.40177366346472 0.5929116876803

C C 0.7385961984475 0.2227019914435 1.4199119972537

C C 0.5802469223522 0.5053629586346 1.2585153424986

C C 1.4165741988589 0.3109233383060 0.91544155247017

C C 0.7939694832097 0.1116434956715 0.8100962175013

H H 1.1391228468087 0.45043504245328 0.5464530353972

H H 0.6941232520670 0.2773048645563 1.4243352690186

H H 0.5470241117752 0.5584338309247 1.2348769363485

H H 1.4173782973361 0.3650145672824 0.95986522580201

H H 0.8344564791221 0.1635532200313 0.7474565633186

H H 0.95745415557583 0.40645148287619 0.5669565803631

H H 0.7727737904387 0.2184212813001 1.5192538727143

H H 0.5214303590035 0.4990176415700 1.3970202966142

H H 1.5315238908982 0.3059264245446 0.7879992064182

H H 0.6533022220162 0.1098829780856 0.8751978179397

H H 1.3044669746993 0.3447671976090 0.4678708896482

H H 0.5343268071703 0.1847919891317 1.3845201944830

H H 0.5359324682274 0.4641320931717 1.06343666614977

H H 1.3416415298372 0.2733155449394 1.1677181506404

H H 1.002192181090264 0.06409876227970 0.5809843162308

H H 1.1559171005692 0.3148248423114 0.4098883113729

H H 0.3971186266447 0.4272209494475 1.2671257906332

H H 1.5339609950563 0.2349775148737 1.008158011111633

H H 0.7983098727869 0.03146661563685 0.6357404514697

H H 1.1871370732076 0.2387963963096 0.6475208156602

H H 0.6587682835822 0.06413846292927 1.3002134291012

H H 0.6709913335894 0.3480902732780 1.05202403406696

H H 1.2439650593403 0.1568681815720 1.1252043819232

H H 0.98774111826230 -0.04895049062403 0.7253398154170

H H 0.97995820897862 0.2577171013600 0.6863822499552

H H 0.7754642143141 0.07563573546941 1.4047044350839

H H 0.6359114172256 0.3606640031814 1.2584519224108

H H 1.3790654215499 0.1635289845748 0.90257541030963

H H 0.7717823959523 -0.03417715612880 0.8806352177964

H H 0.91921161524663 0.40492833227900 1.09849228880581

H H 1.1275285402105 0.2053877508637 0.92285476034934

H H 0.8954357390236 0.0094343162874 1.03313286726151

H H 0.95411620870060 0.3058475135279 0.93449617466033

H H 0.98969352388348 0.1088941502267 1.1300536110441

H H 0.5186019327900 0.1521014462489 1.5723431447493

#END

J.6 PP-2 CIF

data_PPFII

_symmetry_cell_setting   trigonal

_symmetry_space_group_name_H-M   'P 32'

_symmetry_Int_Tables_number   145

loop_

_symmetry_equiv_pos_site_id

_symmetry_equiv_pos_as_xyz

1 x,y,z

2 -y,x-y,2/3+z

3 -x+y,-x,1/3+z

_cell_length_a   6.64326727

_cell_length_b   6.64326727

_cell_length_c   9.60125787

_cell_angle_alpha   90.000000

_cell_angle_beta   90.000000

_cell_angle_gamma   120.000000

_cell_volume   366.963

loop_

_atom_site_label

_atom_site_type_symbol

_atom_site_fract_x

_atom_site_fract_y

_atom_site_fract_z

C C 0.01596654385846 -0.007103170474542 0.09395528235756

N N -0.02686067948053 -0.1706193665484 0.1922607731086

O O -0.07315512385516 0.1170986949121 0.09740575607850

C C 0.1951099771137 0.02527503386097 -0.01941264119432

C C 0.4441082003882 0.1959364471137 0.03256508878296

C C 0.4757473164179 0.4361945058927 -0.003679655052814

C C 0.06113485586220 -0.3355421149927 0.1944405614581

H H 0.2532290052619 -0.2436429620236 0.1939473463811

H H -0.0007723785251607 -0.4512033161828 0.1025257418070

H H 0.5704872176947 0.1631686350255 -0.02261389932837

H H 0.4650527450147 0.1748761110167 0.1445206847866

H H 0.1728693246817 -0.1441752125955 -0.05097171699718

H H 0.65859204844703 0.5699140762710 -0.0194662682060

H H 0.40430435200609 0.4956067996423 0.0803144126849

N N 0.1706193665484 0.14375868706787 -0.1410725602247

C C -0.16983494325273 -0.1951099771137 0.31392069213901

C C -0.0395528105252 -0.4757473164179 0.329653678280519

C C 0.3355421149927 0.39667697085490 -0.1388927718752

#END

APPENDIX K: Chapter 15 Supporting Information

Table K.1 Calculated vibrational frequencies and mode descriptions for the two L-glutamic acid polymorphs.

α-GLU		β-GLU	
Freq	Mode Description	Freq	Mode Description
1.923	Rotation about b	1.229	Rotation about b
2.070	Translation in c	1.958	Rotation about a
2.120	Rotation about bc	2.050	Rotation about c
2.284	Rotation about a	2.388	Torsion of CH_2-CH bond
2.507	Rotation about c	2.504	Torsional bending of COO⁻ and backbone
2.532	Rotation about b	2.723	Torsion of COOH about the C-C bond
2.613	Rotation about b	2.816	Torsional bending about the backbone
2.713	Torsional bending of COO⁻ and backbone	2.923	Torsion of CH_2-CH bond
2.840	Torsion of COOH about the C-C bond	3.075	Torsion of COO⁻ about the C-C bond
2.988	Torsion of COO⁻ about the C-C bond	3.313	Torsion about the CH_2-CH_2 bond
3.071	Torsional bending about the backbone	3.350	Torsion about the backbone with COO⁻ and COOH rotation
3.160	Torsion of COO⁻ and COOH about the C-C bonds	3.428	Torsion about the backbone with COO⁻ and COOH rotation
3.330	Torsion of COO⁻ and COOH about the C-C bonds	3.536	Torsion about the CH_2-CH_2 bond
3.600	Torsion about the CH_2-CH_2 bond	3.584	Torsion of COOH about the C-C bond
3.820	Torsion about the backbone with COO⁻ and COOH rotation	3.706	Torsion about the backbone

Table K.2. Relative energetic values for the two studied glutamic acid polymorphs (kJ/mol).

	PBE			PBE-D3		
	Electronic	Molecular Conformational	Cohesive	Electronic	Molecular Conformational	Cohesive
α-GLU	0	0	0	0	0	0
β-GLU	+8.23	+3.97	+4.26	+3.69	+4.83	-1.14

K.1 α-GLU Experimental CIF

data_AlphaGLu

_audit_creation_method   SHELXL-2014/6

_chemical_name_systematic   ?

_chemical_name_common   ?

_chemical_melting_point   ?

_chemical_formula_moiety   ?

_chemical_formula_sum

 'C5 H9 N O4'

_chemical_formula_weight   147.13

loop_

 _atom_type_symbol

 _atom_type_description

 _atom_type_scat_dispersion_real

 _atom_type_scat_dispersion_imag

 _atom_type_scat_source

 'C' 'C'   0.0033   0.0016

 'International Tables Vol C Tables 4.2.6.8 and 6.1.1.4'

 'H' 'H'   0.0000   0.0000

 'International Tables Vol C Tables 4.2.6.8 and 6.1.1.4'

 'N' 'N'   0.0061   0.0033

 'International Tables Vol C Tables 4.2.6.8 and 6.1.1.4'

'O' 'O' 0.0106 0.0060

'International Tables Vol C Tables 4.2.6.8 and 6.1.1.4'

_space_group_crystal_system   orthorhombic

_space_group_IT_number   19

_space_group_name_H-M_alt   'P 21 21 21'

_space_group_name_Hall   'P 2ac 2ab'

_shelx_space_group_comment

;

The symmetry employed for this shelxl refinement is uniquely defined

by the following loop, which should always be used as a source of

symmetry information in preference to the above space-group names.

They are only intended as comments.

;

loop_
 _space_group_symop_operation_xyz
 'x, y, z'
 '-x+1/2, -y, z+1/2'
 '-x, y+1/2, -z+1/2'
 'x+1/2, -y+1/2, -z'

_cell_length_a   7.0120(6)

_cell_length_b   8.7622(7)

_cell_length_c   10.2729(8)

_cell_angle_alpha   90

_cell_angle_beta   90

_cell_angle_gamma   90

_cell_volume   631.17(9)

_cell_formula_units_Z   4

_cell_measurement_temperature   95(2)

_cell_measurement_reflns_used   ?

_cell_measurement_theta_min   ?

_cell_measurement_theta_max   ?

_exptl_crystal_description   Block

_exptl_crystal_colour   Colorless

_exptl_crystal_density_meas   ?

_exptl_crystal_density_method   ?

_exptl_crystal_density_diffrn   1.548

_exptl_crystal_F_000   312

_exptl_transmission_factor_min   ?

_exptl_transmission_factor_max   ?

_exptl_crystal_size_max   0.12

_exptl_crystal_size_mid   0.08

_exptl_crystal_size_min   0.06

_exptl_absorpt_coefficient_mu   0.135

_shelx_estimated_absorpt_T_min   ?

_shelx_estimated_absorpt_T_max   ?

_exptl_absorpt_correction_type   multi-scan

_exptl_absorpt_process_details   'SADABS V2012/1 (Bruker AXS Inc.)'

_diffrn_ambient_temperature   90(2)

_diffrn_radiation_wavelength   0.71073

_diffrn_radiation_type   MoK\a

_diffrn_radiation_source   'fine-focus sealed tube'

_diffrn_radiation_monochromator   graphite

_diffrn_measurement_device_type   'Bruker APEX-II CCD'

_diffrn_measurement_method   '\f and \w scans'

_diffrn_detector_area_resol_mean   ?

_diffrn_reflns_number   25388

_diffrn_reflns_av_unetI/netI   0.0261

_diffrn_reflns_av_R_equivalents   0.0460

_diffrn_reflns_limit_h_min   -10

_diffrn_reflns_limit_h_max   10

_diffrn_reflns_limit_k_min   -13

_diffrn_reflns_limit_k_max   13

_diffrn_reflns_limit_l_min   -15

_diffrn_reflns_limit_l_max   15

_diffrn_reflns_theta_min   3.056

_diffrn_reflns_theta_max   33.145

_diffrn_reflns_theta_full   25.242

_diffrn_measured_fraction_theta_max   0.991

_diffrn_measured_fraction_theta_full   1.000

_diffrn_reflns_Laue_measured_fraction_max   0.991

_diffrn_reflns_Laue_measured_fraction_full   1.000

_diffrn_reflns_point_group_measured_fraction_max   0.986

_diffrn_reflns_point_group_measured_fraction_full 1.000

_reflns_number_total   2372

_reflns_number_gt   2132

_reflns_threshold_expression   'I > 2\s(I)'

_reflns_Friedel_coverage   0.708

_reflns_Friedel_fraction_max   0.978

_reflns_Friedel_fraction_full   1.000

_reflns_special_details

;

Reflections were merged by SHELXL according to the crystal

class for the calculation of statistics and refinement.

_reflns_Friedel_fraction is defined as the number of unique

Friedel pairs measured divided by the number that would be

possible theoretically, ignoring centric projections and

systematic absences.

;

_computing_data_collection   'Bruker APEX2 (Bruker, 2011)'

_computing_cell_refinement   'SAINT V8.30C (Bruker AXS Inc., 2013)'

_computing_data_reduction   'SAINT V8.30C (Bruker AXS Inc., 2013)'

_computing_structure_solution   'SHELXL-2013 (Sheldrick, 2013)'

_computing_structure_refinement   'SHELXL-2013 (Sheldrick, 2013)'

_computing_molecular_graphics   'CrystalMaker (Palmer, 2010)'

_computing_publication_material   'Bruker SHELXTL (Bruker, 2011)'

_refine_special_details   ?

_refine_ls_structure_factor_coef Fsqd

_refine_ls_matrix_type   full

_refine_ls_weighting_scheme   calc

_refine_ls_weighting_details

'w=1/[\s^2^(Fo^2^)+(0.0438P)^2^+0.0868P] where P=(Fo^2^+2Fc^2^)/3'

_atom_sites_solution_primary   ?

_atom_sites_solution_secondary   ?

_atom_sites_solution_hydrogens   difmap

_refine_ls_hydrogen_treatment   refall

_refine_ls_extinction_method   none

_refine_ls_extinction_coef   .

_refine_ls_abs_structure_details

;

 Flack x determined using 835 quotients [(I+)-(I-)]/[(I+)+(I-)]

 (Parsons, Flack and Wagner, Acta Cryst. B69 (2013) 249-259).

;

_refine_ls_abs_structure_Flack   -0.1(3)

_chemical_absolute_configuration ?

_refine_ls_number_reflns   2372

_refine_ls_number_parameters   127

_refine_ls_number_restraints   0

_refine_ls_R_factor_all   0.0431

_refine_ls_R_factor_gt   0.0335

_refine_ls_wR_factor_ref   0.0788

_refine_ls_wR_factor_gt   0.0739

_refine_ls_goodness_of_fit_ref   1.047

_refine_ls_restrained_S_all   1.047

_refine_ls_shift/su_max   0.001

_refine_ls_shift/su_mean   0.000

loop_

 _atom_site_label

 _atom_site_type_symbol

 _atom_site_fract_x

 _atom_site_fract_y

 _atom_site_fract_z

 _atom_site_U_iso_or_equiv

 _atom_site_adp_type

 _atom_site_occupancy

 _atom_site_site_symmetry_order

 _atom_site_calc_flag

 _atom_site_refinement_flags_posn

 _atom_site_refinement_flags_adp

 _atom_site_refinement_flags_occupancy

 _atom_site_disorder_assembly

 _atom_site_disorder_group

O001 O 0.87535(17) 0.59616(11) 0.58514(10) 0.0159(2) Uani 1 1 d . . . . .

O002 O 0.67471(15) 0.56552(12) 0.87814(9) 0.0145(2) Uani 1 1 d . . . . .

O003 O 0.70556(16) 0.76389(13) 1.01470(10) 0.0155(2) Uani 1 1 d . . . . .

O004 O 0.88651(18) 0.81142(13) 0.46910(10) 0.0195(2) Uani 1 1 d . . . . .

N005 N 0.45804(17) 0.91948(14) 0.84805(11) 0.0118(2) Uani 1 1 d . . . . .

C006 C 0.66795(18) 0.70685(15) 0.90638(12) 0.0109(2) Uani 1 1 d . . . . .

C007 C 0.90141(19) 0.74462(15) 0.57311(13) 0.0123(2) Uani 1 1 d . . . . .

C008 C 0.61017(18) 0.81631(15) 0.79670(12) 0.0102(2) Uani 1 1 d . . . . .

C009 C 0.9485(2) 0.82369(17) 0.69938(13) 0.0139(2) Uani 1 1 d . . . . .

C00A C 0.7777(2) 0.91543(16) 0.75094(13) 0.0131(2) Uani 1 1 d . . . . .

H1 H 0.513(4) 0.987(3) 0.906(2) 0.030(6) Uiso 1 1 d . . . . .

H2 H 0.364(3) 0.861(2) 0.8862(18) 0.015(4) Uiso 1 1 d . . . . .

H3 H 0.405(3) 0.975(3) 0.778(2) 0.028(6) Uiso 1 1 d . . . . .

H4 H 0.555(3) 0.763(2) 0.7248(19) 0.013(5) Uiso 1 1 d . . . . .

H5 H 0.846(4) 0.546(3) 0.510(2) 0.037(6) Uiso 1 1 d . . . . .

H6 H 0.819(3) 0.975(2) 0.8222(19) 0.018(5) Uiso 1 1 d . . . . .

H7 H 0.734(3) 0.987(2) 0.681(2) 0.020(5) Uiso 1 1 d . . . . .

H8 H 0.989(3) 0.753(2) 0.764(2) 0.023(5) Uiso 1 1 d . . . . .

H9 H 1.053(3) 0.892(2) 0.679(2) 0.025(5) Uiso 1 1 d . . . . .

K.2 β-GLU Experimental CIF

data_BetaGLU

_audit_creation_method   SHELXL-2013
_chemical_name_systematic
;
 ?
;
_chemical_name_common   ?
_chemical_melting_point   ?
_chemical_formula_moiety   ?
_chemical_formula_sum
 'C5 H9 N O4'
_chemical_formula_weight   147.13

loop_
 _atom_type_symbol
 _atom_type_description
 _atom_type_scat_dispersion_real
 _atom_type_scat_dispersion_imag
 _atom_type_scat_source
 'C' 'C'   0.0181   0.0091
 'International Tables Vol C Tables 4.2.6.8 and 6.1.1.4'
 'H' 'H'   0.0000   0.0000

'International Tables Vol C Tables 4.2.6.8 and 6.1.1.4'

'N' 'N' 0.0311 0.0180

'International Tables Vol C Tables 4.2.6.8 and 6.1.1.4'

'O' 'O' 0.0492 0.0322

'International Tables Vol C Tables 4.2.6.8 and 6.1.1.4'

_space_group_crystal_system   orthorhombic

_space_group_IT_number   19

_space_group_name_H-M_alt   'P 21 21 21'

_space_group_name_Hall   'P 2ac 2ab'

_shelx_space_group_comment

;

The symmetry employed for this shelxl refinement is uniquely defined

by the following loop, which should always be used as a source of

symmetry information in preference to the above space-group names.

They are only intended as comments.

;

loop_

 _space_group_symop_operation_xyz

'x, y, z'

'x+1/2, -y+1/2, -z'

'-x, y+1/2, -z+1/2'

'-x+1/2, -y, z+1/2'

_cell_length_a   5.1392(3)

_cell_length_b   6.8794(4)

_cell_length_c   17.2457(11)

_cell_angle_alpha   90

_cell_angle_beta   90

_cell_angle_gamma   90

_cell_volume   609.72(6)

_cell_formula_units_Z   4

_cell_measurement_temperature   438(2)

_cell_measurement_reflns_used   ?

_cell_measurement_theta_min   ?

_cell_measurement_theta_max   ?

_exptl_crystal_description   Plates

_exptl_crystal_colour   Colorless

_exptl_crystal_density_meas   ?

_exptl_crystal_density_method   ?

_exptl_crystal_density_diffrn   1.603

_exptl_crystal_F_000   312

_exptl_transmission_factor_min   ?

_exptl_transmission_factor_max   ?

_exptl_crystal_size_max   0.13

_exptl_crystal_size_mid   0.10

_exptl_crystal_size_min   0.05

_exptl_absorpt_coefficient_mu   1.210

_shelx_estimated_absorpt_T_min   ?

_shelx_estimated_absorpt_T_max   ?

_exptl_absorpt_correction_type   multi-scan

_exptl_absorpt_process_details   'SADABS V2012/1 (Bruker AXS Inc.)'

_diffrn_ambient_temperature   90(2)

_diffrn_radiation_wavelength   0.71073

_diffrn_radiation_type   MoK\a

_diffrn_radiation_source   'fine-focus sealed tube'

_diffrn_radiation_monochromator   graphite

_diffrn_measurement_device_type   'Bruker APEX-II CCD'

_diffrn_measurement_method   '\f and \w scans'

_exptl_special_details
;
 ?
;

_diffrn_ambient_temperature   438(2)

_diffrn_radiation_wavelength   1.54178

_diffrn_radiation_type   CuK\a

_diffrn_source   ?

_diffrn_measurement_device_type   ?

_diffrn_measurement_method   ?

_diffrn_detector_area_resol_mean ?

_diffrn_reflns_number   6775

_diffrn_reflns_av_unetI/netI   0.0113

_diffrn_reflns_av_R_equivalents 0.0167

_diffrn_reflns_limit_h_min   -6

_diffrn_reflns_limit_h_max   5

_diffrn_reflns_limit_k_min   -8

_diffrn_reflns_limit_k_max   8

_diffrn_reflns_limit_l_min   -20

_diffrn_reflns_limit_l_max   20

_diffrn_reflns_theta_min   5.129

_diffrn_reflns_theta_max   69.595

_diffrn_reflns_theta_full   67.679

_diffrn_measured_fraction_theta_max   0.954

_diffrn_measured_fraction_theta_full 0.982

_diffrn_reflns_Laue_measured_fraction_max   0.954

_diffrn_reflns_Laue_measured_fraction_full 0.982

_diffrn_reflns_point_group_measured_fraction_max   0.942

_diffrn_reflns_point_group_measured_fraction_full 0.977

_reflns_number_total   1089

_reflns_number_gt   1088

_reflns_threshold_expression   'I > 2\s(I)'

_reflns_Friedel_coverage   0.606

_reflns_Friedel_fraction_max   0.924

_reflns_Friedel_fraction_full   0.969

_reflns_special_details

;

Reflections were merged by SHELXL according to the crystal

class for the calculation of statistics and refinement.

_reflns_Friedel_fraction is defined as the number of unique

Friedel pairs measured divided by the number that would be

possible theoretically, ignoring centric projections and

systematic absences.

;

_computing_data_collection   'Bruker APEX2 (Bruker, 2011)'

_computing_cell_refinement   'SAINT V8.30C (Bruker AXS Inc., 2013)'

_computing_data_reduction   'SAINT V8.30C (Bruker AXS Inc., 2013)'

_computing_structure_solution   'SHELXL-2013 (Sheldrick, 2013)'

_computing_structure_refinement   'SHELXL-2013 (Sheldrick, 2013)'

_computing_molecular_graphics   'CrystalMaker (Palmer, 2010)'

_computing_publication_material   'Bruker SHELXTL (Bruker, 2011)'

_refine_special_details

;

 ?

;

_refine_ls_structure_factor_coef Fsqd

_refine_ls_matrix_type   full

_refine_ls_weighting_scheme   calc

_refine_ls_weighting_details

'w=1/[\s^2^(Fo^2^)+(0.0272P)^2^+0.1639P] where P=(Fo^2^+2Fc^2^)/3'

_atom_sites_solution_primary   ?

_atom_sites_solution_secondary   ?

_atom_sites_solution_hydrogens   mixed

_refine_ls_hydrogen_treatment   mixed

_refine_ls_extinction_method   none

_refine_ls_extinction_coef   .

_refine_ls_abs_structure_details

;

 Flack x determined using 411 quotients [(I+)-(I-)]/[(I+)+(I-)]

 (Parsons and Flack (2004), Acta Cryst. A60, s61).

;

_refine_ls_abs_structure_Flack   0.07(3)

_chemical_absolute_configuration ?

_refine_ls_number_reflns   1089

_refine_ls_number_parameters   95

_refine_ls_number_restraints   0

_refine_ls_R_factor_all   0.0205

_refine_ls_R_factor_gt   0.0204

_refine_ls_wR_factor_ref   0.0558

_refine_ls_wR_factor_gt   0.0558

_refine_ls_goodness_of_fit_ref   1.176

_refine_ls_restrained_S_all   1.176

_refine_ls_shift/su_max   0.000

_refine_ls_shift/su_mean   0.000

loop_

 _atom_site_label

 _atom_site_type_symbol

 _atom_site_fract_x

 _atom_site_fract_y

 _atom_site_fract_z

 _atom_site_U_iso_or_equiv

 _atom_site_adp_type

 _atom_site_occupancy

 _atom_site_site_symmetry_order

 _atom_site_calc_flag

 _atom_site_refinement_flags_posn

 _atom_site_refinement_flags_adp

 _atom_site_refinement_flags_occupancy

 _atom_site_disorder_assembly

 _atom_site_disorder_group

O1 O 1.0010(2) 0.44619(16) 0.42202(6) 0.0129(3) Uani 1 1 d . . . . .

H2 H 0.913(4) 0.443(3) 0.3803(13) 0.019 Uiso 1 1 d . U . . .

O2 O 0.3312(2) 0.58240(18) 0.73635(6) 0.0123(3) Uani 1 1 d . . . . .

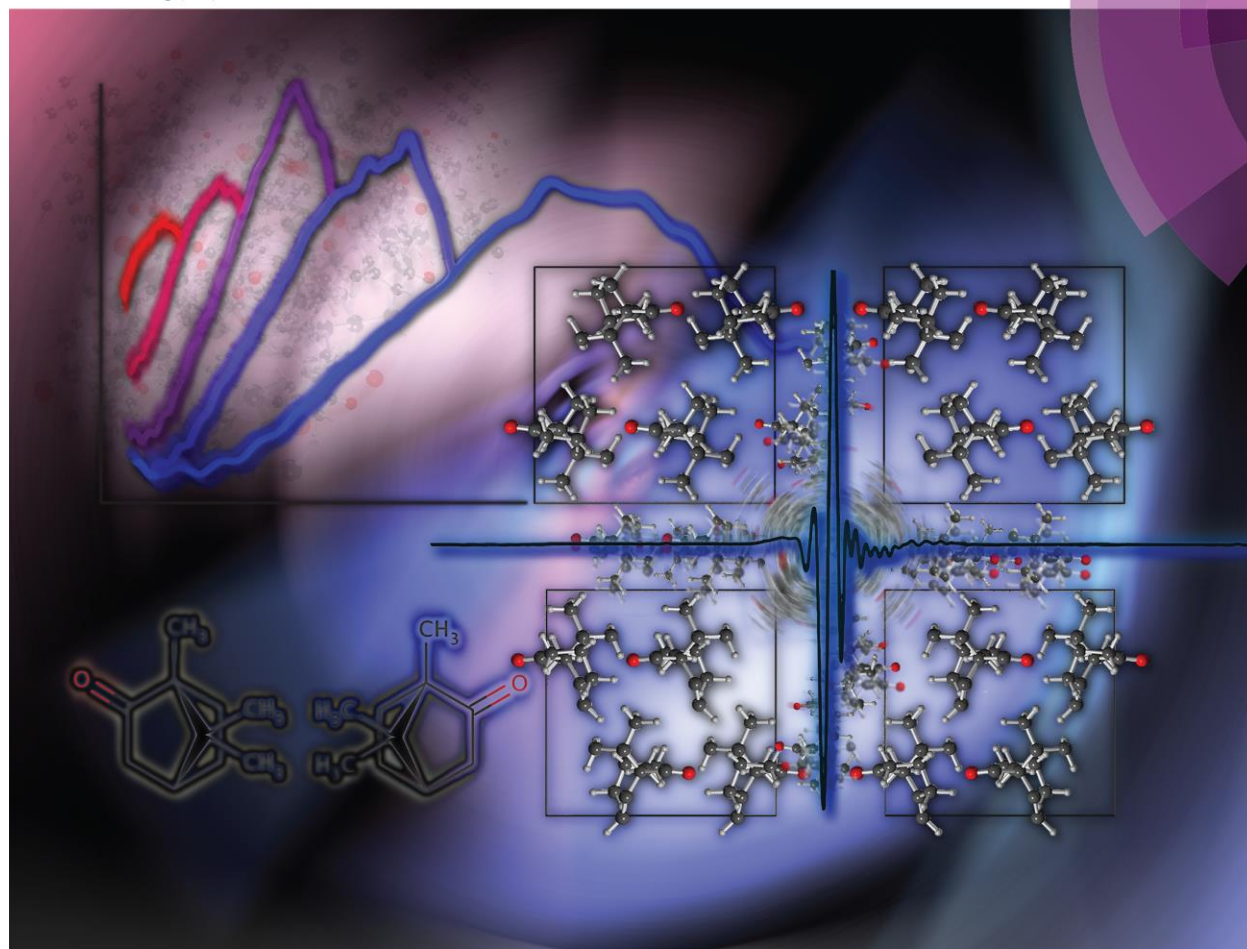O3 O 0.7233(2) 0.59193(17) 0.79314(6) 0.0123(3) Uani 1 1 d . . . . .

O4 O 0.6388(2) 0.56793(17) 0.47588(6) 0.0145(3) Uani 1 1 d . . . . .

N1 N 0.9120(3) 0.7969(2) 0.66832(8) 0.0094(3) Uani 1 1 d . . . . .

H1 H 1.0432 0.7451 0.6949 0.014 Uiso 1 1 calc R U . . .

H3 H 0.8479 0.8979 0.6943 0.014 Uiso 1 1 calc R U . . .

H4 H 0.9689 0.8365 0.6222 0.014 Uiso 1 1 calc R U . . .

C1 C 0.7035(3) 0.6479(2) 0.65743(9) 0.0089(3) Uani 1 1 d . . . . .

H9 H 0.5741 0.6957 0.6203 0.011 Uiso 1 1 calc R U . . .

C2 C 0.8167(3) 0.4551(2) 0.62887(8) 0.0112(3) Uani 1 1 d . . . . .

H6 H 0.6728 0.3683 0.6177 0.013 Uiso 1 1 calc R U . . .

H5 H 0.9150 0.3979 0.6711 0.013 Uiso 1 1 calc R U . . .

C3 C 0.9926(3) 0.4616(2) 0.55744(9) 0.0123(4) Uani 1 1 d . . . . .

H7 H 1.1217 0.5626 0.5651 0.015 Uiso 1 1 calc R U . . .

H8 H 1.0844 0.3388 0.5537 0.015 Uiso 1 1 calc R U . . .

C4 C 0.8565(3) 0.4986(2) 0.48138(9) 0.0105(3) Uani 1 1 d . . . . .

C5 C 0.5723(3) 0.6072(2) 0.73572(9) 0.0090(3) Uani 1 1 d . . . . .

APPENDIX L: Featured Cover of *Physical Chemistry Chemical Physics,* vol. 17, issue 10, 2015.

APPENDIX M: Featured Cover of *Chemical Communications,* vol. 51, issue 89, 2015.

ChemComm

Chemical Communications

www.rsc.org/chemcomm

ROYAL SOCIETY
OF CHEMISTRY
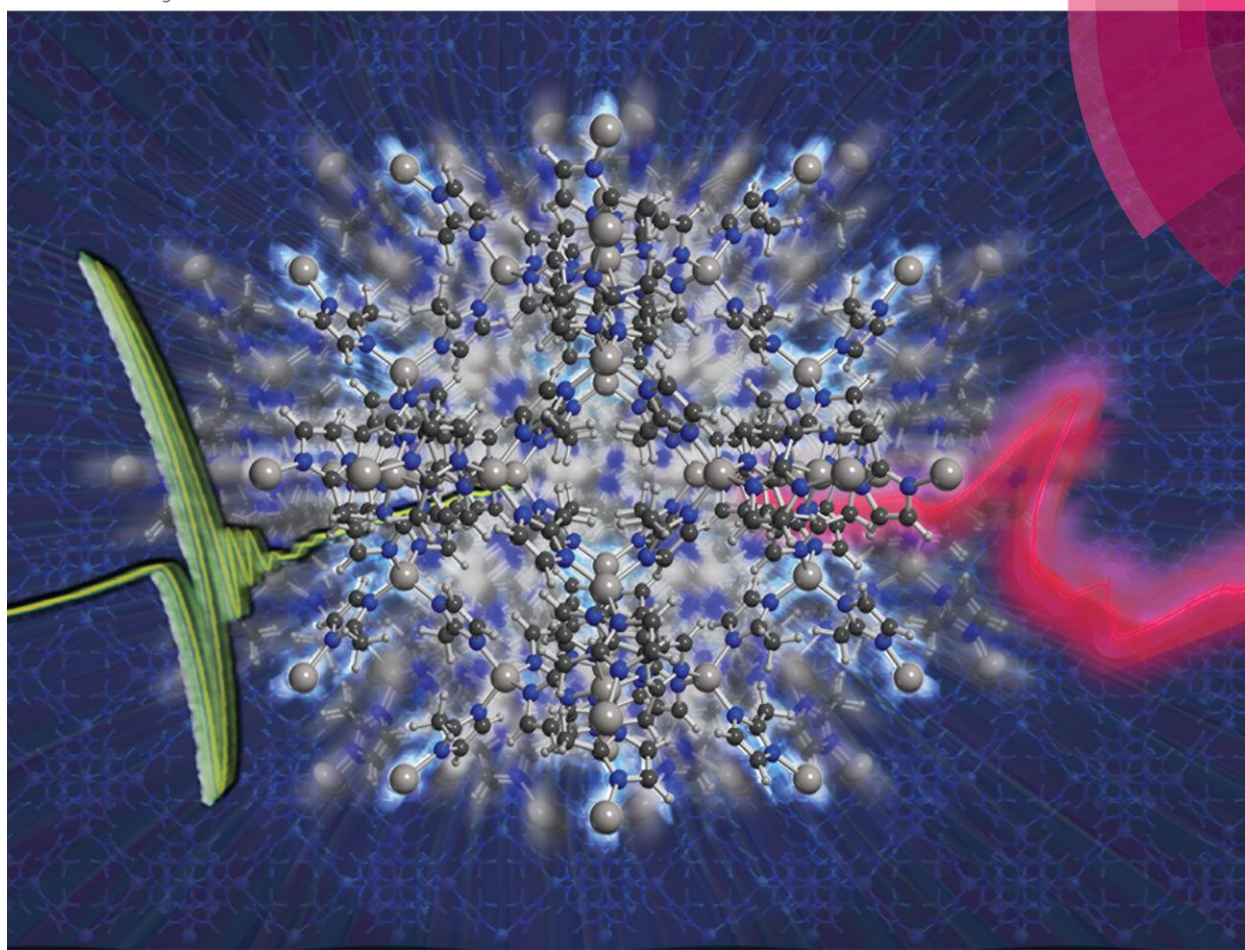
COMMUNICATION
J. Axel Zeitler *et al.*
Investigation of the terahertz vibrational modes of ZIF-8 and ZIF-90 with
terahertz time-domain spectroscopy

Michael Thomas Ruggiero

Department of Chemistry, Syracuse University, Syracuse, NY 13244-4100

Phone: +1 (516) 417-4218 Email: mtruggie@syr.edu

Education

Doctor of Philosophy in Physical Chemistry February 2016
Syracuse University – Syracuse NY

Master of Philosophy in Physical Chemistry August 2014
Syracuse University – Syracuse, NY

Bachelor of Science in Chemistry (Mathematics Minor) May 2012
State University of New York, College at Geneseo – Geneseo, NY

Research Experience

Syracuse University, Syracuse, NY
Ph. D. Candidate, Advisor: Prof. Timothy M. Korter

- Combined experimental time-domain terahertz spectroscopy (far infrared) and solid-state density functional theory (DFT) calculations to study the intermolecular and intramolecular interactions in crystalline solids.
- Attention has been paid to biologically-relevant metal-containing organics to better understand the role of metal cations in natural reactions.
- Characterization of metal-containing compounds for the study of historical artwork and documents through investigation of the pigments terahertz vibrational spectra
- Method development for the *ab. initio* CRYSTAL14 code, using the FORTRAN90 and python programming languages.

University of Torino, Turin, Italy
Invited Researcher, Host: Prof. Roberto Orlando

- Development and Implementation of new algorithms for use in the CRYSTAL density functional theory software package.
- Investigation of various theoretical methods to enhance the understanding of intermolecular forces in solid-materials.
- Use of the FORTRAN90 programming language for all implemented algorithms.

SUNY College at Geneseo, Geneseo, NY
Undergraduate Research, Advisor: Prof. Jeffrey J. Peterson

- Studied the optical and electronic properties of semiconducting nanocrystals.
- Experiment design, synthesis, and characterization were all included in responsibilities.
- Lead selenide (PbSe) and cadmium selenide (CdSe) were primarily used.
- Low-temperature fluorescence, UV-visible-near infrared absorbance, and nuclear magnetic resonance were used for nanocrystal characterization.

Teaching Experience

Teaching Assistant, Syracuse University, Syracuse, NY

Physical Chemistry I & II Lecture and Laboratory   Fall 2012-Spring 2014

General Tasks: Assistance in designing and teaching laboratory experiments to advanced undergraduate students. Responsibilities included pre-laboratory instruction, experimental set-up and break-down, post-laboratory assistance (office hours), and grading scientific reports.

Grants/Honors/Awards

Syracuse University Certificate in Teaching College Science	Spring 2013
SUNY Geneseo Deans List	Fall 2011 and Spring 2012

Laboratory Skills

Experimental Techniques

Mid and Far Infrared Spectroscopy (FTIR, ATR, THz), Single-Crystal and Powder X-ray Diffraction, Organic and Inorganic Synthesis, Nuclear Magnetic Resonance, Thermal Gravimetric Analysis, Differential Scanning Calorimetry, Isothermal Titration Calorimetry, Raman Spectroscopy, Raman Microscopy, Mass Spectroscopy, Gas Chromatography, Liquid Chromatography, and High Performance Liquid Chromatography.

Computational Techniques

Extensive experience with the CRYSTAL *ab. initio* software package, and experience with other quantum mechanical programs such as GAUSSIAN, Quantum ESPRESSO, Vienna *Ab. Initio* Software Package (VASP). Fluent in the python and FORTRAN programming languages, with additional experience in Java, C++, MATLAB, and Javascript.

Publications

M. T. Ruggiero, J. Sibik, J. A. Zeitler, T.M. Korter. Exploring the Influence of Cation Identity on the Structures and Terahertz Spectra of Glutamic Acid Salts. *In Preparation.*

M. T. Ruggiero, J. Sibik, J. A. Zeitler, T.M. Korter. Examination of L-Glutamic Acid Polymorphs by Solid-State Density Functional Theory and Terahertz Spectroscopy. *In Preparation.*

M. T. Ruggiero, J. Sibik, R. Orlando, J. A. Zeitler, T.M. Korter. Measuring the Elasticities of Poly-L-Proline Helices with Terahertz Spectroscopy. *In Preparation.*

M. T. Ruggiero, J. Gooch, J. Zubieta, T. M. Korter. Evaluation of Range-Corrected Density Functionals for the Simulation of Pyridinium-Containing Molecular Crystals. *The Journal of Physical Chemistry A. In Press* (2015).

M. T. Ruggiero, T. M. Korter. The Crucial Role of Water in Shaping Low-Barrier Hydrogen Bonds and Implications for Enzymatic Catalysis. *Physical Chemistry Chemical Physics, In Press* (2015).

M. T. Ruggiero, T. M. Korter. Uncovering the Terahertz Spectrum of Copper Sulfate Pentahydrate. *The Journal of Physical Chemistry A*, 120(2), 227-232 (2016).

M. T. Ruggiero, A. Erba, R. Orlando, T. M. Korter. Origins of Contrasting Copper Coordination Geometries in Crystalline Copper Sulfate Pentahydrate. *Physical Chemistry Chemical Physics*, 17 (46), 31023-31029 (2015).

A. Erba, **M. T. Ruggiero,** T. M. Korter, R. Dovesi. Piezo-Optic Tensor of Crystals from Quantum-Mechanical Calculations. *The Journal Chemical Physics*, 143 (14), 144504 (2015).

N. Y. Tan, **M. T. Ruggiero,** C. Orellana-Tavra, T. Tian, A. D. Bond, T. M. Korter, D. Farien-Jimenez, J. A. Zeitler. Investigation of the Terahertz Vibrational Modes of ZIF-8 and ZIF-90 with Terahertz Time-Domain Spectroscopy. *Chemical Communications*, 51 (89), 16037-16040 (2015). (Featured on Journal Front Cover)

M. T. Ruggiero, T. Bardon, M. Strlic, P. F. Taday, T. M. Korter. The Role of Terahertz Polariton Absorption in the Characterization of Crystalline Iron Sulfate Hydrates. *Physical Chemistry Chemical Physics*, 17 (14), 9326-9334 (2015).

D. V. Nickel, **M. T. Ruggiero,** T. M. Korter, D. M. Mittleman. Terahertz Disorder-Localized Rotational Modes and Lattice Vibrational Modes in the Oreintationally Disordered and Ordered Phases of Camphor. *Physical Chemistry Chemical Physics*, 17 (10), 6671-7078 (2015). (Featured on Journal Front Cover)

M. T. Ruggiero, T. Bardon, M. Strlic, P. F. Taday, T. M. Korter. Assignment of the Terahertz Spectra of Crystalline Copper Sulfate Hydrates via Solid-State Density Functional Theory. *The Journal of Physical Chemistry A*, 118 (43), 10101-10108 (2014).

Presentations

M. T Ruggiero, T. M. Korter. Metal-Mediated Proton Transfer in Maleic Acid and Implications for Enzyme Catalysis. 249th ACS National Meeting, Denver, CO, United States. March 22-26, 2015.

I. Corcione, J. J. Peterson, W. C. Stephens, **M. T Ruggiero**. Low Temperature, Size-Selective Fluorescence Spectroscopy of PbSe Quantum Dots. 249th ACS National Meeting, Denver, CO, United States. March 22-26, 2015.

M. T. Ruggiero, T. M. Korter. Assisgnment of the Terahertz Spectra of Crystalline Copper Sulfate and Its Hydrates via Solid State Density Functional Theory. MSSC2014 − *Ab Initio* Modelling in Solid State Chemistry, Imperial College, London, United Kingdom. September 15-19, 2014.

M. T. Ruggiero, T. M. Korter. Terahertz Spectroscopy for Characterizing Copper Sulfate in Historical Inks. Quantum ESPRESSO Workshop, Pennsylvania State University, State College, PA, USA. June 16-20, 2014.

M. T Ruggiero, T. M. Korter. Substituent Effects on Pyridinium Ring Stacking Interactions in the Solid State. 246th ACS National Meeting, Indianapolis, IN, United States. September 8-12, 2013.

M. T. Ruggiero, T. M. Korter. Substituent Effects on Pyridinium Ring Stacking Interactions in the Solid State. MSSC2013, Turin, Italy. September 1-5, 2013.

W. C. Stephens, **M. T. Ruggiero,** M. S. Azzaro, J. J. Peterson. Low Temperature Photoluminescence Excitation Spectroscopy of PbSe Quantum Dots. 245th ACS National Meeting, New Orleans, LA, United States. April 7-11, 2013.